

Pertanika Journal of

**SCIENCE &  
TECHNOLOGY**

**JST**

**VOL. 25 (S) JAN. 2017**

*A special issue devoted to*  
**Contemporary Issues Towards Smart Sustainable Engineering Solution**

Guest Editors

**Siti Anom Ahmad, Ribhan Zafira Abdul Rahman, Wan Zuha Wan Hasan,  
Mohd Amran Mohd Radzi, Suhaidi Shafie, Noor Izzri Abdul Wahab & Nashiren Farzilah Mailah**



**PERTANIKA**  
JOURNALS

**A scientific journal published by Universiti Putra Malaysia Press**

## *Journal of Science & Technology*

### About the Journal

#### Overview

Pertanika Journal of Science & Technology (JST) is the official journal of Universiti Putra Malaysia published by UPM Press. It is an open-access online scientific journal which is free of charge. It publishes the scientific outputs. It neither accepts nor commissions third party content.

Recognized internationally as the leading peer-reviewed interdisciplinary journal devoted to the publication of original papers, it serves as a forum for practical approaches to improving quality in issues pertaining to science and engineering and its related fields.

JST is a **quarterly** (January, April, July and October) periodical that considers for publication original articles as per its scope. The journal publishes in **English** and it is open to authors around the world regardless of the nationality.

The Journal is available world-wide.

#### Aims and scope

Pertanika Journal of Science and Technology aims to provide a forum for high quality research related to science and engineering research. Areas relevant to the scope of the journal include: bioinformatics, bioscience, biotechnology and bio-molecular sciences, chemistry, computer science, ecology, engineering, engineering design, environmental control and management, mathematics and statistics, medicine and health sciences, nanotechnology, physics, safety and emergency management, and related fields of study.

#### History

Pertanika was founded in 1978. A decision was made in 1992 to streamline Pertanika into three journals as Journal of Tropical Agricultural Science, Journal of Science & Technology, and Journal of Social Sciences & Humanities to meet the need for specialised journals in areas of study aligned with the interdisciplinary strengths of the university.

After almost 25 years, as an interdisciplinary Journal of Science & Technology, the revamped journal now focuses on research in science and engineering and its related fields.

#### Goal of *Pertanika*

Our goal is to bring the highest quality research to the widest possible audience.

#### Quality

We aim for excellence, sustained by a responsible and professional approach to journal publishing. Submissions are guaranteed to receive a decision within 14 weeks. The elapsed time from submission to publication for the articles averages 5-6 months.

#### Abstracting and indexing of *Pertanika*

Pertanika is almost 40 years old; this accumulated knowledge has resulted in Pertanika JST being abstracted and indexed in SCOPUS (Elsevier), Thomson (ISI) Web of Knowledge [BIOSIS & CAB Abstracts], EBSCO & EBSCOhost, DOAJ, ERA, Cabell's Directories, Google Scholar, MyAIS, ISC & Rubriq (Journal Guide).



### Future vision

We are continuously improving access to our journal archives, content, and research services. We have the drive to realise exciting new horizons that will benefit not only the academic community, but society itself.

### Citing journal articles

The abbreviation for Pertanika Journal of Science & Technology is *Pertanika J. Sci. Technol.*

### Publication policy

Pertanika policy prohibits an author from submitting the same manuscript for concurrent consideration by two or more publications. It prohibits as well publication of any manuscript that has already been published either in whole or substantial part elsewhere. It also does not permit publication of manuscript that has been published in full in Proceedings.

### Code of Ethics

The Pertanika Journals and Universiti Putra Malaysia takes seriously the responsibility of all of its journal publications to reflect the highest in publication ethics. Thus all journals and journal editors are expected to abide by the Journal's codes of ethics. Refer to Pertanika's **Code of Ethics** for full details, or visit the Journal's web link at [http://www.pertanika.upm.edu.my/code\\_of\\_ethics.php](http://www.pertanika.upm.edu.my/code_of_ethics.php)

### International Standard Serial Number (ISSN)

An ISSN is an 8-digit code used to identify periodicals such as journals of all kinds and on all media—print and electronic. All Pertanika journals have ISSN as well as an e-ISSN.

Journal of Science & Technology: ISSN 0128-7680 (*Print*); ISSN 2231-8526 (*Online*).

### Lag time

A decision on acceptance or rejection of a manuscript is reached in 3 to 4 months (average 14 weeks). The elapsed time from submission to publication for the articles averages 5-6 months.

### Authorship

Authors are not permitted to add or remove any names from the authorship provided at the time of initial submission without the consent of the Journal's Chief Executive Editor.

### Manuscript preparation

Refer to Pertanika's **INSTRUCTIONS TO AUTHORS** at the back of this journal.

Most scientific papers are prepared according to a format called IMRAD. The term represents the first letters of the words **I**ntroduction, **M**aterials and **M**ethods, **R**esults, **A**nd, **D**iscussion. IMRAD is simply a more 'defined' version of the "IBC" [Introduction, Body, Conclusion] format used for all academic writing. IMRAD indicates a pattern or format rather than a complete list of headings or components of research papers; the missing parts of a paper are: *Title, Authors, Keywords, Abstract, Conclusions, and References*. Additionally, some papers include Acknowledgments and Appendices.

The *Introduction* explains the scope and objective of the study in the light of current knowledge on the subject; the *Materials and Methods* describes how the study was conducted; the *Results* section reports what was found in the study; and the *Discussion* section explains meaning and significance of the results and provides suggestions for future directions of research. The manuscript must be prepared according to the Journal's **INSTRUCTIONS TO AUTHORS**.

### Editorial process

Authors are notified with an acknowledgement containing a *Manuscript ID* on receipt of a manuscript, and upon the editorial decision regarding publication.

Pertanika follows a **double-blind peer-review** process. Manuscripts deemed suitable for publication are usually sent to reviewers. Authors are encouraged to suggest names of at least three potential reviewers at the time of submission of their manuscript to Pertanika, but the editors will make the final choice. The editors are not, however, bound by these suggestions.

Notification of the editorial decision is usually provided within ten to fourteen weeks from the receipt of manuscript. Publication of solicited manuscripts is not guaranteed. In most cases, manuscripts are accepted conditionally, pending an author's revision of the material.

As articles are double-blind reviewed, material that might identify authorship of the paper should be placed only on page 2 as described in the first-4 page format in Pertanika's **INSTRUCTIONS TO AUTHORS** given at the back of this journal.

### **The Journal's peer-review**

In the peer-review process, three referees independently evaluate the scientific quality of the submitted manuscripts.

Peer reviewers are experts chosen by journal editors to provide written assessment of the **strengths** and **weaknesses** of written research, with the aim of improving the reporting of research and identifying the most appropriate and highest quality material for the journal.

### **Operating and review process**

What happens to a manuscript once it is submitted to *Pertanika*? Typically, there are seven steps to the editorial review process:

1. The Journal's chief executive editor and the editorial board examine the paper to determine whether it is appropriate for the journal and should be reviewed. If not appropriate, the manuscript is rejected outright and the author is informed.
2. The chief executive editor sends the article-identifying information having been removed, to three reviewers. Typically, one of these is from the Journal's editorial board. Others are specialists in the subject matter represented by the article. The chief executive editor asks them to complete the review in three weeks.

Comments to authors are about the appropriateness and adequacy of the theoretical or conceptual framework, literature review, method, results and discussion, and conclusions. Reviewers often include suggestions for strengthening of the manuscript. Comments to the editor are in the nature of the significance of the work and its potential contribution to the literature.

3. The chief executive editor, in consultation with the editor-in-chief, examines the reviews and decides whether to reject the manuscript, invite the author(s) to revise and resubmit the manuscript, or seek additional reviews. Final acceptance or rejection rests with the Editor-in-Chief, who reserves the right to refuse any material for publication. In rare instances, the manuscript is accepted with almost no revision. Almost without exception, reviewers' comments (to the author) are forwarded to the author. If a revision is indicated, the editor provides guidelines for attending to the reviewers' suggestions and perhaps additional advice about revising the manuscript.
4. The authors decide whether and how to address the reviewers' comments and criticisms and the editor's concerns. The authors return a revised version of the paper to the chief executive editor along with specific information describing how they have answered the concerns of the reviewers and the editor, usually in a tabular form. The author(s) may also submit a rebuttal if there is a need especially when the author disagrees with certain comments provided by reviewer(s).

5. The chief executive editor sends the revised paper out for re-review. Typically, at least one of the original reviewers will be asked to examine the article.
6. When the reviewers have completed their work, the chief executive editor in consultation with the editorial board and the editor-in-chief examine their comments and decide whether the paper is ready to be published, needs another round of revisions, or should be rejected.
7. If the decision is to accept, an acceptance letter is sent to all the author(s), the paper is sent to the Press. The article should appear in print in approximately three months.

The Publisher ensures that the paper adheres to the correct style (in-text citations, the reference list, and tables are typical areas of concern, clarity, and grammar). The authors are asked to respond to any minor queries by the Publisher. Following these corrections, page proofs are mailed to the corresponding authors for their final approval. At this point, **only essential changes are accepted**. Finally, the article appears in the pages of the Journal and is posted on-line.



Pertanika Journal of

# **SCIENCE & TECHNOLOGY**

*A special issue devoted to*  
Contemporary Issues Towards Smart Sustainable Engineering Solution

**Vol. 25 (S) Jan. 2017**  
(Special Edition)

Guest Editors

Siti Anom Ahmad, Ribhan Zafira Abdul Rahman, Wan Zuha Wan Hasan,  
Mohd Amran Mohd Radzi, Suhaidi Shafie, Noor Izzri Abdul Wahab & Nashiren Farzilah Mailah

A scientific journal published by Universiti Putra Malaysia Press



## EDITOR-IN-CHIEF

**Mohd Adzir Mahdi**

*Physics, Optical Communications*

## CHIEF EXECUTIVE EDITOR

**Nayan Deep S. Kanwal**

*Environmental Issues – Landscape Plant Modelling Applications*

## UNIVERSITY PUBLICATIONS COMMITTEE

**Mohd Azmi Mohd Lila, Chair**

## EDITORIAL STAFF

### Journal Officers:

Kanagamalar Silvarajoo, *ScholarOne*

Lim Ee Leen, *ScholarOne*

### Editorial Assistants:

Zulinaardawati Kamarudin

Florence Jiyom

## COPY EDITORS

Doreen Dillah

Crescentia Morais

Pooja Terasha Stanslas

## PRODUCTION STAFF

### Pre-press Officer:

Kanagamalar Silvarajoo

### Layout & Typeset:

Lilian Loh Kian Lin

## WEBMASTER

Mohd Nazri Othman

## PUBLICITY & PRESS RELEASE

Magdalene Pokar (*ResearchSEA*)

Florence Jiyom

## EDITORIAL OFFICE

### JOURNAL DIVISION

Office of the Deputy Vice Chancellor (R&I)

1<sup>st</sup> Floor, IDEA Tower II

UPM-MTDC Technology Centre

Universiti Putra Malaysia

43400 Serdang, Selangor Malaysia.

Gen Enq.: +603 8947 1622 | 1619 | 1616

E-mail: [executive\\_editor.pertanika@upm.my](mailto:executive_editor.pertanika@upm.my)

URL: <http://journals-id.upm.edu.my>

## PUBLISHER

**Kamariah Mohd Saidin**

UPM Press

Universiti Putra Malaysia

43400 UPM, Serdang, Selangor, Malaysia.

Tel: +603 8946 8855, 8946 8854

Fax: +603 8941 6172

E-mail: [penerbit@putra.upm.edu.my](mailto:penerbit@putra.upm.edu.my)

URL: <http://penerbit.upm.edu.my>

## EDITORIAL BOARD

2015-2017

**Abdul Halim Shaari**

*Superconductivity and Magnetism, Universiti Putra Malaysia, Malaysia.*

**Adem Kilicman**

*Mathematical Sciences, Universiti Putra Malaysia, Malaysia.*

**Ahmad Makmom Abdullah**

*Ecophysiology and Air Pollution Modelling, Universiti Putra Malaysia, Malaysia.*

**Ali A. Moosavi-Movahedi**

*Biophysical Chemistry, University of Tehran, Tehran, Iran.*

**Amu Therwath**

*Oncology, Molecular Biology, Université Paris, France.*

**Angelina Chin**

*Mathematics, Group Theory and Generalisations, Ring Theory, University of Malaya, Malaysia.*

**Bassim H. Hameed**

*Chemical Engineering: Reaction Engineering, Environmental Catalysis & Adsorption, Universiti Sains Malaysia, Malaysia.*

**Biswa Mohan Biswal**

*Medical, Clinical Oncology, Radiotherapy, Universiti Sains Malaysia, Malaysia.*

**Christopher G. Jesudason**

*Mathematical Chemistry, Molecular Dynamics Simulations, Thermodynamics and General Physical Theory, University of Malaya, Malaysia.*

**Hari M. Srivastava**

*Mathematics and Statistics, University of Victoria, Canada.*

**Ivan D. Rukhlenko**

*Nonlinear Optics, Silicon Photonics, Plasmonics and Nanotechnology, Monash University, Australia.*

**Kaniraj R. Shenbaga**

*Geotechnical Engineering, Universiti Malaysia Sarawak, Malaysia.*

**Kanury Rao**

*Senior Scientist & Head, Immunology Group, International Center for Genetic Engineering and Biotechnology, Immunology, Infectious Disease Biology and System Biology, International Centre for Genetic Engineering & Biotechnology, New Delhi, India.*

**Karen Ann Crouse**

*Chemistry, Material Chemistry, Metal Complexes – Synthesis, Reactivity, Bioactivity, Universiti Putra Malaysia, Malaysia.*

**Ki-Hyung Kim**

*Computer and Wireless Sensor Networks, AIOU University, Korea.*

**Kunnawee Kanitpong**

*Transportation Engineering-Road Traffic Safety, Highway Materials and Construction, Asian Institute of Technology, Thailand.*

**Megat Mohd Hamdan**

**Megat Ahmad**

*Mechanical and Manufacturing Engineering, Universiti Pertahanan Nasional Malaysia, Malaysia.*

**Miralini Kandiah**

*Public Health Nutrition, Nutritional Epidemiology, UCSI University, Malaysia.*

**Mohamed Othman**

*Communication Technology and Network, Scientific Computing, Universiti Putra Malaysia, Malaysia.*

**Mohd. Ali Hassan**

*Bioprocess Engineering, Environmental Biotechnology, Universiti Putra Malaysia, Malaysia.*

**Mohd Sapuan Salit**

*Concurrent Engineering and Composite Materials, Universiti Putra Malaysia, Malaysia.*

**Narongrit Sombatsompop**

*Engineering & Technology: Materials and Polymer Research, King Mongkut's University of Technology Thonburi (KMUTT), Thailand.*

**Prakash C. Sinha**

*Physical Oceanography, Mathematical Modelling, Fluid Mechanics, Numerical Techniques, Universiti Malaysia Terengganu, Malaysia.*

**Rajinder Singh**

*Biotechnology, Biomolecular Sciences, Molecular Markers/ Genetic Mapping, Malaysia Palm Oil Board, Kajang, Malaysia.*

**Renuganth Varatharajoo**

*Engineering, Space System, Universiti Putra Malaysia, Malaysia.*

**Riyanto T. Bambang**

*Electrical Engineering, Control, Intelligent Systems & Robotics, Bandung Institute of Technology, Indonesia.*

**Sabira Khatun**

*Engineering, Computer Systems & Software Engineering, Applied Mathematics, Universiti Malaysia Pahang, Malaysia.*

**Shiv Dutt Gupta**

*Director, IHMR, Health Management, Public Health, Epidemiology, Chronic and Non-communicable Diseases, Indian Institute of Health Management Research, India.*

**Suan-Choo Cheah**

*Biotechnology, Plant Molecular Biology, Asiatic Centre for Genome Technology (ACGT), Kuala Lumpur, Malaysia.*

**Wagar Asrar**

*Engineering, Computational Fluid Dynamics, Experimental Aerodynamics, International Islamic University, Malaysia.*

**Wing Keong Ng**

*Aquaculture, Aquatic Animal Nutrition, Aqua Feed Technology, Universiti Sains Malaysia, Malaysia.*

**Yudi Samyudia**

*Chemical Engineering, Advanced Process Engineering, Curtin University of Technology, Malaysia.*

## INTERNATIONAL ADVISORY BOARD

2017-2019

**Adarsh Sandhu**

*Editorial Consultant for Nature Nanotechnology and Contributing Writer for Nature Photonics, Physics, Magneto-resistive Semiconducting Magnetic Field Sensors, Nano-Bio-Magnetism, Magnetic Particle Colloids, Point of Care Diagnostics, Medical Physics, Scanning Hall Probe Microscopy, Synthesis and Application of Graphene, Electronics-inspired Interdisciplinary Research Institute (EIIRIS), Toyohashi University of Technology, Japan.*

**Graham Megson**

*Computer Science, The University of Westminster, U.K.*

**Kuan-Chong Ting**

*Agricultural and Biological Engineering, University of Illinois at Urbana-Champaign, USA.*

**Malin Premaratne**

*Advanced Computing and Simulation, Monash University, Australia.*

**Mohammed Ismail Elnaggar**

*Electrical Engineering, Ohio State University, USA.*

**Peter G. Alderson**

*Bioscience, The University of Nottingham, Malaysia Campus.*

**Peter J. Heggs**

*Chemical Engineering, University of Leeds, U.K.*

**Ravi Prakash**

*Vice Chancellor, JUIT, Mechanical Engineering, Machine Design, Biomedical and Materials Science, Jaypee University of Information Technology, India.*

**Said S.E.H. Elnashaie**

*Environmental and Sustainable Engineering, Penn. State University at Harrisburg, USA.*

**Suhash Chandra Dutta Roy**

*Electrical Engineering, Indian Institute of Technology (IIT) Delhi, India.*

**Vijay Arora**

*Quantum and Nano-Engineering Processes, Wilkes University, USA.*

**Yi Li**

*Chemistry, Photochemical Studies, Organic Compounds, Chemical Engineering, Chinese Academy of Sciences, Beijing, China.*

## ABSTRACTING/INDEXING

*Pertanika* is now over 35 years old; this accumulated knowledge has resulted the journals being indexed in SCOPUS (Elsevier), Thomson (ISI) Web of Knowledge [BIOSIS & CAB Abstracts], EBSCO, DOAJ, Google Scholar, AGRICOLA, ISC, Citefactor, Rubriq and MyAIS. JST is also indexed in ERA.



The publisher of *Pertanika* will not be responsible for the statements made by the authors in any articles published in the journal. Under no circumstances will the publisher of this publication be liable for any loss or damage caused by your reliance on the advice, opinion or information obtained either explicitly or implied through the contents of this publication.

All rights of reproduction are reserved in respect of all papers, articles, illustrations, etc., published in *Pertanika*. *Pertanika* provides free access to the full text of research articles for anyone, web-wide. It does not charge either its authors or author-institution for refereeing/publishing outgoing articles or user-institution for accessing incoming articles.

No material published in *Pertanika* may be reproduced or stored on microfilm or in electronic, optical or magnetic form without the written authorization of the Publisher.

Copyright © 2017 Universiti Putra Malaysia Press. All Rights Reserved.





## Preface

We are pleased to present this special issue of the Pertanika Journal of Science and Technology (JST). This issue is a compilation of 38 out of 73 selected papers that were presented at the 2016 International Conference on Electrical and Electronic Technology (ICEETech2016), held at Universiti Putra Malaysia from 22<sup>nd</sup> to 26<sup>th</sup> August 2016. The remaining 35 papers will be published in the subsequent issue. These papers were subjected to the usual stringent peer reviewing process before publication. ICEETech2016 was organised by Universiti Putra Malaysia, Kyushu Institute of Technology, Japan and Prince of Songkla University, Thailand.

Themed '*Inculcating Great Minds towards Smart Sustainable Engineering Solution*', the ICEETech2016 topics include but not limited to: Power System and Protection, Renewable & Sustainable Energy, High Voltage, Dielectric Insulation, Machine, Power Electronics, Energy Efficient Transportation Engineering, Robotic Automation, Control System and Signal Processing, Biomedical Engineering, Intelligent System, Sensor Technology, System-on-Chip, MEMS and NEMS, IC Packaging and Test and Nanoelectronics.

We would like to thank all the contributors as well as the reviewers who have made this JST ICEETech2016 a successful endeavour. It is hoped that this publication would encourage researchers around the world to be more active in publishing their research papers.

We record our deepest appreciation to Dr. Nayan Kanwal of the Journal Division and his editorial team at Pertanika, Universiti Putra Malaysia. Their assistance was invaluable in realising the publication of this Pertanika Special Issue.

### **Guest Editors:**

Siti Anom Ahmad (*Assoc. Prof. Dr.*)  
Ribhan Zafira Abdul Rahman (*Dr.*)  
Wan Zuha Wan Hasan (*Assoc. Prof. Dr.*)  
Mohd Amran Mohd Radzi (*Assoc. Prof. Dr.*)  
Suhaidi Shafie (*Assoc. Prof. Dr.*)  
Noor Izzri Abdul Wahab (*Assoc. Prof. Dr.*)  
Nashiren Farzilah Mailah (*Dr.*)

**January 2017**



**Pertanika Journal of Science & Technology**  
**Vol. 25 (S) Jan. 2017**

**Contents**

<b>Contemporary Issues Towards Smart Sustainable Engineering Solution</b>	
Impact of Different Lifting Height and Load Mass on Muscle Performance using Periodogram <i>Shair, E. F., Ahmad, S. A., Abdullah, A. R., Marhaban, M. H. and Mohd Tamrin, S. B.</i>	1
A Single-stage LED Driver with Voltage Doubler Rectifier <i>Nurul Asikin, Zawawi, Shahid Iqbal and Mohamad Kamarol, Mohd Jamil</i>	9
An Integrated System Wide Reactive Power Management Strategy for Transmission and Distribution System based on Techno Economic Analysis <i>Jun Huat Tang, Mau Teng Au, Asnawi bin Mohd Busrah, Mohd Hafiz bin Mat Daud, Lau Chee Chong, Khairuddin bin Abdullah</i>	19
Opportunity for Using WLAN with IEC 61850 and the Future of this Protocol <i>N. H. Ali, Borhanuddin. M. Ali, O. Basir, M. L. Othman, F. Hashim and E. Aker</i>	25
Enhancement of DNA Microarray Images using Mathematical Morphological Image Processing <i>Asral Bahari Jambek, Khairul Anuar Mat Said and Nasri Sulaiman</i>	39
Memory Polynomial with Binomial Reduction in Digital Pre-distortion for Wireless Communication Systems <i>Hong Ning Choo, Nurul Adilah Abdul Latiff, Pooria Varahram and Borhanuddin Mohd Ali</i>	49
Performance Comparison of Image Normalisation Method for DNA Microarray Data <i>Omar Salem Baans, Asral Bahari Jambek, Uda Hashim and Nor Azah Yusof</i>	59
Real-time Human Motion Analysis and Grasping Force using the OptiTrack System and Flexi-force Sensor <i>N. F. Elya Saidon, Chikamune Wada, Siti A. Ahmad, Ribhan Zafira Abdul Rahman, Kiyotaka Eguchi, Yoshiyuki Tomiyama and Farida Izni Abd Rahman</i>	69

Control of Wastewater Treatment by using the Integration MATLAB and LabVIEW <i>Ilanur Muhaini Mohd Noor and Muhamad Kamal M. A.</i>	77
LLC Resonant Converter with Series-Connected Primary Windings of Transformer for PEV Battery Charging <i>Shahid Iqbal, M. Imran Shahzad and Soib Taib</i>	85
Partial Measurement of Planar Surface Ion Balance Analysis <i>Sayan Plong-ngooluam, Nattha Jindapetch, Phairote Wounchoum and Duangporn Sompongse</i>	95
Reliably Optimal PMU Placement using Disparity Evolution-based Genetic Algorithm <i>Yoshiaki Matsukawa, Mohammad Lutfi Othman, Masayuki Watanabe and Yasunori Mitani</i>	103
Statistical Optimisation of Process Parameters on the Efficiency of N-TiO <sub>2</sub> Dye Sensitised Solar Cell Using Response Surface Methodology (RSM) <i>Buda Samaila, Suhaidi Shafie, Suraya Abdul Rashid, Haslina Jafaar and Ali Khalifa</i>	111
Classification of Aromatic Herbs using Artificial Intelligent Technique <i>A. Che Soh, U. K. Mohamad Yusof, N. F. M. Radzi, A. J. Ishak and M. K. Hassan</i>	119
A Corrective Action Scheme for Contingency Monitoring of Transmission Line Overloading <i>Mohammad Lutfi Othman, Mahmood Khalid Hadi and Noor Izzri Abdul Wahab</i>	129
Electrical Characteristics of Rubber Wood Ash Filled Natural Rubber at High Frequency <i>Salakjit Nilborworn, Krerkchai Thongnoo and Pornchai Phukpattaranont</i>	139
Unbalanced Self-Sensing Actuation Circuit Effects on Vibration Control in Piezoelectric Systems <i>Kiattisak Sengchuai, Boworn Panyavoravaj and Nattha Jindapetch</i>	149
Parametric Tracking Across Multiple Cameras <i>Patrick Sebastian, Yap Vooi Voon and Richard Comley</i>	159
Optimal Location and Size of Distributed Generation to Reduce Power Losses based on Differential Evolution Technique <i>Noor Izzri Abdul Wahab, Ahmed Sahib Hammadi and Mohammad Lutfi Othman</i>	169

Simulation of Interleaved Current Fed Full Bridge Converter for Fuel Cell Electrical Vehicle <i>Koay Boon Kit, Nasrudin Abd Rahim and Siti Rohani Sheikh Raihan</i>	179
Double Series Resonant DC-DC Converter with Uniform Voltage Stress on High Voltage Transformers <i>Nor Azura, Samsudin, Soib, Taib and Shahid, Iqbal</i>	187
PCA based Feature Extraction for Classification of Stator-Winding Faults in Induction Motors <i>Thanaporn Likitjarernkul, Kiattisak Sengchuai, Rakkrit Duangsoithong, Kusumal Chalermyanont and Anuwat Prasertsit</i>	197
Effect of Boron and Oxygen Doping to Graphene Band Structure <i>Siti Fazlina bt Fauzi and Syarifah Norfaezah bt Sabki</i>	205
Seasonal Variation of Transmission Line Outages in Peninsular Malaysia <i>I. Mohamed Rawi, M.Z.A. Ab-Kadir and M. Izadi</i>	213
FDTD Computational Simulation for SAR Observation towards Breast Hyperthermia Cancer Procedure <i>Kasumawati Lias and Norlida Buniyamin</i>	221
Application of Evolutionary Programming for the Placement of TCSC and UPFC for Minimisation of Transmission Losses and Improvement of Voltage Profile <i>Nur Ashida Salim, Nabila Ismail, Muhammad Murtadha Othman</i>	231
Method of Determining Load Priority using Fuzzy Logic for Adaptive Under Frequency Load Shedding Technique <i>A. I. M. Isa, H. Mohamad, K. Naidu, N. Y. Dahlan and I. Musirin</i>	239
Synchronous Reference Frame Fundamental Method in Shunt Active Power Filter for Mitigation of Current Harmonics <i>S. Musa and M. A. M. Radzi</i>	249
A Study of Negative Bias Temperature Instability (NBTI) in p-MOSFET Devices <i>H. Hussin and M. F. Zainudin</i>	257
Planar Sensors Array for Water Contaminants Detections <i>Aizat Azmi, Sallehuddin Ibrahim, Ahmad Amsyar Azman, and Mohd Amri Md Yunus</i>	267
Optimising PID Controller using Slope Variation Method for Positioning Radio Telescope <i>N. Mohamad Zaber, A. J. Ishak, A. Che Soh, M. K. Hasan and A. N. Ishak</i>	275

Enhanced Time of Use Electricity Pricing for Commercial Customers in Malaysia <i>Nur Azrina Mohd Azman, Md Pauzi Abdullah, Mohammad Yusri Hassan, Dalila Mat Said and Faridah Hussin</i>	285
Evaluation of Inverter Reliability Performance Due to Negative Bias Temperature Instability (NBTI) Effects in Advance CMOS Technology Nodes <i>M. F. Zainudin, H. Hussin and A. K. Halim</i>	295
Compound Learning Control for Formation Management of Multiple Autonomous Agents <i>Syafiq Fauzi Kamarulzaman and Hayyan Al Sibai</i>	305
Binary Classification Using SVM for Sick and Healthy Chicken Based on Chicken's Excrement Image <i>Nurhanna Abdul Aziz and Mohd Fauzi Bin Othman</i>	315
A Single DC Source 41-level 115V, 400Hz Cascaded Multilevel Inverter <i>Ahmad, Syukri Mohamad and Norman, Mariun</i>	325
Dielectrophoresis and AC Electroosmosis Force on Fluid Motion in Microfluidic using Latex Particles <i>Nurul Amziah Md Yunus, Mohd Nazim Mohtar, Khaldon Mohammed Almadhagi and Izhal Abdul Halin</i>	333
Application of Sliding Mode Control with Extended High Gain Observer to Stabilize the Underactuated Quadrotor System <i>Elya M. N, S. B. Mohd Noor, Ribhan Zafira A. R. and Syaril Azrad</i>	343

## Impact of Different Lifting Height and Load Mass on Muscle Performance using Periodogram

Shair, E. F.<sup>1,3\*</sup>, Ahmad, S. A.<sup>1</sup>, Abdullah, A. R.<sup>3</sup>, Marhaban, M. H.<sup>1</sup>  
and Mohd Tamrin, S. B.<sup>2</sup>

<sup>1</sup>Department of Electrical and Electronic Engineering, Faculty of Engineering,  
Universiti Putra Malaysia, 43400 UPM, Serdang, Selangor, Malaysia

<sup>2</sup>Department of Environmental and Occupational Health, Faculty of Medicine and Health Sciences,  
Universiti Putra Malaysia, 43400 UPM, Serdang, Selangor, Malaysia

<sup>3</sup>Faculty of Electrical Engineering, Universiti Teknikal Malaysia Melaka, Malacca, Malaysia

### ABSTRACT

Musculoskeletal disorders (MSDs) caused by muscle fatigue have been a major problem for industry which needs to be resolved to save costs related to human resource development (extra training and compensation). Detailed fatigue monitoring researches aimed at finding the best fatigue indices is not new although studies on the causes of fatigue can be explored further. Identification analysis is required to monitor the factors that influence muscle performance characteristic of surface electromyography (sEMG) signal. Periodogram monitoring technique applies a frequency domain signal and represents the distribution of the signal power over the frequency. It is a technique that allows the tracing of small changes in the behaviour of sEMG signal when external parameters are varied. This technique is used in this paper to monitor the sEMG signal changes in muscle performance when the lifting height and load mass are varied. The periodogram amplitude, which represents the power, increases with the rise in lifting height and load mass. From the frequency representation of the periodogram, the root mean square voltage ( $V_{rms}$ ) is calculated where the muscle performance characteristic could be further identified. The  $V_{rms}$  also shows a similar trend when the lifting height and load mass are varied proving the periodogram technique is useful to monitor changes in the muscle performance during manual lifting.

*Keywords:* Periodogram, electromyography, frequency representation, manual lifting

### ARTICLE INFO

#### Article history:

Received: 24 August 2016

Accepted: 02 December 2016

#### E-mail addresses:

ezreen@utem.edu.my;

gs4417@student.upm.edu.my (Shair, E. F.),

sanom@upm.edu.my (Ahmad, S. A.),

abdulr@utem.edu.my (Abdullah, A. R.),

mhm@upm.edu.my (Marhaban, M. H.),

shamsul\_bahri@upm.edu.my (Mohd Tamrin, S. B)

\*Corresponding Author

### INTRODUCTION

Musculoskeletal disorders (MSDs) due to manual lifting are viewed as one of the main source of occupational injury, influencing the quality of life of industrial laborers worldwide.

Since most of the MSDs are caused by muscle fatigue, studies have concentrated on finding the best fatigue indices (González-Izal et al., 2010). For sometime now, surface electromyography (sEMG) has been perceived as a solid instrument to assess muscle condition in biomechanics applications. The sEMG signal is a measure of the electrical activity in human body produced by skeletal muscles (Merlo & Campanini, 2010). sEMG is commonly utilized in research due to the fact that it is non-invasive and convenient to use (Shair, Zawawi, Abdullah, & Shamsudin, 2015). Since the characteristics of the sEMG signal itself is complicated and non-stationary, accurate analysis and scrutinizing of sEMG signal has been greatly valued.

Generally, there are three types of methods to analyse the sEMG signals: time domain, frequency domain and time-frequency domain. Even though the trend now is to use time-frequency domain the time domain and frequency domain continue to be popular (Tkach, Huang, & Kuiken, 2010). Different techniques have been used to identify the effects of outside factors such as lifting height and load mass in manual lifting on muscle performance. Kamarudin (Kamarudin, Ahmad, Hassan, Yusoff, & Dawal, 2014) in her paper presented the effects of different lifting height, load mass and twist angle to the biceps and triceps muscles, and to the subject's heart rate based on the time representation. Roy, Bonato, & Knaflitz, 1998 have experimentally assessed the differences in back muscle function for static and dynamic lifting based on the instantaneous median frequency.

Identification analysis is required to monitor the factors that play a part in performance characteristics. The periodogram changes waveform information from time domain into frequency domain and represents the dissemination of the signal power over frequency. Time domain signal would only demonstrate the time for any changes in phenomena that are likely to occur in the signal, whereas frequency domain signal able to distinguish and clarify the magnitude (power) behaviour of the signal based on the individual or band of frequency.

Previous studies were mostly concerned with the utilization of periodogram technique on fault detection, leakage current and power quality (Dhahbi-Megrache & Beroual, 2015). This despite several researches having applied the periodogram for bio-signal processing.

Performance monitoring of muscle signal using periodogram is used in this study. The muscle signals, scientifically known as EMG signals from right biceps brachii are captured to assess the effects of varying the lifting height and load mass during manual lifting tasks using periodogram. The analytical domain is limited to assess the effects on various lifting conditions without focusing on muscle fatigue monitoring as a platform for future in-depth monitoring.

## **EXPERIMENTAL SETUP**

### **Subjects**

Five healthy male volunteers and five women volunteers were chosen for the study. None of them had a history of injury, either upper-limb disorder, lower-limb disorder or back disorder.



Their ages are between 21 to 25 years, and mean height and weight are 163 cm and 61.5 kg respectively. The complete demographic data of the subjects are shown in Table 1.

Table 1  
*Subject's demographic data*

Criteria	Minimum	Mean	Maximum
Age (Year)	21	23	25
Body weight (kg)	48	61.5	75
Body height (cm)	156	163	170

### Fatigue Exercise Protocol

Subjects were requested to stand straight  $0^\circ$  in front of the shelf and were required to lift the load (5 kg and 10 kg) onto the 75 cm shelf repetitively until experiencing muscle fatigue. This is when the simulation time stopped. The lifting height is then changed to 140 cm. The movement of the forearm makes eccentric contraction in biceps brachii muscle. Every contraction was partitioned into four phases as in Figure 1. Details of the phases are shown as follows:

Phase 1: Subject takes the load

Phase 2: Travelling the load onto the shelf

Phase 3: Place the load onto the shelf

Phase 4: Release the load

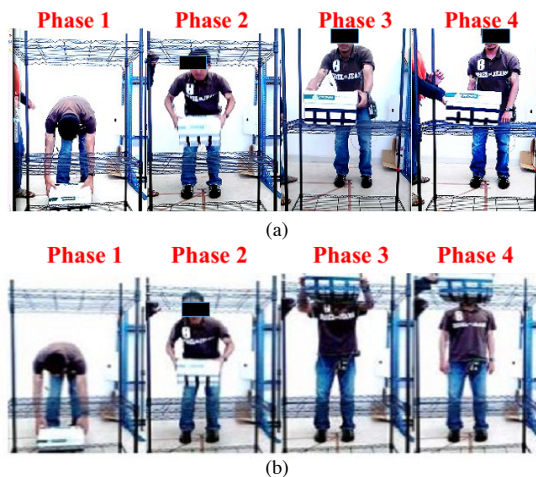


Figure 1. (a) Phases involved in each lifting for 75 cm lifting height;  
(b) phases involved in each lifting for 140 cm

### sEMG Data Collection

The sEMG signals from the right biceps brachii were recorded, sampled at 1500 Hz and filtered by a low pass filter of 500 Hz using Noraxon TeleMyo 2400T G2 and MyoResearch XP Master Research software. The location of Ag/AgCl electrodes (diameter 10mm) was aligned parallel to the fibres of the biceps brachii. To secure the electrodes, the electrodes are fixed onto the skin surface with an anti-allergic tape. Before attaching the electrodes, skin surface is cleansed using BD Alcohol Swabs of 70% Isorophyl Alcohol, and leave to dry before rubbing with the Signa Gel which is highly conductive, then only the electrodes are attached. The electrode placement is shown in Figure 2, where the biceps brachii label as (A) and the reference electrode is (B).

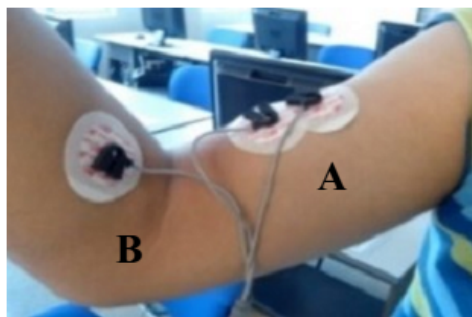


Figure 2. sEMG electrode placement on right biceps brachii

The Non-Invasive Assessment of Muscle (SENIAM) guideline was referred to obtain maximum pickup area of the EMG signals and to ensure that the signal from each subject is stable. The data of the signal were then processed by using Matlab R2011a.

### Periodogram Analytical Model

Raw data of the EMG signals were post-processed using periodogram. The periodogram changes waveform information from the time space into the frequency space and represents the dissemination of the signal power over frequency, which is called the power spectrum. The periodogram can be defined as

$$S_v(f) = \left| \frac{1}{T} \int_{-\frac{T}{2}}^{\frac{T}{2}} v(t) e^{-j2\pi f t} dt \right|^2 \quad (1)$$

where  $S_v(f)$  is the periodogram in frequency domain and  $v(t)$  is the voltage waveform of the raw sEMG signal.

The instantaneous root means square voltage ( $V_{rms}(t)$ ) can be calculated from the periodogram as follows:

$$V_{rms}(t) = \sqrt{\int_{-\frac{f_{max}}{2}}^{\frac{f_{max}}{2}} S_v(f) df} \quad (2)$$

where  $f_{max}/2$  is the maximum frequency of interest and  $S_v(f)$  is the periodogram.

## EXPERIMENTAL RESULTS

Figure 3 shows the raw EMG signal at various lifting height and load mass obtained from the fatigue exercise experiment for 1 subject. These figures show a decreasing trend in the number of repetitions and time taken for the subject to experience muscle fatigue as the lifting height and load mass are increased. Similar trends were also seen for the other 9 subjects. At lifting height of 75 cm and load mass of 5 kg, the number of repetition is 36 liftings with the time

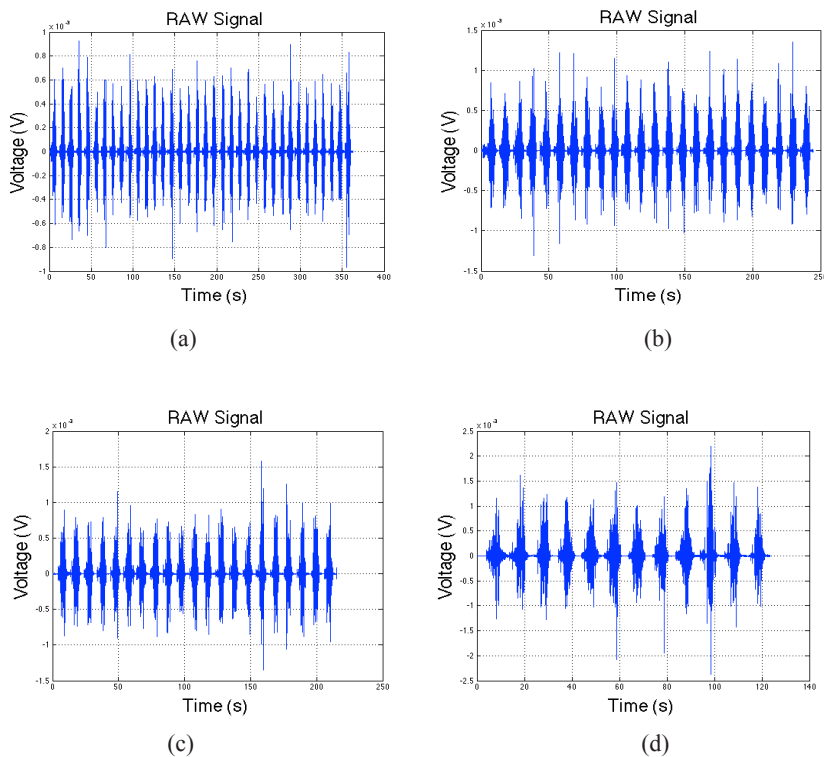


Figure 3. Raw EMG signal for (a) 5 kg load mass, 75 cm lifting height; (b) 5 kg load mass, 140 cm lifting height; (c) 10 kg load mass, 75 cm lifting height; (d) 10 kg load mass, 140 cm lifting height

taken to experienced fatigue is the highest (362.8 s) compared to the other three liftings. This trend is followed by lifting height of 140 cm and load mass of 5 kg, lifting height of 75 cm and load mass of 10 kg, and lifting height of 140 cm and load mass of 10 kg, with 24 liftings (244.6 s), 21 liftings (215.1 s) and 12 liftings (123.3 s) respectively.

Periodogram algorithm is then applied to the raw EMG signal to obtain the frequency representation of the signal. The periodogram results for different lifting height and load mass are shown in Figure 4. The signal of periodogram shows the distribution of the waveform signal power for the Y-axis over the frequency for the X-axis. Each signal from the periodogram shows similar frequency trend, however the amplitude value of the power spectrum for different lifting has a slight changed. The result indicates that the value of the amplitude (power) increased when the lifting height and load mass increased. The maximum power exists in the power spectrum for different liftings starting from 75 cm lifting height and 5 kg load mass, 140 cm lifting height and 5 kg load mass, 75 cm lifting height and 10 kg load mass, 140 cm lifting height and 10 kg load mass are  $1.187 \times 10^{-12}$  W,  $6.153 \times 10^{-12}$  W,  $5.104 \times 10^{-12}$  W and  $1.35 \times 10^{-11}$  W respectively.

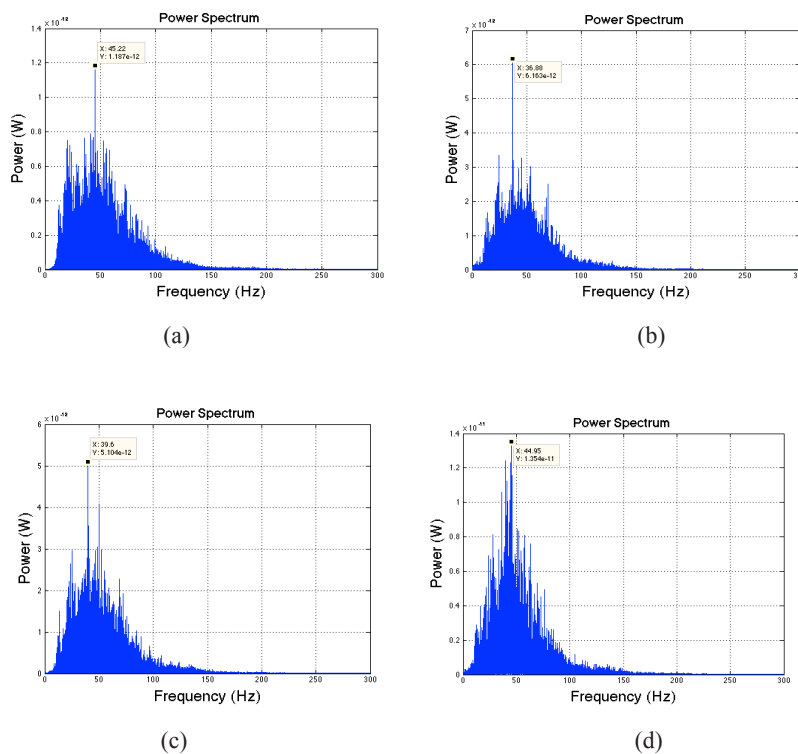


Figure 4. Power spectrum for (a) 5 kg load mass, 75 cm lifting height; (b) 5 kg load mass, 140 cm lifting height; (c) 10 kg load mass, 75 cm lifting height; (d) 10 kg load mass, 140 cm lifting height

From the power spectrum, muscle strength is estimated by calculating the  $V_{rms}$  values. The periodogram data of  $V_{rms}$  and maximum power with various lifting height and load mass is presented in Figure 5. These values are the mean values taken from all of the 10 subjects. It can be seen that  $V_{rms}$  are slightly increased from 0.0012 V, 0.0017 V, 0.0018 V and 0.0024 V as the lifting height and load mass are increased. Similar trend also showed by the EMG signal maximum power values. Hence, the overall results for periodogram data of  $V_{rms}$  and maximum power at various lifting conditions are presented in Table 2.

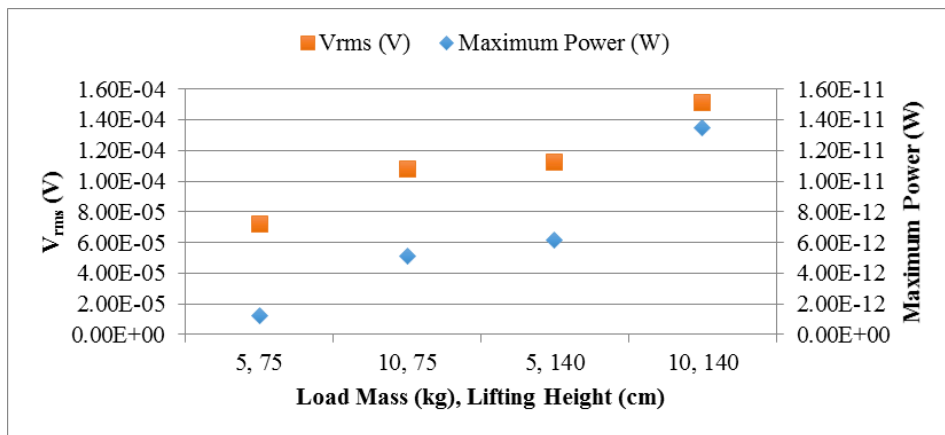


Figure 5. Periodogram data of maximum power and  $V_{rms}$  at various load mass and lifting height

Table 2

Periodogram data of various load mass and lifting height

Lifting Height (cm)	75		140	
Load Mass (kg)	5	10	5	10
Maximum Power (W)	1.19E-12	5.10E-12	6.16E-12	1.35E-11
$V_{rms}$ (V)	7.19E-05	1.08E-04	0.0018	0.0024

## CONCLUSION

An experimental study based on analysis of the periodogram power spectrum was performed to monitor the effects of different lifting height and load mass on muscle performance. Results indicate the number of lifting repetitions which could be performed before the subject experiences muscle fatigue. The findings show the relationship between the lifting height and load mass on muscle performance. Apart from that, it indicates that both the amplitude of the periodogram, which represents the power and the  $V_{rms}$  (strength) are increased as the lifting height and load mass are increased. Consequently, the EMG signal characteristic of various lifting height and load mass could be well presented by using periodogram.

## ACKNOWLEDGEMENT

Control System and Signal Processing research group of Universiti Putra Malaysia (UPM), together with Rehabilitation and Assistive Technology research group of Universiti Teknikal Malaysia Melaka, supported this work. All experiments were performed at the Advanced Digital Signal Processing Research Laboratory and were funded by the Ministry of Higher Education Malaysia (MOHE).

## REFERENCES

- Dhabhi-Megrache, N., & Beroual, A. (2015). Time–Frequency Analyses of Leakage Current Waveforms of High Voltage Insulators in Uniform and Non-Uniform Polluted Conditions. *IET Science, Measurement and Technology*, 9(8), 945–954. doi:10.1049/iet-smt.2015.0116
- González-Izal, M., Malanda, A., Navarro-Amézqueta, I., Gorostiaga, E. M., Mallor, F., Ibañez, J., & Izquierdo, M. (2010). EMG Spectral Indices and Muscle Power Fatigue during Dynamic Contractions. *Journal of Electromyography and Kinesiology*, 20(2), 233–240. doi:10.1016/j.jelekin.2009.03.011
- Kamarudin, N. H., Ahmad, S. A., Hassan, M. K., Yusoff, R. M., & Dawal, S. Z. (2014). Muscle Contraction Analysis During Lifting Task. In *IEEE Conference on Biomedical Engineering and Sciences* (pp. 8–10). Miri, Sarawak, Malaysia.
- Merlo, A., & Campanini, I. (2010). Technical Aspects of Surface Electromyography for Clinicians. *The Open Rehabilitation Journal*, 3, 98–109. doi:10.2174/1874943701003010098
- Roy, S. H., Bonato, P., & Knaflitz, M. (1998). EMG Assessment of Back Muscle Function During Cyclical Lifting. *Journal of Electromyography and Kinesiology*, 8(4), 233–245. doi:10.1016/S1050-6411(98)00010-8
- Shair, E. F., Zawawi, T. N. S. T., Abdullah, A. R., & Shamsudin, N. H. (2015). sEMG Signals Analysis Using Time-Frequency Distribution for Symmetric and Asymmetric Lifting. In *2015 International Symposium on Technology Management and Emergent Technologies (ISTMET)* (pp. 233–237).
- Tkach, D., Huang, H., & Kuiken, T. a. (2010). Study of Stability of Time-Domain Features for Electromyographic Pattern Recognition. *Journal of Neuroengineering and Rehabilitation*, 7, 1–13. doi:10.1186/1743-0003-7-21

## A Single-stage LED Driver with Voltage Doubler Rectifier

**Nurul Asikin, Zawawi<sup>1\*</sup>, Shahid Iqbal<sup>1</sup> and Mohamad Kamarol, Mohd Jamil<sup>1</sup>**

<sup>1</sup>*School of Electrical and Electronic Engineering, Universiti Sains Malaysia, Nibong Tebal, 14300 Penang, Malaysia*

### ABSTRACT

In this paper, a configuration of a single-stage AC-DC converter and a high voltage resonant controller IC L6598 for LED street light driver is discussed. The converter is obtained by integrating two boost circuits and a half-bridge LLC resonant circuit. A voltage double rectifier circuit is adopted as output to lower the voltage stress on transformer and the associated core. The two boost circuits work in boundary conduction mode (BCM) to achieve the power factor correction (PFC). The converter works in soft-switching mode allowing the power switches to operate in zero-voltage-switching (ZVS) and the output diodes to operate in zero-current-switching (ZCS). This reduces the switching losses and enhances the efficiency. The converter features lower voltage stress on the power switches and the bus voltage is reduced to slightly higher than the peak input voltage. Therefore, the converter can perform well under high-input-voltage. Here, the DC bus and the output filter capacitances are greatly reduced. So, electrolytic capacitor-less converter can be realized for a long lifetime LED driver. Simulation results from PSpice are presented for a 100-W prototype.

*Keywords:* LED driver, boost circuit, LLC, power factor correction, street lighting, voltage doubler

### INTRODUCTION

Recently, light-emitting diode (LED) has become popular for street lighting due to its energy savings capacity and low maintenance

costs. Switching from incandescent lights to LEDs can also help reduce greenhouse gas emissions from power plants in addition to providing better light quality and eliminating mercury waste disposal (“Energy Efficient,” 2013).

An appropriate converter that can support a wide range of universal input ac voltages is desirable. Therefore, AC-DC conversion stage is a compulsory to drive the system powered from ac source. Switching converter is usually chosen due to its economical driving solutions, but the conventional AC-

#### ARTICLE INFO

##### *Article history:*

Received: 24 August 2016

Accepted: 02 December 2016

##### *E-mail addresses:*

[nurulasikin@hotmai.com](mailto:nurulasikin@hotmai.com) (Nurul Asikin, Zawawi),

[shahisidu@hotmail.com](mailto:shahisidu@hotmail.com) (Shahid Iqbal),

[eekamarol@usm.my](mailto:eekamarol@usm.my) (Mohamad Kamarol, Mohd Jamil)

\*Corresponding Author

DC switching converters have poor performances in PF and harmonic distortion. In order to achieve input current shaping, an additional PFC stage is added in front of the converters. In spite of its good performance, these two-stage converters are usually expensive, bigger in size and energy inefficient compared to the single-stage converters. To simplify the circuit and improve the reliability of the system, single-stage AC-DC converters were proposed (Gacio et al., 2011; Lin et al., 2006; Lu et al., 2008). PFC circuit and the DC-DC converter were integrated into one stage by sharing one or more switches. However, the integrated switch was subjected to high voltage stress and operated in hard switching which decreases the circuit efficiency.

A single-stage LLC resonant converter has the advantage of soft-switching characteristics and can achieve high efficiency. However, the single-stage PFC converters based on half-bridge resonant structure (Chen et al., 2012; Kang et al., 2002; Lai & Shyu, 2007) continued to maintain a high bus voltage twice the input peak voltage. On the contrary, the converter in Seok & Kwon, 2001 demonstrated a lower bus voltage, and less voltage stress on the switching devices. Wang et al. (2010) proposed a single-stage LED driver which comprises an interleaving boost circuit and half-bridge LLC resonant circuit. The two boost circuits work in DCM to obtain PFC function. With proper switching frequency, the primary-side switches operate in ZVS and the secondary-side diodes operate in ZCS. Cheng and Yen (2011) implemented the same topology and reduced one capacitor at the input side. Later, Wang et al. (2015) improved the topology by replacing the two boost inductors with a single inductor that was shared by the two boost circuits. Both boost circuits worked in BCM. However, the driver is more complex and larger in terms of its size since it uses pulse transformer for the driving circuit.

In this paper, the configuration of a single-stage LED driver proposed in Wang et al., 2015 and a resonant controller ICL658 is used to design a 100-W prototype for application under 240-V AC input. Since the voltage divider capacitors can fulfil the same role, the driver eliminated the DC input filter capacitor after the input bridge rectifier. By employing the output-voltage doubler rectifier on the secondary side, a higher voltage conversion ratio is obtained with a lower turn ratio transformer. The reduced turn ratio increases the overall efficiency. The transformer size also can be decreased. Here, the output voltage is shared by two output filter capacitors. So, a smaller capacitance with lower voltage rating capacitor can be used. Since, the DC bus and the output filter capacitance are incredibly downsized; film type capacitor can be utilized. Hence, a longer life span for the LED driver can be achieved.

### Structure of the proposed circuit

Figure 1 shows the proposed configuration of LED driver with a resonant controller and a control circuit. The driver consists of a full-bridge rectifier, two voltage divider capacitors  $C_1$  and  $C_2$ , two boost diodes  $D_1$  and  $D_2$ , a boost inductor  $L_b$ , two power switches  $S_1$  and  $S_2$ , a bus voltage capacitor  $C_{bus}$ , a resonant capacitor  $C_r$ , a transformer with resonant inductor  $L_r$  and magnetizing inductor  $L_m$ , two output diodes  $D_{r1}$  and  $D_{r2}$ , two output capacitors  $C_{r1}$  and  $C_{r2}$  and LED street light module. Here,  $C_{S1}$  and  $C_{S2}$  are the parasitic capacitors, while  $D_{S1}$  and  $D_{S2}$  are the parasitic diodes of switches  $S_1$  and  $S_2$ . Two boost circuits are obtained by integrating the switches of half-bridge LLC resonant circuit.  $C_{bus}$ ,  $D_1$ ,  $L_b$ ,  $S_1$ , and  $D_{S2}$  constitute one boost circuit, whereas  $C_{bus}$ ,  $D_2$ ,  $L_b$ ,  $S_2$ , and  $D_{S1}$  constitute another boost circuit.  $C_{bus}$  and  $L_b$  are shared by the two boost



circuits. A high voltage resonant controller IC manufactured by ST Microelectronics, L6598 would be used to drive the two switches alternately with a certain dead time and switching duty cycle nearly 0.5. The dead time provided between the conduction of the high-side switch and low-side switch will allow the switches to turn on with ZVS. The auxiliary voltage  $V_{aux}$  supply a constant voltage to the resonant controller for driving the switches.

### Principle of the operation

This driver has ten operational modes in a single switching period. The steady state operating waveforms of the driver are demonstrated in Figure 2. In the following, the descriptions for the operational modes are elaborated.

**Mode 1** ( $t_0 - t_1$ ): At time  $t_0$ , switch  $S_2$  is already turned off. Resonant current  $i_r$  flows in opposite direction through switch  $S_1$  to discharge parasitic capacitor  $C_{S1}$ . Hence, drain-source voltage  $V_{DS1}$  decreases to zero and parasitic diode  $D_{S1}$  is turned on. During this time, boost inductor  $L_b$  discharges energy via  $D_{S1}$ ,  $C_{bus}$ ,  $D_2$ , and  $C_2$ . On the secondary side, diode  $D_{r1}$  is turned on and current  $i_{Dr1}$  increases. So, the voltage across magnetizing inductor  $L_m$  is clamped by output voltage. Resonant inductor  $L_r$  and resonant capacitor  $C_r$  form a resonant tank. Afterward, gate signal  $V_{GS1}$  arrives to turn on  $S_1$  in ZVS. At the end of this mode,  $i_r$  becomes zero.

**Mode 2** ( $t_1 - t_2$ ): Within this time interval, resonant current  $i_r$  flows in positive direction and increases with sinusoidal shape.

**Mode 3** ( $t_2 - t_3$ ): At time  $t_2$ , parasitic diode  $D_{S1}$  is turned off. Resonant current  $i_r$  flows through  $C_{bus}$  and  $S_1$ . Magnetizing current  $i_m$  continues to decrease linearly. At the end of this mode, boost inductor  $L_b$  is completely discharged until current  $i_{Lb}$  becomes zero.

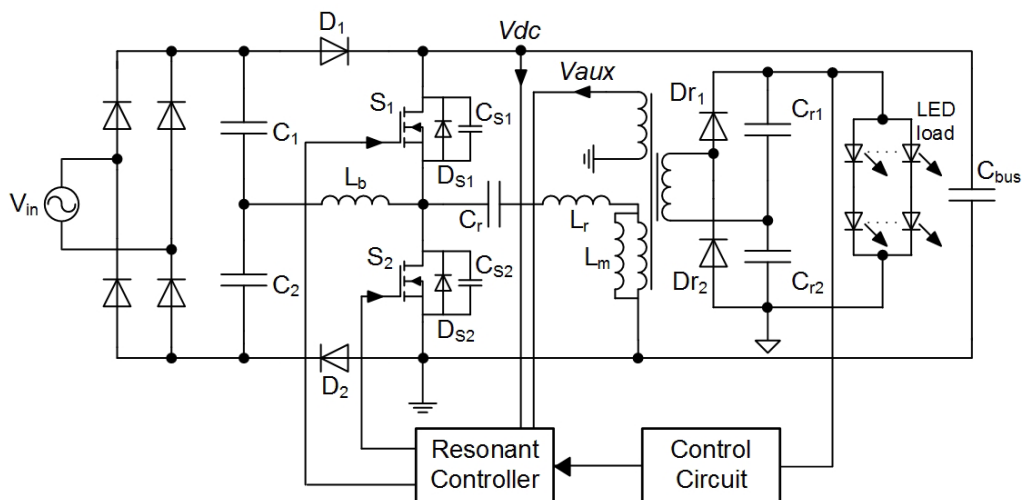


Figure 1. The proposed configuration of LED driver with a resonant controller and a control circuit

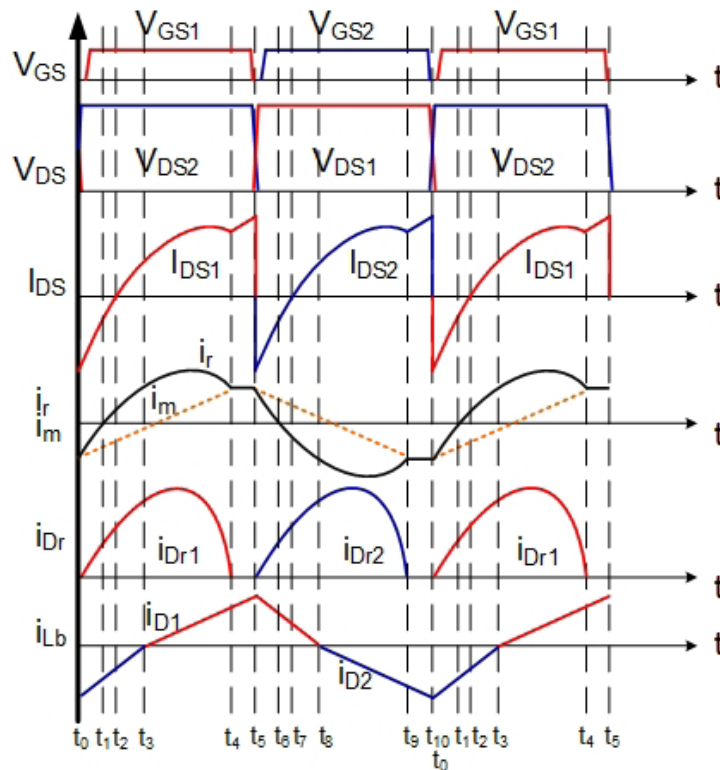


Figure 2. The steady state operating waveforms of the driver

**Mode 4** ( $t_3 - t_4$ ): At time  $t_3$ ,  $C_1$  charges  $L_b$  via  $D_1$  and  $S_1$ . Magnetizing current  $i_m$  becomes zero, then changes its flow to positive direction and continues to increase linearly to the maximum value. Resonant current  $i_r$  also increases until reaching the peak value then decreases until the value is equal to  $i_m$ . The difference current between  $i_r$  and  $i_m$  flows through the primary winding of the transformer and power is supplied to the load. Here, diode current  $i_{Dr1}$  increases to the peak value and then decreases to zero.

**Mode 5** ( $t_4 - t_5$ ): At time  $t_4$ , diode  $D_{r1}$  is turned off in ZCS. The secondary side circuit is separated from the primary side circuit. So, the voltage across  $L_m$  is no longer clamped by output voltage. Hence,  $L_m$  involves in the resonant tank with  $L_r$  and  $C_r$ . At this time,  $i_r$  and  $i_m$  are equal. The current continues to flow through  $C_{bus}$  and  $S_1$ . At the end of this mode, switch  $S_1$  is turned off. Parasitic capacitor  $C_{S1}$  is charged and drain-source voltage  $V_{DS1}$  increases to bus voltage. Boost inductor  $L_b$  is fully charged and  $i_{Lb}$  reaches peak value.

**Mode 6** ( $t_5 - t_6$ ): At time  $t_5$ , resonant current  $i_r$  flows through switch  $S_2$  and discharges parasitic capacitor  $C_{S2}$ . Hence, drain-source voltage  $V_{DS2}$  decreases to zero and parasitic diode  $D_{S2}$  is turned on. During this time, boost inductor  $L_b$  discharges energy via  $C_1$ ,  $D_1$ ,  $C_{bus}$ , and  $D_{S2}$ . On the secondary side, diode  $D_{r2}$  is turned on and current  $i_{Dr2}$  increases. So, the voltage across  $L_m$  is clamped by output voltage. Resonant inductor  $L_r$  and resonant capacitor  $C_r$  form a resonant tank. Afterward, gate signal  $V_{GS2}$  arrives to turn on  $S_2$  in ZVS. At the end of this mode,  $i_r$  decreases to zero.

**Mode 7** ( $t_6 - t_7$ ): During this mode, resonant current  $i_r$  flows in negative direction and increases with sinusoidal shape.

**Mode 8** ( $t_7 - t_8$ ): At time  $t_7$ , parasitic diode  $D_{S2}$  is turned off. Resonant current  $i_r$  flows through  $S_2$ . Magnetizing current  $i_m$  continues to decrease linearly. At the end of this mode, boost inductor  $L_b$  is completely discharged until current  $i_{Lb}$  becomes zero.

**Mode 9** ( $t_8 - t_9$ ): At time  $t_8$ ,  $C_2$  charges  $L_b$  via  $S_2$  and  $D_2$ . Magnetizing current  $i_m$  becomes zero, then changes its flow to negative direction and continues to increase linearly to the maximum value. Resonant current  $i_r$  also increases until reaching the peak value then decreases until the value is equal to  $i_m$ . The difference current between  $i_r$  and  $i_m$  flows through the primary winding of the transformer and power is supplied to the load. Here, diode current  $i_{Dr2}$  increases to the peak value and then decreases to zero.

**Mode 10** ( $t_9 - t_{10}$ ): At time  $t_9$ , diode  $D_{r2}$  is turned off in ZCS. The secondary side circuit is separated from the primary side circuit. So, the voltage of  $L_m$  is no longer clamped by output voltage. Hence,  $L_m$  involves in the resonant tank with  $L_r$  and  $C_r$ . At this time,  $i_r$  and  $i_m$  is equal. The current continues to flow through switch  $S_2$ . At the end of this mode, switch  $S_2$  is turned off. Parasitic capacitor  $C_{S2}$  is charged and drain-source voltage  $V_{DS2}$  increases to bus voltage. Boost inductor  $L_b$  is fully charged and  $i_{Lb}$  reaches peak value.

From the waveforms, the boost inductor current  $i_{Lb}$  is naturally in BCM state. The two boost circuits charge and discharge the energy to boost inductor  $L_b$  alternately in one switching period.

The switch is turned on when the drain-source voltage is zero. During this time, the parasitic diode carries reverse current before the switch conducts forward current. Hence, there are no turn on switching losses exist in the switches. Furthermore, when the switch is turned off, the parasitic capacitor will be charged and the drain-source voltage increases. At the same time, the parasitic capacitor of the opposite switch will be discharged and the energy stored is returned to the dc source. Here, capacitive loss is eliminated. This help to erase the turn off switching losses. Thus, the switches operate alternately with ZVS.

On the secondary side, output diodes are turned off with ZCS. Then, the secondary side is separated from the primary side and the output filter capacitors will supply energy to the LEDs.

### Design consideration

A prototype of an LED driver is designed for application under 240-V AC input. Here, the LED street light module consists of six strings with two LEDs per string. The LED has steady state rated performance of 26.5V/320mA. The switching frequency  $f_s$  of LLC resonant circuit must satisfy the range  $f_m < f_s < f_r$  for the switches to work in ZVS and the secondary side diodes to work in ZCS. Here, the switching frequency is set to  $0.9 f_r$ . A large value of  $L_m$  is used to obtain a lower bus voltage in variation of the load. The utilized components for the driver are shown in detail in Table 1.

Table 1  
Component list

Component	Symbol	Value
Voltage Divider Capacitor	$C_1, C_2$	330nF
Boost Inductor	$L_b$	200uH
Resonant Capacitor	$C_r$	10nF
Leakage Inductor	$L_r$	110uH
Magnetizing Inductor	$L_m$	990uH
Bus Capacitor	$C_{bus}$	90uF
Output Capacitor	$C_{r1}, C_{r2}$	47uF

### Simulation result

In this paper, a 100-W prototype with 53V output for an LED street light module is simulated using PSpice. Figure 3 shows the waveforms of the input voltage  $v_{in}$  and input current  $i_{in}$ . The input current is in phase with the input voltage, so the PFC function is obtained. The sinusoidal waveform without shape distortion portray that the current consist of fundamental component, so a low current THD can be estimated.

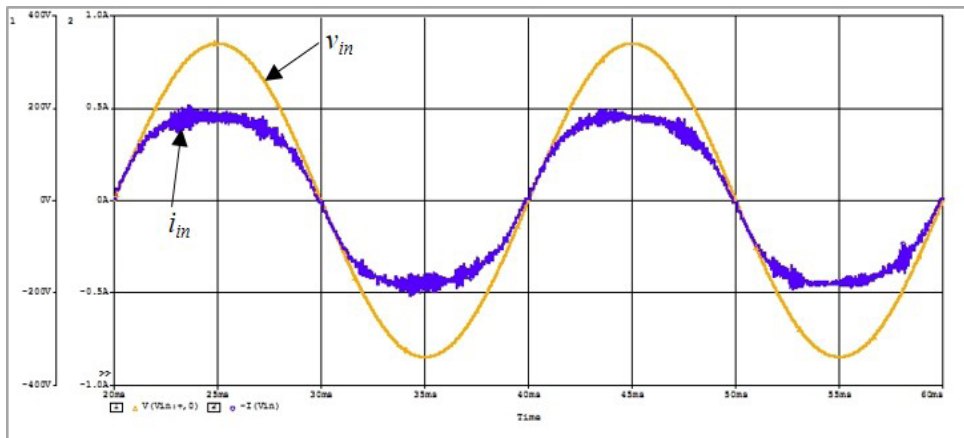


Figure 3. The waveforms of the input voltage  $v_{in}$  and input current  $i_{in}$

Figure 4 shows the waveforms of  $V_{DS1}$ ,  $V_{GS1}$  and  $I_{DS1}$ . The switch gate voltage  $V_{GS1}$  comes after the switch drain-source voltage  $V_{DS1}$  turned to zero. During this time, the switch conducts reverse current. This is demonstrating that the switches work in ZVS mode. Figure 5 shows the waveforms of the switch drain-source voltage  $V_{DS1}$  and diode current  $i_{Dr1}$ . The diode current slowly decreases to zero and there is a short time it to keep it at zero value, which shows that the secondary side diodes turn off in ZCS mode.

### A Single-Stage Converter for Driving LEDs

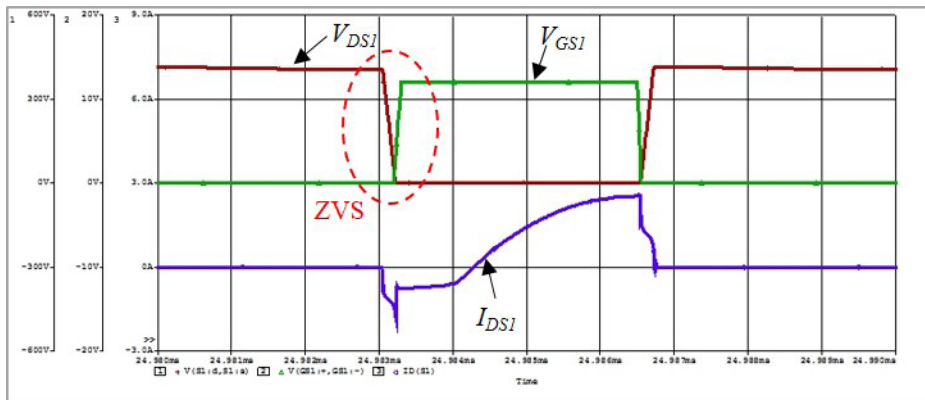


Figure 4. The waveforms of the switch drain-source voltage  $V_{DS1}$ , switch gate voltage  $V_{GS1}$  and switch current  $I_{DS1}$

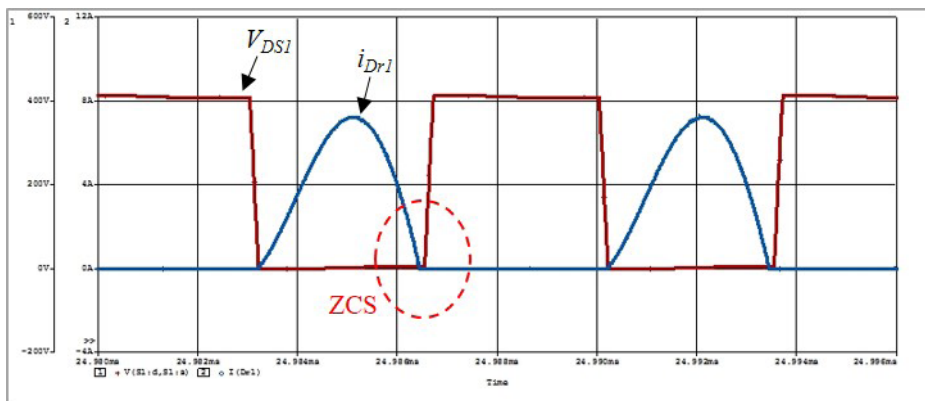


Figure 5. The waveforms of the switch drain-source voltage  $V_{DS1}$  and output diode current  $i_{Dr1}$

Figure 6 shows the waveforms of  $V_{DS1}$ ,  $i_r$ ,  $i_{Dr1}$  and  $i_{Lb}$  in 100-W full-load stage. The resonant current  $i_r$  has a step shape and the diode current  $i_{Dr1}$  works in ZCS. The switching frequency is 141 kHz.

Figure 7 shows the waveforms of output voltage  $V_o$  and output current  $I_o$ . The voltage is 53 V, and the current is 1.9 A, hence, the output power is approximately 100 W. The voltage ripple is lower than 1 V, while the current ripple is lower than 100 mA, which is an acceptable value to drive the LEDs without flicker.

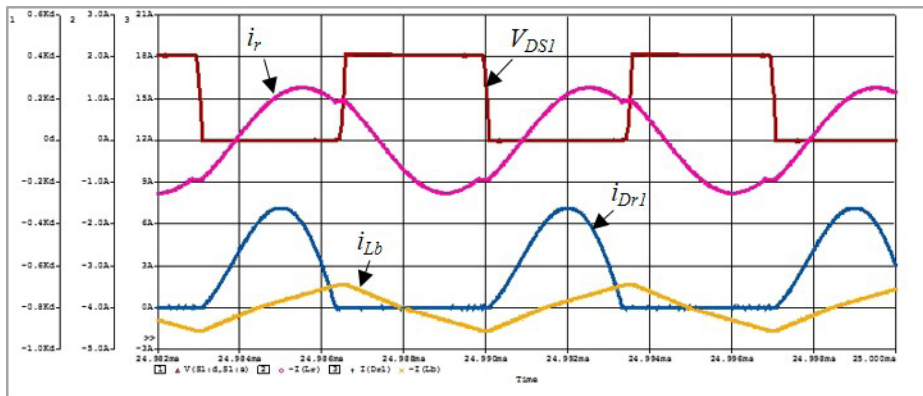


Figure 6. The waveforms of the switch drain-source voltage  $V_{DS1}$ , resonant current  $i_r$ , output diode current  $i_{Dr1}$  and boost inductor current  $i_{Lb}$

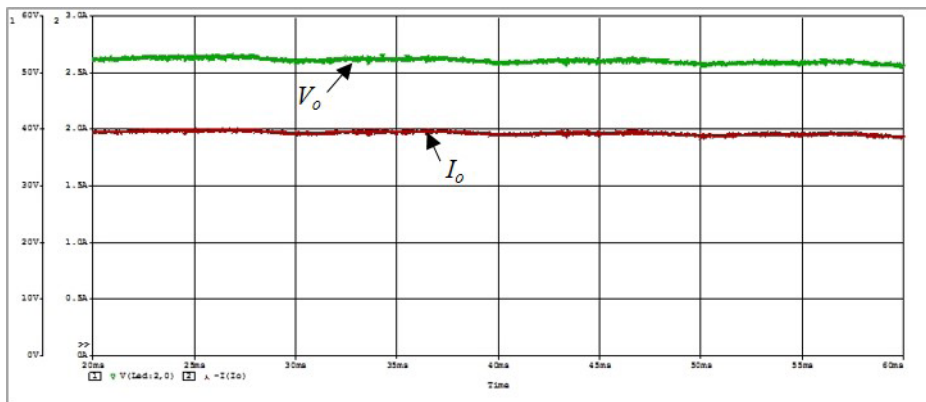


Figure 7. The waveforms of the output voltage  $V_o$  and output current  $I_o$

## CONCLUSION

A 100-W single-stage LED driver based on two boost circuits and a half-bridge type LLC resonant circuit is simulated under 240-V AC input. The boost circuits share a single inductor that operate in BCM to obtain the PFC. Input voltage is divided by two capacitors, so the voltage stress of the switches is reduced by half and the driver is suitable for high-input-voltage condition. The value of the magnetizing inductor is selected to be high so that the bus voltage is low in variation of the power. Both switches work with soft-switching characteristics in order to achieve a high conversion efficiency. Simulation results showed that the bus voltage was about 400V, which is higher than the input peak voltage. Here, ideal elements were selected, thus, the switches or components losses were not considered throughout the simulation.

## ACKNOWLEDGEMENT

The authors would like to thank the Universiti Sains Malaysia for providing all necessary facilities and equipment to make this research possible. This work was supported by Fundamental Research Grant Scheme (FRGS) 203/PELECT/6071307 from Ministry of Education Malaysia.

## REFERENCES

- Chen, S. Y., Li, Z. R., & Chen, C. L. (2012). Analysis and design of single-stage AC/DC LLC resonant converter. *IEEE Transactions on Industrial Electronics*, 59(3), 1538-1544.
- Cheng, C. A., & Yen, C. H. (2011, June 21-23). A single-stage driver for high power LEDs. Paper presented at the IEEE Conference on Industrial Electronics and Applications (pp. 2666-2671).
- Gacio, D., Alonso, J. M., Calleja, A. J., Garcia, J., & Rico-Secades, M. (2011). A universal-input single-stage high-power-factor power supply for HB-LEDs based on integrated buck-flyback converter. *IEEE Transactions on Industrial Electronics*, 58(2), 589-599.
- Kang, F. S., Park, S. J., & Kim, C. U. (2002). ZVZCS single-stage PFC AC-to-DC half-bridge converter. *IEEE Transactions on Industrial Electronics*, 49(1), 206-216.
- Lai, C. M., & Shyu, K. K. (2007). A single-stage AC/DC converter based on zero voltage switching LLC resonant topology. *IET Electric Power Applications*, 1(5), 743-752.
- Lau, S. P., Merrett, G. V., & White, N. M. (2013, May). Energy-efficient street lighting through embedded adaptive intelligence. In *Advanced Logistics and Transport (ICALT), 2013 International Conference on* (pp. 53-58). IEEE.
- Lin, J. L., Yao, W. K., & Yang, S. P. (2006). Analysis and design for a novel single-stage high power factor correction diagonal half-bridge forward AC-DC converter. *IEEE Transactions on Circuits and Systems I: Regular Papers*, 53(10), 2274-2286.
- Lu, D. D. C., Iu, H. H. C., & Pjevalica, V. (2008). A single-stage AC/DC converter with high power factor, regulated bus voltage, and output voltage. *IEEE Transactions on Power Electronics*, 23(1), 218-228.
- Seok, K. W., & Kwon, B. H. (2001). A novel single-stage half-bridge AC-DC converter with high power factor. *IEEE Transactions on Industrial Electronics*, 48(6), 1219-1225.
- Wang, Y., Guan, Y., Ren, K., Wang, W., & Xu, D. (2015). A single-stage LED driver based on BCM boost circuits and LLC converter for street lighting system. *IEEE Transactions on Industrial Electronics*, 62(9), 5446-5457.
- Wang, Y., Zhang, X., Wang, W., & Xu, D. (2010, Oct 10-13). *A novel interleaved single-stage AC/DC converter with high power factor and ZVS characteristic. Paper presented at the International Conference on Electrical Machines and Systems (ICEMS)* (pp. 249-254).







## An Integrated System Wide Reactive Power Management Strategy for Transmission and Distribution System based on Techno Economic Analysis

Jun Huat Tang<sup>1\*</sup>, Mau Teng Au<sup>2</sup>, Asnawi bin Mohd Busrah<sup>1</sup>,  
Mohd Hafiz bin Mat Daud<sup>1</sup>, Lau Chee Chong<sup>3</sup>, Khairuddin bin Abdullah<sup>1</sup>

<sup>1</sup>TNB Research Sdn Bhd, Kajang 43300, Selangor, Malaysia,

<sup>2</sup>Universiti Tenaga Nasional, Kajang 43300, Selangor, Malaysia

<sup>3</sup>Tenaga Nasional Berhad, Petaling Jaya 46200, Selangor, Malaysia

### ABSTRACT

This paper presents a methodology to determine the economic power factor at the point of power transfer between transmission and distribution (T & D) system for a vertically integrated utility company. An integrated reactive power management strategy is developed to optimize the planting up of reactive power compensation devices in the transmission and distribution system. The transmission and distribution network is modelled and simulated using commercially available software to analyse the transmission network losses, capacity released and voltage stability due to capacitor plant up. Economic analysis on the total cost of ownership of capacitor banks is used to determine the economic benefits of technical losses reduction and capacity released in transmission and distribution equipment through the planting up of capacitor bank. The proposed methodology can be used by a vertically integrated power utility where a single utility own both the transmission and distribution system. A software base data analytic, power system automation and economic analysis tool was developed to facilitate the planning engineer in reactive power planning and management.

*Keywords:* Reactive power management

### ARTICLE INFO

#### *Article history:*

Received: 24 August 2016

Accepted: 02 December 2016

#### *E-mail addresses:*

[tangjunhuat@tnbr.com.my](mailto:tangjunhuat@tnbr.com.my);

[tangjh\\_8@hotmail.com](mailto:tangjh_8@hotmail.com) (Jun Huat Tang),

[Mtau@uniten.edu.my](mailto:Mtau@uniten.edu.my) (Mau Teng Au),

[asnawi.busrah@tnb.com.my](mailto:asnawi.busrah@tnb.com.my) (Asnawi bin Mohd Busrah),

[hafiz.matdaud@tnbr.com.my](mailto:hafiz.matdaud@tnbr.com.my) (Mohd Hafiz bin Mat Daud),

[laucc@tnb.com.my](mailto:laucc@tnb.com.my) (Lau Chee Chong),

[khairuddin.abdullah@tnbr.com.my](mailto:khairuddin.abdullah@tnbr.com.my) (Khairuddin bin Abdullah)

\*Corresponding Author

### INTRODUCTION

Reactive power management in transmission network aims at addressing issues related to voltage stability in a power system under normal operating conditions. Inadequate reactive power in the transmission system could lead to voltage collapse (U.S.-Canada Power System Outage Task Force, 2014). In the distribution system, the main objective

of having adequate reactive power is to minimize technical losses and to release equipment capacity. Voltage management based on reactive power control in the distribution system is not as effective when compared with transmission system due to the nature of distribution system where the X/R ratio is high. The total costs of ownership for capacitor banks depends on the voltage and its manufacturer. As such, capacitor plant up in transmission and distribution system is optimized based on the selection of capacitor bank according to its voltage level and design under technical constraints such as physical space, network topology and availability. An integrated approach in reactive power planning and planting up can help to save costs and benefit a vertically integrated utility company.

Various methods have been proposed by researchers to optimize the management of reactive power (Singh & Srivastava, 2012); (Shourvarzi, Vaziri Mirzaei, Mehdizadeh Afroozi, & Rostami, 2012). In recent years, many publications have focused on optimal location, sizing and control strategy of reactive power management in the network with distributed generation or renewable energy resources (Hu, Dong, Lu, Xu, & Lianjie Lv, 2012). A comprehensive literature survey on the European practices in voltage and VAR control is published in (Mousavi & Cherkaoui, 2011).

Majority of the publications are focused on the optimal reactive power management on either transmission or distribution system. The methods proposed in the literature are applicable for deregulated electricity market where the coordination between transmission and distribution is minimal, and distribution operator adopted the concept “pay as you use” for reactive power. Furthermore, the proposed solution for optimal reactive power management involves complex optimization technique and heavy computation.

This paper describes an integrated approach in capacitor bank plant up for a transmission and distribution system. The first step is to establish the economic power factor at the point of power transfer between the transmission and distribution system. By applying total costs of ownership for each type of capacitor bank of different voltage level, economic benefits in terms of reduction in technical losses and capacity released in equipment is optimized by calculating the internal rate of return of each case of capacitor bank plant up. The optimum strategy is based on techno-economic analysis and network availability. Parameters required for the proposed methodology includes transmission and distribution network data, peak load demand data, unit cost of energy, and unit savings from capacity release.

## **METHODOLOGY**

Typically, in a power system, most of the reactive power is consumed by the electrical loads. Reactive power transfer between the transmission and distribution system is recorded by energy meters installed on the secondary side of power transformers in the Main-In-Take substations. In this study, system wide power factor profile is first established by analysing the owner factor at each of the Main-In-Take substation. Power system studies were done on the transmission network to determine the optimal power factor at the Main-In-Take substation that yields the highest economic benefits.

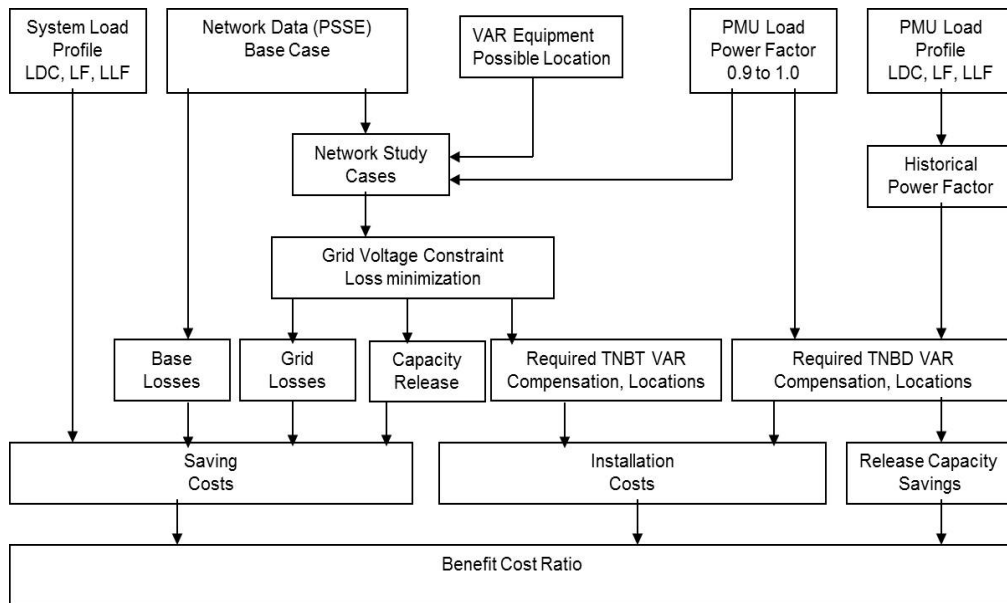


Figure 1. Process flow for integrated reactive power management

The quantum of capacitor banks to be planted in the distribution system is determined based on the optimal power factor at the Main-In-Take substation. Three different types of capacitor bank are considered; medium voltage (MV) capacitor bank, ground mount (GMLV) low voltage capacitor bank and low voltage pole top (LVPT) capacitor bank. Economic benefits based on internal rate of return are calculated for each of the three types of capacitor bank. Figure 1 shows the process flow of the integrated capacitor plant up based on the economic power factor to be maintained at the PMUs.

## TECHNICAL ANALYSIS

In the technical analysis, the network data, load demand and existing power factor for the load was obtained from the utility company. The entire transmission network is modelled in the power system simulation software with optimal power flow (OPF) and the results (technical losses and total loading in MVA) are saved as base case. The OPF is repeated using different power factor from 0.9 to 1.0. The result of OPF at different power factor is compared to the technical losses and loading in MVA for the base case. The difference is the saving/benefit obtained from reactive power management. Figure 2 shows the example of capacity release at different power factor.

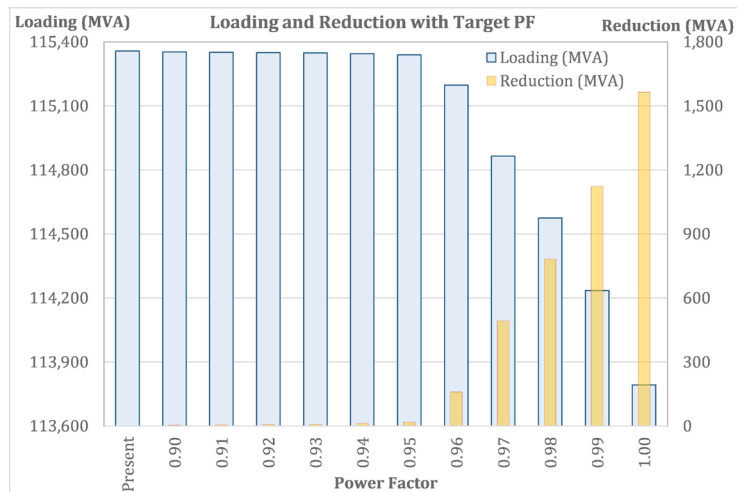


Figure 2. Example of capacity release chart

## ECONOMIC ANALYSIS

From the technical analysis, the studies were able to establish the technical losses reduction, capacity released and capacitor bank required to achieve the target power factor. Financial savings is taken from the product of capacity released and energy losses multiply by its respective dollar/unit (\$/MVA and \$/kWh).

### Capacity Released

The capacity released would benefit utility companies in terms of deferment of investment in new infrastructure, which typically consists of construction costs of new substations, transformers and auxiliary equipment. In addition, by releasing the transformer capacity the utility company would be able to minimize risk of power interruption to customers through demand management in the event of a fault in the system.

### Technical Losses Reduction

Technical losses indicate the energy efficiency of the transmission and distribution system in supply power to customer loads. Operating at economic power factor by placing capacitor banks at strategic locations in the power system are effective and economical ways to minimize technical losses.

### Capacitor Cost

Capacitor bank is a low cost reactive power compensation device compared to other technology such as STATCOM. Therefore, capacitor bank is widely used by power utility. Capacitor bank rated at different voltage level has different capacity, life span and maintenance cost. To have a fair comparison, total cost of ownership (TCO) is introduced to compare the most optimum reactive power compensation strategy. TCO is calculated based on the formula below: -

$$TCO (RM) = [Initial\ cost + Maintenance\ cost + Disposal\ cost - Less\ value] \text{ unit cost} \quad (1)$$

### RESULTS AND DISCUSSION

The benefit cost ratio is calculated based on ratio of overall cost saving to total cost of capacitor installation. The result in figure 3 shows the most economic power factor to be maintained at Main-In-Take Substation which is 0.97. Consequently, this 0.97 power factor is used to determine system wide strategies in capacitor bank plant up in the distribution system.

In this study, it has been determined that 120 MVAR of capacitor bank should be planted per year over the next 8 years in the distribution system to mitigate the deficit in reactive power requirement based on 0.97 economic power factor at PMU. Plant up of 120 MVAR per year is taking into consideration of practicality at site such as outage requirement, civil work, cabling and installation work.

A sample result on capacitor bank plant up in the distribution system is shown in Table 1. In this example, 75% of the total 120 MVAR required will be planted up at 11kV (5 MVAR capacitor bank). This is equivalent to approximately 90 MVAR or 18 units of 5 MVAR 11kV capacitor bank. This is follow by 10 % of GMLV capacitor bank and 15% of LVPT capacitor bank. With the plant up as shown in Table 1, it is expected that the quantum of reactive power transfer from transmission to distribution system would be gradually reduced. Consequently, the whole generation, transmission and distribution system would be more energy efficient as the distribution system is capable of meeting its reactive power demand locally which is achievable in year 2023.

Figure 3 shows the overall optimization chart from the reactive power optimization study. It is shown that the most economic power factor in between transmission and distribution system is 0.97. This is because the benefit over cost ratio at power factor of 0.97 is the highest.

Table 1  
*Plant-up Strategy in Distribution System based on 120 MVAR/YR*

5 MVAr 11kV Cap Bank		180 kVAR GMLV Cap Bank		18 kVAR LVPT Cap Bank	
Percentage	No of Units	Percentage	No of Units	Percentage	No of Units
75%	18	10%	67	15%	1,000

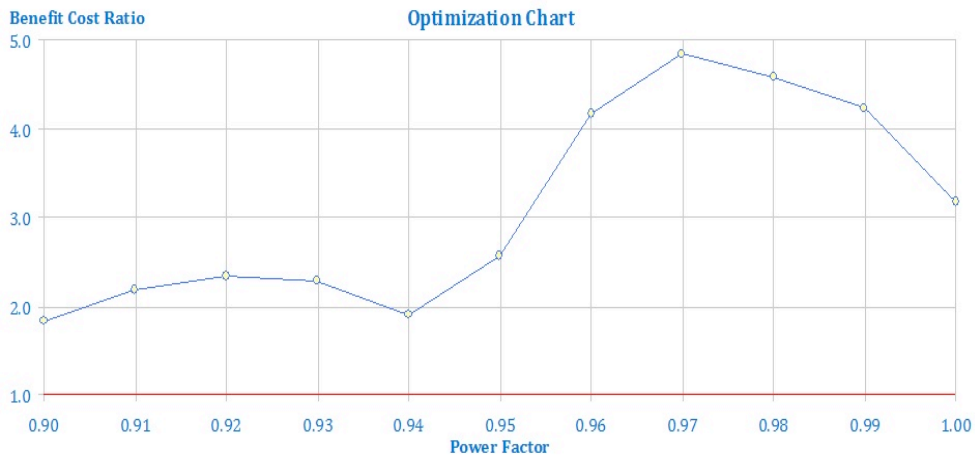


Figure 3. Benefits over cost ratio at different targeted power factor

## CONCLUSION

An integrated VAR management methodology based on techno economic analysis is proposed to determine the economic power factor in transmission and distribution networks. The proposed methodology is suitable where transmission and distribution system belongs to the same utility company. A Microsoft Access data based and automation tools was developed for short term and long term reactive power planning and analysis.

## ACKNOWLEDGEMENTS

The authors would like to thank TNB Research for financial support, and TNB Transmission and Distribution Division for their kind assistance in providing the relevant data.

## REFERENCES

- Hu, W., Dong, S., Lu, Q., Xu, F., & Lianjie Lv. (2012). Coordinated optimizing control strategy between power generators and power grid in Inner Mongolia. In *47th International Universities Power Engineering Conference (UPEC)*. London.
- Mousavi, O. A., & Cherkaoui, R. (2011). *Literature Survey on Fundamental Issues of Voltage and Reactive Power Control*. EPF Lausanne – Power System Group .
- Shourvarzi, R., Vaziri Mirzaei, M., Mehdizadeh Afroozi, N., & Rostami, M. (2012). Distribution management and optimal supply of reactive power in restructured power systems using PSO Algorithm. In *7th International Power Electronics and Motion Control Conference (IPEMC)*. Harbin.
- Singh, H., & Srivastava, L. (2012). Multi-objective Reactive Power Management using Differential Evolution. *IEEE 5th India International Conference on Power Electronics (IICPE)*. Delhi.
- U.S.-Canada Power System Outage Task Force. (2014). *Final Report on the August 14, 2003 Blackout in the United States and Canada: Causes and Recommendations*.

## **Opportunity for Using WLAN with IEC 61850 and the Future of this Protocol**

**N. H. Ali<sup>1\*</sup>, Borhanuddin. M. Ali<sup>1</sup>, O. Basir<sup>1</sup>, M. L. Othman<sup>2</sup>, F. Hashim<sup>1</sup> and E. Aker<sup>2</sup>**

<sup>1</sup>*Department of Computer and Communication Systems Engineering, Faculty of Engineering, Universiti Putra Malaysia, 43400 UPM, Serdang, Selangor, Malaysia*

<sup>2</sup>*Department of Electrical and Electronic Engineering, Faculty of Engineering, Universiti Putra Malaysia, 43400 UPM, Serdang, Selangor, Malaysia*

---

### **ABSTRACT**

The unified protocols are unified in application interface, models, and seamless. They generate one standard protocol, one world called IEC 61850. IEC 61850 integrate the security, interoperability, modelling, mapping to a substation, and reliability. Presently, the more expensive fiber based Ethernet LAN is the most prevalent technology for medium and low voltage distribution substations. To circumvent this problem Wireless Local Area Network (WLAN) has been investigated for its suitability for applications that are compliant to IEC 61850: automation and metering; control and monitoring; and over-current protection. In this paper the IEEE 802.11n WLAN is studied when used in various IEC 61850 supported applications for substation automation. It also discusses the benefits of using GOOSE message to protect and control applications and the use of IEC 61850.

*Keywords:* IEC 61850, GOOSE, WLAN, Smart Grid

---

### **ARTICLE INFO**

*Article history:*

Received: 24 August 2016

Accepted: 02 December 2016

*E-mail addresses:*

[nasir200420022000@yahoo.ca](mailto:nasir200420022000@yahoo.ca) (N. H. Ali),

[borhan@upm.edu.my](mailto:borhan@upm.edu.my) (Borhanuddin, M. Ali),

[obasir@uwaterloo.ca](mailto:obasir@uwaterloo.ca) (O. Basi),

[lutfi@upm.edu.my](mailto:lutfi@upm.edu.my) (M. L. Othman),

[fazirulhisyam.hashim@gmail.com](mailto:fazirulhisyam.hashim@gmail.com) (F. Hashim),

[hadi.aker@yahoo.com](mailto:hadi.aker@yahoo.com) (E. Aker)

\*Corresponding Author

### **INTRODUCTION**

Control and Protection engineers are often faced with many problems that can be stated with alternative easy inquiry “To IEC 61850 or Not to IEC 61850”. The answers regarding too many engineering works in control and automation in the substations is obviously yes. IEC61850 protocol is the only one that supports systems based on multi-vendor Intelligent Electronic Devices (IEDs) networked together to provide protection, monitoring, automation, metering, and control



functions. The interoperability of equipment and systems is ensured by providing compatibility between interfaces, protocols, and data models.

This paper presents stations implementing this new IEC 61850 standard and applications examples which are organized for them. The IEC 61850 standard applicability and viability as the recognized communication standard for substations automation are excellent. Therefore, it is possible with IEC 61850-GOOSE to achieve high speed communication for interlocking switchgears across bays (substations). The ‘generic object-oriented substation event’ is abbreviated as GOOSE, a service of fast communication that is independent of the communication between the client (centralized station controller) and the server (bay control unit). The WLAN is being widely organized in smart networks (Parikh et al., 2010). The WLAN was studied extensively for home automations and industrial applications due to its simplicity (Gungor et al., 2010). A few examples of research in WLAN for control, monitoring and protection have been described in (Ali et al., 2015). Numerous automation systems which use WLAN has defined in (Parikh et al., 2013) and the application of the same Wireless Local Area Network (WLAN) in substations was done as well (Abdel-Latif et al., 2009). In the above-mentioned articles, performances of wireless LAN have been evaluated for the applications of IEC 61850 based smart network supply substation. They classify possible applications of smart distribution and show that the WLAN technology can achieve technical and economic advantages in these applications. In this paper, we focus on the presentation of the ETE Delay of GOOSE message using the multipoint to point (Access Point) network. The influence of Radio Frequency Interference (RFI), and Electro-Magnetic Interference (EMI) effect, was assumed to be the Gaussian probability density function distribution. The rest of this paper is organized as follows: after this section; focuses on the GOOSE message for IEC 61850, and section 3 describes the Future for IEC 61850. Finally, the conclusion is given in section 4.

### **GOOSE MESSAGE FOR IEC 61850**

Using the goose message in control and protection application will improve the reliability, performance, and efficiency of the system. The Transmission Control Protocol (TCP) is a connection-oriented protocol, the devices at the end points establish an end-to-end connection before any data is sent. TCP protocol is more reliable, because they guarantee that data will arrive in the proper sequence. Regarding to their principles TCP cannot meet the protection application requirements. This has led to another type of communication based on a connectionless technique. Using this technique of communication between Intelligent Electronic Devices (IEDs) means there is no assurance that the data will be received. Due to that IEC 61850 protocol has presented specific mechanisms to ensure the transfer of data to the receivers.

Peer-to-peer (P2P) communication standard used for IEC 61850 makes the control and protection very attractive. P2P communications in IEC 61850 can used unicast, or multicast for data delivery, enabling the IEDs to manage and exchange of information with all devices. In order to obtain high-speed control and protection in Substation Automation Systems (SASs), the system must meet specific requirements. The performance transfer time requirements needed for control, protection, monitoring, and recording are different based on IEC 61850.



Regarding to the definition of time transfer, the GOOSE communication is much better than hardware interface communication. Priority tagging improves the performance of protection, while the availability of VLAN improves the security and flooded the network.

Protection and control based on P2P communication in compliance with IEC 61850 was designed by the way that can meet the different requirements. The concept of event model not according to commands, but based on sending an indication that particular event is happening. This way will be support high speed and reliable communication between different IEDs and enabling to replace the hardwire signal between devices by using message exchange, as a result, the protection and automation control improved. The GOOSE communication messages based on a publisher/subscriber techniques. The publisher multicast GOOSE message to the different subscriber-servers or clients. As mentioned the GOOSE message replace the hard-wired signal in IEC 61850 When it is used for protection and control, then the GOOSE message introduces a different way that ensure the received information. It used the repetition techniques with varying time interval between the recurrent message until a new variation happening. The GOOSE messages recurrent with a growing time from  $T_{min}$  to  $T_{max}$ . The reiteration with  $T_{max}$  continues forever, until the next event happens and the recurrent rate start again with  $T_{min}$  see Figure 1. The GOOSE message having data attributes likes the sequence number (sqNum) and state number (stNum) which can be used for obrusion finding. Then using GOOSE message for protection and control in substation automation system will reduce the installation cost; improve the reliability, overcoming the limitations of binary interfaces, and reduce maintenance.

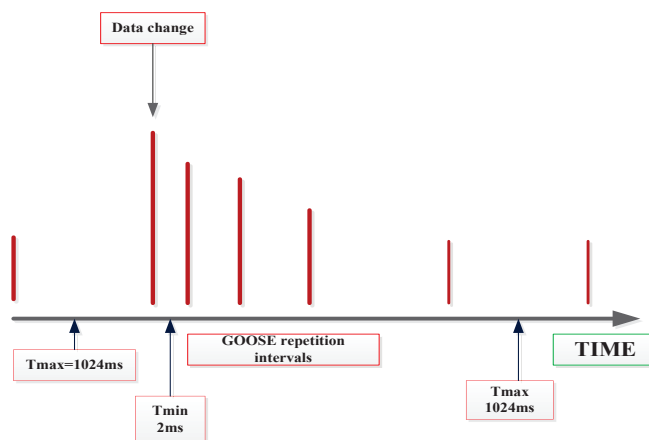


Figure 1. Reliability of the GOOSE messages

## MULTICAST GOOSE MESSAGE BENEFIT FOR FEEDER PROTECTION

Referring to Figure 2, the voltage drops when a fault occurs in feeder 2 in a distribution system results in an inrush condition after the clearing of the fault, this may lead to the undesired operation of protection elements of multifunctional relays on the healthy feeders. Once a fault on the feeder 2 that it is protecting is detected by a protection feeder IED, a GOOSE message will be sent to all other protection feeder IEDs telling them to guess an inrush as a result of the voltage recovery following the fault clearing.

Each of the protection feeder IEDs on the healthy feeders subscribes to GOOSE messages from all adjacent feeder protection IEDs and when it receives a message indicating adjacent feeder fault, it adapts its settings for the period of time that the expected inrush condition is going to last. This scenario was done as shown in Figure 2 using WLAN IEEE 802.11n with packet length 100 bytes for GOOSE message, and the fault feeder sends GOOSE message with repetition as shown in Figure 3, while the health feeder sends the GOOSE message as shown in Figure 4.

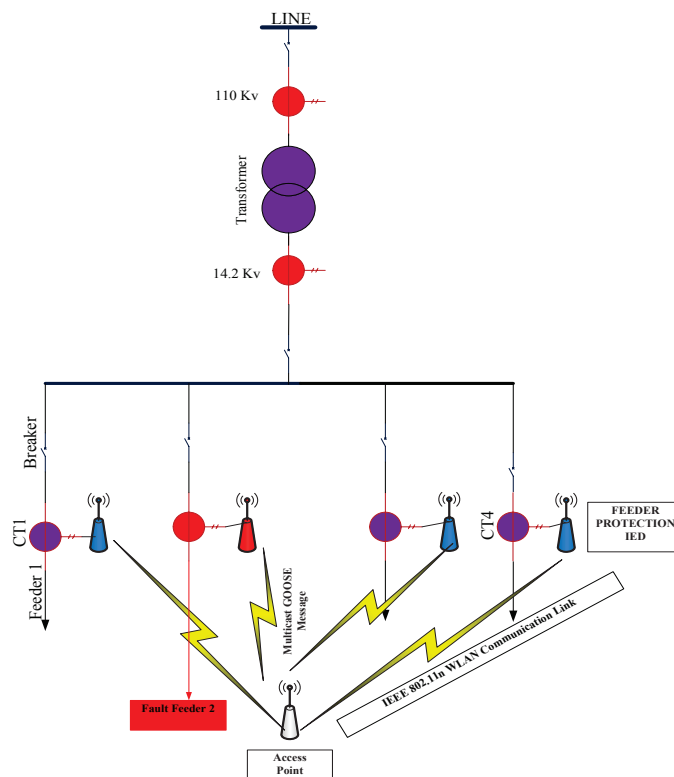


Figure 2. GOOSE message for fault feeder's distribution

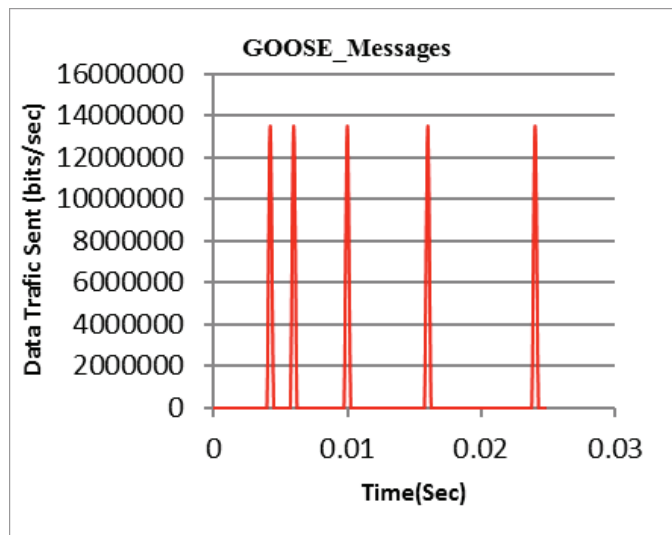


Figure 3. GOOSE message from Fault Feeders

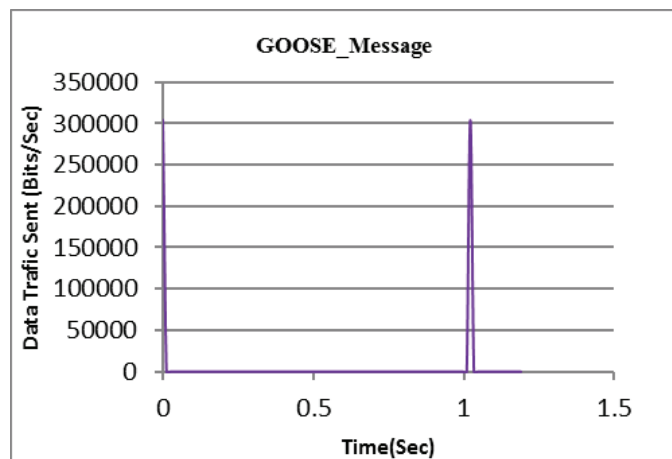


Figure 4. GOOSE message from Health Feeders

The ETE delay performance of this scenario at different path streaming and different signal to noise ratio was mentioned in Table 1. From Table 1 we can see that the ETE delay using WLAN Technology achieve the time delay requirements mentioned in IEC 61850-5. Except the case when the signal to noise ratio equal 19dB. In this scenario only require publishing and subscribing to GOOSE messages from the adjacent protection feeders' IEDs. Table 2 represent the same result at 5.0 GHz band of IEEE 802.11n, from Table 2 we can observe that delay is less compared to 2.4 GHz, but distance for 5.0 GHz is less.

Table 1  
*ETE performance for IEEE 802.11n at 2.4 GHz Band*

(S/N) signal to Noise ratio (dB)	Stream	Minimum ETE delay (ms)	Maximum ETE delay (ms)
36.5	1	0.2	0.65
29	1	0.2	0.65
19	1	10	20
22	4	0.05	0.15

Table 2  
*ETE performance for IEEE 802.11n at 5.0 GHz Band*

(S/N) signal to Noise ratio (dB)	Stream	Minimum ETE delay (ms)	Maximum ETE delay (ms)
33	4	0.055	0.085
33	1	0.070	0.090
22	1	0.090	0.095
22	4	0.06	0.09

### **CENTRALIZED LOAD SHEDDING USING WLAN GOOSE MESSAGE.**

Allocated load shedding is a new idea, in which, every individual allocation feeder to be prepared with an IED which could accomplish the function of load shedding and calculate the frequency. That means also every feeder relays requires having a voltage input that generally specifies a higher cost device of high end. Nevertheless, this kind of a device not only offers protection, but recording, measurements and other required functions also, and improved consistency of the system of load shedding.

While in centralized load shedding a single relay in the substation acts as one step of the scheme of load shedding and performs measurement of frequency at one point in the substation. When more than one step is required, extra under-frequency relays would be used.

Centralized systems of load shedding have also been used nowadays in the microprocessor based relays world. However, voltage relay and specified frequency could be used to do the functions of complex load shedding in several steps and according to different standards as specified by the plan of defence. The breakers tripping could be completed using GOOSE messages. The group of loads that need to be shed would be determined by the device of load-shedding, starting generally with lower priority loads. When using GOOSE messages, the network would receive a message suggesting which step has operated and the distribution feeder IEDs subscribing to this message would tumble their related breakers. Referring to Figure 5 the centralized shedding was implemented based on wireless LAN for three feeders communicate with centralized shedding IED using GOOSE message, the feeders send the load status each 50ms with packet length 100 bytes and each feeder having a different priority. The centralized load IED received the GOOSE message from feeders, and take voltage reading and

with advanced calculation if there is any instability in the frequency it will be send GOOSE message to trip minimum priority feeder. This simulation can be seen in Table 3 at different signal to noise ratio. The ETE delay achieved the requirement mention in IEC 61850-5. Table 4 shows the performance of WLAN at 5.0 GHz. The ETE delay at 5.0 GHz is less than at 2.4 GHz but it is more sensitive to the noise and distance between different nodes. The attribute parameter for this scenario used 100 bytes packet length, the feeder send status each 20 ms and the load shedding IED send a packet at rate 50 ms. This result was obtained using opnet 18.0 license simulators.

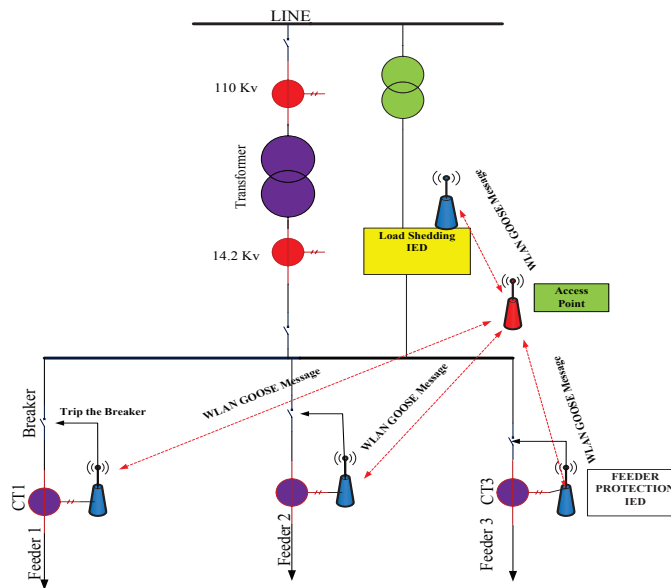


Figure 5. Centralized shedding based on wireless LAN

Table 3  
ETE performance for IEEE 802.11n at 2.4 GHz Band

(S/N) Signal to Noise ratio in (dB)	stream	Minimum ETE delay (ms)	Maximum ETE delay (ms)
20	4	0.1	1.1
35	4	0.05	0.7
36	1	0.07	1.0
24	1	0.08	1.3
18	1	0.2	3

Table 4  
*ETE performance for IEEE 802.11n at 5.0 GHz Band*

(S/N) Signal to Noise ratio in (dB)	stream	Minimum ETE delay (ms)	Maximum ETE delay (ms)
23	1	0.4	0.9
23	4	0.35	0.8
32	4	0.05	0.5
32	1	0.05	0.35
18	1	0.25	1.7

### FAST DISTRIBUTION BUS PROTECTION SCHEME

Using overcurrent relays is the normal way for protecting distribution bus. Usually, downstream feeder IEDs delays the upstream protection IED (IED-1) via coordination interval, i.e. approximately 400-500 ms or more. In the case of a fault in feeder, this coordination interval is injected to let downstream feeder IED before bus IED. Nevertheless, if there is a fault on bus, overcurrent protection of the bus would be delayed by this coordination delay (400 ms to 500 ms). Hence, delay could be extremely decreased via installing WLAN communication of a low cost as clarified below:

In this structure, peer-to-peer IEC 61850 GOOSE message could be used for signal sending from feeder protection IEDs to bus overcurrent IED. This structure needs only non-directional elements of overcurrent protective, with communication channel of a low cost (i.e. wireless LAN). In case of feeder fault, a fault would be detected by two IEDs: first, corresponding feeder IED, and second upstream bus IED. Thus, BLOCK command will immediately be sent by feeder IED using IEC 61850 GOOSE message, and the fault will be isolated by feeder IED. Furthermore, if the distribution substation bus has a fault, none of the feeder IEDs would detect the fault, and thus, no BLOCK message will be received by bus IED, and bus IED will be normally operated after an approximate delay of 60 ms. Therefore, coordination delay could be decreased from 400-500 ms down to 60 ms. The life of components installed on upstream of distribution bus will be improved by this structure, i.e. distribution transformer, as the fault current time going over these components lessens. See Figure 6. The ETE delay of GOOSE Block message can be seen in Figure 7. This delay increased as a signal to noise ratio decrease. This result was obtained when WLAN IEEE 802.11n work under single stream, and 400 ns Guard Interval, the fault feeder send GOOSE message at 1,000 Hz rate and packet length equal 100 bytes, while health feeder send GOOSE message at rate 1 sec.

### FUTURE WITH IEC 61850

IEC 61850 was originally designed based on the assumption that the bandwidth of the communication network will not be a limiting factor. For LANs with transmission speeds of 100 Mbit/s or greater, this assumption holds true in most cases. But for SS-to-SS communication,

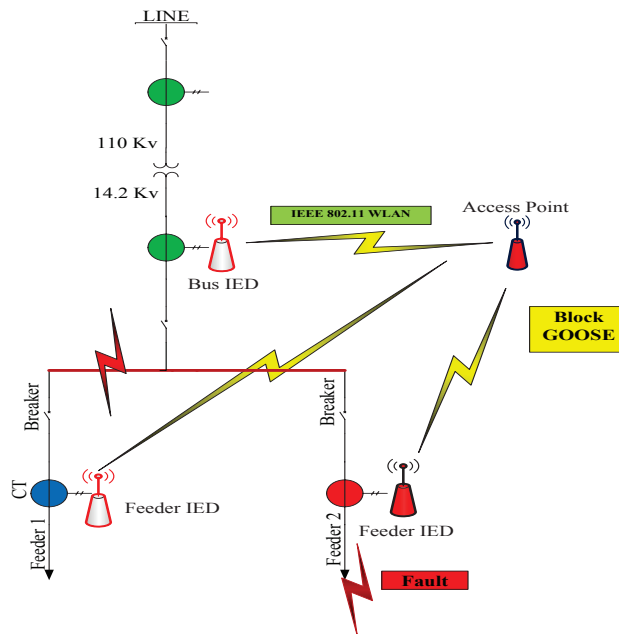


Figure 6. The concept of the fast distribution bus protection scheme

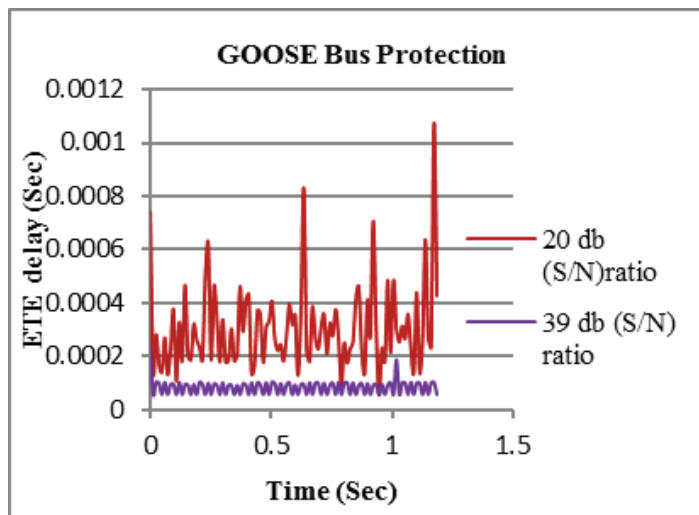


Figure 7. ETE GOOSE Message for Fast Bus protection

such communication paths generally does not exist requiring bandwidth limits be taken into account.

Apart from possible performance issues, the function D2 in station D shall be able to access function E2 in station E as if both would reside in the same local substation network.

There are two methods for that tunnelling approach and gateway approach as mentioned in IEC 61850-90-1. See Figure 8.

The operations of communication between SS-CC are described regarding to the different use situations. In this domain three main groups of users can be known. Distribution system operators (DSO), industrial power system operators and Transport system operators (TSO). Their conditions on the SS-CC communication are very different. There are two ways for communication between SS-CC to access the IEDs in the substation, first, using direct communication or using proxy/gateway as shown in Figure 9.

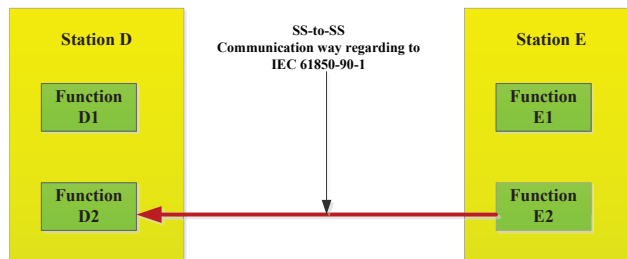


Figure 8. Substation to substation communication

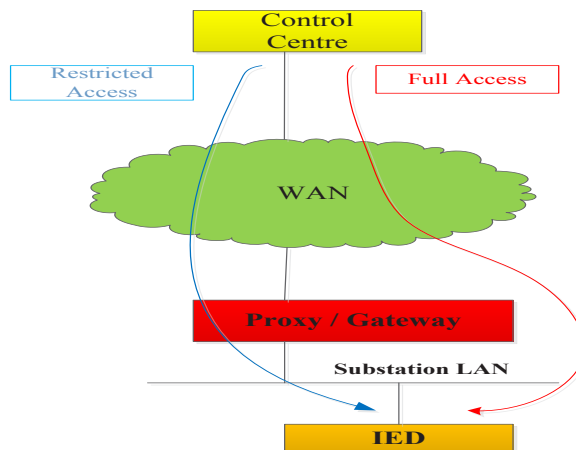


Figure 9. Proxy/gateway concept



## FULL ACCESS

Full access functions control Centre access the IEDs directly without pass through proxy/gateway. This allows performing the same operations with the device as if it would be connected to the same network. Cyber security must be afforded for the connection to fulfil the security demands. “Tunnelling” is a way to join multiple communication networks. Using tunnelling as a communication link the substation network it becomes as a part of control centre network. The control centre can address the devices in substation network directly. Tunnel will be known by switch and routers in the network. The router can be connected to two independent communication path infrastructures to achieve redundancy. This way will provide communication path failure protection. Parallel redundancy for communication failure protection fit the demands of the industrial power system and other applications. For example, the remote services of IEDs (Figure 10).

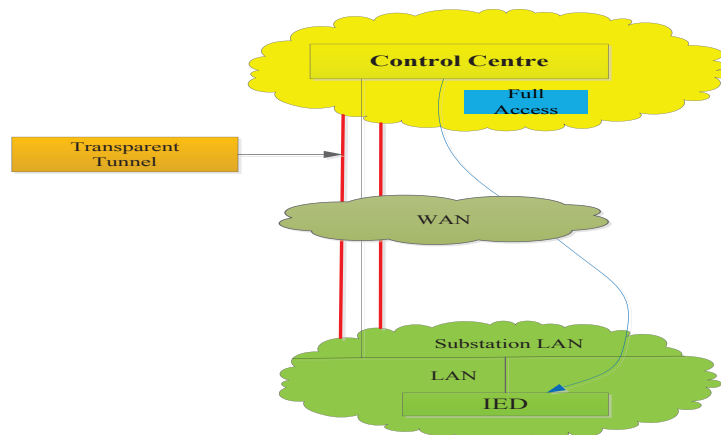


Figure 10. Full access to IED

## RESTRICTED ACCESS

The restricted access is used for different applications, and not limited to, SCADA applications. Restricted access application means that there is no direct access the devices. Presented data and services by proxy/gateway only can be used by those devices. The proxy idea has been part of the IEC61850 protocols standard from the beginning. It defines devices that present one by one copy of logical devices from other IEDs to a client. The proxy/gateway has been extended for the function of the SS-CC communications to enables the renaming and rearrangement of information. This enables condensing and filters substation data. Furthermore, renames the data to switch from device oriented addressing to topological addressing. Then proxy/gateway access method improve the security because only those device data and services which are accessible from the outside that are configured in the proxy/gateway. IEC62351 is used for the SS-CC link to provide cyber security.

IEC 61850 Growth dramatically and will be used in Hydro power (IEC 61850-7-410), Distributed energy resources (IEC 61850-7-420), wind power (IEC 61400-25), Gate way mapping to IEC 60870-5-101/104 (IEC 61850-80-1), Between substations (IEC 61850-90-1), Between substation and control Centre (IEC 61850-90-2), GOOSE and Process Bus over IP Multicast for Synchrophasor communication (IEC 61850-90-5), and new mapping for IEC 61850 for using in the smart grid or web services. To integrate DER with IEC 61850 over Extensible Messaging and Presence Protocol (XMPP), The IEC 61850 specifies a method of exchanging non-time-critical data through any kinds of network, including public networks, using IEC 61850-8-2 Specific communication service mapping (SCSM) – Mapping to Extensible Messaging Presence Protocol (XMPP). The IEC 61850-8-2 is complementary to the existing SCSM (8-1); not competing sees Figure 11, and Figure 12 for more details.

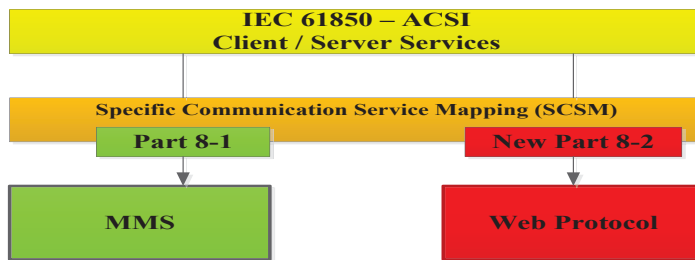


Figure 11. Specific communication service mapping- Mapping to Extensible Messaging Presence Protocol

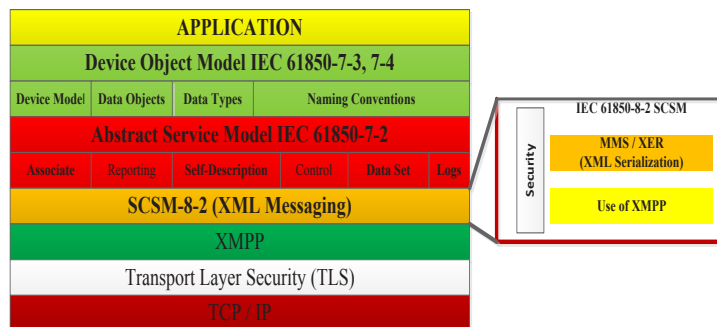


Figure 12. Protocol Stack for IEC 61850-8-2

## CONCLUSION

The GOOSE model lets the protection development, as well as the development of control systems, that give some important advantages comparing to conventional hard-wired systems. The GOOSE benefit includes reduced installation costs, improved flexibility, improved interoperability, reliability and performance, reduced maintenance. IEC 61850 substation architectures provide significant benefits to users and flexibility to accomplish new objectives that are too costly with legacy technology. Justification is challenging but realistic. IEC 61850-

8-2 extends the IEC 61850 technology by a mapping based on XMPP. It provides a secure and powerful communication for public networks considering end-to-middle and end-to-end security relations, IEC 61850-8-2 is intended to use for power management and demand response of DER (distributed energy resources).

## REFERENCES

- Abdel-Latif, K. M., Eissa, M. M., Ali, A. S., Malik, O. P., & Masoud, M. E. (2009). Laboratory investigation of using Wi-Fi protocol for transmission line differential protection. *IEEE Transactions on Power Delivery*, 24(3), 1087-1094.
- Ali, N. H., Ali, B. B. M., Basir, O., Othman, M. L., & Hashim, F. B. (2015, December). WLAN oriented optimization of process bus in IEC 61850-based substation communication network. In *3rd International Renewable and Sustainable Energy Conference (IRSEC)* (pp. 1-6). IEEE.
- Gungor, V. C., Lu, B., & Hancke, G. P. (2010). Opportunities and challenges of wireless sensor networks in smart grid. *IEEE transactions on Industrial Electronics*, 57(10), 3557-3564.
- Parikh, P. P., Kanabar, M. G., & Sidhu, T. S. (2010, July). Opportunities and challenges of wireless communication technologies for smart grid applications. In *IEEE PES General Meeting* (pp. 1-7). IEEE.
- Parikh, P. P., Sidhu, T. S., & Shami, A. (2013). A comprehensive investigation of wireless LAN for IEC 61850-based smart distribution substation applications. *IEEE Transactions on Industrial Informatics*, 9(3), 1466-1476.





## Enhancement of DNA Microarray Images using Mathematical Morphological Image Processing

Asral Bahari Jambek<sup>1\*</sup>, Khairul Anuar Mat Said<sup>1\*</sup> and Nasri Sulaiman<sup>2,3</sup>

<sup>1</sup>*School of Microelectronic Engineering, Universiti Malaysia Perlis, Perlis, Malaysia*

<sup>2</sup>*Department of Electrical and Electronic Engineering, Faculty of Engineering, Universiti Putra Malaysia, 43400 UPM, Serdang, Selangor, Malaysia*

<sup>3</sup>*Institute of Advance Technology (ITMA), Universiti Putra Malaysia, 43400 UPM, Serdang, Selangor, Malaysia*

### ABSTRACT

DNA microarray images contain spots that represent the gene expression of normal and cancer samples. As there are numerous spots on DNA microarray images, image processing can help in enhancing an image and assisting analysis. The mathematical morphology is proposed to enhance the microarray image and analyse noise removal on the image. This follows an experiment in which the erosion, dilation, opening, closing, white top-hat (WTH) and black top-hat (BTH) operations were applied on a DNA microarray image and its results analysed. Noise was completely removed by the erosion operation and the images were enhanced.

*Keywords:* DNA microarray image, mathematical morphology, image enhancement

### INTRODUCTION

Microarray technology is widely known for allowing scientists to analyse the gene expression. Furthermore, microarrays make it easier to compare between normal and cancerous cells. For this study, deoxyribonucleic acid (DNA) microarray

containing microscopic DNA spots were deposited on the surface of a glass slide. Firstly, two samples of cDNAs (normal and cancerous cells) were labelled with different fluorescent dyes (Cy3 and Cy5) (Belean et al., 2015; Helmy & El-taweel, 2013). Then, both samples were hybridized on the same glass slide. The glass slide was scanned using a green and red laser after the hybridization process was completed. A composite image was produced and the intensities of each spot were analysed. The sample that was labelled using Cy3 produced a green colour, while the sample labelled using Cy5 produced a red colour. If the two samples were in equal abundance, the yellow colour would have

### ARTICLE INFO

#### *Article history:*

Received: 24 August 2016

Accepted: 02 December 2016

#### *E-mail addresses:*

asral@unimap.edu.my (Asral Bahari Jambek),

anuarsaid91@gmail.com;

keoinuar@gmail.com (Khairul Anuar Mat Said),

nasri\_sulaiman@upm.edu.my (Nasri Sulaiman)

\*Corresponding Author

appeared; if neither sample was present, it would have appeared as a black colour (Qin et al., 2005). Therefore, the gene expression of the DNA microarray images can be monitored. The DNA microarray images may contain noises and contaminations arising from the scanning process or other previous process stages (Qin et al., 2005; Wang et al., 2013). These problems can affect the whole microarray image process. Thus, image processing is proposed as a means to minimize or eliminate such problems.

Microarray image processing contains the following three stages: (1) gridding, which is a process of segmenting the microarray image into partitions, with each partition having only one spot; (2) segmentation, which is a process of differentiating between the foreground and background features; and (3) intensity extraction, which is a process of calculating the intensity that is available on the image (Harikiran et al., 2012; J et al., 2011). The noises on the microarray image are a major problem during the entirety of image processing. Some of them may generate wrong information about the gene expression. Besides, missing spots on the microarray image may also appear. Thus, the process of spot recognition is a difficult as the microarray image consists of noises that interrupt the image acquisition (J et al., 2013). It is more convenient if the noise is removed or minimized early. Image enhancement is an important method because it can recover several useful details of the image (Bai et al., 2012).

In this paper, mathematical morphological image processing was performed on a DNA microarray image and analysed. The operations were programmed using the MATLAB software; the output image for each operation is discussed. In the literature review several applications that have used mathematical morphology in image processing are presented, and followed by an explanation of the methodology adopted. The section on result and discussion all the experimental results are discussed, and followed by the conclusion.

## LITERATURE REVIEW

Mehta et al. (2015) proposes the combination of pre-processing morphology and entropy calculation to enhance the ultrasound images of the gall bladder. The ultrasound images are first converted into greyscale and then into a black and white image using a threshold filter. The threshold value of this work is set at 0.18. By converting the image into a black and white able to distinguish between the foreground and background features. The erosion and dilation operations are used to improve the clarity of the image, in which the erosion shrinks the foreground features, while the dilation enlarges the foreground features. Results show the ultrasound image clearly shows the location of the gallstone and is better than the input image.

Mittal & Dubey (2013) proposes using morphological image processing for early detection of rheumatoid arthritis (RA). This disease is commonly caused by inflammation in the joints, fingers and knees. The erosion process shrinks the foreground features of the image, while the dilation process enlarges the foreground features of the image. Both processes use the same structuring element (SE) as a probe, while showing that morphological image processing provides a better understanding of the ultrasound image and monitoring of RA.

Yuan & Li (2015) demonstrates a switching morphological and median (SMM) filter for noise removal. Morphological operations, such as erosion, dilation, opening and closing, are applied in order to eliminate the noise. The noise pixel can be estimated by combining the output

of the conditional morphological filter with that of the improved median filter. This method produces higher peak signal-to-noise ratio (PSNR) values compared to boundary discriminative noise detection (BDND), fast switching median (FSM), convolution noise detection-based switching median (CNDSM), opening-closing sequence (OCS), efficient edge-preserving (EEP) and noise adaptive fuzzy switching median (NAFSM) filters. Based on the result, the proposed method removes the noise effectively and the details of the image are well preserved.

Rong-yu et al. (2012) are concerned with observing space objects using a full-frame transfer CCD camera to detect and locate stars and moving objects in space. During the observation, the CCD images that are produced contain a smearing effect because the camera shutter is often removed. The effect degrades the image quality and increases the difficulty of object recognition. The author proposes mathematical morphology in order to eliminate the smearing effect as well as improve the detection rates and position accuracies of stars and moving objects. The dilation operation filters the maximum value depending on the structural body. The erosion operation filters the minimum value depending on the structural body. The opening operations eliminate the bright details that reduce the size of a structural body. The closing operation eliminates the dark details that reduce the size of an SE. This paper uses TopHat and Spread TopHat methods to remove the long-strip signals in the CCD image. The structural body plays an important role in morphological results, such that different structural bodies give different results. Results show mathematical morphology improves the detection rate and position accuracies of stars and moving objects by eliminating the smearing effect.

Zhang et al. (2011) proposes using an improved morphological edge detection method for an edge detection operator and an iterative thresholding method for a better thresholding value in order to identify foreign fibres in cotton products. Dilation and erosion algorithms are used in the edge detection operator. Each colour (R, G and B) is then taken into account in the image, while the improved morphological edge detection consists of the edge detection for each colour, which is called the edge intensity value; if the value of it is greater than the given threshold, it is considered as edge pixels from the image. Therefore, the iterative method is a method to select the threshold value automatically because different situations lead to different light intensities. Based on the result, the proposed methods provide a better accuracy for the segmentation of foreign fibres and improve the processing time compared to conventional methods.

Mathematical morphological image processing operations helps to enhance the features on the image. Different applications will use different operations of mathematical morphology. Table 1 shows the comparison between different applications that apply mathematical morphological operation, which will be discussed later. Yuan & Li (2015) uses the SMM filter to determine the noise pixels in relation to the removal process. TopHat and Spread TopHat transforms in method (Rong-yu et al., 2012) are discussed, in which the smearing effect may be eliminated by choosing suitable SEs. Zhang et al. (2011) uses a combination of morphological edge detection and iterative thresholding to improve the segmentation process in order to identify foreign fibres in cotton. From the five applications, it can be seen that mathematical morphological operations may enhance the image and preserve image information well. In the next section, the experiment undertaken in this work is presented.

Table 1  
Comparison of different applications

Method	(Mehta et al., 2015)	(Mittal & Dubey, 2013)	(Yuan & Li, 2015)	(Rong-yu et al., 2012)	(Zhang et al., 2011)
Application	Medical	Medical	Case study	Astronomy	Agriculture
Type of image	Colour	Greyscale	Greyscale	Greyscale	Colour
Threshold	Yes	No	No	No	Yes
Accuracy	N/A	N/A	N/A	N/A	N/A
Complexity	Low	Low	Normal	Normal	Normal
Special feature	N/A	N/A	SMM	TopHat and Spread TopHat	Morphological edge detection and iterative thresholding

## METHODOLOGY

This section discusses mathematical morphological image processing of microarray image (Microarrays Inc., 2016). The mathematical morphological process is programmed using the MATLAB software. Figure 1(a) shows a part image with a size of  $441 \times 431$  pixels, compared with the real microarray image of  $2200 \times 7300$  pixels, which is used as the input image for this work. Figure 1 (b) shows the SE that is used as a probe for mathematical morphology. An SE of a disk shape, with a radius of four pixels, is chosen as the input image to be used, containing DNA spots, which are generally in circle shape. Therefore, the disk shape in structuring is used to produce similarity with the information interest on the input image. The spots on the input image provide the important information, so that the SE of mathematical morphology may enhance the spots area that forms the background. The size of the SE depends on the spot size. In this work, the radius of four pixels is chosen because the average size (diameter) of the spots on the input image is 8~9 pixels.

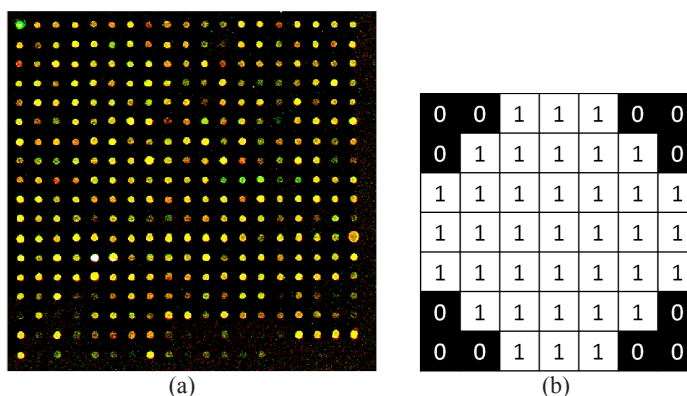


Figure 1. (a) Input image of a  $441 \times 431$  pixels region from a real microarray image of  $2200 \times 7300$  pixels; (b) the SE of a disk shape with a radius of four pixels



## Mathematical Morphological Image Processing

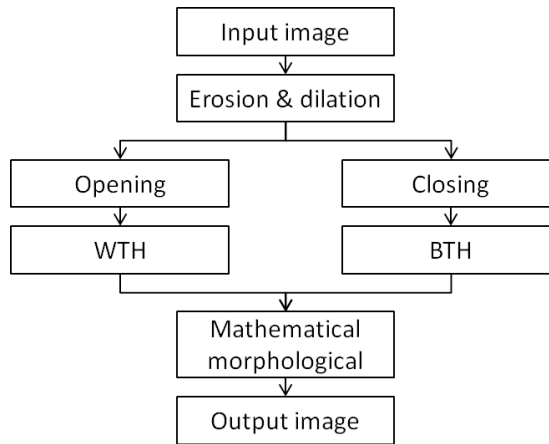


Figure 2. The flowchart of mathematical morphological image processing

Figure 2 shows the flowchart of mathematical morphological image processing where the basic process is erosion and dilation. Erosion is a process of removing the foreground features of an image, while dilation is a process of adding the foreground features on the image. Both the erosion and dilation processes depend on the SE. Opening is a process to remove the foreground objects that are smaller than the SE. Closing is a process of removing the background objects that smaller than the SE. Both opening and closing control the uses of erosion and dilation to enhance the foreground and background features. During the opening, the input image (IM) will undergo erosion first, followed by dilation. Meanwhile, in closing, the IM will undergo dilation first, followed by erosion. The major process of mathematical morphology involves the white top-hat (WTH) and the black top-hat (BTH). The WTH enhances the foreground features on the image in line with the different results obtained between the IM and the opening operation. BTH enhances the background features of an image giving results that differ from the closing operation and the IM. Mathematical morphology is the result of the IM added to the WTH, then subtracted from the BTH. The opening, closing, WTH, BTH and overall operations are defined as follows (Li et al. 2015):

$$\textit{Opening} = \textit{IM} \ominus \textit{SE} \oplus \textit{SE} \quad (1)$$

$$\textit{Closing} = \textit{IM} \oplus \textit{SE} \ominus \textit{SE} \quad (2)$$

$$\textit{WTH} = \textit{IM} - \textit{Opening} \quad (3)$$

$$\textit{BTH} = \textit{Closing} - \textit{IM} \quad (4)$$

$$\text{Mathematical morphological} = IM \oplus WTH - BTH \quad (5)$$

where  $\ominus$  and  $\oplus$  respectively denote the erosion process and the dilation process.

## RESULTS AND DISCUSSION

In the previous section, the mathematical morphological algorithm was presented. The algorithm was run on the input image as shown in Figure 1(a) using the SE shown in Figure 1 (b). In this section, the experimental result for each process in the mathematical morphological operation will be presented. All the workings are performed using the MATLAB software running on the Windows operating system. Firstly, the input image will convert into the greyscale image, as shown in Figure 3 (a). The image result for each operation is zoomed in with  $161 \times 166$  pixels, which contain  $7 \times 7$  spots for ease of analysing and understanding each operation, as shown in Figure 3 (b).

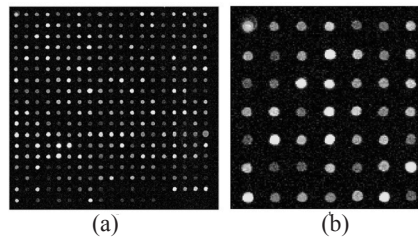
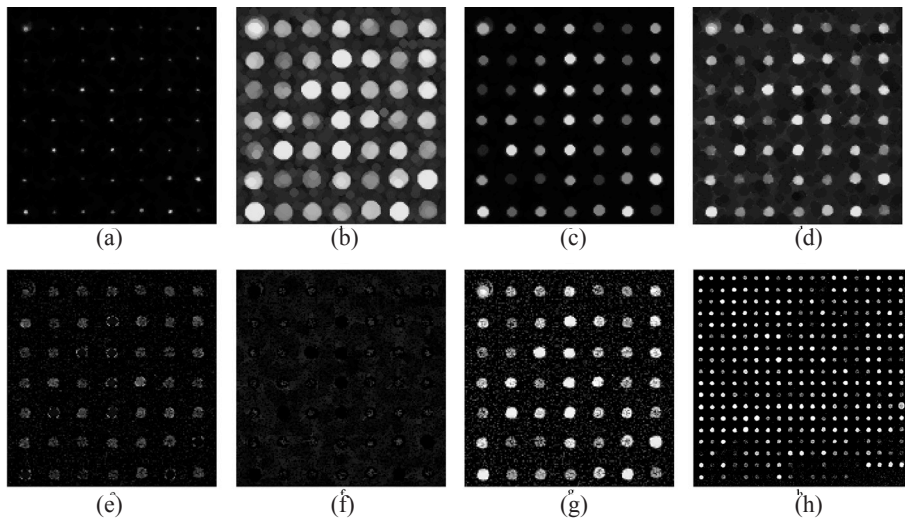


Figure 3. (a) The greyscale image of the input image; (b) the rescale input image consists of  $7 \times 7$  spots

### Opening, Closing, Erosion and Dilation Operations

The erosion operation shrinks the foreground features depending on the SE, as shown in Figure 4 (a). Based on the result, the spots (foreground features) on the image shrink due to the erosion operation. The shrinking causes a decrease in the foreground area compared to the input image. At this point, the noises that are smaller than the SE are completely removed. Besides, the spots that are smaller than the SE can also be removed, so selecting the appropriate size of the SE is important for this operation. The dilation operation enlarges the foreground features depending on the SE, as shown in Figure 4 (b). Based on the result, the spots (foreground features) on the image become larger due to the dilation operation. The enlargement causes a decrease in the background area compared to the input image. At this point, the noises are also enlarged with the spots which might combine with other foreground features if the size of the SE is too large.

In the opening and closing operations, opening is a process to remove the foreground objects that are smaller than the SE while closing is a process of removing the background objects that are smaller than the SE. From the result in Figure 4 (c), it shows that the opening operation removes the foreground object that is smaller than the SE compared to the input image. Based on the result, the opening operation is generally run as the dilation operation on the image result from the erosion operation in Figure 4 (a). From the erosion operation, the foreground object that is smaller than the SE is already removed. Thus, the opening operation is



*Figure 4.* (a) The result of the erosion operation; (b) the result of the dilation operation; (c) the result of the opening operation; (d) the result of the closing operation; (e) the result of the WTH operation; (f) the result of the BTH operation; (g) the result of the mathematical morphological operation; (h) the final result of the full scale of the input image

the result of the enlargement of the foreground object that remains after the erosion operation. The opening operation follows the mathematical theoretical state, as given at (1).

The result in Figure 4 (d), shows that the closing operation removes the background object that is smaller than the SE compared to the input image. Based on the result, the closing operation is generally run alongside the erosion operation on the image resulting from the dilation operation in Figure 4 (b). From the dilation operation, the foreground features are enlarged, with some of them combining with other spots or noises. Thus, the closing operation is the result of shrinking the foreground object on the image resulting from the dilation operation. The closing operation follows the mathematical theoretical state given at (2).

### **Mathematical Morphological, WTH and BTH Operations**

Next, the major operations in mathematical morphology take place, which concern the WTH and the BTH. The WTH is the difference between the input image and the opening operation result, as stated in (3). Based on the result in Figure 4 (e), the pixel in the remaining in the foreground is better than the image of the opening operation. The BTH is the difference between the closing operation result and the input image, as stated in (4). Based on the result in Figure 4 (f), the foreground features that remain are the exceeded pixels in the foreground on the image result from the closing operation compared to the input image. Finally, from the result of the WTH and the BTH, the enhancement of the image can be produced. The mathematical morphological operation is a process where the input image is added to the image produced from the WTH operation which is then subtracted with the image result from the BTH operation, as stated in (5). Based on the result in Figure 4 (g), the image becomes sharper and clearer compared to the input image. Figure 4 (h) shows the final result of mathematical morphology on the full-scale input image (Figure 3 (a)).

## CONCLUSION

This paper shows the mathematical morphological image processing has better enhancement of the microarray image. The erosion and dilation are the fundamental operations to the mathematical morphology, while the opening and closing operations to enhance the foreground and background features, respectively. Lastly, the mathematical morphological operation produces the enhancement image by adding the input image and the WTH image, and then subtracting the BTH image. The results show the mathematical morphological image processing compared to the input image. Besides, during the erosion operation, the noises are completely removed.

## ACKNOWLEDGEMENT

This research was supported by the Science Fund 2015 from the Ministry of Science, Technology and Innovation (MOSTI), Malaysia.

## REFERENCES

- Bai, X., Zhou, F., & Xue, B. (2012). Image enhancement using multi scale image features extracted by top-hat transform. *Optics and Laser Technology*, 44(2), 328–336.
- Belean, B., Terebes, R., & Bot, A. (2014). Low-complexity PDE-based approach for automatic microarray image processing. *Medical and Biological Engineering and Computing*, 53(2), 99–110.
- Harikiran, J., NarasimhaRao, Y., Saichandana, B., Lakshmi, P. V., & Kiran Kumar, R. (2012). Spot Edge Detection in Microarray Images Using Bi-Dimensional Empirical Mode Decomposition. *Procedia Technology*, 4, 227–231.
- Helmy, A. K., & El-Taweel, G. S. (2013). Regular gridding and segmentation for microarray images. *Computers and Electrical Engineering*, 39(7), 2173–2182.
- J, N., Rangarajan, L., S.S, M., & .N, H. K. (2011). Application of Mathematical Morphology for the Enhancement of Microarray Images. *International Journal of Advances in Engineering & Technology*, 1(5), 329–336.
- J, N., S, M. S., & Pradeep, D. (2013). A Fully Automatic Approach for Enhancement of Microarray Images. *Journal of Automation and Control Engineering*, 1(4), 285–289.
- Li, N., Jia, L., & Zhang, P. (2015). Detection and volume estimation of bubbles in blood circuit of hemodialysis by morphological image processing. In *Proceedings of the 2015 7th IEEE International Conference on Cybernetics and Intelligent Systems, CIS 2015 and Robotics, Automation and Mechatronics, RAM 2015* (pp. 228–231).
- Mehta, N., Arya, L., & Pant, M. (2015). A Novel Approach for the Analysis of US Images. *Computing for Sustainable Global Development (INDIACom), 2015 2nd International Conference*, 868–872.
- Microarrays Inc. (2016). Expert Laboratory Services. Retrieved February 19, 2016, from <http://www.microarrays.com/services.php>

- Mittal, A., & Dubey, S. (2013). Analysis of MRI images of Rheumatoid Arthritis through morphological image processing techniques. *International Journal of Computer Science Issues*, 10(2), 118–122.
- Qin, L., Rueda, L., Ali, A., & Ngom, A. (2005). Spot detection and image segmentation in DNA microarray data. *Applied Bioinformatics*, 4(1), 1–11.
- Rong-Yu, S., Chang-Yin, Z., Yi-ding, P., Jian-Ning, X., & Chen, Z. (2012). Use of Mathematic Morphological Operators for Processing the Smearred Images of A Camera without Shutter. *Chinese Astronomy and Astrophysics*, 36(3), 340–352.
- Wang, Z., Zineddin, B., Liang, J., Zeng, N., Li, Y., Du, M., ... Liu, X. (2013). A novel neural network approach to cDNA microarray image segmentation. *Computer Methods and Programs in Biomedicine*, 111(1), 189–198.
- Yuan, C., & Li, Y. (2015). Switching median and morphological filter for impulse noise removal from digital images. *Optik*, 126(18), 1598–1601.
- Zhang, X., Li, D., Yang, W., Wang, J., & Liu, S. (2011). A fast segmentation method for high-resolution color images of foreign fibers in cotton. *Computers and Electronics in Agriculture*, 78(1), 71–79.





## Memory Polynomial with Binomial Reduction in Digital Pre-distortion for Wireless Communication Systems

Hong Ning Choo<sup>1\*</sup>, Nurul Adilah Abdul Latiff<sup>1</sup>, Pooria Varahram<sup>2</sup> and Borhanuddin Mohd Ali<sup>1</sup>

<sup>1</sup>Department of Computer and Communication Systems Engineering, Faculty of Engineering, Universiti Putra Malaysia, 43400 UPM, Serdang, Selangor, Malaysia

<sup>2</sup>Department of Electronic Engineering, National University of Ireland Maynooth, Maynooth, Co. Kildare, Ireland

### ABSTRACT

One of the biggest power consuming devices in wireless communications system is the Power Amplifier (PA) which amplifies signals non-linearly when operating in real-world systems. The negative effects of PA non-linearity are energy inefficiency, amplitude and phase distortion. The increases in transmission speed in present day communication technology introduces Memory Effects, where signal spreading happens at the PA output, thus causing overhead in signal processing at the receiver side. PA Linearization is therefore required to counter the non-linearity and Memory Effects. Digital Pre-distortion (DPD) is one of the outstanding PA Linearization methods in terms of its strengths in implementation simplicity, bandwidth, efficiency, flexibility and cost. DPD pre-distorts the input signal, using an inversed model function of the PA. Modelling of the PA is therefore vital in DPD, where the Memory Polynomial Method (MP) is used to model the PA with memory effects. In this paper, the MP method is improved in Memory Polynomial using Binomial Reduction method (MPB-imag-2k). The method is simulated using a modelled ZVE-8G Power Amplifier and sampled 4G (LTE) signals. It was found MPB-imag-2k is capable of achieving comparable anti-scattering/anti-distortion in MP for non-linearity order of 3, memory depth of 3 and pre-amplifier gain of 2.

*Keywords:* Power Amplifier, PA Linearization, Digital Pre-Distortion, 4G, Memory Polynomial

### ARTICLE INFO

#### Article history:

Received: 24 August 2016

Accepted: 02 December 2016

#### E-mail addresses:

eddiechoohn@gmail.com (Hong Ning Choo),  
nuruladilah@upm.edu.com (Nurul Adilah Abdul Latiff),  
pooria.varahram@nuim.ie (Pooria Varahram),  
borhan@upm.edu.com (Borhanuddin Mohd Ali)

\*Corresponding Author

### INTRODUCTION

The non-linearity of the Power Amplifier (PA) causes output signal distortion in amplitude and phase (Chen et al., 2014; Choo, 2012; Choo et al., 2013; Ding et al., 2004; Ding, 2004; Liu et al., 2014; Morgan et al., 2006; Parta et al., 2014; Pinal & Pere, 2007). The

simplistic solution of avoiding the PA's non-linearity is to back-off the PA to operate only in the linear region. Besides resulting in poor energy efficiency, the backed-off solution causes higher operational cost. Today's high speed transmission technology such as Wideband Code Division Multiple Access (WCDMA) and Orthogonal Frequency Division Multiplexing (OFDM) causes high Peak to Average Power Ratios (PAPR) in communication systems, which encourages the PA to be backed off further from its saturation point. Low efficiency of the PA contributes to waste of power, which is an undesired additional cost in the telecommunication industry. The business needs of the industry justify the demand of linearizing the PA, to eliminate the undesired effects of inefficiency, distortions and power wastage.

The Digital Pre-Distortion (DPD) technique linearizes the cheaper non-linear power amplifiers, resulting in a lower overall cost of the communication system (Choo, 2012; Choo et al., 2013; Techsource-asia, 2012; Varahram et al., 2010). DPD offers many advantages in terms of cost, power management, reliability and handling if compared to the other analog methods (Choo, 2012; Choo et al., 2013; Varahram et al., 2009; Varahram et al., 2010).

<b>Nomenclature</b>	
DPD	Digital Pre-distortion
OFDM	Orthogonal Frequency Division Multiplexing
MOR	Multiplication Operations Reduction
MP	Memory Polynomial
MPB	Memory Polynomial with Binomial Reduction
PA	Power Amplifier
PAPR	Peak to Average Power Ratios
WCDMA	Wideband Code Division Multiple Access

## **MODEL DESCRIPTION**

### **Digital Pre-distortion (DPD)**

The pre-distorter behaves as an inversed function of the PA. The PA input signal is first pre-distorted at the pre-distorter, and then directed into the PA. The two connecting sequential functions: inversed non-linear pre-distorter and the non-linear PA, results in a linear output (Pinal & Pere, 2007; Techsource-asia, 2012; Varahram et al., 2009; Varahram et al., 2010).

Digital Pre-distortion (DPD) is where the pre-distortion is conducted at baseband digital domain. DPD is one of the most cost effective PA linearizing methods with the least compromise on efficiency (Ding et al., 2004; Ding, 2004; Varahram et al., 2009; Varahram et al., 2010; Choo, 2012; Techsource-asia, 2012; Choo et al., 2013; Chen et al., 2014). Accurate modelling of the non-linearity PA is required in-order to calculate the pre-distorter function as an inversed model of the PA.



### Memory Polynomial (MP)

Volterra Series is traditionally used to model non-linear systems. However, the complexity increases exponentially when the PA non-linearity order increases 0-0. The Memory Polynomial (MP) method utilizes the diagonal kernels of the Volterra Series, resulting in a reduced number of coefficients. MP is widely explored and built on top in (Chen et al., 2014; Liu et al., 2014; Morgan et al., 2006; Xie & Zeng, 2012; Yu & Jiang 2013). The MP method is shown below (Ding et al., 2004; Ding, 2004):

$$z(n) = \sum_{\substack{k=1 \\ k \text{ odd}}}^K \sum_{q=0}^Q a_{kq} x(n-q) |x(n-q)|^{k-1} \quad (1)$$

Where  $Q$  is the memory depth,  $K$  is the non-linearity order.  $x(n)$  is the PA Input Signal, and is  $a_{ka}$  the inversed of the PA coefficients, which is also the MP coefficients.

The Least Squares (LS) method is used to obtain the MP coefficients (Ding et al., 2004; Ding, 2004). The input signal  $x(n)$  is replaced with the output signal  $y(n)$ , yields the following:

$$z(n) = \sum_{\substack{k=1 \\ k \text{ odd}}}^K \sum_{q=0}^Q a_{kq} y(n-q) |y(n-q)|^{k-1} \quad (2)$$

(2) in matrix form:

$$z = Y \cdot a \quad (3)$$

Where

$$z = [z(0), z(1), \dots, z(N-1)]^T \quad (4)$$

$$Y = [y_{10}, \dots, y_{K0}, \dots, y_{1Q}, \dots, y_{KQ}] \quad (5)$$

$$y_{KQ} = [y_{KQ}(0), y_{KQ}(1), \dots, y_{KQ}(N-1)]^T \quad (6)$$

$$a = [a_{10}, \dots, a_{K0}, \dots, a_{1Q}, \dots, a_{KQ}]^T \quad (7)$$

The least square solutions in (3) could be rewrite as:

$$a = (Y^{conj} \cdot Y)^{-1} Y^{conj} z \quad (8)$$

**Memory Polynomial with Binomial Reduction (MPB)**

The MP equation in (1) is rephrased, where non-linearity order,  $k$ , and linearity order,  $q$  starts from 0:

$$z(n) = \sum_{k=0}^K \sum_{q=0}^Q a_{kq} x(n-q) [x(n-q)_{real}^2 + x(n-q)_{imag}^2]^k \tag{9}$$

Using the binomial theorem below

$$(x + a)^n = \sum_{k=0}^n \binom{n}{k} x^k a^{n-k} = \sum_{k=0}^n \binom{n}{k} a^k x^{n-k} \tag{10}$$

The non-linear portion of the basis function is restructured as:

$$[x(n-q)_{real}^2 + x(n-q)_{imag}^2]^k = x(n-q)_{imag}^{2k} \sum_{h=0}^k \binom{k}{h} \left[ \frac{x(n-q)_{real}}{x(n-q)_{imag}} \right]^{2h} \tag{11}$$

$$[x(n-q)_{real}^2 + x(n-q)_{imag}^2]^k = x(n-q)_{real}^{2k} \sum_{h=0}^k \binom{k}{h} \left[ \frac{x(n-q)_{imag}}{x(n-q)_{real}} \right]^{2h} \tag{12}$$

Let the binomial basis function of (11) represented as

$$y = \sum_{h=0}^k \binom{k}{h} \left[ \frac{x(n-q)_{real}}{x(n-q)_{imag}} \right]^{2h} = \sum_{h=0}^k \binom{k}{h} x^{2h} \tag{13}$$

Similarly, let the binomial basis function of (12) represented as

$$y = \sum_{h=0}^k \binom{k}{h} \left[ \frac{x(n-q)_{imag}}{x(n-q)_{real}} \right]^{2h} = \sum_{h=0}^k \binom{k}{h} x^{2h} \tag{14}$$

Let

$$y = \sum_{h=0}^k \binom{k}{h} x^{2h} \approx x^j \tag{15}$$

where  $-5 \leq x \leq 5$  and  $3 \leq k \leq 5$

The value of  $j$  is explored by using the macro-matching graph method as shown in Figure 1, Figure 2 and Figure 3.

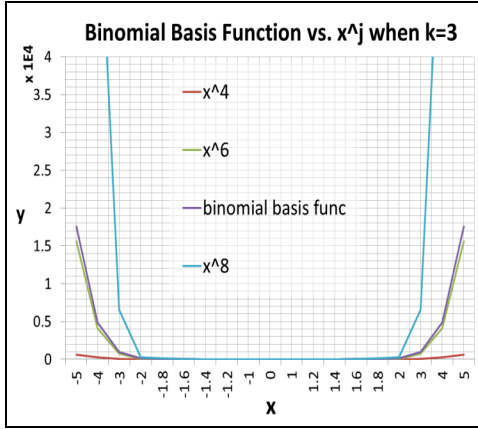


Figure 1. Binomial Basis Function vs.  $x^j$  when  $k = 3$

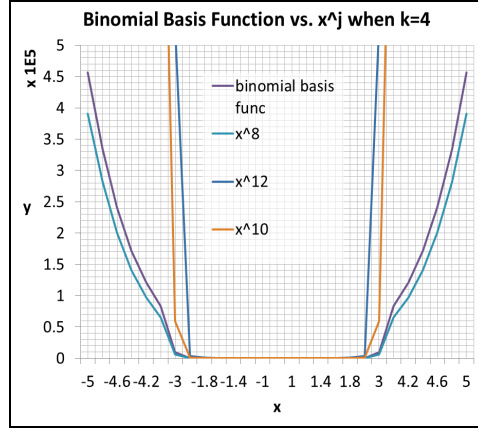


Figure 2. Binomial Basis Function vs.  $x^j$  when  $k = 4$

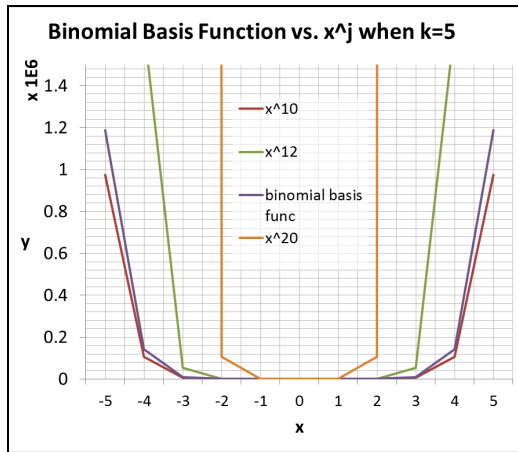


Figure 3. Binomial Basis Function vs.  $x^j$  when  $k = 5$

The binomial basis function equivalent is shown in Table 1 below:

Table 1  
Binomial basis function equivalent

Non-linearity order, k =3 (Figure 1)	k =4 (Figure 2)	k =5 (Figure 3)
$y = \sum_{h=0}^3 \binom{3}{h} x^{2h} \approx x^6$	$y = \sum_{h=0}^4 \binom{4}{h} x^{2h} \approx x^8$	$y = \sum_{h=0}^5 \binom{5}{h} x^{2h} \approx x^{10}$

The following could be concluded:

$$\sum_{h=0}^k \binom{k}{h} x^{2h} \approx x^{2k} \tag{16}$$

Substituting (16) into (13), (11) and (9) gives MPB-real-2k equation below:

$$z(n) = \sum_{k=0}^K \sum_{q=0}^Q a_{kq} x(n-q) x(n-q)_{real}^{2k} \tag{17}$$

Similarly, substituting (16) into (14), (12) and (9) yields MPB-imag-2k:

$$z(n) = \sum_{k=0}^K \sum_{q=0}^Q a_{kq} x(n-q) x(n-q)_{imag}^{2k} \tag{18}$$

## RESULTS AND DISCUSSION

### Amplitude and Phase Distortion Correction

Figure 4 shows the AMAM graph for MPB-imag-2k vs. MP with Non-linearity Order (K) = 3; Memory Depth (M) = 3, and Pre-amp Gain = 2. Pre-distortion (MPB) is capable of resolving the scattering of PA output signal observed.

Figure 5 shows the AM/PM graph for MPB-imag-2k vs. MP with Non-linearity Order (K) = 3, Memory Depth (M) = 3, and Pre-amp Gain = 2. The pre-distorted PA output is capable of resisting phase distortion, where the phase difference between output and input signal is close to zero.

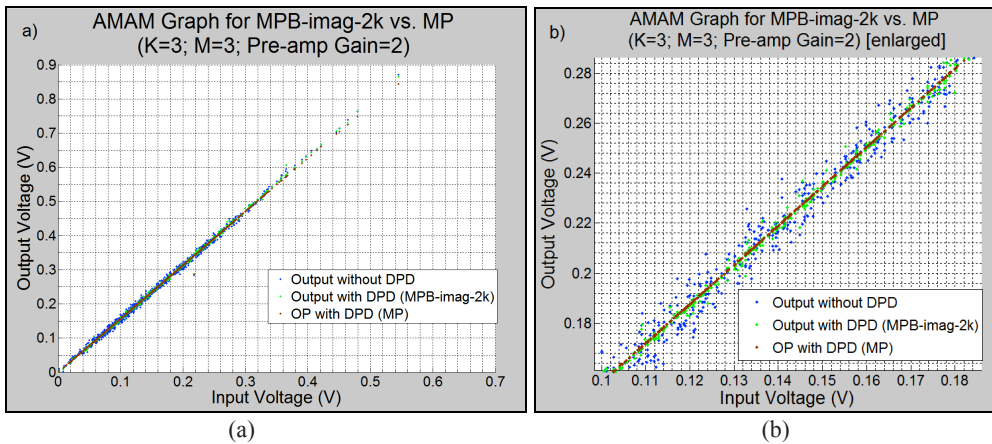


Figure 4. (a) AMAM Graph for MPB-imag-2k vs. MP with Non-linearity order=3, Memory Depth=3, and Pre-amplifier Gain=2; (b) Enlarged image of the AMAM graph

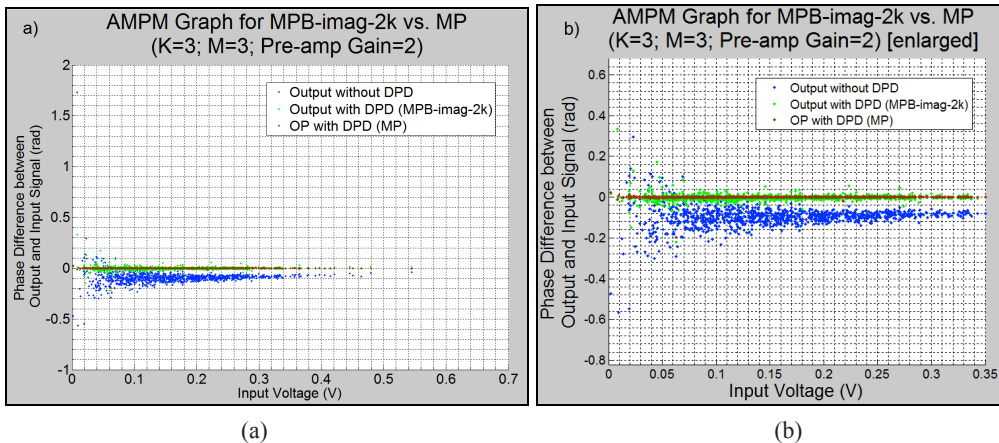


Figure 5. Figure 5. (a) AMPM Graph for MPB-imag-2k vs. MP with Non-linearity Order=3, Memory Depth=3, and Pre-amplifier Gain=2; (b) Enlarged image of the AMPM graph

### Resource Optimization on Multiplication Operations Reduction

MPB is compared with MP on resources reduction in terms of multiplication operations. Table 2 and 3 shows the respective formulas used to calculate the required multiplication operations.

Table 2  
Multiplication Operations Calculation Formula for MP

Method Formula	$z(n) = \sum_{k=0}^K \sum_{q=0}^Q a_{kq} x(n-q) \sqrt{x(n-q)_{real}^2 + x(n-q)_{imag}^2}^{-2k}$
Multiplications Operations Calculation Formula	$Q(1 + 3(2K))$

Table 3  
 Multiplication Operations Calculation Formula for MP

Method Formula	$z(n) = \sum_{k=0}^K \sum_{q=0}^Q \alpha_{kq} x(n-q) x(n-q)_{imag}^{2k}$
Multiplications Operations Calculation Formula	$Q(1 + 2(K))$

The net reduction of multiplication operations are calculated by finding the difference between the two formulas, which results in Multiplication Operations Reduction (MOR) in Table 4.

Table 4

Table 4  
 MOR of MPB (MPB-imag-2k) against MP

MPB (MPB-imag-2k) from Table 2	MP from Table 3	MOR
$Q(1 + 2(K))$	$Q(1 + 3(2K))$	$4(K)$

## CONCLUSION

MPB is an improved MP Model which uses the Binomial Reduction Method at the MP Basis Function. This results in linearly reduced multiplication operations but with matching PA Linearization Performance in MP, especially in anti-scattering and anti-phase-distortion.

## REFERENCES

Chen, W., Zhang, S., Liu, Y. J., Ghannouchi, F. M., Feng, Z., & Liu, Y. (2014). Efficient Pruning Technique of Memory Polynomial Models Suitable for PA Behavioral Modeling and Digital Predistortion. *IEEE Transactions on Microwave Theory and Techniques*, 62(10), 2290-2299.

Choo, H. N. (2012). *DSP implementation of digital pre-distortion in wireless systems*. (Degree Dissertation). Universiti Putra Malaysia.

Choo, H. N., Varahram, P., & Ali, B. M. (2013, November). DSP implementation of Digital Pre-distortion in wireless communication systems. In *Communications (MICC), 2013 IEEE Malaysia International Conference on* (pp. 207-212). IEEE.

Ding, L., Zhou, G. T., Morgan, D. R., Ma, Z., Kenney, J. S., Kim, J., & Giardina, C. R. (2004). A robust digital baseband predistorter constructed using memory polynomials. *IEEE Transactions on Communications*, 52(1), 159-165.

Ding, L. (2004). *Digital predistortion of power amplifiers for wireless applications* (Doctoral dissertation). Georgia Institute of Technology. Retrieved from [http://www.academia.edu/download/34086448/ding\\_lei\\_200405\\_phd.pdf](http://www.academia.edu/download/34086448/ding_lei_200405_phd.pdf)

Liu, Y. J., Zhou, J., Chen, W., & Zhou, B. H. (2014). A robust augmented complexity-reduced generalized memory polynomial for wideband RF power amplifiers. *IEEE Transactions on Industrial Electronics*, 61(5), 2389-2401.

- Morgan, D. R., Ma, Z., Kim, J., Zierdt, M. G., & Pastalan, J. (2006). A generalized memory polynomial model for digital predistortion of RF power amplifiers. *IEEE Transactions on Signal Processing*, 54(10), 3852-3860.
- Parta, H., Ercegovic, M. D., & Pamarti, S. (2014, August). RF digital predistorter implementation using polynomial optimization. In *2014 IEEE 57th International Midwest Symposium on Circuits and Systems (MWSCAS)* (pp. 981-984). IEEE.
- Pinal, P. L. G., & Pere, L. (2007). *Multi Look-Up Table Digital Predistortion for RF Power Amplifier Linearization*. (Doctoral dissertation). Universitat Politècnica de Catalunya. Retrieved from <http://upcommons.upc.edu/handle/10803/6915>
- Techsource-asia. (2012). *Digital predistortion: Seeing clearly in the house of mirrors*. Retrieved from <http://techsource-asia.com/news/press-room/detail/25-digital-predistortion--seeing-clearly-in-the-house-of-mirrors.html>
- Varahram, P., Mohammady, S., Hamidon, M. N., Sidek, R. M., & Khatun, S. (2009). Digital Predistortion Technique for Compensating Memory Effects of Power Amplifiers in Wideband Applications. *Journal of Electrical Engineering*, 60(3), 129-135.
- Varahram, P., Mohammady, S., Hamidon, M., Sidek, R. M., & Khatun, S. (2010). Complex Gain Predistortion in WCDMA Power Amplifiers with Memory Effects. *The International Arab Journal of Information Technology*, 7(3), 333-341.
- Vella-Coleiro, G. (2011). Improving the Efficiency of RF Power Amplifiers with Digital Predistortion. In *26th Annual MTT-AP Symposium and Mini Show*.
- Xie, D., & Zeng, Z. (2012, March). An Improved Adaptive Algorithm for Digital Predistortion. In *Proc. IEEE International Conference on Computer Science and Electronics Engineering*. [S. 1.]: IEEE Press (pp. 340-343).
- Yu, X., & Jiang, H. (2013). Digital predistortion using adaptive basis functions. *IEEE Transactions on Circuits and Systems I: Regular Papers*, 60(12), 3317-3327.







## Performance Comparison of Image Normalisation Method for DNA Microarray Data

Omar Salem Baans<sup>1\*</sup>, Asral Bahari Jambek<sup>1\*</sup>, Uda Hashim<sup>2</sup> and Nor Azah Yusof<sup>3</sup>

<sup>1</sup>*School of Microelectronic Engineering, University Malaysia Perlis, 02600 Arau, Perlis, Malaysia.*

<sup>2</sup>*Institute of Nano Electronic Engineering, University Malaysia Perlis, 02600 Arau, Perlis, Malaysia*

<sup>3</sup>*Department of Malaysia Chemistry, Faculty of Science, Universiti Putra Malaysia, 43400 UPM, Serdang, Selangor, Malaysia*

### ABSTRACT

Normalisation is a process of removing systematic variation that affects measured gene expression levels in microarray experiment. The purpose is to get a more accurate DNA microarray result by deleting the systematic errors that may have occurred when making the DNA microarray slide. In this paper, four normalisation methods of Global, Lowess, Quantile and Print-tip are discussed, tested and their final results compared in the form of Matrixes and graphs. Ideal and real microarray slides have been used for this project. It was found that the Print-tip normalisation method showed the closest results to the real result for an ideal microarray slide and it has a straight median line final graph. The Print-tip normalisation method uses more than one normalization factor that is divided among intervals which are dependent on the values of the addition of red and green logarithm.

*Keywords:* DNA, Microarray, Normalisation, Global, Lowess, Quantile, Print-tip, Background correction, M-A plot

### INTRODUCTION

Gene expression measurements provide clues on the regulatory mechanism, biochemical pathways and broader cellular function. By

gene expression is the transformation process of gene's information into proteins. The formal transformational pathway of protein begins with the DNA (deoxyribonucleic acid) which is copied to the mRNA (messenger ribonucleic acid) and, finally this molecule passes from nucleus to cytoplasm carrying the information to build proteins (Belean et al., 2011).

There are many microarray analysis software packages in the market. Each software program is concerned with three main tasks: 1) gridding or addressing, which is

#### ARTICLE INFO

##### Article history:

Received: 24 August 2016

Accepted: 02 December 2016

##### E-mail addresses:

omersalim4901@gmail.com (Omar Salem Baans),

asral@unimap.edu.my (Asral Bahari Jambek),

uda@unimap.edu.my (Uda Hashim),

azahy@upm.edu.com (Nor Azah Yusof)

\*Corresponding Author

the process of specifying coordinate to every spot on the slide 2) segmentation which decides the classification of each pixel either as foreground which corresponds to be an interest spot or as background which acts as an error or noise 3) Intensity Extraction which is the step to calculate green and red for foreground fluorescence intensity for each spot on the array (Borda et al., 2011; Rao et al., 2008).

Processes to inspect the results and correct the errors are: 1) background correction method obtained by subtracting the value of the background intensity from the value of foreground intensity or any other suitable method to neglect the effect of background intensity 2) normalisation method which is the objective of this research (Yang et al., 2001).

Normalisation is the process of removing systematic variations that affect measured gene expression levels in microarray experiments. The purpose of normalisation is to adjust for effects which arise from variations in the microarray technology rather than from biological differences between the RNA samples or between the printed probes. Imbalances between the red and green dyes may arise from differences between the labelling efficiencies or scanning properties of the two dyes complications perhaps by the use of different scanner settings (Geeleher et al., 2009). The aim of this paper is to review various methods that discuss and compare DNA microarray normalization.

In section II several normalization algorithms are elaborated, while section IV discusses the comparison of these various methods. Section V and VI presents the methodology and results of analysis of the different methods. The conclusion follows in section VII.

## LITERATURE REVIEW

Discussion on the normalisation of DNA microarray is currently well developed. Before we review some of them, we will explain the two types of graphs that can show normalisation quality. First, (log M vs. log R) as shown in Figure 1(a). Second, M-A plot is 45° rotation of standard scatter plot as shown in Figure 1(b). Write R and G for the background-corrected red and green intensities for each spot. Normalisation is usually applied to the log-ratios of expression, which will be written ( $M = \log R - \log G$ ). The log-intensity of each spot will be written ( $A = (\log R + \log G)/2$ ), a measure of the overall brightness of the spot. (The letter M is a mnemonic for minus while A is a mnemonic for addition) (Dudoit et al., 2002).

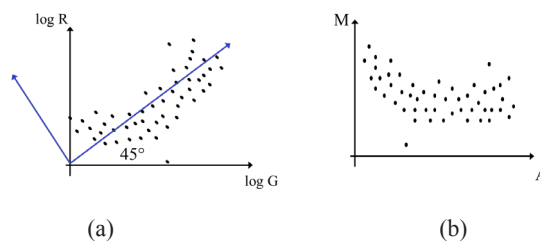


Figure 1. (a) Log R vs. Log G; (b) M-A Plot

This section will discuss and elaborate the methods of DNA microarray normalisation and identify the most suitable for further microarray analysis. The first method is Global normalisation: the underlying assumption of this approach is that the total of mRNA labelled with either R value (sum of red intensities) or G value (sum of green intensities) is equal. While the intensity for any one spot may be higher in one channel than the other, when averaged over thousands of spots in the array, these fluctuations should average out. In this method, the value of  $c$  out of  $\log(R/G)$ . The  $c$  value is equal to the main assumption that equal to  $\log$  of the total R over total G which can be expressed by the variable  $K$  (Yang et al., 2002). The intensity-dependent lowess normalisation runs a line through the middle of the MA plot, shifting the  $M$  value of the pair  $(A, M)$  by  $c=c(A)$ , as shown in Equation 3. One estimate of  $c(A)$  is made using the loess function: Locally Weighted Scatterplot Smoothing (Berger et al., 2004; Bilban et al., 2002).

$$\log_2 R/G \rightarrow \log_2 R/G - c = \log_2 R/(kG) \tag{1}$$

$$K = \sum R/G \tag{2}$$

$$\log_2 R/G \rightarrow \log_2 R/G - c(A) = \log_2 R/(k(A)G) \tag{3}$$

In the Print-tip normalisation, each  $M$ -value ( $\log R - \log G$ ) is normalised by subtracting from it the corresponding value of the tip group loess curve that is dependent on  $A$  value ( $[\log R + \log G]/2$ ) while its value should be fixed. The normalised  $\log$ -ratios ( $N$ ) are the residuals from the tip group loess regressions. A simpler form of Print-tip is shown in Equation 4 where  $\text{loess}(A)$  is the global loess curve plotted in Figure 2. Refer to Figure 3 for the final figure of the Print-tip normalisation (Smyth et al., 2003). The Quantile normalisation method is undertaken by rearranging the genes in each column as in second table in Figure 4. Following which the mean in each row is replaced the whole row by the mean value as shown in the third table in Figure 4. Finally, reorder each gene in its original place with its new value.

$$N = M - \text{loess}(A) \tag{4}$$

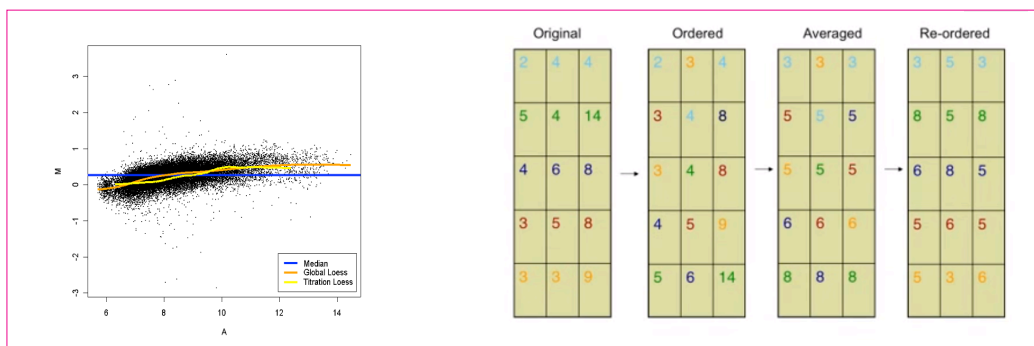


Figure 2. Global normalisation

Figure 3. Print-tip normalisation; Figure 4. Quantile normalisation

### COMPARISON OF DIFFERENT NORMALISATION APPROACHES

In this section, the existing system algorithm as discussed in section III will be analysed and discussed to find out the similarities and variations among the different normalisation methods. Table 1 summarized the comparison of these algorithms.

From Table 1, it can be seen that, all the methods are using mainly the value of M which equal to log of red intensity minus log of green intensity. However, three methods have different value to subtract from M. To illustrate, Global normalisation use the log of addition of each of red and green intensity while the other two methods are using median and global median.

In term of the final shape of the normalisation on M-A graph, there are similarities between Lowess and Print-tip methods because both have a straight median line in the value of (M=0) due to their similarities on subtracting the mean or median from M. However, in Global normalisation, there is a curve around the value of (M=0) due to the subtraction of the total R and G. Quantile normalisation method does not use M-A plot, consequently its final graphs do not always take a straight line of the mean on the (M=0). According to this review, we suggest Print-tip normalisation method to be used because when comparing to the global normalisation its final figure is simpler and easier to read and can also easily be compared to various plots. Straight line on (M=0) is easier to read than the Global and lowess normalisation curve.

Table 1  
Comparison between different system algorithms

No.	[1]	[2]	[3]	[4]
Method	Global	Lowess	Print Tip	Quantile
Function	Log (R/ KG)	Log (R/ G) – c(A)	N= M- loess (A)	Mean of rows after reorder
Variable	$K = \sum R/G$	LOWESS function	Global Loess	NA
Shape on M-A graph	Curve	Straight line on (M=0)	Straight line on (M=0) but has some variation	It does not meet M-A plot.

### METHODOLOGY

Using Matlab, we developed a code that can extract the intensity for 100 spots. Using 100 spots instead of the whole microarray slide make the process easier and simpler especially to compare the many algorithms used. In order to examine the suitable method which would be more accurate and suitable for this project, an ideal microarray image spots in Figure 5(a), and a real microarray slide in Figure 5(b) were used. Matlab usually reads the image intensity as matrix by pixel, for example our image after cropping is 220\*227 pixels while it has only 100 spots. Thus, each spot has around 20 pixel diameters. Next, it calculates the foreground and background then subtract the background value from foreground, and using threshold equal to zero will not allow negative values to appear. In the ideal image the value of background is fixed (Rb = Gb =3) while foreground value is a variant from 0 to 225 as shown in Matrix 1. Then, according to the normalisation method, the formula codes were applied.

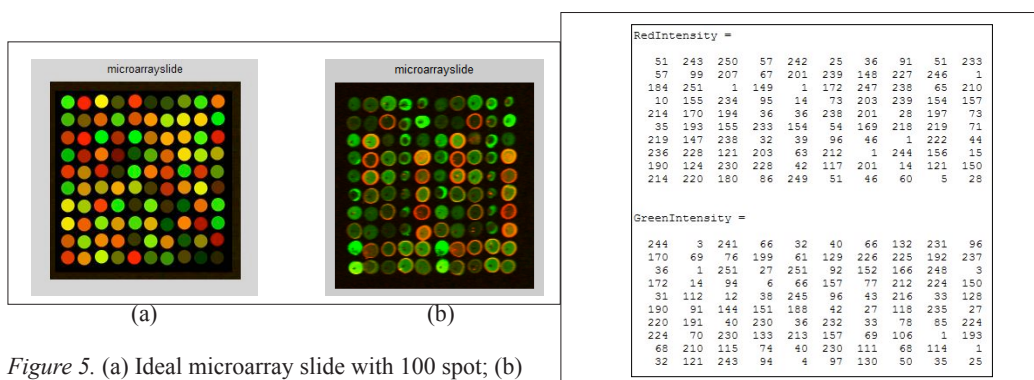


Figure 5. (a) Ideal microarray slide with 100 spot; (b) Real microarray slide with 100 spot;

Matrix 1. Original Intensity of the ideal spots

For Global Normalisation, loops were used to find the total of red and green intensities values for all 100 spots. Then taking the logarithm of the total value and subtracts it from the value of  $M$  according to Equation number 1 and 2. Similarly, in the Lowess method, mean of  $m$  values was calculated then subtracted, to be on the centre ( $M=0$ ) according to equation number 3. However, Quantile normalisation is much different than the previous two methods, because it does not require calculation of  $A$  and  $M$  values. But it requires sorting the matrix in each column. Then taking the average in each row and finally put each new value in its original location as shown in Figure 5. Finally, Print-tip normalisation,  $A$  values (addition of logarithm) has been divided into four groups ( $<5$ ,  $<6$ ,  $<7$  and else) and according to each group, mean value of  $M$  was taken and defined into variable call  $PT$ . After that, the  $PT$  value was subtracted from  $M$  according to its group. Next section will discuss the results of the various methods tested.

## RESULT AND DISCUSSION

First of all, there is a different in the last result for all the four methods in terms of last intensities values and  $M-A$  displaying graphs. Global normalisation and Lowess share a similarity especially when we compare the difference between the green and the red intensity for the same spots. Similarly, Print-tip normalisation which has a similar graph but there is a different according to the interval groups. However, the results for quantile normalisation are fluctuating and the different is larger than all of the other normalisation methods. Normalisation results for the ideal and normal microarray slide are shown in matrix 1 and 2, and  $M-A$  graphs in Figure 6 and 7 respectively. As we saw in Matrix 1 above, there are red and green intensities for 100 spots as well as in Matrix 2 below. Thus, we have 4 matrixes with the size of  $(10 \times 10)$ . The first and second for the red and green intensities of ideal image in Matrix 2 while the third and fourth for the red and green intensities for the slide image. Figure 6 and 7 depict  $M-A$  plots for ideal and slide image before any method of normalisation was performed. Thus, the illustrations will help us compare them with the next results of various normalisation methods.

RedIntensity =												
5	15	22	11	11	4	16	9	12	14			
11	6	36	19	30	8	4	41	20	22			
10	87	13	12	5	8	88	31	16	3			
5	56	23	15	156	8	75	19	11	163			
4	63	21	8	67	3	89	33	11	76			
8	32	11	6	47	13	26	20	11	73			
13	6	20	7	68	15	5	24	8	84			
15	9	6	10	109	32	14	8	9	115			
10	53	25	32	44	10	83	38	48	45			
70	34	13	23	30	51	30	22	38	26			

GreenIntensity =												
30	50	99	39	16	31	42	102	46	9			
31	30	31	28	110	27	22	29	27	43			
66	126	26	34	30	68	120	19	39	37			
59	33	85	35	108	61	32	83	30	108			
32	96	100	17	51	35	91	85	16	52			
29	51	47	14	88	36	56	46	14	86			
78	44	35	21	23	96	34	32	16	23			
55	50	17	13	74	49	49	18	29	74			
152	37	45	96	100	133	37	43	93	91			
185	52	34	102	69	126	47	28	108	73			

Matrix 2. Red and Green Intensity before norm of the slide image;

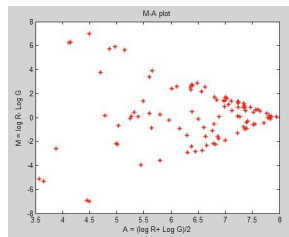


Figure 6. M-A plot before normalisation of the ideal image;

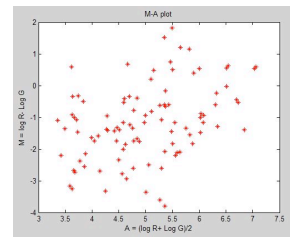


Figure 7. M-A plot before normalisation of the slide image

Matrixes 3 and Matrix 4 show the results of global normalisation for ideal and real DNA microarray slide. Firstly, they show  $k$  and  $c$  values,  $c$  is the logarithm of the total of red intensities over the total of green intensities ( $k$ ) which is equal to 0.0274 in ideal image and  $-0.2358$ , and that explains to us why the normalisation is important and how the variety of  $c$  increased for the real microarray slide image. Thus, the difference between the last and original results in the real microarray slide is larger.

m =												
0.1756												
RedLowNorm =												
49	230	237	55	229	25	35	87	49	221			
55	95	198	64	191	226	141	215	233	2			
175	238	2	142	2	163	234	225	63	199			
11	147	222	91	13	70	192	226	146	149			
203	41	184	35	55	225	191	29	187	70			
34	183	147	221	146	52	160	207	208	68			
208	140	225	32	38	92	45	2	210	43			
224	216	115	132	61	201	2	231	148	14			
180	118	218	216	41	112	191	15	115	143			
203	208	171	82	236	49	45	58	6	28			
GreenLowNorm =												
261	5	258	72	36	44	72	142	247	104			
182	75	82	213	66	139	242	241	206	233			
60	3	268	30	268	99	163	178	265	8			
184	16	101	8	72	168	83	227	240	161			
35	121	14	42	262	104	47	231	37	138			
203	98	155	162	201	46	30	127	251	30			
235	205	44	246	40	248	37	84	92	240			
240	74	246	143	228	168	75	114	3	207			
74	225	124	80	44	246	120	74	123	3			
36	130	260	101	6	105	140	55	39	28			

Matrix 3. Red and Green Intensity for global norm of the ideal image

m =												
-1.1662												
RedLowNorm =												
9	24	35	18	18	8	26	15	20	23			
18	11	56	30	47	14	8	63	32	35			
17	132	21	20	9	14	134	68	26	6			
9	86	36	24	236	14	114	30	18	246			
8	96	33	14	102	6	138	51	18	114			
14	50	18	11	72	21	41	32	18	111			
21	11	32	12	104	24	9	38	14	128			
24	15	11	17	165	50	23	14	15	174			
17	81	39	50	68	17	126	99	74	69			
107	53	21	36	47	78	47	35	59	41			
GreenLowNorm =												
21	33	67	27	12	22	29	69	32	7			
22	21	22	20	75	19	16	21	19	30			
48	88	19	24	21	97	81	14	27	26			
41	23	58	25	73	42	23	57	21	73			
23	65	68	13	35	25	62	58	12	36			
21	59	33	11	60	25	59	32	11	59			
53	31	25	15	17	65	24	23	12	17			
37	38	13	10	51	34	34	13	21	51			
103	26	31	65	68	90	26	30	63	62			
125	36	24	69	47	85	33	20	73	50			

Matrix 4. Red and Green Intensity for global norm of real slide image

Lowess normalisation results for ideal and real DNA microarray slide are shown in Matrix 5 and 6. First it shows  $(m)$  values,  $m$  is the mean  $M$  value for 100 spots which equal to the difference between logarithms of red and green intensities for each spot separately.  $(m)$  is equal to 0.1756 in ideal image and  $-1.1662$  explaining why the normalisation process is important and how does the variety of  $c$  increase for the real microarray slide image. Also, it is greater than  $c$  values (for global normalisation). The difference  $t$  between the last and original results in real microarray slide is larger than the different in global normalisation.



## Image Normalisation Methods for DNA Microarray Data

<p><b>Matrix 5: Red and Green Intensity for global norm of the ideal image</b></p> <pre> 0.1756 RedLowNorm = 49 230 237 55 229 25 35 87 49 221 55 95 196 64 191 226 141 235 233 2 175 238 2 142 2 163 234 225 63 199 11 147 222 91 15 70 192 226 146 149 203 161 184 35 35 225 191 20 187 70 34 183 147 221 146 92 160 207 208 68 208 140 223 32 38 92 45 2 210 43 224 216 115 192 61 201 2 231 148 16 180 118 218 216 41 112 191 15 115 143 203 208 171 82 236 49 45 88 6 28  GreenLowNorm = 261 5 258 72 36 44 72 142 247 104 182 75 82 213 66 139 242 241 206 283 40 3 268 30 248 99 163 178 248 8 184 16 103 8 72 168 83 227 240 161 35 121 14 42 262 104 47 231 37 138 209 98 155 162 201 46 90 127 251 30 235 205 44 246 40 248 37 44 92 240 240 76 246 143 228 168 75 114 3 207 74 225 124 80 44 246 120 74 133 3 96 130 260 101 6 105 140 55 39 28                 </pre>	<p><b>Matrix 6: Red and Green Intensity for global norm of real slide image</b></p> <pre> -1.1662 RedLowNorm = 9 24 35 18 18 8 26 15 20 23 18 11 56 30 47 14 8 63 32 35 17 132 21 20 9 14 134 48 26 6 9 86 36 24 236 14 114 30 18 246 8 96 33 14 102 6 135 51 18 116 14 50 18 11 72 21 41 32 19 111 21 11 32 12 104 24 9 38 14 128 24 15 11 17 165 50 23 14 15 174 17 81 39 50 68 17 124 59 74 69 107 53 21 36 47 78 47 35 59 41  GreenLowNorm = 21 35 67 27 12 22 29 69 32 7 22 21 22 20 75 19 16 21 19 30 45 85 19 24 21 47 81 14 27 26 41 23 58 25 73 42 33 57 21 73 23 65 68 13 35 25 42 58 12 36 21 35 33 11 60 25 39 32 11 59 53 31 25 15 17 65 24 23 12 17 37 35 13 10 51 34 34 13 21 51 103 26 31 65 68 90 24 30 63 42 125 36 24 69 47 85 33 20 73 50                 </pre>
---	--

*Matrix 5.* Red and Green Intensity for global norm of the ideal image

*Matrix 6.* Red and Green Intensity for global norm of real slide image

Quantile normalisation results for ideal and real DNA microarray slide are shown in Matrix 7 and 8. Quantile normalisation method differs from global and Lowess normalisations in that it does not require fixed values of (c) or (m). Rather an average of the columns after sorting the matrix in each row as explained before in section 2. Thus, we can see in Matrix 8 that (67, 85, 124, 18 and so on) are repeated in each column of matrix QRN, and also the other values for QGN are similar in Matrix 8. There are 10 fixed numbers repeated in each column of each matrix.

<p><b>Matrix 7: R &amp; G Intensity for Quant. Norm. of the ideal image</b></p> <pre> QRN = 67 229 243 67 229 18 50 124 50 243 85 18 149 85 211 243 124 192 243 18 124 243 18 192 18 192 243 211 67 229 18 85 211 149 50 85 229 229 124 211 192 124 124 50 67 229 192 67 192 149 50 149 67 243 192 67 149 149 211 124 229 67 229 18 85 124 67 18 229 85 243 211 50 211 149 211 18 243 149 50 149 50 192 229 124 149 211 50 85 192 211 192 85 124 243 50 85 85 18 67  QGN = 236 32 187 72 32 18 72 123 187 99 99 72 48 216 99 123 236 236 123 236 48 18 236 32 236 48 216 167 236 32 123 48 72 18 123 167 123 187 167 167 18 167 18 48 216 72 48 216 32 123 167 123 123 187 167 32 18 99 216 72 187 216 32 236 48 236 32 48 72 216 216 99 167 167 187 187 99 72 18 187 72 236 99 99 72 216 167 32 99 18 32 187 216 123 18 99 187 18 48 48                 </pre>	<p><b>Matrix 8: R &amp; G Intensity for Quant. norm of the real slide image</b></p> <pre> QRN = 9 16 38 23 9 9 16 9 28 9 38 6 78 42 14 14 6 78 42 14 23 78 14 28 6 16 55 38 38 6 14 42 42 38 78 23 38 14 14 78 6 55 28 14 38 6 78 42 16 38 16 23 9 6 28 38 23 16 23 28 42 9 23 9 42 42 9 28 6 42 55 14 6 16 55 55 14 6 9 55 28 38 55 78 23 28 42 55 78 23 78 28 16 55 16 78 28 23 55 16  QGN = 25 44 104 73 20 25 44 120 73 20 30 20 30 44 120 20 20 36 36 36 57 120 25 52 30 57 120 25 57 30 52 25 73 57 104 52 25 73 52 120 36 104 120 30 36 30 104 104 25 44 20 57 57 25 57 36 73 57 20 73 73 36 44 36 25 73 30 44 30 25 44 52 20 20 52 44 57 20 44 57 104 30 52 104 73 120 36 52 104 104 120 73 36 120 44 104 52 30 120 52                 </pre>
---	---

*Matrix 7.* R & G Intensity for Quant. Norm. of the ideal image

*Matrix 8.* R & G Intensity for Quant. norm of the real slide image

Finally, Print-tip normalisation gave the results for the red and green intensities for the ideal microarray image in Matrix 9 and real microarray slide in Matrix 10. M-A graphs for the results are displayed in Figure 8 and 9 respectively. PT values in Matrix 9 and 10 are represented by the normalisation values among the four intervals for each image. For example, in Matrix 9, PT equals -0.0664, 0.2457, 0.1445 and 0.2633. These values were subtracted from M (the different between logarithms of red and green intensities for each spot) according to the values of A for the same spot. These intervals are (<5, <6, <7 and else), so each interval has its own normalisation values; and that is why, at times, we can see the obvious different

between the normalised and un-normalised values in some intervals according to the values of PT. Besides that, Figure 9 represents the M-A plot for Print-tip normalization of real image slide which show more different from its original slide except by the values of PT especially in the first interval when  $PT = -1.5263$  among the interval ( $A$  less than 5).

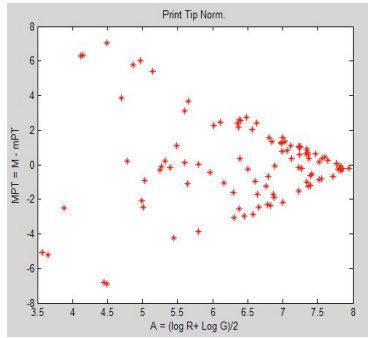


Figure 8. M-A Plot for Print tip norm of the Ideal Image

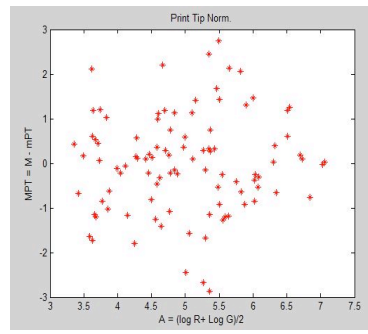


Figure 9. M-A Plot for Print tip norm of the Slide Image

PT =									
	-0.0664	0.2487	0.1445	0.2633					
RedPTNorm =									
50	250	230	54	232	24	34	88	50	214
56	96	198	65	193	220	137	209	226	3
176	258	3	143	3	165	227	219	61	216
11	144	215	89	16	71	195	220	142	145
208	187	178	94	36	219	193	28	189	71
35	178	143	214	142	51	162	200	201	67
201	136	228	32	37	89	44	3	204	43
217	218	112	187	61	195	3	224	161	15
182	115	211	210	40	108	185	14	117	155
205	202	166	83	230	50	45	56	7	30
GreenPTNorm =									
258	4	266	74	35	45	74	140	244	107
180	74	81	211	66	143	249	248	212	233
39	2	247	30	247	98	168	183	273	4
189	17	105	7	66	167	83	234	247	166
34	124	15	43	259	107	47	209	36	136
201	101	159	167	208	47	30	131	259	31
249	211	44	249	41	256	38	78	95	237
247	75	294	447	225	174	69	118	2	212
73	232	128	83	45	254	123	76	121	2
35	134	268	100	6	104	138	56	36	26

PT =									
	-1.5263	-0.9235	-0.6295	0.5579					
RedPTNorm =									
11	28	32	21	21	9	29	14	23	26
21	12	51	34	43	16	9	58	36	40
19	110	24	23	11	16	111	55	29	7
11	79	34	28	130	16	105	28	21	156
9	80	31	16	94	7	112	47	21	107
16	46	21	12	60	24	38	36	21	93
20	12	36	14	96	23	11	43	16	118
28	17	12	19	137	46	26	16	17	145
16	75	36	46	56	16	116	54	61	58
89	49	24	34	43	65	43	40	49	38
GreenPTNorm =									
19	31	73	24	11	19	26	75	28	6
19	19	24	18	81	17	14	22	17	26
40	103	16	21	19	41	98	12	24	23
36	25	63	22	133	37	24	61	19	133
20	78	74	11	38	22	74	68	11	39
18	38	29	9	72	22	42	28	9	70
58	27	22	15	18	71	21	20	11	18
32	31	11	9	61	37	30	12	15	61
112	28	34	71	82	98	28	32	76	74
150	39	21	75	51	103	35	18	88	54

Matrix 9. Red and Green Intensity for PT norm of the ideal image

Matrix 10. Red and Green Intensity for PT norm of real slide image

From the Matrixes and graphs discussed above, it can be observed the global and Lowes are almost similar; Print-tip, an advanced version of them, gave results that was close to Matrix 1 and 2. However, Quantile differed greatly than the correct one and its graphs fluctuate away from the goal. Furthermore, the graphs of real image Print-tip normalization shows the expected result for real slide image in Figure 9 due to the clustering around the straight line when ( $M = 0$ ). These findings support the view of Smyth that the “print-tip loess normalization provides a well-tested general purpose normalization method which gives good results on a wide variety of arrays” and best combined with diagnostic plots of the data. When the diagnostic plots show that biases still remain in the data after normalization, additional steps such as quantile normalization of the arrays may be undertaken (Smyth et al., 2003).



## CONCLUSION

In this paper, normalization is defined as a process to delete systematic error. Four most commonly used normalization algorithms such as Global, Lowess, Quantile and Print-tip were tested and compared to find the most suitable approach in a general normalization process. For that purpose, a Matlab code was built for each method for two slides; the ideal and real microarray slides. The results shown in the form of Matrix of red and green intensities and M-A graph show that Global, Lowess and Print-tip are more accurate in comparison with an ideal image result while Print-tip has the advantages than the other two especially in term of final graph shape.

## ACKNOWLEDGMENT

This research was funded by Science Fund, Ministry of Science, Technology and Innovation (MOSTI), Malaysia (2015).

## REFERENCES

- Belean, B., Borda, M., LeGal, B., & Malutan, R. (2011, August). FPGA technology and parallel computing towards automatic microarray image processing. In *Telecommunications and Signal Processing (TSP), 2011 34th International Conference on* (pp. 607-610). IEEE.
- Berger, J. A., Hautaniemi, S., Järvinen, A. K., Edgren, H., Mitra, S. K., & Astola, J. (2004). Optimized LOWESS normalization parameter selection for DNA microarray data. *BMC Bioinformatics*, 5(1), 1
- Bilban, M., Buehler, L. K., Head, S., Desoye, G., & Quaranta, V. (2002). Normalizing DNA microarray data. *Current Issues in Molecular Biology*, 4, 57-64.
- Borda, M., Belean, B., Terebes, R., & Malutan, R. (2011, November). FPGA based SoC for automated cDNA microarray image processing. In *E-Health and Bioengineering Conference (EHB), 2011* (pp. 1-4). IEEE.
- Dudoit, S., Yang, Y. H., Callow, M. J., & Speed, T. P. (2002). Statistical methods for identifying differentially expressed genes in replicated cDNA microarray experiments. *Statistica Sinica*, 111-139.
- Geeleher, P., Morris, D., Hinde, J. P., & Golden, A. (2009). BioconductorBuntu: a Linux distribution that implements a web-based DNA microarray analysis server. *Bioinformatics*, 25(11), 1438-1439.
- Rao, Y., Lee, Y., Jarjoura, D., Ruppert, A. S., Liu, C. G., Hsu, J. C., & Hagan, J. P. (2008). A comparison of normalization techniques for microRNA microarray data. *Statistical Applications in Genetics and Molecular Biology*, 7(1).
- Smyth, G. K., & Speed, T. (2003). Normalization of cDNA microarray data. *Methods*, 31(4), 265-273.
- Yang, Y. H., Buckley, M. J., & Speed, T. P. (2001). Analysis of cDNA microarray images. *Briefings in Bioinformatics*, 2(4), 341-349.
- Yang, Y. H., Dudoit, S., Luu, P., Lin, D. M., Peng, V., Ngai, J., & Speed, T. P. (2002). Normalization for cDNA microarray data: a robust composite method addressing single and multiple slide systematic variation. *Nucleic Acids Research*, 30(4), e15-e15.



## Real-time Human Motion Analysis and Grasping Force using the OptiTrack System and Flexi-force Sensor

N. F. Elya Saidon<sup>1\*</sup>, Chikamune Wada<sup>2</sup>, Siti A. Ahmad<sup>1</sup>, Ribhan Zafira Abdul Rahman<sup>1</sup>, Kiyotaka Eguchi<sup>2</sup>, Yoshiyuki Tomiyama<sup>2</sup> and Farida Izni Abd Rahman<sup>1</sup>

<sup>1</sup>Department of Electrical and Electronic Engineering, Universiti Putra Malaysia, 43400 UPM, Serdang, Selangor, Malaysia

<sup>2</sup>Graduate School of Life Science and Systems Engineering, Kyushu Institute of Technology, Hibikino 2-4, Wakamatsu-ku, Kitakyushu, Fukuoka, 808-0196, Japan

### ABSTRACT

Biologically inspired robotic hands have important applications in industry and biomedical robotics. The grasping capacity of robotic hands is crucial for a robotic system. This paper presents an experimental study on the finger force and movements of a human hand during the grasping operation in real-time. It focuses on two topics; measuring grasping force using Flexi-force sensors and analysing human hand action during grasping operation. The findings show that lifting required higher forces compared with grasp force in the static phase.

*Keywords:* Hand grasping, Flexi-force sensors, motion capture systems

### INTRODUCTION

Hands are important for almost all activities. Robotic hands are developed with the aim of mimicking the human hand in terms of

dexterity and reliability especially in grasping operations.

In robotic hand sensors are required for the location of the fingertips contact position, measurement of the force applied on the object, and determination of the grasp configuration. Trying to arrive at the best method to measure fingers force is an important aspect of research (Monroy et al., 2009; Ye & Auner, 2003; Kazerooni et al., 2004; Dipietro et al., 2008; Adnan et al., 2012; et al., 2013).

To date, a number of studies have reported the use of force sensor to measure finger force. According to Paredes-Madrid et al., the best

### ARTICLE INFO

#### Article history:

Received: 24 August 2016

Accepted: 02 December 2016

#### E-mail addresses:

nurfarahelya91@gmail.com (N. F. Elya Saidon),  
wada@brain.kyutech.ac.jp (Chikamune Wada),  
sanom@upm.edu.my (Siti A. Ahmad),  
ribhan@upm.edu.my (Ribhan Zafira Abdul Rahman),  
o966006k@mail.kyutech.jp818 (Kiyotaka Eguchi),  
ms071121@gmail.com (Yoshiyuki Tomiyama),  
iznie8393@yahoo.com (Farida Izni Abd Rahman)

\*Corresponding Author

sensor devices for measuring the finger force should have the following list of the characteristics such as repeatability for measuring the high reading, small physical size, light weight, low cost and may be function at a high temperature (Paredes-Madrid et al., 2010). Maeno, et al., 2004; Edussooriya et al., 2008; De et al., 2015) proposed a control strategy to detect slipping off a grasped object using a Flexi-force. However, in order to have a good grasp, not only a force sensation, but also grasping strategies are thought to be important for firm grasping.

According to clinicians, the index finger and thumb are responsible for at least 75% of overall hand functions (Park et al., 2009). There is insufficient evidence in robotic literature on thumb behaviour, despite its important role in grasping operation. To collect information about thumb and fingers during grasping, optoelectronic motion analysis is used (Cordella et al., 2014).

There is little published data on grasping behaviour, this study aims to parameterize the grasping operation in relation to human motion and identify the kinematic parameters and forces related to particular grasping tasks.

## BACKGROUND STUDY

### Anatomy of Human Hand

The human hand consists of 27 bones, 14 of which are digital bones of the fingers and thumb. Figure 1 shows the skeleton structure of the human hand. A human hand consists of five digits; thumb, index finger, middle finger, ring finger, and little finger. Fingers consist of joints and bones which have similar characteristics, but the thumb has slightly different characteristics (Ungureanu, Stanciu & Menyhardt 2006). Each finger has three links, only the thumb has two joints.

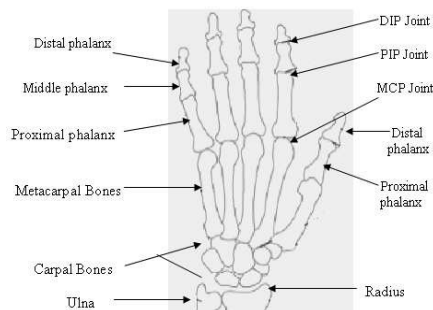


Figure 1. Joints of fingers (Institute for Quality and Efficiency in Health Care, 2012)

The fingers constitute of three interlinking segments: proximal phalange (PP), middle phalange (MP) and distal phalange (DP). The thumb is made up of two segments: proximal phalange (PP) and distal phalange (DP). The first phalanx is connected to the metacarpal bone that constitutes the palm and is connected to the carpal bones. The joints of the fingers are named:

Distal Interphalangeal (DIP), Proximal Interphalangeal (PIP) and Metacarpophalangeal (MCP) joints. The joints for the thumb named: Interphalangeal (IP) and Carpometacarpal (CMC). Joints of the hand vary in the number of degrees of freedom (DOF) they possess. For fingers, Distal Interphalangeal (DIP) and Proximal Interphalangeal (PIP) joints contribute to 1 DOF due to rotational movement while Metacarpophalangeal (MCP) contribute 2 DOF due to adduction-abduction and rotational motion. On the other hand, thumb possesses 5 DOF where Interphalangeal (IP) and Carpometacarpal (CMC) contributes 1 DOF.

### **Grasping Force**

Grasps are defined as a set of contacts on the surface of the object. During grasping, the object is compressed and force generated on the gripper finger to prevent the object from slipping. Many researchers have used piezoresistive Flexi-force to measure finger force (Edussooriya, et al., 2008). This sensor is particularly useful in studying finger force based on the divers advantages; low cost, good sensitivity, simple construction and enhances accuracy.

### **Motion Analysis**

Different kinematic hand models have been proposed using OptiTrack Motion. This system is composed of an infrared (IR) camera, passive ballshaped markers, calibration and analysis software. The ballshaped markers produce X, Y and Z coordinate values are tracked by the infrared cameras and analyze in VENUS 3D software. Using optoelectronic system MOTIVE Software, all marker position must be detected by the cameras (Dutta, 2012; Han & Lee, 2013). If the cameras failed to capture some markers for certain conditions, the cameras were re-positioned.

## **METHODOLOGY**

This project is to analyse human motion and pressure that is applied in grasping a paper cup weighing 200 g and with a radius 26 mm and height of 80 mm. The participant is required to fully extend the fingers and grasp the object with the right hand and lift it to a height of 4cm. Prior to data collection, the subject received an explanation of the experiment. The subject was asked to grasp paper cup using index finger and thumb.

### **Experimental setup**

This project combined two system simultaneously using motion capture system and Flexi-force sensor system. Figure 2 shows the block diagram of the proposed system.

Flexi-force sensors are connected to DAQ hardware and LabVIEW software to acquire sensors signal and facilitate analysis. Motion capture system was used OptiTrack camera to collect data during grasping operations and. Microsoft Visual Studio to program the Arduino UNO and synchronise two signals of the system. The frequency of both systems was set to 100Hz. Lamp act as indicated to compare the signal between both systems.

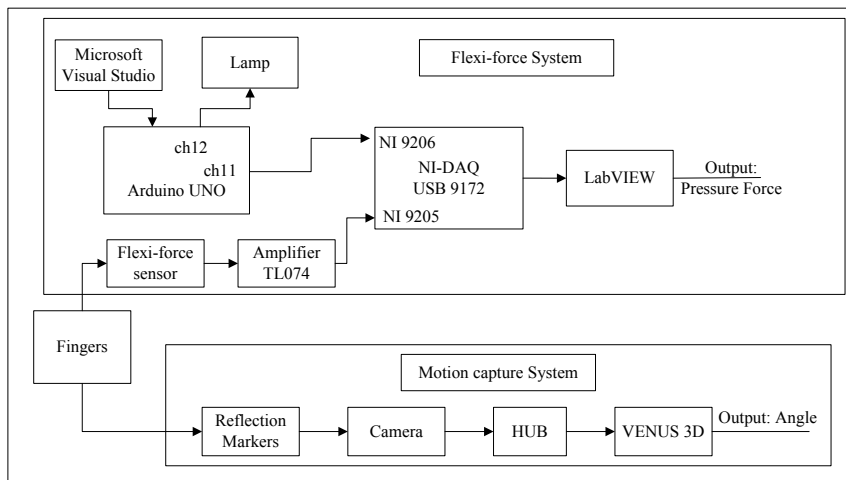


Figure 2. Block diagram of the proposed system)

### Flexi-force Sensor

In this paper, the LabVIEW based DAQ system is used to evaluate and measure the pressure force using Flexi-force sensor (0-25)lb/(110N) for real-time robotic hand control. Flexi-force sensors were attached to the fingertips of index finger and thumb as shown in Figure 3.

The Flexi-force sensor sends the signal to DAQ within millivolts range. Hence, sensor is connected to amplifier TL074 and the output voltage is connected DAQ and calibrated using a strain gauge by applying a known uniform weight to the sensing area using different weight. A linear interpolation between the voltage and pressure is plotted and the values were written in LabVIEW to analyse the measurement. Then output voltage from the sensor is converted to the pressure to measure pressure force during grasping.



Figure 3. Flexi-force sensor position

## Hand Motion Tracking

In this experiment, six cameras were positioned around the experimental area to detect the marker position and hand motion during grasping operation. We placed twelve reflection markers on the volunteer's right hand and on the object; eight markers were secured at every tip and joint of the index finger and thumb including DIP, PIP, MCP joints with IP and CMC joints of the thumb and four on the object as shown in Figure 4. Eyelash glue is used to fix the small marker. To minimize artefacts due to skin movements or marker occlusion, procedure for positioning markers on the hand has been chosen (Cordella, F. et al., 2014).

The marker position on the cup is able to extract the position of the object with respect to the object radius, height and location of the object during grasping. The motion analysis measures the joints angles by reconstructing the marker position in VENUS 3D software. Joint angles were defined as zero when the finger in fully extended posture.

## Data Analysis

A specific program was written in Microsoft Visual Studio to synchronise both systems. Motion capture system and LabVIEW software were run simultaneously to record grasping operation and the lamp as an indicator to synchronise the signals.

For starting configuration, all fingers were fully extended and the thumb was adducted. The marker position was recorded in starting position and during the whole motion until hand grasped the object. After grasping, subject held the object for a while until auditory cue then lifts the cup to 4 cm high and gradually release grasp until the object slipped. The process was repeated four consecutive times and all data were recorded. The joints angle measured for DIP joint of index finger and IP joint for thumb during grasping operation as shown in Figure 4.

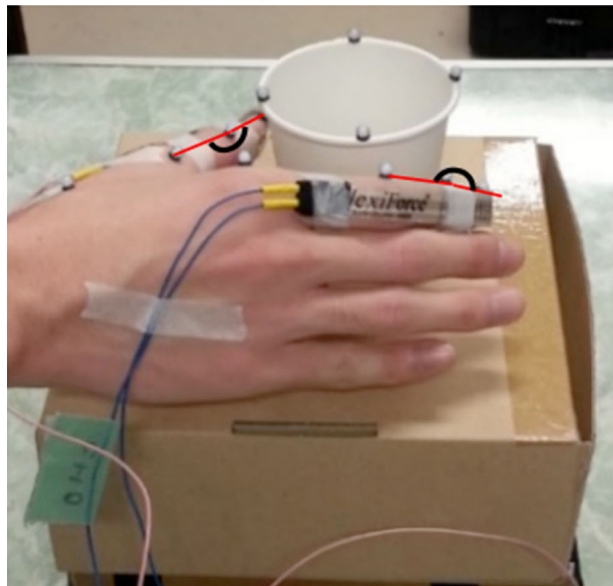


Figure 4. Markers position on volunteer's right hand

## RESULTS AND DISCUSSION

To date, this force measurement system and motion tracking has been applied to study the grasp between index finger and thumb. Figure 5 shows the experimental data on sensor and grasping behaviour of the grasp. The angle measured is DIP for index and IP for the thumb as shown in Figure 4. The graph divide the actions of lifting an object and setting it back down into seven states as shown in Table 1.

Figure 5 shows the sub-phases of movement which identified due to significant variations produced by the motion capture and measuring system (T1-T7); reaching, grasping, lifting, stable, slipping, release and original position. Using both systems allows the identification of variables which relevance to description of the movement.

Table 1  
Hand motion states

State	T1	T2	T3	T4	T5	T6	T7
Action	Reach	Grasp	Lift	Hold	Slip	Release	Original hand position

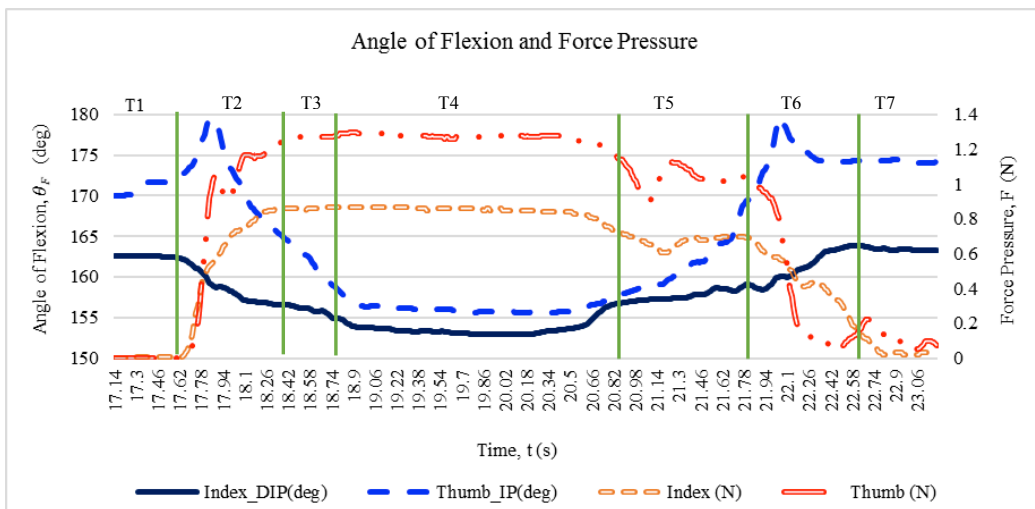


Figure 5. Angle of flexion and grasping force

The grasping force during lifting, stable and slippery states were measured and shown in Table 2.

An initial objective of the project was to identify the relationship between the grasping operation, the sensory system and human motion. Figure 5 presents the data while performing the grasp based on flexion angle of index finger and thumb and grasping force. Based on the results, the correlation between angle of flexion and force measurement is established. During



the grasping and lifting of a cup between the fingertips, the subject manipulated the cup for stable grasping and grasp force simultaneously caused small vibration in the data.

Another important finding was the force required to lift, grasp and release as shown in Table 2 shows during the first 2 s of contact with the cup are small compared to the forces needed to lift the cup off the table. The force required to lift the cup builds up gradually from the time of initial contact. The results confirm that lifting requires higher forces than grasping in the static phase due to gravitational force needed to lift an object. However, these results were not very encouraging because of the object's weight and the subject's limitation.

Table 2  
*Descriptive analysis of the forces*

	Contact Force, $F_c$ (N) Mean $\pm$ SD	Lifting Force, $F_L$ (N) Mean $\pm$ SD	Stable Force, $F$ (N) Mean $\pm$ SD	Slippery Force, $F_s$ (N) Mean $\pm$ SD
Thumb	0.800 $\pm$ 0.484	1.279 $\pm$ 0.009	1.266 $\pm$ 0.016	1.064 $\pm$ 0.078
Index	0.557 $\pm$ 0.312	0.862 $\pm$ 0.007	0.837 $\pm$ 0.013	0.688 $\pm$ 0.041

## CONCLUSION

This paper analyses index finger and thumb motion during grasping. Results indicate lifting requires more force than stable force. This research extends our knowledge of force required to model robot hand controller system.

## ACKNOWLEDGEMENT

This work is supported by the East Policy 2.0 Grants Programme (LEP 2.0).

## REFERENCES

- Adnan, N. H., Khairunizam, W. A. N., & Shahrman, A. B. (2012). Accurate measurement of the force sensor for intermediate and proximal phalanges of index finger. *International Journal of Computer Applications*, 45(15), 59-65.
- Adnan, N. H., Wan, K., Shahrman, A., Za'ba, S. K., Desa, H., & Aziz, M. A. A. (2012). The development of a low cost data glove by using flexible bend sensor for resistive interfaces. In *2nd Int. Malaysia-Ireland Joint Symposium on Engineering, Science and Business*.
- Ali, M. H., Khairunizam, W. A. N., Adnan, N. H., Seah, Y. C., Bakar, J. A. A., & Razlan, Z. M. (2013). Analysis of finger movement by using motion information from GloveMAP and motion capture system. *International Journal of Mechanical and Mechatronics Engineering*, 13(3).
- Cordella, F., Zollo, L., Salerno, A., Accoto, D., Guglielmelli, E., & Siciliano, B. (2014). Human hand motion analysis and synthesis of optimal power grasps for a robotic hand. *International Journal of Advanced Robotic Systems*, 11(37), 1-14.
- De Maria, G., Falco, P., Natale, C., & Pirozzi, S. (2015, May). Integrated force/tactile sensing: The enabling technology for slipping detection and avoidance. In *2015 IEEE International Conference on Robotics and Automation (ICRA)* (pp. 3883-3889). IEEE.

N. F. Elya Saidon, Chikamune Wada, Siti A. Ahmad, Ribhan Zafira Abdul Rahman, Kiyotaka Eguchi,  
Yoshiyuki Tomiyama and Farida Izni Abd Rahman

- Dipietro, L., Sabatini, A. M., & Dario, P. (2008). A survey of glove-based systems and their applications. *IEEE Transactions on Systems, Man, and Cybernetics Part C: Applications and Reviews*, 38(4), 461-482.
- Dutta, T. (2012). Evaluation of the kinect™ sensor for 3-D kinematic measurement in the workplace. *Journal of Applied Ergonomics*, 43(4), 645-649.
- Edussooriya, C. U. S., Hapuachchi, H. S. S., Rajiv, D., Ranasinghe, R. A. H., & Munasinghe, S. R. (2008). Analysis of grasping and slip detection of the human hand. In *International Conference on Information and Automation for Sustainability* (pp. 261-266).
- Han, S., & Lee, S. (2013). A vision-based motion capture and recognition framework for behavior-based safety management. *Journal of Automation in Construction*, 35, 131-141.
- Kazerooni, H., Fairbanks, D., Chen, A., & Shin, G. (2004, May). The magic glove. In *Robotics and Automation, 2004. Proceedings. ICRA'04. 2004 IEEE International Conference on* (Vol. 1, pp. 757-763). IEEE.
- Maeno, T., Kawamura, T., & Cheng, S. C. (2004). Friction estimation by pressing an elastic finger-shaped sensor against a surface. *IEEE Transactions on Robotics and Automation*, 20(2), 222-228.
- Monroy, M., Ferre, M., Barrio, J., Eslava, V., & Galiana, I. (2009, April). Sensorized thimble for haptics applications. In *2009 IEEE International Conference on Mechatronics*.
- Paredes-Madrid, L., Torruella, P., Solache, P., Galiana, I., & de Santos, P. G. (2010, May). Accurate modeling of low-cost piezoresistive force sensors for haptic interfaces. In *Robotics and Automation (ICRA), 2010 IEEE International Conference on* (pp. 1828-1833). IEEE.
- Park, W. I., Kwon, S. C., Lee, H. D., & Kim, J. (2009, June). Thumb-tip force estimation from sEMG and a musculoskeletal model for real-time finger prosthesis. In *2009 IEEE International Conference on Rehabilitation Robotics* (pp. 305-310). IEEE.
- Ungureanu, L., Stanciu, A., & Menyhardt, K. (2006, October). Actuating a human hand prosthesis: model study. In *2nd WSEAS International Conference on Dynamical Systems and Control, Bucharest Romania*.
- Ye, Z., & Auner, G. (2003, June). Haptic interface prototype for feedback control on robotic integration of smart sensors. In *Control Applications, 2003. CCA 2003. Proceedings of 2003 IEEE Conference on* (Vol. 2, pp. 995-1000). IEEE.



## **Control of Wastewater Treatment by using the Integration MATLAB and LabVIEW**

**Ilanur Muhaini Mohd Noor and Muhamad Kamal M. A.**

*Bio-Inspired System and Technology Research Group, Malaysia-Japan International Institute of Technology (MJIT), Universiti Teknologi Malaysia (UTM), Kuala Lumpur, Malaysia*

### **ABSTRACT**

This research attempts to enhance of the ability of Fuzzy Logic Controller in controlling wastewater treatment system, highlighting the pH parameter in factory wastewater treatment plants. The research not only covers methods to monitor and track the pH level in wastewater tank but more importantly, the control of total wastewater volume by neutralising the pH. Fuzzy logic control has gained more attention in the control of continuous processes. It utilised both, in the context of deciding and tracking set-points, and to control the total unwanted water capacity. This paper also discusses suitable level of pH required which will not damage the water ecosystem. The self-learning fuzzy logic control with adaptive capabilities alert operator in charge of the pH level automatically. This research includes the design and development a graphical user interface (GUI) to show the process of pH neutralisation in wastewater treatment. A fast response system is achieved through GUI which could be monitored and control remotely using laptop or smartphone, from anywhere. This proposed design will inform engineers and technicians about the status of the current reading of parameters in the wastewater treatment system without the hassle of going to the site or control room of the wastewater treatment plant.

*Keywords:* Fuzzy Logic Controller, pH, MATLAB, LabVIEW

### **INTRODUCTION**

This research has been carried out to analyse fuzzy logic used in controlling process tank

in industrial wastewater systems. The process of wastewater treatment is complicated and nonlinear. This research introduces an effective and robust control approach to control concentration in a wastewater treatment process. In this research, focus will be on pH, which is one of the parameters involved in wastewater treatment. In wastewater treatment, the pH is controlled to maintain the pH to neutral value which is within the range of 6 to 8 according to

#### **ARTICLE INFO**

*Article history:*

Received: 24 August 2016

Accepted: 02 December 2016

*E-mail addresses:*

ilanur@hotmail.com (Ilanur Muhaini Mohd Noor)

mkamalma@upm.my (Muhamad Kamal M.A)

\*Corresponding Author

statistics from United Nations (UNDESA, 2006). Neutralisation is a process of adding acid or alkali solution to waste water in order to obtain the neutral pH range (pH 7). pH (hydronium potential) neutralisation process control plays an important role in the control of pH level in numerous industries such as biotechnology, manufacturing, chemical, sewage treatment, paper factory, pharmaceutical, agriculture, food processing, research laboratories, rain water harvesting, waste water treatment and many other industries where a certain pH level has to be maintained for suitable applications. pH levels of waste water produced by factories have to be controlled and maintained at neutral range before the effluent is discharged in accordance to environmental regulations. The focus of this research is to design and implement a fuzzy controller to obtain a neutral pH for the wastewater treatment plant using LabVIEW software and to simulate the pH level of mix tank with randomly sensed pH values before analysing the non-linear system.

The main idea of the research is to control the flow rate of acid liquid and alkali liquid into the mix tank to maintain the mix tank at neutral pH which is 7. The manner in which the flow rate is quantified depends on whether the quantity flowing is a solid, liquid or gas. For solid, it is appropriate to measure the rate of mass flow, whereas in the case of liquid and gases, flow is usually measured in terms of the volume flow rate. The system will calculate the concentration (M) based on the pH value after the wastewater pH value in the mix tank is sensed. If the pH value is 7, then no acid or base will be pumped into the mix tank but if it is less or more than 7, then it will recalculate the concentration value so that a specific amount of acid or base will be added. Results of the output level of the mix tank after randomly accomplishing inputs from pH sensor in the mix tank. By implementing fuzzy algorithms based on the pH level sensed by the sensor the valve opening of respected acid or alkali solution can be generated in order to achieve the neutral range. Wright and Kravaris (1991) said that “by measuring the effluent pH it is impossible to uniquely determine the effluent ion concentrations and by manipulating the titration stream flow rate it is impossible to move the effluent concentrations to arbitrary values”. Hence, as the influent stream changes, the titration curve also changes significantly, so an efficient system is necessary in producing satisfactory results. A strategic method to solve nonlinearity and time delay in pH control was introduced by Wang et al. (2009) where predictive control model was used based on hierarchical optimisation in rolling mill waste water treatment (Takekawa et al., 2010). Fuzzy control was applied to a “P” and “PD” plant to perform pH control by De Azevedo et al. (2011) for neutralising rain water in order to reuse it; a comparison was also done between the controllers. An analysis of the system was done under two different circumstances, namely where only error was considered for the plant input and variation of error was considered in the other situation. Fuzzy logic based PID control of pH neutralisation process was carried out by researchers Jebarani, D, I. & Rammohan, T. (2014) for waste water treatment systems. The input to the fuzzy control was based on the feedback from the output values of the PID controller and with reference to set point whereby a new value is set for the PID flow rate controller.

## METHODOLOGY

### The pH value and Molar Concept

The pH value of a substance is directly related to the ratio of the hydrogen ion  $[H^+]$  and the hydroxyl ion  $[OH^-]$  concentrations. If the  $H^+$  concentration is greater than  $OH^-$ , the material is acidic, i.e., the pH value is less than 7. If the  $OH^-$  concentration is greater than  $H^+$ , the material is basic, with a pH value greater than 7. If equal amounts of  $H^+$  and  $OH^-$  ions are present, the material is neutral, with a pH of 7. Acids and bases have free hydrogen and hydroxyl ions respectively. Since pH is a logarithmic function, a change of one pH unit represents a ten-fold change in hydrogen ion concentration. There are miscellaneous bacteria involved in anaerobic sludge digestion (Feng et al., 2009) and the growth rate is affected by pH. A mole of a compound is defined as Avogadro's number of molecules ( $6.02 \times 10^{23}$  molecules), which has a mass approximately equal to the molecular weight, expressed in grams. For example, sodium hydroxide, NaOH, which has a molecular weight of  $23+16+1=40$ , would have 40 grams in a mole. Since the atomic weight of the hydrogen ion ( $H^+$ ) is one (1), there is one gram of hydrogen ions in a mole of hydrogen. A solution with a pH of 10 has  $1 \times 10^{-10}$  moles of hydrogen ions, or  $10^{-10}$  grams in a one litre solution (Cosmin et al., 2012).

### Fuzzy Logic Controller

In this research, the aim is to maintain the pH level of wastewater mix tank to pH 7 which is the neutral pH. Based on the value of pH sensed by the pH sensor in the mix tank, either one of the tank which consists of acid or alkali will be pumped into the mix tank. If the pH sensor in the mix tank shows pH less than 7, it is considered as acidic. Therefore, a certain amount of alkali will be pumped into the mix tank to maintain the pH to neutral value. If the pH sensor in the mix tank shows pH more than 7 (between 8-14) then it is considered as base. Therefore, certain amount of acid will be pumped into the mix tank to maintain the pH to neutral value. If the pH sensed by sensor in the mix tank shows the pH to be exactly 7, then both valve for alkali and acid will be closed to make sure that none of it is pump into the mix tank. Advantages of using a fuzzy logic system is that it has the capability of controlling nonlinearity by formalising the set of rules set by human to act intelligently in providing the output.

### Construction of System Using Fuzzy Logic Toolbox

The Fuzzy Logic Toolbox could create and edit fuzzy inference systems. These systems could be created using graphical tools or command-line functions, or it could be generated automatically using either clustering or adaptive neuro-fuzzy techniques (Sabri & Almshat, 2015). In the Fuzzy Inference System or FIS Editor, the first step is to design the fuzzy controller. In this editor, the input and output variable are included. The Mamdani (2004) method is used for the system.

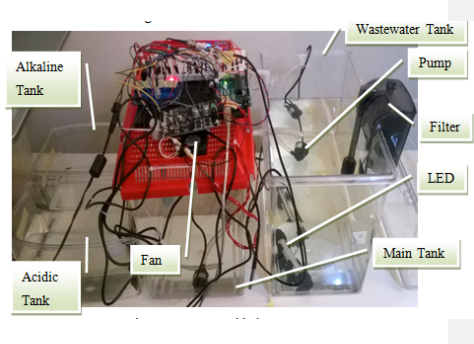
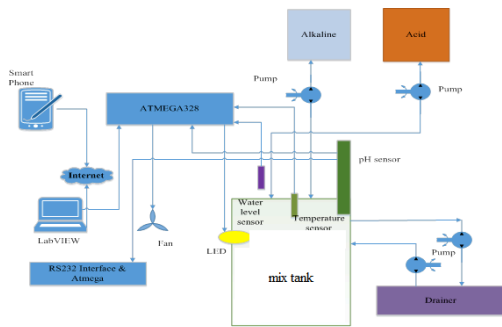


Figure 2.0. Hardware components interfaced with LabVIEW      Figure 2.1. Low cost prototype

A low-cost microcontroller was used (Arduino Uno) to control the whole system (Figure 2.0). A research was carried out with low cost prototype (Figure 2.1) which can be interfaced with the GUI created and provided faster response in the neutralisation process. The main control element in the neutralisation system is the control valve. Even though low cost components and materials were used, it did not compromise the outcome. It has to be noted that there must not be any delay in the polling of data and controlling of the system between the GUI and the prototype. Testing was done after interfacing the hardware with the GUI using serial cable. Control signals were sent from the GUI and the response was observed from the prototype. The wiring diagram is the control circuitry illustration (Figure 2.2) sketched using Proteus software. As shown in Figure 2.2, controller was connected to three different inputs and outputs mechanism.

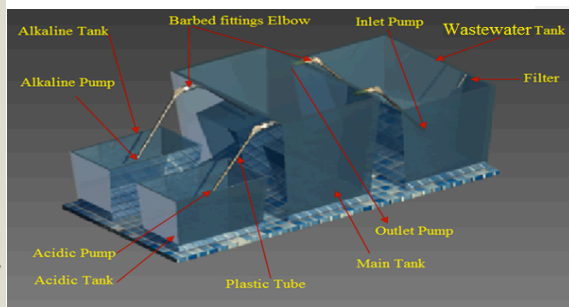
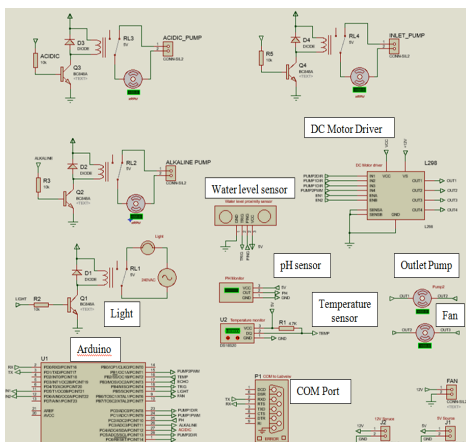


Figure 2.2. Wiring diagram

Figure 2.3. 3D

## Design of the prototype

The position, size and the number of the tanks were selected due to their availability and reduced power consumption as shown in Figure 2.3. If tanks are not placed at the same level, there will be increased power consumption because pumps are operating against gravity with higher elevation difference.

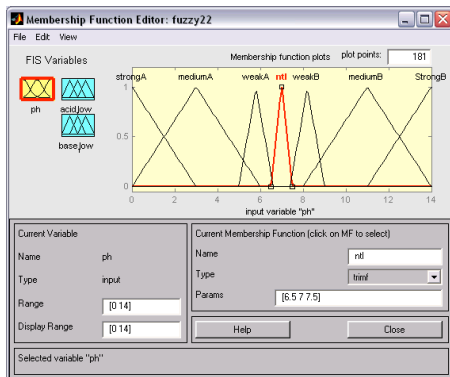


Figure 3.1. Membership Function Editor of pH

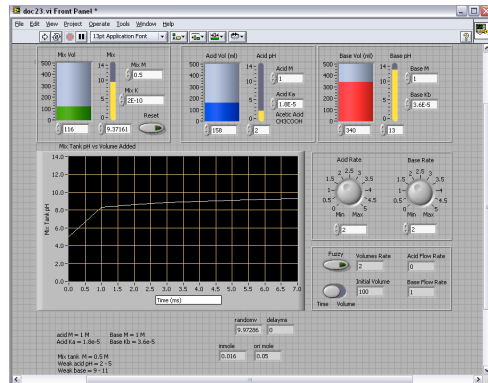


Figure 3.2. Front panel of the completed project

## RESULTS AND DISCUSSION

To measure the current pH (to remain at or near neutral level or within some range), and have control over two valves for the acid tank and alkali (base) tank to be pumped into the mix tank, the following steps need to be followed as shown in Membership Function Editor of Figure 3.1:

- i) Establish fuzzy membership functions for pH, such as “Strong acid”, “Medium acid”, “Weak acid”, “Neutral”, “Weak Base”, “Medium Base” and “Strong Base”. This will need to be done for pH rate of change or any other derivatives of pH as well.
- ii) Establish fuzzy membership functions (Figure 3.1) for the two outputs flow rate, one for acid tank and the other for base tank, such as “Off”, “Slow”, “Medium” and “Fast”.
- iii) Write rules linking the desired outputs to the given inputs, for example: (if pH is strong acid (strong A) then acid flow is off and base\_flow is fast)

The front panel (Figure 3.2) is where the Graphical User Interface (GUI) is located. Users could set in any first value of the pH, and it will generate automatically random pH value to be simulated. In the real situation, this first value is being sensed by the pH sensor in the plant and the signal is sent to the software via data acquisition (DAQ card). At the same time, volume of wastage in the mix tank will be reduced and which can be viewed in this panel. There are two indicators: pH level indicator and volume indicator in the mix tank. Another two sets of similar tank volume and pH indicator is shown for acid and alkali tanks. The simulation could be viewed in two different forms. One by inserting the fuzzy system in the system and the other one without it. The graph could also be viewed in two different units. One is pH versus time



and the other is pH versus volume inserted. Acid and base flow rate could be adjusted by using two knobs, which resemble valves, at the right side of the front panel. In the programming section (block diagram) in Figure 3.3, it consists of few subs VI, function icon, and a loop including the pH of Acid, pH of Base, Number of Mol, For Loop, Subtract Icon, Add Icon, Less Icon, MATLAB script editor to call MATLAB fuzzy logic controller file into LabVIEW environment and MATLAB m-files programming modules on various tasks.

When the pH is 1.862 (Figure 3.4) which is acidic, there will be no acid flow into the mix tank but there will be 0.56ml/ms of base flows into the mix tank. Therefore, in the rule viewer of Figure 3.4, acid flow = 0 and base flow = 0.56ml/ms. When the pH is 12.78 (Figure 3.5) which is alkaline, there will be no base flow into the mix tank but there will be 0.601ml/ms of acid flows into the mix tank. Therefore, in the rule viewer of Figure 3.5, acid flow = 0.601ml/ms and base flow = 0.

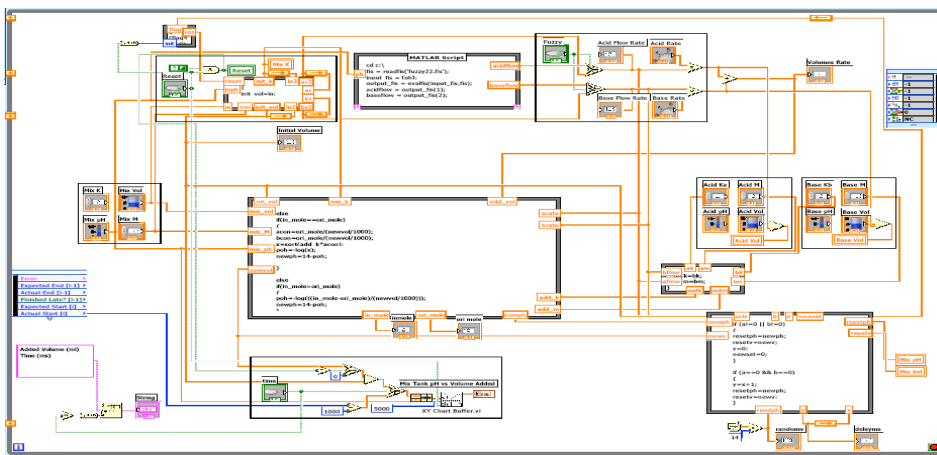


Figure 3.3. Block diagram (programming) of the whole research

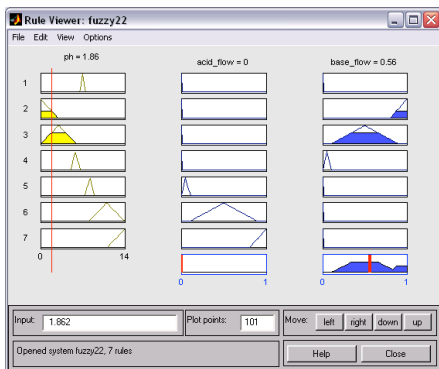


Figure 3.4. Rule viewer at pH 1.862

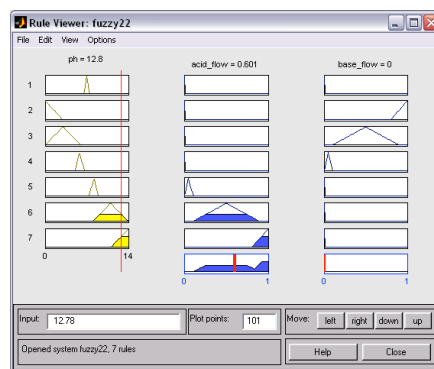


Figure 3.5. Rule viewer at pH 12.78



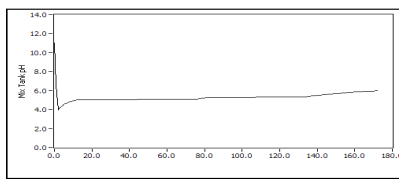


Figure 3.7. pH sensed in Mix tank versus time

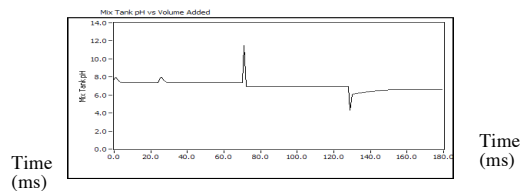


Figure 3.8. pH in Mix tank versus time

### Results of the output level of the mix tank after randomly accomplishing inputs from pH sensor in the mix tank

In Figure 3.6, as soon as the pH level in the mix tank is 11, the system will drop the pH level in mix tank to pH 4 for the first 2.0 ms. After 2.0 ms, it will slowly increase to neutral starting from pH 4 to pH 7. This figure shows the time from 0 ms to 180.0 ms. For Figure 3.7, as soon as the pH level in the mix tank is 8, the system will drop the pH level in mix tank to pH 7 for the first 70.0 ms. After 70.0 ms it drastically increases to pH 11. This happens due to chemical reaction but it drastically drops to neutral at 73.0ms. This figure shows the time from 0ms to 180.0 ms. This chemical reaction again happens at 130.0 ms but increases to the neutral value again after that. This shows that even though it is hard to predict when the chemical reaction drastically changes the graph but a well-designed system could bring the pH value back to the desired neutral value. Therefore, the characteristics of Figure 3.6 and Figure 3.7, show that even though the time exceeds to 180ms, the system maintains the mix tank pH at values which approaches neutral. The objective of this research was to maintain pH level at neutral in the mix tank which was achieved here. Huan et al. (2014) proposed network via wireless system to android phone. This system will enable engineers and technicians to be alert about the status of the current reading of parameters in the wastewater treatment system without hassle to go to the site or control room of the wastewater treatment plant.

### CONCLUSION

The system that had been created could maintain the pH level at neutral whenever random values are supplied to the mix tank. This mix tank is especially important in the industrial area because industries usually throw their prerequisite liquid which could affect the environment. This research has shown that pH control is a non-linear and it could be controlled using fuzzy logic controller. The system could be remotely controlled from anywhere by using online system connected to the proposed project. The rating of the overall system performance can be up to 95%.

### REFERENCES

Cosmin, D., Ramona, H., Ruben, c. & Ioan, n. (2012). Modelling and Internal Model Control Strategy of pH Neutralization Process. *Institute of Electrical and Electronics Engineers*, 12, 1579-1582.

- de Azevedo Dantas, A. F. O., de Lima, F. A., Maitelli, A. L., & Dantas, G. F. (2011, November). Comparative study of strategies for fuzzy control P and PD applied to a pH plant. In *IECON 2011-37th Annual Conference on IEEE Industrial Electronics Society* (pp. 516-521). IEEE.
- Huan, J., Liu, X., Li, H. Wang, H. & Zhu, x. (2014) A monitoring and control system for aquaculture via wireless network and android platform. *Journal of Sensors and Transducers*, 169, 250-256.
- Jebarani, D, I. & Rammohan, T. (2014). Fuzzy Logic based PID Controller for pH Neutralization Process. *International Journal of Computer Applications*, 95(6), 36-39.
- L.Y. Feng, Y.Y. Yan, Y.G. Chen (2009). Kinetic analysis of waste activated sludge hydrolysis and short-chain fatty acids production at pH 10. *Journal of Environment Science*, 21(5), 589–594.
- Mamdani, E.H. (2004). Soft computing as a tool, Fuzzy Systems. In *Proceedings of IEEE International Conference on*, (Vo.1, pp. 31 – 31). IEEE.
- Sabri, I., & Almshat, H. (2015). Implementation of fuzzy and PID controller to water level system using LabVIEW. *International Journal of Computer Applications*, 116(11), 6-10.
- Takekawa, M., Aoki, J., Nakaya, M., Ohtani, T. & Ohtsuka, T. (2010). An Application of Nonlinear Model Predictive Control using C/GMRES method to a pH Neutralization Process. In *SICE Annual Conference, Taipei*, 18th -21st August 2010. (pp. 1494-1496).
- Wang, W., Long, W., & Hu, L. (2009, May). Nonlinear Model Predictive Control of pH in Rolling Mill Wastewater Treatment. In *Intelligent Systems and Applications, 2009. ISA 2009. International Workshop on* (pp. 1-5). IEEE.
- Wright, R. A., & Kravaris, C. (1991). Nonlinear control of pH processes using the strong acid equivalent. *Industrial and Engineering Chemistry Research*, 30(7), 1561-1572.

## **LLC Resonant Converter with Series-Connected Primary Windings of Transformer for PEV Battery Charging**

**Shahid Iqbal<sup>1</sup>, M. Imran Shahzad<sup>1,2</sup> and Soib Taib<sup>1</sup>**

<sup>1</sup>*School of Electrical & Electronic Engineering, University Sains Malaysia, 14300 Nibong Tebal, Pulau Penang, Malaysia*

<sup>2</sup>*Department of Applied Physics, Federal Urdu University of Arts, Science & Technology, G-7/1, 44000 Islamabad, Pakistan*

### **ABSTRACT**

This paper proposes a half-bridge LLC resonant converter with two resonant tanks for plug-in electric vehicle (PEV) battery charging. Each resonant tank is connected with one of the centre-tapped primary windings of the power transformer. Both resonant tanks are fed alternately by a half cycle of the switching pulse in one period. The converter is designed to operate below resonance zero-voltage switching (ZVS) region to reduce switching losses and to achieve output DC voltage range 250V-420V with 400V input DC voltage for depleted PEV battery. MATLAB Simulink is used to simulate the circuit with 1.5 kW maximum power and the simulation results show that the converter can meet the constant-current, constant-voltage (CC-CV) charging requirements of the depleted PEV battery.

*Keywords:* LLC resonant converter, PEV battery charger, FHA

### **INTRODUCTION**

Due to the threat of fossil fuel depletion, global warming and environmental issues, the interest in PEVs is growing continuously. High power density, high efficiency, smooth and quick charging are the desired features expected

from onboard PEV chargers. Lithium-ion (Li-ion) battery packs are preferred for PEVs due to their salient features including slow depletion of energy, high energy density, and no memory effect and a charging profile of single cell Li-ion battery is shown in Figure 1 (a) (Wang et al., 2014c). In this profile, 1V-2.5V is a deeply depleted battery voltage range and 2.5V-4.2V is the normally depleted battery voltage range. Thus, the depleted battery voltage range of 100 cells in series for PEV battery pack can be extracted from this profile which maps to 250V-420V. The battery charging consists of constant-current (CC) and constant-voltage (CV) charging

#### **ARTICLE INFO**

*Article history:*

Received: 24 August 2016

Accepted: 02 December 2016

*E-mail addresses:*

shahid.iqbal@usm.my (Shahid Iqbal),

ishzd@yahoo.com (M. Imran Shahzad),

soibtaib@usm.my (Soib Taib)

\*Corresponding Author

stages. In CC charging stage, the voltage varies between 250V and 420V range starting from the initial voltage of the battery using constant charging current. In CV charging stage, the charging voltage is kept constant at 420V while the current decreases and when it drops down to a minimum threshold, charging stops.

Figure 1 (b) shows a commonly used power architecture of a two stage PEV battery charging system with power factor correction (PFC) stage and DC/DC conversion stage (Junjun et al., 2014). The PFC stage converts the line AC voltage to a regulated DC voltage and takes care of harmonic distortion to keep the power factor near unity. The DC/DC converter regulates current for CC charging and voltage for CV charging modes providing galvanic isolation. At this stage, ZVS resonant converters are preferred to enhance charging efficiency. In particular,, LLC series resonant converters have desired features such as ZVS operation on primary and ZCS operation on secondary side, short circuit protection capability and good voltage regulation over light load (Wang et al., 2014a, 2014b). This paper is focused on DC/DC stage of battery charger (see Figure 1).

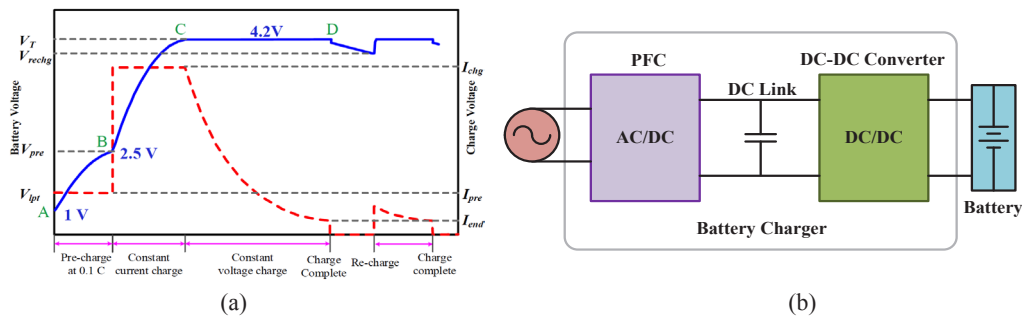


Figure 1. (a) Charging profile of a Li-ion battery cell; (b) Power architecture of a battery charger

Researchers proposed many PEV battery charging solutions using LLC resonant converter with constant or variable DC-link voltage. For fixed DC-link voltage case, around 400V DC is regulated at DC-link and charging voltage range is achieved by switching frequency variation of LLC converter. Wang et al. (2014a) achieved 320V-420V range using full-bridge LLC converter and 250V-420V range is achieved by (Wang et al., 2014c) and simulation results are given. Junjun et al. (2014) achieved 250V-450V range and presented the design methodology. Wang et al. (2014b) achieved 320V-420V output voltage range using LLC converter operating around resonance frequency and variable input voltage at DC-link. The DC-link voltage is controlled at AC/DC conversion stage. All these studies used full-bridge LLC converter with four switches.

This paper proposed an LLC resonant converter with two resonant tanks for DC/DC stage of PEV battery charger using half-bridge configuration with only two switches which will eventually reduce cost. The converter achieved the charging voltage range of 250V-420V with below resonance frequency operation using only two power switches compared to full-bridge used by (Wang et al., 2014a, 2014b). Simulation results are presented to verify the operation

of the converter. The rest of the paper is organised as follows: Section 2 describes the proposed converter while in section 3, equivalent AC circuit of the converter with gain characteristics and design procedure are presented. In section 4, simulation results are given and conclusion is drawn in section 5.

### PROPOSED LLC CONVERTER WITH TWO RESONANT TANKS

The schematic of proposed LLC resonant converter with series-connected primary windings of the centre-tapped transformer is shown in Figure 2. The proposed converter consists of a DC source, half-bridge, two resonant tanks  $RCT1$  and  $RCT2$ , a centre-tapped transformer, a bridge rectifier with output filter capacitor  $C_o$ , and the output load  $R_L$ .  $RCT1$  consists of resonant capacitor  $C_{r1}$ , resonant inductor  $L_{r1}$ , and magnetising inductance  $L_{m1}$  and similarly  $RCT2$  consists of  $C_{r2}$ ,  $L_{r2}$ , and  $L_{m2}$ . The two power switches are connected to the primary windings  $N_{p1}$  and  $N_{p2}$  through  $RCT1$  and  $RCT2$ . The series resonant tanks  $RCT1$  and  $RCT2$  are alternatively fed from DC source by turning on power switches  $S_2$  and  $S_1$  respectively with complimentary half switching cycles. Therefore, double power is transferred to the load in every switching cycle and input current is fetched twice in a switching cycle compared with half bridge converter.

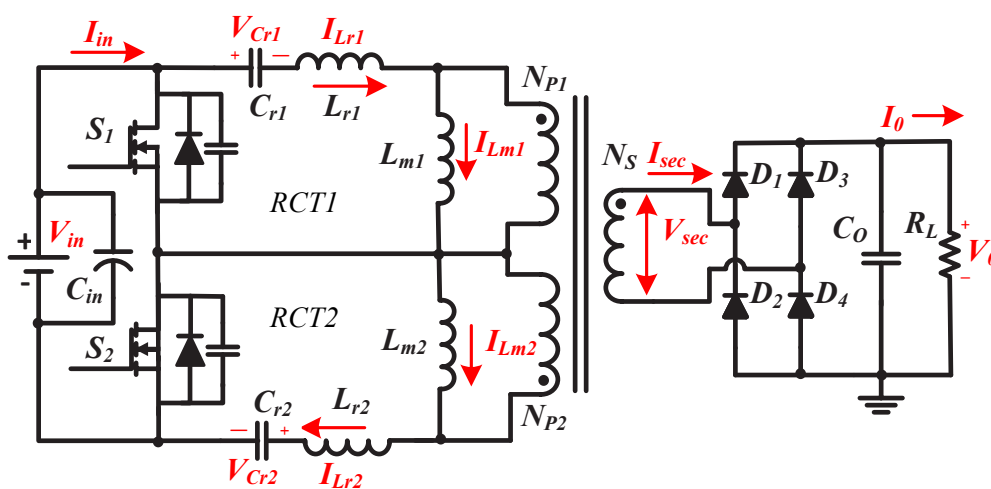


Figure 2. Proposed converter schematic

The primary windings  $N_{p1}$  and  $N_{p2}$  share the load equally and thus, half of the total current flows through each resonant tank. This reduces the components' stress to half in the resonant tanks compared with the conventional half-bridge LLC resonant converter topology which reduces the associated ohmic losses. Since there is only one transformer in the circuit, the core losses are also reduced compared with the topology proposed by (Lin & Wu 2011) with two transformers.

### GAIN CHARACTERISTICS OF LLC CONVERTER

As the resonant tanks  $RCT1$  and  $RCT2$  are symmetrical, therefore, the analysis of gain characteristics of only one resonant tank will be sufficient. The AC equivalent circuit of  $RCT1$  is shown in Figure 3 (a). The input to the tank is a square wave with minimum zero to maximum value equal to the input voltage. To analyse the gain characteristics we apply fundamental harmonic approximation (FHA) approach. The fundamental components of tank input voltage and resonant current are given as;

$$V_{ab1}(t) = \frac{2}{\pi} \sin(\omega_s t) \text{ and } i_{Lr1}(t) = \sqrt{2} I_{Lr1} \sin(\omega_s t - \phi) \quad (1)$$

where  $I_{Lr1}$  is the RMS value of tank current  $i_{Lr1}$  and  $\phi$  is the current phase shift relative to tank voltage. The fundamental component of voltage across  $Np_1$  is given as:

$$V_{Lm1}(t) = \frac{4nV_0}{\pi} \sin(\omega_s t) \quad (2)$$

Where  $V_0$  is the output voltage and  $n$  is the transformer turns ratio. The primary windings share the current equally and the maximum primary current in each winding in terms of output current  $I_0$  is given as:

$$i_p(\text{max}) = \frac{i_s(\text{max})}{2n} = \frac{\pi I_0}{4n} \quad (3)$$

Thus, the equivalent AC resistance reflected to the primary side is given as:

$$R_{ac1} = \frac{V_{Lm1}(\text{max})}{i_p(\text{max})} = \frac{16n^2}{\pi^2} R_0 \quad (4)$$

With  $R_0 = V_0/I_0$ , and this shows that the reflected load is four times of that reflected in converter presented by (Lin & Wu, 2011). The voltage gain can be obtained from AC equivalent circuit in Figure 4 (a) as:

$$G = \frac{2nV_{01}}{V_{ab1}} = \left| \frac{sL_{m1} \parallel R_{ac1}}{Z_{in1}(s)} \right| = \left| \frac{sL_{m1} \parallel R_{ac1}}{\frac{1}{sC_{r1}} + sL_{r1} + sL_{m1} \parallel R_{ac1}} \right| = \frac{k}{\sqrt{\left(1 + k - \frac{1}{f_n^2}\right)^2 + Q^2 k^2 \left(f_n - \frac{1}{f_n}\right)^2}} \quad (5)$$

Where  $k = L_{m1}/L_{r1}$ ,  $Q = Z_{in1}/R_{ac1} = \left(\sqrt{L_{r1}/C_{r1}}\right)/R_{ac1}$ ,  $f_n = f_s/f_{r1}$ ,  $f_{r1} = 1/2\pi\sqrt{L_{r1}C_{r1}}$ ,

with  $f_s$  as switching frequency and  $f_{r1}$  as resonant frequency. The output voltage curves versus switching frequency with quality factor  $Q$  for the three key operating points B, C and D in the charging profile in Figure1 (a) are shown in Figure 3 (b). Using design procedure by (Shahzad et al., 2014) the tank parameters are calculated as:  $L_{r1} = L_{r2} = 46.6 \mu\text{H}$ ,  $L_{m1} = L_{m2} = 141.5 \mu\text{H}$ ,  $C_{r1} = C_{r2} = 23.8 \text{ nF}$ ,  $n = 0.7974$ ,  $k = 3.4$ , and  $Q = 0.44$ .

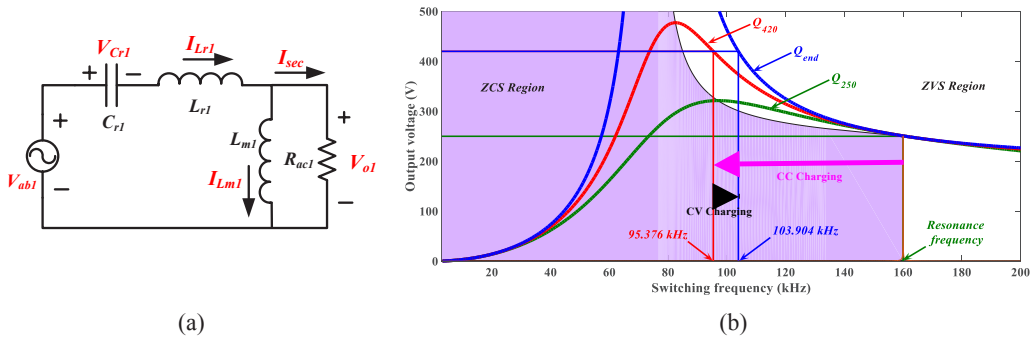


Figure 3. (a) AC Equivalent circuit; (b) Output voltage versus switching frequency curves for three key operating points B, C and D

### SIMULATION RESULTS

Figure 4 shows simulation model of the proposed LLC resonant converter using MATLAB Simulink. The simulation results show the operation of converter at key operating points B, C and D in charging profile using CC-CV method. The converter achieves the charging voltage range of 250V-420V operating below resonance frequency in the ZVS region. At each key operating point, simulation results are presented in two combinations. Each combination shows the operating waveforms of tanks input voltages  $V_{ab1}$  and  $V_{ab2}$ , resonant capacitor voltages  $V_{Cr1}$  and  $V_{Cr2}$ , resonant currents  $I_{Lr1}$  and  $I_{Lr2}$ , and magnetising currents  $I_{Lm1}$  and  $I_{Lm2}$ . The second combination shows the waveforms of secondary voltage  $V_{sec}$  and secondary current  $I_{sec}$ , rectifier diode currents  $I_{D1}$  and  $I_{D2}$ , and switches current  $I_{sw1}$  and  $I_{sw2}$ .

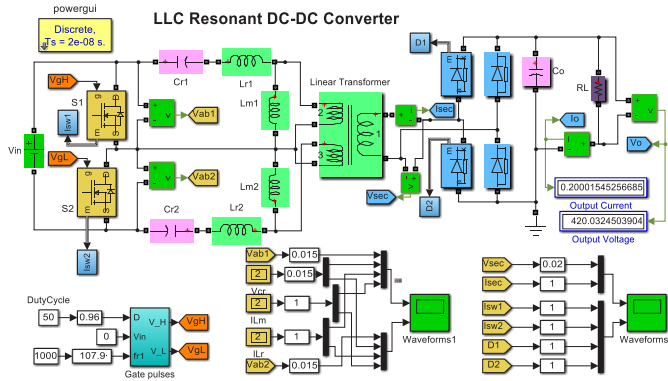


Figure 4. MATLAB simulation model of the proposed LLC converter

Figure 5 shows the operation of converter at resonance frequency with minimum circulating current. The power switches have ZVS turn-on and the turn-off current is 2A, whereas the secondary rectifiers have ZCS operation. The converter is operating at key operating point B with charging voltage  $V_0 = 250V$  at constant current as  $I_0 = 3.57A$  and is the minimum voltage point in a normally depleted battery. From this voltage to 420V, the battery is charged at constant maximum current.

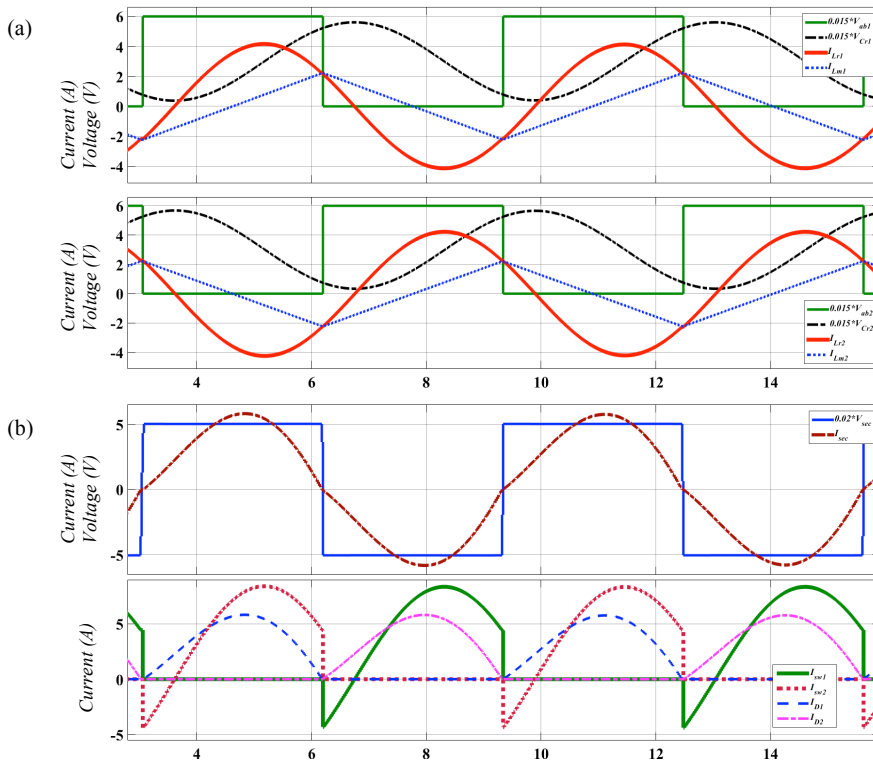


Figure 5. Operation waveforms at key point B. (a) First Combination; (b) Second Combination



Figure 6 shows the operation of converter at minimum switching frequency 98.6 kHz which is the point with maximum power during charging operation. The power switches have ZVS turn-on and the turn-off current is 3.7A with ZCS operation of secondary diodes. The converter is operating at key operating point C with output voltage  $V_o = 420V$  and constant current  $I_o = 3.57A$ . At this point, the mode transition from CC charging to CV charging occurs.

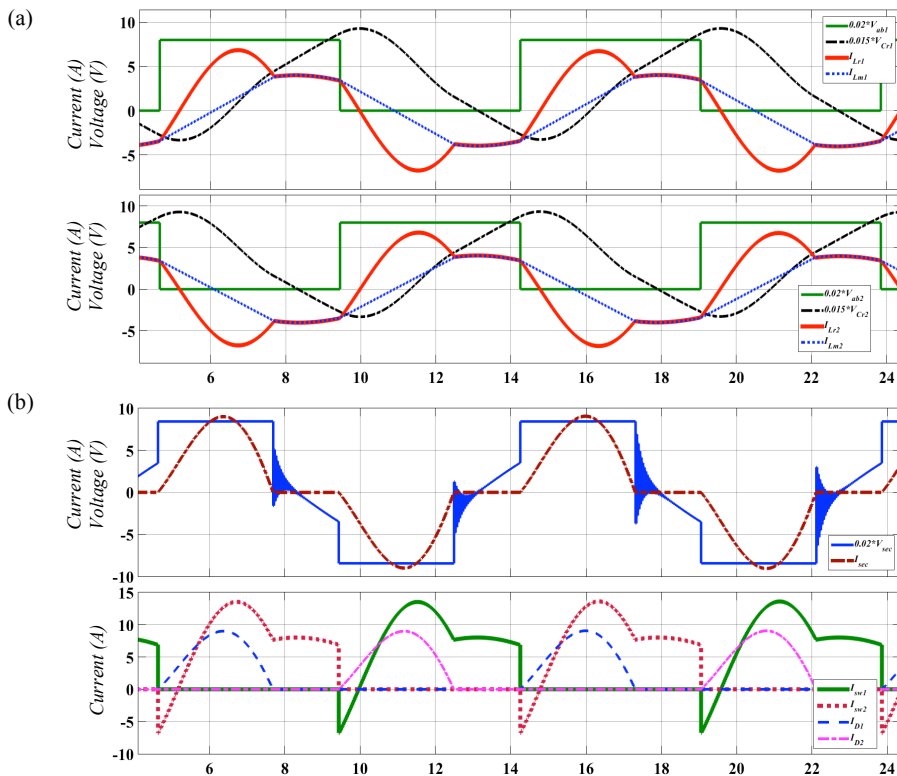


Figure 6. Operation waveforms at key point C. (a) First Combination; (b) Second Combination

Figure 7 shows the operation of converter at switching frequency 104.3 kHz which is the key operating point D with minimum power during charging process. The power switches have ZVS turn-on and the turn-off current is 3.7A with ZCS operation of secondary rectifier diodes. The converter is operating with output voltage  $V_o = 420V$  and threshold current as  $I_o = 0.2A$ . At this point the charging process is terminated.

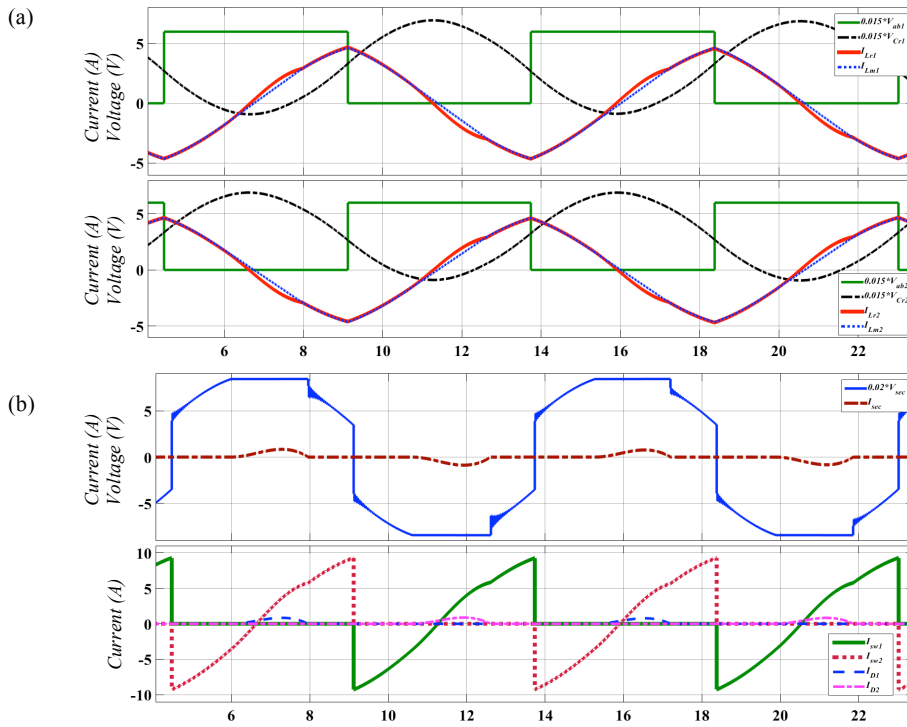


Figure 7. Operation waveforms at key point D. (a) First Combination; (b) Second Combination

### CONCLUSION

This paper proposed an LLC resonant converter with half-bridge configuration, two resonant tanks, and series-connected primary windings of the transformer for depleted PEV battery charging. The converter has been designed to operate below resonance frequency in the ZVS region to achieve primary switches ZVS and secondary rectifier diodes ZCS operation. The Converter has been simulated in MATLAB to achieve output voltage range of 250V-420V with 1.5 kW maximum power and 400V input DC voltage. Simulation results showed that the converter can successfully achieve all the key operating points in the charging profile of Li-ion battery pack using half-bridge configuration instead of full-bridge in conventional topologies.

## ACKNOWLEDGEMENT

The authors thank Universiti Sains Malaysia (USM) for providing the necessary facilities to make this research possible. This work was supported by FRGS Grant 203/PELECT/6071307 from USM.

## REFERENCES

- Junjun, D., Siqi, L., Sideng, H., Mi, C. C., & Ruiqing, M. (2014). Design Methodology of LLC Resonant Converters for Electric Vehicle Battery Chargers. *IEEE Transactions on Vehicular Technology*, 63(4), 1581-1592. doi:10.1109/TVT.2013.2287379
- Lin, B. R., & Wu, S. F. (2011). ZVS Resonant Converter With Series-Connected Transformers. *IEEE Transactions on Industrial Electronics*, 58(8), 3547-3554. doi:10.1109/TIE.2010.2089946
- Shahzad, M. I., Iqbal, S., & Taib, S. (13-14 Oct. 2014). *LLC series resonant converter with PID controller for battery charging application*. Paper presented at the Energy Conversion (CENCON), 2014 IEEE Conference on.
- Wang, H., Dusmez, S., & Khaligh, A. (2014a). Design and Analysis of a Full-Bridge LLC-Based PEV Charger Optimized for Wide Battery Voltage Range. *IEEE Transactions on Vehicular Technology*, 63(4), 1603-1613. doi:10.1109/TVT.2013.2288772
- Wang, H., Dusmez, S., & Khaligh, A. (2014b). Maximum Efficiency Point Tracking Technique for LLC-Based PEV Chargers Through Variable DC Link Control. *IEEE Transactions on Industrial Electronics*, 61(11), 6041-6049. doi:10.1109/TIE.2014.2311399
- Wang, H., Dusmez, S., & Khaligh, A. (2014c, March 2014). *A novel approach to design EV battery chargers using SEPIC PFC stage and optimal operating point tracking technique for LLC converter*. Paper presented at the Applied Power Electronics Conference and Exposition (APEC), 2014 Twenty-Ninth Annual IEEE





## Partial Measurement of Planar Surface Ion Balance Analysis

Sayan Plong-ngooluam<sup>1,2\*</sup>, Nattha Jindapetch<sup>2</sup>, Phairote Wouchoum<sup>2</sup> and Duangporn Sompongse<sup>1</sup>

<sup>1</sup>Western Digital (Thailand) CO., LTD. Bang Pa-in, Phra Nakhon Si Ayutthaya, 13160, Thailand

<sup>2</sup>Department of Electrical Engineering, Faculty of Engineering, Prince of Songkla University, Hat Yai, Songkhla, 90112, Thailand

### ABSTRACT

This paper reports the experimental results of the partial surfaces ion balance analysis on ionised planar surface to identify the fine-grained level of ioniser balance measurement. The standard 6"×6" charged plate was exposed to ionised air supplied through the DC corona ioniser to measure the ion balance. A one square inch charged plate had been used to measure the ion balance in the 36-segment partial measurement points which were ordinary arranged on that planar surface. The 36-segment partial results were analysed to image the ion balance distribution on that planar surface. The experiment revealed that fined-grained levels could be identified behind the coarsely results which had been measured by the standard charged plate. The surface plot could image the ion balance distribution on that planar surface which was ionised by the ioniser thoroughly. This ion balance imaging could be used to enhance ioniser performance analysis related to ion balance and distribution along the ionised surface.

*Keywords:* Ion balance, ioniser measurement, partial surface, ion balance distribution

### INTRODUCTION

The electrostatic discharge (ESD) had been a problem in electronics industry because the ESD events could damage devices, harm the

systems or induce particulate contamination on the charged surfaces due to electrostatic forces (ESD Association, 2014). In general, ground connecting is a simple method for making an equipotential surface to drain out the electrostatic charges to the system ground. However, this method is less effective for removing electrostatic charges from the insulator surface or conductive particles (Glor, 1985; Robinson, Brearey & Szafraniec, 2009) due to the availability of conduction and conductivity in them. To prevent these electrostatic issues, air ionization is widely used to remove the electrostatic charges from

#### ARTICLE INFO

##### Article history:

Received: 24 August 2016

Accepted: 02 December 2016

##### E-mail addresses:

Sayan.Plong-ngooluam@wdc.com (Sayan Plong-ngooluam),

Nattha.s@psu.ac.th (Nattha Jindapetch),

Phairote.w@psu.ac.th. (Phairote Wouchoum),

Duangporn.Sompongse@wdc.com (Duangporn Sompongse)

\*Corresponding Author

the insulator surfaces or the tiny conductive objects unable to connect the ground cable. The air ioniser provides the opposite polarity ions to neutralize the electrostatic charges on the object. It is necessary to measure the balance of these supplied ions because the ionisers could generate electrostatic charges while the sourced ions are unbalanced.

The ANSI/ESD STM3.1-2015 (ESD Association, 2015) is a standard test method (STM) for characterising the ioniser performance. It describes the ion balance as the electrostatic potential value caused by the ion collecting on a floated 6"×6" conductive plate with 20pF capacitances. This configuration was agreed with a typical silicon wafer at the time of drafting the standard in the late of 1980s (Rodrigo, Bellmore, Diep, Jarrett, Jonassen, Newberg, & Turangan, 2004). However, many manufacturers of electronics working on the small scale require the ion balance within +/-1V or tighter to ensure the safety of electrostatic sensitive (ESDS) devices (Kraz, 2004). They might concern to the precision of ion balance measurement because the actual devices are much smaller than the standard charged plate. The smaller plate reports a less ion balance voltage than a larger plate (Rodrigo et al., 2004). The small charged plate analysers were launched to serve the sub-1V ion balance measurement such as the ioniser controllers on US patents 6,985,346 B2 (Kraz, Cruz, & Martin, 2006), US 7,522,402 B2 (Kraz, Cruz, & Martin, 2009) and the biased-plate monitor (Crowley, Ignatenko, & Levit, 2004). These analysers provide alternative methods to identify the ion balance with the miniaturized plates to collect the ions from ioniser and correlate the result to the standard charged plate monitor result described on STM.

Ions distribution as reported in the electrohydrodynamics theory depends on the drift velocities and the airflow velocities of particular ioniser models (Ohsawa, 2013). The electrostatic potential on each foot-step might not uniform due to fluid dynamic functions. The modelling (Plong-ngooluam, Jindapetch, Wouchoum, & Sompongse, 2015) has mentioned that ion balance measurement precision could be enhanced by the surface dividing. This simulated result still needs the field measurement in the ionised environment to validate its feasibility.

In this work, the ion balance on the 6"×6" planar surface was partially analysed by the miniaturized charged plate, arranged in the same area as the standard charged plate measurement. The partial results were imaged by the surface plot to express the ion balance distribution along the 6"×6" planar surface which was neutralized by the ionised air from the DC corona ioniser.

## ION BALANCE MEASUREMENT

The ioniser is an equipment that provides either positive or negative air ions to neutralize the electrostatic charges on the surface or a tiny object. The typical corona ioniser generates the ions through the collision between the neutral molecules and electrons which are accelerated by an electric field which exceeds the inception level (Ohsawa, 2005). The emitted air ions could attract an object surface and neutralize it. Ion balance can be described by the electrostatic potential ( $V$ ) of the positive ion ( $n_p$ ) and negative ion densities ( $n_n$ ) as

$$\nabla^2 V = \frac{-e(n_p - n_n)}{\epsilon_0}, \quad (1)$$

where  $e$  is an elementary charge and  $\epsilon_0$  is the permittivity of free space.

The motions of positive ion ( $n_p$ ) and negative ion ( $n_n$ ) in (1) depend on the air velocity as

$$\frac{\partial n_p}{\partial t} + \nabla \cdot (n_p \mathbf{u}_p) - D_p \nabla^2 n_p = -\beta n_p n_n \quad \text{Positive,} \quad (2)$$

$$\frac{\partial n_n}{\partial t} + \nabla \cdot (n_n \mathbf{u}_n) - D_n \nabla^2 n_n = -\beta n_p n_n \quad \text{Negative,} \quad (3)$$

where  $\mathbf{u}_p$  and  $\mathbf{u}_n$  are air velocities of positive and negative ion mobilities,  $D_p$  and  $D_n$  are positive and negative ion diffusion coefficients, and  $\beta$  is the ion-ion recombination coefficient.

Since the ion balance is defined by the electrostatic potential value caused by an accumulation of positive and negative ions, it could be expressed by the ratio of the total amount of charge ( $Q$ ) which is accumulated on that plate and ion receiving plate capacitance ( $C$ ) as

$$V = \frac{Q}{C}. \quad (4)$$

Assume that charge distribution on the ion receiving surface and electrostatic field are uniform, the total amount charge ( $Q$ ) can be defined as

$$Q = \rho_s A, \quad (5)$$

where the  $\rho_s$  is the density of charge on the ion receiving surface ( $A$ ). This charge density is the summed result of ion balancing term of (1) which can be defined as

$$\rho_s = e(n_p - n_n). \quad (6)$$

By the substitution (5) on (4), the electrostatic potential ( $V$ ) proportionally depends on the ion receiving surface and the charge density as

$$V = \frac{\rho_s A}{C}. \quad (7)$$

Based on this assumption, it could be concluded that the ion balance which is measured by the smaller surface will be lower than that of a larger surface when the ion distribution is uniform and the plate capacitance is fixed conditions. However, the surface charge density on (6) depends on the ion motion (2) and (3) which are concerning to the air velocity. The 6"×6" planar surface with the fixed 20pF capacitance which is constituted by the STM might not represent the suitable grain result which depends on the ion motions.

## EXPERIMENTAL SETUP AND ANALYTICAL METHOD

This section describes the apparatus, the ioniser configuration, the 6"×6" charged plate, the arrangement of the 1"×1" charged plate, and the partial measurement evaluation.

## Apparatus

The charged plate analyser Trek model 157 with the standard 20pF 6"×6" planar surface plate was used to measure the ion balance as the standard ioniser measurement. A partial measurement was performed using the 1"×1" miniaturized plate. With this plate, the total capacitance still fixed at 20pF as same as the standard plate capacitance. The 36-segment partial measurement points were ordinary arranged over the standard 6"×6" planar surface plate as shown in Figure1. The DC corona ioniser MKS model 5802i was installed over the non-obstructive workstation with a grounded surface. The ioniser was located at the centre of the workstation with 60 cm in height from the grounded surface. The charged plates were placed at 45 cm under the ioniser facing with the 15 cm from the grounded surface as describes on the STM.

## Partial Measurement Evaluation

Evaluation began by adjusting the ioniser balance to -1.0 Volt which was measured by the standard 6"×6" plate following which ioniser the standard 6"×6" plate was moved out then placed the 1"×1" charged plate and measured the ion balance at the arranged points as shown in Figure1. The measurement was performed from the first segment through the 36th segment sequentially. Then repeat the evaluation with the 0.0 Volt and +1.0 Volt ion balance adjustment.

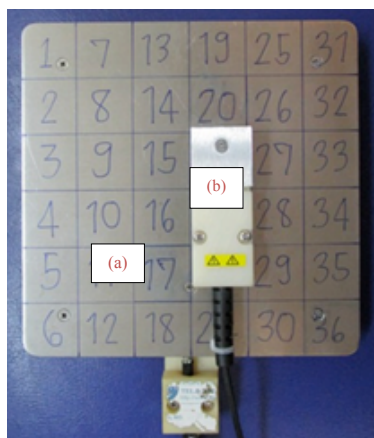


Figure 1. The partial measurement point on the planar surface arranging; (a) The standard 6"×6" charged plate, (b) The 1"×1" square plate

## Analytical Method

The Minitab, a statistical software, provides the wireframe plot to image the relationship between three variables in the x, y and z coordination. In this work, the 36-segment partial measurement results were assigned as response values z which were arranged in the x-y plane according to the plate arrangement in Figure 1. The Minitab also provides the distance method (Ryan, Joiner, & Cryer, 2010) to interpolate the unknown data points between measured data points.



All data points which are interpolated by this method always within the range of measured data points. It works well in a wide range of circumstances. The number of x and y meshes could be determining the resolution of the regular grid. In this experiment, the distance method was using to interpolate the ion balance distribution over the 6"×6" planar surface with the regular 50×50 mesh from the 6×6 measured data points as the arrangement in Figure 1. This interpolation is proposed to enhance the fine-grained levels of ion balance results beyond the actual results measured by the 36-segment partial surface.

## RESULTS AND DISCUSSIONS

The partial measurement had reported the results in the six rows and six columns. The rows are intersections in the y axis and intersections in the x axis. The ion balance distributions have been analysed and imaged with the wireframe plot with the 50×50 meshes data interpolation using distance method. The partial measurement results of ion balance from the -1.0 Volt ioniser adjustment are summarized in Table 1. The measurement values varied from -1.0 to -0.4 Volt. These results could be used to image the ion balance distribution as shown in Figure 2. The image is expressing the fine-grained levels over the 6"×6" planar surface and vary around -0.5 Volt from the settled point which was adjusted and measured by the standard 6"×6" charged plate.

Table 1  
*The partial measurement results of ion balance from the ioniser with -1.0 Volt adjustment (unit in Volt)*

	C1	C2	C3	C4	C5	C6
R1	-0.8	-0.7	-0.4	-0.8	-0.7	-0.7
R2	-0.8	-0.7	-0.6	-0.8	-0.9	-0.8
R3	-0.9	-0.8	-0.5	-0.8	-0.9	-0.6
R4	-0.6	-0.8	-0.7	-0.8	-0.8	-0.8
R5	-0.7	-0.7	-0.7	-0.8	-0.7	-1.0
R6	-0.7	-0.7	-0.7	-0.7	-0.8	-0.9

The partial measurement results of ion balance from the 0.0 Volt ioniser adjustment are summarized in Table 2. The measurement values were varying from -0.3 to 0.3 Volt. This result proves that the tested ioniser is capable with the sub 1V ion balance control workstation requirement because all data points are within the range of +/-1 Volt. The ion balance distribution image of the 0.0 Volt ioniser adjustment expresses the fine-grained levels which vary around +/-0.3 Volt from the settled point is shown in Figure 3. However, the minimum and the maximum points are not locating in the same positions as the ion balance image in Figure 2. The suspicion might be the variation of the turbulence of the air that was driven by the fan unit which was install in the ioniser. This turbulence could affect to the ions mobility mechanisms in the ions transport region, regarding to the electrohydrodynamics theory which is the interactive mechanism between the electric fields and the surrounding fluid.

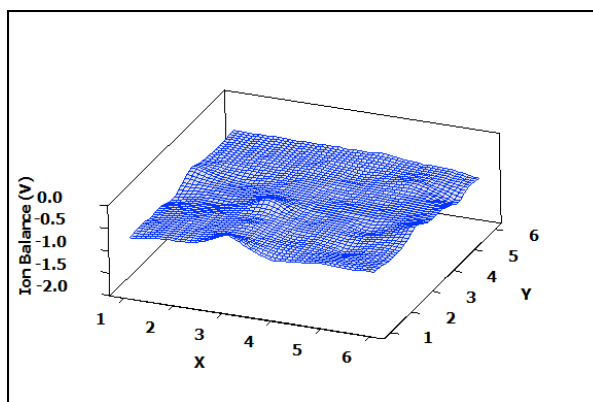


Figure 2. The ion balance distribution image with -1.0 Volt ioniser adjustment

Table 2

The partial measurement results of ion balance from the ioniser with 0.0 Volt adjustment (unit in Volt)

	C1	C2	C3	C4	C5	C6
R1	0.0	0.1	0.3	0.0	-0.1	-0.2
R2	0.0	0.0	0.1	0.3	-0.1	-0.1
R3	0.0	0.0	0.0	0.0	0.2	-0.2
R4	0.1	0.0	0.1	0.0	0.0	0.0
R5	0.0	0.1	-0.3	0.0	-0.1	0.2
R6	0.0	0.3	-0.3	0.0	0.0	0.2

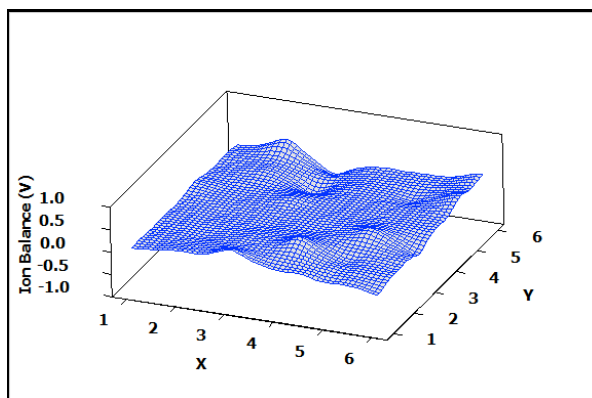


Figure 3. The ion balance distribution image with 0.0 Volt ioniser adjustment

The partial measurement results of ion balance from the 1.0 Volt ioniser adjustment are summarized in Table 3. The measurement values varied from 0.5 to 1.7 Volt. The ion balance distribution image is illustrated by the wireframe plot as shown in Figure 4. The fine-grained levels of ion balance are expressing over the 6"×6" planar surface as same as the ion balance distribution images from the -1.0 Volt and the 0.0 Volt adjustments. Based on these results,

the ion balance was distributed over the 6"×6" planar surface with +/-0.5 Volt variation. It validated the ioniser capability which needs for the workstation which requires to control the ion balance within +/-1 Volt because these fine-grained levels could be identified by the partial measurement technique. The ion balance results on the regular 50×50 mesh of the wireframe plots consist of measurement data points and interpolated data points. These data points were plotted at the at the x-y intersections of the mesh.

Table 3  
The partial measurement results of ion balance from the ioniser with 1.0 Volt adjustment (unit in Volt)

	C1	C2	C3	C4	C5	C6
R1	0.8	1.6	0.7	0.7	0.7	1.0
R2	0.8	1.6	0.7	0.9	0.5	1.1
R3	0.8	0.7	0.7	0.5	0.5	0.8
R4	0.8	0.8	0.1	0.8	0.7	0.7
R5	0.5	1.0	0.7	0.7	0.6	0.7
R6	0.7	0.8	0.7	0.6	1.1	0.7

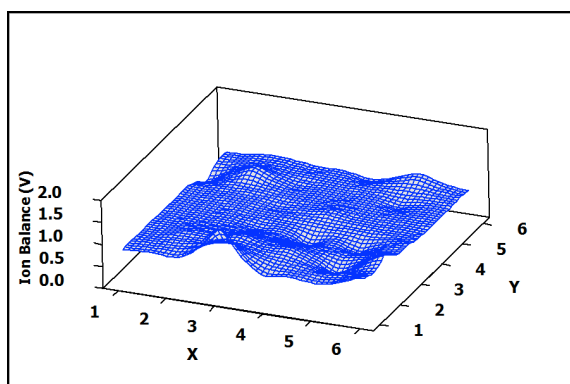


Figure 4. The ion balance distribution image with 1.0 Volt ioniser adjustment

## CONCLUSION

Experimental results validated that partial surface measurement could identify the fine-grained levels of ion balance measurement result which could not be identified by the standard charged plate measurement. The results show the variation of the voltage levels on different areas of the planar surface, indicating different areas have different voltages. The ion balance results measured by the large planar surfaces are losing such fine-grained voltage levels on different areas of the planar surface because the given result is the summation of all ions which are collected from the whole surface.

The above partial measurement results also identified the ionised air uniformity over the 6"×6" planar surface which is subjected to be neutralized. The partial measurement results

also provides methods for suitable plate improvement of the ion balance measurement of electrostatic protective areas.

## ACKNOWLEDGEMENT

The authors would like to express the deepest gratitude to the ESD development laboratory, department of Technical Support Engineering, Western Digital (Thailand) Company Limited for the workstation and equipment support. This research was financially supported by the matching fund contract no. PHD56I0059 between Thailand Research Fund (TRF) and “Western Digital (Thailand) Company Limited” under the Research and Researchers for Industries (RRI) project.

## REFERENCES

- Crowley, J. M., Ignatenko, A., & Levit, L. B. (2004). Biased-plate characterization of pulsed DC ionisers. *Journal of Electrostatics*, 62, 219-230.
- ESD Association (2014). *Electrostatic discharge (ESD) technology roadmap-revised*, 7900 Turin Road, Bldg. 3, Rome, NY.
- ESD Association (2015). ANSI ESD STM 3.1-2015, *The Protection of Electrostatic Discharge Susceptible Items-Ionization*. 7900 Turin Road, Bldg. 3, Rome, NY.
- Glor, M. (1985). Hazards due to electrostatic charging of powders. *Journal of Electrostatics*, 16(2-3), 175-191.
- Kraz, V. (2004, September). Notes on maintaining sub-1V balance of an ioniser. In *Electrical Overstress/Electrostatic Discharge Symposium Proceedings* (p. 194). ESD Association.
- Kraz, V., Cruz, S., & Martin, K. A. (2006). *US Patent No. US 6,985,346 B2*. Washington, DC: U.S. Patent and Trademark Office.
- Kraz, V., Cruz, S., & Martin, K. A. (2009). *US Patent No. US 7,522,402 B2*. Washington, DC: U.S. Patent and Trademark Office.
- Ohsawa, A. (2005). Modeling of charge neutralization by ioniser. *Journal of Electrostatics*, 63(6), 767773.
- Ohsawa, A. (2013). 2-D electrohydrodynamic simulations towards zero offset voltage with corona ionisers. *Journal of Electrostatics*, 71, 116-124. Patent and Trademark Office.
- Plong-Ngooluam, S., Jindapetch, N., Wouchoum, P., & Sompongse, D. (2015). 3-D Computational Simulations of Electrostatic Potential in Partial Surfaces towards the Precision of Ion Balance Analysis. In *Applied Mechanics and Materials* (Vol. 781, pp. 308-311). Trans Tech Publications.
- Robinson, K., Brearey, R., & Szafraniec, J. (2009). Sheet sticking caused by charge flow in a buried conducting layer. *Journal of Electrostatics*, 67(5), 781-788.
- Rodrigo, R., Bellmore, D., Diep, J., Jarrett, T., Jonassen, N., Newberg, C., & Turangan, J. (2004, September). CPM study: discharge time and offset voltage, their relationship to plate geometry. In *Electrical Overstress/Electrostatic Discharge Symposium Proceedings* (p. 200). ESD Association.
- Ryan, B. F., Joiner, B. L., & Cryer, J. D. (2010). *MINITAB Handbook: Update for Release 16, 6th Edition*. Brooks/Cole Publishing Co., Pacific Grove, CA, USA.



## Reliably Optimal PMU Placement using Disparity Evolution-based Genetic Algorithm

Yoshiaki Matsukawa<sup>1</sup>, Mohammad Lutfi Othman<sup>2\*</sup>, Masayuki Watanabe<sup>1</sup> and Yasunori Mitani<sup>1</sup>

<sup>1</sup>Department of Electrical & Electronic Engineering, Kyushu Institute of Technology, 1-1, Sensui-cho Tobata-ku Kitakyushu Fukuoka 804-8550, Japan

<sup>2</sup>Centre for Advanced Power and Energy Research (CAPER),

Department of Electrical and Electronic Engineering, Faculty of Engineering, Universiti Putra Malaysia, 43400 UPM, Serdang, Selangor, Malaysia

### ABSTRACT

Phasor Measurement Units (PMUs) are an important component in Wide Area Protection (WAP)- based operations in power systems. It is needed that a certain placement scheme of PMUs is suggested if power system scale gets larger. The optimal placement of PMU in power systems has been considered and formulated in order to reduce the number of installed PMUs while accomplishing a desired level of reliability of observation. Optimal PMU Placement (OPP) problem as the combinatorial optimization problem has been formulated to determine the minimum PMU location in the power system. In this paper, Disparity Evolution-type Genetic Algorithm (DEGA) based on disparity theory of evolution is applied. Genetic Algorithm (GA) is employed for the purpose of comparison with DEGA. The optimization model is solved for IEEE 118 standard bus system. DEGA can find better placement suggestion compared with GA because of the nature of evolution that models the double spiral structure of DNA to hold the diversity of population.

*Keywords:* Observability, Phasor Measurements, Genetic Algorithm, optimization

### ARTICLE INFO

#### Article history:

Received: 24 August 2016

Accepted: 02 December 2016

#### E-mail addresses:

p349532y@mail.kyutech.jp (Yoshiaki Matsukawa),

lutfi@upm.edu.com (Mohammad Lutfi Othman),

watanabe@ele.kyutech.ac.jp (Masayuki Watanabe),

mitani@ele.kyutech.ac.jp (Yasunori Mitani)

\*Corresponding Author

### INTRODUCTION

Phasor Measurement Unit (PMU) plays a role in acquiring data to estimate the state of power system. This role is important in Wide Area Protection (WAP), where it provides reliable security prediction and optimized coordinated actions to mitigate or prevent large area disturbances. PMU can measure information of phase differences between different points

synchronously because it uses GPS (Global Positioning System). The phase value synchronized by GPS can be calculated by PMU, and stored in the server over the internet. Using such data, it is analysable for oscillation features and power system characteristics. PMU data such as voltages and currents have been used for reliable distance protective relay operation (Othman et al., 2014) Synchro-phasor technology has grown from the PMU in the U.S. Pacific Northwest to a continental network of almost 2,000 PMUs in the past decade, which has helped to improve the reliability of the North American electric power grid since the late 1990s (Rurnett et al., 1994; Overholt et al., 2015).

However, if the scale of power system gets larger, it is needed that the optimal PMU placement scheme is chosen while considering reliability of observability which ensures whether the voltage phasor at that bus can be estimated or not in power system. In addition, the number of PMUs is needed to reduce in order to plan the placement schedule within limited cost. , Ghamsari-Yazdel and Enmaili (2015) reported that the price of a typical base PMU without measurement channels is around USD 20,000 and each measurement channel costs about USD 3,000. Thus, PMUs cannot be placed all buses because of limited budget. Therefore, Optimal PMU Placement (OPP) problem has been identified as a means to address the issue of budget constraint, where OPP works to reduce the number of PMUs placed in the power system while at the same time ensuring reliability of observability.

OPP problem has been proven to be completely NP (Non-deterministic Polynomial-time) by Brueni, Heath (2005) and can be defined as the binary combinatorial optimization problem. Hence, many heuristic algorithms and Integer Programming (IP) have been applied on OPP problem (Manousakis et al., 2012). Genetic Algorithm (GA) is one of the methods that has been proposed to solve combinatorial optimization problems. However, considering realistic system scale, e.g. above 100 bus system, normal GA approach might lapse into the evolution retardation due to missing the diversity of solution if the large number of evolutions is iterated to get better solution. i.e. similar individuals tend to be diffused into population by procedure of GA. This paper presents an application of Disparity Evolution-type Genetic Algorithm (DEGA) based on Disparity Theory of Evolution. GA is used for the purposes of comparing with DEGA. The optimization model is solved for IEEE 118 bus test system. Simulation shows DEGA approach performs better in robustness on 50 iterations. The proposed DEGA approach in this study serves as an important aspect of WAP scheme.

## **PROBLEM FORMULATION**

In this study, reliability based OPP problem is defined as a single objective optimization problem (Khiabani et al., 2014). This section provides the details about single objective PMU placement model.

## Objective Function

In this study, the objective function includes minimization of the number of PMUs and maximization of reliability of observability. The mathematical objective function model is defined as follows:

$$z = \max \left\{ w_1 (ROB - R_{min}) + w_2 \left( \sum_{i=1}^n x_i \right)^{-1} \right\} \quad (1)$$

where  $R_{min}$  is the desired minimum system wide reliability level,  $ROB$  is the overall system reliability of observability,  $\sum_{i=1}^n x_i$  is the total number of buses to be placed in the system,  $n$  is the number of buses.  $w_1$  and  $w_2$  are weight coefficients associated with objective. Equation (1) will be modelled as a fitness function on GA and DEGA in later section.

## The Range PMU Covers

The range of buses by which PMU covers is given. PMU which is placed at a bus measures the voltage phasor of that bus and the current phasors of adjacent lines. PMUs are not necessarily placed at all buses because the voltage phasors of adjacent buses can be obtained using Ohm's law. Thus, PMU placement at a given bus allows the measurement of voltage phasor at that bus directly, and voltage phasors at immediate neighbouring buses by calculation.

Figure 1 (a) shows the example the covering range of buses that one PMU covers. In Figure 1, a PMU which is allocated at bus 3 covers buses 1, 2, 3 and 4 since the PMU makes adjacent buses itself observable.

## Reliability of observability

None of the PMUs are redundant, the failure of any PMU would result in system failure. Thus, it is necessary the reliability of observability is defined. The reliability of observability (Ghamsari-Yazdel and Enmaili, 2015) of the  $i$  th can be given as:

$$r_i = 1 - \prod_{j=1}^{f_i} q_j \quad (2)$$

where  $r_i$  represents the reliability of the  $i$  th bus,  $q_j$  is the probability of failure of the PMU,  $f_i$  denotes the total number of PMUs covering the  $i$  th bus. Also, (2) can be described as:

$$r_i = 1 - \prod_{j=1}^{f_i} (1 - R_{PMU}) \quad (3)$$

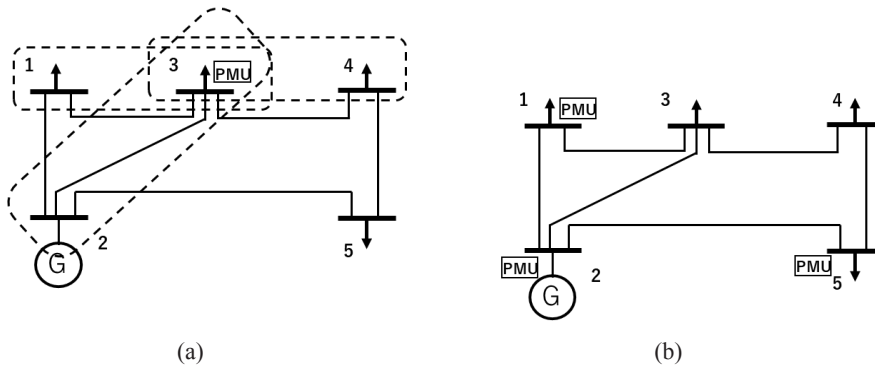


Figure 1. Covering range of the PMU; (b) Reliability example in case of IEEE 5 bus system

where,  $R_{PMU}$  is a value of reliability that one PMU has. For example, consider the IEEE 5 bus system in Figure 1 (b) with PMUs placed at buses 1, 2, and 5. Then it is assumed that one PMU has a reliability of  $R_{PMU} = 0.90$ . At this time, the reliability of observability of bus 4 will be 0.90 because it is observed by one PMU which is placed at bus 5 only. However, bus 1 is covered by two PMUs which are placed at bus 2 and bus 1 itself. Therefore, the reliability of observability of bus 1 is given as  $r_1 = 1 - \{(1 - 0.90) * (1 - 0.90)\} = 0.99$ .

Especially, this study is interested in the maximization of overall system reliability. Then, it is defined by taking direct product of reliability of observability of all buses as follows:

$$ROB = \prod_{i=1}^n r_i \tag{4}$$

where  $n$  is the number of the buses in the power system.

The abovementioned reliability index is included into PMU placement constraints as follows:

$$x_i = \begin{cases} 1 & \text{if the PMU is present at bus } i \\ 0 & \text{otherwise} \end{cases} \tag{5}$$

$$A_{ij} = \begin{cases} 1 & \text{if either } i = j \text{ or } i \text{ is adjacent to } j \\ 0 & \text{otherwise} \end{cases} \tag{6}$$

where  $x_i$  is defined as a binary decision variable vector which represents whether the PMU is placed at  $i$  th bus or not, and  $A_{ij}$  is called connection matrix which represents the connection condition of each bus in the power system. Then, the number of PMUs covering the  $i$  th bus can be introduced as follows:

$$f_i = \sum_{j=1}^n A_{ij} x_j \tag{7}$$

Thus, it can be known how many buses that cover the  $i$  th bus from  $f_i$ .



## DESCRIPTION OF ALGORITHMS

### Disparity Evolution-type Genetic Algorithm

GA is a method to solve the optimization problem by modeling the evolutionary theory. DEGA which was first developed by Maeda (2001) is an improved GA modelled on the disparity theory of evolution (Furusawa and Doi 1998). DEGA exploits the concept of gene reproduction and different mutation rates by faithfully modelling the double spiral structure of DNA. In the disparity theory of evolution, when double DNAs duplicate, they are divided into two kinds of chains that is called leading strand with low mutation rate and lagging strand with high mutation rate. Different mutation rates make DEGA's evolution speed improve by maintaining diversity of solutions, whereas it is difficult to increase diversity in GA's procedure. The procedure of DEGA for OPP problem is described in Figure 2. In this solution approach for OPP problem, a binary encoding is implemented where the string of chromosome means the total number of buses in the system. For representative value in the chromosome, if the PMU is placed on that particular bus, then the representative at that particular bus takes 1, and it takes 0 if otherwise.

```

Algorithm: DEGA (evol, n, pc, pmle, pmla)
//Initialize of 0th generation
k ← 0;
Lek ← a population of n/2 randomly-generated chromosomes (leading strand);
Lak ← bit reversed individuals of Lek (lagging strand);
Pk ← Lek + Lak;
//Evaluate Lek
Compute fitness (i) for each i ∈ Lek;
While (k < evol)
{
    //Create generation k + 1;
    //Crossover (two-point crossover)
    cp1, cp2 ← Generate two random numbers for each Lek and Lak
    Crossover between cp1 and cp2; Select pc*n members of Lek and Lak in Pk; pair them up; produce
    offspring Le'k, La'k;
    Ok ← Le'k + La'k;
    //Mutate
    pm ← Generate random numbers for each gene;
    Mutate for Le'k in Ok; If pm < pmle, then invert the bit; occur at low mutation rate;
    Mutate for La'k in Ok; If pm < pmla, then invert the bit; occur at high mutation rate;
    //Duplicate
    La''k ← create new lagging strand by bit inversion of Le'k;
    Le''k ← create new leading strand by bit inversion of La'k;
    Ok ← Le'k + La'k + Le''k + La''k;
    //Evaluate Le'k, Le''k and select the individuals which survive into next generation by roulette
    selection and elitism
    Compute fitness
    Preserve limited number of elites in Pk, Ok;
    Evaluate each leading strand in the individual; Select the individuals Pk+1 within n by roulette
    selection;
    //Increment
    k ← k + 1;
}
Return the best solution in population;

```

Figure 2. Pseudo-code of the DEGA model

### Fitness Function

The fitness function is defined in order to decide the relative merits of the solution. It is calculated as:

$$fitness = \sum_{j=1}^4 \omega_j \theta_j \quad (8)$$

where, each term  $\theta_j$  is defined as:

$$\theta_1 = \frac{\text{Number of buses covered by PMUs}}{\text{Total number of buses}} \quad (9)$$

$$\theta_2 = \frac{\text{Number of buses that no PMU is placed}}{\text{Total number of buses}} \quad (10)$$

$$\theta_3 = \begin{cases} 1 & ROB \geq R_{min} \\ 0 & ROB < R_{min} \end{cases} \quad (11)$$

$$\theta_4 = ROB \quad (12)$$

$\omega_1$  denotes corresponding weights coefficients with the criteria that are listed above. Equation (8) is customizable by changing each  $\omega_j$ , the summation of all  $\omega_j$  should be 1. In this study, solutions which have high fitness value have a higher chance to be chosen into next generation because the roulette selection is used as the selection method.  $\theta_1$  means the fraction of buses covered by PMUs.  $\theta_2$  is associated with minimizing the number of placed PMUs.  $\theta_3$  denotes the required overall reliability of observability in the system, if the solution cannot satisfy desired reliability, 0 will be given as penalty in this term.  $\theta_4$  directly has the value of reliability of observability. The weight coefficients  $\omega_j$  are configured as shown in Table 1, whereby  $\omega_1$  is set as the highest value to have consideration for the complete observability, and  $\omega_2$  is the second highest value to satisfy the required reliability of observability.  $\omega_4$  is lowest because if solution satisfies the minimum reliability of observability, it is not needed that reliability of observability is improved keenly. After satisfying the reliability, the number of PMUs are reduced.

### SIMULATION STUDY

DEGA and GA are tested on a standard IEEE 118 bus system using MATLAB 2013a. Table 1 shows the parameters of DEGA and GA in this simulation. GA as the standard approach for global optimization is chosen for the purposes of comparison with DEGA. The PMU placements are proposed with desired reliability  $R_{min} = 0.90$ , PMU inherent reliability  $R_{PMU} = 0.99$  for each method. In order to verify robustness of proposed method, the simulations have been tried by 50 iterations using different random numbers. Moreover, this simulation considers the concept of zero injection bus. The results proposed by DEGA and GA are shown in Figure 3 and Tables 2 and 3. The graph in Figure 3; (a) shows the generation characteristics for fitness value in the iterations which get best fitness value in each method, also (b) shows the most inferior fitness case. The graphs show the best and average fitness value in the population

Table 1  
DEGA and GA parameters

Parameter	DEGA	GA
Population size	50	50
Generation limit	10000	10000
Crossover probability	0.4	0.8
Mutation probability	-	0.01
Mutation probability on leading strand	0.01	-
Mutation probability on lagging strand	0.5	-
Number of preserved elites	3	3
$\omega_1$	4/9	4/9
$\omega_2$	1/6	1/6
$\omega^3$	1/3	1/3
$\omega_4$	1/18	1/18

Table 2  
The practical best and most inferior solutions in each method

	The best solution		The most inferior solution	
	DEGA	GA	DEGA	GA
Fitness	0.9214	0.9214	0.9163	0.5970
The number of PMUs	52	52	56	33
ROB	0.9071	0.9075	0.9164	0.5843

Table 3  
The fitness average in 50 iterations

	DEGA	GA
The fitness average	0.9190	0.7659

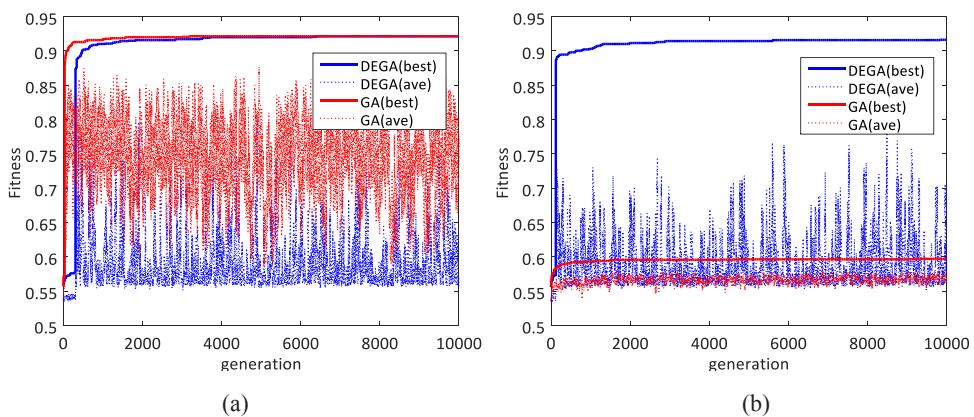


Figure 3. (a) Generation-Fitness characteristics in the best iterations; (b) Generation-Fitness characteristics in the most inferior iterations

of each generation. DEGA seems to have slower convergence rate and lower average fitness value in generations, but finally DEGA got approximately same fitness with GA. However, DEGA can also get sufficient fitness even though GA's evolution stops in the case of Figure 3(b). GA obviously could not satisfy the minimum desired ROB as shown in Table 2. DEGA has better average fitness value in 50 iterations than GA. It can be considered that DEGA can maintain diversity of solution in the progress of evolution because of the procedure. That is why DEGA has lower average fitness value in each generation due to diversity of individuals. Results prove that in OPP problem, DEGA has good capacity to solve the problem in several cases. In some cases of larger system scale, DEGA is expected to be able to find better PMU placement.

## CONCLUSION

This paper proposed the novel GA-based algorithm called DEGA to deal with the issue of OPP problem. Simulations were done in DEGA and GA for IEEE 118 bus system. Results indicate that DEGA could be potentially useful in solving the OPP problem.

## REFERENCES

- Brueni, D. J., & Heath, L. S. (2005). The PMU placement problem. *SIAM Journal on Discrete Mathematics*, 19(3), 744-761.
- Furusawa, M. & Doi, H. (1998). Asymmetrical DNA replication promotes evolution: disparity theory of evolution. *Genetica*, 102, 333-343.
- Ghamsari-Yazdel, M., & Enmaili, M. (2015). Reliability-based Probabilistic Optimal Joint Placement of PMUs and Flow Measurements. *International Journal of Electrical Power & Energy Systems*, 857-863.
- Khiabani, V., Erdem, E., Farahmand, K., & Nygard, K. (2014). Smart Grid PMU Allocation Using Genetic Algorithm. *Journal of Network and Innovative Computing ISSN*, 2, 030-040.
- Maeda, Y. (2001). Modified Genetic Algorithms Based on Disparity Theory of Evolution. *IEEE IFSA World Congress and 20th NAFIPS International Conference*, (Vol. 4, pp. 2235-2240).
- Manousakis, N. M., Korres, G. N., & Georgilakis, P. S. (2012) Taxonomy of PMU Placement Methodologies. *IEEE Transactions on Power Systems*, 27(2), 1070-1077.
- Milosevic, B., & Begovic, M. (2003). Nondominated Sorting Genetic Algorithm for Optimal Phasor Measurement Placement. *IEEE Transactions on Power Systems*, 18(1), 69-75.
- Negnevitsky, M. (2011). *Artificial Intelligence: A Guide to Intelligent Systems*. Third Edition, Person Education Limited.
- Othman, M. L., Aris, I. N., & Abdul, Wahab, I. (2014). Modeling and Simulation of Industrial Numerical Distance Relay Aimed at Knowledge Discovery in Resident Event Report. *Simulation: Transactions of Society for Modeling and Simulation International*, 90(6), 660-686.
- Overholt, P., Ortiz, D. and Silverstein, A. (2015). Synchrophasor Technology and the DOE. *IEEE Power and Energy Magazine*, September/October, 14-17.
- Rurnett, R. O. Jr., Butts, M. M., et al. (1994). Synchronized Phasor Measurements of a Power System Event. *IEEE Trans. On Power Systems*, 9(3), 1643-1650.



## Statistical Optimisation of Process Parameters on the Efficiency of N-TiO<sub>2</sub> Dye Sensitised Solar Cell Using Response Surface Methodology (RSM)

Buda Samaila<sup>1</sup>, Suhaidi Shafie<sup>1,2\*</sup>, Suraya Abdul Rashid<sup>1,3</sup>, Haslina Jafaar<sup>2</sup> and Ali Khalifa<sup>2</sup>

<sup>1</sup>Institute of Advanced Technology, Universiti Putra Malaysia, 43400 UPM, Serdang, Selangor, Malaysia

<sup>2</sup>Department of Electrical and Electronics Engineering, Faculty of Engineering, Universiti Putra Malaysia, 43400 UPM, Serdang, Selangor, Malaysia

<sup>3</sup>Department of Chemical Engineering, Faculty of Engineering, Universiti Putra Malaysia, 43400 UPM, Serdang, Selangor, Malaysia

### ABSTRACT

In this study, nitrogen doped titanium dioxide-based dye-sensitised solar cell was successfully fabricated using screen printing technique to discover the optimisation of process parameters for the solar cell efficiency using response surface methodology (RSM). Parameter optimisation has been a major concern in solar cell fabrication. The selected parameters were: nitrogen concentration (15-25 mg of urea), the film thickness (25-60 µm) and dye loading time (12-24 hours), the optimum condition which yields the highest efficiency of 3.5% was at 15 mg nitrogen concentration, 25 µm film thickness and 24-hours dye loading time. Film thickness was found to have a significant influence on efficiency while the loading time exceeding 18 hours has the least significant effect.

*Keywords:* Dye-sensitised, solar cell, nitrogen, screen printing, optimisation

### INTRODUCTION

Energy, fresh water and air are the most important commodities for human existence. Fossil fuels such as petroleum, natural gas, and coal are the most widely used sources of energy for industrial and domestic purposes. The rapid depletion finite reserves and environmental concerns such as greenhouse gas emissions are some of the drawbacks of these highly efficient carbon-based fuels.

#### ARTICLE INFO

##### Article history:

Received: 24 August 2016

Accepted: 02 December 2016

##### E-mail addresses:

budasamaila@gmail.com (Buda Samaila),  
suhaidishafie@upm.edu.my (Suhaidi Shafie),  
suraya\_ar@upm.edu.my (Suraya Abdul Rashid),  
(Haslina Jafaar)  
allikhalifa@yahoo.com (Ali Khalifa)

\*Corresponding Author

Solar energy is a renewable source of energy that has attracted global attention as a substitute for fossil fuels owing to its numerous advantages of being a naturally infinite resource.

This study attempts to provide a unique design that optimises process parameters in the fabrication of N-doped-based DSSC which yields maximum efficiency for end-use electricity generation. The study also investigated the effects of nitrogen concentration, dye loading time and film thickness in the performance of N-TiO<sub>2</sub>-based DSSC using Surface Response Methodology (SRM) for the determination of the best-optimised model.

In order to achieve high conversion efficiency, there must be an efficient collection of nearly all the photogenerated electrons which means that the incident-photon to-current-efficiency should be close to unity under visible light region. This can be realised if the carrier diffusion length ( $L_n$ ) is greater than the film thickness ( $d$ ) (Grätzel, 2005)

$$L_n = \sqrt{D_e \tau_r}$$

where  $D_e$  is the diffusion coefficient and  $\tau_r$  is the electron life time. However, the film should be optimally controlled as each TiO<sub>2</sub> particle is a potential electron trap.

Dye loading time needs to be optimised to ensure homogeneity of dye concentration in the TiO<sub>2</sub> pores as well as to prevent non-radiative decay of exciton and static quenching resulting from a large aggregation of dye molecules (Hardin, 2010). Nitrogen-doped TiO<sub>2</sub> has noble photovoltaic properties, therefore, it has received much attention due to the narrowing of the band gap and shifting of the absorption edge to the visible region of the solar spectrum.

Since its introduction in 1951 by Box and Wilson, RSM has been widely used as a unique statistical tool for engineering system design, optimisation and prediction of system's input-output relationship.

The mathematical model obtained from SRM enables reproducibility of the system optimal working condition by establishing an empirical relationship between variable factors and desired product response (Chowdhury et al., 2012; Khalid, 2012). In the current study, a statistical model has been developed based on varied experimental trails in order to determine the influence of the different process parameters on the overall performance of the fabricated Nitrogen-doped Titanium dioxide (N-TiO<sub>2</sub>) - based Dye-sensitised Solar Cell (DSSC) device.

A quadratic model based on Central Composite Design (CCD) was developed and with Nitrogen concentration, Dye loading time and Film thickness as variable factors and cell efficiency as a response. The model was further improved using regression analysis and subsequent examination using analysis of variance (ANOVA) to determine its corresponding accuracy.

## MATERIALS AND METHODS

### Materials

Titanium Dioxide (TiO<sub>2</sub>), Fluorine Tin oxide (FTO) coated glass (7sq<sup>-1</sup>), Di-2 Cis-bis (isothiocyanato) bis-bipyridyl-4-4'-dicarboxylato ruthenium (ii) (N719) dye were all obtained from Sigma-Aldrich Co., (USA). Urea was purchased from R&M Chemicals and electrolyte was obtained from Kyutech Laboratory, Japan.

### Fabrication of DSSC device

The N-TiO<sub>2</sub> was prepared by mixing 500 mg of TiO<sub>2</sub> with the required amount of Urea as a source of nitrogen (from 15 mg to 25 mg) in a motor and carefully grounded until a homogenous mixture was obtained before it was annealed in a furnace at 500°C for 30 minutes. The fabrication of N-TiO<sub>2</sub>-based photoanode was achieved using the following procedure, Initially, 500 mg of N-TiO<sub>2</sub> composite was mixed with a solution containing 10 mL ethanol, 5 mL of distilled water and ethyl cellulose (1 g) in a 200 mL beaker and stirred for 12 hours using a magnetic stirrer to obtain an N-TiO<sub>2</sub> paste; subsequently, the paste was coated on an FTO-coated glass substrate by screen printing technique using a mesh with the desired thickness and the obtained film was sintered in a furnace at 450°C for 30 minutes. The resultant photoanode was immersed in an ethanolic solution of 0.2M N719 dye for required duration of between 12 and 24 hours. A complete DSSC device was assembled as follows: a platinum coated FTO glass cathode was placed on the photoanode separated by a polymer-based spacer and electrolyte solution was subsequently introduced into the cell through a pre-drilled hole on the cathode.

The current-voltage measurement was done using a solar simulator which provides AM 1.5 simulated solar radiation, I-V curve of the solar cell device was recorded by applying a bias voltage and simultaneously measuring the corresponding photogenerated current with a Keithly Source Meter (Keithly 2611, USA) under 100mWcm<sup>-2</sup> light intensity.

### Experimental Design

Central composite Design (CCD) full factorial in the design-Expert software version 6.0.6 was used to evaluate three independent variables, namely amount of nitrogen, film thickness and dye loading time on five level points (see Table 1). This produced 20 experimental sets as represented in equation (1) below:

$$\text{Number of experiment} = 2^k + 2k + 6 \quad (1)$$

Where k is the number of independent variables.

Table 1  
*Independent variable coded levels*

Factor	Name	Centre	Level	
			Low Level	High Level
X <sub>1</sub>		20	15	25
X <sub>2</sub>	Film Thickness (µm)	42.5	25	60
X <sub>3</sub>	Dye loading time (h)	18	12	24

The empirical model for the efficiency of N-TiO<sub>2</sub>-based solar cell was developed by performing the experimental sets obtained from a complete design matrix as shown in Table 2.

Table 2  
*VSM design matrix and experimental results*

Run	X <sub>1</sub>	X <sub>2</sub>	X <sub>3</sub>	Y
1	25	60	24	2.7
2	20	42.5	18	3.1
3	15	25	24	3.5
4	15	25	12	3.3
5	20	42.5	18	3.1
6	20	42.5	18	3.1
7	15	60	12	2.8
8	25	25	12	3.4
9	15	42.5	18	2.5
10	20	42.5	42	3
11	25	25	24	3.1
12	20	42.5	18	3
13	20	42.5	18	3
14	20	42.5	12	2.9
15	20	42.5	18	3.1
16	20	60	18	2.7
17	20	25	18	3.4
18	15	60	24	2.9
19	40	42.5	18	2
20	25	60	12	2.6

The relationship between the variable factors X<sub>1</sub>, X<sub>2</sub>, X<sub>3</sub> and the response Y is expressed as follows.

$$Y = F(X_1, X_2, X_3) \quad (2)$$

Where F represents the response function.

In this case, a polynomial model based on Taylor's expansion series (Khuri & Mukhopadhyay, 2010) was chosen and represented as follows:

$$Y = b_0 + \sum_{i=1}^k b_i x_i + \sum_{i,j=1}^k b_{ij} x_i x_j + e \quad (3)$$



Putting the predicted solar cell efficiency  $Y$  and the variable  $X_1, X_2, X_3$  representing the amount of nitrogen, film thickness and dye loading time respectively, equation 3 is expressed as:

$$f(x) = \beta_0 + \beta_1X_1 + \beta_2X_2 + \beta_3X_3 + \beta_{12}X_1X_2 + \beta_{13}X_1X_3 \quad (4)$$

## RESULTS AND DISCUSSION

### Development of Regression Model

At the end of the experiment, a carefully selected regression model based on the highest order polynomial was developed for the DSSC efficiency ( $Y$ ) as dependent variable while the independent variables  $X_1, X_2, X_3$  represent amount of nitrogen (weight of urea), film thickness and dye loading time respectively. The empirical model is represented in equation (5) as below:

$$Y = 3.05 - 0.067X_1 - 0.3X_2 + 0.027X_3 - 0.05X_1^2 + 0.04X_2^2 - 0.009X_3^2 - 0.013X_1X_2 - 0.063X_1X_3 + 0.037X_2X_3 \quad (5)$$

the linear terms  $X_1, X_2,$  and  $X_3$  represent the effect of the individual variable on the efficiency while the multiple variable terms show the interaction of variable on the response and the quadratic effect was represented by the squares of the terms.

The predicted versus actual efficiency plot is shown in Figure 1, from the plot, the predicted value was observed to be closer to the experimental value of the solar cell efficiency, the coefficient of determination ( $R^2$ ) is calculated to be equal to 0.9680 which shows a near unity correlation between the predicted and actual cell efficiency which is an indication of the effectiveness of the developed model.

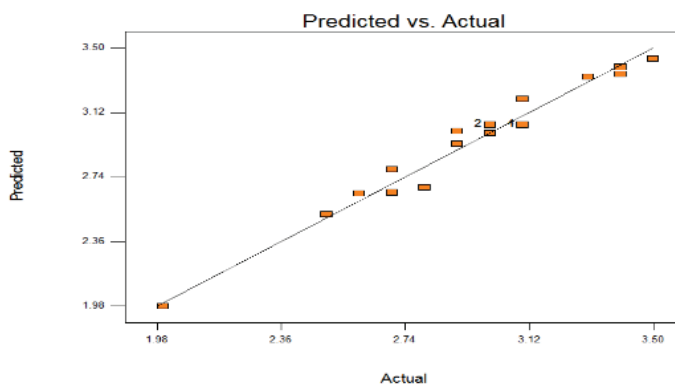


Figure 1. Plot of predicted against actual values

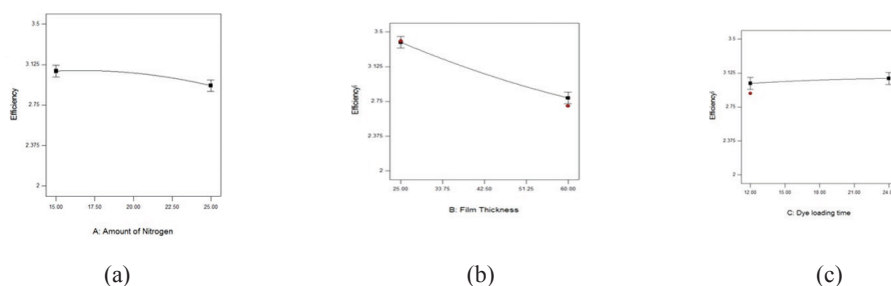


Figure 2. Response surface plot for efficiency dependence on (a) amount of nitrogen, (b) Film thickness and (c) dye loading time

Figure 2(a), (b) and (c) shows the effect of the amount of nitrogen, film thickness and dye loading time on the overall efficiency of the solar cell. Figure 2(a) shows the dependence of the cell performance on the film thickness, efficiency decreased 3.2% to 2.8% as the thickness increases from 25 microns to 60 microns which is attributable to an increase in recombination sites along the electron path length.

The optimal nitrogen concentration was found to be 15 and 17 mL and there was no strong dependence of cell efficiency with an increase in nitrogen concentration (Guo et al., 2011) as the efficiency decreases by only 0.1% as the nitrogen concentration was increased from 15 to 25 mL as shown in Figure 2(b). Additionally, there was no strong dependence of efficiency on the increase in dye loading from 12 hours to 24 hours.

Table 3  
Summary of statistical parameters for the ANOVA regression model

Model summary	
Source	Quadratic
Standard deviation	0.086
R <sup>2</sup>	0.9680
Adjusted R <sup>2</sup>	0.9392
Sum of Squares	1.12
Degrees of freedom	3
Mean square	0.37
F value	50.25

### Current vs. Voltage curve

The J-V curves of the solar cells prepared under different conditions are shown in Figure 3 (A= highest thickness, B= lowest thickness and C= highest dye loading time) and from the plot it is clear that sample B and sample C have the same open circuit voltage - the difference between the Lowest Unoccupied Molecular Orbital (LUMO) and the redox potential of the electrolyte (Roy et al., 2010). However, the reduction in film thickness which is also a reduction of carrier

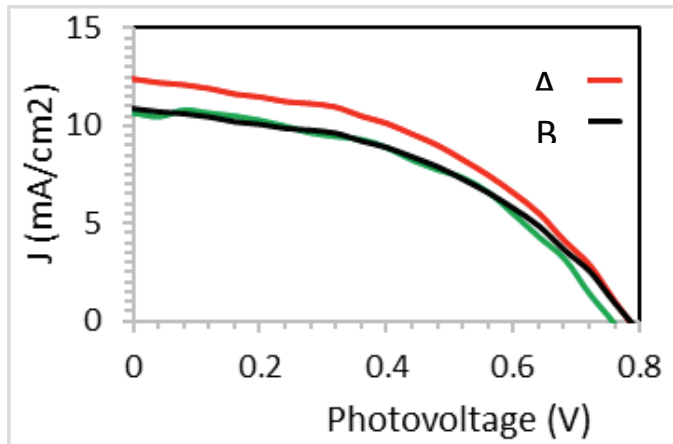


Figure 3. Current- Voltage relationship of DSSC under different process condition

Table 4  
Analysis of Variance (ANOVA) and lack of fit test response of the developed quadratic model

Source of Variance	Sum of Squares	Degree of freedom	Mean Squares	F Values	Prob > F
Model	2.25	9	0.25	33.6	< 0.0001
X <sub>1</sub>	0.18	1	0.18	24.46	0.0006
X <sub>2</sub>	0.9	1	0.9	120.78	< 0.0001
X <sub>3</sub>	0.00711	1	0.00711	0.95	0.3517
X <sub>1</sub> <sup>2</sup>	0.98	1	0.98	131.89	< 0.0001
X <sub>2</sub> <sup>2</sup>	0.007217	1	0.007217	0.97	0.3483
X <sub>3</sub> <sup>2</sup>	0.0088	1	0.0088	1.18	0.3027
X <sub>1</sub> X <sub>2</sub>	0.00125	1	0.00125	0.17	0.6908
X <sub>1</sub> X <sub>3</sub>	0.031	1	0.031	4.19	0.0678
X <sub>2</sub> X <sub>3</sub>	0.011	1	0.011	1.51	0.2473
Residual	0.075	10	0.007452		
Lack of Fit	0.061	5	0.012	4.59	0.06
Pure Error	0.013	5	0.002667		
Total	2.33	19			

diffusion length, leads to an increase of current density from 10.8mA cm<sup>2</sup> in sample B to 12.4 mA cm<sup>2</sup> in sample C due to the low electron-hole recombination. The lower efficiency of the sample is attributed to the high film thickness.

## CONCLUSION

A statistical model was developed using response surface methodology through sequential experimental settings to determine the ideal number of different variables influencing the

efficiency of N-TiO<sub>2</sub> based DSSC, the optimum condition was at 15mg nitrogen concentration, 25 μm photoanode film thickness and 12 hour dye loading time. The model was useful in ensuring efficiency by restricting the process variable for efficient output in industrial applications.

## REFERENCE

- Chowdhury, Z. Z., Zain, S. M., Khan, R. A., Ahmad, A. A., & Khalid, K. (2012). Application of response surface methodology (RSM) for optimizing production condition for removal of Pb (II) and Cu (II) onto kenaf fiber based activated carbon. *Research Journal of Applied Sciences, Engineering and Technology*, 4(5), 458–465.
- Grätzel, M. (2005). Solar energy conversion by dye-sensitized photovoltaic cells. *Inorganic Chemistry*, 44(20), 6841–51. <http://doi.org/10.1021/ic0508371>
- Guo, W., Shen, Y., Boschloo, G., Hagfeldt, A., & Ma, T. (2011). Influence of nitrogen dopants on N-doped TiO<sub>2</sub> electrodes and their applications in dye-sensitized solar cells. *Electrochimica Acta*, 56(12), 4611–4617. <http://doi.org/10.1016/j.electacta.2011.02.091>
- Hardin, B. E. (2010). *Increased light harvesting in dye-sensitized solar cells using Förster resonant energy transfer*. Stanford University. Retrieved from <http://purl.stanford.edu/td264yn6201>
- Kao, M. C., Chen, H. Z., Young, S. L., Kung, C. Y., & Lin, C. C. (2009). The effects of the thickness of TiO<sub>2</sub> films on the performance of dye-sensitized solar cells. *Thin Solid Films*, 517(17), 5096–5099. <http://doi.org/10.1016/j.tsf.2009.03.102>
- Khuri, A. I., & Mukhopadhyay, S. (2010). Response surface methodology. *Wiley Interdisciplinary Reviews: Computational Statistics*. <http://doi.org/10.1002/wics.73>
- Lim, S. P., Pandikumar, A., Huang, N. M., Lim, H. N., Gu, G. C., & Ma, T. L. (2014). Promotional effect of silver nanoparticles on the performance of N-doped TiO<sub>2</sub> photoanode-based dye-sensitized solar cells. *Rsc Advances*, 4(89), 48236–48244. <http://doi.org/10.1039/c4ra09775k>
- Narayan, M. R. (2012). Review: Dye sensitized solar cells based on natural photosensitizers. *Renewable and Sustainable Energy Reviews*, 16(1), 208–215. <http://doi.org/10.1016/j.rser.2011.07.148>
- Roy, P., Kim, D., Lee, K., Spiecker, E., & Schmuki, P. (2010). TiO<sub>2</sub> nanotubes and their application in dye-sensitized solar cells. *Nanoscale*, 2(1), 45–59. <http://doi.org/10.1039/b9nr00131j>

## Classification of Aromatic Herbs using Artificial Intelligent Technique

A. Che Soh\* , U. K. Mohamad Yusof, N. F. M. Radzi, A. J. Ishak and M. K. Hassan

*Department of Electrical and Electronic Engineering, Faculty of Engineering, Universiti Putra Malaysia, 43400 UPM, Serdang, Selangor, Malaysia*

### ABSTRACT

Herbs have unique characteristics such as colour, texture and odour. In general, herb identification is through organoleptic methods and is heavily dependent on botanists. It is becoming more difficult to identify different herb species in the same family based only on their aroma. It is because of their similar physical appearance and smell. Artificial technology, unlike humans, is thought to have the capacity to identify different species with precision. An instrument used to identify aroma is the electronic nose. It is used in many sector including agriculture. The electronic nose in this project was to identify the odour of 12 species such as lauraceae, myrtaceae and zingiberaceae families. The output captured by the electronic nose gas sensors were classified using two types of artificial intelligent techniques: Artificial Neural Network (ANN) and Adaptive Neuro-Fuzzy Inference System (ANFIS). From the result, ANFIS has 94.8% accuracy compared with ANN at 91.7%.

*Keywords:* Artificial Neural Network, Adaptive Neuro-Fuzzy Inference System

### INTRODUCTION

The leaves of the plant that do not develop persistent woody tissue are called herbs (Chen

et al., 2012). What make herbs valuable is their taste, aroma, health and medicinal properties, commercial significance, pesticide properties and colour sources (Fischer, 2010; Haddi et al., 2013; Konduru et al., 2015). The presence of phytochemical in the form of volatile compound gives herbs their characteristic aroma. Beneficial properties found in herbs are terpenes, steroids, phenolic compounds, amino acids, lipids, and alkaloids (Ganora, 2008). Researchers recognise plant species by analysing the physical form or the texture of the herbs (Husin et al., 2012; Ishak et al., 2009; Zalikha, 2011).

#### ARTICLE INFO

##### *Article history:*

Received: 24 August 2016

Accepted: 02 December 2016

##### *E-mail addresses:*

azuracs@upm.edu.my (A. Che Soh),  
umi.mpputm@gmail.com (U. K. Mohamad Yusof),  
nfmr86@gmail.com (N. F. M. Radzi),  
asnorji@upm.edu.my (A. J. Ishak),  
khair@upm.edu.my (M. K. Hassan)

\*Corresponding Author

Humans identify different herb species by using their sensory panels. However, critics have pointed out that our sense of smell is subjective and is usually inaccurate. Hence, this severely limits our identification capability. Among the factors that can influence the human sensory system are physical, mental health, tiredness and other conditions of the body (Tudu et al., 2009). On the other hand, the main problem in identifying different herbs in the same family is their physical appearance (they may look and smell alike). Even botanists face difficulty identifying different herbs based on their aroma.

In recent years, researchers have used chemical gas and liquid to differentiate the aroma of different herbs. It is a complex procedure and an expensive one involving an aroma-detecting equipment (Fischer 2010). Volatile gas from herbs are analysed using complicated and expensive experiment involving gas chromatography (GC) with a selective mass spectrometric (MS) detector. The result is accurate but involves various experiments, time consuming, and costly (Fischer, 2010). There is a demand for new technology that provides good results in real time with low cost, simple procedures and user friendly. Consequently, the electronic nose sensor was invented to detect aroma (Wilson, 2013). The device is popular in the herbs industry because it has several advantages such as the ability to provide chemical and physical information of the plant in real time (Dinrifo, 2011; Haddi et al., 2013; Wilson, 2013). It can also detect simple or complicated smell. An electronic nose consists of an array of electronic chemical sensors with partial specificity and an applicable pattern-recognition system (Wilson & Baietto, 2009). In biological olfactory system, the odour of sample will be obtained from the smell process before that information is processed by the brain. The neural system will recognise the sample and identify the odour. In an electronic nose system on the other hand, raw data from the odour signal is captured by the gas sensor array and processed using algorithm formulated such as neural network to identify the odour. The output or the result will be acquired from the database of the system.

A particularly significant and interesting aspect of electronic nose system is the classification of herb species. Pattern recognition systems focus on recognise patterns and regularities in data. Basically, the system was trained from labelled training data in supervised learning. Unlabelled data is identified by the formulated algorithm to discover previously unknown patterns in unsupervised learning. Prediction problems in pattern recognition relate to classification, regression and clustering (Guterriez, 2002). The pattern recognition is a problem of assigning an object to a class. The most common classification algorithm used in artificial olfactory system is artificial neural network (Amari et al., 2006; Dinrifo, 2011; Husin, 2012; Ihsan et al., 2009; Li, 2007). Artificial neural networks (ANN) technique used in chemical vapour recognition have proven to be suitable in analysing and recognising patterns for complex data. The design of artificial neural network is inspired by the human brain. The structure of ANN consists of a pyramid of layers, where the neurons are organised and linked to the external environment by input and output layers. Every neuron is a basic information-processing unit that can calculate its activation level given the inputs and numerical weights. The weights are modified to bring the network input and output behaviour in line with the environment (Dinrifo, 2011; Guterriez, 2002; Li et al., 2007).

Comparison of artificial neural networks (ANN) with fuzzy inference systems (FIS), showed that the neural network was difficult to use due to prior knowledge rule or it has to be learnt from scratch. Among the disadvantages of the neural network system are complex learning algorithms and difficult to extract knowledge. Compared with fuzzy inference systems, it can incorporate prior rule-base, interpretable by if-then rules, simple interpretation and implementation. However, the fuzzy system is unable to acquire linguistic knowledge. Additionally, knowledge must be provided. Therefore, an integrated system that combines the FIS and ANN modelling concept is an advantage and complements each other (Gulbag & Temurtas, 2006).

There are not many studies that look at identification of herbs in the same family based on their aroma. Therefore, the aim of this study is to explore, analyse and show the difference between herbs based on their aroma. Mohamad Yusof et al. (2015) employed an electronic nose to classify 12 herb species from three aromatic herbs families, namely *Lauraceae*, *Myrtaceae*, and *Zingiberaceae* was studied by. This artificial intelligence was effective in acquiring signals and advantageous for sample preparation compared with other systems. Raw data from the odour signal is captured by the gas sensor array in electronic nose system. The signal = is processed using several standard normalisation techniques to give better interpretation of data. The objective of this paper is to compare the performance of two types of artificial intelligent techniques. The artificial neural network (ANN) and adaptive neuro-fuzzy inference system (ANFIS) is employed using normalised data for herbs classification. The accuracy of classification of both techniques is presented for 12 herb species in three families. The performance of both techniques will be evaluated based on of the accuracy of the system to classify the herbs species.

## THEORY AND METHODS

### Experiment Overview

Electronic nose was used to classify 12 aromatic herbs species from Lauraceae, Myrtaceae, and Zingiberaceae family by Mohamad Yusof et al. (2015). The list of herbs was chosen and collected with the consultation of botanist from Bioscience Institute based on the availability of samples from Agricultural Conservatory Park, Universiti Putra Malaysia. The scientific name of the sample is listed in Table 1. Due to fast response, affordable cost, low power consumption and large number of target gas detection, multiple metal oxide gas sensors from Figaro were selected as shown in Table 2 to detect a broad range of chemical compound according to the phytochemical of the herbs 15 g applied for each species as a sample.

### Artificial Neural Network (ANN)

The ANN model is designed from two to five inputs to find the best result of herbs classification. Training was done by using scaled conjugate gradient backpropagation method. Data was divided into 70% training, 15% testing and of the rest for validation. Sigmoid activation function was used in neural network of the study. The architecture of neural network in this research is

Table 1  
*Scientific name of twelve herb species*

Family Name	Abbreviation	Scientific Name
Lauraceae	LCI	1. <i>Cinnamomum Iners</i>
	LCV	2. <i>Cinnamomum Verum</i>
	LCP	3. <i>Cinnamomum Porrectum</i>
	LLE	4. <i>Litsea Elliptica</i>
Myrtaceae	MSA	5. <i>Syzygium Aromaticum</i>
	MSP	6. <i>Syzygium Polyanthum</i>
	MMA	7. <i>Melaleuca Alternifolia</i>
	MRT	8. <i>Rhodomyrtus Tomentosa</i>
Zingiberaceae	ZSK	9. <i>Scaphoclamys Kunstleri</i>
	ZET	10. <i>Etilingera Terengganuensis</i>
	ZZZ	11. <i>Zingiber Zerumbet</i>
	ZEC	12. <i>Elettariopsis Curtisii</i>

Table 2  
*The selected FIGARO MOS gas sensor for electronic nose*

Sensor Type	Abbreviation	Type of gas detection
TGS 2610	Sensor 1	Butane, propane, liquefied petroleum gas
TGS 2611	Sensor 2	Methane, natural gas
TGS 2620	Sensor 3	Alcohol, toluene, xylene, volatile organic compound
TGS 823	Sensor 4	Organic solvent vapours
TGS 832	Sensor 5	Halocarbon, Chlorofluorocarbon

made up of the input from sensor 1, sensor 2, sensor 3, sensor 4 and sensor 5, 20 hidden layers and 12 species of herbs as the output. Every node from the input layer is connected to a node from the hidden layer. On the other hand, every node from the hidden layer is connected to a node in the output layer. Each link is associated with the weight  $w_{ij}$ .

The input layer represents the raw information that is fed into the network. Every single input to the network is duplicated and sent to the nodes in hidden layer. Data is accepted from the input layer by the hidden layer. It uses the input values and is modified based on weight,  $w_{ij}$  value. The new value will be sent to the output layer. After that, there will be another modification based on the weight,  $w_{jk}$  from the connection between hidden and output layer. Finally, the output layer processes the information received from the hidden layer and produces the output for 23 herbs species. The two layers feed-forward back propagation structure is illustrated in Figure 1(a).

### Adaptive Neuro-Fuzzy Inference System (ANFIS)

The ANFIS is another classification technique used in this study. To build the fuzzy inference system into the structure, the subtractive clustering was selected. For better performance in



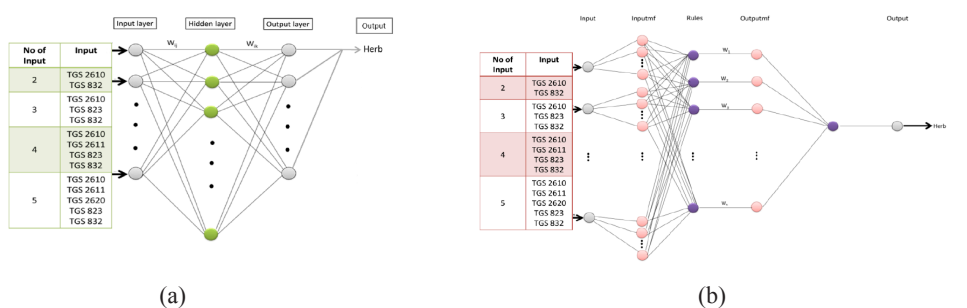


Figure 1. (a) Structure of ANN; b) Structure of ANFIS

the training phase, hybrid optimisation method was adopted. This is because it is faster and the results are closest compared with the back propagation gradient descent optimisation method. Sensor 1 to sensor n input layer is the first layer of the ANFIS structure. Premise or antecedent parameters of the ANFIS are contained in the second layer. It is dedicated to the fuzzy sub-space. The consequent parameters of the fifth layer were used to optimise the network. In the hybrid learning algorithm, the node outputs go forward until layer five and the consequent parameters are identified by least-square method during the forward pass. In the backward pass, error signals propagate backwards and the premise parameters are updated by gradient descent method. The structure of ANFIS in this project is shown in Figure 1(b).

Throughout the learning process, the parameters associated with the membership functions changed. A gradient vector facilitates the computation of these parameters. It provides a measurement of the fuzzy inference system modelling the input or output data for a given set of parameters. When the gradient vector is obtained, any of several optimisation routines can be applied in order to adjust the parameters to reduce measurement errors. This error measure is usually defined by the sum of the squared difference between actual and desired outputs. The ANFIS uses either back propagation or a combination of least squares estimation and back propagation to estimate membership function parameter.

The following are the rules for Sugeno-type fuzzy-rule-based model for five-input ANFIS:

- If (TGS2610 is LCI) and (TGS2611 is LCI) and (TGS2620 is LCI) and (TGS823 is LCI) and (TGS832 is LCI) then (HERBSPECIES is CinnamomumIners) (1)
- If (TGS2610 is LCP) and (TGS2611 is LCP) and (TGS2620 is LCP) and (TGS823 is LCP) and (TGS832 is LCP) then (HERBSPECIES is CinnamomumVerum) (1)
- If (TGS2610 is LCV) and (TGS2611 is LCV) and (TGS2620 is LCV) and (TGS823 is LCV) and (TGS832 is LCV) then (HERBSPECIES is CinnamomumPorrectum) (1)
- If (TGS2610 is LLE) and (TGS2611 is LLE) and (TGS2620 is LLE) and (TGS823 is LLE) and (TGS832 is LLE) then (HERBSPECIES is LitseaElliptica) (1)
- If (TGS2610 is MMA) and (TGS2611 is MMA) and (TGS2620 is MMA) and (TGS823 is MMA) and (TGS832 is MMA) then (HERBSPECIES is MelaleucaAlternifolia) (1)

- If (TGS2610 is MRT) and (TGS2611 is MRT) and (TGS2620 is MRT) and (TGS823 is MRT) and (TGS832 is MRT) then (HERBSPECIES is RhodomyrtusTomentosa) (1)
- If (TGS2610 is MSA) and (TGS2611 is MSA) and (TGS2620 is MSA) and (TGS823 is MSA) and (TGS832 is MSA) then (HERBSPECIES is SyzygiumAromaticum) (1)
- If (TGS2610 is MSP) and (TGS2611 is MSP) and (TGS2620 is MSP) and (TGS823 is MSP) and (TGS832 is MSP) then (HERBSPECIES is SyzygiumPolyanthum) (1)
- If (TGS2610 is ZEC) and (TGS2611 is ZEC) and (TGS2620 is ZEC) and (TGS823 is ZEC) and (TGS832 is ZEC) then (HERBSPECIES is ElettariopsisCurtisii) (1)
- If (TGS2610 is ZET) and (TGS2611 is ZET) and (TGS2620 is ZET) and (TGS823 is ZET) and (TGS832 is ZET) then (HERBSPECIES is EtlingeraTerengganuensis) (1)
- If (TGS2610 is ZSK) and (TGS2611 is ZSK) and (TGS2620 is ZSK) and (TGS823 is ZSK) and (TGS832 is ZSK) then (HERBSPECIES is ScaphoclamysKunstleri) (1)
- If (TGS2610 is ZZZ) and (TGS2611 is ZZZ) and (TGS2620 is ZZZ) and (TGS823 is ZZZ) and (TGS832 is ZZZ) then (HERBSPECIES is ZingiberZerumbet) (1)

The ANFIS training process first determines the fuzzy sets and the number of sets of each input variable and shape of their membership function. Training data passes through the neural network and with adjusts the input parameters to identify the relationship between input and output, and to minimise the errors. The expected output of the ANFIS will be the 12 herb species. The best structure was determined by the lowest value of the error given by the ANFIS model.

## RESULTS AND DISCUSSIONS

The classification techniques in this research were implemented using ANN and ANFIS. The result of classification using ANN is shown in Table 3. Two and Five inputs of classification were done and the percentage of accuracy is given to indicate the performance of the system. The lowest percentage for 83.4% of accuracy obtained from two inputs structure of ANN. Three input systems, TGS 25610, TGS 823 and TGS 832, yielded 85.8% accuracy and less error value for 9.769E-3 compared with two inputs. With four inputs, the accuracy increases to 90.2% and 8.868E-3 value of training error. Meanwhile, five inputs show provides the highest accuracy at 91.7% to classify the sample herbs and the lowest value of training error among the other inputs. Increasing the number of inputs increases value of accuracy and with less training errors.

Table 3  
Result of classification using ANN

Input	Network	MSE	Accuracy
TGS 2610, TGS 832	[2 20 12]	1.948E-2	83.4 %
TGS 2610, TGS 823, TGS 832	[3 20 12]	9.769E-3	85.8 %
TGS 2610, TGS 2611, TGS 823, TGS 832	[4 20 12]	8.868E-3	90.2 %
TGS 2610, TGS 2611, TGS 2620, TGS 823, TGS 832	[5 20 12]	7.554E-3	91.7 %

Next, the ANN network was evaluated with testing data for five inputs to show performance of the system. From the results in Table 4, ANN yielded 84.2% accuracy for classification process. The testing data is independent from the training data whereby the former contains more noise compared with training data resulting in the accuracy to be slightly lower and the MSE error to be slightly higher.

Table 4  
*Result of classification using ANN*

Dataset	MSE	Accuracy
Training	7.554E-3	91.7 %
Testing	2.742E-2	84.2 %

In the ANFIS classification method, the highest percentage of classification was given by five inputs of ANFIS structured as 94.8% of accuracy with RMSE value 2.472E-4. The classification accuracy for four inputs was achieved at 94.7% with a difference of only 0.1% from five inputs. Furthermore, the three inputs produced 92.7% of accuracy and 4.301E-4 of RMSE. The lowest percentage is made up from two inputs which showed 85.4% accuracy. Table 5 shows classification using ANFIS technique. The ANFIS structure was also evaluated using testing data. The result as in Table 6 shows that percentage of accuracy is getting lower. Human error that may have occurred during the experimental procedure may influence data collection and lower the quality of testing data.

Table 5  
*Result of classification using ANFIS*

Input	FIS	MSE	Accuracy
TGS 2610, TGS 832		8.6912E-4	85.4 %
TGS 2610, TGS 823, TGS 832	Fuzzy	4.301E-4	92.7 %
TGS 2610, TGS 2611, TGS 823, TGS 832	Subtractive	2.713E-4	94.7 %
TGS 2610, TGS 2611, TGS 2620, TGS 823, TGS 832	Clustering	2.472E-4	94.8 %

Table 6  
*Comparison of error and accuracy for training set and testing set*

Dataset	RMSE	Accuracy
Training	2.472E-4	94.8 %
Testing	3.965E-4	92.7 %

The k-fold cross-validation method was used to validate the performance of the classifier in the electronic nose system as shown in Table 7. The K-fold cross validation is run several times, each with a different random arrangement in order to obtain an accurate estimate to the accuracy of a classifier. The ANFIS showed higher accuracy compared with ANN with lower value of true error where the former reported 94.8 % of true error while the latter (ANN) reported 91.2 % of true error. Hence, ANFIS was validated as better classifier compared with ANN in this research to classify 12 herb species of three families.

Table 7  
*K-fold cross-validation results for ANN and ANFIS*

ACCURACY	NO. OF EXPERIMENT			
	EXP. 1	EXP. 2	EXP. 3	TRUE ERROR
ANN	90.9 %	91.6 %	91.1 %	91.2 %
ANFIS	92.1 %	94.8 %	97.6 %	94.8 %

## CONCLUSION

In this study, we have considered two types of artificial intelligent techniques for classification purposes. The classification of the 12 herbs was successfully done using artificial neural network and adaptive neuro-fuzzy inference system. The ANFIS technique gives better performance with higher percentage of accuracy (94.8%) to classify the herb species compared with the ANN technique (91.7%). Cross-validation showed the best classifier was ANFIS by comparing the true error for both ANN and ANFIS. The results showed the proposed structure of electronic nose system was viable and hence, the objective of this study was achieved. The study had also contributed to improving the artificial olfactory system.

## ACKNOWLEDGEMENT

The authors acknowledge with gratitude the financial support supported by Fundamental Research Grant Scheme, Ministry of Higher Education, Malaysia, FRGS/2/2013/TK02/UPM/02/5, and Project Title: Formulation of Algorithm to Classify Distinctive Odors Pattern of Aromatic Plant Species using Hybrid Artificial Intelligence Techniques and Universiti Putra Malaysia Grant Scheme (Geran Putra IPS) (Project Title: Development of E-Tongue Device for Herb Recognition System). Special thanks also goes to Institute of Bioscience, Universiti Putra Malaysia for providing samples of herbs.

## REFERENCES

- Amari, A., Barbri, N. E., Llobet, E., Bari, N. E., Correig, X., & Bouchikhi, B. (2006). Monitoring the Freshness of Moroccan Sardines with a Neural-Network Based Electronic Nose. *Sensors (Basel, Switzerland)*, 6(10), 1209–1223.
- Chen, C., Muhamad, A., & Ooi, F. (2012). Herbs in exercise and sports. *Journal of Physiological Anthropology*, 31(1), 4.

- Dinrifo, R.R. (2011) Neural network-based electronic nose for cocoa beans quality assessment. *Agricultural Engineering International: CIGR Journal*, 13(4), 1–17.
- Fischer, D.C.H. (2010). Handbook of herbs and spices. *Brazilian Journal of Pharmaceutical Sciences*, 46(4), 821–822.
- Ganora, L. (2008). Herbal Constituents Foundations of Phytochemistry. *Louisville, Colorado: Herbalchem Press*, 1–15.
- Gulbag, A., & Temurtas, F. (2006). A study on quantitative classification of binary gas mixture using neural networks and adaptive neuro-fuzzy inference systems. *Sensors Actuators, B Chem.*, 115(1), 252–262.
- Guterriez. (2002). LECTURE 1: Pattern Recognition Course Introduction. *Texas A&M University*, 1–20.
- Haddi, Z., Alami, H., El Bari, N., Tounsi, M., Barhoumi, H., Maaref, A., Jaffrezic-Renault, N., & Bouchikhi, B. (2013). Electronic nose and tongue combination for improved classification of Moroccan virgin olive oil profiles. *Food Research International*, 54(2), 1488-1498.
- Husin, Z., Shakaff, A.Y.M., Aziz, A.H.A., Farook, R.S.M., Jaafar, M.N., Hashim, U., & Harun, A. (2012). Embedded portable device for herb leaves recognition using image processing techniques and neural network algorithm. *Computers and Electronics in Agriculture*, 89, 18-29.
- İhsan Ömür Bucak, & Bekir Karlık. (2009). Hazardous Odor Recognition by CMAC Based Neural Networks. *Sensors*, 7308–7319.
- Ishak, A.J., Hussain, A., & Mustafa, M.M. (2009). Weed image classification using Gabor wavelet and gradient field distribution. *Comput. Electron. Agric.*, 66(1), 53–61.
- Konduru, T., Rains, G.C., & Li, C. (2015). A customized metal oxide semiconductor-based gas sensor array for onion quality evaluation: system development and characterization. *Sensors (Basel)*, 15(1), 1252–1273.
- Li, C., Heinemann, P., & Sherry, R. (2007). Neural network and Bayesian network fusion models to fuse electronic nose and surface acoustic wave sensor data for apple defect detection. *Sensors Actuators B Chem.*, 125(1), 301–310.
- Mohamad Yusof, U.K., Che Soh, A., Radzi, N.F.M., Ishak, A.J., Hassan, M.K., Ahmad, S.A., & Khamis, S. (2015). Selection of Feature Analysis Electronic Nose Signals Based on the Correlation Between Gas Sensor and Herbal Phytochemical. *Australian Journal of Basic and Applied Sciences*, 9(5), 360-367.
- Tudu, B., Kow, B., Bhattacharyya, N. & Bandyopadhyay, R. (2009). Normalization techniques for gas sensor array as applied to classification of black tea. *International Journal on Smart Sensing and Intelligent Systems*, 2, 1-14.
- Wilson, A.D. (2013). Diverse applications of electronic-nose technologies in agriculture and forestry. *Sensors (Basel)*, 13(2), 2295–2348.
- Wilson, A.D., & Baietto, M. (2009). Applications and advances in electronic-nose technologies. *Sensors (Basel)*, 9(7), 5099–5148.
- Zalikha, Z. (2011). Plant Leaf Identification Using Moment Invariants & General Regression Neural Network. In *11th IEEE International Conference on Hybrid Intelligent Systems*, (pp. 430-435).



## A Corrective Action Scheme for Contingency Monitoring of Transmission Line Overloading

Mohammad Lutfi Othman\*, Mahmood Khalid Hadi and Noor Izzri Abdul Wahab

*Centre for Advanced Power and Energy Research (CAPER), Dept. of Electrical and Electronic Engineering, Faculty of Engineering, Universiti Putra Malaysia, 43400 UPM, Serdang, Selangor, Malaysia*

### ABSTRACT

Special Protection Schemes (SPSs), are corrective action schemes that are designed to protect power systems against severe contingency conditions. In planning of SPSs, protecting transmission network from overloading issue due to critical situations has become a serious challenge which needs to be taken into account. In this paper, a Special Protection and Control Scheme (SPCS) based on Differential Evolution (DE) algorithm for optimal generation rescheduling has been applied to mitigate the transmission line overloading in system contingency conditions. The N-1 contingency has been performed for different single line outages under base and increased load in which generation rescheduling strategy has been undertaken to overcome the overloading problem. Simulation results are presented for both pre-and post system emergency situations. The IEEE 30-bus test system was utilised in order to validate the effectiveness of the proposed method.

*Keywords:* Special Protection Scheme, transmission line overloading, line contingency, generation rescheduling, Differential Evolution (DE) algorithm

### INTRODUCTION

Special Protection Schemes (SPSs), also known as Corrective Action Schemes (CASs),

are schemes aimed at creating an incredible system contingency condition in order to initiate pre-determined preventive actions, not only the isolation of faulted elements but also to overcome the consequences of severe system conditions in addition to maintaining good system performance. The corrective actions comprise changing system demand (load shedding), changing utility generation and system configuration in order to maintain system stability and an acceptable bus voltage or branch power flow. The operation of SPSs

#### ARTICLE INFO

##### *Article history:*

Received: 24 August 2016

Accepted: 02 December 2016

##### *E-mail addresses:*

[lutfi@upm.edu.my](mailto:lutfi@upm.edu.my) (Mohammad Lutfi Othman),

[mhm\\_mhm\\_80@yahoo.com](mailto:mhm_mhm_80@yahoo.com) (Mahmood Khalid Hadi),

[izzri@upm.edu.my](mailto:izzri@upm.edu.my) (Noor Izzri Abdul Wahab)

\*Corresponding Author

is presented by the incidence of disturbances such as frequency and/or voltage instability, transient angular instability, and instability resulting from cascade transmission line tripping (Vinnakota et al., 2008).

<b>Nomenclature</b>	
$P_i, Q$	Active and reactive power injected to the system at bus $i$ .
$V_i, V_j$	Bus voltage magnitude at buses $i$ and $j$ .
$G_{ij}, B_{ij}$	Self-conductance and susceptance of the element between bus $i$ and $j$ .
$\theta_{ij}$	Voltage angle between bus $i$ and $j$ .
$P_{Gi}, Q_{Gi}$	Active and reactive power generated bus $i$ .
$P_{Li}, Q_{Li}$	Active and reactive power consumed in bus $i$ .
$P_{Gi}^{min}, P_{Gi}^{max}$	Minimum and maximum generation limits of active power at bus $i$ .
$Q_{Gi}^{min}, Q_{Gi}^{max}$	Minimum and maximum generation limits of reactive power at bus $i$ .
$V_i^{min}, V_i^{max}$	Minimum and maximum voltage limits of bus $i$ .
$NB$	Number of system buses.

The main goals of applying the special protection schemes are to (Seyedi & Sanaye-Pasand, 2009):

- To operate the power systems within their acceptable limits.
- To increase system security through critical disturbances, and
- To improve the power system operating conditions.

Due to the growing complexity of utility operation, many factors such as growth in demand, increased power imports/exports have stressed the transmission network during its normal operation. In designing SPS, protecting of transmission lines from overloading risk in critical contingencies is a significant challenge which needs to be taken into account. This could happen due to some disturbances such as line and/or transformer outage, load perturbation, and when there is no communication between system generation and transmission grids. To avoid a network collapse in overloading situations, some corrective actions are needed such as load shedding and/or generation rescheduling strategies, phase shift transformers, and



transmission line switching (Awais et al., 2015). Load shedding and generation rescheduling schemes are commonly utilised to overcome grid overloading issue and in which no more reserves are needed. Building new transmission lines to meet N-1 contingency condition is costly and time-consuming. Overloading issues could take place due to unexpected line and/or generator outage, a sudden increase in system demand, and failure of any of system component and resulted in cascade line outages and system collapse. One of the most effective and obvious approaches to relieve line overload is the generation rescheduling plan under system disturbances (Pandiarajan & Babulal, 2014). Alleviation of transmission line overloading has been performed using different techniques. Balaraman Kamaraj (2012) had applied a generation rescheduling method based on back propagation neural network to predict line overloading amount and mitigation of this overload according to N-1 contingency conditions. In (Sharma and Srivastava, 2008), an algorithm based on neural network presented for identification of the overloaded lines and prediction of overloading amount in the overloaded lines for different generation / loading conditions. Congestion management via optimal generation rescheduling based on Particle Swarm Optimization (PSO) algorithm was proposed in (Dutta & Singh, 2008). In (Hagh & Galvani, 2010), a modified Genetic Algorithm was used to find the location and the load amount to be shed and generation rescheduling in post contingency conditions such as line overloading as well as voltage violations.

In this paper, generation rescheduling methodology has been performed based on Differential Evolution (DE) algorithm to alleviate transmission line overloading along with the severity index philosophy. The validation of the applied algorithm was examined on IEEE 30-bus system with the aid of the power flow analysis. Line overloads according to sudden line outage was also considered.

## METHODOLOGY

### Mathematical Formulation

The major aim of the presented algorithm is to determine the optimum power rescheduling based on minimising severity and to overcome the overloading in post contingency. Thus, a minimum severity index has been considered as the objective function in this study. During the proposed solution of the problem, the optimal rescheduling values are subjected to the operating constraints and are divided into two groups:

- Equality constraints:

Equality constraints in a power system represent active and reactive power injected to the system buses as shown below:

$$P_i = V_i \sum_{j=1}^{NB} V_j (G_{ij} \cos \theta_{ij} + B_{ij} \sin \theta_{ij}) \quad \text{where } P_i = P_{Gi} - P_{Li} \quad (1)$$

$$Q_i = V_i \sum_{j=1}^{NB} V_j (G_{ij} \sin \theta_{ij} - B_{ij} \cos \theta_{ij}) = Q_{Gi} - Q_{Li} \quad (2)$$

- Inequality constraints:

Active and reactive power generated, bus voltage magnitude, as well as line flow limits are considered as inequality constraints and can be represented as follows:

$$P_{Gi}^{min} \leq P_{Gi} \leq P_{Gi}^{max} \quad i = 1, 2 \dots \dots NG \quad (3)$$

$$V_i^{min} \leq V_i \leq V_i^{max} \quad i = 1, 2 \dots \dots NB \quad (4)$$

$$S_{ij} \leq S_{ij}^{max} \quad i = 1, 2 \dots \dots NL \quad (5)$$

### Severity index (SI)

The severity state of any power system contingency condition which is associated to a line overloading can be presented in terms of the severity index formula that refers to the stress in a power system during a post contingency condition (Alsac & Stott, 1974; Balaraman & Kamaraj, 2012):

$$SI = \sum_{k=1}^{ovl} \left( \frac{S_{ij}}{S_{ij}^{max}} \right)^{2m} \quad (6)$$

where:  $SI$  = severity index,  $S_{ij}$  = line flow in a branch between bus  $i$  and  $j$ ,  $S_{ij}^{max}$  = maximum line flow limit,  $ovl$  = a set of overloaded lines, and  $m$  = an integer exponent.

The line flow is obtained from one of the load flow solutions such as Newton-Raphson method which has been applied in this work. Only overloaded lines are considered when computing the severity index for security assessment and the value of  $m$  is fixed to 1 to avoid the masking effects (Balaraman & Kamaraj, 2012). For a secure operation in power system, the value of  $SI$  must be zero. The greater the value of  $SI$ , the more severe contingency will be.

## OVERVIEW OF DIFFERENTIAL EVOLUTION

Differential evolution (DE) defined as simple, and population set based direct search algorithm. It is a high performance optimisation algorithm and easy to understand and implement. It was first proposed by Storn and Price (Storn & Price, 1997). The optimisation steps are similar to the Genetic Algorithm. However unlike GA, which relays on crossover operation, DE algorithm initially employs the mutation (differential) operation, crossover and selection process to guide the search of a solution toward the prospective solution within a search region. Like

other evolutionary algorithms, DE works with population set of candidate solutions known as individuals that randomly generate and improve iteratively by implementing mutation, crossover and selection operations (Singh & Srivastava, 2014). The DE generates a population set of real valued individual vectors  $X_{i,G}$  which called target vector as below:

$$\dots X_{i,G} = X_{j,i,G} \quad i = 1, \dots, NP, \quad G = 0, 1, \dots, G_{max}, \quad j = 1, \dots, D \quad (7)$$

Each individual vector has a population index  $i$ , its range between 1 and  $NP$ , where  $NP$  represents the population size. The parameters in the vectors are indexed by  $j$ , its range between 1 and  $D$  where  $D$  represents the number of variables that need to be optimised. The basic stages of DE algorithm are depicted as following:

### Initialisation

The optimisation process of DE algorithm begins by generating a population set of  $NP$   $D$  dimensional real valued vectors at  $G = 0$ . Each parameter vector is as a candidate for solution to the optimisation process. The initial vector values are selected randomly and limited to lower and upper parameter bounds i.e.  $[X_L, X_H]$ . Where  $X_L = [X_{1,L}, X_{2,L}, \dots, X_{D,L}]$  and  $X_H = [X_{1,H}, X_{2,H}, \dots, X_{D,H}]$ , represent the lower and upper limits for the search region for each individual vector respectively. The initial individual vector can be expressed as:

$$X_{j,i}(0) = X_L + rand(X_H - X_L) \quad (8)$$

where  $rand$  is a random number which is selected between 0 and 1.

### Mutation

In the mutation stage, DE algorithm generates a new candidate solution called a mutant (donor) vector from the initial population by selecting randomly three distinct vectors from the target vector. The mutant vector is created by adding a weighted difference between two of the selected vectors to the third vector from the current generation. These randomly selected vectors are different from the target vector and chosen from the range 1 to  $NP$ . A mutant vector  $V_{j,i,G}$  is expressed as:

$$V_{j,i,G} = X_{r_1,G} + F(X_{r_2,G} - X_{r_3,G}) \quad (9)$$

where  $r_1 \neq r_2 \neq r_3 = \{1, \dots, NP\}$  randomly generated indices.  $X_{r_1,G}$ ,  $X_{r_2,G}$ , and  $X_{r_3,G}$  are randomly chosen vectors from the initial population set.  $F$  represents a mutation factor and selected within the range  $[0,1]$ .

### Crossover

In this step, the mutant vector  $V_{j,i,G}$  and the target vector  $X_{j,i,G}$  are swapped in order to form the trial vector  $U_{j,i,G}$  using an operation named as crossover in order to increase the diversity of a population. This trial vector can be generated by:

$$U_{j,i,G} = \begin{cases} V_{j,i,G} & \text{if } (rand \leq CR \text{ or } j = j_{rand}) \\ X_{j,i,G} & \text{otherwise} \end{cases} \quad (10)$$

where  $CR$  is the crossover factor which controls the diversity of a population and assists the algorithm to escape from the local optimum. Its range between 0 and 1.  $j_{rand} \in [1, 2, \dots, D]$ , represents an index which is randomly chosen to ensure that  $U_{j,i,G}$  gets at least one element from the mutant vector.

In order to avoid the violation of the vector limits and to ensure the vector values lie within the boundary limits after the recombination, a penalty function is applied. The new vector value which violates the constraints is replaced by a random value as:

$$U_{j,i,G} = X_{j,i,L} + rand (X_{j,i,H} - X_{j,i,L}) \quad (11)$$

### Selection

In order to keep the population size fixed, a selection operation is performed to determine which one of the target vectors or the mutant vectors will survive to be in the next generation i.e. ( $G = G+1$ ). The selection operation can be expressed as:

$$X_{i,G+1} = \begin{cases} U_{i,G} & \text{if } J(U_{i,G}) < J(X_{i,G}) \\ X_{i,G} & \text{otherwise} \end{cases} \quad (12)$$

where  $J(X)$  denotes the fitness function to be minimised. Thus, if the fitness value of a trial vector is lower, then it swaps the individual vector along with its corresponding fitness of the target vector through the next generation, else the target value is kept to the population to be survive in the next generation. Therefore, the population set either gets better or remains constant from the fitness function point of view, but never declines. These steps are repeated over each iteration until a maximum number of generations (iterations)  $G_{max}$  is met.

## RESULTS AND DISCUSSIONS

### System contingency analysis

The validation of the proposed DE based SPCS has been examined on IEEE 30 bus system. The algorithms are performed using Matlab and executed in Intel core i3 CPU 2.2 GHz, 2 GB RAM PC. The test system data regarding line parameters, generation limits and base case load are adopted and taken from (Alsac & Stott, 1974). Full a.c power flow (e.g. Newton –

Raphson) method has been applied to determine the variables related to each bus of the power system which comprise four values: voltage magnitude, its phase angle, and real and reactive power flows. The variables are related to each line: active and reactive power flows as well as line losses. In a power system, transmission line overloading may take place due to different reasons comprising line outage. Therefore, N-1 contingency analysis has been conducted under normal demand conditions in order to identify the harmful disturbances during system operation. For each case, pre-and post contingency line flows are obtained by solving the power flow equations to determine which transmission lines get overloaded due to a specific single line outage. From the contingency analysis, line outage 1-2, 1-3, 3-4, 2-5 resulted in overloading some other lines in the system under base and increased load by 10% at all buses conditions.

### The Proposed DE Algorithm

For a secure system operation, the power flows in transmission lines should not override its allowable limits under normal and contingency conditions. Thus, corrective actions should be taken to relieve line overloads. The main objective of this study is to mitigate line overloading by applying generation rescheduling strategy during a system contingency. Optimum generation rescheduling is obtained using DE algorithm.

Generated active power of the system generators are taken as the control variables of the proposed algorithm. Initially, a set of  $P_G$  values are randomly created by DE algorithm within the generation limits such that equation (3) is satisfied for the lower and upper limits. Hence, DE algorithm runs these generated values in the fitness function algorithm to get the values of SI in order to evaluate the problem which needs to be solved. Consequently, the algorithm utilises the mutation and crossover operations in order to get a better and minimum fitness value as much as possible due to its strategy. In this study, the magnitudes of  $F$  and  $CR$  are taken as 0.8 and 0.5 respectively that give best results after many trials. The fitness function of this work is the load flow algorithm to get the line flow and evaluate the severity index. Minimum severity index is considered as the objective function for the proposed algorithm. The optimal active power generation as a corrective action plan is shown in Table 1 for the simulated cases in addition to system losses for each simulated case.

The algorithms were performed for a maximum number of 50 iterations and was run for 10 independent runs. The generation rescheduling values are taken as average from the independent runs. Figure 1 illustrates the variation of the fitness function convergence of DE algorithm runs for the considered base load contingencies and its values are also taken as the average. It is clear from Figure 1 that the DE algorithm converges rapidly and focuses on finding the convenient solutions to the specific issue. The fitness value goes down to its minimum value close to zero. Simulated line outage cases along with the overloaded lines details are tabulated in Table 2 before and after generation rescheduling. The values of  $SI$  are also evaluated for each scenario before rescheduling and the final values of  $SI$  after rescheduling are also given in the last column.

Table 1  
Control variables setting of IEEE 30-bus test system

Case study	Line out of service	Active power generation values (MW)						Power Losses (MW)
		PG1	PG2	PG3	PG4	PG5	PG6	
Base load	1-2	124.87	46.12	41.53	30.97	20.19	32.97	12.82
	1-3	128.65	42.75	39.81	31.18	20.41	29.18	8.30
	3-4	129.07	42.62	35.31	30.81	21.02	32.61	7.92
	2-5	149.59	40.37	32.69	24.46	21.13	28.97	13.32
Base load	1-2	124.87	46.12	41.53	30.97	20.19	32.97	12.82
	1-3	128.65	42.75	39.81	31.18	20.41	29.18	8.30
	3-4	129.07	42.62	35.31	30.81	21.02	32.61	7.92
	2-5	149.59	40.37	32.69	24.46	21.13	28.97	13.32
Increased load by 10% at all buses	1-2	126.78	65.17	46.70	31.71	21.97	33.50	14.06
	3-4	133.14	55.34	45.62	32.25	20.77	36.46	11.83

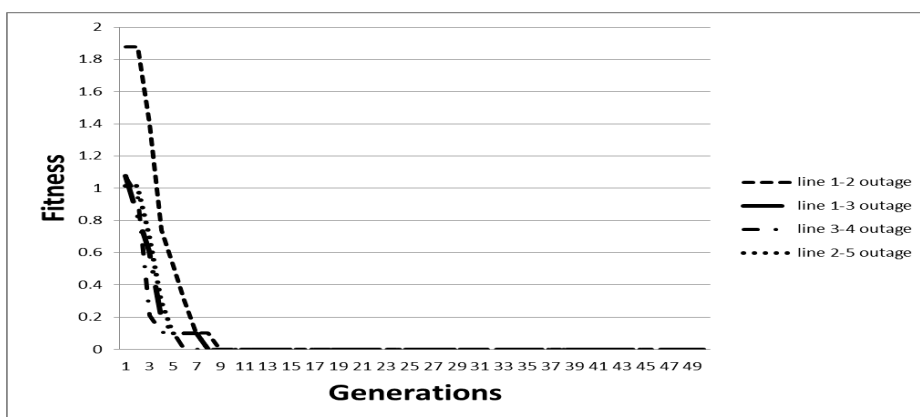


Figure 1. Fitness convergence of the proposed DE algorithm

Table 2  
*Simulated line outage details before and after generation rescheduling*

Case study	Line outage	Overloaded lines	Line limit (MVA)	Before rescheduling		After rescheduling	
				Line flow (MVA)	SI	Line flow (MVA)	SI
Base load	1-2	1-3	130	307.803	16.265	123.144	0
		2-4	65	65.592		24.384	
		3-4	130	279.121		116.283	
		4-6	90	174.058		73.506	
		6-8	32	36.362		13.152	
	1-3	1-2	130	273.019	9.279	128.068	0
		2-4	65	86.154		44.752	
		2-6	65	92.759		47.477	
	3-4	6-8	32	33.188		7.040	
		1-2	130	270.07	9.076	126.559	0
		2-4	65	84.916		42.758	
		2-6	65	91.805		46.112	
	2-5	6-8	32	32.928		8.085	
		1-2	130	164.467	10.885	85.544	0
		2-4	65	74.604		43.368	
		2-6	65	102.858		59.528	
		4-6	90	124.097		71.591	
		5-7	70	110.189		69.689	
Increased load by 10% at all buses	1-2	6-8	32	33.317		12.509	
		1-3	130	369.586	22.580	124.888	0
		2-4	65	77.239		21.141	
		3-4	130	321.795		117.563	
		4-6	90	201.235		76.224	
	3-4	6-8	32	44.791		9.732	
		1-2	130	305.287	11.518	127.499	0
		2-4	65	93.888		47.139	
		2-6	65	101.556		50.865	
		6-8	32	38.874		5.228	

## CONCLUSION

In this paper, an SPCS scheme for transmission line overloading alleviation has been presented based on the Differential Evolution (DE) algorithm. The proposed technique efficiently mitigates the line overloads based on the corrective action through the generation rescheduling philosophy. Contingency conditions due to unexpected single line outage under base and increased load are considered in this study. In order to reveal the efficiency of the performed approach, IEEE 30-bus system was used for the simulation cases. The results show that DE algorithm completely mitigates the line overloading issues in addition to fast fitness convergence.

## ACKNOWLEDGEMENT

The authors would like to acknowledge the financial support from Universiti Putra Malaysia (UPM) under the Geran Putra IPB scheme with the project no. GP-IPB/2013/941210.

## REFERENCES

- Alsac, O., & Stott, B. (1974). Optimal load flow with steady-state security. *Power Apparatus and Systems, IEEE Transactions on, PAS-93*(3), 745-751.
- Awais, M., Basit, A., Adnan, R., Khan, Z. A., Qasim, U., Shafique, T., & Javaid, N. (2015). Overload Management in Transmission System Using Particle Swarm Optimization. *Procedia Computer Science, 52*, 858-865.
- Balaraman, S., & Kamaraj, N. (2012). Cascade BPN based transmission line overload prediction and preventive action by generation rescheduling. *Neurocomputing, 94*, 1-12.
- Dutta, S., & Singh, S. (2008). Optimal rescheduling of generators for congestion management based on particle swarm optimization. *IEEE Transactions on Power Systems, 23*(4), 1560-1569.
- Hagh, M. T., & Galvani, S. (2010). *A multi objective genetic algorithm for weighted load shedding*. Paper presented at the 18th Iranian Conference on Electrical Engineering (ICEE), 2010.
- Pandiarajan, K., & Babulal, C. (2014). Transmission line management using hybrid differential evolution with particle swarm optimization. *Journal of Electrical Systems, 10*(1), 21-35.
- Seyedi, H., & Sanaye-Pasand, M. (2009). Design of new load shedding special protection schemes for a double area power system. *American Journal of Applied Sciences, 6*(2), 317.
- Sharma, S., & Srivastava, L. (2008). Prediction of transmission line overloading using intelligent technique. *Applied Soft Computing, 8*(1), 626-633.
- Singh, H., & Srivastava, L. (2014). Modified differential evolution algorithm for multi-objective VAR management. *and Energy Systems, 55*, 731-740.
- Storn, R., & Price, K. (1997). Differential evolution—a simple and efficient heuristic for global optimization over continuous spaces. *Journal of Global Optimization, 11*(4), 341-359.
- Vinnakota, V. R., Yao, M. Z., & Atanackovic, D. (2008). *Modelling issues of system protection schemes in energy management systems*. Paper presented at the Electric Power Conference, 2008. EPEC 2008. IEEE Canada.





## **Electrical Characteristics of Rubber Wood Ash Filled Natural Rubber at High Frequency**

**Salakjit Nilborworn\*, Krerkchai Thongnoo and Pornchai Phukpattaranont**

*Department of Electrical Engineering, Faculty of Engineering, Prince of Songkla University, Hat Yai, Songkhla 90112, Thailand*

### **ABSTRACT**

The purpose of this study was to identify a method to form rubber composites by incorporating natural rubber (NR) and wood ash from rubber trees with a preliminary electrical properties test. This formulation is intended to improve the rubber composites in order to obtain new materials for high voltage insulators. First, the rubber formulation and processing conditions were optimised before the composites are processed in the laboratory. Second, the interactions between the NR and wood ash were investigated with the following tests: cure time, agglomerate dispersion, SEM images, and the electrical characteristic test. In the electrical characteristic test, the experimental setup was designed for testing the frequency range from 50 Hz to 100 kHz, which is the range of high voltage power line switching frequencies. This energised transient frequency can occur due to switching operations or any other external causes in high voltage systems. Finally, the dielectric property of the rubber composites was evaluated and the equivalent circuit was formulated. The results show that the different properties tested with the new material not only correspond with the filler contents, but also with the frequencies in the transmission lines. The measured data are extracted and converted into other parameters at each frequency. The comparison results are closely matched. Moreover, the results revealed that relative permittivity and the conductivity increases the wood ash filler is increased.

*Keywords:* Rubber composites, high voltage insulator, rubber formulation, electrical characteristic test

### **ARTICLE INFO**

*Article history:*

Received: 24 August 2016

Accepted: 02 December 2016

*E-mail addresses:*

[n.salakchit@gmail.com](mailto:n.salakchit@gmail.com) (Salakjit Nilborworn),

[krerkchai@psu.ac.th](mailto:krerkchai@psu.ac.th) (Krerkchai Thongnoo),

[pornchai.p@psu.ac.th](mailto:pornchai.p@psu.ac.th) (Pornchai Phukpattaranont)

\*Corresponding Author

### **INTRODUCTION**

There is a rapid rise in demand for electricity. Hence, high voltage systems have become crucial power transmission. Power insulators in this high voltage transmission system is one of the indicators of power system stability. Faults in the system frequently occur due to the failure of insulation or an ineffective

design. Both cause degradation in power quality and failure to withstand high voltage stress. Under the high voltage stress, there are four main types of testing methods to ensure stability of high voltage insulators: low and high frequency tests, constant DC test, and an impulse test. In addition to this typical high voltage withstanding capability, a high voltage insulator must also be capable of withstanding different high-frequency disturbances. These disturbances may occur due to switching operations or other external causes. The oscillated frequencies of switching transient can range from 300 Hz to over 10 kHz (Chapman et al., 1999). Thus, the insulating properties should cover all these abnormal spectra.

For this reason, a rubber composite has been designed. In a high powered insulator, rubber composites for high power appliances present many challenges related to their mechanical strength, electrical properties and environmental degradation. Based on their electrical properties, a rubber formulation was prepared by controlling appropriate ingredients using the dielectric constant. After the vulcanising process, the electrical properties of the new material become unpredictable. Thus, the characteristics of the material need to be considered. To ensure their capacity to withstand the disturbance in frequencies, this research reveals the electrical properties of the composite material as a function of frequency.

#### Nomenclature

$R_s, R_p$  series and parallel resistance ( $\Omega$ )

$C_p$  the parallel capacitance (F)

$Z$  impedance ( $\Omega$ )

$\tan \delta$  loss tangent =  $\epsilon''/\epsilon'$

$\epsilon'$  dielectric constant

$\sigma$  conductivity (S/mm)

## MATERIALS AND METHODS

The rubber composites were prepared according to the following procedures: mixing, forming, and vulcanising. First, the raw rubber was mixed in an internal mixture machine. Then all the curative chemicals and additional fillers were added according to the compounding formula design in Table. 1. Next, the procedure for forming the rubber composites were compressed with a designated thickness with a compression machine.

Table 1  
Control variables setting of IEEE 30-bus test system

Ingredients	phr	Approximate $\epsilon'$
Rubber	100	2.7
ZnO	5.0	10
Stearic Acid	1.0	2.3
Antioxidant (TMQ)	1.0	-
Sulphur	2.0	3.5
Rubber Wood Ash (RWA)	0, 5, 10, 20, 30, 40	3.5

The mixing process takes about 12 minutes for each batch. The mixing temperature setting varied between 60°C and 90°C. To ensure the homogeneity of the composites, the mixed rubber was compounded and formed in a typical two-roll mill for 15 minutes. The samples were prepared by varying the volume of RWA contents. It is found that NR/RWA at different formulations affect their cure characteristics and their properties. In general, the dielectric constant for rubber insulators needs to be low. If we design an insulator for appliances, the dielectric constant should be controlled. Table 1 shows typical dielectric constants ( $\epsilon'$ ) of each ingredient.

### EQUIVALENT CIRCUIT OF RUBBER COMPOSITE

The dielectric involving parasitic is a combination of resistance (R) and capacitance (C). It can be lumped as the simplest series and parallel circuit model, which represents the real and imaginary (resistive and reactive) parts of the equivalent circuit. The sample model of the electrical conductivity is shown in Figure 3(a) and its equivalent circuit is shown in Figure 3(b). Based on this equivalent circuit, this hypothesis will provide for the measurement setup which is described in the next section. The agglomerate images of the rubber and the fillers are shown below.

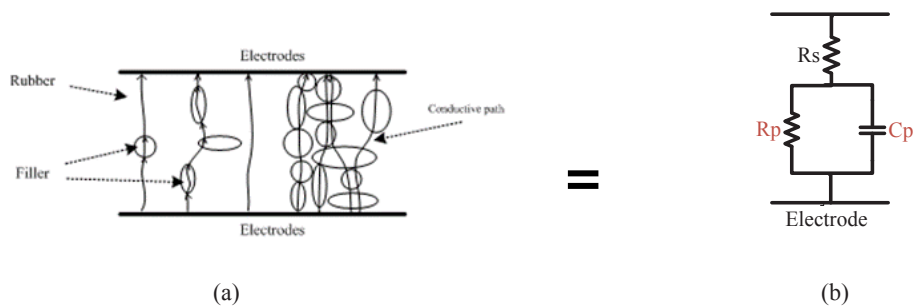


Figure 1. The sample model for (a) the electrical conductivities; (b) an equivalent circuit

## MEASUREMENT SETUP

The test structure is shown in Figure 4. The LCR HiTESTER (HIOKI 3522) was used to measure the electrical values of  $R$ ,  $X$ ,  $C_p$ , and  $Z$ . The applied frequencies were sweeping from 50 to 100 kHz at room temperature (28°C). At least two values of measured data were converted into the desired parameters such as  $|Z|$ ,  $\epsilon'$ ,  $\epsilon''$ ,  $\delta$  and  $\sigma$ . To investigate the electrical properties of the rubber composite, different formulas (0, 5, 10, 20, 30, 40 phr) were measured.

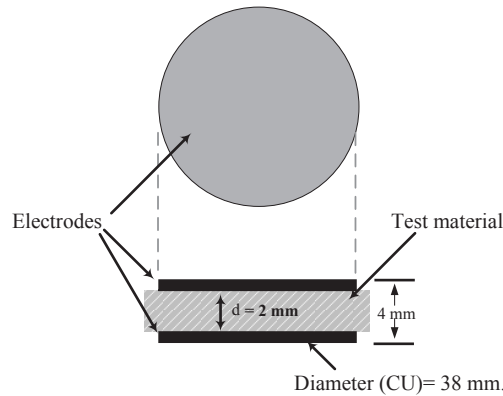


Figure 2. Rubber composite test structure

The test structure consists of two 38 mm diameter circular copper disks to form parallel plate electrodes with rubber composites in between. The disks are separated by a 2 mm thick rubber composite. The separation between the parallel plates is indicated as  $d$ , which is the thickness of the rubber composite. Based on the test structure, the measured data were calculated according to the RCL meter user's manual (Naidu & Kamaraju, 1996).

## RESULTS AND DISCUSSIONS

In this research, the agglomerate shapes of the rubber, as well as the fillers were studied. At first, the amount of filler dispersion can be investigated by an image analysis technique from the Dispergrader according to ASTM D7723. This equipment uses highlights casted by agglomerates presented to measure the dispersion of the fillers in mixed rubber (Alpha technologies, 2016).

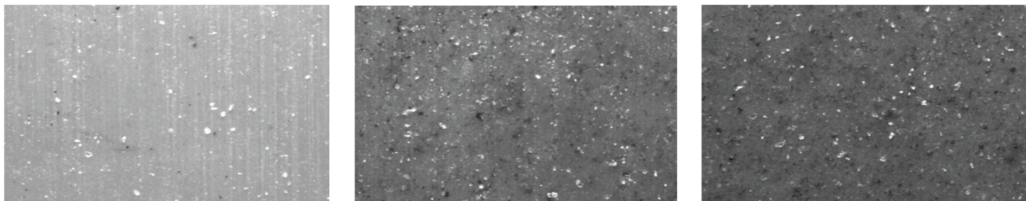


Figure 3. Dispergrader view of NR mixed with RWA 0, 5, 10 phr respectively

The sample images of NR/RWA at 0, 5, 10 parts per hundred of rubber (phr) are shown in Figure 1, when filler particles (white spots) and RWA (black spots) appear between the rubber matrix. The quantitative dispersions are 99.75%, 96.95%, 96.77% respectively. The filler dispersion of the rubber surface (Figure 2) was enlarged by the SEM micrographs for more details.

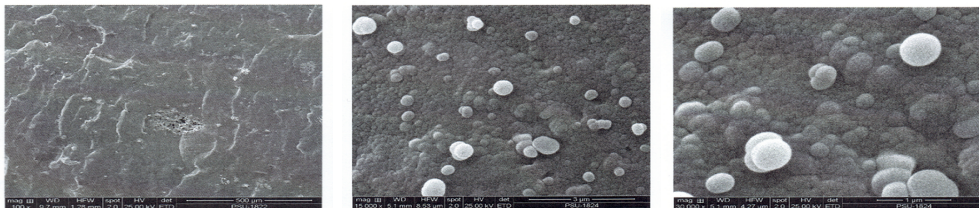


Figure 4. SEM of agglomerates for NR/RWA 10 phr

The purpose of SEM images is to show the agglomerate shapes of rubber and fillers when the RWA content is 10 phr. The images show that the structure of the mixtures is a combination between ellipsoidal and spherical shapes. Based on the RWA contents, the properties of the material depend significantly on the compound compositions. The effects of RWA additive in the compositions on the capacitive and impedance values are shown in Figure 5 and 6 respectively. All measured data were validated with the commonly use electrical insulator, Fr4 (dielectric permittivity  $<5.8 @1\text{MHz}$ ). The measured capacitance value is very high at the lowest frequency. For the frequencies below 300 Hz, the values decrease exponentially and the values are approximately constant at high frequencies. Therefore, the capacitance causes the absolute impedance reduction as shown in Figure 6. Please note that the  $C$  is rather high due to the limitation of the RLC meter at power line frequency (50 Hz).

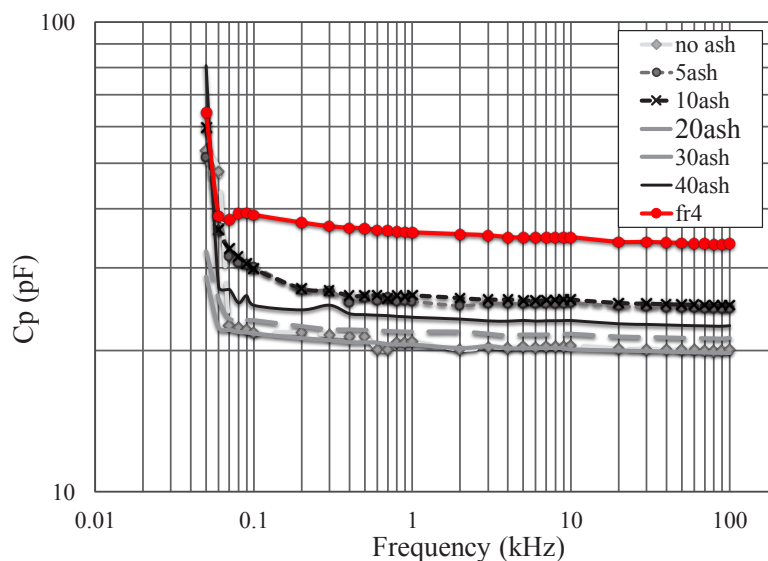


Figure 5. Parallel capacitance as a function of frequencies in logarithmic scale

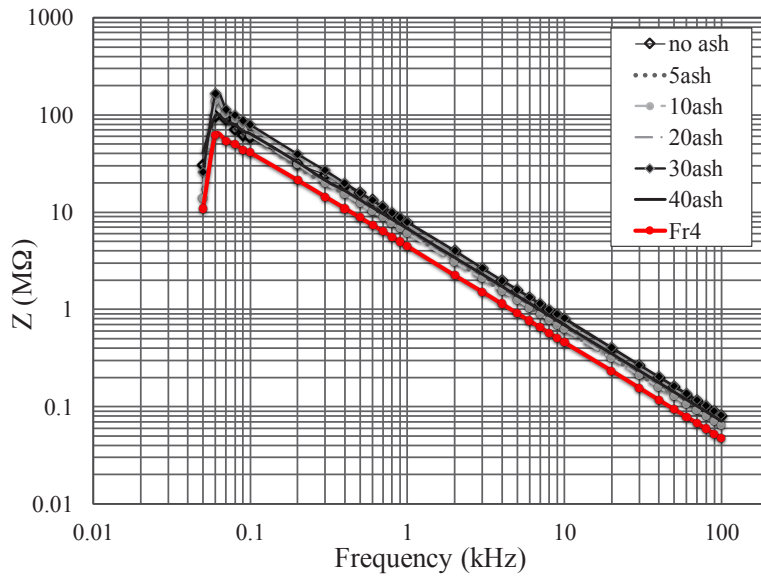


Figure 6. Absolute impedance as a function of frequencies in logarithmic scale

The calculated dielectric loss tangent values and conductivity of the materials are shown in Figures 7 and 8. It shows that dielectric loss tangent values decrease with increasing frequencies and move from a high loss tangent region at the lowest frequency towards a low loss tangent region as the frequency increases.

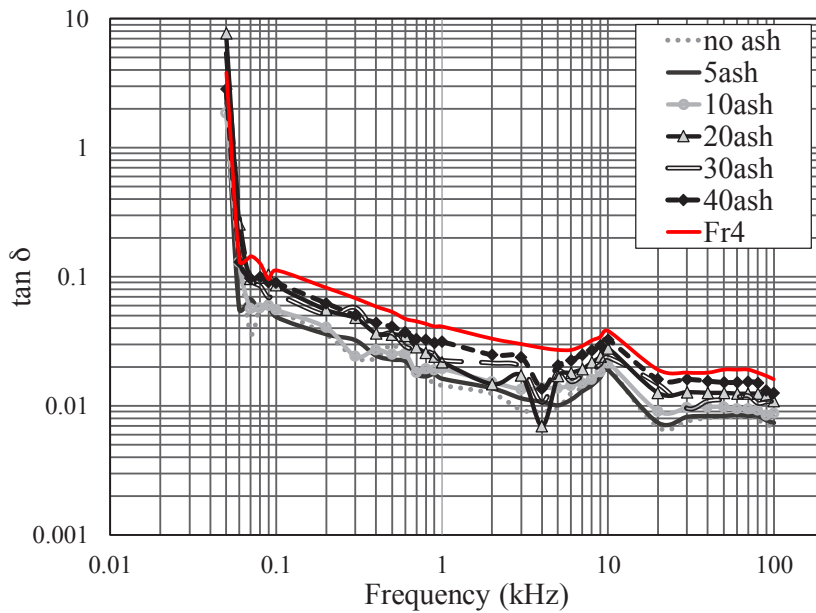


Figure 7. Dielectric loss tangent as a function of frequencies in logarithmic scale

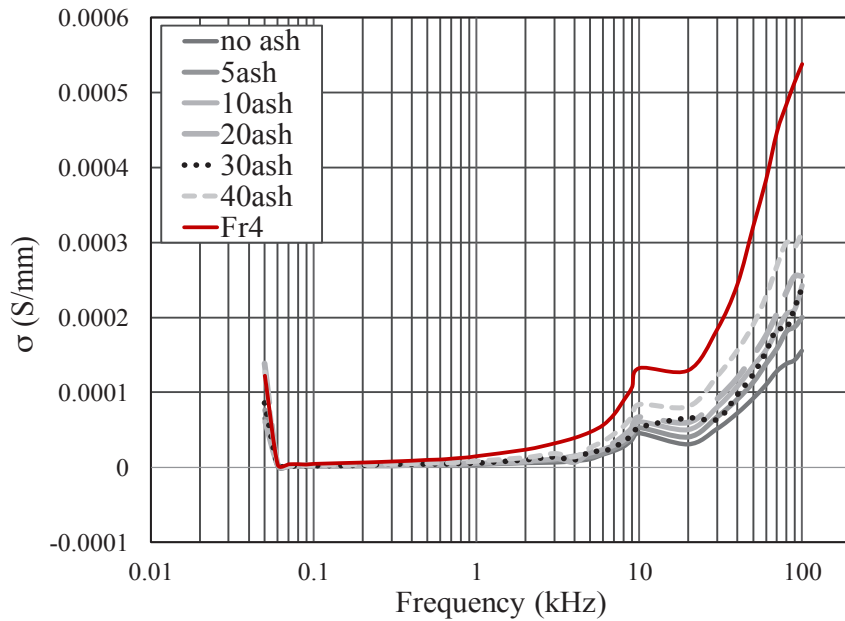


Figure 8. Conductivity as a function of frequencies in logarithmic scale

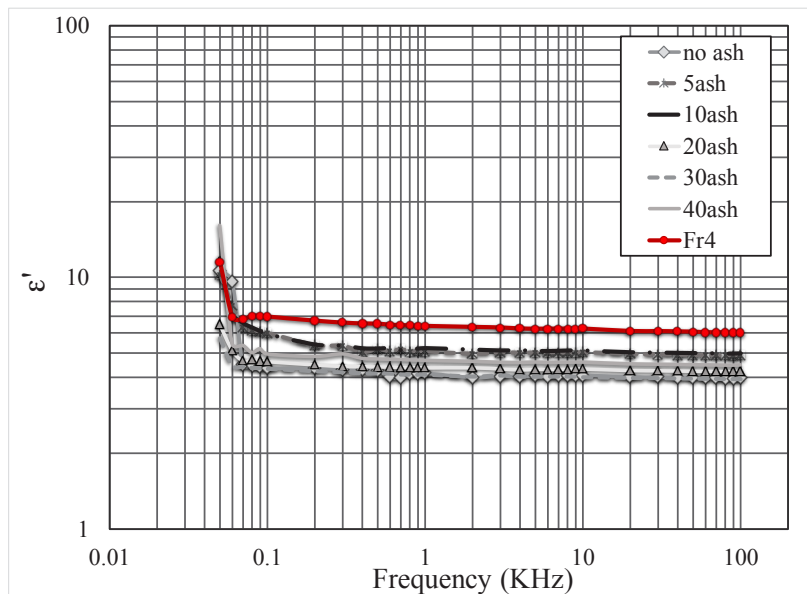


Figure 9. Calculated dielectric constant as a function of frequency

Figure 9 shows the dielectric constant which was calculated from the parallel plate capacitor as  $\epsilon' = C_{pd} / (\epsilon_0 A)$ , where  $d$  represents the thickness of the rubber sheet, the variable  $A$  is the area of the plate electrode and  $\epsilon_0$  is the permittivity of free space,  $8.854 \times 10^{-12}$  F/m.

The impedance which was generated from the equivalent circuits and measured data over the whole frequency range is shown in Figure 10. Calculated data were compared and shown as a good fit with measured data.

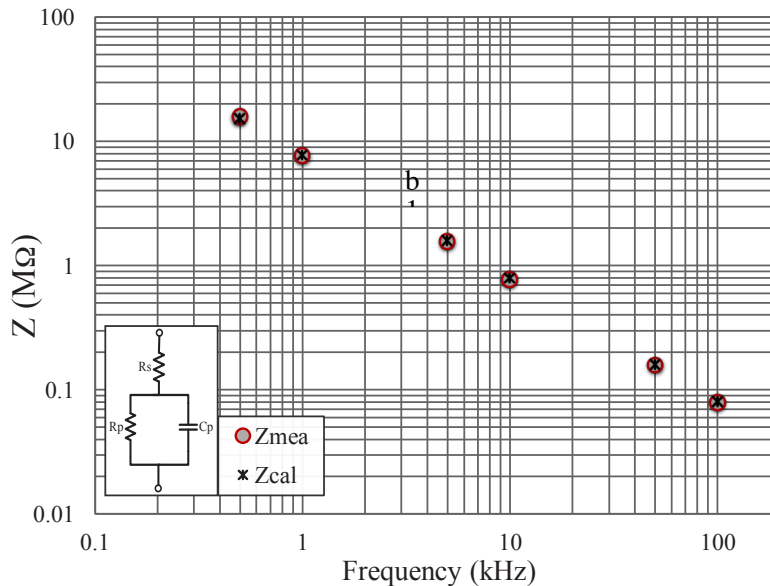


Figure 10. Measured and calculated impedance as a function of frequency

## CONCLUSION

This research presents electrical properties of NR/RWA composite at high frequencies. The natural rubber was formed with different RWA contents. The RWA and other blends influence the electrical properties of the rubber composite, especially when involving transient frequencies in the power line system. The materials exhibited dielectric constant of 4-5 and insulation loss or loss tangent ( $<0.07$ ) in the transient frequency ranges, which are comparable to the dielectric constant of FR4. The measured data agrees with the equivalent circuit which represents the microstructures morphologies of the rubber composite. Thus, these rubber composites can be a good candidate for power line insulators.

However, further tests must be carried out to avoid unexpected breakdown of insulators. These tests include the low-frequency tests, constant DC test, and impulse test. The results obtained from this study can be extended to predict and improve the processes of the rubber composite as a high-voltage insulator.

## ACKNOWLEDGEMENT

The authors would like to thank to the office of the Higher Education Research Promotion for supporting Miss. Salakjit Nilborworn under the CHE-PHD Scholarship Program, Prince of Songkla University.



## REFERENCES

- Alpha technologies. (2016). *disperGRADER aview*. Ohio USA: Alpha Technology.
- Chapman, M. A., Martinez, A., Sabir, E., Wang, K., & Liu, Y. (1999). Switching and fault caused transients in electric power systems. *IEEE Power Engineering Society 1999 Winter Meeting* (p. 1015–1021).
- HIOKI. (2006). *3522-50 LCR HiTESTER Instruction Manual*. Nagano, Japan: HIOKI E.E. Corporation.
- Naidu, M. S., & Kamaraju, V. (1996). *High voltage engineering* (2nd ed.). New York: McGraw-Hill.



## Unbalanced Self-Sensing Actuation Circuit Effects on Vibration Control in Piezoelectric Systems

Kiattisak Sengchuai<sup>1\*</sup>, Boworn Panyavoravaj<sup>2</sup> and Nattha Jindapetch<sup>1</sup>

<sup>1</sup>*Department of Electrical Engineering, Faculty of Engineering, Prince of Songkla University, Hat Yai, Songkhla 90112, Thailand*

<sup>2</sup>*Western Digital (Thailand) CO., LTD. Bang Pa-in, Phra Nakhon Si Ayutthaya 13160, Thailand*

### ABSTRACT

Self-sensing actuation (SSA) is a technique to use a single piezoelectric actuator as both an actuator and a sensor simultaneously. A self-sensing actuation circuit is used to extract a voltage generated by a piezoelectric actuator from a control voltage. However, the SSA circuit must be balanced to obtain an accurate sensing voltage. This paper describes an effect of an unbalanced SSA circuit on the sensing voltage output. The SSA circuit is connected to a piezoelectric system to apply the control voltage and measure the generated voltage simultaneously. The unbalanced SSA circuit is configured by designing an equivalent capacitance parameter to be not equal to a piezoelectric capacitance. The unbalanced SSA circuit effects is evaluated in terms of the step response and the frequency response. An experiment is conducted in an open-loop system and a closed-loop system. In the open-loop system, the sensing voltage is observed when the control voltage is applied to the piezoelectric actuator. In the closed-loop control system, a positive position feedback (PPF) controller is used for vibration control at a resonant frequency of the piezoelectric system. Experimental results show that the unbalanced SSA circuit causes the sensing voltage error when the amplitude of the control voltage is larger than the amplitude of the voltage generated from the piezoelectric actuator. In this case study, the unbalanced SSA circuit does not affect the vibration control at the resonant frequency in the closed-loop system. The vibration of the piezoelectric system at the resonant frequency is attenuated by 16 dB in both the balanced and the unbalanced SSA circuit conditions.

*Keywords:* Self-sensing actuation circuit, unbalanced SSA circuit, piezoelectric actuator, vibration control

### ARTICLE INFO

#### *Article history:*

Received: 24 August 2016

Accepted: 02 December 2016

#### *E-mail addresses:*

ak.kiattisak@hotmail.com (Kiattisak Sengchuai),  
boworn.panyavoravaj@wdcc.com (Boworn Panyavoravaj),  
nattha.s@psu.ac.th (Nattha Jindapetch)

\*Corresponding Author

### INTRODUCTION

Piezoelectric materials are widely employed in electromechanical systems to act as an actuator or a sensor. Advantages of

piezoelectric materials are light weight, high resolution, high bandwidth, fast response, and simple input/output. These piezoelectric materials can be used in many applications, such as vibration control, precision control, health monitoring, and so on. In piezoelectric actuator applications, the mechanical strain (or stress) is produced by applying the electric field (or voltage) to a piezoelectric actuator. In piezoelectric sensor applications, the electrical charge (or voltage) is produced by the mechanical strain (or stress) in a piezoelectric sensor.

Self-sensing actuation (SSA) is a technique to use a single piezoelectric actuator as both an actuator and a sensor simultaneously. The concept of the self-sensing actuation was initially proposed by Dosch, Inman, and Garcla (1992) which was based on a bridge circuit. The advantages of a self-sensing actuation is its lower cost for adding external sensors as well as the piezoelectric materials. In addition, the self-sensing actuation is utilised in different applications, such as a vibration control (Seki & Iwasaki, 2014), a position and force control (Rakotondrabe, Ivan, Khadraoui, Lutz, & Chaillet, 2015), and a mass detection (Faegh, Jalili, & Sridhar, 2013).

Self-sensing actuation circuit is used to separate the voltage generated by a piezoelectric actuator from the control voltage. This control voltage is applied to the same piezoelectric actuator. The SSA circuit was first proposed in Dosch et al. (1992) which was the bridge circuit. The bridge circuit SSA is used for a vibration suppression of a structure, such as a cantilever beam (Ji, Qiu, Wu, Cheng, & Ichchou, 2011), and an R/W head suspension in a hard disk drive (Yamada, Sasaki, & Nam, 2008). This SSA circuit is easy to understand and implement, but it attenuates the control voltage applied to a piezoelectric actuator by a parameter of the circuit. To solve the control voltage attenuation, an indirect-driven SSA (IDSSA) circuit was proposed in Hong, Memon, Wong, and Pang (2010) and Hong and Pang (2012). The IDSSA circuit was implemented in a piezoelectric micro-actuator in a dual-stage hard disk drive for a vibration control at critical resonant modes. However, it is difficult to make this IDSSA circuit balance.

In this paper, we study the effects of an unbalanced SSA circuit on the sensing voltage output of the SSA circuit. The effects of the unbalanced SSA circuit were evaluated in terms of the step response and the frequency response in both the open-loop control system and the closed-loop control system. This paper describes the self-sensing actuation circuit, the experimental setup, the experimental results, and the conclusion.

## SELF-SENSING ACTUATION CIRCUIT

The self-sensing actuation (SSA) circuit is used to extract the voltage generated by the piezoelectric actuator from the control voltage. The structure of the self-sensing actuation circuit was proposed in Hong et al. (2010) as shown in Figure 1. The piezoelectric actuator can be modelled as a series of a voltage source  $V_p$  and a piezoelectric capacitance  $C_p$ . The control voltage  $V_c$  is applied to the piezoelectric actuator via the non-inverting (+) input terminal of the upper operation amplifier. The voltage  $V_p$  generated from the piezoelectric actuator can be extracted by balancing the SSA circuit.

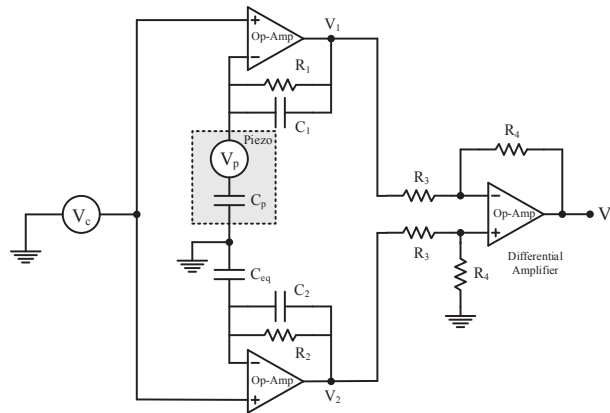


Figure 1. A self-sensing actuation circuit (Hong et al., 2010).

### SSA circuit model

The circuit in Figure 1 is composed of the piezoelectric actuator, four resistors ( $R_1, R_2, R_3, R_4$ ), three capacitors ( $C_{eq}, C_1, C_2$ ), and three operation amplifiers (Op-Amp). This circuit can be analysed by deriving the Laplace transform of  $V_1$  and  $V_2$  as expressed by (1) and (2) respectively.

$$V_1(s) = \left(1 + \frac{R_1 C_p s}{R_1 C_1 s + 1}\right) V_c(s) - \frac{R_1 C_p s}{R_1 C_1 s + 1} V_p(s) \quad (1)$$

$$V_2(s) = \left(1 + \frac{R_2 C_{eq} s}{R_2 C_2 s + 1}\right) V_c(s) \quad (2)$$

If  $R_3 = R_4$ , the sensing voltage  $V$  can be calculated as (3). Note that  $R_3$  and  $R_4$  only affect to the gain of the differential amplifier.

$$V_s(s) = \frac{R_4}{R_3} (V_2(s) - V_1(s)) = \left(\frac{R_2 C_{eq} s}{R_2 C_2 s + 1} - \frac{R_1 C_p s}{R_1 C_1 s + 1}\right) V_c(s) + \frac{R_1 C_p s}{R_1 C_1 s + 1} V_p(s) \quad (3)$$

If  $\omega_c \gg 1/R_1 C_1$  and  $\omega_c \gg 1/R_2 C_2$ , the sensing voltage  $V_s$  can be rewritten as (4), where  $\omega_c$  is the frequency of control voltage  $V_c$ .

$$V_s(s) = \left(\frac{C_{eq}}{C_2} - \frac{C_p}{C_1}\right) V_c(s) + \frac{C_p}{C_1} V_p(s) \quad (4)$$

The sensing voltage  $V_s$  is composed of the control voltage  $V_c$  term and the generated voltage  $V_p$  term. The voltage  $V_p$  generated from the piezoelectric actuator can be decoupled from the control voltage  $V_c$  by balancing the SSA circuit.

### Balanced SSA circuit

The SSA circuit is balanced by designing the parameters  $C_{eq} = C_p$  and  $C_1 = C_2$ . The sensing voltage  $V_s$  is proportional to the generated voltage  $V_p$  as defined in (5).

$$V_s(s) = \frac{C_p}{C_1} V_p(s) \quad (5)$$

### Unbalanced SSA circuit

The parameter  $C_{eq}$  in the SSA circuit cannot be designed to match the piezoelectric capacitance  $C_p$  because the actual piezoelectric capacitance is unknown. Therefore, the parameter  $C_{eq}$  can be defined as (6).

$$C_{eq} = C_{eq0} + \Delta C_{eq} \quad (6)$$

Assume that  $C_{eq0} = C_p$  and  $C_1 = C_2$ , the sensing voltage  $V_s$  can be rewritten as (7). Note that  $C_1$  and  $C_2$  can affect the unbalanced circuit. However, they can be easily designed to have the same value.

$$V_s(s) = \frac{\Delta C_{eq}}{C_2} V_c(s) + \frac{C_p}{C_1} V_p(s) \quad (7)$$

The sensing voltage  $V_s$  in (7) is composed of the control voltage  $V_c$  term and the generated voltage  $V_p$  term. The former term is close to zero when the SSA circuit is balanced. In contrast,  $V_s$  contains both terms when the SSA circuit is unbalanced. In this paper, the effect of the unbalanced circuit on the sensing voltage is studied through the real experiment because the transfer function model of the piezoelectric actuator is unknown.

## EXPERIMENTAL SETUP

The block diagram of the experiment is shown in Figure 2. The SSA circuit is implemented according to the SSA circuit in Figure 1. It is connected to the piezoelectric system to apply the control voltage to the piezoelectric actuator and measure the voltage generated from the piezoelectric actuator. The piezoelectric system is composed of two piezoelectric actuators. One piezoelectric actuator is used as the self-sensing actuator, and the other is used as a disturbance source of the system. The sensing voltage measured from the SSA circuit is fed to the MATLAB

Simulink in the computer via A/D of the NI PCI-6024E board. The control voltage generated by the MATLAB Simulink is applied to the piezoelectric actuator via D/A of the NI board. The sampling frequency of A/D and D/A is 50 kHz. The experimental setup is shown in Figure 3.

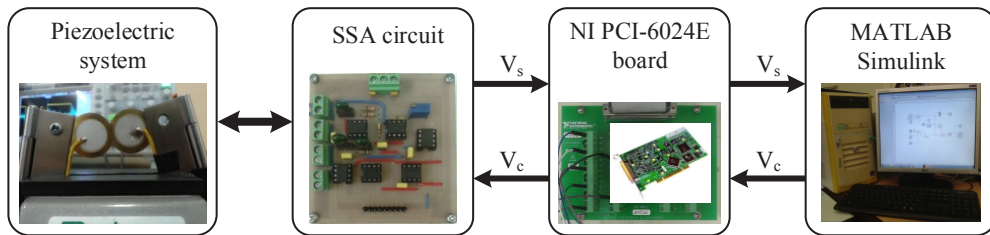


Figure 2. The experiment block diagram

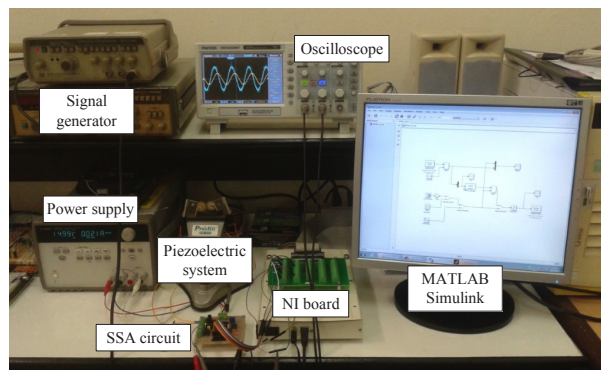


Figure 3. The experimental setup

The SSA circuit is implemented in a print circuit board (PCB). The operation amplifiers in the circuit are implemented by the LF351 op-amp chips which have high bandwidth and high input impedance. The values of parameters in the SSA circuit are listed in Table 1.

Table 1  
Circuit parameters

Circuit parameters	Value
$C_p$	26 nF
$C_1 = C_2$	22 nF
$R_1 = R_2$	10 M $\Omega$
$R_3 = R_4$	10 k $\Omega$

In the experiment, the step response and the frequency response is studied in both the open-loop control system and the closed-loop control system. In the step response test, the control voltage  $V_c$  is applied by the step signal with 1 V amplitude. In the frequency response test, the control voltage  $V_c$  is applied by the swept sine signal in the frequency range of 100 Hz to 10 kHz with 1 V amplitude. The frequency response  $V_s/V_c$  of the SSA circuit with the piezoelectric system is obtained by applying the control voltage  $V_c$  and measuring the sensing voltage  $V_s$ .

## EXPERIMENTAL RESULTS

The experiments are conducted in the open-loop system and the closed-loop system to study the effects of unbalanced SSA circuit on the sensing voltage output. The balanced SSA circuit is configured by designing the parameter  $C_{eq} \approx C_p$ . The unbalanced SSA circuit can be configured by designing the parameter  $C_{eq} \neq C_p$ . In this paper, the parameter  $C_{eq}$  is designed to 23 nF ( $C_{eq} < C_p$ ) and 29 nF ( $C_{eq} > C_p$ ).

### Open-loop system

The step responses of the open-loop system are shown in Figure 4. These responses demonstrate the effect of the balanced and unbalanced SSA circuit conditions on the sensing voltage  $V_s$ . The sensing voltage of the balanced SSA circuit demonstrates that the generated voltage  $V_p$  relates to the vibration of the piezoelectric system at the resonant frequency. In the unbalanced SSA circuit, the sensing voltage is composed of the control voltage and the generated voltage  $V_p$ . Obviously, this behaviour conforms to (7). The unbalanced SSA circuit causes the sensing voltage error because the amplitude of the generated voltage is smaller than the amplitude of the control voltage.

The frequency responses of the open-loop system with the balanced and unbalanced SSA circuit conditions are shown in Figure 5. The frequency response result shows the resonant frequency of the piezoelectric system at 2.9 kHz. The frequency response of the balanced and the unbalanced SSA circuit conditions are the same at the resonant frequency because

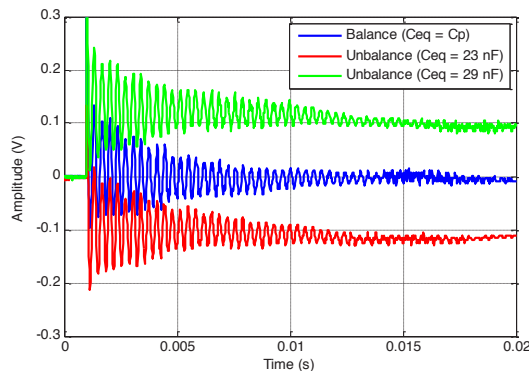


Figure 4. The step responses of the open-loop system



### Unbalanced Self-Sensing Actuation Circuit Effects

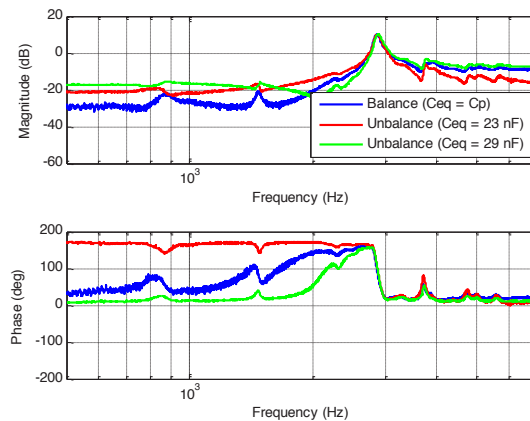


Figure 5. The frequency responses of the open-loop system

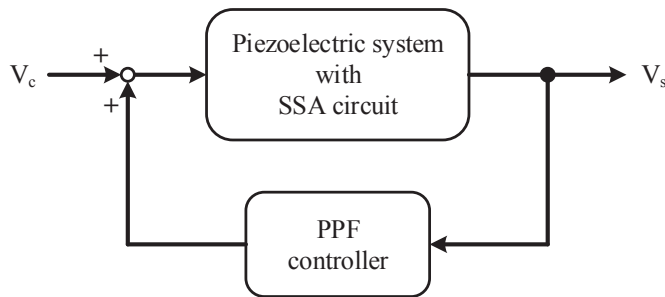


Figure 6. The closed-loop control system block diagram.

the amplitude of the generated voltage is larger than the amplitude of the control voltage. However, the unbalanced SSA circuit effects can be observed at the other frequencies because the piezoelectric system slightly responds and the amplitude of the generated voltage is smaller than the amplitude of the control voltage.

### Closed-loop system

The block diagram of the closed-loop control system for the vibration control at the resonant frequency is shown in Figure 6. The positive position feedback (PPF) controller is used to control the vibration of the piezoelectric system. The sensing voltage  $V_s$  measured from the SSA circuit is fed back to the PPF controller. In this paper, the transfer function of the PPF controller defined in Sasaki, Inoue, and Yamada (2012) is used as shown in (8).

$$G_c(s) = K \frac{\omega^2}{s^2 + 2\zeta\omega s + \omega^2} \quad (8)$$

where  $\omega$  is the natural frequency of the controller,  $\zeta$  is the damping ratio of the controller, and  $K$  is the gain of the controller. In this experiment, the natural frequency is 2.9 kHz ( $\omega = 2900$ ), the damping ratio is 0.2 ( $\zeta = 0.2$ ), and the gain is -0.7 ( $K = -0.7$ ). The PPF controller is implemented on the MATLAB Simulink.

The step responses of the open-loop system and the closed-loop system with the balanced and unbalanced SSA circuit conditions are shown in Figure 7. These responses show the effectiveness of the vibration control by using the sensing voltage  $V_s$  measured from the SSA circuit and fed back to the PPF controller. The vibration of the piezoelectric system can be suppressed in the closed-loop control system. However, the sensing voltage output of the SSA circuit is effected from the unbalanced SSA circuit because the amplitude of the control voltage applied by the step signal is larger than the amplitude of the voltage generated by the piezoelectric actuator as shown in Figure 7(b) and (c).

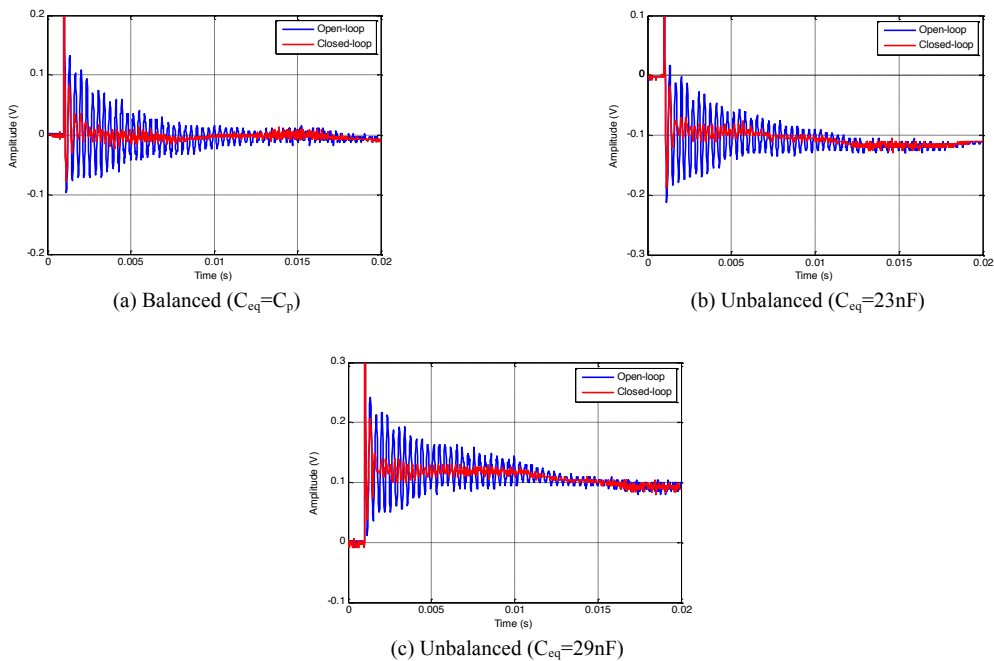


Figure 7. The step responses of the closed-loop system

The frequency responses of the closed-loop control system with the balanced and unbalanced SSA circuit conditions are shown in Figure 8. The vibration of the piezoelectric system is attenuated about 16 dB in both the balanced and the unbalanced SSA circuit conditions at the resonant frequency. In this case study, the unbalanced SSA circuit does not affect to the closed-loop control system because the former (unbalanced SSA circuit) slightly affects the sensing voltage fed back to the controller.

### Unbalanced Self-Sensing Actuation Circuit Effects

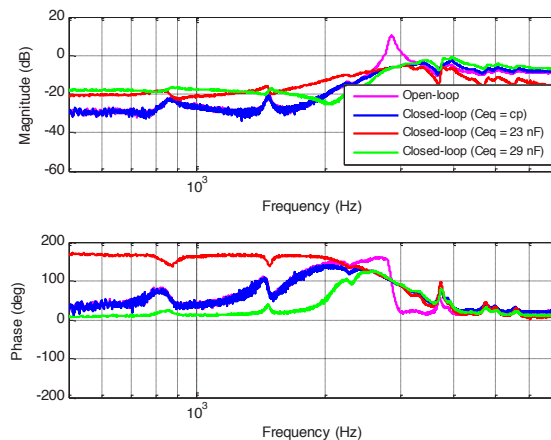


Figure 8. The frequency responses of the closed-loop system.

## CONCLUSION

This paper presents a study of the self-sensing actuation circuit with the piezoelectric system when the circuit is balanced and unbalanced. The unbalanced SSA circuit affects the sensing voltage output of the SSA circuit when the amplitude of the control voltage is larger than the amplitude of the voltage generated from the piezoelectric actuator. In this case study, the unbalanced SSA circuit does not affect the closed-loop control system at the resonant frequency. The vibration of the piezoelectric system at the resonant frequency is attenuated by 16 dB in both the balanced and the unbalanced SSA circuit conditions. The self-sensing actuation circuit can be used with the single piezoelectric actuator to act as both the actuator and the sensor simultaneously for the vibration control in the piezoelectric system. In the future work, the unbalanced SSA circuit effects will be studied by applying the piezoelectric micro-actuator.

## ACKNOWLEDGEMENT

Funds for this research came from Thailand Research Fund (TRF) and Western Digital (Thailand) Company Limited under the Research and Researchers for Industries (RRI) project No. PHD57I0051.

## REFERENCES

- Dosch, J. J., Inman, D. J., & Garcla, E. (1992). A Self-Sensing Piezoelectric Actuator for Collocated Control. *Journal of Intelligent Material Systems and Structures*, 3(1), 166-185.
- Faegh, S., Jalili, N., & Sridhar, S. (2013). A Self-Sensing Piezoelectric MicroCantilever Biosensor for Detection of Ultrasmall Adsorbed Masses: Theory and Experiments. *Sensors*, 13(5), 6089-6108.
- Hong, F., & Pang, C.K. (2012). Robust vibration control at critical resonant modes using indirect-driven self-sensing actuation in mechatronic systems. *ISA Transactions*, 51, 834-840.

- Hong, F., Memon, A.M., Wong, W.E., & Pang, C.K. (2010). Indirect-Driven Self-Sensing Actuation for Dual-Stage HDDs with Improved Robustness. *ASME Information Storage and Processing Systems Conference* (pp. 141–143). Santa Clara, CA, USA.
- Ji, H. L., Qiu, J. H., Wu, Y. P., Cheng, J., & Ichchou, M. N. (2011). Novel Approach of Self-Sensing Actuation for Active Vibration Control. *Journal of Intelligent Material Systems and Structures*, 22(5), 449-459.
- Rakotondrabe, M., Ivan, I.A., Khadraoui, S., Lutz, P., & Chaillet, N. (2015). Simultaneous Displacement/Force Self-Sensing in Piezoelectric Actuators and Applications to Robust Control. *IEEE/ASME Transactions on Mechatronics*, 20(2), 519–531.
- Sasaki, M., Inoue, Y., & Yamada, H. (2012). Active Vibration Control of a Microactuator for the Hard Disk Drive Using Self-Sensing Actuation. *Smart Materials Research*.
- Seki, K., & Iwasaki, M. (2014). Improvement of Bending Vibration Suppression Performance for Galvano Mirror by Self-Sensing Actuation. *IEEJ Journal of Industry Applications*, 3(1), 10–17.
- Yamada, H., Sasaki, M., & Nam, Y. (2008). Active Vibration Control of a Micro-Actuator for Hard Disk Drives using Self-Sensing Actuator. *Journal of Intelligent Material Systems and Structures*, 19, 113-123.



## Parametric Tracking Across Multiple Cameras

Patrick Sebastian<sup>1\*</sup>, Yap Vooi Voon<sup>2</sup> and Richard Comley<sup>3</sup>

<sup>1</sup>*Electrical and Electronic Engineering Department, Universiti Teknologi PETRONAS, 32610 Bandar Seri Iskandar, Perak, Malaysia*

<sup>2</sup>*Department of Electronic Engineering, Faculty of Engineering and Green Technology, Universiti Tunku Abdul Rahman, Kampar, Perak, Malaysia*

<sup>3</sup>*Department of Engineering and Information Science, Middlesex University, The Boroughs, Hendon, London NW4 4BT, United Kingdom*

### ABSTRACT

This paper presents a tracking method based on parameters between colour blobs. The colour blobs are obtained from segmenting the overall target into multiple colour regions. The colour regions are segmented using EM method that determines the normal colour distributions from the overall colour pixel distribution. After segmenting into different regions on the different colour layers, parameters can be generated between colour regions of interest. In this instance, the colour regions of interest are the top and bottom colour regions. The parameters that are generated from these colour regions are the vector magnitude, vector angle and the value difference between colour regions. These parameters are used as a means for tracking targets of interest. These parameters are used for tracking the target of interest across an array of cameras which in this instance are three cameras. Three cameras have been set up with different background and foreground conditions. The summarised results of tracking targets across three cameras have shown that the consistency of colour regions across different cameras and different background settings provided sufficient parameters for targets to be tracked consistently. Example of tracking performance across three cameras were 0.88, 0.67 and 0.55. The remaining tracking performances across three cameras are shown in Table 2. The tracking performance indicate that the parameters between colour regions were able to be used for tracking a target across different cameras with different background scenarios. Based on results obtained, parameters between segmented colour regions have indicated robustness in tracking target of interest across three cameras.

### ARTICLE INFO

#### Article history:

Received: 24 August 2016

Accepted: 02 December 2016

#### E-mail addresses:

patrick\_sebastian@petronas.com.my;

patrick\_sebastian@utp.edu.my (Patrick Sebastian),

yapvv@utar.edu.my (Yap Vooi Voon),

r.comley@mdx.ac.uk (Richard Comley)

\*Corresponding Author

*Keywords:* Blob tracking, parametric tracking, multiple camera, tracking

### INTRODUCTION

Surveillance is an act of monitoring behaviour or activities of a person or a group of people

in an area of interest. In this instance, video surveillance is the utilisation of video cameras to obtain video or visual imagery to observe areas of interest for the purposes of control, recognition and monitoring activities. Government, law enforcement and security organisations monitor human activities for the purpose of maintaining control, recognising and monitoring threats in a large crowd of people (Bredereck et al., 2012; Hommel et al., 2012; Wang et al., 2009). Video surveillance cameras are typically connected to a recording device or recording network. The video captured is usually observed or watched live or through a recording by an operator. A single operator would be able to observe all activities within the view field of a single camera. In surveillance of a large area, multiple video cameras provide complete coverage of the area of interest. In this instance, the operator observing the cameras would have a large number of monitors to observe and this would be difficult for a single operator to observe and track all activities from all cameras at the same time. It is difficult for a human operator to monitor multiple surveillance screens and thus, computer systems can intelligently track targets across multiple cameras in a large-scale surveillance system.

## **BACKGROUND**

Tracking of targets in a surveillance system is based on a number of parameters such as area (Park & Aggarwal, 2002), colour (Zhu, 2009), trajectory and velocity. Apart from the general parameters mentioned earlier for tracking a target, targets can be tracked based on features such as edges, lines, corners (Trucco & Plakas, 2006), limbs and heads (Siebel & Maybank, 2002). With the wide availability of a number of parameters and features, tracking methods can vary from simple tracking methods to complex tracking methods.

### **Colour Space**

The utilisation of different colour spaces which range from RGB, HSV and YCbCr colour spaces have different effects in tracking targets of interest. From available colour spaces, RGB colour space has been deemed the not preferred colour space for tracking as the brightness information is embedded in the respective layers of the RGB colour space. It was found from different studies that colour spaces with chrominance information on separate layers from brightness information such as HSV and YCbCr colour spaces have better tracking capabilities (Chippendale, 2006). Chrominance information such as HS and CbCr layers in the HSV and YCbCr colour space respectively could provide sufficient information to be used for tracking (Chippendale, 2006).

### **Blob Modelling**

Foreground and background views are separated in a video scene by detecting blobs. From detected blobs, a number of blob parameters can be extracted such as blob size, motion, vector and centroid (Trucco & Plakas, 2006). Targets can be tracked by utilising the detected blob (Atsushi et al., 2002) or portions of the blob such as the head (Yan & Forsyth, 2005).

The target of interest in this scenario would be the tracking of a whole person which would lead tracking of the whole blob (Atsushi et al., 2002). For parametric tracking, a single blob can be segmented into separate blobs based on colours of the regions (Wang et al., 2014). Single blobs can be segmented into multiple blobs using methods such as watershed segmentation (Gonzalez et al., 2004) and mean shift segmentation (Yunji et al., 2014). When the single blob is segmented into separate blobs, the centroids (Ali et al., 2006) of each blob can be used to generate the parameters for tracking a multi blob target which is illustrated in Figure 6.

## TRACKING METHODOLOGY

Tracking as used in this paper is based on the parameters that exist between colour regions of each target; colour region segmentation is the first step. Colour region segmentation is also dependent on the colour space that is used. The YCbCr colour space was selected based on better tracking performance compared with RGB and grayscale colour spaces that had been tested in different tracking methods (Sebastian et al., 2010).

Segmenting target of interest into multiple colour regions would begin with the extraction of colour information from the overall colour pixel distribution. Colour region information can be separated into different normal distributions using EM method (Sebastian et al., 2012; Yiming & Guirong, 2014). Each normal distribution parameters are used to generate different colour regions within the overall target blob region. A person can then be modelled or represented as a collection of coloured regions. Different coloured blobs can be used to denote the different portions of a person such as the head, face, torso and lower limbs (Park & Aggarwal, 2002). An example of segmentation is illustrated in the following figures. Figure 1 shows a snapshot input image while Figure 2 and Figure 3 illustrate the pixel distributions of the Cb and Cr layers for the person that is being tracked respectively.

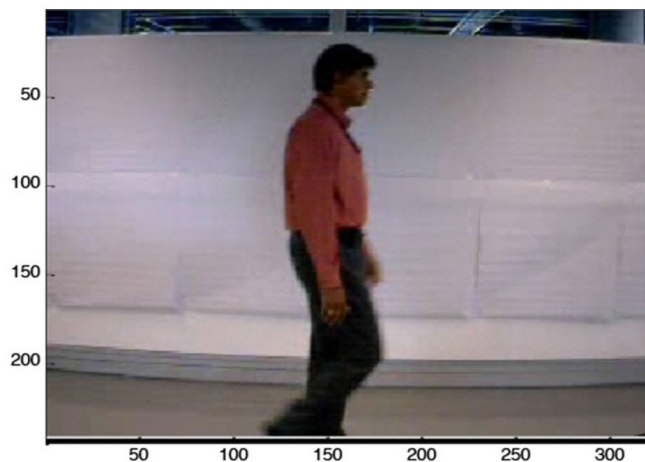


Figure 1. Sample Input Image

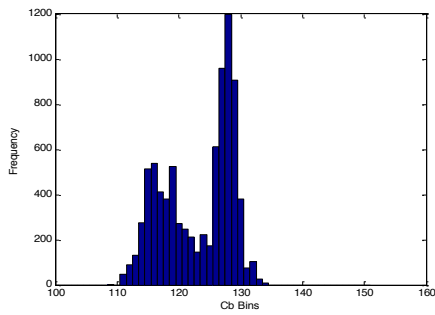


Figure 2. Cb Layer

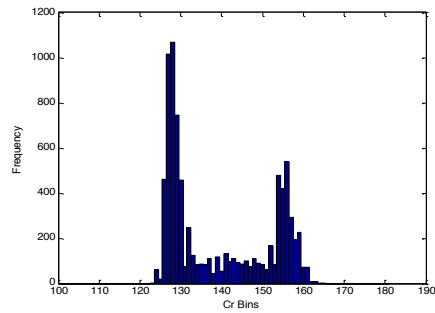


Figure 3. Cr Layer

Based on pixel distributions in Figure 2 and Figure 3 it can be seen that there are multiple peaks in the pixel distribution indicating different colour values and regions. Using the EM method to segment data into different normal distributions, as seen in Figure 4 and Figure 5, for layers Cb and Cr respectively, each detected normal distribution would have its own mean and standard deviation. Each detected distribution parameters would be used to segment the input image into different coloured blobs or regions. The result of the segmentation can be seen in Figure 6 where the centroids of each segmented regions are indicated as crosshairs. The red and green crosshairs are indicators of the centroids from regions detected on the Cb and Cr layers respectively.

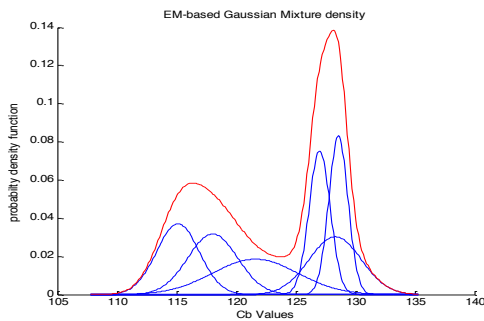


Figure 4. EM Gaussian Mixture on Cb Layer

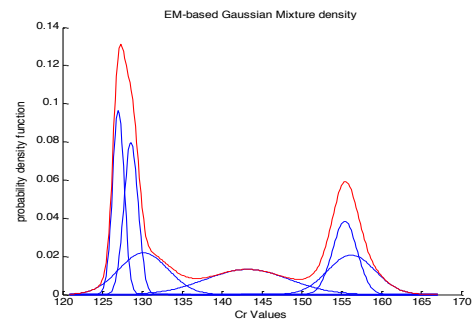


Figure 5. EM Gaussian Mixture on Cr Layer



Figure 6. EM Sample Image Detected Centroids



The next step in tracking target of interest would be the extraction of parameters between colour regions of interest which in this case would be the top and bottom colour regions as reference parameters. The parameters to be used for tracking are the magnitude and angle of the vector between the colour regions. An additional parameter is the difference of the colour region mean values (Sebastian et al., 2012). Combination of data from the vector magnitude, vector angle and colour difference would generate a set of parameters that should be unique for each target of interest. An illustration of extracted data and clustering can be seen in Figures 7 and 8.

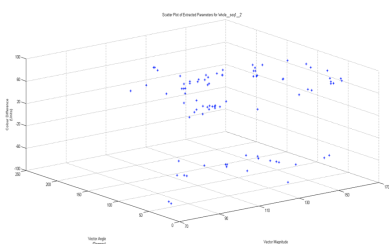


Figure 7. Scatter Plot of Extracted Data

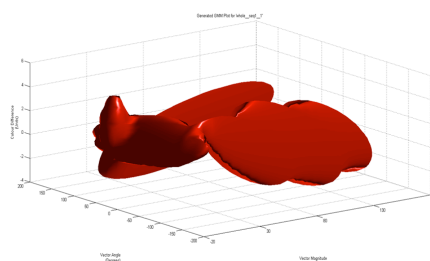


Figure 8. Data clusters of Extracted Data with Parameters

The tracking process is executed by comparing extracted or input parameters against reference parameters. A track is considered to be successful when the input parameters are statistically similar to the reference parameters. Table 1 shows the tracking performance of different tracking methodologies in the YCbCr colour space.

Table 1  
Summarised Compared Tracking Methodology Tracking Data

Input Video	Histogram Similarity Comparison						
	Normalised Cross Correlation	Histogram Intersection	Euclidean Intersection	Chi-Squared 1	Chi-Squared 2	Kullbeck-Leibler	Parameteric Tracking
whole_seq1_1	0.00	0.29	0.19	0.31	0.25	0.27	0.92
whole_seq1_2	0.00	0.24	0.00	0.29	0.29	0.29	0.90
whole_seq1_3	0.00	0.20	0.00	0.15	0.16	0.12	0.95
whole_seq1_4	0.00	0.15	0.20	0.28	0.33	0.35	0.90
whole_seq1_5	0.00	0.20	0.00	0.19	0.28	0.19	0.94

Table 1 compares the tracking performances between different tracking methods. The same set of videos were used in determining the tracking performance for different methodologies investigated. Tracking performances from different tracking methods starting from normalised cross correlation and histogram comparison method had led to the development of parametric



Figure 9. Uneven Illumination



Figure 10. Uneven background



Figure 11. Noisy Environment

tracking method which were done on a single camera. The scores are determined by obtaining the ratio of the detection count of the target against the total count of the target appearance in the camera view field.

Multiple camera tracking setup was done with 3 web cameras with non-overlapping view fields. The overall camera setup was done in an indoor environment with different backgrounds. The cameras had a resolution of 320x240 pixels. Sample images of different background view fields captured by the different cameras are seen in the Figures 9, 10 and 11 where each figure illustrates the different background setup in each camera view field. The different background setup was used to evaluate the utilisation of same set of parameters between blobs as a method for tracking a target across the three cameras.

## RESULTS

In measuring tracking capability or performance, a tracking metric known as track detection rate (TDR) (Ellis, 2002) was used. The tracking performance is determined by statistically comparing the input image parameters against the compiled parameters of the target of interest. A sample of raw tracking results can be seen in Table 2 which compiles the track detection rate in a confusion matrix. In this instance, the confusion matrix lists the tracking results of each input video against the tracking parameter of each target of interest

Table 2  
Sample TDR of Camera 1

Input Video	Reference								
	whole_seq2_1	whole_seq2_2	whole_seq2_3	whole_seq2_4	whole_seq2_5	whole_seq2_6	whole_seq2_7	whole_seq2_8	whole_seq2_9
whole_seq2_1	0.70	0.44	0.36	0.17	0.60	0.06	0.73	0.33	0.20
whole_seq2_2	0.87	0.97	0.87	0.38	0.69	0.11	0.90	0.84	0.34
whole_seq2_3	0.95	0.87	0.96	0.68	0.83	0.60	0.94	0.86	0.57
whole_seq2_4	1.00	1.00	1.00	0.92	0.91	0.29	0.96	0.96	0.53
whole_seq2_5	0.17	0.13	0.13	0.03	0.26	0.00	0.23	0.08	0.06
whole_seq2_6	0.78	0.92	0.77	0.56	0.62	0.55	0.83	0.84	0.23
whole_seq2_7	0.65	0.61	0.57	0.23	0.71	0.04	0.80	0.42	0.10
whole_seq2_8	0.89	0.97	0.92	0.44	0.73	0.21	0.92	0.97	0.48
whole_seq2_9	0.97	1.00	0.99	0.64	0.89	0.35	0.88	0.97	0.96

Comparing the input video against its own reference parameter in Table 2 should show the highest tracking result if the tracking parameters were the correct set of parameters which are highlighted. Compilation of the raw TDR data tracking performance can be seen in Table 3. The values that are recorded in the tables should range from 0 to 1.0 which indicates a correct tracking performance of 0% to 100% correct tracking. Table 3 shows the track results of targets that have successful track across three cameras. Empty cells in Table 3 indicate that correct tracking was not achieved across 3 cameras. The cells with tracking data rates indicate that the target was correctly tracked and had the highest tracking rate. Table 3 displays the number of input videos used for determining tracking performance, number of EM segmentations which indicate the number of colour regions that each tracked target is segmented into and the classification of data that is based on raw data tracking or outlier data removed tracking. Nine videos were used. The number of EM segments ranged from 3 to 6. Tracking was also done based on raw data and outlier removed data. Raw data indicates that all track data points are used in determining track performance whereas the outlier removed data set removes the outlier data track points from the calculation of track performance.

Table 3  
Compiled TDR across 3 cameras

Ref Video	Number of Segmentation and Cameras											
	out6			out5			out4			out3		
Input Video	Cam1	Cam2	Cam3	Cam1	Cam2	Cam3	Cam1	Cam2	Cam3	Cam1	Cam2	Cam3
whole_seq2_1				0.76	0.7	0.82						
whole_seq2_2												
whole_seq2_3				0.89	0.61	0.57	0.94	0.62	0.62	0.64	0.61	0.37
whole_seq2_4	0.87	0.66	0.68	0.92	0.44	0.54				0.19	0.14	0.15
whole_seq2_5												
whole_seq2_6				0.71	0.59	0.26						
whole_seq2_7												
whole_seq2_8												
whole_seq2_9	0.88	0.67	0.55				0.84	0.77	0.57			

Ref Video	Number of Segmentation and Cameras											
	raw6			raw5			raw4			raw3		
Input Video	Cam1	Cam2	Cam3	Cam1	Cam2	Cam3	Cam1	Cam2	Cam3	Cam1	Cam2	Cam3
whole_seq2_1				0.76	0.7	0.78						
whole_seq2_2												
whole_seq2_3				0.92	0.69	0.59						
whole_seq2_4				0.93	0.58	0.57	0.84	0.16	0.23	0.20	0.17	0.10
whole_seq2_5												
whole_seq2_6												
whole_seq2_7				0.83	0.82	0.76						
whole_seq2_8												
whole_seq2_9	0.96	0.74	0.60				0.88	0.83	0.63	0.68	0.42	0.40

Table 3 shows random input videos labelled 'whole\_seq2\_1', 'whole\_seq2\_3', 'whole\_seq2\_4', 'whole\_seq2\_6', 'whole\_seq2\_7' and 'whole\_seq2\_9' had parameters that enabled the specific targets to be tracked across 3 cameras. Where the tracking parameters used in this instance are the combination vector magnitude, vector angle and colour difference that make each target have their own unique combination for tracking across the 3 cameras. The video sequences of 'whole\_seq2\_2', 'whole\_seq2\_5' and 'whole\_seq2\_8' did not generate the necessary tracking parameters for successful tracking across 3 cameras. Video sequence 'whole\_seq2\_5' could not be segmented into different colour regions as that particular target had only one colour for the whole target and thus this particular target could not generate the necessary parameters between colour regions for tracking. Video sequence 'whole\_seq2\_2' and 'whole\_seq2\_8' had the colour regions segmented and detected only on one colour layer. The utilization of parameters between colour regions detected on same colour layer did not give accurate tracking of targets (Sebastian et al., 2012). Apart from the video sequences that did not have any tracking results across three cameras, the other video sequences have tracking results that indicated that the targets are tracked across the three cameras. The tracking performance across three cameras are dependent on the number of colour region that the target of interest is segmented into.

## CONCLUSION

This paper contributes in the area of target tracking in a video surveillance system where tracking the target of interest is based on the parameters between colour regions. The parameters used in tracking the target of interest were vector magnitude, vector angle and colour difference between colour regions. The tracking performance of the parametric tracking was initially compared against other tracking methods such as normalised cross correlation and histogram comparison methods. The results had shown that the parametric tracking had better tracking performance. In the initial evaluation, the targets of interest were tracked on a single camera and the results indicated that parametric track had significantly better tracking performance compared with other tracking methods. The parametric tracking methodology was then extended to tracking a target across an array of cameras. The tracking performance across an array of cameras had shown that the target of interest could be tracked based on the parameters between colour regions. The tracking performance had indicated that the consistent nature of the target colour was one of the primary reasons that the target of interest was able to be tracked across an array of cameras. The results obtained from this paper is an extension of a previous paper that determined that tracking a target was possible by utilising the parameters between the top and bottom colour regions of a target.

## REFERENCES

- Ali, M. A., Indupalli, S., & Boufama, B. (2006, June). *Tracking multiple people for video surveillance*. In First International Workshop on Video Processing for Security, Quebec City, Canada.
- Atsushi, N., Hirokazu, K., Shinsaku, H., & Seiji, I. (2002). Tracking multiple people using distributed vision systems. In *Robotics and Automation, 2002. Proceedings. ICRA'02. IEEE International Conference on* (Vol. 3, pp. 2974-2981). IEEE.

- Bredereck, M., Jiang, X., Körner, M., & Denzler, J. (2012, October). Data association for multi-object tracking-by-detection in multi-camera networks. In *Distributed Smart Cameras (ICDSC), 2012 Sixth International Conference on* (pp. 1-6). IEEE.
- Chippendale, P. (2006). Towards Automatic Body Language Annotation. In *7th International Conference on Automatic Face and Gesture Recognition 2006 (FGR 2006)*.
- Ellis, T. (2002). *Performance Metrics and Methods for Tracking in Surveillance*. Third IEEE International Workshop on Performance Evaluation of Tracking and Surveillance, Copenhagen, Denmark.
- Gonzalez, W., & Woods, R. E. (2004). *Eddins, Digital Image Processing Using MATLAB*. Third New Jersey: Prentice Hall.
- Hommel, S., Grimm, M. A., Voges, V., Handmann, U., & Weigmann, U. (2012, November). An intelligent system architecture for multi-camera human tracking at airports. In *Computational Intelligence and Informatics (CINTI), 2012 IEEE 13th International Symposium on* (pp. 175-180). IEEE.
- Park, S. and J. K. Aggarwal (2002). *Segmentation and Tracking of interacting human body parts under occlusion and shadowing*. Workshop on Motion and Video Computing 2002.
- Sebastian, P., Voon, Y. V., & Comley, R. (2010). Colour space effect on tracking in video surveillance. *International Journal on Electrical Engineering and Informatics*, 2(4), 298-312.
- Sebastian, P., Voon, Y. V., & Comley, R. (2012, December). Parametric tracking of multiple segmented regions. In *Computer Applications and Industrial Electronics (ISCAIE), 2012 IEEE Symposium on* (pp. 185-189). IEEE.
- Siebel, N. T. and S. Maybank (2002). Fusion of Multiple Tracking Algorithms for Robust People Tracking. In *Proceedings of the 7th European Conference on Computer Vision (ECCV 2002)*.
- Trucco, E. and K. Plakas (2006). Video Tracking: A Concise Survey. *IEEE Journal of Oceanic Engineering*, 31(2), 520-529.
- Wang, H., Liu, C., Zhang, X., & Li, Q. (2009, October). Multi-camera tracking based on information fusion in video surveillance. In *Image and Signal Processing, 2009. CISP'09. 2nd International Congress on* (pp. 1-5). IEEE.
- Wang, H., Sang, N., & Yan, Y. (2014, August). Real-time tracking combined with object segmentation. In *Pattern Recognition (ICPR), 2014 22nd International Conference on* (pp. 4098-4103). IEEE.
- Yan, W., & Forsyth, D. A. (2005, January). Learning the behavior of users in a public space through video tracking. In *Application of Computer Vision, 2005. WACV/MOTIONS'05 Volume 1. Seventh IEEE Workshops on* (Vol. 1, pp. 370-377). IEEE.
- Qian, Y., & Guirong, W. (2014, August). Lung nodule segmentation using EM algorithm. In *Intelligent Human-Machine Systems and Cybernetics (IHMSC), 2014 Sixth International Conference on* (Vol. 1, pp. 20-23). IEEE.
- Zhao, Y., Zhang, B., & Zhang, X. (2014, July). Meanshift blob tracking with target model adaptive update. In *Control Conference (CCC), 2014 33rd Chinese* (pp. 4831-4835). IEEE.
- Zhu, Y. F. (2009, December). Background subtraction and color clustering based moving objects detection. In *2009 International Conference on Information Engineering and Computer Science* (pp. 1-5). IEEE.



## **Optimal Location and Size of Distributed Generation to Reduce Power Losses based on Differential Evolution Technique**

**Noor Izzri Abdul Wahab<sup>1\*</sup>, Ahmed Sahib Hammadi<sup>1</sup> and  
Mohammad Lutfi Othman<sup>1</sup>**

*<sup>1</sup>Department of Electrical and Electronic Engineering, Faculty of Engineering, Universiti Putra Malaysia, 43400 UPM, Serdang, Selangor, Malaysia*

---

### **ABSTRACT**

An electric power system generate electricity to meet demands. Distributed Generation (DG) allows electricity to be generated in a small capacity where the customer is located. In this paper, multi-objective functions based on the indices of system performance are formulated and used to determine the best location. The Differential Evolution technique (DE) has been employed to calculate optimal sizing for each location. Unity power factor DG model have been studied in this work and the problems solved with one DG unit. IEEE 14 bus has been used as a test system.

*Keywords:* Distributed Generation (DG), Differential Evolution (DE), multi-objective function (MOF)

---

### **INTRODUCTION**

Major changes in technology, environmental policies and expansion of power markets have enabled the distribution of electricity in a small capacity to power networks (Karimyan, Gharehpetian, Abedi, & Gavili, 2014). The new technology utilises both unconventional and conventional sources of energy. Often, it may be operated by the utility company

or the customer. The operation of a DG unit may be considered random depending on customer load (Aman, Jasmon, Bakar, & Mokhlis, 2012). The location and amount of power delivered from DG (Distributed Generation) units into the distribution system can either increase or decrease the efficiency and stability of the system. Therefore, it's very important to determine the optimal location and size of the DG units before they are inaugurated into the system. In the recent years, numerical calculation approach based on artificial intelligence techniques has been introduced to optimise the operations of the DG. These methods though efficient, are complex and sometimes reproduction of their results may be difficult or impossible. Earlier

---

#### **ARTICLE INFO**

*Article history:*

Received: 24 August 2016

Accepted: 02 December 2016

---

*E-mail addresses:*

[izzri@upm.edu.my](mailto:izzri@upm.edu.my) (Noor Izzri Abdul Wahab),

[ahmed.tuky@yahoo.com](mailto:ahmed.tuky@yahoo.com) (Ahmed Sahib Hammadi),

(Mohammad Lutfi Othman)

\*Corresponding Author

studies have examined optimal placement and sizing and evaluation of impact of the DG unit. Adaptive genetic algorithm (GA) was used to reduce power losses and improve the voltage profile under uncertainties load in (Ganguly & Samajpati, 2015). The PSO method was used to find the best location and to determine the optimal size of DG units for improving voltage stability and reducing power losses (Khanjanzadeh, Arabi, Sedighizadeh, & Rezazadeh, 2011). The PSO method was more accurate than the GA method and the speed of convergence was also fast. Firefly Algorithm (FA) method has been employed to determine optimal location and sizing of DG units in the distribution power networks to minimise the total real power loss of system (Sulaiman, Mustafa, Azmi, Aliman, & Rahim, 2012). The Differential Evolutionary (DE) methodology was proposed to achieve optimal location, size and number of capacitor bank in the distribution networks (Karimi, Shayeghi, Banki, Farhadi, & Ghadimi, 2012). The DE method proved effective in finding the optimal size, location, and number of capacitor banks in terms of speed and accuracy of the results.

In this paper, DE optimisation technique is used to determine the best location and the optimal size of DG unit to reduce power losses and improve the voltage profile of the distribution system.

This paper is organised as follows: The five performance indices relating to DG allocation are discussed in section II. The multi objective functions with corresponding weights are discussed in section -III while optimal sizing and siting of DG unit by using Differential Evolution method (DE) is discussed in section IV. In section V, IEEE 14 bus distribution system, methodology and results of the study are discussed. Section VI concludes the paper.

## OBJECTIVE FUNCTION FORMULATION

Indices show the range of system reliability and in this paper, five indices are used to determine the multi-objective function by giving weight to each index.

- 1. Real and Reactive Power Loss Index:** The real and reactive power loss indices are defined as flowing (Ochoa, Padilha-Feltrin, & Harrison, 2006):

$$LIP = \frac{P_{loss}^{with L}}{P_{loss}^{without}} \quad (1)$$

$$LIQ = \frac{Q_{loss}^{with DG}}{Q_{loss}^{without DG}} \quad (2)$$

where;  $P_{loss}^{with DG}$ ,  $Q_{loss}^{with DG}$ ,  $P_{loss}^{without DG}$  and  $Q_{loss}^{without DG}$  are the total real and reactive power losses after and before inclusion of DG units in the distribution system.



2. **Voltage Deviations Index:** One of the advantages of proper location and size of the DG is the improvement in the system voltage profiles. The voltage deviation index can be defined as:

$$VDI_i = \max_{i=2}^n \left[ \frac{V_{ref} - V_i}{V_{ref}} \right] \quad (3)$$

where,  $V_{ref}$  is the voltage of the reference bus (slack bus) and  $n$  is the number of the buses.

3. **Line Loading Index:** the line flows show an increase or decrease at few existing distribution lines when the DG units are placed in the distribution system. The line loading index definition is from: (Seifinajmi & Sakhavat Sagh, 2014)

$$LLI_i = \max \left( \frac{S_j^{DG}}{S_j^0} \right)^{nl} \quad (4)$$

where,  $S_j^{DG}$  and  $S_j^0$  are the power flows at the branch  $j$  with and without DG.  $nl$  is the number of the branches.

4. **Short Circuit Index:** This index is related to the protection and selectivity issues where it evaluates the maximum short-circuit current variation of the system in two scenarios, with and without DG (El-Zonkoly, 2011).

$$SCI_i = \max \left( \frac{Isc_i^{DG}}{Isc_i^0} \right)_{i=1}^{nb} \quad (5)$$

where,  $Isc_i^{DG}$  and  $Isc_i^0$  are the symmetrical fault current contributions at node  $i$  with and without DG.

The indices proposed in this paper are subject to the following quality and inequality operational constraints:

**Voltage limits:** The voltage drop limits depend on the voltage regulator limits provided by the disco (Kumaraswamy, Tarakalyani, & Prasanth, 2014).

$$V_{min} \leq V_i \leq V_{max} \quad (6)$$

**Line Thermal limits:** Power flow through any distribution feeder must comply with the line thermal capacity.

$$S_i \leq S_{i,max} \quad (7)$$

DG capacity: This section defines the boundary of power generator by DG:

$$P_{min}^{DG} \leq P_i^{DG} \leq P_{max}^{DG} \tag{8}$$

### MULTI OBJECTIVE FUNCTION FORMULATION

By calculating the five indices described in the previous section and taking corresponding weights for each index, the Multi-objective Function can be expressed as in equation 9 (Mancer, Mahdad, & Srairi, 2012).

$$MOF = w_1LIP + w_2LIQ + w_3VDI + w_4LLI + w_5SCI \tag{9}$$

The sum of the absolute values of the weights assigned to all indices should add up to one as shown in the following equation:

$$w_1 + w_2 + w_3 + w_4 + w_5 = 1 \tag{10}$$

The weight values vary according to concerns of engineers and the importance of electrical standards. Additionally,, the weight values are specified to give importance to each index depending on the system. The index that outperforms the others in terms of benefits and importance is given a larger weight.

### DE METHOD FOR OPTIMAL DG ALLOCATION

The DE technique is one of the evolutionary computation methods which depends on stochastic real parameter algorithms. It is used to solve nonlinear, non-differentiable and multimodal objective functions (Kenneth, 1999). The DE is uses a less stochastic approach and a greedy selection compared with other classical EAs to solve optimisation problems. The basic steps of the standard DE algorithm are described as follows:

*Step 1: Initialisation.* The first operation of the DE algorithm is randomly initiated population (NP) of D-dimensional parameter vectors. These vectors represent a candidate solution to solve the optimisation problem. The initial population can be expressed as:

$$X^1 = [X_1^1, X_2^1, \dots, X_i^1], (i = 1, 2, \dots, N_p) \tag{11}$$

$$X_i^1 = X_{lower} + (X_{upper} - X_{lower})RM_i^1 \tag{12}$$

where,  $(X_i^1)$  is a D-dimensional vector, and  $RM_i^1 = [rm_{i,1}^1, rm_{i,2}^1, \dots, rm_{i,D}^1]$ .

*Step 2: Mutation.* Three distinct parameter vectors are sampled randomly from the current population to create donor vectors; these indices are generated once for each mutant operator. The scale of difference between two vectors is added to the third one. The mutation strategy is expressed as:

$$V_i^g = X_{best}^g + F(X_{r1}^g - X_{r2}^g) \tag{13}$$

where,  $X_{r1}^g, X_{r2}^g$  are the randomly selected vectors among the population,  $X_{best}^g$  is the vector with the best fitness value among the individuals, F is a scaling factor.

*Step 3: Crossover.* In crossover operations, the donor vectors  $V \rightarrow_{iG}$  reciprocate with the target vectors  $X \rightarrow_{iG}$  to create the trial vectors  $U \rightarrow_{iG}$ . The trial vectors  $u_{(j,i,G)}$  can be formulated as:

$$u_{i,j}^g = \begin{cases} v_{i,j}^g, & \text{if } (rm_{i,j}^g \leq CR) \text{ or } j = rm_{i,j}^g \\ X_{i,j}^g, & \text{if } (rm_{i,j}^g > CR) \text{ and } j \neq rm_{i,j}^g \end{cases} \tag{14}$$

where,  $u_{i,j}^g$  is a component of  $U_{i1}^g = u_{i,1}^g, u_{i,2}^g, \dots, u_{i,D}^g$

*Step 4: Selection.* After the crossover process, the generated trial vector may be chosen to be a member of the next generation based on the selection criteria, which is given by:

$$X_i^{g+1} = \begin{cases} U_i^g, & \text{if } fitness(U_i^g) < fitness(X_i^g) \\ X_i^g & \text{otherwise} \end{cases} \tag{15}$$

## RESULTS AND DISCUSSIONS

### Test System

The DG unit was assumed to be integrated in an IEEE 14 bus test system. Figure 2 shows the single line diagram of IEEE 14-bus test system which consists of 5 generator buses, 9 load buses and 20 branches. The total real load of the system is 259 MW and reactive load is 112 MVar. The real and reactive power losses in the base case of IEEE 14 bus test system obtained using Newton Raphson method is 13.5929 MW and 56.9096 MVar respectively (Pai, 1979).

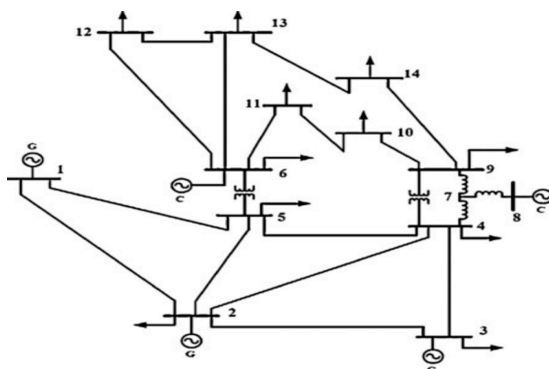


Figure 1. Single line diagram of IEEE 14 test system

## Weights Values

The values of weights in multi-objective function are different based on the engineer's concern. In general, it is not easy to identify suitable weight values for each index. Engineers and operators of plants who have experience with distribution systems should be able to identify the suitable values of the weights. During this study, the values of the weights were assumed positive and W1 related to active power losses is restricted between 0.35 and 0.50, W2 related to reactive power losses is restricted between 0.1 and 0.30 W3 related to voltage division is restricted between 0.1 and 0.30, W4 and W5 related to capacity of line and short circuit level are fixed at 0.10 (see Table 1).

Table 1  
*Set of weights with corresponding fitness values*

Set No	W1	W2	W3	W4	W5	Best fitness
1	0.35	0.20	0.25	0.10	0.10	0.758131
2	0.35	0.25	0.20	0.10	0.10	0.805079
3	0.35	0.30	0.15	0.10	0.10	0.852028
4	0.35	0.15	0.30	0.10	0.10	0.711182
5	0.40	0.20	0.20	0.10	0.10	0.805079
6	0.40	0.30	0.10	0.10	0.10	0.898977
7	0.40	0.10	0.30	0.10	0.10	0.721182
8	0.40	0.25	0.15	0.10	0.10	0.852028
9	0.40	0.15	0.25	0.10	0.10	0.758130
10	0.45	0.20	0.15	0.10	0.10	0.852028
11	0.45	0.15	0.20	0.10	0.10	0.805079
12	0.45	0.10	0.25	0.10	0.10	0.758130
13	0.45	0.25	0.10	0.10	0.10	0.898977
14	0.50	0.15	0.15	0.10	0.10	0.852028
15	0.50	0.20	0.10	0.10	0.10	0.898977
16	0.50	0.10	0.20	0.10	0.10	0.805079

From Table 1, set number 4 which shows the minimum fitness function is selected as a weighting set for MOF eq. (9). Thus, the weights for each index are described as  $w_1=0.35$ ,  $w_2=0.15$ ,  $w_3=0.30$ ,  $w_4=0.10$  and  $w_5=0.10$ .

## Results Considering DG

In order to find the best place for DG units and their respective optimal sizes in the system, the buses that have minimum fitness values will consider their respective size. The results obtained by using DE method are tabulated and shown in Table 2.

Table 2  
Optimal DG size with respective fitness value

Bus No.	Fitness	DG size MW	Bus No.	Fitness	DG size MW
4	0.7109	25.977	11	0.7203	25.7435
5	0.7311	25.6087	12	0.7283	25.9943
7	0.7100	25.6194	13	0.7124	25.7466
9	0.7090	25.8660	14	0.7034	25.9220
10	0.7153	24.3677			

From Table 2, the best three locations with minimum fitness values based on their respective optimal sizes were selected to become candidate buses to install the DG unit in their test system. The associated power losses and voltage levels for each candidate bus are determined using Newton Raphson load flow based on the optimal size of the DG unit. The results are compared in Table 3.

Table 3  
Total power losses of the test system with DG

Bus No	DG size MW	Total Real losses MW		Total Reactive losses MVar		Percentage of reduction	
		Without DG	With DG	Without DG	With DG	P	Q
9	25.8660		10.956	44.141	19.4%	22.4%	
7	25.6194		10.925	45.577	19.6 %	19.9 %	

From Table 3, it is clear bus 14 is an optimal location to install DG unit in the test system according to the percentage of loss. The total real power loss is 10.738 MW (21% loss) while the reduction of the reactive power loss is 43.426MVar (23.9% loss). Table 4 provides optimal location details.

Table 4  
Optimal location details of system with DG

Optimal DG location	Optimal DG size	Parameter of optimal DG location and size						Total real losses	Total reactive losses
		LIP	LIQ	VD	LLC	SC	MOF		
14	25.922	0.799	0.775	0.047	0.946	1.038	0.7072	10.738	43.426

The values of LLC and SCI were increased by an acceptable amount from (0.831) and (0.725) in the normal case to become (0.946) and (1.038) after adding the DG units. Therefore, it is necessary to update the protection devices after including DG units with the distribution system. The voltage levels of test system were increased after including the DG unit within the acceptable limits (0.95-1.1p.u) for generating buses and (0.95-1.05) for load buses (Alsac

& Stott, 1974). Table 5 compares voltage in two cases, without DG and with DG located at the best place with optimal size determined by DE method.

Table 5  
Voltage profile of test system

Bus No.	Type of Bus	Voltage profile		Bus No.	Type of Bus	Voltage profile	
		Without DG	With DG			Without DG	With DG
1	generating	1.0600	1.0600	8	generating	1.0800	1.0800
2	generating	1.0450	1.0450	9	load	1.0305	1.0372
3	generating	1.0100	1.0100	10	load	1.0299	1.0355
4	load	1.0131	1.0183	11	load	1.0461	1.0490
5	load	1.0165	1.0212	12	load	1.0432	1.0452
6	generating	1.0700	1.0700	13	load	1.0466	1.0485
7	load	1.0456	1.0472	14	load	1.0192	1.0426

The DE method improves the voltage levels of almost all buses while ensuring that no voltage level rises above the acceptable limit. Figure 2 provides a comparison.

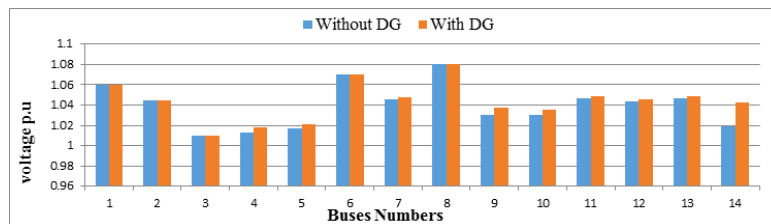


Figure 2. Voltage profile comparison

## CONCLUSION

Optimal size and suitable location of DG unit that supply only active power (Type 1 DG unit) to the system have been addressed in this paper. The best locations and optimal sizes have been identified by minimising the multi-objective index using artificial intelligence methods. Among the many different heuristic optimisation algorithms, DE provides better results in terms of reduction in real and reactive power losses and improving the voltage profile of the distribution system. Reduction in the real power loss is 21% while reduction in the reactive power losses is 23.96%. The voltage level of bus 14 is increased from 1.019 to 1.0426 after integration with the DG unit.

## REFERENCES

Alsac, O., & Stott, B. (1974). Optimal load flow with steady-state security. *IEEE transactions on Power Apparatus and Systems*(3), 745-751.

- Aman, M., Jasmon, G., Bakar, A., & Mokhlis, H. (2012). Optimum capacitor placement and sizing for distribution system based on an improved voltage stability index. *International Review of Electrical Engineering-Iree*, 7(3), 4622-4630.
- El-Zonkoly, A. (2011). Optimal placement of multi-distributed generation units including different load models using particle swarm optimisation. *IET generation, transmission & distribution*, 5(7), 760-771.
- Ganguly, S., & Samajpati, D. (2015). Distributed generation allocation on radial distribution networks under uncertainties of load and generation using genetic algorithm. *IEEE Transactions on Sustainable Energy*, 6(3), 688-697.
- Karimi, M., Shayeghi, H., Banki, T., Farhadi, P., & Ghadimi, N. (2012). Solving Optimal Capacitor Allocation Problem using DE Algorithm in Practical Distribution Networks. *Przeegląd Elektrotechniczny*, 88(7a), 90-93.
- Karimyan, P., Gharehpetian, G., Abedi, M., & Gavili, A. (2014). Long term scheduling for optimal allocation and sizing of DG unit considering load variations and DG type. *International Journal of Electrical Power & Energy Systems*, 54, 277-287.
- Kenneth, V. (1999). Price, An introduction to differential evolution, New ideas in optimization: McGraw-Hill Ltd., UK, Maidenhead, UK.
- Khanjanzadeh, A., Arabi, M., Sedighzadeh, M., & Rezazadeh, A. (2011). Distributed Generation Allocation to Improve Steady State Voltage Stability of Distribution Networks Using Particle Swarm Optimization and Genetic Algorithm. *Canadian Journal on Electrical and Electronics Engineering*, 2(6), 250-254.
- Kumaraswamy, I., Tarakalyani, S., & Prasanth, B. V. (2014). Optimal Location of Distributed Generation on Radial Distribution System for Loss Reduction and Voltage Profile Improvement.
- Mancer, N., Mahdad, B., & Srairi, K. (2012). Multi objective optimal reactive power flow based STATCOM using three variant of PSO. *International Journal of Energy Engineering*, 2(2), 1-7.
- Ochoa, L. F., Padilha-Feltrin, A., & Harrison, G. P. (2006). Evaluating distributed generation impacts with a multiobjective index. *IEEE Transactions on Power Delivery*, 21(3), 1452-1458.
- Pai, M. (1979). Computer techniques in power system analysis EJ. *Tata McGraw-Hill Pub Co Ltd*, 1, 979.
- Seifinajmi, E., & Sakhavat Saghi, M. N. (2014). Optimal Placement of DGs in Radial Distribution Systems Considering Power Quality Improvement and Reduce Losses. *Bull. Env. Pharmacol. Life Sci*, 3, 37-41.
- Sulaiman, M. H., Mustafa, M. W., Azmi, A., Aliman, O., & Rahim, S. A. (2012). *Optimal allocation and sizing of distributed generation in distribution system via firefly algorithm*. Paper presented at the Power Engineering and Optimization Conference (PEDCO) Melaka, Malaysia, 2012 Ieee International.





## **Simulation of Interleaved Current Fed Full Bridge Converter for Fuel Cell Electrical Vehicle**

**Koay Boon Kit\*, Nasrudin Abd Rahim and Siti Rohani Sheikh Raihan**

*UMPEDAC, Level 4, Wisma R&D, Universiti Malaya, Jalan Pantai Baharu, 59990 Kuala Lumpur, Malaysia*

### **ABSTRACT**

Hydrogen fuel cell (HFC) is one of the renewable resources to address fossil fuel depletion and global warming. Its primary advantages are power is generated from renewable fuel hydrogen and the emission is only water. However, HFC supplies power in a slow dynamic response. In fuel cell electrical vehicle (FCEV), energy storage system (ESS), i.e. supercapacitor and battery, is required to immediately compensate the difference between load demand and power supply; the lifetime of HFC is affected by current ripple. In order to manage power flow between HFC and load, HFC is interfaced with a unidirectional DC-DC converter. The converter steps up the terminal fuel cell voltage and regulate the voltage before it is connected to the load. Among the proposed HFC DC-DC converters, interleaved DC-DC converter seems more suitable for FCEV application due to its advantages. When galvanic isolation is required, current fed full bridge converter receives significant consideration as the module of interleaved converter. This paper simulates interleaved current fed full bridge (ICFFB) converter and discusses the suitability of ICFFB for FCEV application.

*Keywords:* Hydrogen fuel cell, DC-DC converter, electric vehicle

### **INTRODUCTION**

Demand for renewable resources is a result of fossil fuel depletion and concerns over global warming. In 2013, the transport sector

accounted for 23% of the global Green House Gas emission, the second largest contributor (International Energy Agency, 2015). Fuel cell electric vehicle (FCEV) is a revolutionary technology that addresses this issue as it emits only water and does not need gasoline fuel.

Hydrogen fuel cell (HFC)/battery/supercapacitor architecture is found to be very fulfilling in the dynamic driving cycle in FCEV (Zandi et al., 2011). The HFC is unable to instantaneously fulfil all the load demand, especially during dynamic load cycle

#### **ARTICLE INFO**

##### *Article history:*

Received: 24 August 2016

Accepted: 02 December 2016

##### *E-mail addresses:*

[bk.koay@siswa.um.edu.my](mailto:bk.koay@siswa.um.edu.my) (Koay Boon Kit),

[nasrudin@um.edu.my](mailto:nasrudin@um.edu.my) (Nasrudin Abd Rahim),

[srohani\\_sr@um.edu.my](mailto:srohani_sr@um.edu.my) (Siti Rohani Sheikh Raihan)

\*Corresponding Author

(Thounthong, Tricoli, & Davat, 2014). Thus, the difference between load demand and power supply from HFC is compensated by energy storage system (ESS), i.e. supercapacitor and battery in FCEV. Moreover, ESS could be recharged by HFC or during regenerative braking. For ease of power flow management, HFC is interfaced with unidirectional DC-DC converter and each ESS component is interfaced with bidirectional DC-DC converter. Besides power flow management, the HFC DC-DC converter step ups and regulates HFC terminal voltage at designated level, since HFC terminal voltage is low and decreases when the HFC current supply increases. While HFC is vulnerable to low frequency ripple, the current source DC-DC converter for HFC is favourable (Wei & Fahimi, 2010). As high ripple current reduces HFC lifetime (Thounthong et al., 2014), the ripple on input current of HFC converter should be low.

In recent years, HFC current source DC-DC converters that have higher efficiency, power handling capability, step-up ratio, lower input current ripple etc. have been invented. The HFC DC-DC converters include non-isolated DC-DC converter (Al-Saffar & Ismail, 2015; Kuo-Ching & Jian-Ting, 2013; Sabzali, Ismail, & Behbehani, 2015), isolated DC-DC converter (Xuancai et al., 2005), interleaved converter (Hegazy, Van Mierlo, & Lataire, 2012; Kong & Khambadkone, 2007; Subsingha & Sarakarn, 2012) etc. Some of the non-isolated DC-DC converters are derived to further increase the step-up ratio without extreme duty cycle by inclusion of coupled inductor (Kuo-Ching & Jian-Ting, 2013), by integration of different DC-DC converters (Al-Saffar & Ismail, 2015; Sabzali et al., 2015) or by using cell multiplier (Rosas-Caro et al., 2015; Wuhua, Weichen, Yan, & Xiangning, 2010). Among the DC-DC converters, interleaved DC-DC converter is preferable for HFC application due to its many advantages of load sharing, have ripple cancellation effect on input current, higher reliability in supplying power etc. (Guilbert, Gaillard, Mohammadi, N'Diaye, & Djerdir, 2015; Kong & Khambadkone, 2007; Phatiphat Thounthong & Davat, 2010). Interleaved converter is constructed by paralleling the input of the identical modules (DC-DC converters) and the phase of the carrier signals are distributed evenly over a cycle and thus, DC-DC converters can be considered as a module for interleaving. When galvanic isolation is not necessary, classical boost converter with a hard switching technique can be considered (Hegazy et al., 2012; Subsingha & Sarakarn, 2012) due to ease of control and analysis. Galvanic isolation is required between supply and the load, full bridge converter is a more popular selection. Compared with push-pull DC-DC converter and half bridge converter, full bridge converter has lower switching stress, higher switch and transformer utilisation.

In this paper, an interleaved current fed full bridge (ICFFB) DC-DC converter consisting of four modules will be simulated in MATLAB. Full bridge converter is chosen as a module due to its advantages. The following sections will discuss in detail the operating principle of ICFFB DC-DC converter, the MATLAB model and the simulation results.

## OPERATION OF ICFFB DC-DC CONVERTER

Figure 1 depicts ICFFB DC-DC converter that consists of four modules (Kong & Khambadkone, 2007). The first module has four switching states. As shown in Figure 2(a), during the first switching state SS1, all switches (S1-S2-S3-S4) is on and inductor L1 is charged (current  $i_l$

increases) while both capacitor C1 and C2 is discharged (each capacitor voltage decreases) supplying power to the load R. In switching state SS2 as shown in Figure 2(b), switches S3-S4 are off and switches S1-S2 are on. Inductor L1 is discharged (current  $i_1$  decreases), i.e. current  $i_1$  enters transformer Tx1 in negative cycle, to transfer energy to capacitor C2 (capacitor C2 voltage increases due to the charging) while capacitor C1 is discharging. Next, switching state SS3 is identical to switching state SS1. Finally, in switching state SS4 as illustrated in Figure 2(c), switches S3-S4 are on and switches S1-S2 are off. Inductor L1 is discharged, i.e. current  $i_1$  enters transformer Tx1 in positive cycle, to transfer energy to capacitor C1 while capacitor C2 is discharging.

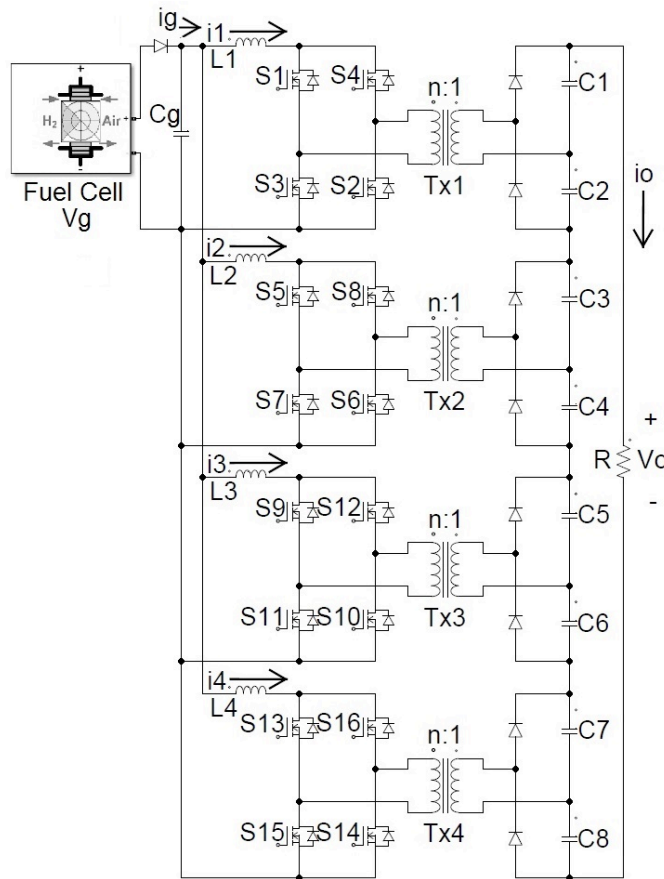


Figure 1. ICFFB DC-DC converter (four modules)

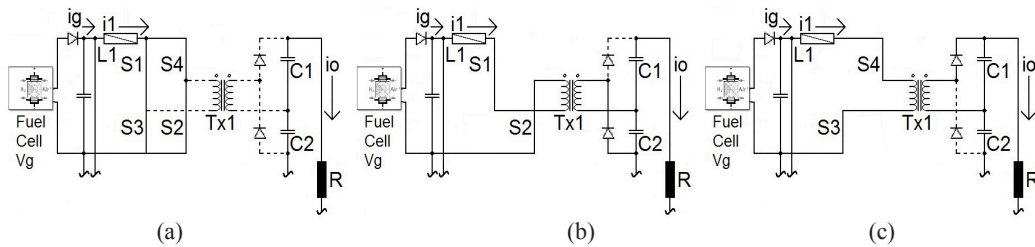


Figure 2. Equivalent circuit for switching state (a) SS1/SS3 (b) SS2 (c) SS4

The first module has switching operation with repeat switching states of SS1, SS2, SS3 and SS4. Meanwhile, each of the remaining modules has similar switching operation that corresponds with the relevant switches, inductor, transformer and capacitors. For example, the second module has switching states involving switches S5-S6-S7-S8, inductor L2, transformer Tx2 and capacitors C3 and C4. 45° phase delay is imposed between the switching of the adjacent modules, i.e. first to fourth modules respectively has the phase delay of 0°, 45°, 90° and 135°. Contrary to Thounthong et al. (2009), the 45° phase delay (between the switching of the adjacent modules) is derived from equation (1), where m is the quantity of modules, since two switches are switched concurrently in each module.

$$\text{Phase Delay} = 2\pi/m \tag{1}$$

By the interleaving of the four modules, capacitor C1 to C8 are connected in series to provide output voltage Vo to load R. The small signal analysis of ICFFB DC-DC converter has been discussed by Kong and Khambadkone (2007). Equation 2 shows the voltage transfer ratio (Kong & Khambadkone, 2007), where Vo is the output voltage, Vcg is the voltage of capacitor Cg, m is the quantity of the modules, n is the transformer winding ratio (n:1) and D is the duty cycle of the switches. Quantity of modules boosts the voltage transfer ratio.

$$\frac{V_o}{V_{cg}} = m \times 2 \times \frac{1}{2n(1-D)} \tag{2}$$

### ICFFB DC-DC CONVERTER MATLAB MODEL

MATLAB model ICFFB DC-DC converter is developed (see Figure 1). Table 1 shows the specification of the converter. The simulation is carried out in MATLAB with open loop system and FC block as the DC voltage source Vg. The FC block possesses characteristic curve of the commercially available fuel cell power module Nexa 1200 (one of the core components in the modular fuel cell training system - Nexa Training System) and the parameter is shown in Table 2 (Heliocentris Energiesysteme GmbH; Heliocentris Energiesysteme GmbH, 2012).

Table 1  
*ICFFB DC-DC converter specification*

Voltage transfer ratio	$V_o/V_{cg}$	2
Inductor	L1 to L4	1.16mH
Capacitor	C1 to C8	470 $\mu$ F
Capacitor	Cg	33 $\mu$ F
Transformer winding ratio	n:1	5:1
Load	R	10 $\Omega$
Switching frequency	f	25kHz
Duty cycle	D	0.6

Table 2  
*Fuel cell block parameter (Nexa 1200)*

Fuel cell voltage	$V_g$	18 – 36V
Rated output power	$P_o$	1200W
Efficiency (at rated output power)	$\eta$	50%
Cell quantity	-	36

Carrier signal of first module to fourth module has the phase delay of 0°, 45°, 90° and 135° respectively to achieve 45° phase delay between the switching of the adjacent modules. Pulse width modulation signals are generated for the switching.

## SIMULATION RESULT

Simulation has been carried for 0.4s and the result is shown in Table 3. The simulation waveforms are shown in Figure 3 and Figure 4. Figure 3(a) shows that the output voltage  $V_o$  is 65.39V with ripple 0.041V. Figure 3(b) shows the waveform of output current  $i_o$  6.54A with ripple 0.0041A when the load is 10 $\Omega$ . Figure 4(a) shows that the fuel cell voltage  $V_g$  31.52V with ripple 2.61V. Figure 4(b) shows the input current  $i_g$  13.24A with ripple 0.021A. Figure 4(c) shows the waveform of inductor current  $i_1$ ,  $i_2$ ,  $i_3$  and  $i_4$  3.31A with ripple 0.12A. Figure 4(d) shows the waveform for voltage capacitor C1, C3, C5 and C7.

Table 3  
*Simulation result*

	Average	Ripple
Output voltage $V_o$ (V)	65.39	0.041
Output current $i_o$ (A)	6.54	0.0041
Fuel cell voltage $V_g$ (V)	31.52	2.61
Capacitor Cg voltage $V_{cg}$ (V)	32.7	0.041
Input current $i_g$ (A)	13.24	0.021
Inductor current $i_1$ , $i_2$ , $i_3$ , $i_4$ (A)	3.31	0.12
Capacitor C1/C3/C5/C7 voltage $V_{c1}/V_{c3}/V_{c5}/V_{c7}$ (V)	8.15	0.36

All inductor currents, each 3.31A, is equal to the input current  $i_g$  13.24A. This shows that the load current is equally shared among the modules. The ripple of each inductor current

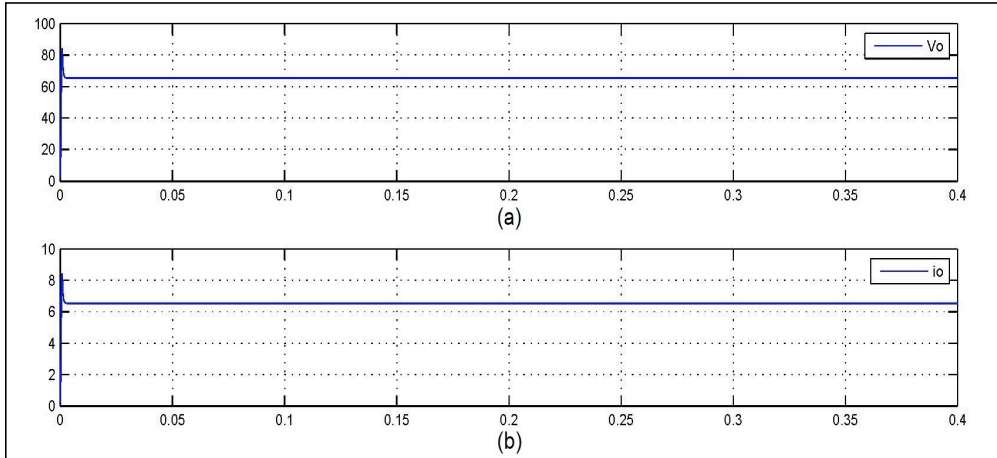


Figure 3. Simulation result (a) output voltage  $V_o$  (b) output current  $i_o$

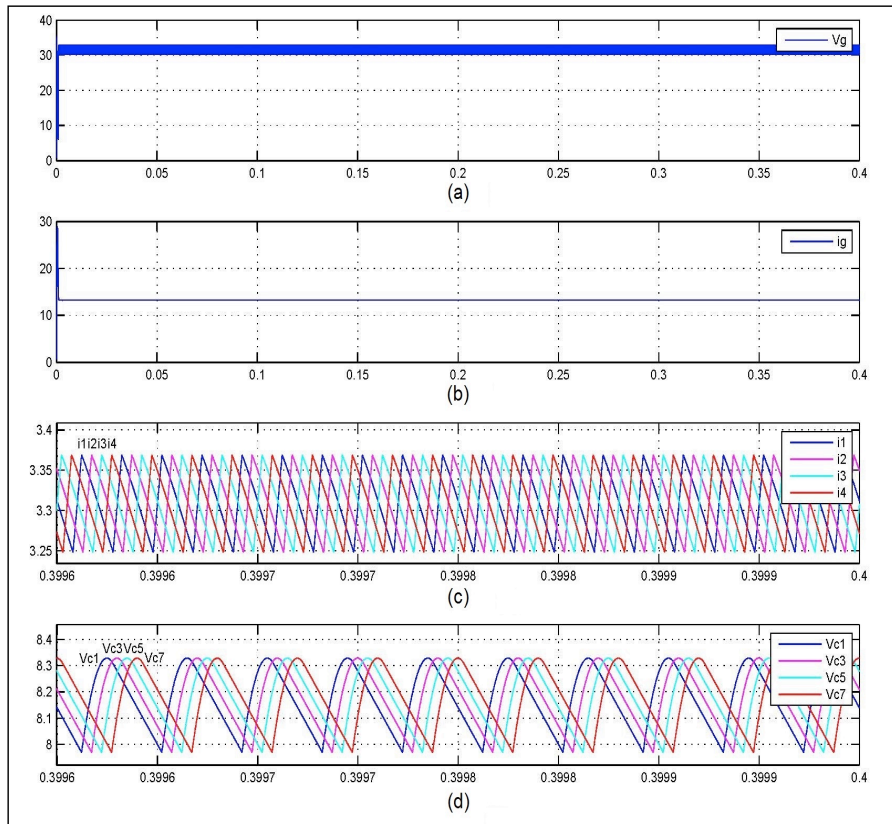


Figure 4. Simulation result (a) fuel cell voltage  $V_g$  (b) input current  $i_g$  (c) inductor current  $i_1, i_2, i_3, i_4$  (d) capacitor voltage  $V_{c1}, V_{c3}, V_{c5}, V_{c7}$

0.12A compensates each other and yields smaller ripple on the input current  $i_g$  0.021A, i.e. ripple cancellation effect. From Figure 4(d), the voltage of each output capacitor is 8.15V. The summation of all capacitors C1 to C8, each 8.15V, is close to the output voltage  $V_o$  65.39V, suggesting the capacitor of smaller voltage rating could be utilised. Table 3 shows the ratio between output voltage  $V_o$  and capacitor  $C_g$  voltage  $V_{cg}$  is two, complying with the voltage transfer ratio that is expressed in equation (2).

## CONCLUSION

This paper simulates ICFFB DC-DC converter that consists of four modules. From the simulation result, each module carries the same load current. Load sharing among the modules in the interleaved converter shows components of smaller rating could be used compared with non-interleaved converter, especially inductor and transformer. Besides, the ripple cancellation effect will minimise the HFC lifetime reduction. Interleaved converter depicts higher reliability in supplying power to the load. If one of the modules malfunctions, interleaved converter is still able to supply power at the total power rating of the remaining modules. The load sharing, ripple cancellation effect, higher reliability and the galvanic isolation between HFC and load are the advantages of ICFFB DC-DC converter for FCEV application.

## ACKNOWLEDGEMENT

The authors would like to thank the Ministry of Higher Education for supporting this research via LRGS research grant LR002-2013B.

## REFERENCES

- Al-Saffar, M. A., & Ismail, E. H. (2015). A high voltage ratio and low stress DC-DC converter with reduced input current ripple for fuel cell source. *Renewable Energy*, 82, 35-43. doi: <http://dx.doi.org/10.1016/j.renene.2014.08.020>
- Guilbert, D., Gaillard, A., Mohammadi, A., N'Diaye, A., & Djerdir, A. (2015). Investigation of the interactions between proton exchange membrane fuel cell and interleaved DC/DC boost converter in case of power switch faults. *International Journal of Hydrogen Energy*, 40(1), 519-537. doi: <http://dx.doi.org/10.1016/j.ijhydene.2014.10.072>
- Hegazy, O., Van Mierlo, J., & Lataire, P. (2012). Analysis, Modeling, and Implementation of a Multidevice Interleaved DC/DC Converter for Fuel Cell Hybrid Electric Vehicles. *Power Electronics, IEEE Transactions on*, 27(11), 4445-4458. doi: 10.1109/TPEL.2012.2183148
- Heliocentris Energiesysteme GmbH. (2012). Nexa Training System-Instruction Manual (2.1 ed.).
- Heliocentris Energiesysteme GmbH. Nexa 1200-Technical Data Sheet.
- Heliocentris Energiesysteme GmbH. Nexa Integration System-1.2 kW Fuel Cell System.
- International Energy Agency. (2015). *CO2 emissions from fuel combustion highlights* (2015 ed.): Organization for Economic Cooperation & Development Stationery Office.



- Kong, X., & Khambadkone, A. M. (2007). Analysis and Implementation of a High Efficiency, Interleaved Current-Fed Full Bridge Converter for Fuel Cell System. *Power Electronics, IEEE Transactions on*, 22(2), 543-550. doi: 10.1109/TPEL.2006.889985
- Kuo-Ching, T., & Jian-Ting, L. (2013, 25-26 Feb. 2013). *High step-up DC/DC converter for fuel cell hybrid electric vehicles*. Paper presented at the Next-Generation Electronics (ISNE), 2013 IEEE International Symposium on.
- Rosas-Caro, J. C., Mayo-Maldonado, J. C., Valderrabano-Gonzalez, A., Beltran-Carbajal, F., Ramirez-Arredondo, J. M., & Rodriguez-Rodriguez, J. R. (2015). DC-DC multiplier boost converter with resonant switching. *Electric Power Systems Research*, 119, 83-90. doi: <http://dx.doi.org/10.1016/j.epr.2014.09.003>
- Sabzali, A. J., Ismail, E. H., & Behbehani, H. M. (2015). High voltage step-up integrated double Boost-Sepic DC-DC converter for fuel-cell and photovoltaic applications. *Renewable Energy*, 82, 44-53. doi: <http://dx.doi.org/10.1016/j.renene.2014.08.034>
- Subsingha, W., & Sarakarn, P. (2012). 4 Phase Interleaved DC Boost Converter for PEMFC Applications. *Procedia Engineering*, 32, 1127-1134. doi: <http://dx.doi.org/10.1016/j.proeng.2012.02.066>
- Thounthong, P., & Davat, B. (2010). Study of a multiphase interleaved step-up converter for fuel cell high power applications. *Energy Conversion and Management*, 51(4), 826-832. doi: <http://dx.doi.org/10.1016/j.enconman.2009.11.018>
- Thounthong, P., Davat, B., Rae, x, l, S., & Sethakul, P. (2009). Fuel cell high-power applications. *Industrial Electronics Magazine, IEEE*, 3(1), 32-46. doi: 10.1109/MIE.2008.930365
- Thounthong, P., Tricoli, P., & Davat, B. (2014). Performance investigation of linear and nonlinear controls for a fuel cell/supercapacitor hybrid power plant. *International Journal of Electrical Power and Energy Systems*, 54, 454-464. doi: <http://dx.doi.org/10.1016/j.ijepes.2013.07.033>
- Wei, J., & Fahimi, B. (2010). Active Current Sharing and Source Management in Fuel Cell-Battery Hybrid Power System. *Industrial Electronics, IEEE Transactions on*, 57(2), 752-761. doi: 10.1109/TIE.2009.2027249
- Wuhua, L., Weichen, L., Yan, D., & Xiangning, H. (2010). Single-Stage Single-Phase High-Step-Up ZVT Boost Converter for Fuel-Cell Microgrid System. *Power Electronics, IEEE Transactions on*, 25(12), 3057-3065. doi: 10.1109/TPEL.2010.2079955
- Xuancai, Z., Dehong, X., Guoqiao, S., Danji, X., Mino, K., & Umida, H. (2005, 2-6 Oct. 2005). *Current-fed DC/DC converter with reverse block IGBT for fuel cell distributing power system*. Paper presented at the Industry Applications Conference, 2005. Fortieth IAS Annual Meeting. Conference Record of the 2005.
- Zandi, M., Payman, A., Martin, J. P., Pierfederici, S., Davat, B., & Meibody-Tabar, F. (2011). Energy Management of a Fuel Cell/Supercapacitor/Battery Power Source for Electric Vehicular Applications. *Vehicular Technology, IEEE Transactions on*, 60(2), 433-443. doi: 10.1109/TVT.2010.2091433



## **Double Series Resonant DC-DC Converter with Uniform Voltage Stress on High Voltage Transformers**

**Nor Azura, Samsudin\*, Soib, Taib and Shahid, Iqbal**

*School of Electrical and Electronic Engineering, Engineering Campus, Universiti Sains Malaysia, 14300 Nibong Tebal, Penang, Malaysia*

### **ABSTRACT**

This paper proposes a novel double series resonant dc-dc converter with uniform voltage stress on a transformer. It consists of a half-bridge inverter with two power switches (IGBTs), two series resonant tank, two high-voltage transformers and a symmetrical voltage multiplier circuit. A symmetrical voltage multiplier circuit is connected at the secondary side of the high voltage transformer to generate desired high voltage dc output. Due to use of voltage multiplier circuit, the proposed converter requires smaller turns ratio of the high voltage transformer, leading to reduction in size and volume of the transformer. The proposed converter operates in discontinuous current mode by varying the switching frequency of the converter. In a discontinuous current mode operation, all the power switches and output diodes of the rectifier circuit turn-on and turn-off under zero current switching conditions. Therefore, it has features of low switching losses and possibility of light-load operation. Besides, it costs less and is smaller in size compared with conventional double series resonant dc-dc converter. It also has a simple operating principle and suitable for high voltage and high power applications. Experimental results confirm the proposed converter performs better than the others.

*Keywords:* Series resonant converter, zero current switching, high voltage, dc-dc converter

### **ARTICLE INFO**

*Article history:*

Received: 24 August 2016

Accepted: 02 December 2016

*E-mail addresses:*

[norazura200584@gmail.com](mailto:norazura200584@gmail.com) (Nor Azura, Samsudin),

(Soib, Taib),

[shahidsidu@gmail.com](mailto:shahidsidu@gmail.com) (Shahid, Iqbal)

\*Corresponding Author

### **INTRODUCTION**

High voltage dc power supplies are used in electrostatic precipitators, particle accelerators, lasers, X-ray systems and industrial test equipment (Kulkarni et al., 2000). A dc high voltage power supply normally consists of a dc-ac inverter, high voltage transformer (HVT), high voltage rectifier and controller, among others. (Jang et al., 2010). The HVT is the most critical

component in high voltage power supplies. The design of the HVT is quite different compare with the conventional transformer. When HVT is used to produce high output voltage, it has a high number of turn's ratio. Due to this reason, the parasitic capacitance referred to the primary side of the transformer is multiplied by the square of two of the number of the turn's ratio. Therefore, a HVT has significant leakage inductance and parasitic capacitance. The parasitic components give voltage and current spikes and affect the performance of the converter (Li et al., 2007).

To overcome the problems causes by HVT, studies have proposed several types of resonant converters. Resonant converters can achieve zero current switching (ZCS) and zero voltage switching (ZVS) at the converter and can operate at a higher switching frequency that can also reduce the size of the converters (Ye et al., 2008). There are various types of the resonant converter topologies such as series resonant converters (SRC), parallel resonant converters (PRC) and series-parallel resonant converters (SPRC). All of these converters have their own merits and demerits. The SRC is often used in the high voltage power supplies because it is free from saturation and has simple frequency control (Pijl et al., 2009), good efficiency both at heavy and light load (Pan et al., 2013) and inherent capability of short circuit protection (Chakraborty et al., 2002). The SRC that operates in a discontinuous current mode (DCM) are mainly used in high voltage application because of advantages when adopting DCM operation which is ZCS turn-on and anti-parallel diodes turn-on and turn-off naturally at the power switches and low switching losses (Singh et al., 2013). Sze Sing et al., (2012) proposed double series resonant high voltage dc-dc converter in order to reduce the conduction loss and improve efficiency. However, this converter has certain drawbacks, namely unequal dc voltage stress on transformers. It is equal to  $V_o/2$  for transformer  $T_1$  while it is zero for transformer  $T_2$ . Due to this reason, transformer  $T_1$  need to be designed with larger isolation distance between primary and secondary windings leading to larger leakage inductance compared with transformer  $T_2$ .

This paper proposes double series resonant dc-dc converter with uniform voltage stress on HVT-based symmetrical voltage multiplier (SVM). In the proposed converter, the secondary windings of the high voltage transformer are connected to the SVM circuit; therefore, the dc voltage stress on the HVTs is uniform. It is equal for both transformers,  $T_1$  and  $T_2$ , respectively because of their common grounding. Therefore, transformer  $T_1$  and  $T_2$  can be designed with same isolation distance between primary and secondary windings so that the value of leakage inductance is same for both transformers,  $T_1$  and  $T_2$ . Furthermore, the proposed converters perform better.

## CIRCUIT DESCRIPTION AND PRINCIPLE OF OPERATION

The proposed double series resonant dc-dc converter with uniform voltage stress on high voltage transformers is shown in Figure 1. The proposed converter circuit consists of half bridge inverter that has two power switches,  $S_1$  and  $S_2$ , two resonant capacitors,  $C_{r1}$  and  $C_{r2}$ , two high voltage transformers,  $T_1$  and  $T_2$ , SVM circuit and output load resistor. The leakage inductances,  $L_{r1}$  and  $L_{r2}$ , are of the primary windings,  $T_1$  and  $T_2$  of the HVTs respectively. The inverter circuit is to invert the lower dc voltage from the input voltage into ac voltage. Power switches  $S_1$  and  $S_2$  operate in complementary fashion with interleaved half switching cycle. The

resonant capacitors,  $C_{r1}$  and  $C_{r2}$  are connected in series with the leakage inductances,  $L_{r1}$  and  $L_{r2}$  respectively. Therefore, two series resonant tank circuits are formed which are resonant tank circuit-1 and resonant tank circuit-2. Resonant tank circuit-1 consists of  $L_{r1}$  and  $C_{r1}$ , and resonant tank circuit-2 consists of  $L_{r2}$  and  $C_{r2}$ . The main purpose of the HVTs is to boost the secondary voltage to desired levels and also to obtain the electrical isolation between primary and secondary side of the HVT circuit. The secondary windings of the transformer are connected to the  $m$ -stage of the SVM circuit. The secondary voltage of the HVTs is multiplied by  $m$ -stage; therefore, maximum output voltage of the SVM circuit is nearly  $V_o = 2m v_{s(max)}$ .

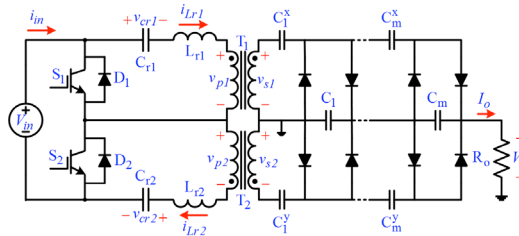


Figure 1. The proposed double series resonant dc-dc converters with uniform voltage stress on high voltage transformers

These series resonant circuits are fed alternatively by operating the power switches with an interleaved half switching cycle. The discontinuous conduction mode (DCM) of operation occurs when the switching frequency,  $f_s$  of the converter is less than half of its resonant frequency,  $f_r$ , i.e.

$$f_s \leq \frac{1}{2} f_r \tag{1}$$

where,  $f_r$  is the natural frequency of resonant tank and expressed as

$$f_r = \text{resonant frequency} = \frac{1}{2\pi\sqrt{L_r C_r}} \tag{2}$$

Here,  $L_r$  is the leakage inductance and  $C_r$  is the resonant capacitor. In the proposed converter, the two resonant capacitors are connected in series to the input dc source through primary windings, so that the voltage stress on these capacitors is reduced to half compared with conventional full-bridge inverter high-voltage dc-dc converter.

### ANALYSIS OF STEADY-STATE OPERATION

The key steady-state waveforms of the proposed converter for one complete switching cycle are shown in Figure 2. There are six modes of operation in one switching cycle and the equivalent circuits of these modes of operation are shown in Figure 3. To simplify the analysis, following assumptions are made:

- All the components are assumed to be identical by  $L_r=L_{r1}=L_{r2}$  and  $C_r=C_{r1}=C_{r2}$ .
- The turns ratio of the transformer is  $k=N_{p1}/N_{s1}=N_{p2}/N_{s2}$  of the transformers,  $T_1$  and  $T_2$  respectively.

The output voltage in the primary side of the transformer is obtained by dividing secondary voltage with transformer turn's ratio,  $k$  and it is assumed that capacitors of the voltage multiplier circuit are large enough so that voltage ripples across these capacitors are significant in a steady-state operation.

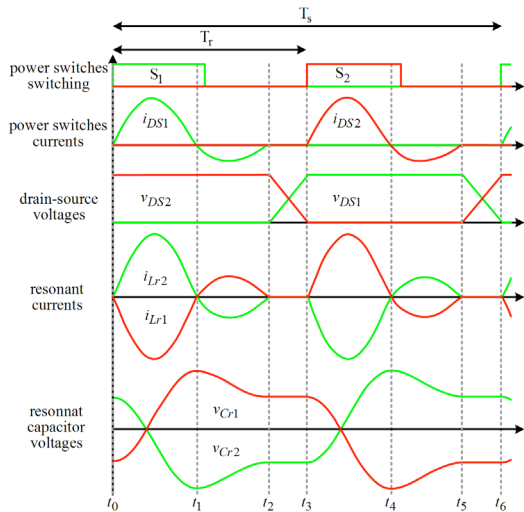


Figure 2. The key steady-state waveform of the proposed resonant converters over one switching cycle

**Mode 1** [ $t_0 \leq t \leq t_1$ ]: This mode begins when the power switch,  $S_1$  is turned on and the resonant currents,  $i_{Lr1}$  and  $i_{Lr2}$  start flowing sinusoidally in the negative and positive directions respectively. Hence, resonant capacitor  $C_{r1}$  is discharging and capacitor  $C_{r2}$  is charging during this mode of the operation. The resonant currents increases from zero, thus  $S_1$  are turn-on with ZCS and dc source supplies power to be consumed by the load and stored in the resonant tank. Input current  $i_{in}$  is identical to the  $i_{Lr2}$  in this mode. This mode ends when the  $i_{Lr1}$  and  $i_{Lr2}$  becomes zero at time  $t=t_1$ . The equivalent circuit for this mode is illustrated in Figure 3(a). The equations of  $i_{Lr1}(t)$ ,  $v_{Cr1}(t)$ ,  $i_{Lr2}(t)$ , and  $v_{Cr2}(t)$  during this mode are given by

$$i_{Lr1}(t) = \frac{-\frac{V_{in}}{2} - \frac{V_o}{4k}}{Z_r} \sin \omega_r t \tag{3}$$

$$v_{Cr1}(t) = \left( -\frac{V_{in}}{2} - \frac{V_o}{4k} \right) (1 - \cos \omega_r t) + \frac{V_{in}}{2} + \frac{V_o}{2k} \quad (4)$$

$$i_{Lr2}(t) = \frac{\frac{V_{in}}{2} + \frac{V_o}{4k}}{Z_r} \sin \omega_r t \quad (5)$$

$$v_{Cr2}(t) = \left( \frac{V_{in}}{2} + \frac{V_o}{4k} \right) (1 - \cos \omega_r t) + \frac{V_{in}}{2} - \frac{V_o}{2k} \quad (6)$$

where  $\omega_r = \frac{1}{\sqrt{L_r C_r}}$ ,  $Z_r = \sqrt{\frac{L_r}{C_r}}$ ,  $L_r = L_{r1} = L_{r2}$ ,  $C_r = C_{r1} = C_{r2}$  and  $k = \frac{N_{S1}}{N_{P1}} = \frac{N_{S2}}{N_{P2}}$

**Mode 2 [ $t_1 \leq t \leq t_2$ ]:** At the beginning of this mode at time  $t=t_1$ , resonant currents,  $i_{Lr1}$  and  $i_{Lr2}$  start flowing through the anti-parallel diode,  $D_1$ , of the power switch,  $S_1$ . During this mode, the  $i_{Lr1}$  and  $i_{Lr2}$  swings sinusoidally in the positive and negative directions respectively. Therefore,  $S_1$  is turn off with ZCS and ZVS conditions. This mode ends when the  $i_{Lr1}$  and  $i_{Lr2}$  reach zero at  $t=t_2$ . The equivalent circuit related to this mode of operation is shown in Figure 3(b). The equations of  $i_{Lr1}(t)$ ,  $v_{Cr1}(t)$ ,  $i_{Lr2}(t)$  and  $v_{Cr2}(t)$  during this mode are given by

$$i_{Lr1}(t) = \frac{\frac{V_{in}}{2} - \frac{V_o}{4k}}{Z_r} \sin \omega_r \left( t - \frac{\pi}{\omega_r} \right) \quad (7)$$

$$v_{Cr1}(t) = \left( \frac{V_{in}}{2} - \frac{V_o}{4k} \right) \left( 1 - \cos \omega_r \left( t - \frac{\pi}{\omega_r} \right) \right) - \frac{V_{in}}{2} \quad (8)$$

$$i_{Lr2}(t) = \frac{-\frac{V_{in}}{2} + \frac{V_o}{4k}}{Z_r} \sin \omega_r \left( t - \frac{\pi}{\omega_r} \right) \quad (9)$$

$$v_{Cr2}(t) = \left( -\frac{V_{in}}{2} + \frac{V_o}{4k} \right) \left( 1 - \cos \omega_r \left( t - \frac{\pi}{\omega_r} \right) \right) + \frac{3V_{in}}{2} \quad (10)$$

**Mode 3 [ $t_1 \leq t \leq t_2$ ]:** At time  $t=t_2$ , the power switch,  $S_1$  are turn-off and the resonant currents,  $i_{Lr1}$  and  $i_{Lr2}$  are zero. As a result, the voltages across resonant capacitors  $v_{Cr1}$  and  $v_{Cr2}$  will be same as at time  $t=t_2$ . The minimum duration of this mode must be greater than zero to ensure DCM operation of the converter. Therefore, no energy transfer occurs from source to load during this mode. The equivalent circuit related to this mode of operation is shown in Figure 3(c). The equations of  $v_{Cr1}(t)$  and  $v_{Cr2}(t)$  during this mode are given by

$$v_{Cr1}(t) = \frac{V_{in}}{2} - \frac{V_o}{2k} \quad (11)$$

$$v_{Cr2}(t) = \frac{V_{in}}{2} + \frac{V_o}{2k} \tag{12}$$

**Mode 4 [ $t_2 \leq t \leq t_3$ ]:** This mode begins at time  $t=t_3$  when the resonant currents,  $i_{Lr1}$  and  $i_{Lr2}$  begin to flow through the power switch,  $S_2$ . The  $i_{Lr1}$  swings sinusoidally in the positive direction and the  $i_{Lr2}$  in the opposite direction. Therefore, the energy stored in the  $L_{r2}$  and  $C_{r2}$  during mode is transferred to the load. This mode ends when the  $i_{Lr1}$  and  $i_{Lr2}$  becomes zero at time  $t=t_4$ . The equivalent circuit for this mode is illustrated in Figure 3(d). The equations of  $i_{Lr1}(t)$ ,  $v_{Cr1}(t)$ ,  $i_{Lr2}(t)$ , and  $v_{Cr2}(t)$  during this mode are given by

$$i_{Lr1}(t) = \frac{\frac{V_{in}}{2} + \frac{V_o}{4k}}{Z_r} \sin \omega_r \left( t - \frac{T_s}{2} \right) \tag{13}$$

$$v_{Cr1}(t) = \left( \frac{V_{in}}{2} + \frac{V_o}{4k} \right) \left( 1 - \cos \omega_r \left( t - \frac{T_s}{2} \right) \right) + \frac{V_{in}}{2} - \frac{V_o}{2k} \tag{14}$$

$$i_{Lr2}(t) = -\frac{\frac{V_{in}}{2} - \frac{V_o}{4k}}{Z_r} \sin \omega_r \left( t - \frac{T_s}{2} \right) \tag{15}$$

$$v_{Cr2}(t) = \left( -\frac{V_{in}}{2} - \frac{V_o}{4k} \right) \left( 1 - \cos \omega_r \left( t - \frac{T_s}{2} \right) \right) + \frac{V_{in}}{2} + \frac{V_o}{2k} \tag{16}$$

**Mode 5 [ $t_3 \leq t \leq t_4$ ]:** At time  $t=t_4$  when the resonant currents,  $i_{Lr1}$  and  $i_{Lr2}$  begin flowing through anti-parallel diode,  $D_2$ , of the power switch,  $S_2$ , in the reverse direction. In this mode,  $S_2$  is turn-off under ZCS and ZVS conditions. In this mode, both resonant tanks transfer energy to the load. This mode ends when the  $i_{Lr1}$  and  $i_{Lr2}$  becomes zero at time  $t=t_5$ . The equivalent circuit related to this mode of operation is shown in Figure 3(e). The equations of  $i_{Lr1}(t)$ ,  $v_{Cr1}(t)$ ,  $i_{Lr2}(t)$ , and  $v_{Cr2}(t)$  during this mode are given by

$$i_{Lr1}(t) = \frac{-\frac{V_{in}}{2} + \frac{V_o}{4k}}{Z_r} \sin \omega_r \left( t - \frac{\pi}{\omega_r} - \frac{T_s}{2} \right) \tag{17}$$

$$v_{Cr1}(t) = \left( -\frac{V_{in}}{2} + \frac{V_o}{4k} \right) \left( 1 - \cos \omega_r \left( t - \frac{\pi}{\omega_r} - \frac{T_s}{2} \right) \right) + \frac{3V_{in}}{2} \tag{18}$$

$$i_{Lr2}(t) = \frac{\frac{V_{in}}{2} - \frac{V_o}{4k}}{Z_r} \sin \omega_r \left( t - \frac{\pi}{\omega_r} - \frac{T_s}{2} \right) \tag{19}$$

$$v_{Cr2}(t) = \left( \frac{V_{in}}{2} - \frac{V_o}{4k} \right) \left( 1 - \cos \omega_r \left( t - \frac{\pi}{\omega_r} - \frac{T_s}{2} \right) \right) - \frac{V_{in}}{2} \tag{20}$$

**Mode 6 [ $t_4 \leq t \leq t_5$ ]:** This mode is same with Mode 3, so the power switch,  $S_2$  is turn-off and the resonant currents  $i_{Lr1}$  and  $i_{Lr2}$  are zero. As a result, the voltages across resonant capacitors  $v_{Cr1}$  and  $v_{Cr2}$  will be constant as at time  $t=t_5$ . The equivalent circuit is shown in Figure 3(f) and equations of  $v_{Cr1}(t)$  and  $v_{Cr2}(t)$  are given by

$$v_{Cr1}(t) = \frac{V_{in}}{2} + \frac{V_o}{2k} \tag{21}$$

$$v_{Cr2}(t) = \frac{V_{in}}{2} - \frac{V_o}{2k} \tag{22}$$

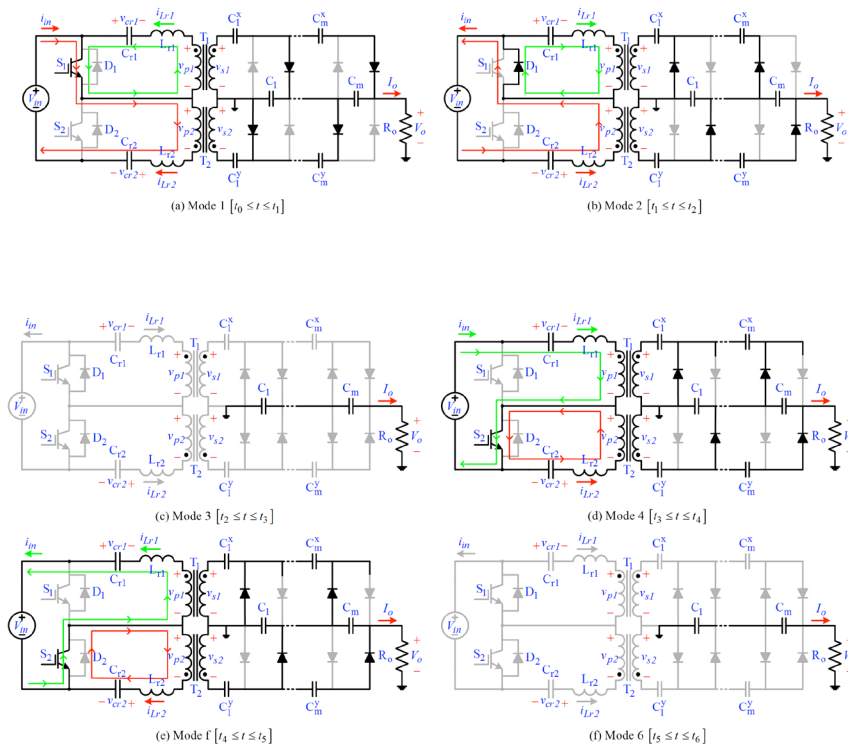


Figure 3. The equivalent circuit of the proposed resonant converter for each operation modes

## RESULTS AND DISCUSSIONS

A prototype of the proposed resonant converter was built and tested to validate the feasibility of the converter. The design specifications of the experimental prototype are as follows:  $V_{in}=100$  V,  $k=5$ ,  $f_r=75$  kHz,  $R_o=20$  k $\Omega$ ,  $C_r=C_{r1}=C_{r2}=110$  nF, and  $L_r=L_{r1}=L_{r2}=46$   $\mu$ H. Figure 4(a) and 4(b) shows the waveforms of the gate signal of the power switches  $V_{GE1}$  and  $V_{GE2}$  and resonant currents,  $i_{Lr1}$  and  $i_{Lr2}$  for switching frequency of 25-kHz and 35-kHz respectively. It can be observed that when the power switch,  $S_1$  is turned on,  $i_{Lr1}$  and  $i_{Lr2}$  flow sinusoidally in the

negative and positive direction respectively. When power switch  $S_2$  is turned-on, then  $i_{Lr1}$  and  $i_{Lr2}$  flow in the positive and negative direction respectively. Thus, the both resonant currents are inverted replica of each other. From the waveforms, power switches  $S_1$  and  $S_2$  are turned ON and OFF at ZCS. Thus, the switching losses are negligible.

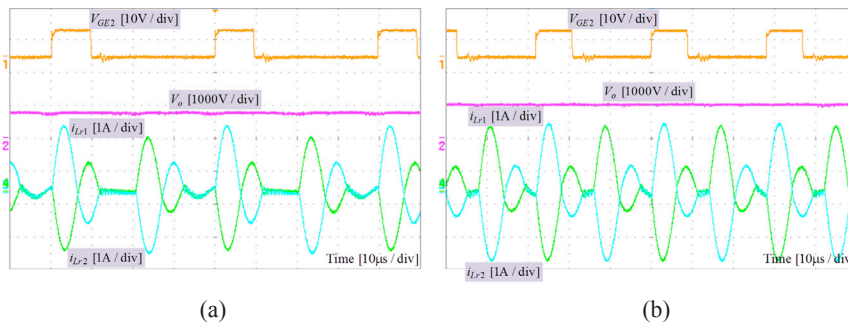


Figure 4. Experimental waveforms of the gate signal of the power switches,  $V_{GE1}$  and  $V_{GE2}$  and resonant currents,  $i_{Lr1}$  and  $i_{Lr2}$  for switching frequency (a) 25-kHz and (b) 35-kHz respectively

Figures 5(a) and 5(b) show the waveforms of the gate signal at the power switch, output voltage,  $V_o$  and resonant currents for switching frequency of 25-kHz and 35-kHz respectively. The output voltage and the amplitude of resonant currents are at the switching frequency of 25-kHz is 772-V and 3.5-A respectively. At the switching frequency 35-kHz, the output voltage and resonant currents is 1020-V and 4.2-A respectively. For a fixed value load resistance, the output voltage and resonant currents are increased when increasing the switching frequency

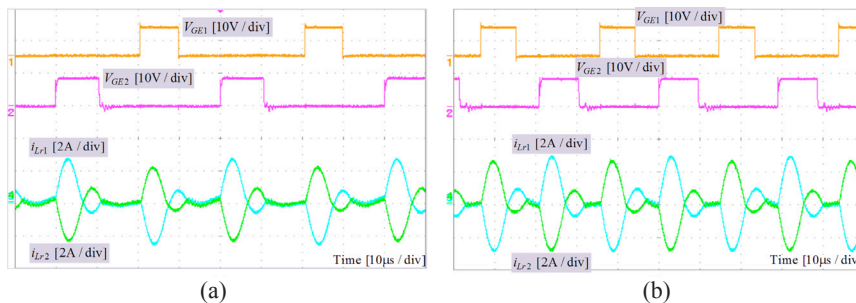


Figure 5. Experimental waveforms of the gate signal of the power switch, output voltage,  $V_o$  and resonant currents,  $i_{Lr1}$  and  $i_{Lr2}$  for switching frequency (a) 25-kHz and (b) 35-kHz respectively

Figures 6(a) and 6(b) shows the waveform of the resonant voltages,  $V_{Cr1}$  and  $V_{Cr2}$  and the resonant currents for the switching frequency of 25-kHz and 35-kHz respectively. It can be observed that resonant capacitors,  $C_{r1}$  and  $C_{r2}$  discharge and charge respectively when the power switches,  $S_1$  is turned on. Similarly, when the power switches,  $S_2$  is turned on,  $C_{r1}$  and  $C_{r2}$  charge and discharge respectively. The peak-to-peak voltages swing of the resonant



capacitors at the Figure 6(a) is smaller compared with Figure 6(b) because of the low switching frequency. Besides, the average resonant voltage  $V_{Cr1}$  and  $V_{Cr2}$  is equal to the  $V_{in}/2$  as shown in Figures 6(a) and 6(b).

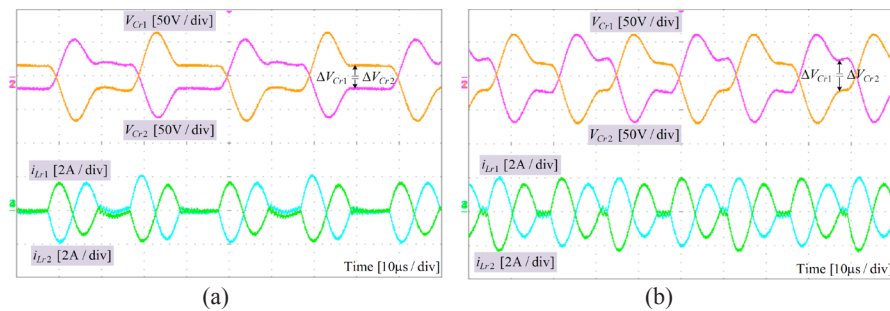


Figure 6. Experimental waveforms of the resonant voltages,  $V_{Cr1}$  and  $V_{Cr2}$  and resonant currents,  $i_{Lr1}$  and  $i_{Lr2}$  for switching frequency (a) 25-kHz and (b) 35-kHz respectively

## CONCLUSION

A double series resonant dc-dc converter with uniform voltage stress on high voltage transformers suitable for high output voltage applications has been proposed in this paper. Symmetrical voltage multiplier (SVM) is used to convert ac output voltage/current at the secondary transformer to dc ones. The SVM facilitates the decrease in the diode ratings, isolation requirement, and transformer turns ratio, as well as facilitates an increase in the total output filter capacitance. The input voltage of 100-V boosts up to 1020-V for switching frequency, 35-kHz with the resonant currents which is 4.2-A in this proposed converter. The proposed converter has shown lower switching losses because the power switches and output diodes operate with ZCS condition under DCM operation.

## ACKNOWLEDGEMENT

The authors would like to thank the Universiti Sains Malaysia for providing facilities and equipment to make this research possible. This work was supported by Research University Grant (RUI) 1001/PELECT/814207 from Universiti Sains Malaysia.

## REFERENCES

- Chakraborty, C., Ishida, M., & Hori, Y. (2002). Novel half-bridge resonant converter topology realized by adjusting transformer parameters. *Journal of IEEE Transactions on Industrial Electronics*, 49(1), 197-205.
- Jang, S. R., Ryoo, H. J., Kim, J. S., & Ahn, S. H. (2010). Design and analysis of series resonant converter for 30kW industrial magnetron. In *Proceedings of Conference on Industrial Electronics Society* (p.415-420). IEEE.

- Kulkarni, R. D., Bisht, D. S., Bhaumik, P. K., Vyas, H. P., & Sinha, R. K. (2000). High current regulated, variable DC power supplies for simulating power transients expected in nuclear reactors. In *Proceedings of International Conference on Industrial Technology* (p.530-535). IEEE.
- Li, J., Niu, Z., Zhang, Z., & Zhou, D. (2007). Analysis of Resonant Converter with Multiplier. In *Proceedings of Conference on Industrial Electronics and Applications* (p.326-331). IEEE.
- Pan, S., Pahlevaninezhad, M., & Jain, P. K. (2013). Adaptive hybrid primary/secondary-side digital control for series resonant DC-DC converters in 48V VR applications. In *Proceedings of Conference on Energy Conversion Congress and Exposition* (p.4920-4925). IEEE.
- Pijl, F. F. A. V. d., Castilla, M., & Bauer, P. (2009). Implementation of an adaptive sliding-mode control for a quantum series-resonant converter. In *Conference on Power Electronics and Applications* (p.1-10). IEEE.
- Singh, Y. V., Viswanathan, K., Naik, R., Sabate, J. A., & Lai, R. (2013). Analysis and control of phase-shifted series resonant converter operating in discontinuous mode. In *Proceedings of Conference on Applied Power Electronics and Exposition* (p.530-535). IEEE.
- Sze Sing, L., Iqbal, S., & Jamil, M. K. M. (2012). A novel ZCS-SR voltage multiplier based high-voltage DC power supply. In *Proceedings of International Conference on Circuits and Systems* (p.2092-2097). IEEE.
- Ye, Z., & Zhixiang, L. (2008). Modeling and design of a pulse phase modulated resonant inverter system. In *Proceedings of International Conference on Telecommunications Energy* (p.1-7). IEEE.

## PCA based Feature Extraction for Classification of Stator-Winding Faults in Induction Motors

Thanaporn Likitjarernkul\*, Kiattisak Sengchuai, Rakkrit Duangsoithong, Kusumal Chalermyanont\* and Anuwat Prasertsit<sup>1</sup>

*Department of Electrical Engineering, Faculty of Engineering, Prince of Songkla University, Hat Yai, Thailand*

### ABSTRACT

Nowadays, induction motors are widely used for many industrial processes. The shorted-turn fault of the stator-winding is the initial point of stator winding faults. This paper proposes using the Principal Component Analysis (PCA) to reduce the dimension of the feature set which is obtained from the Motor Current Signature Analysis (MCSA). The six original features consist of the signal power of the three-phase filtered current signal at 20 Hz to 80 Hz and 120 Hz to 180 Hz of the phases A, B and C. After using the PCA, the dimension of the feature set decreases to two new features. These two new features are then used to classify the shorted-turn phases of the stator-winding by applying the Artificial Neural Network (ANN) classifier. The experimental results demonstrate that the new feature set can decrease the complexity of the system. Additionally, the accuracy rate using the new feature set is higher than using the original feature set. Therefore, the new feature set can properly improve the efficiency of the classification.

*Keywords:* Induction motor, interturn short circuit fault, shorted-turn fault, stator-winding fault, Principal Component Analysis (PCA), Artificial Neural Network (ANN)

### ARTICLE INFO

*Article history:*

Received: 24 August 2016

Accepted: 02 December 2016

*E-mail addresses:*

L.thanapond@gmail.com (Thanaporn Likitjarernkul),

ak.kiattisak@hotmail.com (Kiattisak Sengchuai),

rakkrit.d@psu.ac.th (Rakkrit Duangsoithong),

kusumal.c@psu.ac.th (Kusumal Chalermyanont),

anuwat.p@psu.ac.th (Anuwat Prasertsit)

\*Corresponding Author

### INTRODUCTION

Induction motors are critical components of industries. Approximately 37% of the induction motor faults are those of stator-winding faults and the shorted-turn fault or the interturn short circuit fault of the stator-winding. (Bonaldi et al., 2012). Consequently, a shorted-turn fault detection system is necessary. The shorted-turn fault can be observed in harmonic components of the current signal. A popular detection method

for stator faults is the MCSA which is employed to analyse the motor faults by identifying the current spectra at harmonic components of faults (Jung et al., 2006; Thomson, 2001). The current spectra are calculated by using Fast Fourier Transform (FFT). The advantage of the MCSA is it does not encroach on the motor operations. Commonly, the MCSA method provides many features from the current spectra for the fault detection. These features can be reduced by a feature extraction to decrease the dimension of features and the complexity of the system. The feature extraction transforms the original feature set into a smaller number of features without eliminating the information of features. The combination of feature reduction and an Artificial Intelligence (AI) method for induction motor fault diagnosis can improve the performance of the system (Casimir et al., 2006; Widode et al., 2007; Lei et al., 2008; Do & Chong, 2011; Sawitri et al., 2012; Gholamshahi et al., 2014; Hammo, 2014; Yang et al., 2006).

This paper presents the feature extraction method to reduce the size of the feature set using the PCA. The reduced set of the new feature is used to classify the shorted-turn phases by applying the ANN classifier. The system is verified by experiments, and the experimental results reveal that using the new feature set can improve both the complexity and the accuracy of the system.

## STATOR-WINDING FAULTS

The shorted-turn fault in the stator-winding can be detected by using an air gap flux waveform. This waveform is changed by the distortion of the net MMF which is caused from the short circuit current flowed into the shorted circuit stator-winding. The harmonic frequency components of the air-gap flux waveform in a stator-winding current are calculated by (1),

$$f_{st} = f_i \left( \frac{n}{p} (1-s) \pm k \right) \quad (1)$$

where  $f_{st}$  is the harmonic frequency components,  $f_i$  is the supply frequency,  $p$  is the pole-pairs,  $s$  is the slip,  $k$  is 1, 3, 5, ... and  $n$  is 1, 2, 3, ..., respectively.

The harmonic frequency components depend on a load size which is related to the slip. Normally, the harmonic frequency components dominantly appear when calculation uses parameter  $k = 1$ ,  $n = 3$ , and  $k = 1$ ,  $n = 5$  (Thomson, 2001). In this paper, a three-phase, four-pole ( $p = 2$ ) induction motor is tested at no-load condition. Therefore, the frequency components that are used to detect the shorted-turn fault are 25, 50, 75, 100, 125, 150 and 175 Hz, respectively. The line current power spectra of phase A for the normal motor is shown in Figure 1(a). Whereas, Figure 1(b) shows the harmonic frequency components of the line current power spectra of phase A in a shorted-turn motor. Since spectra components occur at 125 Hz and 175 Hz, the shorted-turn fault can be identified.

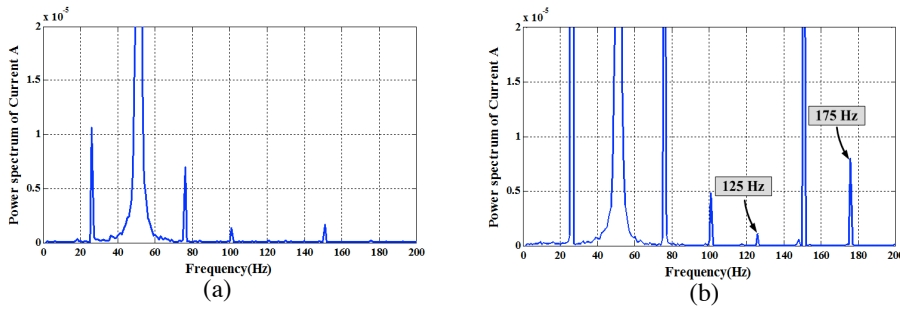


Figure 1. The current power spectra of the phase A (a) the normal motor; (b) the shorted-turn fault in the phase A

### FEATURE GENERATION

The three-phase current signals are measured and used to generate the original features. The original features are calculated by the following methods:

#### Signal power

The shorted-turn fault of the stator-winding can be detected by the air gap flux spectrum analysis. The ranges of the harmonic frequency components for the shorted-turn fault detection are 25, 50, 75, 100, 150, 125 and 175 Hz. Accordingly, each phase of the current signal is filtered by the band-pass filter at 20 Hz to 80 Hz and 120 Hz to 180 Hz. The filtered current signals are used to calculate the signal powers as expressed by (2),

$$P = \frac{1}{N} \sum_{n=1}^N x_n^2 \tag{2}$$

where  $P$  is the signal power,  $x$  is the band-pass filtered signal and  $N$  is the number of samples.

#### Normalization of Data

Since the signal power values at 20 Hz to 80 Hz and at 120 Hz to 180 Hz are very different, then these values should first be normalised. The signal power of each phase is normalised by the min-max normalisation technique. The normalised value can be calculated by (3)

$$x^* = \frac{x - \min(x)}{\max(x) - \min(x)} \tag{3}$$

where  $x^*$  is the normalised value and  $x$  is the signal power value.

### PRINCIPAL COMPONENT ANALYSIS

The feature extraction is one of the methods used for reducing the feature dimension. The PCA (Jolliffe, 1986) is one of the examples of the feature extraction. The dimension of features is reduced by the PCA without eliminating the signal information. The PCA is a technique that

transforms an original feature set into a smaller feature set. The smaller feature set is transformed by using a function that related to the eigenvectors and eigenvalues. The procedures of the PCA have 4 steps. In the first step, the original feature set is used to calculate a covariance matrix as expressed by (4).

$$C_{ij} = \frac{1}{n-1} \sum_{m=1}^n (x_{im} - \bar{x}_i)(x_{jm} - \bar{x}_j) \quad (4)$$

Where  $C_{ij}$  is the covariance matrix between the feature  $i$  and the feature  $j$ ,  $x_{im}$  is the sample  $m$  of the feature  $i$ ,  $\bar{x}_i$  is the average value of the feature  $i$ ,  $x_{jm}$  is the sample  $m$  of the feature  $j$ ,  $\bar{x}_j$  is the average value of the feature  $j$  and  $n$  is the number of samples.

In the second step, the eigenvectors and eigenvalues of the covariance matrix are calculated using (5) and (6), respectively.

$$\mathbf{A} \cdot \mathbf{v} = \lambda \cdot \mathbf{v} \quad (5)$$

$$|\mathbf{A} - \lambda \mathbf{I}| = 0 \quad (6)$$

Where  $\mathbf{A}$  is the covariance matrix,  $\mathbf{v}$  is the eigenvector,  $\lambda$  is the eigenvalue and  $\mathbf{I}$  is the identity matrix.

In the third step, the principal components are the eigenvectors which are selected from the eigenvalue ranking. Finally, the fourth step, the smaller feature set is calculated by (7). The smaller feature set is the new feature set which is used to classify the shorted-turn fault of the stator-winding.

$$\mathbf{Y} = (\mathbf{v}^T \times \mathbf{X})^T \quad (7)$$

Where  $\mathbf{Y}$  is the new feature set matrix,  $\mathbf{X}$  is the original feature set matrix and  $\mathbf{v}$  is the eigenvector.

## ARTIFICIAL NEURAL NETWORK CLASSIFICATION

The ANN is a type of classifier. It is a model that is inspired from the study of biological neural networks. A perceptron is one type of the ANNs that it has many models depended on the number of the hidden layer and the hidden cell. In this paper, a single layer perceptron is used. The perceptron has a learning algorithm for classification and make adjustments to the weights of input and the biases of hidden layer. The updated weights and the updated biases are calculated by (8) and (9), respectively and the output is calculated by (10). The output is calculated by a transfer function which estimates the output by using the total product between the weight vector and the input vector. An error between the output and the target can be calculated by (11). Finally, the last weights and the last biases are used to classify the shorted-turn fault of the stator-winding.

$$\mathbf{W}_{k+1} = \mathbf{W}_k + e_k \cdot \mathbf{p}^T \tag{8}$$

$$b_{k+1} = b_k + e_k \tag{9}$$

$$a_k = f(\mathbf{W}_k \times \mathbf{p} + b_k) \tag{10}$$

$$e_k = t - a_k \tag{11}$$

Where  $\mathbf{w}_{k+1}$  is the new weight matrix,  $\mathbf{w}_k$  is the old weight matrix,  $e_k$  is the error,  $p$  is the input vector,  $b_{k+1}$  is the new bias,  $b_k$  is the old bias,  $a_k$  is the output,  $f$  is the transfer function and  $t$  is the target.

### EXPERIMENTAL SETUP

The three-phase, four-pole, star-connected induction motor is used for the experiment as shown in Figure 2. The motor parameters and ratings are also illustrated in Table 1. The three-phase current signals are measured by three current sensors. National Instrument (NI) data acquisition device at 6,000 Hz sampling rate are used. These measured current signals are filtered at 20 Hz to 80 Hz and 120 Hz to 180 Hz. Then, the filtered signals are used to calculate the power signal, and the results are normalised by (2) and (3), respectively. Therefore, the normalised value is the original feature set which is reduced the dimension of features by the PCA. The block diagram of the experiment is presented in Figure 3. As mentioned before, this paper uses the ANN classifier. Classes of the fault classification include [0 0], [0 1], [1 0] and [1 1]. These classes mean a normal motor and shorted-turn faults in the phase A, B and C, respectively. The total data set contains of six features and 160 samples. The 80 samples are used as the training set, and the 80 samples are used as the test set.

Table 1  
Parameters and ratings of test machines

V	Hz	r/min	kW	cosØ	A
230Δ/400Y	50Hz	1430	2.2	0.79	8.66/4.98
415Y	50Hz	1435	2.2	0.765	4.94

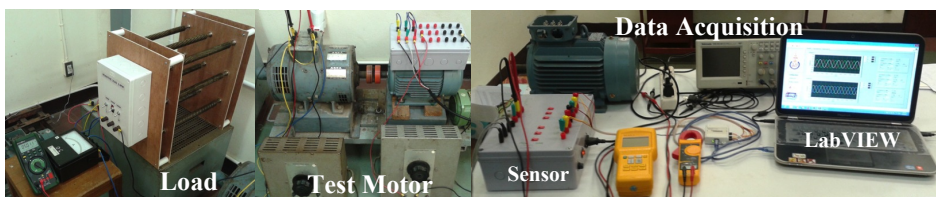


Figure 2. The experimental setup

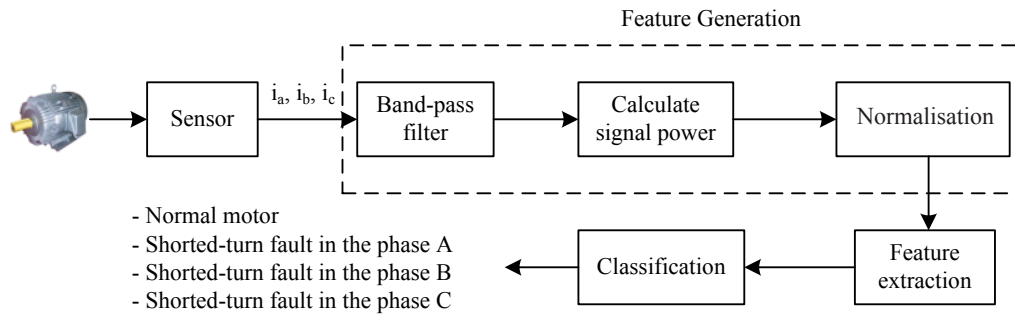


Figure 3. The block diagram of the experiment

### EXPERIMENTAL RESULTS

The original data set has six features: the signal power of the 20 Hz to 80 Hz filtered signal and the 120 Hz to 180 Hz filtered signal in the phase A, B and C. The signal power values are normalised between zero to one. The original data set is reduced the size by the PCA. The PCA can extract up to two features. The two new features can be plotted the scattered graph as presented in Figure 4. From the graph, classes of the fault classification are clearly separated. The new feature set is used to create the learning system. The learning results are also shown in Table 2. From the learning results, it found that the new feature set uses less number of training epoch than the original feature set for all ratio of the train/test data. Similarly, the new feature set has less numbers of error samples than the original feature set. Finally, the efficiency of the classification is illustrated in Table 3. According to such results, the new feature set has the number of training and the classification error less than the original feature set. The new feature set provides an accuracy rate that is higher than the original feature set. As reason of the result, the new feature set is the reduced feature set, but it does not eliminate the information of features. Therefore, the new feature set can decrease the complexity of the system and increase the accuracy rate of the classification system.

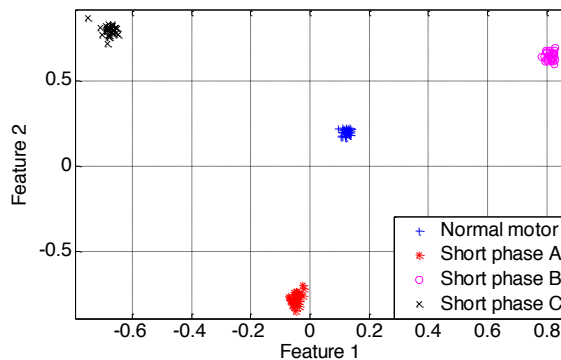


Figure 4. The scattered graph of the new features



Table 2  
The number of training

Train/Test (%)	With the PCA		Without the PCA	
	Epochs	Error	Epochs	Error
30/70	5	0/112	134	4/112
50/50	4	0/80	46	3/80
70/30	3	0/48	40	1/48

Table 3  
The number of training

	Classification (Perceptron ANN)	
	With the PCA	Without the PCA
Training sets	80	80
Test sets	80	80
Epochs	4	46
Classification error (%)	0	3.75
Accuracy rate (%)	100	96.25

## CONCLUSION

This paper is on using the PCA to reduce the dimension of features. The new feature set is used to classify the shorted-turn fault of the stator-winding. Based on our experimental results, the six original features remained in only two new features. This new feature set can decrease the complexity of the classification system. The accuracy rate using the new feature set is 100% and could improve the fault classification system.

## ACKNOWLEDGEMENT

This work has been financial support from the Prince of Songkla University Graduate Studies Grant, No, PSU/95000201/2556, Prince of Songkla University funding contact number ENG560014S and partially supported by Center of Excellence in Wireless Sensor Networks (CoE-WSN), Faculty of Engineering, Prince of Songkla University, Hat Yai, Songkhla, Thailand.

## REFERENCES

- Bonaldi, E. L., de Oliveira, L. E. L., Borges da Silva, J. G., Lambert-Torres, G., & Borges da Silva, L. E. (2012). Predictive maintenance by electrical signature analysis to induction motors. In R. E. Araujo (Eds), *Induction Motors Modelling and Control*. InTech.
- Casimir, R., Boutleux, E., Clerc G., & Yahoui, A. (2006). The use of feature selection and nearest neighbors rule for faults diagnostic in induction motors. *Engineering Applications of Artificial Intelligence*, 19, 169-177.

- Do, V. T., & Chong, U.-P. (2011). Signal model-based fault detection and diagnosis for induction motors using features of vibration signal in two-dimension domain. *Journal of Mechanical Engineering*, 57(9), 655-666.
- Gholamshahi, R., Poshtan, J., & Poshtan, M. (2014). Improving stator winding fault diagnosis in induction motor using dempster-shafer theory. *Electrical and Electronics Engineering: An International Journal (ELELIJ)*, 3(2), 161-173.
- Hammo, R. (2014). *Faults identification in three-phase induction motors using support vector machines*. Spring.
- Jolliffe, I. T. (1986). *Principal Component Analysis*. New York: Springer-Verlag.
- Jung, J.-H., Lee, J.-J., & Kwon, B.-H. (2006). Online diagnosis of induction motors using MCSA. *IEEE Transactions on Industrial Electronics*, 53(6), 1842-1852.
- Lei, Y., He, Z., & Zi, Y. (2008). A new approach to intelligent fault diagnosis of rotating machinery. *Expert Systems with Applications*, 35, 1593-1600.
- Sawitri, D. R., Purnama, I. E., & Ashari, M. (2012). Detection of electrical faults in induction motor fed by inverter using support vector machine and receiver operating characteristic. *Journal of Theoretical and Applied Information Technology*, 40(1), 15-22.
- Thomson, W. T. (2001). On-line MCSA to diagnose shorted turns in low voltage stator windings of 3-phase induction motors prior to failure. *Proceedings of IEEE Conference on Electrical Machines and Drives (IEMDC)* (p. 891-898).
- Widode, A., Yang, B.-S., & Han, T. (2007). Combination of independent component analysis and support vector machines for intelligent faults diagnosis of induction motor. *Expert Systems with Applications*, 32, 299-312.
- Yang, B.-S., Han, T., & Yin, Z.-J. (2006). Fault diagnosis system of induction motors using feature extraction, feature selection and classification algorithm. *JSME International Journal*, 49(3), 734-741.

## Effect of Boron and Oxygen Doping to Graphene Band Structure

Siti Fazlina bt Fauzi\* and Syarifah Norfaezah bt Sabki

School of Microelectronic Engineering, Universiti Malaysia Perlis (UniMAP), Kampus Pauh Putra, 02600 Arau, Perlis

### ABSTRACT

Graphene band structure can be modulated when dopant atoms are introduced into graphene sheets. As a result, there is flexibility in design and optimisation of electronic devices. In this study, the effects of atomic doping to graphene band structure were investigated by using boron and oxygen as dopant atoms. Different dopant concentrations and dopant locations in graphene sub lattices were studied by using a 4x4 graphene sub lattice which consists of 32 carbon atoms. Results show that both dopants cause opening of energy band gap of mono layer graphene. The highest energy band gap ( $E_g$ ) value for graphene doped with boron is 0.52 eV and the highest  $E_g$  value for graphene doped with oxygen is 1.67 eV, in which both results are obtained for highest dopant concentration and farthest dopant's distance in a graphene sheet. This shows that higher dopant concentration and farther dopant's location in a graphene sheet lead to higher energy band gap.

*Keywords:* Graphene, band structure, band gap, boron, oxygen, atomic doping

### INTRODUCTION

Graphene is a carbon allotrope arranged in a honeycomb lattice with an atomically thin layer. It has attracted interest among researchers due to its excellent physics properties as well as its electrical and

mechanical properties. Due to this, a lot of new applications have been explored using graphene, especially as an alternative to replace silicon based transistor. However, monolayer graphene is a zero bandgap material, which means the conduction band and the valence band of graphene meet at one point. It is known that band gap is the difference of energy between the lowest point of conduction band and the highest point of valence band. Band gap also refers to the amount of energy needed to excite the electron in the valence to the conduction band so that electricity can be conducted. Due to that, a band gap is needed in a respective

#### ARTICLE INFO

*Article history:*

Received: 24 August 2016

Accepted: 02 December 2016

*E-mail addresses:*

sitifazlina\_f@yahoo.com (Siti Fazlina bt Fauzi),

norfaezah@unimap.edu.my (Syarifah Norfaezah bt Sabki)

\*Corresponding Author

value so that there will be a clear state where the device can be turned on and off. Therefore, a lot of measures have been taken in order to open a band gap in graphene. For instance, there are studies that had been carried out by applying electric field to bilayer graphene which have resulted in band gap due to the breaking of inversion symmetry between two layers (McCann, 2006; Castro et al., 2007, Oostinga et al., 2008). However, this method reduced the mobility carrier of graphene (Oostinga et al., 2008), in which high mobility carrier can only be obtained in monolayer graphene. Carrier mobility is often observed in determining performance of devices. Maintaining high carrier mobility in monolayer graphene as well as creating a band gap are crucial. Few methods that have been carried to open a band gap in monolayer graphene. Modifying the edge structures such as quantum dots /antidotes (Fujita et al., 1996, Nakada et al., 1996, Son et al., 2006) and nano ribbons (Singh et al., 2010; Fu et al., 2009) have shown that band gap can be opened in monolayer graphene. However, tuning the band gap magnitude by using this method is difficult due to the complexity in controlling the edge structure (Takahashi et al., 2014). Another method that has been proposed to open a band gap in monolayer graphene is by applying uniaxial strain to the graphene sheet (Ni et al., 2008, 2009). However, this method requires a very strong strain in order to open a band gap in monolayer graphene. Doping graphene sheets with heteroatoms (Denis et al., 2009, Dai et al., 2009) is found to be better in creating band gap in monolayer graphene whilst maintaining its high carrier mobility and with better control.

This paper examines the effect of boron and oxygen doping in graphene band structure. Both atoms are known to have the ability to increase the energy band-gap of graphene, Boron is recognised as a P-type dopant when it is included in graphene (Rani et al., 2013) and oxygen is chosen as the dopant due to its atom size which is quite similar to the size of carbon atom and the ability of its valence electrons to make bonds with carbon atoms. In this paper, boron and oxygen atoms are introduced in monolayer graphene sheets in graphene band structure.

## METHODOLOGY

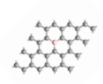
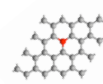
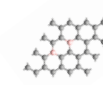
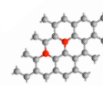
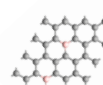
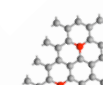
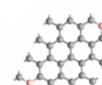
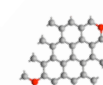
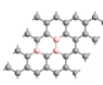
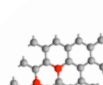
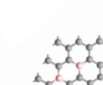
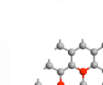
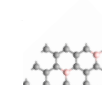
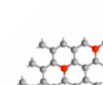
The simulation has been performed using the Atomistix Tool Kit (ATK) simulator by Quantumwise. The band structure of the monolayer graphene sheet is calculated using the semi-empirical Huckel (SE Huckel) calculator. The SE Huckel is able to calculate the band structure of doped graphene faster than the density functional theories (DFT) calculator because it uses simpler models. However, the results from the SE Huckel are similar to the results obtained from DFT calculator.

To perform the simulation, initially, a graphene sheet of 4 x 4 lattices with 32 carbon atoms is made. Boron and oxygen atoms in the graphene sheet are added in different concentrations. The dopant atoms are inserted in the graphene sub lattices in 1, 2 and 3 atoms, which provide 3%, 6% and 9% dopant concentration respectively. The dopant atoms are also arranged in such a way that they are in the same and different sub lattices.

As shown in Table 1, boron atom in the same graphene sub lattice is labelled B1. Boron atoms in different sub lattices are divided into two different positions, which are represented by boron in sub lattice 2 and 3, labelled as B2 and B3 respectively. The same position and

concentration arrangement are also applied for oxygen atoms, and labelled as O1, O2 and O3. The dopant atoms in sub lattice 2 involves the inclusion of dopant atoms in two neighbouring sub lattices, while the dopant atoms in sub lattice 3 separates the dopant atoms in the farthest distance. The dopant atoms arrangement in the graphene sheet is shown in Table 1 below.

Table 1  
Structure of monolayer graphene doped with boron (B) and oxygen (O) atoms at different concentrations and different locations

Dopant concentration	Boron in same sub lattice (B1)	Oxygen in same sub lattice (O1)	Boron in different sub lattice 1 (B2)	Oxygen in different sub lattice 1 (O2)	Boron in different sub lattice 2 (B3)	Oxygen in different sub lattice 2 (O3)
3 %						
6 %						
9 %						

## RESULTS AND DISCUSSION

### Monolayer graphene doped with boron

The inclusion of boron in the graphene sheet changes the properties of graphene into p-type. This is due to the lower number of electron valence in boron compared with carbon that results in the Fermi level of graphene shifting below the Dirac point (or also known as K point). With the Fermi level, the band gap opening is also expected to occur with the inclusion of boron in graphene. As shown in Figure 1 for graphene doped with boron in the same sub lattice (B1) (refer Table 1), the opening of band gap is observed for all 3 different concentrations, with energy gap of 0.16 eV for 3%, 0.21 eV for 6% and 0.37 eV for 9% boron concentration. The linear increment of this energy gap is in agreement with previous studies (see for example, Rani et al., 2013); however, it is slightly different in terms of value. It is suggested that this band gap opening at the K point of monolayer graphene with the inclusion of boron atoms is caused by the broken symmetrical hexagonal structure in the graphene sub lattices (Rani et al., 2013).

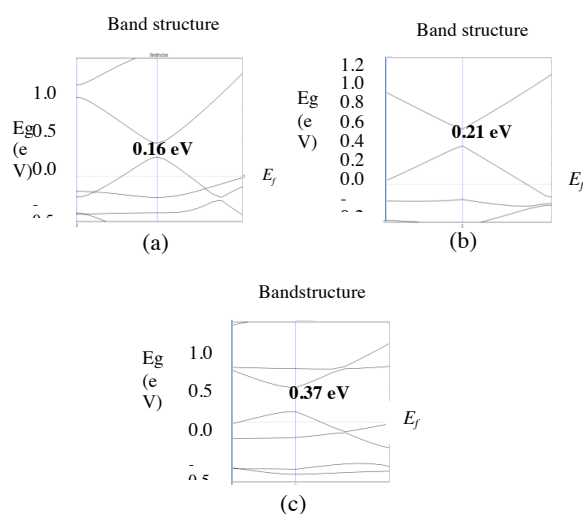
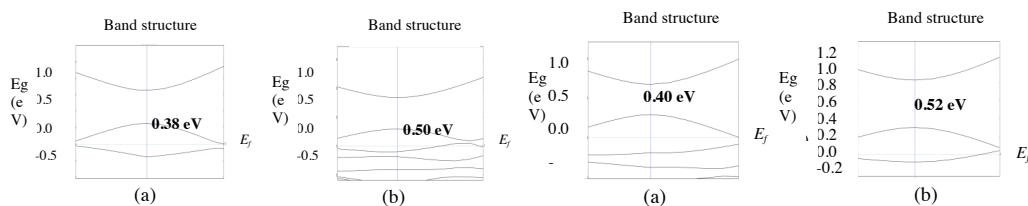


Figure 1. Band structures of graphene doped with boron in the same sub lattice (B1). The boron concentrations are at (a) 3 %, (b) 6% and (c) 9%

The effect of dopant atoms at different graphene sub lattice 1 (B2) is shown in Table) at the same concentration of boron at 6% and 9%. Boron concentration of 6% produces 0.38 eV energy bandgap and 9% produces 0.5 eV energy bandgap, which are higher than energy gap shown in Figure 1. This shows that different locations of boron atoms in the graphene sub lattices plays an important role in altering the graphene band gap at K point. This may happen due to the symmetry in the triangular sub-lattices of graphene formed by the hetero-atoms.

For boron doped in different sub lattice 2 (B3), the energy band structures are shown in Figure 3(a). The energy band gap for 6 % of boron concentration gives the highest value of 0.40 eV compared to 6% boron concentration doped in the same sub lattices (B1) and in different sub lattice 1 (B2). This shows that the distance between each boron atom affects the value of energy bandgap. This result is consistent with the findings of Rani et al. (2013). The same trend is also observed for 9 % of boron concentration doped in different sub lattice 2 (B3) with energy band gap of 0.52 eV, which is also the highest value compared with the 9% boron concentration doped in same sub lattice (B1) and in different sub lattice 1 (B2). The band structures for graphene doped with boron atoms caused the Fermi level to be lower than the top of valence band. This could be because the boron atom has 3 valence electrons, which introduces more holes in the valence band than electrons in the conduction band. The Fermi level shows the probability of holes to occupy lower energy levels in the valence band. The complete results for energy bandgap of boron doped graphene are shown in Table 2.



*Figure 2.* Band structures of graphene doped with boron in different sub lattice 1 (B2). The boron concentrations are at (a) 6% and (b) 9%

*Figure 3.* Band structures of graphene doped with boron in different sub lattice 2 (B3). The boron concentrations are at (a) 6% and (b) 9%

### Monolayer graphene doped with oxygen

As shown in Figure 3 for graphene doped with oxygen in the same sub lattice (O1) (Refer Table 1), the opening of band gap is observed for all three different concentrations, with energy gap of 0.40 eV for 3%, 0.50 eV respectively for 6% and 0.63 eV for 9% boron concentration. The linear increment of this energy gap is also consistent with findings of previous study (Rani et al., 2013) though it is slightly different in the value. The energy gaps for graphene doped with oxygen atoms are larger compared with graphene doped with boron atoms. This may be suggested by the excitation energy for electrons in oxygen that is higher than boron. The number of valence electrons in oxygen and boron also may give rise to this effect. As mentioned earlier, this band gap opening at the K point of monolayer graphene with the inclusion of oxygen atoms is also caused by the broken symmetrical hexagonal structure in the graphene sub lattices (Rani et al., 2013).

For dopant atoms at different graphene sub lattice 1 (O2) (refer Table 1) in Figure 4, boron concentration of 6% produces 0.67 eV energy band gap and 9% produces 0.71 eV energy band gap, which are higher than energy gaps obtained in Figure 4 and also higher than energy gaps for graphene doped with boron as in Figure 2.

For boron doped in different sub lattice 2 (O3) (refer Table 1), the energy band structures are shown in Figure 5. The energy band gap for 6% of oxygen concentration gives the value of 0.93 eV which is higher than 6% oxygen doped in the same sub lattices (O1) and in different sub lattice 1 (O2). The same trend is also observed for 9% of oxygen concentration doped in different sub lattice 2 (O3) with energy band gap of 1.67 eV, which is also higher than 9% oxygen doped in the same sub lattice (O1) and in different sub lattice 1 (O2). The band structures for graphene doped with oxygen atoms caused Fermi level to be higher than the minimum level of conduction band. This happens due to the 6 valence electrons in oxygen that introduce higher number or electrons in the conduction band. The Fermi level shows the probability for electrons to occupy higher levels in the conduction band. The complete results for energy band gap of graphene doped with oxygen are shown in Table 2.

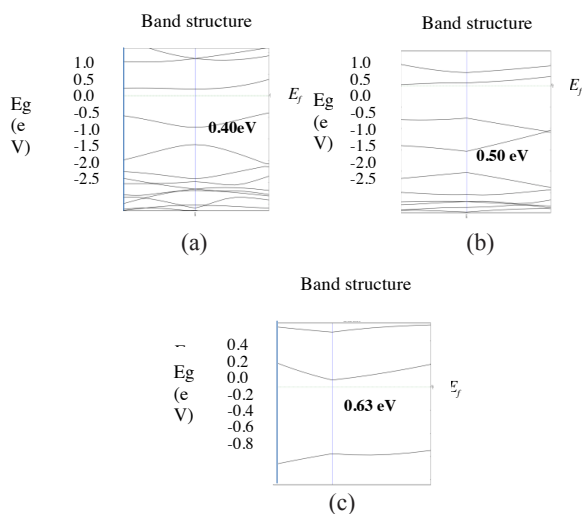


Figure 4. Band structure for graphene doped with oxygen in the same sub lattice (O1). The oxygen concentrations are at (a) 3 %, (b) 6% and (c) 9%

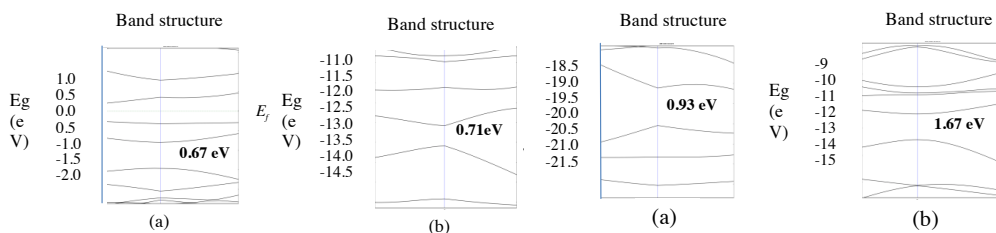


Figure 5. Band structures for graphene doped with oxygen in different sub lattice 1 (O2). The oxygen concentrations are at (a) 6% and (b) 9%

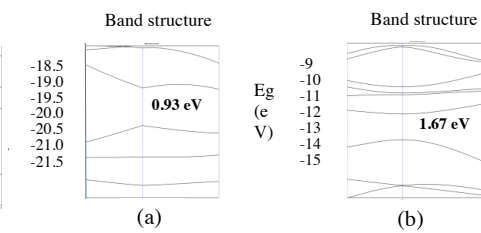


Figure 6. Band structures for graphene doped with oxygen in different sub lattice 2 (O3). The oxygen concentrations are at (a) 6% and (b) 9%

Table 2

Energy band gap for monolayer graphene doped with boron (B) and oxygen (O) at different dopant concentrations and different locations

Dopant concentration [%]	B1	O1	B2	O2	B3	O3
	[Electron Volt - eV]					
3 %	0.16	0.40	0.21	0.40	0.21	0.40
6 %	0.21	0.50	0.38	0.67	0.40	0.93
9 %	0.37	0.63	0.50	0.71	0.52	1.67

## CONCLUSION

The band structure of graphene doped with boron and oxygen atoms are investigated and the energy band gaps of graphene are observed. For graphene doped with boron atoms, the Fermi



level is lower than the top of the valence band, which suggests that there is a probability that majority of holes are occupying the valence band. For graphene doped with oxygen, the Fermi level is higher than the bottom of the conduction band, which suggests that there is a probability that majority of electrons are occupying the conduction band. This suggests the mobility carriers (electrons) in graphene doped with oxygen is higher than graphene doped with boron. It was also observed that higher dopant concentration contributes to larger energy band-gap. The location of dopant atom in a graphene sheet also affect the energy band-gap, whereas the farther the distance between dopant atoms the higher the energy gap. This work shows that graphene band gap is tunable and can be easily controlled using dopant atoms. This tunable band gap is crucial for the design and optimisation of high performance electronic devices.

## REFERENCES

- Castro, E. V., Novoselov, K. S., Morozov, S. V., Peres, N. M. R., Dos Santos, J. L., Nilsson, J., ... & Neto, A. C. (2007). Biased bilayer graphene: semiconductor with a gap tunable by the electric field effect. *Physical Review Letters*, 99(21), 216802.
- Fujita, M., Wakabayashi, K., Nakada, K., & Kusakabe, K. (1996). Peculiar localized state at zigzag graphite edge. *Journal of the Physical Society of Japan*, 65(7), 1920-1923.
- Fürst, J. A., Pedersen, J. G., Flindt, C., Mortensen, N. A., Brandbyge, M., Pedersen, T. G., & Jauho, A. P. (2009). Electronic properties of graphene antidot lattices. *New Journal of Physics*, 11(9), 095020.
- J. Dai, J. Yuan, P. Giannozzi, (2009). *Appl. Phys. Lett.* 95 232105.
- McCann, E. (2006). Asymmetry gap in the electronic band structure of bilayer graphene. *Physical Review B*, 74(16), 161403.
- Nakada, K., Fujita, M., Dresselhaus, G., & Dresselhaus, M. S. (1996). Edge state in graphene ribbons: Nanometer size effect and edge shape dependence. *Physical Review B*, 54(24), 17954.
- Ni, Z. H., Yu, T., Lu, Y. H., Wang, Y. Y., Feng, Y. P., & Shen, Z. X. (2008). Uniaxial strain on graphene: Raman spectroscopy study and band-gap opening. *ACS Nano*, 2(11), 2301-2305.
- Oostinga, J. B., Heersche, H. B., Liu, X., Morpurgo, A. F., & Vandersypen, L. M. (2008). Gate-induced insulating state in bilayer graphene devices. *Nature Materials*, 7(2), 151-157.
- P.A. Denis, R. Faccio, A.W. Momburu, (2009). *ChemPhysChem* 10 715.
- Rani, P., & Jindal, V. K. (2013). Designing band gap of graphene by B and N dopant atoms. *RSC Advances*, 3(3), 802-812.
- Singh, A. K., Penev, E. S., & Yakobson, B. I. (2010). Vacancy clusters in graphene as quantum dots. *ACS Nano*, 4(6), 3510-3514.
- Son, Y. W., Cohen, M. L., & Louie, S. G. (2006). Energy gaps in graphene nanoribbons. *Physical Review Letters*, 97(21), 216803.
- Takahashi, T., Sugawara, K., Noguchi, E., Sato, T., & Takahashi, T. (2014). Band-gap tuning of monolayer graphene by oxygen adsorption. *Carbon*, 73, 141-145.





## Seasonal Variation of Transmission Line Outages in Peninsular Malaysia

I. Mohamed Rawi<sup>1,2\*</sup>, M.Z.A. Ab-Kadir<sup>2</sup> and M. Izadi<sup>2</sup>

<sup>1</sup>Tenaga Nasional Berhad, Brickfields, 50470 Kuala Lumpur, Malaysia

<sup>2</sup>Centre for Electromagnetic and Lightning Protection Research (CELP), Universiti Putra Malaysia, 43400 UPM, Serdang, Selangor, Malaysia

### ABSTRACT

Researchers have observed the impact of climate changes on overhead line outages. It is known that overhead lines are very prone to lightning strikes due to their height and location which are normally in an open and exposed area. Studies have also reported that transmission and distribution lines experience very high failure rates due to lightning strikes. The tropics experience greater lightning activities and have higher peaks where transmission lines suffer frequent line outages. This paper examined studies that have been conducted on line outages due to lightning activities, especially in the tropical areas. Lightning detection system is also discussed as well as how to evaluate line performance. Seasonal variation of lightning occurrences and line outage pattern help to predict lightning occurrences and to optimise a suitable power protection system of overhead lines. It has been widely reported that lightning occurrences and line outages are significantly related and lightning activity was more prevalent during inter monsoon seasons.

*Keywords:* Transmission lines, lightning performance, lightning, tropical weather

### INTRODUCTION

Tropical countries experience more frequent line outages due to lightning flash density

peculiar to the climate. During certain periods of the year, lightning activities are higher and these observations help researchers understand line outage pattern of high voltage systems. Studies also suggest the use of surge protection devices, improve footing resistance and increase insulation level. To date, there has been no agreement among researchers on the best solution for optimising the arrester location on the phases or towers along the line. There is also mismatch with regards to the principle used for estimating line performance.

#### ARTICLE INFO

##### Article history:

Received: 24 August 2016

Accepted: 02 December 2016

##### E-mail addresses:

[iryansirawi@gmail.com](mailto:iryansirawi@gmail.com) (I. Mohamed Rawi),

[mzk@upm.edu.my](mailto:mzk@upm.edu.my) (M. Z. A. Ab-Kadir),

[aryaphase@yahoo.com](mailto:aryaphase@yahoo.com) (M. Izadi)

\*Corresponding Author

This paper discussed practical approaches in electric utilities for evaluating and improving transmission line performance where monsoon or seasonal variation resulted in transmission line outages (Ahmad, Yahya, & Alam, 2008). It also reviews data from lightning detection network (LDN) to evaluate line performance. The methods prescribed by different researchers to predict and manage the issue with line outages are summarised and discussed and future research topics are recommended in this paper.

## LIGHTNING IN TROPICAL COUNTRIES

Tropical countries are located within the “tropics” - a region of the Earth surrounding the Equator, delimiting in altitude by the Tropic of Cancer and Tropic of Capricorn. It is also known as the “torrid zone”. The tropics include all areas on the Earth where Sun reaches a point directly from overhead at least once during every solar year. Observed by NASA and NASDA, analysed by many, world lightning maps were generated in terms of thunder days (or keraunic level) and ground flash density level (GFD). Over the years, it has been reported that lightning occurrences were highest in the tropics (Graham, n.d.). There are 103 tropical countries which encompasses the region of North America, Central America, South America, Caribbean, Central Africa, East Africa, West Africa and Southeast Asia.

Keraunic level was the earliest method used for measuring lightning intensity. It was an acceptable method with inevitable flaws. It is measured in thunder days per year, depending on the number of observation stations. It is also not possible to know the severity of lightning strikes and measurement including cloud-to-cloud lightning, which contributes to 90% of lightning and clearly does not affect system performance. Modern sensors were later invented capable of locating the strike location, discharge time, crest current and it’s polarity and multiplicity of return stroke (Ahmad et al., 2008). The entire lightning detection system (LDS) measures lightning as GED in flashes per km<sup>2</sup> per year. Data from LDS are very important for users to optimise their design and avoid overspending on the cost of the design (Bouquegneau,

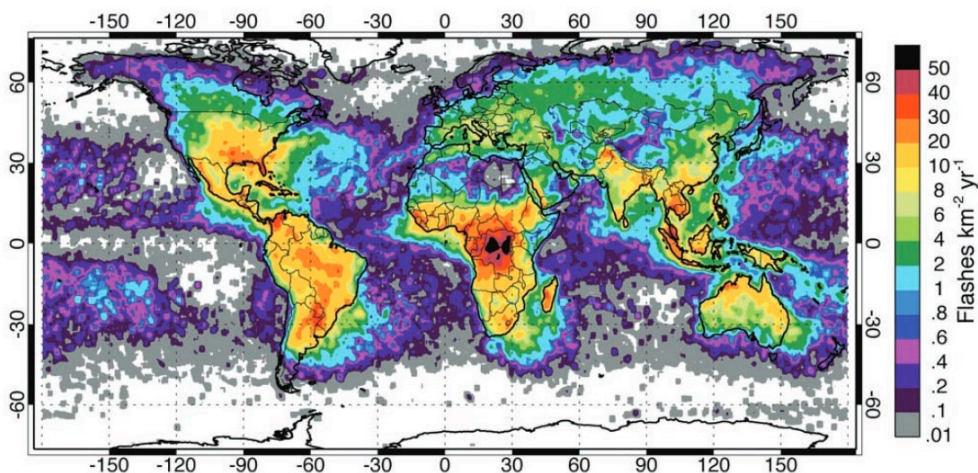


Figure 1. Annualised distribution of total lightning activity in flashes per km<sup>2</sup> per year

2014). Figure 1 shows an intense 50 flashes per km<sup>2</sup> per year in Central Africa and as low as 2 flashes per km<sup>2</sup> per year in Central Europe. These two areas shall not use the same design of (surge protective devices). From the map, areas around the equator experience lightning activity as high as 50 flashes per km<sup>2</sup> per year, referred as ground flash density or isokeraunic level.

Mean annual flash rate in the tropics are also very high (Cecil, Buechler & Blakeslee, 2014), notably in Central Africa. It is also very important to note that observed flash rate in the Malaysia region is between 10 and 30 flashes per km<sup>2</sup> per year.

In the tropics, lightning occurrences are higher in certain months. It is also reported that Southeast Asia has sharp increases of lightning activity in April, particularly Bangladesh which experiences high flash rates in April to May. This is due to shifts in the season from pre-monsoon to monsoon which increases the progression of thunderstorm activity (Cecil et al., 2014). Indonesia and Malaysia have very similar double-peak activity where lightning activity increases in April and October (Ab Kadir et al., 2012; Zoro & Mefiardhi, 2005).

Table 1  
*Lightning statistics*

Description	Location	Source	Value
Average positive flash polarity	South East Brazil <sup>Note 1</sup>	(Pinto et al., 1996)	35%
	Peninsular Malaysia <sup>Note 1</sup>	(Mohamed, 2011)	23.0%
	Peninsular Malaysia <sup>Note 2</sup>	(Abdullah, Yahaya, & Hudi, 2008; Abdullah & Hatta, 2012)	17.6%
Average peak amplitude	Pekan area, Malaysia	(Ibrahim & Ghazali, 2012)	32kA
	Peninsular Malaysia	(Abdullah et al., 2008)	37kA
	Northern Australia	(Abdullah et al., 2008)	37kA
	Java Island, Indonesia	(Abdullah et al., 2008)	37kA (+) 41kA (-)
Highest peak amplitude	Peninsular Malaysia	(Abdullah et al., 2008)	484.4kA
	Japan (non-tropic)	(Takami & Okabe, 2007)	130.2kA
Frequent lightning activity	Peninsular Malaysia	(Kadir et al., 2012; Abdullah et al., 2008; Mohamed, 2011)	April – May Oct – Nov
	Bangladesh	(Cecil et al., 2014)	April - May

<sup>Note 1</sup> One year observation period

<sup>Note 2</sup> Period of observation was for eight years

Table 1 shows that in the tropics, positive flashes are higher, where positive lightning discharges account for 10% or less of global cloud-to-ground lightning activity (Rosa et al., 2000). Average peak amplitude was observed to be around 32kA to 37kA (positive) and 41kA (negative). Peak amplitude of lightning current was also found to be very high compared with other non-tropical countries. A common inter-monsoon period in tropical countries, namely April to May and October to November, indicated higher lightning activities.

## **LIGHTNING DETECTION NETWORK**

### **Use of LDN in performance study**

The Malaysian Meteorological Department (MET) measures the keraunic level in terms of thunder-days ( $T_d$ ) per year. The MET reports that the average recorded thunder-days in Malaysia (specifically in KLIA, Sepang) is 309 per year. The highest recorded thunder-days was in Subang in 1987 where 362 days were reported with lightning activities (Malaysian Meteorological Department, 2016). This analysis was based on readings from 36 weather stations until 2010. However,  $T_d$  was not accurate for system analysis due to several weaknesses, such as its inability to distinguish between intra-cloud lightning which does not harm the system and cloud to ground strokes which could damage it. Furthermore, the counting was limited to the weather stations in nearby areas and level of lightning intensity (kA) was not measured (Whitehead & Driggans, 1990).

The situation has changed after the successful installation and operation of TNB Lightning Detection Network (LDN) in 1994 which has helped researchers to conduct a more holistic lightning study and analysis, thus optimising the system design. Noradlina et al. (2008) reported that over nine million lightning strikes were recorded between 2004 and 2007 while 11.1 million strikes were recorded between 2008 and 2011, taking into account 3.7 million flashes reported with mean multiplicity of three strokes per flash observed by LDN. The system has an accuracy of 500m and 95% detection efficiency whereby it is able to detect lightning 600km from the sensors. The IMPACT ESP sensors uses Time-of-arrival (TOA) and Magnetic Direction Finding (MDF) method in order to satisfy the accuracy and efficiency requirements (Abdullah et al., 2008).

### **Stroke counts and polarities**

In evaluating lightning performance, it is also important to know the stroke polarity. Previous researches have predicted that between 5% and 10% of lightning occurrences are positive flashes. However, percentage of positive flash occurrences are above the stated predicted value, especially in tropical areas. Pinto et al., (1996) observed 63.4% negative and 35.0% positive stroke polarity and the rest are bipolar flashes in Southeastern Brazil between 1992 and 1993. Earlier studies in Malaysia have reported yearly lightning stroke polarity count ranged from the ratio of 69:31 to 86:14 between negative to positive strokes (see Table 2).

Table 2  
*Observation on lightning polarities in Peninsular Malaysia*

Year	Negative strokes	Percentage	Positive strokes	Percentage
2004	1,835,053	69%	843,089	31%
2005	1,681,775	86%	277,417	14%
2006	2,448,549	86%	404,613	14%
2007	1,049,653	85%	187,249	15%
2008	3,131,865	85%	552,645	15%
2009	2,347,809	80%	586,953	20%
2010	1,684,101	82%	369,681	18%
2011	1,997,610	86%	325,194	14%

## TRANSMISSION LINE PERFORMANCE

### Reported line performance by electric utilities

Electric utility companies face a high number of line outages due to lightning. In Southern China for example, statistics indicated about 70% of line outages are resulted from lightning activities (Zhao et al., 2013) while in Brazil, CEMIG declared 67% of transmission line outages are due to the same cause (Cherchiglia et al., 2002). In Indonesia, 66% of 150kV line outages were reported to be due to lightning (Warmi & Michishita, 2015). Similarly, in Australia, Gillespie and Stapleton (2004) reported 40.5% of 275kV network outages were due to lightning.

In evaluating overhead line performance, a list of available standards such as IEEE Std. 1410 an IEEE Std. 1243 can be used. However, it is always a challenge for users from the tropical countries as these standards and procedures are generally designed to be used in non-tropical countries such as United States of America, Canada and Europe (Baharuddin, Abidin, & Hashim, 2006). A recent work by CIGRE WG C4.410 specified calculated on high voltage line performance ranging from 4.7 to 4.9 flashes per km<sup>2</sup> per year which are incomparable to the GFD value in tropical countries which typically are between 10 and 30 flashes per km<sup>2</sup> per year (See Table 3).

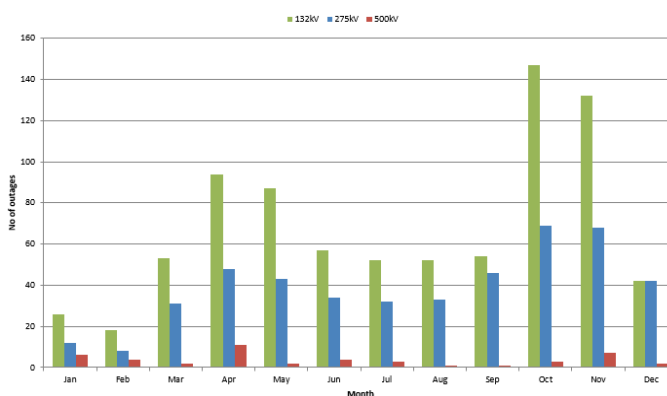


Figure 2. Transmission line outages due to lightning in peninsular Malaysia (from 2002 – 2015)



Table 3  
*Observation on line outage rates in electric utilities*

No	Utility or line name	Country	Tower footing resistance ( $\Omega$ )	No. of shield wires	Line voltage (kV)	Outage rate (per 100km/yr)
Tropical countries						
1	CEMIG	Brazil			34.5	62
2	CEMIG	Brazil			69	40
3	CEMIG	Brazil			138	30.33
4	Angostura-B	Mexico	15	2	115	14.55
5	KKRI-GMSG	Malaysia	10	2	132	4.26
6	ATWR-BTRK	Malaysia	5	2	500	0.51
Non-tropical countries						
1	Ontario-Hydro	Canada	200	1	115	5.72
2	NEA	Australia	10	1	132	1.86
3	ECNSW	Australia			132	4.47
4	Com. Edison	USA			138	4.97
5	Tokyo	Japan			140	2.24
6	TVA	USA	30	2	161	1.99
7	Seq. to Charleston	USA			161	3.83
8	S. Jackson to Cordova	USA			161	0.55
9	SECV	Australia	28	1	220	1.02
10	CIGRE line #30				230	0.24
11	Tokyo	Japan			250	1.12
12	ECNSW	Australia			330	0.93
13	OVEC	USA	5	1	345	4.72
14	CIGRE line #31				345	3.44
15	Johns to Cordova	USA			500	0.3
16	Brown F. to West P.	USA			500	0.94
17	CSPG	China		2	500	0.74
18	Powerlink	Australia	10 - 20		132	3.3
19	Powerlink	Australia	10 - 20		275	0.3 – 0.7
20	Powerlink	Australia	10 - 20		330	0.3 – 0.7

In peninsular Malaysia, transmission line consists of 132 kV, 275kV and 500kV systems. From 2002 until 2015, total number of outages were recorded and compared with the lightning activity throughout the year.

Figure 2 shows a double-peak pattern on the total number of line outages in peninsular Malaysia for all transmission line system voltages i.e. 132kV, 275kV and 500kV. From the statistics, outages due to lightning are higher between April to May and between October to November. This pattern was observed in the annual lightning activities which are also higher during the monsoon interchange season, i.e. inter-monsoon period which are notably from April to May and October to November (Ab Kadir et al., 2012)



## CONCLUSION

In tropical countries, higher outage rate due to lightning is observed. It is therefore important to have extra protection on the transmission lines to avoid frequent interruptions on the power systems by installing transmission line arresters, adopting special grounding designs to provide lower tower footing resistance, installing additional earth wires to provide additional shielding on the phase conductor and increase system insulation level i.e. insulation string length. Lightning activity increases in the tropics during inter-monsoon seasons which are between April to May and October to November. This is consistent with the number of transmission line outages observed in peninsular Malaysia where higher number of outages were reported during these periods. Therefore, extra precautions have to be taken by the system grid owner or the electric utility companies before lightning peak season sets in. This is to avoid recurrence of line outages on overhead transmission lines. Continuous observation on the LDN data is essential to understand lightning behaviour in this lightning-prone region especially with regards to the monsoonal variation.

## REFERENCES

- Ab Kadir, M. Z. A., Misbah, N. R., Gomes, C., Jasni, J., Wan Ahmad, W. F., & Hassan, M. K. (2012). Recent statistics on lightning fatalities in Malaysia. In *31st International Conference on Lightning Protection, ICLP 2012* (p. 5). <http://doi.org/10.1109/ICLP.2012.6344337>
- Abdullah, N., & Hatta, N. M. (2012). Cloud-to-Ground Lightning Occurrences in Peninsular Malaysia and Its Use in Improvement of Distribution Line Lightning Performances. In *IEEE International Conference on Power and Energy (PECon)* (pp. 819–822).
- Abdullah, N., Yahaya, M. P., & Hudi, N. S. (2008). Implementation and Use of Lightning Detection Network in Malaysia. In *2nd IEEE International Conference on Power and Energy (PECon 08)* (pp. 383–386).
- Ahmad, H., Yahya, M. P., & Alam, M. A. (2008). *Recent Advances in Lightning Detection and Protection Studies*. (Z. A. Malek, Ed.) *Universiti Teknologi Malaysia* (1st ed.). Penerbit Universiti Teknologi Malaysia. Retrieved from [www.penerbit.utm.my](http://www.penerbit.utm.my)
- Baharuddin, M. Z., Abidin, I. Z., & Hashim, A. H. (2006). Application of Lightning Performance Analysis for a Tropical Climate Country. In *1st International Power and Energy Conference PECon* (pp. 590 – 595).
- Bouquegneau, C. (2014). The Need for an International Standard on Lightning Location Systems. In *23rd International Lightning Detection Conference*.
- Cecil, D. J., Buechler, D. E., & Blakeslee, R. J. (2014). Gridded lightning climatology from TRMM-LIS and OTD: Dataset description. *Atmospheric Research*, *135-136*, 404–414. <http://doi.org/10.1016/j.atmosres.2012.06.028>
- Cherchiglia, L. C., F., A. C., Reis, R. J. dos, & Amorim, G. E. (2002). CEMIG experience in Improving Transmission Line Lightning Performance using a Lightning Location System. In *CIGRE 2002* (pp. 1–6).
- Graham, A. (n.d.). List Of Tropical Countries - Tropical. Retrieved from <http://www.hobotraveler.com/tropical/list-of-tropical-countries.php>

- Ibrahim, W. I., & Ghazali, M. R. (2012). An Overview of Pekan Lightning Detection System ( PLDS ). In *IEEE International Conference on Power and Energy (PECon)* (pp. 1–6).
- Malaysian Meteorological Department. (2016). Maklumat Iklim. Retrieved from [http://www.met.gov.my/index.php?option=com\\_content&task](http://www.met.gov.my/index.php?option=com_content&task)
- Mohamed, M. (2011). Lightning in the Peninsular Malaysia. *Malaysia Meteorological Department*. Retrieved from [http://www.lightningsafety.com/nlsi\\_lhm/lightning-protection-malaysia-2011.pdf](http://www.lightningsafety.com/nlsi_lhm/lightning-protection-malaysia-2011.pdf)
- Pinto, O. J., Gin, R. B. B., Pinto, I. R. C. A., Mendes, O. J., Diniz, J. H., & Carvalho, A. M. (1996). Cloud-to-ground lightning flash characteristics in southeastern Brazil for the 1992–1993 summer season. *Journal of Geophysical Research: Atmospheres*. <http://doi.org/10.1029/96JD01865>
- Rosa, F. de la, Cummins, K., Deller, L., Diendorfer, G., Galvan, A., Use, J., ... Uman, M. A. (2000). *Characterization of Lightning for Applications in Electric Power Systems (WG 33.01.02)*.
- Takami, J., & Okabe, S. (2007). Observational Results of Lightning Current on Transmission Towers. *IEEE Transactions on Power Delivery*, 22(1), 547–556. <http://doi.org/10.1109/TPWRD.2006.883006>
- Warmi, Y., & Michishita, K. (2015). A Study on Lightning Outages on the 150 Kv Transmission Line of Payakumbuh – Koto Panjang in West Sumatra in Indonesia. In *19th International Symposium on High Voltage Engineering* (pp. 23–28).
- Whitehead, J., & Driggans, R. (1990). TVA'S Experience with the SUNYA Lightning Detection Network. *IEEE Transactions*, 5(4), 2054–2062.
- Zhao, X., Xie, Y., He, H., He, J., Chen, X., & Cai, H. (2013). Lightning Performance Assessment of 500kV Transmission Lines in Southern China. In *IEEE PES Power and Energy Society* (pp. 1–5).
- Zoro, R., & Mefiardhi, R. (2005). Lightning Performance on Overhead Distribution Lines : Field Observation at West Java - Indonesia. In *Power Engineering Conference (IPEC)* (pp. 1–6).

## **FDTD Computational Simulation for SAR Observation towards Breast Hyperthermia Cancer Procedure**

**Kasumawati Lias<sup>1\*</sup> and Norlida Buniyamin<sup>2</sup>**

*<sup>1</sup>PhD Student, Faculty of Electrical Engineering, Universiti Teknologi MARA (UiTM), 40450, Shah Alam, Selangor, Malaysia*

*<sup>2</sup>Associate Professor, Faculty of Electrical Engineering, Universiti Teknologi MARA (UiTM), 40450, Shah Alam, Selangor, Malaysia*

---

### **ABSTRACT**

The radiation absorption distribution of electromagnetic energy into the breast phantom is of fundamental importance in understanding its therapeutic capability emitted by the microstrip applicator for non-invasive hyperthermia procedure. In this paper simple microstrip applicator with rectangular shape is presented. Different operating frequency were investigated to observe radiation absorption distribution, which is measured through specific absorption rate (SAR) parameter. The operational frequency was 915MHz and 2450MHz, the industry, scientific and medical (ISM) frequency range. As simulated by using the finite difference time-domain (FDTD) computational simulation which is known as SEMCAD X solver, the results shed an interesting observation on the SAR when frequency varies, which is shown by the transformation onto the penetration depth and focusing capability onto the breast area to be treated.

*Keywords:* Non-invasive, hyperthermia, SAR, microstrip applicator

---

### **INTRODUCTION**

Evolution in computational electromagnetics has significantly contributed towards the rapid development of novel antenna designs. The

computational electromagnetics is presented by various numerical techniques include the method of moments (MoM), finite element method (FEM) and the finite difference time-domain (FDTD) method, which have been well developed over the years. As a consequence, numerous commercial software packages have emerged. With a powerful personal computer and advanced numerical techniques or commercial software, complex engineered electromagnetic materials in antenna designs can be arrived at.

---

#### **ARTICLE INFO**

*Article history:*

Received: 24 August 2016

Accepted: 02 December 2016

---

*E-mail addresses:*

danza252@gmail.com (Kasumawati Lias),

nbuniyamin@salam.uitm.edu.my (Norlida Buniyamin)

\*Corresponding Author

#### Nomenclature

MoM is method of moment

FEM is finite element method

FDTD is finite difference time-domain

SAR is specific absorption rate

ALARA is as low as reasonably achievable

EFS is effective field size

E field is electric field

Therefore, the exploration on antenna application in medical therapy is conducted with FDTD computational packages known as SEMCAD X to obtain the specific absorption rate (SAR) outcomes on the shape, depth penetration and focusing capability of the electromagnetic antenna. In this study, microstrip antenna or applicator was used. The medical therapy studied is known as hyperthermia cancer procedure. Hyperthermia is an alternative procedure for cancer, using slightly high heat about 41°C – 45°C in order to denature the cancer tissue into the necrotic tissue (Choi, Kim, Kim, & Yoon, 2014; Nguyen, Abbosh, & Crozier, 2015; Rajendran, 2015). The electromagnetic fields have a great influence on the behaviour of all the living systems. The radiation contributes from the electromagnetic may results harmful health effect, especially in case of long exposures to low such as power system. This imposes by as low as reasonably achievable (ALARA) principle (Plewako, Krawczyk, & Grochowicz, 2003). Nevertheless, some benefits can be taken from the effects of the electromagnetic fields on the living being such as hyperthermia cancer procedure, which is discussed and investigated further in this work. As in industrial application, the electromagnetic computation is utilised at early investigation as to allow a better knowledge of the phenomena, and for the purpose of this research, it is allows an optimised design for hyperthermia. SAR is observed as to provide the information on two essential parameters for the hyperthermia, which are penetration depth and focusing capability either both parameters are satisfied enough or vice versa.

Hyperthermia can be either invasive or non-invasive and depends on the position of hyperthermia applicator i.e. whether it is penetrating the body through the skin or radiate from outside the body. Since, non-invasive method may produce less side effects, the investigation of this method is emphasized. According to the mechanisms of heat deposition in tissues by electromagnetic fields, which is discussed in (Plewako et al., 2003), when the tissue's electric dipoles (both permanent and induced) oscillate in response to the E-field of an applied wave, heat is generated by a process analogous to friction. When free charges (electrons and ions) in the tissue are set in motion by the E-field, collisions with immobile atoms and molecules in the tissue generate heat (Plewako et al., 2003). The propensity of the tissue to produce heat for a given sinusoidal E- field magnitude is determined by the values of the imaginary part of its relative permittivity  $\epsilon''$  and its conductivity  $\sigma$  (Plewako et al., 2003). It is important that the internal E-field is responsible for the heat generation. In addition, the internal H-field is not

directly responsible for heating because tissue has a permeability  $\mu$  close to that of free space with no magnetic losses. But the time-varying H-field produces a resulting internal E-field and in this way it causes heating of tissue (Plewako et al., 2003).

Early age of hyperthermia procedure, three heating techniques are applied, which known as capacitive, inductive and radiative. They offer towards simplicity, insensitive with coupling condition and deep penetration, respectively. However, the main deficiency share by these 3 heating techniques, where the penetration depth and fields generated in the tissue are not optimum and this condition may affect other surrounding healthy tissue in negative ways. Currently, there are many types of applicators have been developed and investigated such as in (Choi, Lim, Yoon, & Member, 2016; Ovidio, Bucci, Crocco, Scapatucci, & Bellizzi, 2016) as to obtain the improvement in delivering heat into the targeted treated cancerous tissue. Varieties of results have been shown. Each of the paper aims in providing an improvement towards the investigated therapy through the use of electromagnetic fields, which then transferred in body into heat. Based on the previous works, electromagnetic hyperthermia deficiencies include the penetration depth, focusing, skin burns problem and difficult to control the required temperature for the procedure. Thus, the research is emphasized in determining the improving heating through the utilization of electromagnetic field, which produces by the antenna. The microstrip is selected to be used in this investigation. The microstrip can be developed with small size, lightweight and can be structured either in single or array. Furthermore, the characters of this antenna far outweighs of its limitations. The microstrip also has provided the utmost results towards hyperthermia cancer procedure as discussed in previous works (Drizdal, Togni, & Vrba, 2007; K. B. Lias, Ahmad Narihan, & Buniyamin, 2014; K. Lias & Buniyamin, 2013; Yin, Li, & Li, 2012). In hyperthermia for cancer procedure, the E field, which is produced by the microstrip patch is of prime consideration is transferred in the body into heat. Based on the bioelectromagnetism law (Jaakko Malmivuo & Robert Plonsey, 1995), the energy transferred from the magnet, B field through forces on permanent magnetic dipoles is not prominent in electromagnetic (EM) biological interaction, since most of the biological tissue is nonmagnetic, which means it is contains very few permanent magnetic dipoles.

Radiation is absorbed and distributed towards the cancerous tissue and measured by a measurement parameter known as the specific absorption rate (SAR). The SAR, which is provided in equation (1) is defined as transferred power as in equation (2) divided by the mass of the object. The unit for SAR is W/kg or mW/g.

$$SAR = \frac{\sigma}{2\rho} |E|^2 \quad (\text{W/kg or mW/g}) \tag{1}$$

With  $\sigma$  is the conductivity of tissue (S/m),  $E$  is an electric field (V/m),  $\rho$  is a density of tissue (kg/m<sup>3</sup>).

$$P = \sigma E^2 \quad (\text{W}) \tag{2}$$

The microstrip impacts towards the radiation absorption are observed for hyperthermia cancer procedure with breast is selected as the treated cancerous area.

## RESEARCH METHODOLOGY

The research methodology is conducted with 3 main parts, which are the development of microstrip antenna or also called as a microstrip applicator in hyperthermia for cancer procedure, construction of breast phantom and water bolus, which is integrated in order to provide cooling environment onto the skin surface, where the heat is delivered. The microstrip applicator is developed with 2 different operating frequencies; 915MHz and 2450MHz, which contributes towards different sizes of the applicator. In order to construct the microstrip applicator, the length (L) and width (W) of the rectangular patch is first to be calculated by using the following equations (3) – (9).

$$w = \frac{c}{2f} \times \sqrt{\frac{2}{\epsilon_r + 1}} \quad (3)$$

where  $w$  is the patch antenna width,  $f$  is the operational frequency,  $\epsilon_r$  is the substrate permittivity and  $c$  is the speed of electromagnetic (EM) wave in vacuum, which equal to  $3 \times 10^8 \text{ms}^{-1}$ .

$$\epsilon_{eff} = \frac{\epsilon_r + 1 + \frac{\epsilon_r - 1}{2} \left( 1 + \frac{10h}{w} \right)^{-0.5}}{2} \quad (4)$$

where  $\epsilon_{eff}$  is the effective permittivity of the microstrip line,  $h$  is the thickness of the substrate. The value of the characteristic impedance used mostly  $50\Omega$  and  $75\Omega$ . For this research, the  $50\Omega$  transmission line is used.

$$L_{eff} = \frac{c}{2f \sqrt{\epsilon_{eff}}} \quad (5)$$

$$\Delta L = 0.412 \times h \times \frac{\epsilon_{eff} + 0.3}{\epsilon_{eff} - 0.258} \times \frac{h}{w} \times \frac{w + 0.264}{h + 0.8} \quad (6)$$

$\Delta L$  is used when considering the fringing effect, where  $L_{eff}$  and  $\epsilon_{eff}$  are changed. The fringing effect is resulted due to the propagating of EM wave at the outside of the patch.

$$L = L_{eff} - \Delta L \quad (7)$$

$$L_g = 6h + L \quad (8)$$

$$W_g = 6h + w \quad (9)$$

The substrate used is FR-4 with 2mm thickness and  $\epsilon_r = 4$ . Then, the breast phantom is constructed. The phantom breast tumour/cancer is positioned 100mm deep from the outer side of the breast skin. The radius for breast fat is 100mm, while the breast tumour phantom has a radius of 50mm. The electrical and thermal properties of the breast phantom are tabulated in Table 1. Last but not least is the development of water bolus, which is utilized in providing a cooling environment onto the skin surface of the heating area during hyperthermia procedure

execution. Thickness of the water bolus may affect the shape and the effective field size (EFS) of the SAR distribution pattern (Jaakko Malmivuo & Robert Plonsey, 1995). Water bolus using distilled water as a coolant fluid with  $\epsilon_r$ ,  $\sigma$  and  $\rho$  are 76.7, 5e-005 and 1000, respectively. The illustration of the proposed hyperthermia design of simulation (DoS) for cancer procedure is provided in Figure 1. The FDTD package, SEMCAD X is used to carry out the simulation process in order to obtain the SAR distribution into the breast for hyperthermia procedure. SEMCAD X is a Speag product, which is affordable of toolsets for antenna design and general EM/Thermal simulation. Important theory behind FDTD is firstly proposed by Yee in the year of 1966 (Kulas & Mrozowski, 2011).

Table 1  
Breast Phantom Electrical and Thermal Properties

915MHz					
	Relative Permittivity, $\epsilon_r$	Electrical Conductivity, $\sigma$ (S/m)	Density, $\rho$ (kg/m <sup>3</sup> )	Specific Heat Capacity, C (J/kg/K)	Thermal Conductivity, K (W/m/K)
Breast Fat	4.699	0.1251	1000	2348.33	0.209
Breast Cancer/ Breast Tumour	48.362	2.6531	1000	2352.55	0.789
2450MHz					
Breast Fat	2.884	1.1179	1000	2348.33	0.209
Breast Cancer/ Breast Tumour	18.254	30.2181	1000	2352.55	0.789
Breast Fat	2.884	1.1179	1000	2348.33	0.209
Breast Cancer/ Breast Tumour	18.254	30.2181	1000	2352.55	0.789

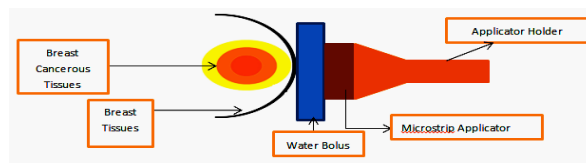


Figure 1. Illustration of the Proposed Applicator for Hyperthermia Cancer Procedure

## RESULT AND DISCUSSION

Based on the equations (3) – (9), the rectangular microstrip applicator specifications for 915MHz and 2450MHz are as tabulated in Table 2. The arrangement for the purpose of this simulation study is demonstrated in Figure 2. The EM simulation is conducted in order to obtain the  $S_{11}$ , E field and SAR distribution pattern. The  $S_{11}$  for 915MHz and 2450MHz are presented in Figure3, where it shows that the  $S_{11}$  for 915MHz and 2450MHz is around -13dB and -17dB, respectively. Based on the bioelectromagnetism interaction, the penetration of electromagnetic fields into biological tissues is decreased as frequency increases.

Table 2  
Rectangular Microstrip Applicator Parameters

915MHz	2450MHz
Length (L) = 83mm	Length (L) = 30mm
Width (W) = 104mm	Width (W) = 39mm
Ground Length (Lg) = 95mm	Ground Length (Lg) = 44mm
Ground Width (Wg) = 118mm	Ground Width (Wg) = 51mm

The frequency and wavelength are related proportionally or asynchronously, while penetration depth and wavelength is synchronously related. The frequency-wavelength relationship is described in equation (10) and equation (11) presents the depth penetration-wavelength relationship.

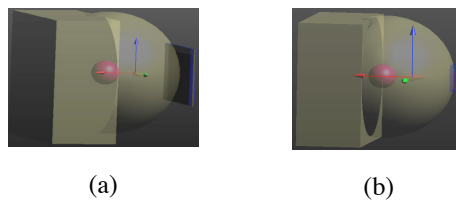


Figure 2. Full arrangement of hyperthermia for cancer procedure (a) 915MHz (b) 2450MHz

$$f = \frac{c}{\lambda} \tag{10}$$

Where  $f$  is frequency,  $c$  is the speed of light,  $3.0 \times 10^8 \text{ ms}^{-1}$  and  $\lambda$  is wavelength.

$$D = \frac{I}{2 \left[ \frac{2\pi}{\lambda} \sqrt{\epsilon} \left( 1 + \frac{\sigma}{\omega \epsilon_0 \epsilon} \right)^{0.5} \right]^2} \tag{11}$$

Where  $\lambda$  is a wavelength,  $\epsilon$  is a material permittivity,  $\epsilon_0$  is a permittivity of free space,  $\sigma$  is the conductivity of tissue (S/m),  $\omega$  is an angle frequency.

The  $\left[ \frac{2\pi}{\lambda} \sqrt{\epsilon} \left( 1 + \frac{\sigma}{\omega \epsilon_0 \epsilon} \right)^{0.5} \right]^2$  is known as absorption coefficient ( $\alpha$ ). By that, the equation (11) can be simplified to equation (12).

$$D = \frac{I}{2\alpha} \tag{12}$$

In Table 3, it is observed that electric field changes when the applicator distance is altered. The yellow colour represents the hottest temperature. When the distance is increased, the E field value is decreased. However, the E field distribution is insignificantly changed especially in term of the shape when the distance is increased. E field is transferred in the body into heat, which is the desired outcome of the hyperthermia procedure. When we observed from Table



3, the E field value is higher for 2450MHz than 915MHz. This is theoretically supported by the Planck-Einstein equation, equation (13).

$$E = hf = \frac{hc}{\lambda} \tag{13}$$

with  $h = 6.62607004 \times 10^{-34} \text{ m}^2 \text{ kg} / \text{s} \dots$

Also in equation (14), it is given that E field is concurrently related with frequency. This is called as the wave equation by Maxwell's, at position and time .

$$E(r,t) = E_0 \cos(\omega t - k \cdot r + \phi_0) \tag{14}$$

With  $E_0$  is constant vector,  $k$  is wave number and  $\phi_0$  is constant scalar. The angular

frequency,  $\omega = 2\pi f$  . Besides, the E field and SAR are also changed simultaneously, especially in term of the distribution pattern, which is described through equation (1). SAR is changed significantly with frequency. Nonetheless, the depth is satisfied for both frequencies with and without water bolus integration, which is up to 100mm. The depth is taken into consideration the brighter area, where the absorption is high. For 2450MHz, it is better in term of focusing capability if compared to 915MHz, where the unnecessary radiation area, which is at the vicinity breast area to be treated, is less.

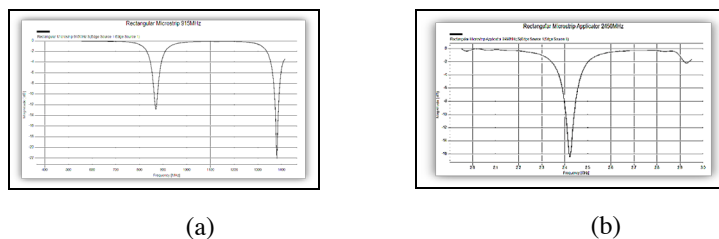


Figure 3. S<sub>11</sub> for Rectangular Microstrip Applicator (a) 915MHz (b) 2450MHz

In addition, the SAR has varied depending on the conductivity of the material,  $\sigma$ . The higher the frequency contributes to higher  $\sigma$ . This is due to the part of loss caused by the motion of the bound charges as tissue with higher water content, such as muscle and breast tumour/cancer, is more lossy for a given E field magnitude than drier tissue as bone and fat.

The findings of this research are at par and even enhance in certain criteria such as the depth penetration and also the focusing capability, if compared to other research findings, which have been conducted previously, despite, with different design of simulation background environment. As for instance, 105mm and 60mm penetration depth were achieved with circular patch (Drizdal et al., 2007) and compact patch applicator (Ammann, Curto, Mcevoy, See, & Chen, 2009; Lim, Choi, Yoon, & Kim, 2015), respectively. On the other hand, when water

Table 3  
E-field and SAR Distribution Pattern for 915 and 2450MHz

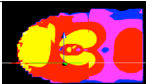
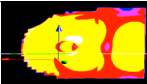
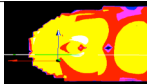
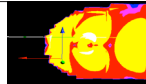
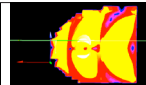
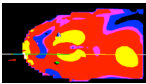
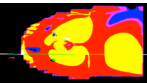
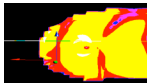
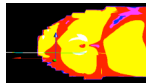
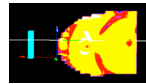
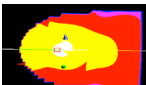
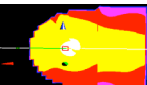
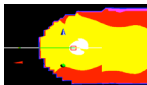
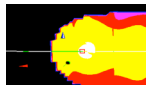
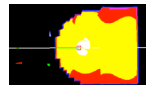
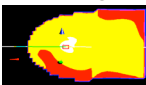
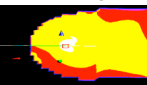
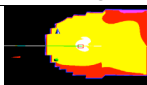
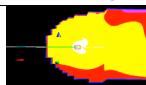
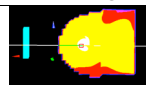
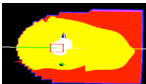
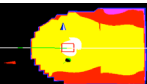
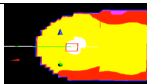
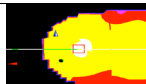
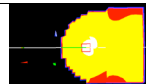
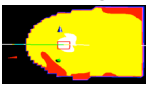
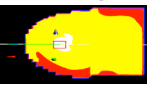
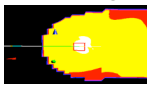
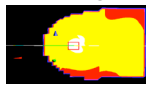
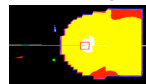
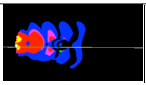
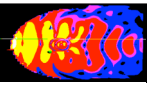
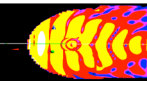
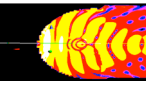
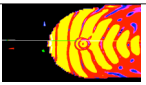
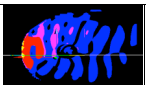

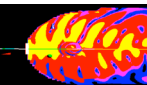
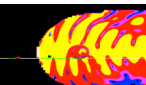
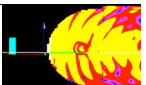
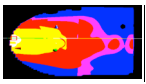
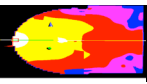
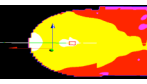
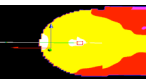
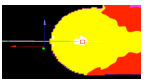
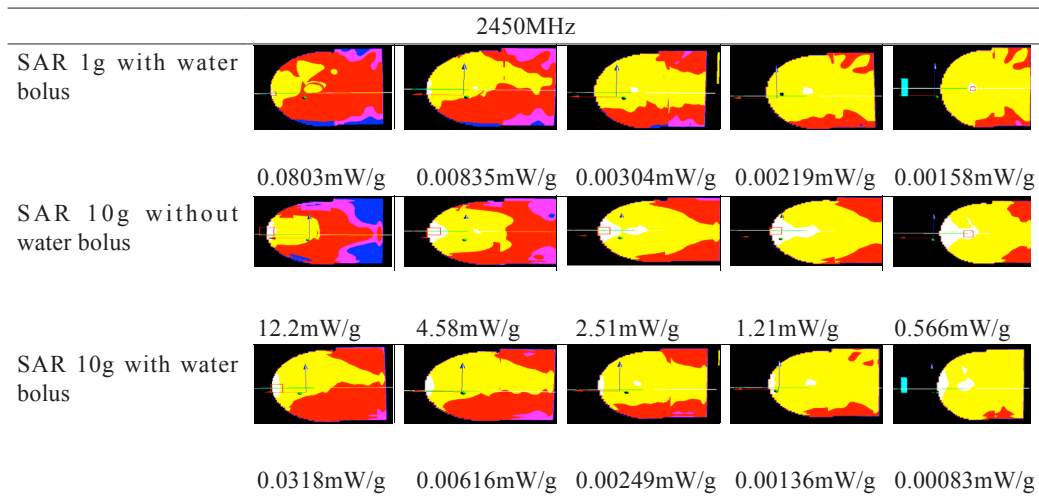
		915MHz				
		Direct on the skin	20mm	40mm	60mm	100mm
E field distribution without water bolus						
E field distribution with water bolus		300V/m	129V/m	123V/m	110V/m	8.78V/m
						
SAR 1g without water bolus		71.8V/m	24.8V/m	19.7V/m	13.5V/m	8.78V/m
						
SAR 1g with water bolus		1.84mW/g	1.56mW/g	1.35mW/g	0.975mW/g	0.502mW/g
						
SAR 10g without water bolus		0.0398mW/g	0.0366mW/g	0.0276mW/g	0.0194mW/g	0.0141mW/g
						
SAR 10g with water bolus		1.23mW/g	1.05mW/g	0.922mW/g	0.67mW/g	0.355mW/g
						
		0.0257mW/g	0.0242mW/g	0.0186mW/g	0.0133mW/g	0.00974mW/g
		2450MHz				
E field distribution without water bolus						
E field distribution with water bolus		2.97X103V/m	328V/m	181V/m	137V/m	113V/m
						
SAR 1g without water bolus		159V/m	14.4V/m	7.92V/m	5.5V/m	4.12V/m
						
		20.3mW/g	5.8mW/g	3.08mW/g	2.01mW/g	1.22mW/g

Table 3  
*E-field and SAR Distribution Pattern for 915 and 2450MHz (continue)*



bolus is added, it is significantly observed that the E field and SAR distribution are changed in shape and depth. Hence, by adding the water bolus, it may reshape the effective field size (EFS), while keeping the vicinity of the targeted area cool during the execution of hyperthermia procedure, which also contributes towards minimal skin burn impact.

### CONCLUSION

The simulation study on the SAR is conducted using the FDTD computational packages, SEMCAD X by Speag. Different operating frequencies are used to carry out the simulation study. Design of simulation (DoS) is provided in Figure 1. As observed from the results, different frequencies may provide satisfied depth, either with or without the integration of water bolus. Focus is better for 2450MHz. The integration of the water bolus assisted in providing the cooling environment on the vicinity of the targeted area during the hyperthermia procedure and help prevent skin burn. Furthermore, the water bolus also reshaping the E field and SAR contour and depth.

### ACKNOWLEDGEMENT

The authors gratefully acknowledge and thank University Teknologi MARA (UiTM) for providing facilities for this research.

### REFERENCES

Ammann, M. J., Curto, S., Mcevoy, P., See, T. S. P., & Chen, Z. N. (2009). A Stable Near-Field Antenna Hyperthermia Applicator for Various Tissue Types and Topologies. *Loughborough Antennas and Propagation Conference*, (November), 76–79.

- Choi, W. C., Kim, K. J., Kim, J., & Yoon, Y. J. (2014). Compact microwave radiator for improving heating uniformity in hyperthermia system. *IEEE Antennas and Wireless Propagation Letters*, 13, 1345–1348. <http://doi.org/10.1109/LAWP.2014.2333033>
- Choi, W. C., Lim, S., Yoon, Y. J., & Member, S. (2016). Design of Noninvasive Hyperthermia System Using Transmit-Array Lens Antenna Configuration. *IEEE Antennas and Wireless Propagation Letters*, 15, 857–860.
- Drizdal, T., Togni, P., & Vrba, J. (2007). Microstrip Applicator for Local Hyperthermia. *2007 International Conference on Electromagnetics in Advanced Applications*, 1047–1049. <http://doi.org/10.1109/ICEAA.2007.4387489>
- Jaakko Malmivuo & Robert Plonsey. (1995). *Bioelectromagnetism - Principles and Applications of Bioelectric and Biomagnetic Fields*. Nature (Vol. 233). Oxford University Press, New York. <http://doi.org/10.1038/233288a0>
- Kulas, L., & Mrozowski, M. (2011). Electromagnetics and Network Theory and their Microwave Technology Applications, 293–307. <http://doi.org/10.1007/978-3-642-18375-1>
- Lias, K. B., Ahmad Narihan, M. Z., & Buniyamin, N. (2014). An Antenna with an Embedded EBG Structure for Non Invasive Hyperthermia Cancer Treatment. In *2014 IEEE Conference on Biomedical Engineering and Sciences, 8 - 10 December 2014, Miri, Sarawak, Malaysia*.
- Lias, K., & Buniyamin, N. (2013). An Overview of Cancer Thermal Therapy Technology based on Different Types of Antenna Exposure. *ICEESE 2013*, 90–95.
- Lim, S., Choi, W. C., Yoon, Y. J., & Kim, H. (2015). Modified rectangular patch antenna for improving heating uniformity in hyperthermia application. *IEEE Antennas and Propagation Society, AP-S International Symposium (Digest), 2015-Octob(c)*, 734–735. <http://doi.org/10.1109/APS.2015.7304754>
- Nguyen, P. T., Abbosh, a., & Crozier, S. (2015). Microwave Hyperthermia for Breast Cancer Treatment Using Electromagnetic and Thermal Focusing Tested on Realistic Breast Models and Antenna Arrays. *IEEE Transactions on Antennas and Propagation*, 63(10), 4426–4434. <http://doi.org/10.1109/TAP.2015.2463681>
- Ovidio, B., Bucci, M., Crocco, L., Scapatucci, R., & Bellizzi, G. (2016). On the Design of Phased Arrays for Medical Applications. *Proceedings of the IEEE*, 104(3), 633–648. <http://doi.org/10.1109/JPROC.2015.2504266>
- Plewako, J., Krawczyk, A., & Grochowicz, B. (2003). Electromagnetic Hyperthermia – Foundations and Computer Modelling. *11th International Symposium on Electromagnetic Fields in Electrical Engineering*, 337–342.
- Rajendran, T. (2015). Comparison Study of Microwave Patch Antennas At 434 MHz for Intra Cavitary Hyperthermia Applicator Design.
- Yin, D.-X., Li, M., & Li, J. L.-W. (2012). Non-invasive breast cancer thermotherapy studies using conformal microstrip antennas. *Isape2012*, 159–162. <http://doi.org/10.1109/ISAPE.2012.6408733>.



## **Application of Evolutionary Programming for the Placement of TCSC and UPFC for Minimisation of Transmission Losses and Improvement of Voltage Profile**

**Nur Ashida Salim<sup>1\*</sup>, Nabila Ismail<sup>1</sup>, Muhammad Murtadha Othman<sup>1</sup>**

*<sup>1</sup>Faculty of Electrical Engineering, Universiti Teknologi MARA, 40450 Shah Alam, Selangor*

### **ABSTRACT**

Flexible AC Transmission System (FACTS) devices are used in to improve stability and loadability of transmission networks as well as minimise losses . Types of FACTS that are normally used are Thyristor Controller Series Compensator (TCSC) and Unified Power Flow Controller (UPFC) which is to control power flow and stability of the power system at a certain location. The TCSC is suitable because it can be installed in a long transmission line system while UPFC can solve any reactive power problems. The objective of this study is to minimise total power losses and to improve the voltage profile by using FACTS devices in the transmission system. This paper proposes a static voltage stability index (SVSI) to determine the size and placement of TCSC and the Evolutionary Programming (EP) technique. The results of the transmission line losses and voltage profile using TCSC and UPFC are compared in order to demonstrate which FACTS device can produce better results. The IEEE 14 bus system is used in this study to validate the findings.

*Keywords:* Evolutionary Programming (EP), Thyristor Controlled Series Compensator (TCSC), Unified Power Flow Controller (UPFC), Flexible AC Transmission System (FACTS), Static Voltage Stability Index (SVSI)

### **ARTICLE INFO**

*Article history:*

Received: 24 August 2016

Accepted: 02 December 2016

*E-mail addresses:*

[nurashida606@salam.uitm.edu.my](mailto:nurashida606@salam.uitm.edu.my) (Nur Ashida Salim),

[nabila\\_bigfoot@yahoo.com](mailto:nabila_bigfoot@yahoo.com) (Nabila Ismail),

[mamat505my@yahoo.com](mailto:mamat505my@yahoo.com) (Muhammad Murtadha Othman)

\*Corresponding Author

### **INTRODUCTION**

Industry and consumer demand for power is increasing load requirement and can cause an overload in the transmission system leading to voltage collapse. Building a new transmission line (Abdullah, Musirin, & Othman, 2010a) or to decreasing power losses by injecting the Flexible AC Transmission System (FACTS) devices into the systems can resolve this problem. However, building

another transmission line to solve the problem is complicated and not cost efficient. Therefore, FACTS is one of the devices used to solve the problem using an existing transmission line. The FACTS is a powerful electronic device used to control power flow in the power system. The FACTS device is capable of managing the network efficiently and it can be used to improve voltage stability, stability and transient stabilities of complex power systems.

Voltage stability can be divided into fast voltage stability index (FVSI), static voltage stability index, (SVSI), voltage stability index (VSI), and line stability index (LQP) (Abedelatti et al., 2015; Stoenescu et al., 2009). Voltage stability is a very important parameter to save the system from voltage collapse. Reducing or adding reactive power load before reaching the point of voltage collapse is one of the methods to preserve the system (Lakkireddy et al., 2015). Power losses will increase if reactive power is high. The rapid increase in power demand leads to instability in the system to result in contingency and outage. It will cause an overloading of the transmission line and affect quality of power (Shah & Prajapati, Jan-June 2015). In order to maintain voltage stability, FACTS devices are used in power systems to control the power flow in certain lines and improve security of transmission lines. The TCSC is one of the suitable types of FACTS that is smooth and flexible to control line impedance with fast responses (Abdullah et al., 2010a). To perform sensitivity analysis and ranking process, it depends on the real power flow index sensitivity and reduction of total system reactive power losses to find a suitable location to install the FACTS (Tlijani, Guesmi, Abdallah, & Ouali, 2012). The UPFC has its own unique features because it can combine all parameters of power flow, voltage, line impedance and phase angle (Kumar & Reddy, 2014).

The aim of this project is to minimise transmission line losses and ensure static voltage stability. This project proposed TCSC and UPFC as the FACTS device to control the power flow, voltage stability and power losses in the system. The TCSC can control the long transmission line (Rajaram, Reka, & Murali, 2010) reactance at high speed condition (Nishida, Hirabayashi, & Iwamoto, 2006). The UPFC can solve reactive power problems. Before installing the FACTS devices, the optimal location and the sizing of FACTS must be identified. The EP techniques are used to optimise the fitness which can be represented by using mathematical equations. It will find the best location to inject the FACTS, sizing of the FACTS, the value of power losses and minimum voltage profile after injecting TCSC and UPFC respectively. The IEEE-14 bus system is applied as the test system in order to install the FACTS devices.

### **Thyristor Controlled Static Compensator (TCSC) modelling**

The TCSC is represented as a capacitive or inductive compensation. It is injected in series to a line (terminal) and allow alteration in impedance of the transmission path of the power flow by increasing or decreasing the value of reactance in line branch, XLI which is the reactance of transmission line where the TCSC is located (Abdullah, Musirin, & Othman, 2010b). The constraint limit for TCSC is given by equation (1) (Abdullah et al., 2010b).

$$(-0.8 \times X_L) \leq X_{TC} \quad (1)$$

### Unified Power Flow Controller (UPFC) Modelling

The UPFC is a combination of TCSC and SVC devices. The TCSC devices are installed in the transmission line while SVC is installed at the bus. The SVC can operate as inductive and capacitive compensation. It is controlled by bus voltage absorbing or injecting reactive power. The constraint limit for UPFC is given by equation (2) and (3) (Abdullah et al., 2010b).

$$(-0.8 \times X_L) \leq X_{TCSC} \leq 0.2 \times X_L \quad (2)$$

$$(-0.8 \times X_L) \leq X_{TCSC} \leq 0.2 \times X_L \quad (3)$$

### FACTS PLACEMENT

The first step is to determine the location of the TCSC and UPFC devices. They are installed at the weakest bus or heavily loaded in the system to reduce the losses (Abdullah et al., 2010a). The SVSI method is used in this study to determine the placement of the FACTS devices. The index shows the level of stability of each transmission line. The line that gives the value of SVSI nearest or equal to 1 indicate that the line is unstable. The FACTS are installed on the instability transmission line. The SVSI are derived from the power flow between two buses, bus  $i$  and bus  $j$ . The SVSI mathematical formulation is given as below by equation (4).

$$SVSI_{ji} = \frac{\sqrt{(X_{ji}^2 + R_{ji}^2)(P_{ji}^2 + Q_{ji}^2)}}{\|V_i\|^2 - 2(X_{ji})(Q_{ji}) - 2(R_{ji})(P_{ji})} \quad (4)$$

### METHODOLOGY

The first step is to determine the location of the TCSC and UPFC devices. They are installed at the weakest bus or heavily loaded in the system to reduce the losses. They SVSI method is used in this study to determine the placement of the FACTS devices. The index shows the level of stability of each transmission line. The line that gives the value of SVSI nearest or equal to 1 indicates that the line is unstable. If value of SVSI less than 1, the system is stable. After determining a suitable location, EP technique is used in the system to optimise the fitness.

### Static Voltage Stability Index (SVSI)

The following steps are used determine the SVSI value for TCSC installation:

- a) Perform the load flow programme using the Newton Raphson iterative technique.
- b) Calculate value of SVSI for every line in the system at the base condition by using equation (2).
- c) Set the loading factor. Then, perform the load flow and re-calculate the new SVSI.
- d) Increase the reactive power demand. Repeat steps b) and c) for the increased reactive power demand. This process will stop if the load flow solution diverges.
- e) Collect and sort the SVSI in descending order.



- f) Repeat steps c) until e) for another load bus.
- g) Extract the maximum reactive power demand for the highest value of SVSI for every load bus.
- h) Sort the maximum loadability (demand) obtained in step g) in ascending order. The smallest maximum loadability (demand) is ranked the highest and it is the weakest in the system.

Once the SVSI has been identified, then the placement of the TCSC and UPFC is based on the SVSI results.

### Evolutionary Programming (EP)

The EP technique is used in the system to optimise the fitness, represented using mathematical equations. The EP consists of initialisation, fitness, mutation, combination, selection, new generation and convergence test. The following steps are followed to optimise EP.

- a) Set loading factor to stress the system or increase the load demand. Calculate SVSI to define the weakest bus as a location to install the FACTS (TCSC and UPFC).
- b) Initialization: Set random initial population. In this study, it sets the random number by referring IEEE-14 bus system. The random number is depending on the location and how many FACTS devices have to be installed into the system. In this system, it just selects one location and has one random number to install the FACTS device.
- c) Fitness: It is to optimize objective function. In this study, it uses two times of fitness. The first is after installation and second is after mutation. In this fitness, it calculates losses, voltage minimum, voltage index, maximum, minimum and average to display in mutation.
- d) Mutation: Generate new population (offspring) to select individual parents using Gaussian elimination method. Each element of the individual parent can be calculated using equation (5) and (6).

$$x_{i+m,j} = x_{i,j} + N(0, \sigma_{i,j}^2) \tag{5}$$

$$\sigma_{i,j} = \beta (x_{j \max} - x_{j \min}) \left( \frac{f_i}{f_{\max}} \right) \tag{6}$$

where

$x_{i+m,j}$  = Parents mutation (offspring)

$x_{i,j}$  = Parents

$N(0, \sigma_{i,j}^2)$  : = Gaussian random variable with mean  $\mu$  and variance

$\beta$  = mutation scale,  $0 < \beta < 1$

$x_{i,\max}$  = maximum random number of every variable

$x_{i,\min}$  = minimum random number of every variable

$f_i$  = fitness for  $i^{\text{th}}$  random number

$f_{\max}$  = maximum fitness



- e) Mutate fitness 2. It is similar to step b).
- f) Combination: Combine the offspring and parents, which are fitness 1 and fitness 2.
- g) Selection: The selection is performed based on the combination process. Rank the process and select the best result. It is used as a survival to choose the next generation.
- h) Convergence criterion: It is to determine the stopping criteria. It refers to the difference between maximum fitness and the minimum fitness of the objective function. It will converge if it approaches the stopping criteria. The stopping criteria can be calculated using equation (7).

$$fitness_{max} - fitness_{min} \leq 0.01 \quad (7)$$

## RESULTS AND DISCUSSIONS

The IEEE14-bus test system is used as a case study. It consists of 20 interconnected lines, 1 slack bus, 9 load buses, 4 generator buses and 20 transformers tap changer. The base power is 100 MVA and the load bus 14 is selected to perform the test as it is the weakest bus. Two constrains were used in this system before performing the optimisations. The constrains are the total loss and must be less than  $P_{loss}$  and the voltage minimum after must be more than  $V_{set}$ .  $P_{loss}$  and  $V_{set}$  are total power loss and voltage set before injecting the TCSC and UPFC.

### TCSC and UPFC as FACTS device

Table 1 shows the bus rank with base case SVSI to define the best location to install the TCSC. Results show that the highest value of voltage stability index is at bus 14, 0.802p.u. However, in this study, determining the most suitable location to install the FACTS depends on the lowest maximum loading because the best location is at the fastest location to diverge when injecting the load at the point. From Table 1, it shows that bus 14 is the lowest maximum loading and it will be the weakest bus and line 20 is heaviest line with a voltage stability value of 0.802p.u.

Table 1  
Bus rank base SVSI for IEEE-14 bus system

Rank	Weak Bus	Heavily Line	Maximum loading (MVAR)	SVSI (p.u)
1	14	20	100	0.802
2	9	9	220	0.665
3	7	8	290	0.440
4	10	9	160	0.412
5	13	13	250	0.388
6	6	4	520	0.275
7	11	11	170	0.233
8	8	2	500	0.184
9	12	12	150	0.055

Based on the results in Table 2, Figure 1 and Figure 2, the comparison of transmission line losses and voltage stability before and after injecting the TCSC is tabulated. Load demand is increased gradually to observe the best placement and sizing for FACTS because different load demand will have different location to inject FACTS depending on which line is the weakest using SVSI method. In this study, power losses decrease due to the increasing load demand from 80 to 100MVAR. From Table 2 and Figure 1, it shows the graph for transmission losses for TCSC and UPFC. At load demand 100MVAR, the transmission losses before injecting FACTS is 58.612MW. After injecting UPFC, transmission losses decrease to 27.504MW (53.07% losses) and after injecting TCSC, it reduces to 51.324MW, 12.43% lower than before installing FACTS. Therefore, it can be seen clearly that the transmission line losses can be reduced in a bigger percentage by installing UPFC compared with TCSC. Table 1 and Figure 2 show the graph for voltage stability for TCSC and UPFC. At loading of 100MVAR, the value of voltage stability before injecting the FACTS is 0.802 and after injecting the TCSC and UPFC, the voltage stability is 0.394 and 0.027p.u respectively. It shows that installing UPFC into IEEE-14 bus system makes it more stable compared with TCSC.

Table 2  
Comparing results for total loss and SVSI of bus 14 before and after TCSC installation

Load Demand (MVAR)	Transmission Losses (MW)			% Δ Loss		SVSI (p.u)		
	Pre	Post TCSC	Post UPFC	TCSC	UPFC	Pre	Post TCSC	Post UPFC
80	41.722	41.134	27.523	1.41	34.03	0.529	0.382	0.027
85	44.491	43.374	27.463	2.51	38.27	0.584	0.416	0.056
90	47.902	45.871	27.512	4.24	42.57	0.645	0.346	0.031
95	52.394	48.448	27.512	7.53	47.49	0.718	0.373	0.044
100	58.612	51.324	27.504	12.43	53.07	0.802	0.394	0.027

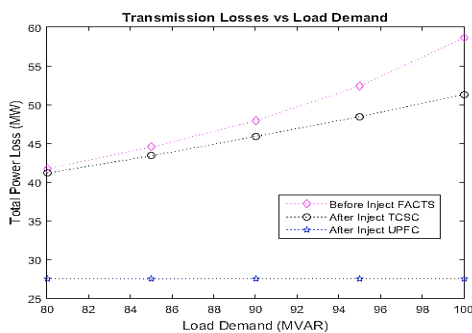


Figure 1. Comparison of transmission line losses for TCSC and UPFC

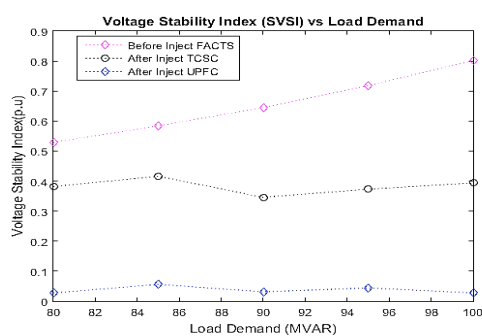


Figure 2. Comparison of Voltage Stability Index (SVSI) for TCSC and UPFC

Table 3 and Figure 3 show the voltage profile before and after installing the TCSC and UPFC. Voltage profile is increased after installing the TCSC and UPFC. Voltage profile is increased after installing the TCSC in the system. After injecting the TCSC and UPFC, the minimum voltage is increased. Before injecting TCSC and UPFC, the value of minimum voltage is 0.7383V, at load demand, 80MVAR. The minimum voltage increase after injecting TCSC and UPFC is 0.7435V and 0.788 respectively. For the other loading condition, the voltage profile also increases after the installation of TCSC and UPFC. This shows that the installation of UPFC improves the voltage profile of the system.

Table 3  
Voltage Profile at Bus 14

Load Demand (MVAR)	Voltage Profile (V)		
	Pre (TCSC and UPFC)	Post TCSC	Post UPFC
80	0.7383	0.7435	0.788
85	0.7146	0.7206	0.771
90	0.6879	0.6951	0.752
95	0.6551	0.6642	0.732
100	0.6149	0.6260	0.710

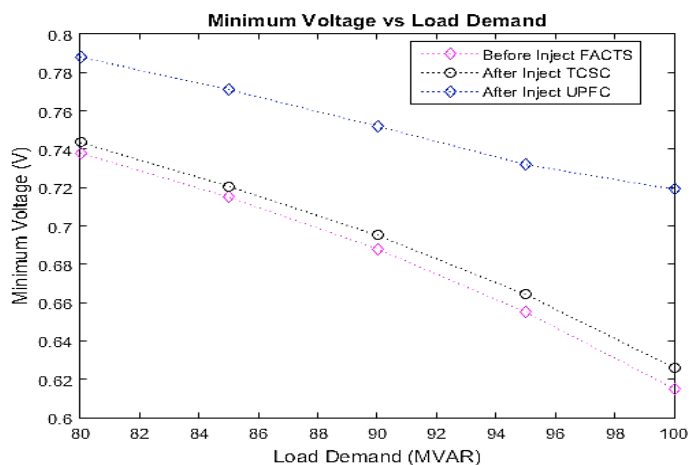


Figure 3. Comparison of Minimum Voltage for TCSC and UPFC

## CONCLUSION

The FACTS is a powerful device that controls transmission line losses and improves minimum voltage. In this paper, the application of TCSC and UPFC by adopting the Evolutionary Programming to reduce transmission line losses and improve minimum voltage in the IEEE 14-bus system has been successfully performed. Results show that FACTS devices can improve minimum voltage and reduce power losses in the system. The UPFC shows much better performance compared with TCSC as it provides more stability and a faster response.

## ACKNOWLEDGEMENT

The authors would like to thank Research Management Institute (RMI), Universiti Teknologi MARA, Malaysia and the Ministry of Higher Education (MOHE), Malaysia for funding this study through research grant RAGS/1/2014/TK03/UiTM//6.

## REFERENCES

- Abdullah, N. R. H., Musirin, I., & Othman, M. M. (2010, November). Thyristor Controlled Series Compensator planning using Evolutionary Programming for transmission loss minimization for system under contingencies. In *Power and Energy (PECon), 2010 IEEE International Conference on* (pp. 18-23). IEEE.
- Abdullah, N. R. H., Musirin, I., & Othman, M. M. (2010). Transmission loss minimization and UPFC installation cost using evolutionary computation for improvement of voltage stability. In *Proceedings of the 14th International Middle East Power Systems Conference Cairo University, Egypt* (pp. 825-830).
- Abedelatti, AE, Hashim, H, Abidin, IZ, & Sie, Adrian WH. (2015). Weakest Bus Based on Voltage Indices and Loadability. *The 3rd National Graduate Conference (NatGrad2015)*.
- Ishit, A. S., & Yogesh, R. P. (Jan-June 2015). Implementation of TCSC for Enhancement of ATC. *International Journal of Electrical and Electronic Engineers*, 7(1), 99-105.
- Kumar, C. V., & Reddy, P. B. (2014). Comparison of Facts Devices to Reduce Power System Losses and Improvement in Voltage Stability by Using Optimization Technique. *International Journal of Science and Research (IJSR)*, 4(10), 2246-2250.
- Lakkireddy, J., Rastgoufard, R., Leevongwat, I., & Rastgoufard, P. (2015, March). Steady state voltage stability enhancement using shunt and series FACTS devices. In *Power Systems Conference (PSC), 2015 Clemson University* (pp. 1-5). IEEE.
- Nishida, K., Hirabayashi, S., & Iwamoto, S. (2006, October). Operation strategy of TCSC considering stability ATC. In *2006 IEEE PES Power Systems Conference and Exposition* (pp. 705-710). IEEE.
- Rajaram, D. M., Reka, N., & Murali, D. (2010). Comparison of FACTS devices for power system stability enhancement. *International Journal of Computer Applications (0975-8887)*, 8(4).
- Stoenescu, E., Corcau, J. I., & Grigorie, T. L. (2009, February). Static voltage stability analysis of a power system. In *Proceedings of the 4th IASME/WSEAS International Conference on Energy & Environment (EE'09)*.
- Tlijani, K., Guesmi, T., Abdallah, H. H., & Ouali, A. (2012, March). Optimal location and parameter setting of TCSC based on Sensitivity analysis. In *2012 First International Conference on Renewable Energies and Vehicular Technology* (pp. 420-424). IEEE.



## Method of Determining Load Priority using Fuzzy Logic for Adaptive Under Frequency Load Shedding Technique

A. I. M. Isa<sup>1</sup>, H. Mohamad<sup>1\*</sup>, K. Naidu<sup>2</sup>, N. Y. Dahlan<sup>1</sup> and I. Musirin<sup>1</sup>

<sup>1</sup>Faculty of Electrical Engineering, Universiti Teknologi MARA, 40450 Shah Alam, Selangor, Malaysia

<sup>2</sup>Electrical Engineering Department, Faculty of Engineering Universiti of Malaya, 50603 Kuala Lumpur, Malaysia

### ABSTRACT

Power systems are usually exposed to numerous disturbances that can have an adverse effect on system operation. Insufficient generation could lead to frequency declination and subsequently system collapse in the absence of immediate control action. Frequency Load Shedding (UFLS) is a technique commonly applied to overcome overloading and restore the system frequency. This paper presents an adaptive load shedding approach to determine the best location with minimum amount of load to be shed. Load Ranking Fuzzy Logic (LRFL) is used to rank the load based on their sensitivity and stability index. In order to achieve this, the proposed strategy is verified using 11 kV Malaysian distributed network consisting of different type of loads connected with single and multiple Distribution Generator (DG). The simulation results show that the proposed strategy successfully stabilizes the system's frequency.

*Keywords:* Distribution Generator, Under Frequency Load Shedding, Load Ranking based Fuzzy Logic, Load Priority

### INTRODUCTION

Power system stability is of critical importance and proper contingency plans are

required to ensure its reliability and security is maintained. With increasing demand for electricity, power systems are being operated at levels that are closer to their limits, thereby, increasing risks. .

Moreover, power systems are constantly exposed to various disturbances which could affect its operation. If the power system is not designed properly poor connection or disconnection of system elements can arise (Seyedi & Sanaye-Pasand, 2009 & Haotian, Chun Sing & Loi Lei, 2014; ).

#### ARTICLE INFO

##### Article history:

Received: 24 August 2016

Accepted: 02 December 2016

##### E-mail addresses:

ama;omaozzati\_isa@yahoo.com (A.I.M. Isa),

hasmaini@salam.uitm.edu.my (H. Mohamad),

vkanendra@gmail.com (K. Naidu),

nofri79@gmail.com (N.Y. Dahlan),

i\_musirin@yahoo.co.uk(I. Musirin)

\*Corresponding Author

In the presence of load generation imbalance, the system frequency is affected. The frequency deviation could be detrimental to the system operation if mitigating action is not taken. It could cause cascading failure, loss of synchronization and finally total collapse of the system (Ahsan et al., 2012; Kanimozhi, Selvi, & Balaji, 2014; Rad & Abedi, 2008). So, it is very important to implement a protection scheme that preserves the stability and security of power system.

Frequency Load Shedding (UFLS) is an emergency protection scheme to protect the system from frequency instability when the generation is unable to meet load demand. The most commonly used UFLS in industry is to set the frequency level, time delay and amount of load to be shed at specified set values in the distribution relay (Seyedi & Sanaye-Pasand, 2009). Drawbacks of this method, adaptive UFLS method is introduced. The adaptive method is improved by estimating the amount of power imbalance based on Rate of Change of Frequency (ROCOF). The control signal based on adaptive UFLS is send to the control centre and the decision to shed the appropriate amount of load is made.

In the load shedding method, many researches have considered voltage stability analysis as an indicator to determine the critical bus in the transmission line (J, 2013; Van Cutsem, Moors, & Lefebvre, 2002). Due to the quick nature of system collapse, it is important to determine the critical busses in the system order to avoid voltage instability. In (Sapari, Mokhlis, Bakar, & Dahalan, 2014), authors have introduced Load Stability Index (LSI) as an indicator to determine the critical load busses in the distribution network. By using the sensitivity information, an optimization problem is determined and the optimal load shedding amount established. The variation in the sensitivities with respect to the load shedding amount is initially investigated. The resulting non-linear optimization problem needs to be solved in order to obtain the best location and minimum amount of load to be shed.

With this in mind an adaptive load shedding technique using Load Ranking based Fuzzy Logic (LRFL) was introduced. The proposed technique considers load stability index (LSI) and Rate of Change of Power (ROCOP) in case of high demand and ensures the overall system is balanced in order to prevent from total system collapse. The objective of this technique is to choose the load optimally so it could prevent frequency decay and maintain load generation balance.

## **PROBLEM FORMULATION**

### **Overall Concept of Adaptive UFLS**

The proposed Adaptive UFLS scheme uses Load Ranking based Fuzzy Logic (LRFL) to stabilize the system by shedding the minimum amount of load at optimal location. LRFL comprises of two steps. In the first step, it will receive the input of Load Stability Index (LSI) and Rate of Change of Power (ROCOP) from the PSCAD and continuously monitor these values. The second steps, from the values obtained in first steps it will rank load according to the fuzzy rules into three categories i.e. non-vital, semi-vital, and vital load. The Load Shedding Controller will determine the amount of load that needs to be shed based on the amount of power imbalance. The overall concept of the proposed Adaptive UFLS technique is illustrated in Figure 1.

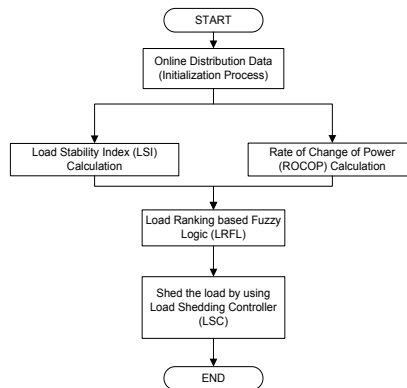


Figure 1. Overall concept of adaptive UFLS

### Modelling the Load Ranking based Fuzzy Logic (LRFL)

Load ranking strategy was used based on MATLAB’s fuzzy logic controller. The first step is to determine the fuzzy set parameters by normalising and fuzzification of the input values. LRFL consist of two inputs and one output which are LSI, ROCOP and Load Ranking (LR) respectively. The input of LSI is fuzzified into Non-Critical (NC), Critical (C), Semi-Critical (SC) and Most-Critical (MC) while the input of ROCOP is fuzzified into Low (L), Very-Low (VL), Extra-Low (EL), and Very-Extra-Low (VEL). The fuzzified output of load ranking values are Non-Vital (NV), Semi-Vital (SV), and Vital (V). Depending on the input values, LRFL will rank the load. The membership function for the state variable and output control are defined and constructed. LRFL input and output membership function are shown in Figures 2, 3 and 4. The Second step of LRFL is fuzzy rule base and interference mechanism. The rule base helps LRFL in making decisions based on input and output control action. The IF-THEN rule is applied as shown in Table 1.

Table 1  
LRFL module

Parameter		Load Stability Index (LSI)			
Rate of Change of Power (ROCO)	Rules	NC	C	SC	MC
	L	NV	NV	NV	NV
	VL	NV	NV	NV	SV
	EL	NV	NV	SV	V
	VEL	SV	SV	V	V

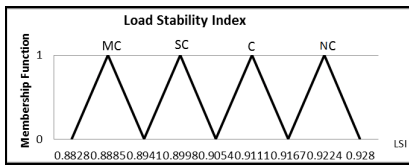


Figure 2. LSI membership function

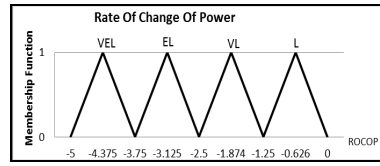


Figure 3. ROCOP membership function

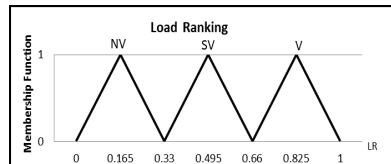


Figure 4. Load ranking membership function

### Load Stability Index (LSI)

The stability index is used as an indicator for voltage instability in the power system network. The stability of the system relies between two busses and the values is between 0-1 as presented in Figure 5. The stability index is given in equation (Sapari et al., 2014):

$$|V_i|^4 - 4 \times \{P_j X_{ij} - Q_j r_{ij}\}^2 - 4 \times \{P_j X_{ij} - Q_j x_{ij}\}^2 \times |V_i|^2 \geq \quad (1)$$

In the LSI, both real power,  $P$  and reactive power,  $Q$  is considered as shown in equation (1). The bus with a LSI near to “0” is considered as a critical bus in the system.

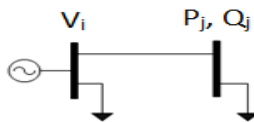


Figure 5. Stability index of distribution generator

### Rate of Change of Power (ROCOP)

Rate of Change of Power (ROCOP) is normally used to assess the influence of active power variations (frequency and voltage) in the power system. In case when inertia is high in the system, for example when generator is operating parallel with the grid the impact is negligible. However, for isolated operation, the ROCOP parameter is used to take into account the state of the system frequency and voltage. The ROCOP parameter is effective on the distribution system which has an imbalance load compared to the system with balance load (Redfern, Barrett, & Usta, 1997).



### Load Shedding Controller (LSC)

The principle operation of Load Shedding Controller (LSC) is shown in Figure 6. The LSC algorithm will always checks for system disturbance and continuously monitors the breaker status and system frequency. The main function of LSC is to calculate power imbalance based on the swing equation as shown in Equation 2.

$$\Delta P = P_m - P_e = \left( 2 \times \sum \frac{H_i}{f_n} \right) \times \frac{df_{coi}}{dt} \dots \dots (2)$$

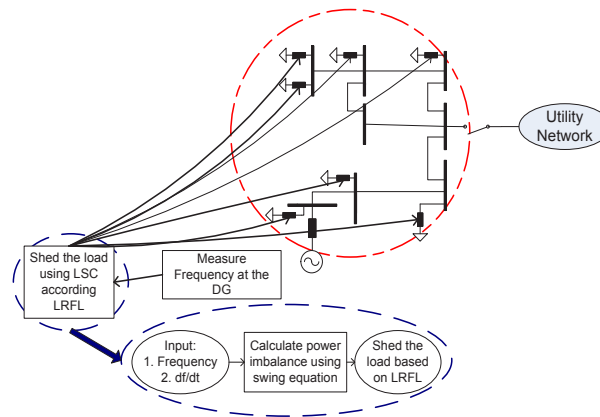


Figure 6. Principle operation of LSC

## CASE STUDY

### Test Network

Test system shown in Figure 7 is used to validate the performance and accuracy of proposed Adaptive UFLS technique. The system is connected to a 50 Hz, 33kV and 100MVA generator. The system consists of one unit mini hydro generator rated at 2MW and seven lumped loads. There are 2 units of 33/11 kV step-down transformers which are rated at 20 MVA and 1 units of 11/3.3 kV step-down transformer which is rated at 2MVA.

### Load Sensitivity Case Study based on LRFL

The proposed Adaptive UFLS technique is tested in a distribution network for islanding operation. The islanding scenario is created by disconnecting utility breakers from the distribution network at t=10.0s. Due to power mismatch between generation and load, frequency declination occurs. Without a proper UFLS technique, the frequency will continue to decline until system collapse. As mentioned earlier, the LSI and ROCOP based ranking uses priority sequence of loads to be shed. Table 2 shows the load profile for each load in the distribution network.

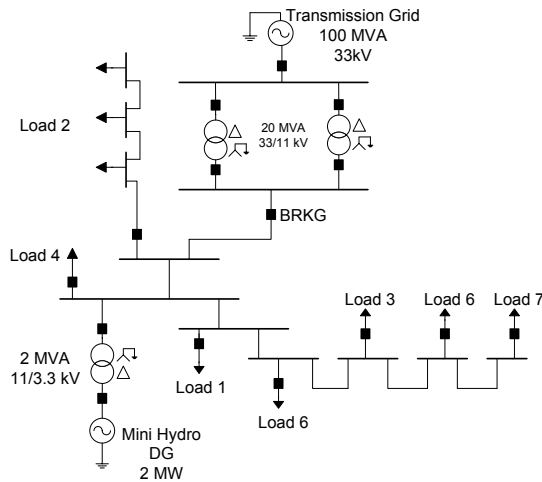


Figure 7. Test system

Table 2  
Load Profile Table

Load	LSI	ROCOP	Load Values		Load Ranking	
			P (MW)	Q (MVAR)	Adaptive UFLS	Proposed UFLS
1	0.8827	-0.3809	0.0748	0.0464	NV1	NV2
2	0.9279	-0.5852	0.0976	0.0606	NV2	NV1
3	0.8853	-1.2651	0.1582	0.092	NV3	NV3
4	0.9205	-2.453	0.2786	0.1606	SV1	SV2
5	0.8953	-1.2471	0.1658	0.0906	SV2	SV1
6	0.9001	-3.774	0.5345	0.3074	V1	V2
7	0.8853	-3.679	0.5061	0.2827	V2	V1

Both LSI and ROCOP indicate the sensitivity status of each load in the system. In LSI “0” represents a critical load and “1” represent a stable load. For ROCOP, the lowest value represents critical load in the system. In this research, the sensitivities of loads are monitored throughout the simulation process.

### CASE 1: Islanding Operation at 0.14 MW Power Mismatch

In the first case, an islanding scenario with a power mismatch of t 0.14 MW is carried out. The total load demand for this case is 1.81 MW and the power supply from mini hydro is 1.67 MW, and the grid supply the remaining power. The system is islanded by opening the grid’s breaker at t=10.0 s.

When the grid is disconnected from the system, the proposed Adaptive UFLS technique monitors the system frequency to determine if threshold limit of 49.5Hz is violated. If the frequency drops below the threshold limit, the LRFL is activated to rank the load based on their

sensitivities and LSC will estimate the power imbalance and total load to be shed. Depending on the amount calculated and the load rank, the technique will trip certain number of load breaker in order to stabilize the frequency.

Table 3  
Adaptive UFLS Parameter for Islanding Operation at 0.14 MW Power Mismatch

Parameter	Without load shedding	Adaptive UFLS	Proposed Adaptive UFLS
Power Imbalance	0.14	0.14	0.14
Total Load Shed	0	0.0748	0.0976
Load Disconnected	No load	Load 1	Load 2
Frequency Undershoot	47.5 Hz	48.5 Hz	49.0 Hz

Based on the test system, there are 7 loads (Load 1-Load 7). The load is categorized into non-vital, semi-vital and vital load as shown in Table 2. The ranking of loads is based on LRFL, where it will rank the loads based on their sensitivities of LSI and ROCOP. The loads will be shed according to its priority where the Non-vital load will be shed first.

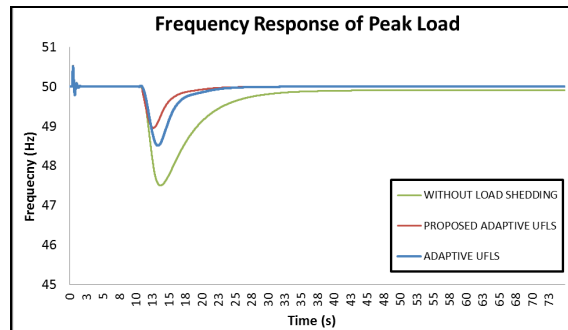


Figure 8. Frequency response during islanding operation at 0.14 MW power mismatch

The power imbalance which is calculated based on the swing equation is 0.14 MW as shown in Table 3. Only a single load needs to be shed which is load 2 (0.0976 MW). By using the proposed adaptive UFLS technique, the frequency drop to 49.0 Hz as shown in Figure 8. It can be clearly seen that the proposed adaptive UFLS technique has a better frequency response compared to conventional and previous adaptive UFLS technique and system without load shedding.

### CASE 2: Load Increment in Islanded System

In the load increment case, an additional load ( $P = 0.6$  MW and  $Q = 0.3106$  MVAR) is connected to the system at  $t = 25$ s. Obviously, the excess load leads to frequency instability, unless load shedding technique is initiated. Table 4 shows the parameters of the proposed adaptive UFLS

technique for load increment. In this case, load 2 is initially shed the moment the system islanded. Load 1, Load 3 and Load 4 is selected to be shed after the additional load is added to the network. As a result, frequency is restored to its nominal value.

Table 4  
*Adaptive UFLS Parameter for Load Increment in Islanded System*

Parameter	Without load shedding	Adaptive UFLS	Proposed Adaptive UFLS
Power Imbalance	0.6	0.6	0.6
Total Load Shed	0	0.4216	0.5116
Load Disconnected	No load	Load 2, Load3 and Load 5	Load 1, Load 3 and Load 4
Frequency Undershoot	47 Hz	47.3 Hz	47.9 Hz

Figure 9 shows the frequency response for load increment scenario. In this situation, the frequency drops until 49 Hz due to the islanding event in case 1. By using the proposed technique, the frequency is able to return to its nominal value. To further verify the effectiveness of this technique, additional load is applied to the system. Despite this, the proposed technique is able to restore the nominal frequency of the system.

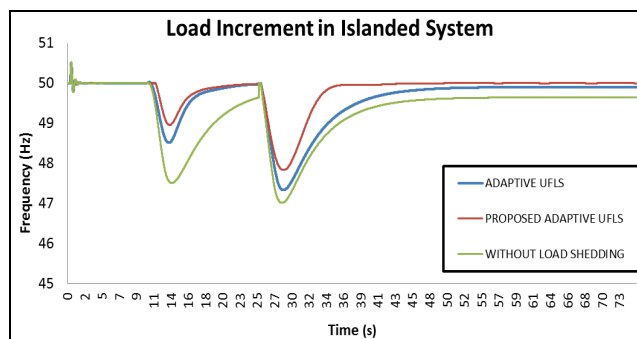


Figure 9. Frequency response for load increment scenario

## CONCLUSION

This paper presents an Adaptive Under-Frequency Load Shedding (UFLS) scheme based on Load Ranking based Fuzzy Logic (LRFL) for distribution network. The algorithm for LRFL was developed using MATLAB's (Fuzzy Controller). The power imbalance or disturbance magnitude is determined by the swing equation and the algorithm of Adaptive UFLS is implemented in the PSCAD simulation software. The accuracy and effectiveness of the proposed Adaptive UFLS technique is investigated on a distribution test system. Two different cases involving power mismatch of 0.14 MW and load increment were investigated. Simulation results have shown that the proposed technique has successfully performed load shedding by

ranking shedding the load according to the power imbalance and thereby restores the frequency back to its nominal value.

## ACKNOWLEDGEMENT

This work was supported by the University of Technology MARA (UiTM), Malaysia under FRGS grant project (Grant Code: 600-RMI/FRGS 5/3 (35/2015))

## REFERENCES

- Ahsan, M. Q., Chowdhury, A. H., Ahmed, S. S., Bhuyan, I. H., Haque, M. A., & Rahman, H. (2012). Technique to Develop Auto Load Shedding and Islanding Scheme to Prevent Power System Blackout. *Power Systems, IEEE Transactions on*, 27(1), 198-205. doi: 10.1109/tpwrs.2011.2158594
- Haotian, Z., Chun Sing, L., & Loi Lei, L. (2014, 12-15 Oct. 2014). *A novel load shedding strategy for distribution systems with distributed generations*. Paper presented at the Innovative Smart Grid Technologies Conference Europe (ISGT-Europe), 2014 IEEE PES.
- J, T., ; J, Liu. ; F, Ponci. ; A, Monti. (2013). Adaptive Load Shedding Based on Combined Frequency and Voltage Stability Assessment Using Synchrophasor Measurement. *IEEE Transactions on Power Systems*, 28(2), 2035-2047.
- Kanimozhi, R., Selvi, K., & Balaji, K. M. (2014). Multi-objective approach for load shedding based on voltage stability index consideration. *Alexandria Engineering Journal*, 53(4), 817-825. doi: <http://dx.doi.org/10.1016/j.aej.2014.09.005>
- Rad, B. F., & Abedi, M. (2008, 22-24 May 2008). *An optimal load-shedding scheme during contingency situations using meta-heuristics algorithms with application of AHP method*. Paper presented at the Optimization of Electrical and Electronic Equipment, 2008. OPTIM 2008. 11th International Conference on May 22-24, 2008.
- Redfern, M. A., Barrett, J. I., & Usta, O. (1997, 25-27 Mar 1997). *A new loss of grid protection based on power measurements*. Paper presented at the Developments in Power System Protection, Sixth International Conference on (Conf. Publ. No. 434).
- Sapari, N. M., Mokhlis, H., Bakar, A. H. A., & Dahalan, M. R. M. (2014, 24-25 March 2014). *Online stability index monitoring for load shedding scheme in islanded distribution network*. Paper presented at the Power Engineering and Optimization Conference (PEOCO), 2014 IEEE 8th International.
- Seyedi, H., & Sanaye-Pasand, M. (2009). New centralised adaptive load-shedding algorithms to mitigate power system blackouts. *Generation, Transmission and Distribution, IET*, 3(1), 99-114. doi: 10.1049/iet-gtd:20080210
- Van Cutsem, T., Moors, C., & Lefebvre, D. (2002, 2002). *Design of load shedding schemes against voltage instability using combinatorial optimization*. Paper presented at the Power Engineering Society Winter Meeting, 2002. IEEE.





## Synchronous Reference Frame Fundamental Method in Shunt Active Power Filter for Mitigation of Current Harmonics

S. Musa<sup>1,2\*</sup> and M. A. M. Radzi<sup>1</sup>

<sup>1</sup>Department of Electrical and Electronic Engineering, Faculty of Engineering, Universiti Putra Malaysia, 43400 UPM, Serdang, Selangor, Malaysia

<sup>2</sup>Department of Electrical Engineering, College of Engineering, Kaduna Polytechnic, Kaduna, Nigeria

### ABSTRACT

This research presents compensation of current harmonic disturbance in power system network using shunt active power filter. In this paper, harmonic extraction using Synchronous Reference Frame Fundamental technique (SRFF) was investigated for three phase 3-wire system. It proposes a method based on direct current measurement of load currents using a band pass filter at low cut off frequencies to improve the filtering ability in highly contaminated loads. The proposed filter consists of second order low pass and high pass filters cascaded together at suitable frequencies, estimated based on the output of these units to mitigate the current harmonics. The performance of the system was simulated in Matlab Platform and evaluated considering total harmonic distortion of the source current in a three-phase balanced network. The simulation results show the ability of the proposed tracking scheme to accurately estimate harmonics.

*Keywords:* Shunt active power filter (SAPF), power quality, harmonics, synchronous reference frame (SRF), Low pass filter, high pass filter, band pass filter

### INTRODUCTION

Non-linear loads, such as power electronic converters, generate harmonic current and voltage into power system network leading to low power quality. This poor power

quality may trigger improper function of devices arising from balanced or unbalanced non-sinusoidal currents. The harmonic spectrum of some common nonlinear loads like uninterrupted power supply, switching mode power supplies and fluorescent lamps consists of odd order harmonics, dominated by 3rd, 5th and 7th harmonic components and compensating them would go a long way eliminating large bulk of harmonic currents (Gautam, Yunqing, Kafle, Kashif, & Hasan, 2014). Various harmonic mitigating devices

#### ARTICLE INFO

##### Article history:

Received: 24 August 2016

Accepted: 02 December 2016

##### E-mail addresses:

sumusa115@gmail.com (S. Musa),

amranmr@upm.edu.my (M. A. M. Radzi)

\*Corresponding Author

have been developed to adequately compensate not just harmonic current but also compensate reactive power, as well as unbalanced nonlinear and fluctuating loads. Thus, sinusoidal voltage and current with unity power factor will be supplied to the load. Shunt active power filter has been proven to be effective in compensating harmonic current and reactive power (Salam, Cheng, & Jusoh, 2006)(Jacob, Abraham, Prakash, & Philip, 2014)(Bojoi et al., 2005). It is designed to draw compensation current or voltage, from the utility, so that it cancels out the harmonic components on the ac side by injecting an equal but-opposite voltage or current distortion into the network.

The SAPF is connected in parallel to the load at PCC as shown in Figure 1. In a design of shunt active power filter, the controller is divided into : detection, dc bus control and current control (Newman, Zmood, & Holmes, 2002). The selection of methods to be adopted is a compromise between accuracy and computational intensity that influences real time application. Estimation of reference signal is initiated through detection of essential voltage/current signals to generate accurate system variables (information).The derivation of compensation signal from the disrupted wave that consists of both fundamental and harmonic contents, can be done by two different methods, either frequency domain or time domain approaches. In frequency domain, control strategy to extract compensating commands is based on Fourier analysis of the distorted voltage or current signals. Among its drawbacks, this technique involves a lot of mathematical computation which requires time to be executed. Also for efficient performance, a good and fast processor must be considered. Control strategy in time domain does not require much calculation, and are easy to be implemented (Singh, Al-haddad, & Chandra, 1999). It is based on instantaneous derivation of compensation commands in the form of either voltage or current signals of distorted signals (voltage or current).

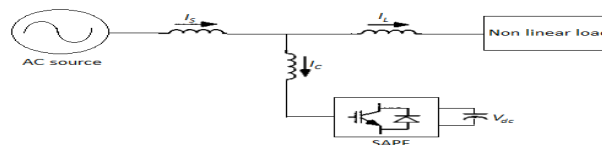


Figure 1. Shunt active power filter

Conventional current detection methods are usually based on harmonic detection of load currents using well-known control strategies in time domain, namely, instantaneous power theory (p-q theory) (Kale & Ozdemir, 2005), synchronous reference frame (SRF) (d-q theory) (Sundaram & Venugopal, 2016; Salim, Benchoula, & Goléa, 2011; Firouzjah, Sheikholeslami, Karami-Mollaei, & Heydari, 2009), synchronous detection method (George & Basu, 2008) etc. The control strategy based on synchronous reference frame (d-q theory) is the most widely popular because of its good performance in abnormal conditions and easy implementation (Giri Prasad, Dheeraj, & Naveen Kumar, 2012). Figure 2 shows block diagram of the harmonic current detection of this scheme. One way to improve accuracy and dynamics is the SRF technique which has faster response and small overshoot. In order to address problems HPF and low pass filter (LPF) were combined to develop a band pass filter (BPF). In LPF, its dc signal output has no phase shift and hence no delay. This design should improve the



performance of the SRF technique in mitigating current harmonics. Second order LPF and HPF were used to produce a fourth order BPF due to the fact that higher order filters will provide better performance in term of accuracy, which improves filtering process in compensating low order harmonics, which are not completely eliminated by other control strategies This design is simple and easy to be implemented. The BPF is tuned in terms of bandwidth, attenuation and centre frequency to obtain the desired total harmonic distortion (THD). In Section 2, the proposed control strategy of the harmonic detection technique is explained. In Section 3, details of harmonic extraction with BPF, and in Section 4, simulation results are presented and discussed. Finally, section 5 presents the summary of the study.

### HARMONIC CURRENT DETECTION TECHNIQUE.

The detection method used is the SRF technique, where the load current is transformed to rotating reference frame dq with  $\theta$  being the transformation angle. In this method,  $\theta$  as time varying angle represents the angular position of reference frame which is rotating at constant speed in synchronizing with the fundamental frequency of the AC system.

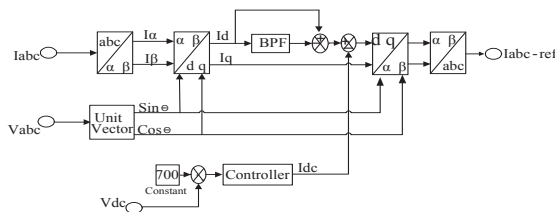


Figure 2. Block diagram of SRF method

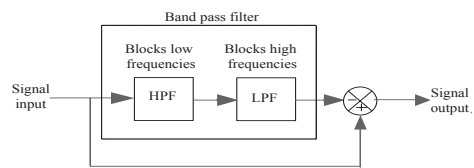


Figure 3. Cascaded HPF and LPF to band pass filter

Presented in Figure 2, is a block diagram of harmonic current detection technique as described in the following steps. In calculating the reference current for shunt active power filter using the SRF method, five steps are involved.

Step one starts with the three-phase supply current  $i_a$ ,  $i_b$  and  $i_c$  are transformed to 2- $\phi$  ( $\alpha$ - $\beta$ ) current in stationary reference frame  $i_\alpha$  and  $i_\beta$  as shown below.

$$\begin{bmatrix} i_\alpha \\ i_\beta \end{bmatrix} = \sqrt{\frac{2}{3}} \begin{bmatrix} 1 & -\frac{1}{2} & \frac{1}{2} \\ 0 & \frac{\sqrt{3}}{2} & -\frac{\sqrt{3}}{2} \end{bmatrix} \begin{bmatrix} i_a \\ i_b \\ i_c \end{bmatrix} \tag{1}$$

Step two involves changing from the  $\alpha - \beta$  plane to current reference in d-q frame, using a unit vector for generation of sine and cosine signals required for synchronization with the various phase to neutral voltages. The d-q currents obtained consist of AC and DC parts. The fundamental component of current becomes fixed DC part and the AC part represents the harmonic components. These harmonic components can easily be extracted using the BPF, as cascaded second order LPF and HPF, as shown in Figure 3.

Current expression in d-q reference frame, is given in equation 2

$$\begin{bmatrix} i_d \\ i_q \end{bmatrix} = \begin{bmatrix} \sin(\theta) & -\cos(\theta) \\ \cos(\theta) & \sin(\theta) \end{bmatrix} \begin{bmatrix} i_\alpha \\ i_\beta \end{bmatrix} \quad (2)$$

where  $\theta$  represent, the phase angle of voltage.

In step three, the detection of harmonics becomes a matter of removing the AC signal with the BPF.

$$\begin{bmatrix} i_d \\ i_q \end{bmatrix} = \begin{bmatrix} \tilde{i}_d & i_d \\ \tilde{i}_q & i_q \end{bmatrix} \quad (3)$$

Thus,  $i_\alpha$  and  $i_\beta$  are obtained as given below in step four:

$$\begin{bmatrix} i_\alpha \\ i_\beta \end{bmatrix} = \begin{bmatrix} \sin(\theta) & -\cos(\theta) \\ \cos(\theta) & \sin(\theta) \end{bmatrix} \begin{bmatrix} i_d \\ i_q \end{bmatrix} \quad (4)$$

The reference current  $i_{\alpha-ref}$  and  $i_{\beta-ref}$  is given by

$$\begin{bmatrix} i_{\alpha-ref} \\ i_{\beta-ref} \end{bmatrix} = \begin{bmatrix} \sin(\theta) & -\cos(\theta) \\ \cos(\theta) & \sin(\theta) \end{bmatrix} \begin{bmatrix} \tilde{i}_d + i_{dc} \\ \tilde{i}_q \end{bmatrix} \quad (5)$$

Finally, in step five, the abc reference frame is obtained using inverse transformation so that, current is as given below:

$$\begin{bmatrix} i_{\alpha-ref} \\ i_{\beta-ref} \\ i_{c-ref} \end{bmatrix} = \sqrt{\frac{2}{3}} \begin{bmatrix} \tilde{1} & 0 \\ -\frac{1}{2} & \frac{\sqrt{3}}{2} \\ \frac{1}{2} & -\frac{\sqrt{3}}{2} \end{bmatrix} \begin{bmatrix} i_{\alpha-ref} \\ i_{\beta-ref} \end{bmatrix} \quad (6)$$

The extracted harmonic current reference is compared with output current from inverter or filter current, thus, generating the required switching pulses for the inverter.

## DESIGN OF BAND-PASS FILTER

In order to mitigate low order harmonics and reactive power with BPF, two second-order LPF and HPF were designed and cascaded. In the fundamental dq-frame, overall harmonic compensation is achieved due to the fact that fundamental frequency is transposed to dc-signal. Its together with all harmonics using both LPF and HPF from the load current, gives a band of selected harmonic current spectrum. The literature suggests that fundamental d-q-frame does not allow specific selective harmonic current compensation; however, it has an interesting property in having characteristic of harmonic orders, in each is designed for one pair i.e.  $k=6n \pm 1$  of positive and negative sequence harmonics (Gautam et al., 2014; Lascu, Asiminoaei, Boldea, & Blaabjerg, 2007). There is therefore an advantage to compensate two harmonic orders at once. In (Lascu et al., 2007) specific loads, such as diode or thyristor rectifiers for example, the 5th harmonic consists of only negative-sequence component and that of 7th harmonic has only positive component. Both harmonics are derived from the sixth harmonic in fundamental reference frame, so that only a single regulator in the fundamental positive-sequence reference frame could be used for both harmonics. At lower cut-off frequencies with pass band to be set at 10 Hz, the BPF is tuned in terms of bandwidth, attenuation and centre frequency at the

desired harmonic frequency. With appropriate cut-off frequencies of BPF (as determined by equations 9 and 10), separation of fundamental and harmonic currents from measured system load current was achieved. This approach, effectively mitigates almost completely the more harmful harmonics from the load current, which are not sufficiently attenuated with other control schemes. Numerical filtering is a key issue in determining accuracy and dynamics of the harmonic detection mechanism. In selecting the characteristics of filter, a compromise between these two has to be made. These are determined by the cut-off frequency and order of the filter; filters with higher order and lower cut-off frequency improve attenuation of harmonics but, at a cost of slowed down response in event of load variation. Therefore, the trade-off is between accuracy and speed (response time) should be discovered.

Equations 7-10 are given below, used for determining filter parameters:

$$\text{Bandwidth } BW = f_2 - f_1. \quad (7)$$

$$\text{Quality factor } Q = \frac{f_0}{BW} \quad (8)$$

$$\text{High pass filter cut-off frequency } f_1 = \sqrt{\left(\frac{BW}{2}\right)^2 + f_0^2} - \frac{BW}{2} \quad (9)$$

$$\text{Low pass filter cut-off frequency } f_2 = \sqrt{\left(\frac{BW}{2}\right)^2 + f_0^2} + \frac{BW}{2} \quad (10)$$

Where BW = Bandwidth, Q = Quality factor,  $f_1$  = low cut-off frequency,  $f_2$  = high cut-off frequency,  $f_0$  = centre frequency.

## RESULTS AND ANALYSIS

The shunt APF performance was investigated using Matlab/Simulink software in the simulation study. A 3- $\phi$  voltage supply with uncontrolled rectifier with resistor-inductor (RL) load (non-linear load) is used as the test system. To mitigate harmonics, shunt APF is connected with the test system via filter inductor L. Figures 4 to 6 below displayed the related results from the simulation work. The THD due to non-linear load of distorted line current is 25.60% as depicted in Figure 4 from fast Fourier transform (FFT) analysis of load current before compensation. This result, clearly shows that, supply current is distorted due to presence of non-linear load. The harmonic spectrum of the distorted waveform is displayed in Figure 4a. In order to eliminate the current harmonics, the shunt active power filter successfully reduced THD of source current to 1.16% (as obtained from FFT analysis shown in Figure 4b). Figure 5a shows waveform of load current before compensation, while Figure 5b displays the source current after compensation, Figure 6a displays the compensation current, and Figure 6b displays DC bus capacitor voltage. The analyses were carried out for the proposed BPF, and with LPF too, for comparison.

Table 1 shows findings obtained from the analyses. The BPF shows a better performance in terms of THD. The smaller bandwidth results in better finding. At lower cut-off frequency with pass band of 10 Hz, the BPF produces good performance. With appropriate cut-off frequencies of BPF, separation of fundamental and harmonic currents from the measured load current was

achieved, and this shows effectiveness of the configuration in mitigating low order harmonics. Different loads were test to verify the performance of the SAPF with both LPF and BPF. The result is presented in Table 2. Again, the BPF has displayed better performance in mitigating current harmonics.

Table 1  
THD with and without shunt active power filter

Harmonic order	THD %		
	Without SAPF	With SAPF LPF tr = 0.159	With SAPF BPF tr = 0.17
1 <sup>st</sup>	100.00	100.00	100.00
3 <sup>rd</sup>	0.00	1.23	0.20
5 <sup>th</sup>	20.96	0.58	0.24
7 <sup>th</sup>	9.92	0.33	0.24
9 <sup>th</sup>	0.00	0.15	0.03
11 <sup>th</sup>	7.63	0.18	0.17
13 <sup>th</sup>	4.94	0.14	0.14
THD%	25.60	3.00	1.16

Table 2  
THD with and without shunt active power filter

Loads	THD %	
	LPF	BPF: (LPF & HPF)
50Ω 100mH	3.64	1.11
20Ω 20mH	3.32	1.49
40Ω 100mH	2.90	1.18
30Ω 10mH	2.90	1.25
30Ω 5mH	2.90	1.25
40Ω 10mH	2.98	1.16
40Ω 90mH	2.91	1.16
30Ω 50mH	3.00	1.25

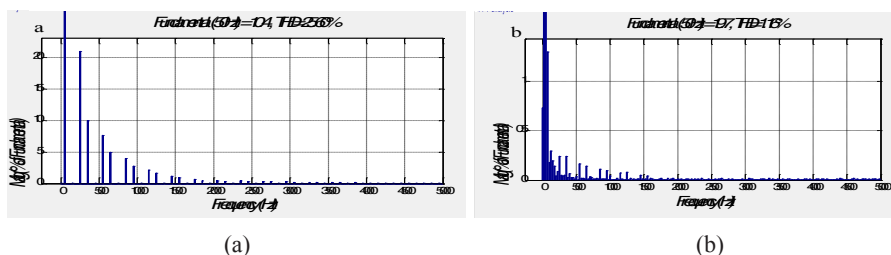


Figure 4. FFT analysis of source current (a) before and (b) after compensation

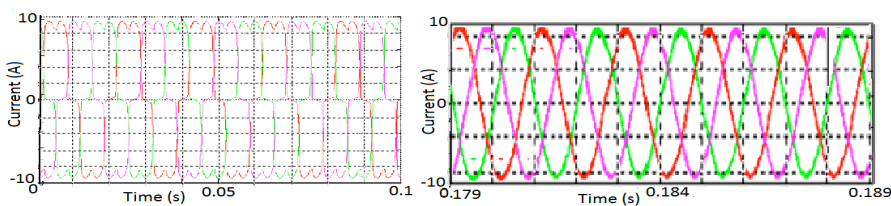


Figure 5. (a) Source current before compensation (b) Source current after compensation

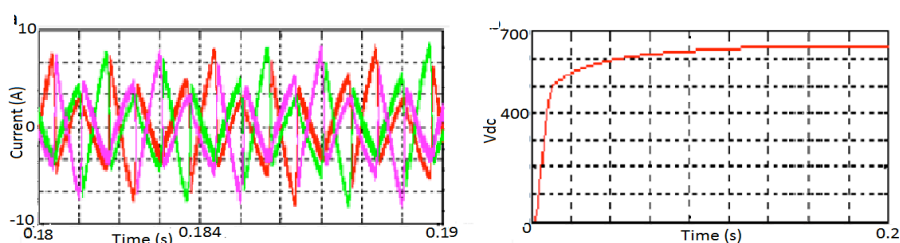


Figure 6. (a) Compensation current

Figure 6. (b) DC bus capacitor voltage

## CONCLUSION

In this work, an improvement in filtering performance of the dq reference frame technique was presented. This was achieved by combining the properties of HPF and LPF in developing BPF. Interestingly, the dc output signal of LPF has zero phase shift; therefore, it has no delay. Second order LPF and HPF were used to produce fourth order BPF, as higher order filters provide better performance, being more accurate thus improving the filtering process. In compensating low order harmonics, which are not completely eliminated by other control strategies. The design is simple and easy to be implemented. The simulation results show effectiveness of this method in mitigating low order harmonics in the system with THD reducing from 25.60% to 1.16%.

## REFERENCES

- Asiminoael, L., Blaabjerg, F., & Hansen, S. (2007). Detection is key-Harmonic detection methods for active power filter applications. *IEEE Industry Applications Magazine*, 13(4), 22-33.
- Bojoi, R. I., Griva, G., Bostan, V., Guerriero, M., Farina, F. and, & Profumo, F. (2005). Current Control Strategy for Power Conditioners Using Sinusoidal Signal Integrators in Synchronous Reference Frame. *IEEE Transactions on Power Electronics*, 20(6), 1402–1412.
- Firouzjahi, K. G., Sheikholeslami, a., Karami-Mollaei, M. R., & Heydari, F. (2009). A predictive current control method for shunt active filter with windowing based wavelet transform in harmonic detection. *Simulation Modelling Practice and Theory*, 17(5), 883–896. <http://doi.org/10.1016/j.simpat.2009.02.008>
- Gautam, S., Yunqing, P., Kaffle, Y., Kashif, M., & Hasan, S. U. (2014). Evaluation of Fundamental d-q Synchronous Reference Frame Harmonic Detection Method for Single Phase Shunt Active Power Filter. *International Journal of Power Electronics and Drive System*, 4(1).
- George, M., & Basu, K. P. (2008). Performance Comparison of Three-Phase Shunt Active Power. *American Journal of Applied Sciences*, 5(11), 1424–1428.
- Giri Prasad, A., Dheeraj, K., & Naveen Kumar, A. (2012). Comparison of Control Algorithms for Shunt Active Filter for Harmonic Mitigation. *International Journal of Engineering Research and Technology (IJERT)*, 1(5), 1–6.
- Jacob, A., Abraham, B. T., Prakash, N., & Philip, R. (2014). A Review of Active Power Filters In Power System Applications. *International Journal of Advanced Research in Electrical, Electronics and Instrumentation Engineering*, 3(6), 10253–10261.

- Kale, M., & Ozdemir, E. (2005). Harmonic and reactive power compensation with shunt active power filter under non-ideal mains voltage. *Electric Power Systems Research*, 74, 363–370. <http://doi.org/10.1016/j.epsr.2004.10.014>
- Lascu, C., Asiminoaei, L., Boldea, I., & Blaabjerg, F. (2007). High Performance Current Controller for Selective Harmonic Compensation in Active Power Filters. *IEEE Transactions on Power Electronics*, 22(5), 1826–1835.
- Newman, M. J., Zmood, D. N., & Holmes, D. G. (2002). Stationary Frame Harmonic Reference Generation for Active Filter Systems. *IEEE Transactions on Industry Applications*, 38(6), 1591–1599.
- Salam, Z., Cheng, T. P., & Jusoh, A. (2006). Harmonics Mitigation Using Active Power Filter : A Technological Review. *Elektrika*, 8(2), 17–26.
- Salim, C., Benchouia, M. T., & Goléa, A. (2011). Harmonic current compensation based on three-phase three-level shunt active filter using fuzzy logic current controller. *Journal of Electrical Engineering and Technology*, 6(5), 595-604.
- Singh, B., Al-haddad, K., & Chandra, A. (1999). Power Quality Improvement. *IEEE Transactions on Industrial Electronics*, 46(5), 960–971.
- Sundaram, E., & Venugopal, M. (2016). Electrical Power and Energy Systems On design and implementation of three phase three level shunt active power filter for harmonic reduction using synchronous reference frame theory. *International Journal of Electrical Power and Energy Systems*, 81, 40–47. <http://doi.org/10.1016/j.ijepes.2016.02.008>

## A Study of Negative Bias Temperature Instability (NBTI) in p-MOSFET Devices

H. Hussin<sup>1,2\*</sup> and M. F. Zainudin<sup>1,2</sup>

<sup>1</sup>Faculty of Electrical Engineering, Universiti Teknologi Mara (UiTM), 40450 Shah Alam, Selangor, Malaysia

<sup>2</sup>Integrated Microelectronics System and Application Research Group, Universiti Teknologi Mara (UiTM), 40450 Shah Alam, Selangor, Malaysia

### ABSTRACT

Negative bias temperature instability (NBTI) is a common phenomenon in a p-channel MOSFET device under a negative gate-to-source voltage at a high stress temperature. This paper presents the NBTI characterisation based on different analysis methods and stress conditions on p-MOSFET devices. The atomic hydrogen concentration is probed at interface, Poly-Si and channel of p-MOSFET under study using SILVACO TCAD tool. In addition, the behaviour of the permanent and recoverable component was investigated based on AC stress at different stress conditions using Modelling Interface Generation (MIG) tool. The results show that increases in temperature, negative voltage stress gate and decreases in frequency increase the threshold voltage shift, thus enhancing NBTI degradation.

*Keywords:* NBTI, temperature, voltage stress gate, frequency, threshold voltage ( $V_{th}$ ), AC, DC, recovery

### INTRODUCTION

Negative bias temperature instability (NBTI) occurs in p-channel MOSFET that operates with negative gate-to-source voltage at elevated temperature. NBTI contributes to degradation of transistor parameters which are

increasing of the threshold voltage, decreasing of transconductance, drain current, channel mobility and subthreshold slope. NBTI not only degrade circuit performance, it can also results in circuit failures (R. Entner, 2014). A gradual shift of threshold voltage ( $V_{th}$ ) over time is commonly observed due to the application of voltage stress on the gate, temperature, and the duty cycle for AC only of the stressing voltage under static stress (DC) and dynamic stress (AC) (Mishra, Pandey, & Alam, 2012).

#### ARTICLE INFO

##### Article history:

Received: 24 August 2016

Accepted: 02 December 2016

##### E-mail addresses:

hanimh@salam.uitm.edu.my (H. Hussin),

mfitrizainudin@gmail.com (M. F. Zainudin)

\*Corresponding Author

**NBTI mechanism based on R-D model**

The model used to define the NBTI mechanism is the rate-diffusion (R-D) model, according to which the electric field was able to break Si-H bonds located at the Silicon-oxide interface. H was released in the substrate where it migrates. The remaining dangling bond Si- (Pb centre) contribute to the threshold voltage degradation. On top of the interface states generation some pre-existing traps located in the bulk of the dielectric (and supposedly nitrogen related), were filled with holes coming from the channel of pMOS. Those traps can be emptied when the stress voltage was removed. This  $V_{th}$  degradation can be recovered over time (Mishra et al., 2012; R. Entner, 2014, Ang, Member, Teo, Ho, & Ng, 2011). Figure 1 shows that released hydrogen diffuses into the gate oxide during stress and returns back to the interface when stress was removed. The active region of the NBTI mechanism was uniformly distributed over the channel according to a one-dimensional problem. Figure 2 depicts that a hole can tunnel to a Si-H bond during inversion of the p-MOSFET and it can take one electron of the covalent bonding away. After that, the hydrogen atom diffuses away with its electron and leaves a positively charged interface trap behind (Entner, 2014).

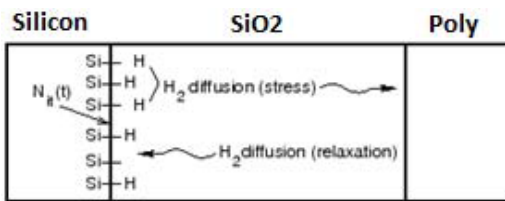


Figure 1. Schematic description of the R-D model (Entner, 2014)

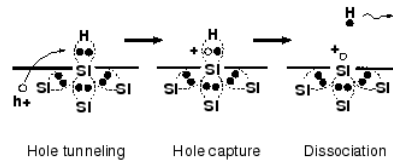


Figure 2. Mechanism for breaking interfacial Si-H bonds by inversion-layer holes (Entner, 2014)

In NBTI, different stress conditions will result in changes in threshold voltage. The methods used in characterizing NBTI degradation causes degradation due to recovery effect to differ (Mishra et al., 2012). Increased defects will lead to shorter device lifetime and device failure. The relationship between the defect shown by the equation below. As the threshold was increased due to the NBTI, the drain current ( $I_D$ ) and transconductance ( $g_m$ ) also degraded. A shift in the threshold voltage ( $\Delta V_{TH}$ ) of the PMOS transistor is proportional to the interface trap generation due to NBTI, which can be expressed as

$$\Delta V_{th} = \frac{qN_{it}(t)}{C_{ox}} (1-m) \tag{1}$$

Where  $m$  represents equivalent  $V_T$  shifts due to mobility degradation (or model parameter),  $q$  is the electronic charge, and  $N_{it}(t)$  is the interface trap generation, which is the most important factor in evaluating performance degradation due to NBTI for R-D model (Mishra et al., 2012).



### Generation and Recovery of Interface Trap

Based on the pre-existing interface traps and creation of the new interface states, there were two components of NBTI which were permanent and temporary as shown in Figure 3 (Mishra et al., 2012). Permanent NBTI was known as non-recoverable because of the new interface trap generation. Meanwhile, temporary NBTI was known as recoverable because of some pre-existing traps present in the gate oxide was filled with holes from the PMOS channel and the hole can be emptied when the stress voltage was removed (Mishra et al., 2012). The component that effect most of the increasing of threshold voltage was mainly due to the permanent NBTI rather than temporary which partly effect threshold voltage (Mishra et al., 2012).

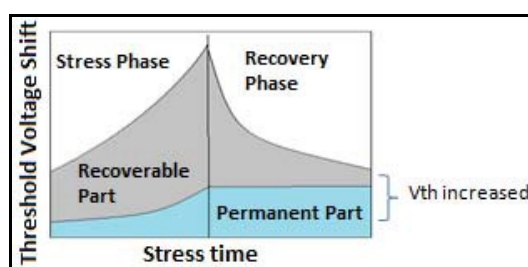


Figure 3. Temporary and permanent phase of NBTI (Mishra et al., 2012)

An early hypothesis was made based on the review paper by Mahapatra (Mahapatra et al., 2013), in negative stress bias ( $V_G$ ) results in increasing of NBTI phenomenon although the magnitude depends on gate oxide field ( $E_{ox}$ ). NBTI phenomena shown to be a temperature dependant where it increases at elevated temperature based on Arrhenius law. Gate oxide field, temperature and stress time can be summarized to be related in increasing of NBTI phenomena by a simple analytic formula (Franco, 2014):

$$\Delta V_{th} \approx \left( -\frac{E_A}{k_B T} \right) \left( \frac{|V_G - V_{th0}|}{t_{ox}} \right)^Y t_{stress}^n \quad (2)$$

Where  $E_A$  is an apparent activation energy,  $k_B$  is the Boltzmann constant and  $T$  is the stress temperature.

In this paper, we probe atomic hydrogen concentration at different location of p-MOSFET device interface, Poly-Si and channel using SILVACO TCAD. The threshold voltage shift of p-MOSFET based on different stress condition in DC and AC analysis were analysed and the behaviour of the permanent and recoverable component of p-MOSFET subject to AC stress we studied.

### METHODOLOGY

In this project, SILVACO TCAD and Modelling Generation (MIG) were the simulation tools used to study the NBTI phenomenon. Figure 4 shows a process flow of creating device structure and characterization process using ATHENA and ATLAS respectively. The atomic hydrogen

concentration was probed at interface, Poly-Si and channel of p-MOSFET as to observe the generation of interface trap at three different location in the MOSFET device (Coulombs, 2010). In this work, a conventional SiO<sub>2</sub> p-MOSFET device with gate length of 1µm was created as shown in Figure 5.

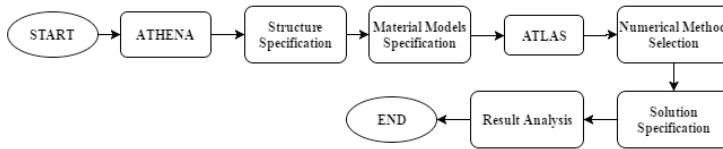


Figure 4. The process design flow in SILVACO TCAD

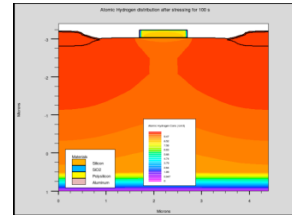


Figure 5. A submicron device structure of p-MOSFET

The MIG was a simulation tool used to estimate the change in the interface trap ( $\Delta N_{IT}$ ), hence threshold voltage shift ( $\Delta V_T$ ), resulting from NBTI phenomena, based on the voltage, temperature and stress conditions given. It can be used to mimic the experimental condition by indicating the points where  $\Delta V_T$  measurement has to be taken, including the effect of delay (due to  $\Delta V_T$  measurement time required by the setup). Finally, based on the measured  $\Delta V_T$  under DC (continuous stress) condition, projection of lifetime,  $t_{life}$  (the time at which the device will degrade up to a certain value of  $\Delta V_T$ ) can be made at both DC and AC (periodic stress, having duty cycle of 50%) (Islam, n.d.).

## EXPERIMENTAL RESULTS

### Effect of Different Probing Location based on Different Stress Temperature and Stress Voltage

A stress was applied to this submicron device by varying the voltage stress and temperature. Based on the result of the simulation, the hydrogen concentration was studied at three different location: centre of the interface, Poly-Si gate contact and Si channel (Coulombs, 2010). The atomic hydrogen concentration was observed as to understand the breaking of Si-H bond during the stress phase and hydrogen passivation during the recovery phase (Mishra et al., 2012).

Temperature ranging from 300K to 420K was applied with same voltage stress on the gate oxide of -2V. The applied temperatures were within the range of 100°C to 150°C, within which significant NBTI degradation was observed (Hussin, Soin, Bukhori, Abdul Wahab, & Shahabuddin, 2014). A total dangling bond density of  $1 \times 10 \text{ cm}^{-2}$  was assumed (initially passivated 100%) (Coulombs, 2010). However, the result shown that the total dangling bond was not passivated at 100%. This was due to the submicron device structure does not completely created properly in SILVACO ATHENA.

Based on Figure 6 – Figure 8, the atomic hydrogen concentration at 420K shows higher concentration than temperature at 398K and 300K. This was because under a high temperature

the hydrogen diffuses much more faster which was why at temperature 420K has higher concentration than 398K and 420K. The hydrogen diffuse more in centre of interface than in Poly-Si contact and Si contact due to the electric field break Si-H bond at the centre of the interface located at the Silicon-oxide interface (Entner, 2014).

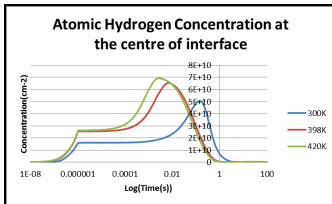


Figure 6. Atomic hydrogen concentration at the centre of the Interface

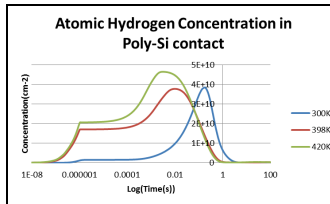


Figure 7. Atomic hydrogen concentration in Poly-Si contact

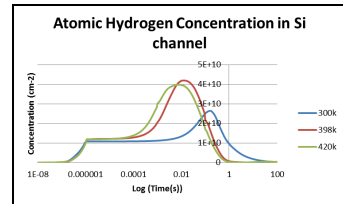


Figure 8. Atomic hydrogen concentration in Si channel

Next, negative voltage stress on the gate oxide from range -1.5V to -2.5V were applied. This time the temperature were set to constant temperature of 398K. The collected data were used to fit the model parameters for NBTI simulation (Wittmann et al., 2005). The applied stress voltages,  $V_S$ , were varied between -1.2 V and -2.52 V such that the oxide electric field ( $E$ ) was maintained within the range of  $6 \text{ MV cm}^{-1}$  to  $11 \text{ MV cm}^{-1}$  in both p-MOSFETs with different Equivalent Oxide Thickness (EOT), thus replicating stress conditions in real-life experiments (Hussin et al., 2014). The expected total dangling bond was also the same during temperature stress:  $1 \times 10^{12} \text{ cm}^{-2}$ .

Figure 9 – Figure 11 show the atomic hydrogen concentration at three different location. The concentration at voltage stress of -2.5V was higher than voltage stress of -1.5V and -2V. The higher the temperature and voltage stress will result in higher hydrogen passivation (Mishra et al., 2012). Thus, generate more interface trap which later result in increasing the threshold voltage ( $V_{TH}$ ). Increasing in threshold voltage ( $V_{TH}$ ) will result the NBTI degradation.

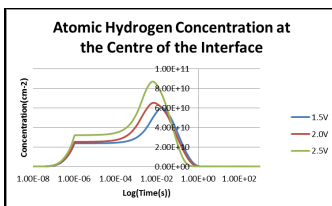


Figure 9. Atomic hydrogen concentration at the centre of the Interface

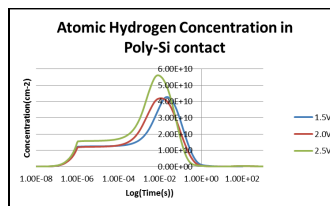


Figure 10. Atomic hydrogen concentration in Poly-Si contact

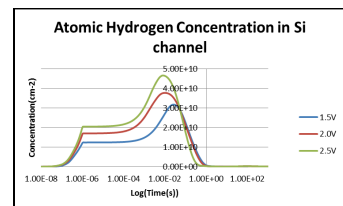


Figure 11. Atomic hydrogen concentration in Si channel

### Effect of Different Stress Condition based on AC Measurement

In AC analysis, similar range of temperature stress and voltage stress used in DC analysis will be applied. In addition, a frequency from a range of 0.001Hz to 0.01Hz as to account for AC measurement was applied. The permanent and recovery component plays an important role to study the NBTI characterization. The recovery mechanism can be observed when a device was subject to a train of stressing pulses which was known as AC stress (Mishra et al., 2012).

During the first phase of the clock cycle,  $V_{th}$  increases due to the stress applied, and then it decreases again in the second half of the cycle when the stress was removed as shown in the Figure 12 below (Mishra et al., 2012). As shown in the figure, a CMOS inverter was drawn and when the  $V_g$  i.e. input gate voltage is zero (i.e.  $V_{gs} = -V_{DD}$ ), the PMOS will be in the stress phase and when  $V_g$  is  $V_{DD}$  (i.e.  $V_{gs} = 0$ ) then PMOS will be in relaxation phase as shown (Mishra et al., 2012). It is important to understand the stress and recovery phenomenon in p-MOSFET devices as the operation of CMOS inverter can significantly affect by the reliability issues specifically the NBTI occurrence in a p-MOSFET devices.

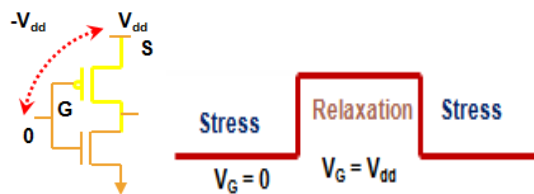


Figure 12. Pulse showing stress and relaxation phase of a PMOS (Mishra et al., 2012)

Figure 13 shows the permanent and recoverable component of the p-MOSFET device under stress of temperature at  $125^{\circ}\text{C}$ , voltage stress gate at  $-2.0\text{V}$  and frequency at  $0.001\text{Hz}$ . The permanent component,  $\Delta V_t^s$  was created as the new interface trap generation when the device was put under stress meanwhile the recovery component,  $\Delta V_t^r$  was obtained when some pre-existing traps present in the gate oxide was filled with holes from the PMOS channel and the hole can be emptied when the stress voltage was removed (Hussin et al., 2014). The device was stressed and relaxed until 5000s in 5 cycle. The threshold voltage ( $V_{TH}$ ) increase slightly for each cycle at the end of applied stress and recovery.

### Effect of Different Stress Condition based on Permanent and Recoverable Component

Figure 14 and 15 show the permanent and recoverable threshold voltage ( $V_{TH}$ ) under three different stress condition: temperature (range from  $75^{\circ}\text{C}$  to  $150^{\circ}\text{C}$ ), voltage stress gate (range from  $-1.6\text{V}$  to  $-2.3\text{V}$ ) and frequency (range  $0.001\text{Hz}$  to  $0.01\text{Hz}$ ). The permanent component in Figure 14 can be obtained by subtracting the threshold voltage ( $V_{TH}$ ) at the end of recovery with the threshold voltage ( $V_{TH}$ ) at the beginning of stress (Hussin et al., 2014). Same with the permanent component, the recovery component in Figure 15 also can be obtained by subtracting the  $V_{TH}$  at the end of recovery and  $V_{TH}$  at the beginning of the recovery (Hussin et al., 2014).

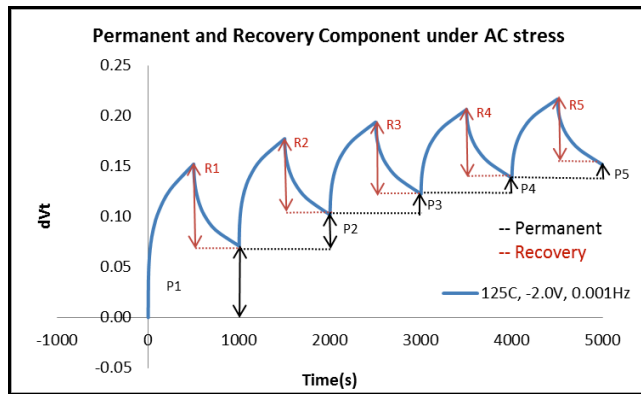


Figure 13. Permanent and Recoverable component at different temperature under AC stress

The permanent and recoverable shift  $V_{TH}$  decreases as the cycle increases. This result was consistent with the self-limiting recovery perspective, where in the recovery is dependent on the number of stress cycles (Hussin et al., 2014). This degradation mechanism, in which a reduction in the recovery is observed, can be explained by the influence of increasing stress recovery cycles that can contribute to greater structural relaxation; consequently, the oxide network was distorted and the hole traps cannot be recovered, thus being transformed into a more permanent form (Hussin et al., 2014). The graph was obtained using the same method in paper (Ang et al., 2011; Grasser et al., 2010; Hussin et al., 2014; Jia et al., 2013).

The threshold voltage shift increases as the frequency decreases. This is due to at high frequency, there was an asymmetry of the delays between dissociation and annealing (Entner, 2014). It can be speculated that a short delay exists between the availability of holes and their capture by Si-H bonds. It can be assumed that the slower starting of the dissociation process was responsible for the reduced threshold shift in the higher frequency (Entner, 2014).

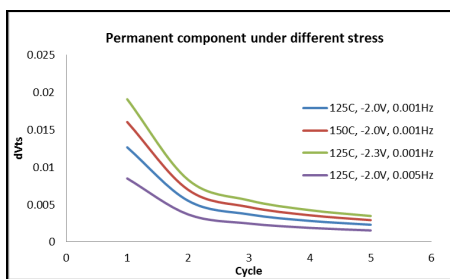


Figure 14. Permanent component of different stress under AC stress

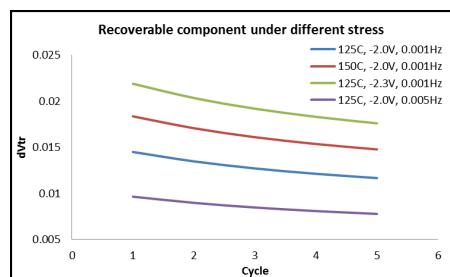


Figure 15. Recoverable component of different stress under AC stress

## DISCUSSION

Concentration of atomic hydrogen on three different locations on p-MOSFET were influenced by temperature and negative voltage stress ( $V_G$ ). Higher temperature results in a higher probability of hydrogen diffusion in the centre of the interface to gate oxide from the breaking of Si-H bond due to the electric field during the stress phase. The process of breaking the Si-H bond becomes much faster at elevated temperature until at its peak of stress time before it diffuses back into  $\text{SiO}_2$  to recombine back into Si-H bond during the recovery phase. The negative voltage stress ( $V_G$ ) with a magnitude of the gate oxide field ( $E_{OX}$ ) creates the electric field which is capable of breaking the Si-H bonds. As the  $V_G$  increases, the electric field becomes much stronger, which causes more Si-H bonds to break to produce a hydrogen atom. As the atomic hydrogen concentration increases, the  $V_{TH}$  shift also increases, which lead to NBTI degradation effects. In DC stress, the threshold voltage shift ( $V_{TH}$ ) increases with the applied stress time. For AC stress, there are stress phase and the recovery phase in each cycle in a specific period of time. The stress time and recovery time, reduce for the next cycle. This result to less permanent and recovery component in the next cycle. The permanent and recoverable component decreases over time in each cycle due to less stress and recovery time for each cycle.

Temperature and negative voltage stress (with a magnitude of oxide field) are well-known NBTI dependence. Therefore, it is very crucial to determine the range of applied stress voltage and temperature during the NBTI characterization process to reduce the possibility of other defect mechanisms such as Time Dependent Dielectric Breakdown (TDDB) and hot carrier injection (HCI) occur. Higher frequency also reduces NBTI degradation in AC analysis. In view of the recovery process being significant in reducing the NBTI effects, to ensure no recovery contribution during the stress-measure-stress characterization process, other techniques such as fast and ultra-fast on-the-fly (OTF) techniques can be used as this method do not suffer from recovery artefacts and are suitable for measuring degradation from short to long t-stress (Mahapatra et al., 2013).

## CONCLUSION

This paper presents the NBTI degradation phenomenon for DC and AC analysis, which the underlying mechanisms based on R-D model. The Silvaco TCAD tool was used as to understand the behaviour of interface trap concentration. Using the MIG tool, higher temperature and negative voltage stress gate well as lower frequency results in higher threshold voltage shift. The permanent and recoverable threshold voltage shift decreases as the cycle increases during AC measurement. A Two Stage the underlying mechanism includes the pre-existing effect together with the interface trap can be used in future work as to enhance the understanding of NBTI degradation in p-MOSFET devices with different technologies such as high-k devices and advanced FinFET technology with regard to the recoverable component issues.

## ACKNOWLEDGMENT

This work was supported by Ministry of Higher Education (MOHE) under Fundamental Research Grant Scheme (FRGS: 600-RMI/FRGS 5/3 (31/2015)). Authors would like to thank Integrated Microelectronics System and Application Research Group (IMSaA) and Faculty of Electrical Engineering, UiTM Shah Alam for the support in making this study a success.

## REFERENCES

- Ang, D. S., Member, S., Teo, Z. Q., Ho, T. J. J., & Ng, C. M. (2011). Reassessing the Mechanisms of Negative-Bias Temperature Instability by Repetitive Stress / Relaxation Experiments, 11(1), 19–34.
- Coulombs, Q. (2010). Simulating Negative Bias Temperature Instability of p-MOSFETS. *The Simulation Standard*, 9–13.
- Entner, R. (2014). *NBTI Reliability Analysis*. Retrieved November 6, 2014, from <http://www.iue.tuwien.ac.at/phd/wittmann/node10.html>
- Franco, J. (2014). *Degradation Mechanisms - Reliability of High Mobility SiGe Channel MOSFETs for Future CMOS Applications* (Springer S). Springer Science+Business Media Dordrecht. <http://doi.org/10.1007/978-94-007-7663-0>
- Grasser, T., Aichinger, T., Reisinger, H., Franco, J., Wagner, P.-J., Nelhiebel, M., ... Kaczer, B. (2010). On the “permanent” component of NBTI. *2010 IEEE International Integrated Reliability Workshop Final Report*, 2–7. <http://doi.org/10.1109/IIRW.2010.5706472>
- Hussin, H., Soin, N., Bukhori, M. F., Abdul Wahab, Y., & Shahabuddin, S. (2014). New Simulation Method to Characterize the Recoverable Component of Dynamic Negative-Bias Temperature Instability in p-Channel Metal–Oxide–Semiconductor Field-Effect Transistors. *Journal of Electronic Materials*, 43(4), 1207–1213. <http://doi.org/10.1007/s11664-014-2978-8>
- Islam, A. E. (n.d.). User ’ s Manual for Modeling Interface-defect Generation ( MIG ).
- Jia, J. Y., Liu, P., Xue, F., Tien, J., Cai, A., Dhaoui, F., ... McCollum, J. (2013). High voltage PMOS FET NBTI results and mechanism. *2013 IEEE International Integrated Reliability Workshop Final Report*, 154–156. <http://doi.org/10.1109/IIRW.2013.6804182>
- Mahapatra, S., Member, S., Goel, N., Member, S., Desai, S., Gupta, S., ... Alam, M. A. (2013). *A Comparative Study of Different Physics-Based NBTI Models*, 60(3), 901–916.
- Mishra, R. K., Pandey, A., & Alam, S. (2012). Analysis and Impacts of Negative Bias Temperature Instability ( NBTI ), 2–5.
- R. Entner. (2014). *Negative Bias Temperature Instability*. Retrieved April 1, 2014, from <http://www.iue.tuwien.ac.at/phd/entner/node24.html>
- Wittmann, R., Puchner, H., Hinh, L., Ceric, H., Gehring, A., & Selberherr, S. (2005). *Simulation of Dynamic NBTI Degradation for a 90nm CMOS Technology*, 3, 29–32.







## Planar Sensors Array for Water Contaminants Detections

Aizat Azmi, Sallehuddin Ibrahim, Ahmad Amsyar Azman, and Mohd Amri Md Yunus\*

*Innovative Engineering Research Alliance, Control and Mechatronic Engineering Departments, Faculty of Electrical Engineering, Universiti Teknologi Malaysia, 81310 Johor Bahru, Johor, Malaysia*

### ABSTRACT

Planar electromagnetic sensors are widely used in many applications due to its low cost, simple architecture, and fast response. Currently, there are many types of membranes which have been introduced to remove contaminants from an aqueous solution. Hence, the water quality could be maintained and safe to consume. The objective of this paper is to apply and investigate the effectiveness of a selective membrane in detecting nitrate, phosphate, zinc, and nickel ions by means of planar electromagnetic sensors array (PESA). The samples have four different concentration levels, 5 ppm, 25 ppm, 75 ppm, and 100 ppm. The selective membrane's performance is evaluated based on absolute average sensitivity ( $|Z\%$ ). This performance is compared with conventional coating such as incralac. The developed membrane consists of two elements which are polymer and solvent. Modified silica is selected as a polymer material while N-(2-Aminoethyl)-3 Aminopropyltrimethoxysilane is selected as a solvent. The selection of these materials is based on their ability to attract the contaminants in the aqueous solution and hence increased the selectivity. The proposed sensor with a membrane shows its higher sensitivity compared to incralac. The highest sensitivity is 338 % which observed in the presence of membrane for the nickel detection. Meanwhile, the lowest sensitivity using membrane is 12 % for zinc detection.

*Keywords:* Planar electromagnetic sensor array, water contaminants, star configuration, water supply quality

### ARTICLE INFO

*Article history:*

Received: 24 August 2016

Accepted: 02 December 2016

*E-mail addresses:*

azizat\_alfateh@yahoo.com (Aizat Azmi),  
salleh@fke.utm.my (Sallehuddin Ibrahim),  
amsyar240390@gmail.com (Ahmad Amsyar Azman),  
amri@fke.utm.my (Mohd Amri Md Yunus)

\*Corresponding Author

### INTRODUCTION

Tremendous developments in the agricultural and industrial sectors have directly affected the water supply quality. Agricultural activities, farm animals, and industry are the primary causes for increases in non-metallic impurities in water resources. These impurities or foreign substances may contain

various diseases and therefore dangerous to humans. A high concentration of nitrate in drinking water can lead to gastric cancer, blue baby syndrome, and Parkinson's disease (World Health Organization, 2011). For instance, zinc can have a corrosive effect on human skin and damage the nervous membrane. Therefore, it is very important to have a standard guideline to monitor the level of contaminants in water. A rapid and efficient system for contaminants detection at lower concentration levels can be useful. Table 1 lists the standard of contaminants in drinking water set by the World Health Organization (WHO).

Table 1  
*Contaminants standard in drinking water*

Pollutants	WHO	EPA
Nitrate	0.05	-
Phosphate	5 ppm	-
Zinc	5 ppm	5 ppm
Copper	1.0 ppm	1 ppm
Arsenic	0.05 ppm	0.01 ppm
Lead	0.05 ppm	0.015 ppm

Many researches have proposed various methods to detect these contaminants above in water, such as spectrophotometric, chromatography (Kodamatani et al., 2009), potentiometry (Hassan, 1976), amperometric, and biosensor (Albanese et al., 2010). However, these methods have their own drawbacks such as exposure towards emission of hazardous gases, measurement error due to interference from other contaminant, kinetic charge transfer at electrode surface are low thus direct reduction of nitrate is characterized by poor sensitivity and reproducibility, low sample throughput and large scale equipment, lengthy analysis time, costly instrumentation requirements, as well as utilization of toxic reagents and carrier solution, and limitation of large sample size required. Due to these issues, PESA is introduced to determine the near-to-the-surface properties, such as dielectrics, permeability and conductivity (Ong et al., 2001) (Hofmann et al., 2005). The applications of PESA can be found in food safety, sheep skin estimation, and bacterial content detection (Ong et al., 2001) (Yunus et al., 2009) (Hofmann et al., 2005), where the sensors are sensitive to the different magnetic susceptibilities and dielectric properties of each material (Nor et al., 2013) (Ong et al., 2001). Research (Yunus et al., 2015) proved that the coating layer could vary the sensitivity of the sensor. On the other hand, protective layer could protect the sensor surface from extreme chemical reaction from contaminants. This research focuses on developing PESA with different types of coating to detect nitrate, phosphate, zinc, and nickel.

## **PESA FOR NITRATE, PHOSPHATE, ZINC, AND NICKEL DETECTION**

### **PESA Architecture and Detection Principle**

In this section, the architecture and detection principle of PESA for contaminants measurement are elaborated. PESA consists of a series-connected meander sensor and an interdigital sensor.

The sensor array is fabricated in a thin substrate such as a printed circuit board (PCB) using the conventional PCB fabrication technique. The meander sensor consists of several loops or coils of electrodes and is designed to be spiral or square shape. The interdigital sensor consists of positive and negative electrodes and is designed to be parallel between positive and negative electrode. The ground electrode is placed at the bottom of the interdigital sensor. The combination of the meander and interdigital type provides the best sensitivity. The architecture of the sensor array is illustrated in Figure 1.

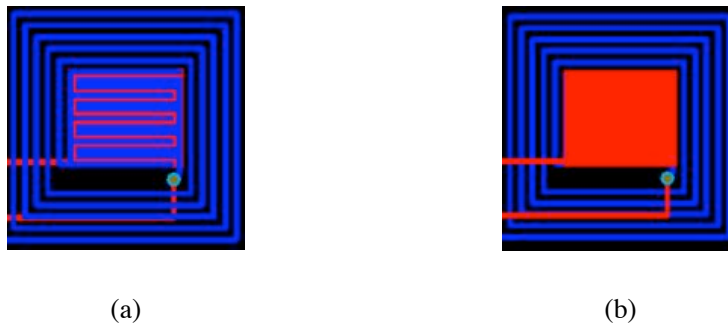


Figure 1. Planar electromagnetic sensor architecture (a) Top view (b) Bottom view

According to Figure 1, the sensors consist of a meander sensor and an interdigital sensor which are connected in series. The proposed dimension of meander sensor is 20 mm × 20 mm. A meander sensor is built based on five loops of coils. The interdigital sensor is designed based on consecutive positive electrode and negative electrode. The proposed interdigital width for positive electrode and negative electrode are 0.5 mm and 1 mm respectively. In this research, planar electromagnetic sensor with star array configuration is used. Based on research in (Nor et al., 2013, 2015), star array configuration has the highest sensitivity. Figure 2 illustrates the star configuration and equivalent electrical circuit diagram.

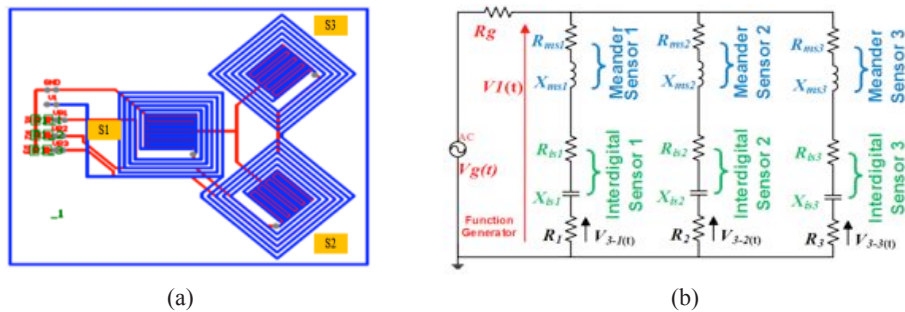


Figure 2. (a) star configuration; (b) equivalent electrical circuit diagram

Three sensors namely  $S_1$ ,  $S_2$  and  $S_3$  are placed in a star array configuration. These three sensors are placed 10 mm apart.  $S_2$ , and  $S^3$  which are placed  $45^\circ$  and  $-45^\circ$  respectively from  $S_1$ . The schematic diagram of the meander sensor and interdigital sensor is shown in blue. The ground plane connection on the other side of the PCB is presented in red. In this research, the equivalent electrical circuit of the sensor is illustrated in Figure 2 (b). According to Figure 2 (b), the sensor is connected to a function generator where  $R_g$  is the output resistance with a nominal value of  $50 \Omega$ .  $R_1$  denotes the series surface mount resistor connected to sensor 1 ( $S_1$ ), as shown in Figure 2 (a). Therefore, current  $I_{3-1}$  can be calculated from

$$I_{3-1} = \frac{V_{3-1}}{R_1} \tag{1}$$

where  $I_{3-1}$  and  $V_{3-1}$  are the rms value of current through the sensor and voltage across  $R_1$  respectively. The absolute total impedance for sensor  $S_1$ ,  $Z_1$  is given by

$$Z_1 = \frac{V_1}{I_{3-1}} \tag{2}$$

where  $V_1$  is the rms value of the input voltage signal. Consider that  $\theta_1$  is the phase difference between  $V_1(t)$  with  $V_{3-1}(t)$  in degree, taking  $V_{3-1}(t)$  or  $I_{3-1}$  as a reference. The total impedance of sensor  $S_1$ ,  $Z_1$ , can be written as:

$$Z_1 = \frac{V_1 \angle \theta_1}{I_{3-1} \angle 0^\circ} \tag{3}$$

The same method of calculation can be used to calculate the impedance for both sensors  $S_2$  and  $S_3$  by using Equations (1) to (3).

## EXPERIMENTAL SETUP AND ANALYSIS

The experimental setup is categorized into three parts; they are sensor, system, and sample. Firstly, the PESA with a star array configuration is fabricated. This sensor is then coated with membrane. A function generator supply AC source to PESA. Meanwhile, the oscilloscope is used for the data acquisition. LabVIEW software is used for data display and analysis. Figure 3 illustrates the experimental setup of the research. 10 Volts peak-to-peak voltages is supplied by means of function generator at each terminal sensor. Four channels oscilloscope that being link online with PC and a holder to hold the sensor which was immersed into a beaker and prepared samples. The oscilloscope is interfaced to a PC where the output signals and the sensor's impedance was recorded and calculated consecutively using LabVIEW software for a period of times. In this research, the frequency is set from 1 kHz to 20 MHz. In order to characterize the effect of coating on sensor performance, the whole procedure is repeated using PESA coated with Incralac. Four types of different samples were prepared. There are nitrate, phosphate, zinc, and nickel solution at different concentration level (5ppm, 25ppm, 75ppm, and 100ppm). The samples are subjected to PESA.

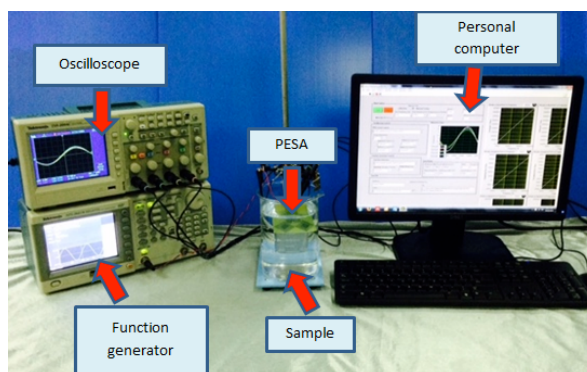


Figure 3. Experimental setup for nitrate, phosphate, zinc, and nickel samples

### MEMBRANE POLYMER DOPE DEVELOPMENT PROCEDURE

All the reagents are analytical grade unless otherwise stated. Firstly, silica powder (10.1348 g) and N-Methyl-2-pyrrolidone (NMP) are mixed for 30 minutes using stirrer machine (IKA RW 20 digital) at the speed of 500 rotation per minute (rpm). This mixing process is demonstrated in Figure 4(a). Secondly, the mixture of silica and NMP were inserted into ultrasonic cleaner machine (3MX) for degassing process. This process takes 60 minutes to disperse the particles in the mixture. The illustration of degassing process is shown in Figure 4(b). Then, 25 g of poly-sulfone (PSF) is added into the mixture of silica and NMP. To ensure the mixture mixed thoroughly, the PSF is inserted gradually and stirred using IKA machine for 4 hours in 750 rpm as illustrated in Figure 4(c). Next, NMP (10 g) is added into the mixture and leave it for 24 hours. Lastly, the mixture is left in ultrasonic cleaner machine (3MX) for 3 hours for degassing process. Figure 4(d) demonstrates the membrane polymer dope which consists of silica, NMP and PSF.

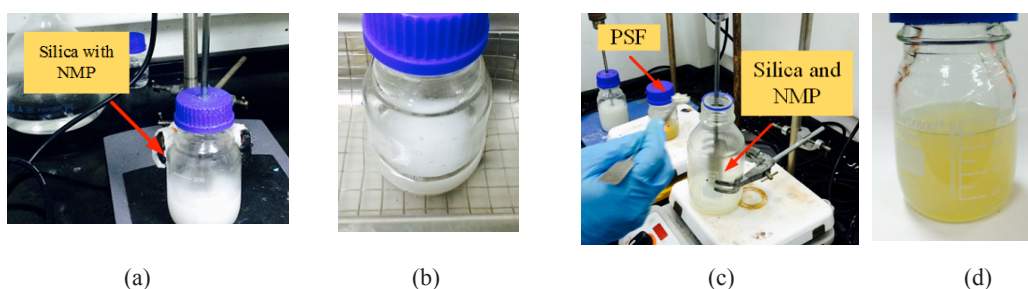


Figure 4. Experimental setup for nitrate, phosphate, zinc, and nickel samples

The prepared membrane is then transferred into the beaker for the coating process. Robot arm is employed to hold the planar electromagnetic sensor and helps to immerse the sensor into the beaker for almost 10 seconds. Then, the sensor is pulled out slowly in order to get smooth coating surface. Finally, the coated sensor is inserted into the oven for 24 hours at 50°C.

## RESULT AND DISCUSSION

Figure 5 and Figure 6 depict the impedance,  $Z$  using PESA with a star configuration for different concentrations of nitrate and phosphate solution respectively. The graphs in Figure 5 and Figure 6 show the impedance for both sensor which are coated with membrane and Inralac. Based on the measured data, it can be seen that the total impedance responses vary with the different samples of nitrate and phosphate. Basically, for the star array sensor, the total impedance value decreases as the concentration of these contaminants solution increased from 5 ppm to 100

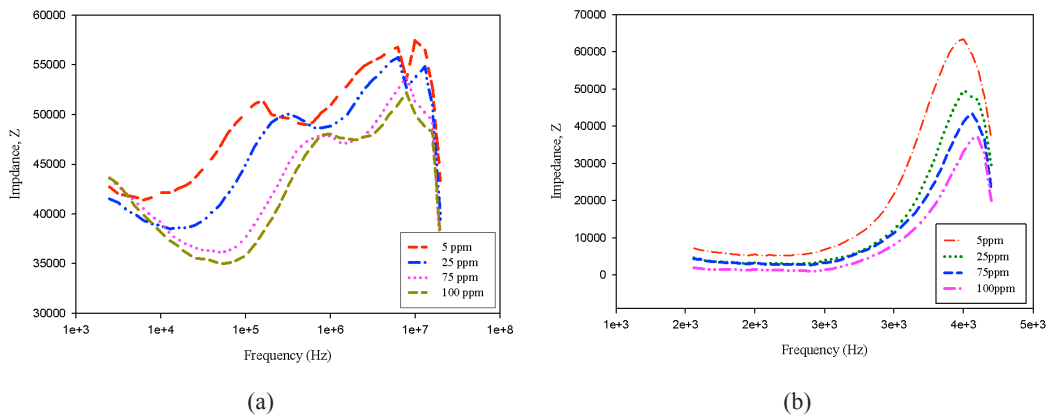


Figure 5. Impedance for different concentration level of nitrate (a) coated with Inralac; (b) coated with membrane

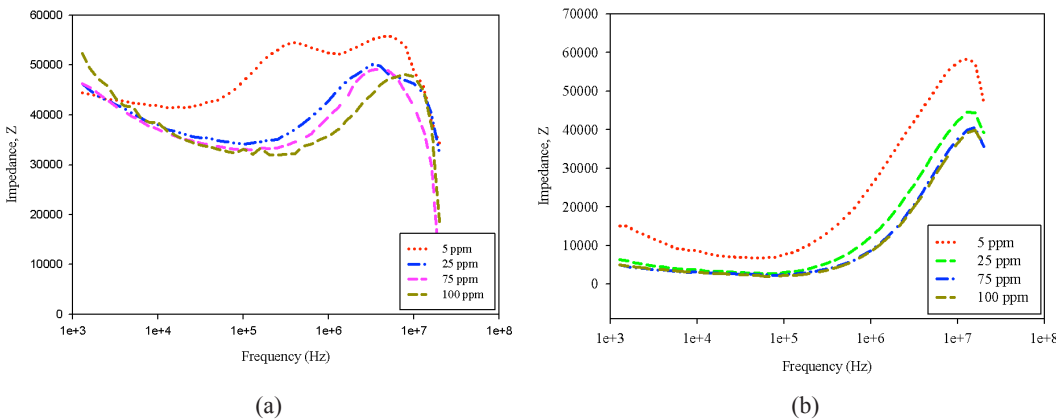


Figure 6. Impedance for different concentration level of phosphate (a) coated with Inralac; (b) coated with membrane

ppm. Hence, it shows that the presence of contamination in water could increase the water conductivity. At the same time, the permittivity of the medium under test also increase with the increased in contamination level. The obtained data in this research agreed with the paper in (Nor et al., 2015; Wang et al., 2015).

Table 2

*Absolute sensitivity, |Z%| for different concentration level of nitrate, phosphate, nickel, and zinc*

Part per million (ppm)	Nitrate		Phosphate		Nickel		Zinc	
	Membrane	Incralac	Membrane	Incralac	Membrane	Incralac	Membrane	Incralac
5	14-99	47-55	20-28	8-56	2-331	1-52	77-224	0.27-71
25	26-99	42-64	13-98	12-61	0-338	0.5-45	93-192	2-60
75	35-100	38-60	35-99	6-65	1-92	2.7-55	12-94	0.02-69
100	42-100	34-60	36-99	6-62	1.8-93	0.55-62	93-204	1-71

Table 2 summarized the absolute average impedance sensitivities, |Z%| for nitrate, phosphate, zinc, and nickel. Sensitivity is calculated based on the equation in (Yunus et al., 2015). Based on the result, PESA with star configuration could distinctly differentiate or give a vary response for different concentration of nitrate, phosphate, zinc, and nickel. PESA coated with membrane shows higher sensitivity compared to Incralac for all measured samples. The highest sensitivity is 338 % which observed in the presence of membrane for the nickel detection. In the meanwhile, the lowest sensitivity using membrane is 12 % for zinc detection. However, for Incralac coating, the highest sensitivity is 71 % and the lowest sensitivity is 0.02 %. The absolute impedance sensitivity value has increased approximate two times higher than the sensor coated with Incralac. The absorption of the nitrate ion on the membrane has changed the nature of the output (impedance). Hence, makes the PESA to be more sensitive to all measured samples.

## CONCLUSION

The membrane and Incralac coaters have been successfully coated on the PESA surfaces. The results demonstrate that the PESA could give different responses for different contaminant concentrations values in different ranges of frequencies. The result indicates that PESA coated with membrane has the highest sensitivity. In the future, an artificial neural network (ANN) classification method will be employed to increase the validity and to estimate the level of contamination of water samples taken from natural sources, such as rivers or lakes.

## ACKNOWLEDGEMENT

The authors would like to acknowledge the financial assistance from the Ministry of Science, Technology and Innovation (MOSTI) Malaysia which provides the Science Fund (Vote No. 03-01-06-SF1216), in part Fundamental Research Scheme Grant (FRGS) from the Ministry of Higher Education Research (MOHE) Malaysia (Vote No. 4F594), and Universiti Teknologi Malaysia for providing the facilities.



## REFERENCES

- Albanese, D., Di Matteo, M., & Alessio, C. (2010). Screen Printed Biosensors for Detection of Nitrates in Drinking Water. In *20th European Symposium on Computer Aided Process Engineering -ESCAPE20* (p. 283-288).
- Hassan, S. S. (1976). Ion-Selective Electrodes in Organic Functional Group Analysis: Microdetermination of Nitrates and Nitramines with Use of the Iodide Electrode. *Talanta*, *23*(10), 738–40.
- Hofmann, M. C., Kensy, F., Büchs, J., Mokwa, W., & Schnakenberg, U. (2005). Transponder-Based Sensor for Monitoring Electrical Properties of Biological Cell Solutions. *Journal of Bioscience and Bioengineering*, *100*(2), 172–177.
- Kodamatani, H. Yamazaki, S., Saito, K., Tomiyasu, T., & Komatsu, Y. (2009). Selective Determination Method for Measurement of Nitrite and Nitrate in Water Samples Using High-Performance Liquid Chromatography with Post-Column Photochemical Reaction and Chemiluminescence Detection. *Journal of Chromatography A*, *1216*(15), 3163–3167.
- Nor, A. S. M., Faramarzi, M., Yunus, M. A. M., & Ibrahim, S. (2015). Nitrate and Sulfate Estimations in Water Sources Using a Planar Electromagnetic Sensor Array and Artificial Neural Network Method. *IEEE Sensors Journal*, *15*(1), 497–504.
- Nor, A. S. M., Yunus, M. A. M., Nawawi, S. W., & Ibrahim, S. (2013). Low-Cost Sensor Array Design Optimization Based on Planar Electromagnetic Sensor Design for Detecting Nitrate and Sulphate. In *Proceedings of the International Conference on Sensing Technology, ICST* (p.693–98). Wellington.
- Ong, K. G., Wang, J. S., Singh, R. S., Bachas, L. G., & Grimes, C. A. (2001). Monitoring of Bacteria Growth Using a Wireless, Remote Query Resonant-Circuit Sensor: Application to Environmental Sensing. *Biosensors and Bioelectronics*, *16*(4-5), 305–12.
- Wang, X., Wang, Y. L., Mukhopadhyay, S. C., Tian, M., & Zhou, J. (2015). Mechanism and Experiment of Planar Electrode Sensors in Water Pollutant Measurement. *IEEE Transactions on Instrumentation and Measurement*, *64*(2), 516–523.
- WHO. (2011). *WHO Guidelines for Drinking Water Quality*. Nitrate and Nitrite in Drinking Water. World Health Organization.
- Yunus, M. A. M., Kasturi, V., Mukhopadhyay, S. C., & Gupta, G. S. (2009). Sheep Skin Property Estimation Using a Low-Cost Planar Sensor. *Instrumentation and Measurement Technology Conference* (p.482 - 486). Singapore.
- Yunus, M. A. M., Ibrahim, S., Altowayti, W. A. H., San, G. P. (2015). Selective Membrane for Detecting Nitrate E Ased on Planar Electromagnetic Sensors Array. *Control Conference (ASCC), Asian* (p. 1-6). Kota Kinabalu.



## Optimising PID Controller using Slope Variation Method for Positioning Radio Telescope

N. Mohamad Zaber<sup>1\*</sup>, A. J. Ishak<sup>1</sup>, A. Che Soh<sup>1</sup>, M. K. Hasan<sup>1</sup> and A. N. Ishak<sup>2</sup>

<sup>1</sup>Department of Electrical and Electronic Engineering, Faculty of Engineering,  
Universiti Putra Malaysia, 43400 UPM, Serdang, Selangor, Malaysia

<sup>2</sup>National Space Agency (ANGKASA) Lot 2233, Jln Turi, Sg. Lang, Banting, Selangor, Malaysia

### ABSTRACT

Radio telescope is an application that requires a precise position control as it should point to the exact coordinate so that it could receive the desired signal. The main idea of this paper is to optimise the PID controller by introducing slope variation method in order to control the position of a radio telescope. This proposed method is also validated with the presence of disturbance, such as wind gust disturbance with different speed amplitude. The results indicate that the proposed optimisation method has a better result with no overshoot and able to attenuate wind gust disturbance when compared with conventional PID controller.

*Keywords:* PID optimisation, position control, radio telescope

### INTRODUCTION

For a large radio telescope, it is essential it receives the intended signal while keeping its position accuracy. The challenges of maintaining its accuracy is increased when the radio telescope exposed to disturbances

and nonlinearities such as wind disturbance, saturation, backlash and many more. In order to sustain the accuracy, different control method and strategies are used.

Cho et al., had utilised  $H_{\infty}$  using step tracking algorithm to control the antenna system (Cho et al., 2003) where this method satisfied the requirement of the system. Referring to (Sahoo and Roy 2014; Garcia-Sanz et al., 2012), QFT method had been used, where Suresh Kumar Sahoo et al. mentioned that the performance of the controller is satisfactory and meet the stability specifications with overshoot of 2.24% and very low steady state error. It takes into account the plant uncertainty in designing the

#### ARTICLE INFO

##### Article history:

Received: 24 August 2016

Accepted: 02 December 2016

##### E-mail addresses:

nsaida.mzaber@gmail.com (N. Mohamad Zaber),

asnorji@upm.edu.my (A. J. Ishak),

azuracs@upm.edu.my (A. Che Soh),

khair@upm.edu.my (M. K. Hassan),

asnor@angkasa.gov.my (A. N. Ishak)

\*Corresponding Author

QFT controller. On the other hand, Garcia-Sanz et al., had considered saturation constraints in the simplified rigid body model of an existing extra-large radio telescope. The robustness of the designed QFT had been able to overcome the disturbance even in the influence of saturation nonlinearity. However,  $H_\infty$  and QFT methods require a lot of mathematical formulation and understanding and hence become complicated.

Fuzzy logic controller then emerged as this method express mathematical equation based on phrases and thus make it understandable. Fuzzy logic has been used widely in controlling the radio telescope such as by (Okumus et al., 2012; 2013). Okumus et al., had employed several fuzzy membership functions such as triangle, trapezoid, Gaussian, bell and Cauchy and compared the performance between them. The best membership function was then used in self-tuning fuzzy logic controller where it showed an improvement in terms of overshoot and rise time. Nevertheless, expert knowledge of the system is required prior to implementing fuzzy logic controller so that fuzzy rules and its range can be properly set. Not only that, the process of designing fuzzy logic controller is still depending on trial-and-observation practice (Chen et al., 1993). Somehow, this condition caused difficulties in determine fuzzy rules and its range.

On contrary, PID controller has been used since decades ago due to its simplicity, easy to understand and implement and also able to control wide range of system applications (Qiu et al., 2014; Rahmani et al., 2012; Namazov, 2010; Yousef, 2012; Qiu et al., 2014). It is one of the earlier control methods that still commonly used now. PID controller work by adjusting and tuning its parameters' value until the desired output is met. However, this process consumes time and requires a lot of adjusting and tuning process. Thus, the purpose of this paper is to optimize the PID controller by introducing slope variation method and improve the performance of the controller including reduce the time consumed during tuning process.

## MODELLING OF RADIO TELESCOPE

Radio telescope consists of two parts:

- DC servo motor
- Parabolic antenna dish (load)

In this section, the procedure in obtaining radio telescope model is presented.

### DC Servo Motor

Servo motor is a type of motor for operation involving position control as well as speed control. Input of this radio telescope is obtained from potentiometer which then converted to voltage and fed into a dc servo motor. Torque,  $T_m$ , developed by servo motor will rotate the antenna dish with desired speed,  $\omega_m$ . The motor is driven only when there is difference between input and output. The larger the value, the greater the motor input voltage, and the faster motor turned (Nise, 2011). DC servo motor is modelled by converting the motor equation into Laplace transfer function.

### Parabolic Antenna Dish (Load)

In this paper, the load is a parabolic antenna dish with diameter of 18 m. This dish is mounted on the servo motor. Generally, a radio telescope is made of two axes; azimuth (rotate side-to-side direction) and elevation (moving up-down direction). In this paper the azimuth axis is studied. The angle of rotation for azimuth axis is between 0 - 360°. Figure 1 below illustrates the azimuth and elevation axis of a radio telescope as well as the schematic diagram of dc servo motor.

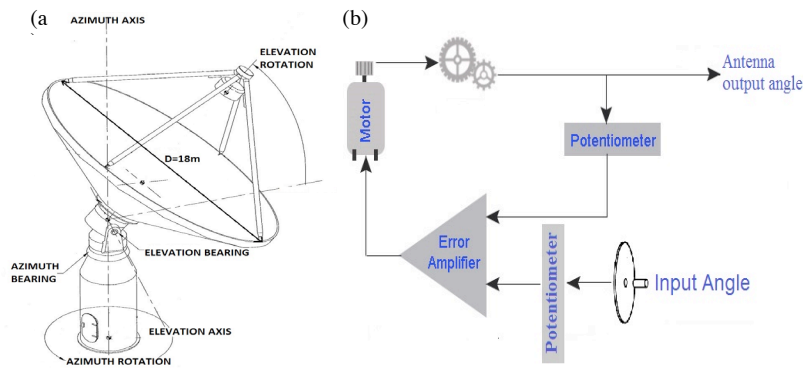


Figure 1. (a) Radio telescope; (b) Schematic diagram of DC servo motor within radio telescope system

### METHODOLOGY

PID controller was used in this project where it attempts to minimize the error generated by the system. The structure of PID controller is as Figure 2 below.  $K_p$ ,  $K_i$  and  $K_d$  values are tuned to achieve the radio telescope performance criteria, in terms of overshoot, rise time, settling time and steady state error. In this paper, Ziegler-Nichols (ZN) heuristic method and the proposed PID optimization using slope variation method are implemented. Designed controller is validated by introducing wind gust disturbance into the system.

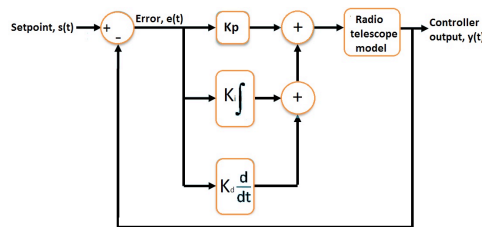


Figure 2. PID controller structure

### ZN Parameter Tuning

PID controller is tuned using ZN method where only  $K_p$  value is varied while others are set to zero.  $K_p$  value is tuned until it reaches natural frequency i.e. constant oscillation. Then  $K_i$  and  $K_d$  values obtained by applying equation (1) where  $T_{int}$ ,  $T_{der}$  are integral and derivative time constant.

$$C(s) = K_p \left( 1 + \frac{1}{T_{int}s} + \frac{T_{der}s}{1 + T_{der}s} \right) \tag{1}$$

### Optimising PID Controller

The proposed optimisation of PID controller is done by considering the slope of the output response whenever PID parameters are varied as shown in Figure 3. The slope value is observed once output reach set point. This observation is important as it will affect overshoot and steady state error values. Eq. (2) below express the slope equation of the output response where  $y(t_h)$  is the highest output response.

$$Slope, sl_1 = \frac{y(t_h) - y(t_{h-1})}{t}; slope, sl_2 = \frac{y(t_{h+1}) - y(t_h)}{t} \tag{2}$$

This optimisation is done following steps below:

- $K_p$  value is tuned until the set point reach. The highest output response is determined and slope values are calculated.
- $K_d$  is increased while keeping the attention to the slope value until the acceptable overshoot is met.
- $K_i$  is tuned in eliminating the steady state error by ensuring the slope values are always close to zero.

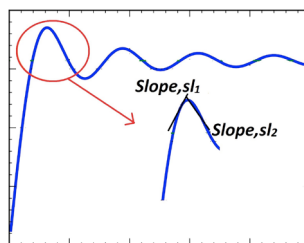


Figure 3. Slope at maximum response

### Wind Model

Wind disturbance is one of the external factors that could affect the performance of the radio telescope by deviating it from desired position (Gawronski, 2008). Generally, there are two types of wind loads that act towards the radio telescope antenna dish; namely steady-state and dynamic (gust) load (Gawronski, 2004). In this paper, only dynamic load is considered. This

wind gust disturbance model is presented in the form of torque,  $T_g$ , act upon radio telescope drive,  $T_m$ , in which it gives increment to the total torque,  $T$ , as shown in Figure 3. Wind gust is generated from white noise of unit standard deviation that being formed from Davenport filter with a constant value,  $k_w$ .

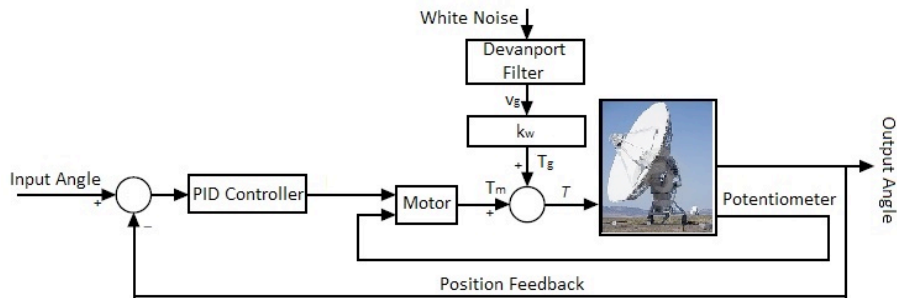


Figure 4. Wind disturbance acting on the antenna dish

The wind torque,  $T_g$ , is actually acquired from and related to the velocity gust value,  $v_g$ , where it is a component of wind velocity,  $v_w$ , and steady state wind velocity,  $v_s$ , as per equation (3). The wind gust component,  $v_g$ , is a random process with zero mean together with a Davenport spectrum. From here, the  $T_w$  is obtained by linearizing equation (4) i.e. wind quadratic law for torque  $T$  and steady state wind,  $v_s$ , which produce equation (5).

$$v_w = v_s + v_g \tag{3}$$

$$\text{Torque, } T = k_w v_s^2 \tag{4}$$

$$T_g = 2k_w v_s v_g \tag{5}$$

## RESULTS AND DISCUSSION

The output of the simulation is presented and discussed in this section. Tuning PID parameters using ZN method somehow is tedious and time consuming. After tuning the  $K_p$  values, it turned out that the response cannot produce constant oscillation as shown in Figure 4 (a-d). Thus, the PID parameters are then set using trial-and-error method where  $K_p$  value is choose by referring to the ZN output that gives better result compared to other values. Thus, the obtained parameters value is  $K_p=20$ ,  $K_i=0.5$  and  $K_d=3$ .

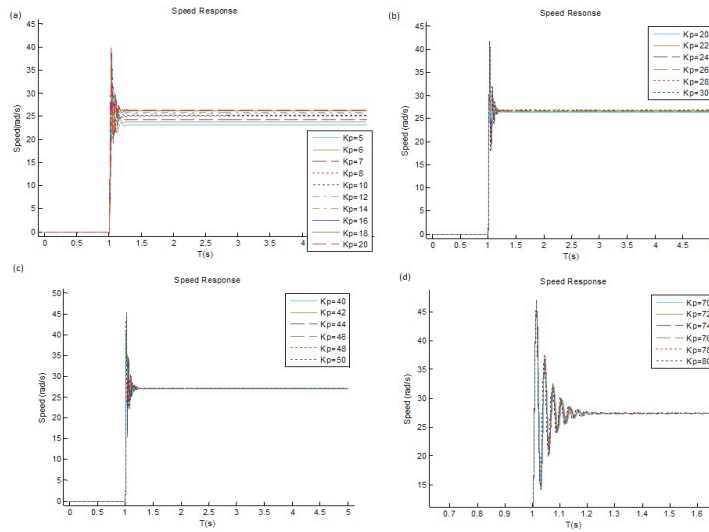


Figure 5. Tuning PID parameters using ZN method

### Speed Loop

This speed loop shows the speed response for both PID and optimised PID using slope variation method without load. PID-slope variation method showed a more accurate output and faster response where it recorded a rise time of 0.09s when compared to PID with 0.3s.

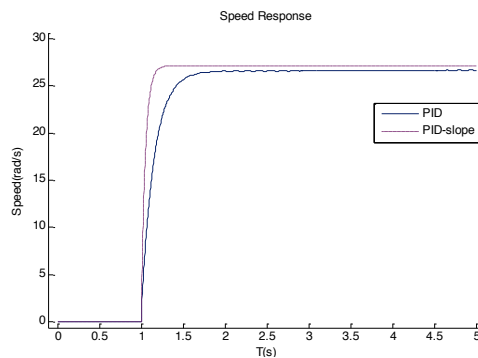


Figure 6. Comparison of speed response between PID and PID-slope variation method

### Position Loop

Figure 7 shows that the optimisation of PID using slope variation method is able to reach set point without overshoot. The analysis of the output is as Table 1.

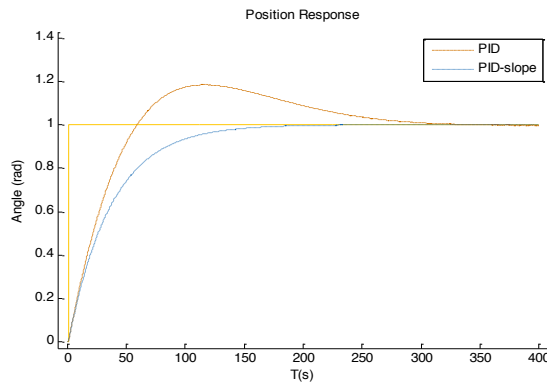


Figure 7. Position response

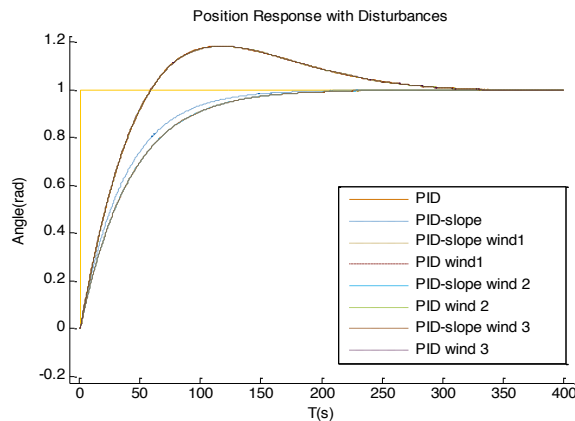


Figure 8. Position response with presence of wind gust disturbance

Referring to Figure 8, when wind gust disturbance with different speed amplitude (2 (wind 1), 4 (wind 2) and 6 (wind 3)) introduced to the system, PID-slope variation took a bit longer time i.e. difference of about 11.32s to reach 90% of the output (for all speed) compared when there is no disturbance. This situation is common as it has to face the resistance of the wind. On the other hand, conventional PID controller cannot attenuate wind gust disturbance and produce overshoot to the system, similar as without disturbance.

Table 1  
*Analysis of output response of radio telescope*

	Without disturbance		Wind disturbance	
	PID	PID-slope variation	PID	PID-slope variation
Rise time, Tr (s)	43.5	79.3	43.5	91.64
% Overshoot	18.4	0	18.4	0

## CONCLUSION

This paper presents the analysis of positioning radio telescope positioning by optimizing PID controller using slope variation method and conventional PID controller. Results showed that the proposed optimization method produces better results and being able to attenuate wind gust disturbances.. It also has a tolerable rise time for a 18m radio telescope.

## ACKNOWLEDGEMENT

This research was supported by Agensi Angkasa Negara, Ministry of Science, Technology and Innovation (MOSTI) and research grant Universiti Putra Malaysia.

## REFERENCES

- Chen, C. L., & Chen, P. C. (1993). Analysis and design of fuzzy control system. *Fuzzy Sets and Systems*, 57(2), 125-140.
- Cho, C. H., Lee, S. H., Kwon, T. Y., & Lee, C. (2003). Antenna control system using step tracking algorithm with  $H_{\infty}$  controller. *International Journal of Control, Automation and Systems*, 1(1), 83-92.
- Garcia-Sanz, M., Ranka, T., & Joshi, B. C. (2012, July). High-performance switching QFT control for large radio telescopes with saturation constraints. In *Aerospace and Electronics Conference (NAECON), 2012 IEEE National* (pp. 84-91). IEEE.
- Gawronski, W. (2004). Modeling wind-gust disturbances for the analysis of antenna pointing accuracy. *IEEE Antennas and Propagation Magazine*, 1(46), 50-58.
- Gawronski, W. (2008). *Modeling and control of antennas and telescopes*. Springer book.
- Namazov, M., & Basturk, O. (2010). DC motor position control using fuzzy proportional-derivative controllers with different defuzzification methods. *Turkish Journal of Fuzzy Systems*, 1(1), 36-54.
- Nise, N. S. (2011). *Control System Engineering* (6<sup>th</sup> Ed). John Wiley & Sons, Inc.
- Okumus, H. I., Sahin, E., & Akyazi, O. (2012). Antenna azimuth position control with classical PID and fuzzy logic controllers. In *2012 International Symposium on Innovations in Intelligent Systems and Applications* (pp. 1-5).
- Okumus, H. I., Sahin, E., & Akyazi, O. (2013, November). Antenna azimuth position control with fuzzy logic and self-tuning fuzzy logic controllers. In *Electrical and Electronics Engineering (ELECO), 2013 8th International Conference on* (pp. 477-481). IEEE.



- Qiu, D., Sun, M., Wang, Z., Wang, Y., & Chen, Z. (2014). Practical wind-disturbance rejection for large deep space observatory antenna. *IEEE Transactions on Control Systems Technology*, 22(5), 1983-1990.
- Rahmani, R., Mahmodian, M. S., Mekhilef, S., & Shojaei, A. A. (2012, December). Fuzzy logic controller optimized by particle swarm optimization for DC motor speed control. In *Research and Development (SCORED), 2012 IEEE Student Conference on* (pp. 109-113). IEEE.
- Sahoo, S. K., & Roy, B. K. (2014, February). Antenna azimuth position control using Quantitative feedback theory (QFT). In *Information Communication and Embedded Systems (ICICES), 2014 International Conference on* (pp. 1-6). IEEE.
- Yousef, A. M. (2012). Experimental set up verification of servo DC motor position control based on integral sliding mode approach. *WSEAS Transactions on Systems and Control*, 7(3), 87- 96.





## Enhanced Time of Use Electricity Pricing for Commercial Customers in Malaysia

Nur Azrina Mohd Azman, Md Pauzi Abdullah\*, Mohammad Yusri Hassan, Dalila Mat Said and Faridah Hussin

<sup>1</sup>Faculty of Electrical Engineering, Universiti Teknologi Malaysia, 81310 Johor Bahru, Malaysia

<sup>2</sup>Centre of Electrical Energy Systems, Institute of Future Energy, Universiti Teknologi Malaysia, 81310 Johor Bahru, Malaysia

### ABSTRACT

Malaysia has introduced a new Time of Use (ToU) tariff scheme known as Enhanced ToU (EToU) for commercial and industrial customers. EToU is a more detailed pricing scheme where one day time frame is divided into six period blocks as compared to only two period blocks in the existing ToU. Mid-peak tariff is introduced to the existing peak and off-peak tariff. Off-peak rate for EToU is significantly lower than the existing off-peak rate but the peak rate is much higher. EToU is designed to motivate users to reduce their consumption during peak hours or shift the load to mid-peak or off-peak hours, which if done correctly can reduce the electricity bill while maintaining electricity consumption. This new EToU scheme will benefit consumers if they are able to shift consumption from peak-hours into mid-peak or off-peak hours. This paper assesses the amount of load shifting that is required based on customers' load profile and EToU rates. The load profile data of an office building in Putrajaya, Malaysia is used as a case study.

*Keywords:* Time-of-Use, load profile, electricity consumption

### ARTICLE INFO

*Article history:*

Received: 24 August 2016

Accepted: 02 December 2016

*E-mail addresses:*

nurazrina\_123@yahoo.com (Nur Azrina Mohd Azmana),

pauzi@fke.utm.my (Md Pauzi Abdullah),

yusrih@fke.utm.my (Mohammad Yusri Hassan),

dalila@fke.utm.my (Dalila Mat Saida),

faridahh@fke.utm.my (Faridah Hussin)

\*Corresponding Author

### INTRODUCTION

Tenaga Nasional Berhad (TNB), the electricity utility supplier in Malaysia has introduced a new EToU tariff scheme as an alternative to the existing ToU tariff. Under EToU scheme, there are three different rates for electricity consumption (kWh) charge: Peak, Mid-Peak and Off-Peak. For maximum demand (kW) charge, there are two different rates: Peak and Mid-Peak. These rates are only applicable on weekdays (Monday to Friday). For weekends

(Saturday, Sunday) and Public Holidays, only Off-Peak rate are used throughout the day and maximum demand charge is waived. The new EToU scheme is offered as an option to any Low Voltage, Medium Voltage and High Voltage consumers under the following tariff category; i) Commercial: Tariff C1, C2 ii) Industrial: Tariff D, Ds, E1, E1s, E2, E2s, E3, and E3s (TNB, 2016). EToU provides price signals for customers to control their electricity usage and encourage Demand Side Management. It allows consumers to lower their electricity bill by using less electricity during peak hours or by shifting their consumption to Mid-Peak and Off-Peak hours, when the rates are lower. However, EToU may also result in higher electricity bill if customers are not able to shift their consumption. This paper presents a simple method to help customers decide whether they should opt for the new EToU scheme or stick to the old ToU scheme.

This paper is divided into six sections. The basic concept of ToU is discussed in Section 2. The relationship between ToU and DSM is presented in section 3. The mathematical formulation of the assessment method is described in section 4. Results obtained from the case study are presented in Section 5. Finally, section 6 concludes the paper.

Nomenclature	
ToU	Time of Use
EToU	Enhanced Time of Use
DSM	Demand Side Management
HVAC	High Voltage Alternate Current

### ToU Electricity Pricing

ToU is an electricity tariff system based on consumers' usage hour. It varies over different time period in a day and fixed within the same time period. Unlike Real Time Pricing (RTP) that varies all the time depending on wholesale market price and Fixed-Tariff Pricing that doesn't vary at all. Comparisons between different pricing methods can be found in Nazar, N.S.M., et al, 2012. ToU pricing method divides time into different period blocks with different tariff rates for each block. Generally, peak hour periods are charged higher tariff unlike, RTP that reflects the real wholesale market price, ToU reflects the long-term cost of producing electricity. Commonly, there are three ToU period blocks categories i.e. Peak, Mid-peak and Off-peak hours. At peak hours, utility need to deliver the highest generation. During this period, the utilities provide maximum amount of energy and use the highest number of system capacity. Use of less fuel-efficient generation plant is often required during these hours. Transmission and distribution system losses also increased, adding to increase need of supply. Although the peak hour is just a small number of hours each day, the cost implication is significantly high. At off peak hours, the utilities use a relatively small amount of total system capacity, thus it does not contribute to the need for the development of facilities. Mid-peak is when the cost of electricity production is between peak and off-peak. Significant ToU rates difference between the peak, mid-peak and off-peak hours are required to ensure the effectiveness of ToU pricing (Hussin et al, 2014).

ToU pricing is intended to encourage consumers to shift their electricity usage from peak hours into off-peak or mid-peak hours. Customers have the option to shift their electricity consumption based on the price; consuming electricity during off-peak or mid-peak period will increase savings as the electricity rates are significantly lower. Where shifting consumption levels are not possible ToU tariffs can encourage some customers to use alternative sources, such as diesel generators on site. In short, ToU pricing encouraged response from electricity consumer and hence become the most important component in DSM Program.

### **ToU in DSM Program**

Typical daily consumer demand has peaks, which result in high generation costs. Demand Side Management (DSM) program encourages the end user to be more energy efficient to reduce these peaks. Examples of DSM measures include lighting retrofits, HVAC improvements, and automation. Some investment cost is required to implement these measures. Another important DSM measure which is cost free yet effective is load shifting i.e. shifting the load or consumption from peak to off-peak hours. For this measure to succeed, electricity consumers must be encouraged to change their electricity consumption based on the supplier's need. In other words, they must shift their load consumption to the targeted hours. It can be done by using price signal such as TOU tariffs, which specify different prices for different times of the day. The difficult part is to determine the most efficient price rate that signals the consumer to change the electricity usage behaviour (de Sa Ferreira et al, 2013). ToU must give the right signal to the consumer so that the objective of ToU can be achieved. The success of DSM program through ToU tariff depends on the following criteria: i) The right signal; utilities must ensure the accurate signal is being channelled to the electricity customer whether by electricity price or other incentive to customer to encourage load shifting ii) DSM should benefits both customer and utilities, iii) a good program would produce the expected outcome to both parties fairly.

### **ToU in selected Countries and Malaysia**

Many countries have already implemented ToU electricity tariff for commercial customers. Different countries have different ToU design and tariff rates due to their unique load profile pattern as well as their needs and objectives. Table 1 shows the ToU period blocks that is currently being implemented to commercial customers in Sri Lanka, South Africa, New York, California, and Malaysia. Different ToU period blocks with different tariff were defined for 24 hours' consumption i.e. peak, mid-peak and off-peak block. From Table 1, it can be seen that the peak-hour block for Sri Lanka is from 6.30pm until 10.30pm, which is aside from the office buildings' common working hours (8am-5pm). Mid-peak block is from 5.30am until 6.30pm. For South Africa, there are two peak hour blocks i.e. from 7am to 10am and from 6pm until 8pm. About 80% of the office buildings' common working hours fall in mid-peak hour blocks i.e. from 10am to 6pm. For USA (New Jersey, Pennsylvania, New York), peak-hour tariff is allocated for 7 hours (from 12pm until 7pm) whereas for California, peak-hour tariff is allocated for 6 hours (from 12pm until 6pm). Meanwhile in Malaysia, the old ToU scheme consists of only two ToU blocks i.e. peak hours (from 8am until 10pm) and off-peak

**Table 1**  
*ToU Period Blocks in Selected Countries (TNB, 2016; Ceylon Electricity Board (CEB), 2016; eThekweni Municipality, 2016; Orange & Rockland, 2016; Pacific Gas and Electric Company (PG&E), 2016; Suruhanyaya Tenaga, 2016)*

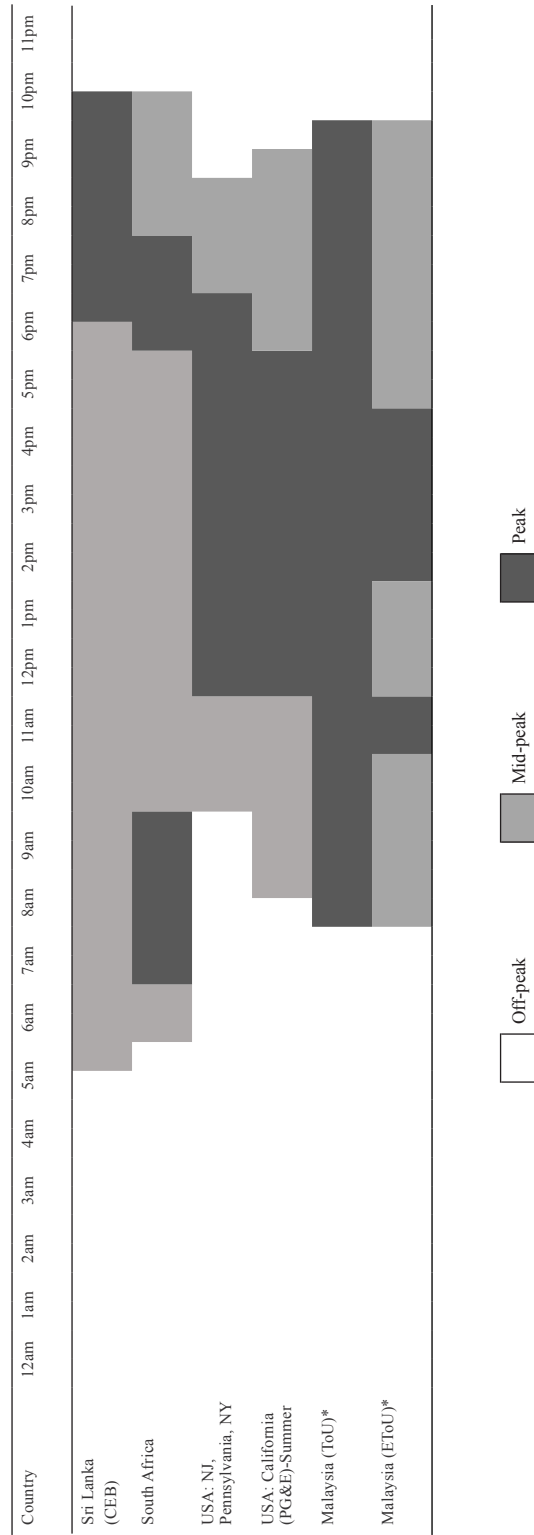


Table 2  
ToU Prices in Selected Countries

No	Country	Time of Use Electricity Details	
		Period	Price
1	Sri Lanka (CEB) (CEB, 2016)	Peak	Rs 23.00/kWh
		mid-peak	Rs 7.30/kWh
		off-peak	Rs 5.30/kWh
2	South Africa (eThekweni Municipality, 2016)	peak	c 25758/kWh
		mid-peak	c 12887/kWh
		off-peak	c 6278/kWh
3	USA: New Jersey, Pennsylvania, New York (Orange & Rockland, 2016)	peak	\$ 8.218/kWh
		mid-peak	\$ 1.976/kWh
		off-peak	\$ 0.263/kWh
4	USA: California (PG&E)- summer (PG&E, 2016)	peak	\$ 0.16585/kWh
		mid-peak	\$ 0.11897/kWh
		off-peak	\$ 0.09367/kWh
5	Malaysia (ToU)* (TNB, 2016; Suruhan Tenaga, 2016)	peak	RM 0.365/kWh
		off-peak	RM 0.365/kWh
	Malaysia (EToU)* (TNB, 2016; Suruhan Tenaga, 2016)	peak	RM 0.584/kWh
		mid-peak	RM 0.357/kWh
		off-peak	RM 0.281/kWh

Note. \*Commercial customers at medium voltage (tariff C1)

hours (from 10pm until 8am). Starting from January 2016, a new ToU scheme known as Enhanced Time of Use (EToU) was introduced to commercial consumers. EToU consists of six ToU blocks with peak, mid-peak and off-peak tariffs as shown in Table 1. Peak hour tariff is allocated two times during office buildings' common office hours i.e. 1 hour (from 11am to 12pm) and another 3 hours (from 2pm to 5pm).

## METHOD FOR ETOU ASSESSMENT

If a consumer manages to reduce electricity bill through EToU tariffs without having to change their electricity consumption pattern, the new EToU scheme is undoubtedly better than the old ToU. Hence, the consumer may switch to the new scheme such as peak-hour load into mid-peak or off-peak hour periods. This section presents the mathematical formulation to evaluate the minimum amount of peak load shifting required for a given load profile and ToU tariffs.

Total electricity bill for the new EToU scheme must be less or at least equal to the old ToU scheme:

$$\sum_{\text{all hour } i} [ToU_{\text{hour } i}^{\text{new tariff}} \times P_{\text{hour } i}^{\text{new consump}}] \leq \sum_{\text{all hour } i} [ToU_{\text{hour } i}^{\text{old tariff}} \times P_{\text{hour } i}^{\text{old consump}}] \quad (1)$$

Where:

$$ToU_{\text{hour } i}^{\text{new tariff}} = ToU_{\text{hour } i}^{\text{old tariff}} + \Delta ToU_{\text{hour } i} \quad (2)$$

$$P_{hour\ i}^{new\ consump} = P_{hour\ i}^{old\ consump} + \Delta P_{hour\ i} \tag{3}$$

Rewriting equation (1) yields the following;

$$\sum_{all\ hour\ i} \left[ \Delta TOU_{hour\ i}^{new\ tariff} \times \frac{P_{hour\ i}^{old\ consump}}{P_{Total}^{old\ consump}} \right] + \left[ TOU_{hour\ i}^{new\ tariff} \times \frac{\Delta P_{hour\ i}}{P_{Total}^{old\ consump}} \right] \leq 0 \tag{4}$$

Where:

$$hour\ i = \{off - peak\ hour\ i, mid - peak\ hour\ i, peak - hour\ i\} \tag{5}$$

For the total electricity consumption remains the same after load shifting, then

$$\sum \Delta P_{off-peak\ hour\ i} + \sum \Delta P_{mid-peak\ hour\ i} + \sum \Delta P_{peak\ hour\ i} = 0 \tag{6}$$

Assuming the electricity consumption during peak-hours can only shifted to off-peak hours;

$$\sum \Delta P_{mid-peak\ hour\ i} = - \sum \Delta P_{peak\ hour\ i} \tag{7}$$

Thus, the total electricity consumption that must be shifted from peak to mid-peak hours;

$$P_{Total}^{shifted\ peak\ to\ mid-peak} \geq \frac{- \sum_{all\ hour\ i} \left[ \Delta TOU_{hour\ i} \times \frac{P_{hour\ i}^{old\ consump}}{P_{Total}^{old\ consump}} \right]}{\sum TOU_{mid-peak\ hour\ i} - \sum TOU_{peak\ hour\ i}} \tag{8}$$

Applying the EToU data into equation (8), the minimum peak load shift requirement for different load percentage share between peak, mid-peak and off-peak is tabulated in a bubble chart given in Figure 1.

Bubble chart in Figure 1 shows the minimum load shift requirement according to the peak, mid-peak and off-peak. Consumers need to calculate the percentage of mid-peak and off-peak

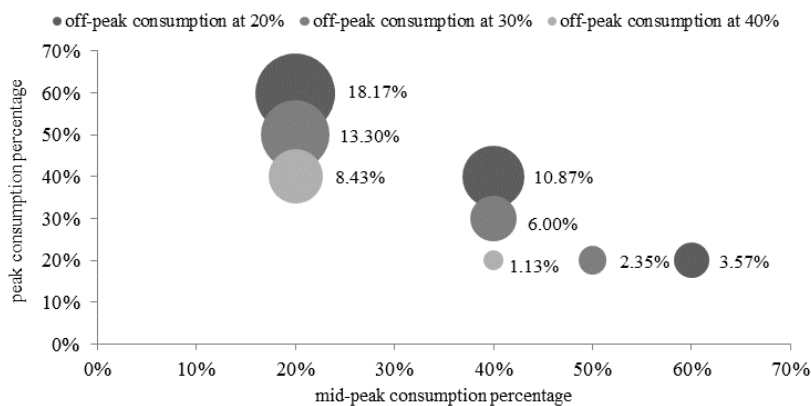


Figure 1. Bubble chart of minimum load shift requirement for different peak, mid and off-peak percentage share



consumption in order to know the minimum load shifting needed for EToU program to work. From Figure 1, it is known that when a customer percentage share of mid-peak and off-peak is 40%, a minimum shifting of peak period to mid-peak period consumption is 1.13%.

**CASE STUDY**

The objective of this case study is to assess the impact of the new EToU scheme for a government office building in Putrajaya, Malaysia. Figure 2 shows the hourly electricity consumption of the building during weekdays and weekends. It can be seen that the consumption for weekdays is high during working hours (8am-5pm) and low outside of working hours. During weekends, the consumption is low throughout the day. To ease calculation, it is assumed that the profile for weekdays and weekends are fixed throughout a month. Also, only electricity consumption (kWh) charge is considered.

The second column of Table 3 shows the electricity consumption for one month for each period block while the third column shows the percentage share between off-peak, mid-peak and peak hours, which is 41%, 41% and 18% respectively. The bubble chart in Figure 1 shows that load shifting around 1% is required (from peak to mid-peak hours) for the new EToU scheme to give cheaper kWh bill than the existing ToU scheme. To test these findings a base case is it is assumed that the building switched to EToU scheme without making any shifting in its daily consumption. The one month electricity bill through EToU and ToU scheme is given o the second row of Table 4. It can be seen that the EToU scheme gives higher bill than ToU scheme. For the second case, the electricity consumption during peak hours is shifted to mid-peak hours by 3% (of the total consumption). The results in Table 4 show that EToU scheme provides lower electricity bill than ToU, which validates the results given by the bubble chart in Figure 1.

Since the goal of EToU is to promote load shifting, switching tariff scheme alone without shifting consumption may result in higher electricity bill. Electricity customers can utilize the presented method to compare the two schemes. If they able to shift their load as suggested, they should opt for the new EToU scheme. If not, they should stick to the existing ToU scheme.

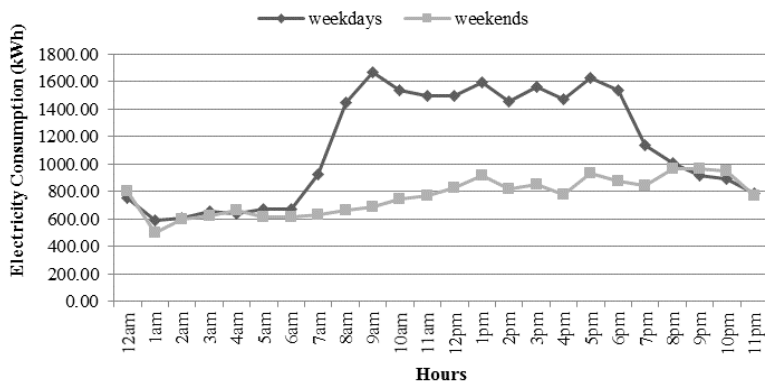


Figure 2. Average electricity consumption of an office building for weekdays and weekends

Table 3  
*Electricity consumption of the building during different EToU period block*

Period block category	Electricity Consumption	Percentage Share
off-peak	305735 kWh	41%
mid-peak	307528 kWh	41%
peak	131667 kWh	18%
Total	744930 kWh	100%

Table 4  
*Electricity bill comparison between ToU and EToU scheme of the building for each case*

Case	ToU	EToU
Base case	RM 271,899	RM 272,592
Load shifting case	RM 271,899	RM 267,520

## CONCLUSION

This paper compared Malaysia’s new Enhanced Time of Use (EToU) tariff schemes with the old ToU scheme. A mathematical method to estimate EToU’s load shifting based on customers’ electricity consumption profile was presented. Results from the case study support the method used allowing consumers to use it as a tool in cost-benefit analysis when deciding on the new EToU. Further studies on this method can be done by modelling the consumption and load shifting in visual basic/MATLAB software in order to provide easier usage in future works.

## ACKNOWLEDGMENT

This work was supported by the Malaysian Ministry of Higher Education (MOHE) and Universiti Teknologi Malaysia (UTM) through Fundamental Research Grant Scheme (FRGS) vot 4F746.

## REFERENCES

- Ceylon Electricity Board. (2016, March11). *Tariff Plan*. Retrieved from <http://www.pucsl.gov.lk/english/wp-content/uploads/2014/03/2009-tariff-notice.pdf>
- de Sá Ferreira, R., Barroso, L. A., Lino, P. R., Carvalho, M. M., & Valenzuela, P. (2013). Time-of-use tariff design under uncertainty in price-elasticities of electricity demand: A stochastic optimization approach. *IEEE Transactions on Smart Grid*, 4(4), 2285-2295.
- eThekwini Municipality. (2016, March 11). *Electricity Tariffs 2015-2016*. Retrieved from [http://www.durban.gov.za/Resource\\_Centre/Services\\_Tariffs/Electricity](http://www.durban.gov.za/Resource_Centre/Services_Tariffs/Electricity)[http://www.durban.gov.za/Resource\\_Centre/Services\\_Tariffs/ElectricityTariffs/ElectricityTariffs2015-2016.pdf](http://www.durban.gov.za/Resource_Centre/Services_Tariffs/ElectricityTariffs/ElectricityTariffs2015-2016.pdf)
- Hussin, N. S., Abdullah, M. P., Ali, A. I. M., Hassan, M. Y., & Hussin, F. (2014, October). Residential electricity time of use (ToU) pricing for Malaysia. In *Energy Conversion (CENCON), 2014 IEEE Conference on* (pp. 429-433). IEEE.

- Nazar, N. S. M., Abdullah, M. P., Hassan, M. Y., & Hussin, F. (2012, December). Time-based electricity pricing for Demand Response implementation in monopolized electricity market. In *Research and Development (SCORED), 2012 IEEE Student Conference on* (pp. 178-181). IEEE.
- Orange & Rockland. (2016, March 10). *Tariffs & Regulatory Documents*. Retrieved from <http://www.oru.com/programsandservices/timeofuserate/>
- Pacific Gas and Electric Company. (2016, March 11). *Time-of-Use Plans*. Retrieved from <http://www.pge.com/en/mybusiness/rates/typ/toupricing.page>
- Suruhanjaya Tenaga. (2016, May 4). *Enhanced Time of Use Etou Tariff Scheme*. Retrieved from <http://www.st.gov.my/index.php/download-page/category/124-sesi-penerangan-sit-dan-etou.html>
- Son, J., Hara, R., Kita, H., & Tanaka, E. (2015, November). Operation scheduling considering demand response in a commercial building with chiller system and energy storage system. In *Power and Energy Engineering Conference (APPEEC), 2015 IEEE PES Asia-Pacific* (pp. 1-5). IEEE.
- Tenaga Nasional Berhad. (2016, 4th May 2016). *Tnb Enhanced Time Of Use (Etou)*. Available: <https://www.tnb.com.my/faq/etou>



## Evaluation of Inverter Reliability Performance Due to Negative Bias Temperature Instability (NBTI) Effects in Advance CMOS Technology Nodes

M. F. Zainudin<sup>1,2</sup>, H. Hussin<sup>1,2\*</sup> and A. K. Halim<sup>1</sup>

<sup>1</sup>Faculty of Electrical Engineering, Universiti Teknologi Mara (UiTM), 40450 Shah Alam, Selangor, Malaysia

<sup>2</sup>Integrated Microelectronic Systems and Applications Research Group, Universiti Teknologi Mara (UiTM), 40450 Shah Alam, Selangor, Malaysia

### ABSTRACT

Negative bias temperature instability (NBTI) is the most concern issue CMOS devices with the scaling down of the CMOS technologies. NBTI effect contributes to P-MOSFET device degradation which later reduce the performance and reliability of CMOS circuits. This paper presents a reliability simulation study based on R-D model on CMOS inverter circuit. HSPICE MOSRA model together with the Predictive Technology Model (PTM) was used as to incorporate the NBTI model in the circuit reliability simulation study for different technology nodes. PTM of High Performance (HP) models of 16nm, 22nm, 32nm and 45nm were used in this simulation study. The atomic hydrogen based model was integrated in the simulation. The results show that in a CMOS inverter circuit, the threshold voltage shift of p-MOSFET under NBTI stressing increased as the year progressed. The threshold voltage shift was observed to increase up to 45.1% after 10 years of operation. The time exponent,  $n \sim 0.232$  of the threshold voltage shift observed indicates that the defect mechanism contributed to the degradation is atomic hydrogen. The propagation delay increased to 19.5% over a 10-year period. s up to 19.5% from the zero year of operation until 10 years of the operation. In addition, the time propagation delay increased as year increased when the technology nodes smaller. The finding is important for understanding reliability issues related to advanced technology nodes in CMOS circuits study.

*Keywords:* NBTI, CMOS Inverter, Predictive Technology Model, HSPICE MOSRA, circuit reliability

### ARTICLE INFO

*Article history:*

Received: 24 August 2016

Accepted: 02 December 2016

*E-mail addresses:*

mfitrizainudin@gmail.com (M. F. Zainudin),

hanimh@salam.uitm.edu.my (H. Hussin),

Abd\_Karimi@salam.uitm.edu.my (A. K. Halim)

\*Corresponding Author

### INTRODUCTION

Negative bias temperature instability (NBTI) is a well-known issue in CMOS devices compared to other issues such as hot carrier injection (HCI). Since it is first reported in the 1960s (Deal et al., 1967) many researchers

are studying the NBTI properties to see its impact on CMOS devices and a several ways to reduce the degradation effect.

NBTI increases with an increase of negative stress gate bias ( $V_G$ ), temperature (Ho et al., 2013) and NBTI shows power-law time dependence for moderate to very long stress time (t-stress) (Haggag et al., 2007) which can be described with an empirical description below :

$$\Delta V_{TH} \approx C \exp\left(-\frac{E_A}{k_B T}\right) \left(\frac{|V_G - V_{TH0}|}{t_{ox}}\right)^{n} t_{stress} \quad (1)$$

where  $E_A$  is an apparent activation energy (typically in range of 60-80 meV),  $k_B$  is the Boltzmann constant,  $T$  is a temperature,  $V_G$  is a negative stress gate bias,  $t_{ox}$  is an oxide thickness, and  $n$  is a power-law time exponent with range between 0.1 and 0.25 (Franco et al., 2014). An oxide electric field ( $E_{ox} \approx |V_G - V_{TH0}| / t_{ox}$ ) clearly shown to be another parameter which lead to NBTI degradation by varying  $t_{ox}$ . Hence, an idea of implementing that features to study on the circuit reliability and performance were used in this work.

According to Mahapatra (Mahapatra et al., 2013), the author declared that NBTI results in positive charge build-up in the gate insulator and causes temporal shift in device parameters such as linear and saturation drain currents ( $\Delta I_{DLIN}$  and  $\Delta I_{DSAT}$ ), subthreshold slope ( $\Delta S$ ), threshold voltage ( $\Delta V_{TH}$ ), and transconductance ( $\Delta g_m$ ). Threshold voltage shift ( $\Delta V_{TH}$ ) due to NBTI effect gives a fractional change of drain current for MOSFETs in both linear (2) and saturation region (3). MOSFETs in the saturation region shown twice degradation than in the linear region.

$$I_{Dlin} \approx \frac{W\mu_{eff}C_{ox}}{L} (V_G - V_T)V_D \Rightarrow \frac{1}{I_D} \frac{dI_D}{dV_T} = -\frac{\Delta V_T}{V_G - V_T} \quad (2)$$

$$I_{Dsat} \approx \frac{W\mu_{eff}C_{ox}}{L} (V_G - V_T)^2 \Rightarrow \frac{1}{I_D} \frac{dI_D}{dV_T} = -\frac{2\Delta V_T}{V_G - V_T} \quad (3)$$

The delay time is:

$$t_d = \frac{C|V_{DD}|}{I_D} = \frac{2LC}{W\mu_{eff}C_{ox}(V_{DD} - V_T)^2} \quad (4)$$

where  $C$  is the capacitance and  $V_{DD}$  the supply voltage. Since NBTI effect results in reducing of  $\mu_{eff}$  and increasing of  $V_T$ , the delay time is also increase (Schroder, 2007).

Inverters, the nucleus of all digital designs which simplified the designing process for complex structures such as NAND gates, flip-flop and microcontroller once its operation and properties are clearly understood (Berkeley, 1999). NBTI effect on the inverter can be studied to see its impact on the inverter reliability performance.

Finding on aging analysis and design (Parthasarathy et al., 2014) which focused NBTI study on propagation delay shown that threshold voltage change causes an increase in the propagation delay. NBTI studies on power gating designs (Lee et al., 2011; Rossi et al., 2016) shown that NBTI does not affect the average power. However, the result of power gating design is used to study the device performance based on the device lifetime. Technology scaling causes the nominal voltage decreases which results in slower switching speeds (Bild et al., 2011).

In this paper, the effect of inverter performance and reliability on NBTI degradation are investigated based on increasing the threshold voltage. Propagation delay, switching speed, noise margin and average power consumption of different parameter stress are analyzed and discussed in section III.

### METHODOLOGY

The inverter circuit was used to perform a reliability and performance study using the built-in aging models integrated into Synopsys HSPICE. MOSFET Model Reliability Analysis (MOSRA) was used to predict the long-term reliability and performance of the device. The reliability and performance of a CMOS technology become more challenging as the technology is scaled down. NBTI degradation shown to increase with an increase of negative stress gate bias (VG) in the previous study(Ho et al., 2013). However, oxide field (EOX) also plays an important role on the NBTI degradation effect (Chenouf, Djeddar, Benadelmoumene, Tahi, & Goudjil, 2015).

A high performance (HP) of PTM technology models were used with different technology nodes (16nm to 45nm). A nominal supply voltage(Vdd) based on each technology parameter was used for the different technology sizes. The simulation was simulated under a 10 years of stress time and constant temperature of 27oC. The inverter sizing ratio for NMOS used in this simulation was 2:1. The width and length (W/L) for PMOS is twice than NMOS which was 4:1. For example, W/L for PMOS and NMOS used for HP 16nm technology were 64nm/16nm and 32nm/16nm respectively.

Then, the NBTI model will be implemented in MOSRA flow for HSPICE circuit simulation as shown in Figure 1. EOL (end of lifetime) of a MOSFET device can be described as the device operation time where a key measure of device performance, such as  $I_{dsat}$ , degrades by a given percentage (typically, 10%) of its fresh (un-aged) value (Synopsys, 2009). The inverter was simulated under a two-phase simulation (pre-stress simulation phase and post-stress simulation phase) in the MOSRA flow.

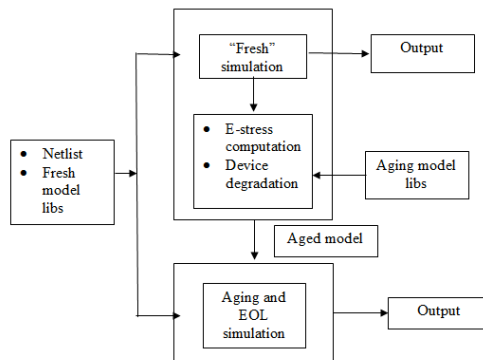


Figure 1. HSPICE MOSRA process flow

The result is then extrapolated to calculate the total device performance degradation after a user-specified time of circuit operation (age) (Synopsys, 2009). Threshold voltage shift ( $\Delta V_{TH}$ ) was calculated. The rise time, fall time and average power consumption can be obtained by referring to HSPICE design hierarchy (Nekovei, 2006). The rise time and fall time were used to calculate the propagation delay. Transient analysis was used to obtain the rise/fall time and average power consumption while DC analysis was used to obtain switching speed (Akshay Sridharan, 1988a, 1988b). The Voltage Transfer Curve (VTC) can be plotted by using Synopsys CosmosScope after the DC analysis simulation. Later, noise margin can be obtained from the VTC.

## RESULT AND DISCUSSION

In this section, the effect of NBTI on threshold voltage shift ( $\Delta V_{th}$ ) of p-MOSFETs and the circuit performance in terms of propagation delay ( $t_{pd}$ ), switching speed, and average power dissipation of an inverter were analysed based on year of operation and different technology nodes.

### Aging Effect

Years of operation are from 1 year to 10 years and measured at year 1, year 5 and year 10. The behavior of the inverter in terms of the threshold voltage shift, propagation delay, switching speed and average power dissipation was observed and analyzed. The factors that cause the change in the inverter behavior were identified according to device year of operation and different technology nodes.

Figure 2 shows that as the years of operation increases, the threshold voltage shift,  $\Delta V_{th}$  also increases. The inverter with 1 year of operation produced less  $\Delta V_{th}$  than 5 years and 10 years. As a result,  $\Delta V_{th}$  increases up to 45.1% from the first year to 10 years of operation.  $\Delta V_{th}$  follows a power-law of the stress time using formula in (1). Based on the graph, A is equal to 0.0559 with n equal to 0.232. Thus, from the result the graph follows the power-law of the stress time where  $n \sim 0.25$  reflects that the atomic hydrogen is the defect mechanism (Franco et al., 2014).

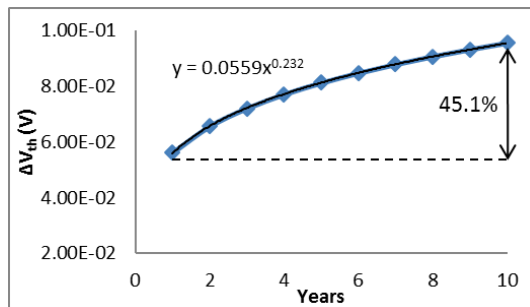


Figure 2. The relationship between threshold voltage shift and aging year



Next, Figure 3 shows that as the inverter aged year increases, the propagation delay,  $t_{pd}$  also increases. The lowest propagation delay between the measured years of operation is during the zero year of operation. The propagation delay increase over 10 years and increases up to 19.5% from the zero year of operation until 10 years of the operation. As a conclusion, the propagation delay increases as the stress time increases. This is similar to previous work where the propagation delay increased due to NBTI effects (Parthasarathy et al., 2014).

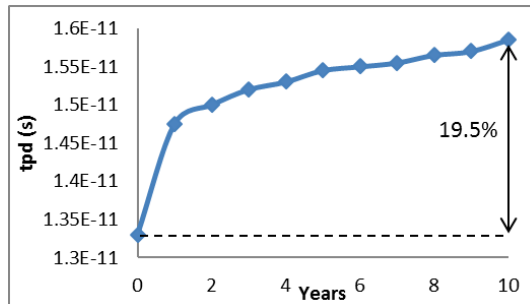


Figure 3. The relationship between propagation delay and aging year

However, the switching speed for the inverter remains constant in Figure 4 for each 1 year, 5 years and 10 years. This is due to constant ratio of W/L is used during the simulation.  $V_M$  can be increase by larger ratio which mean making the PMOS wider (Parthasarathy et al., 2014). Since the W/L ratio used remains the same, so there is no change in switching speed. It can be concluded that the switching speed does not affected by NBTI.

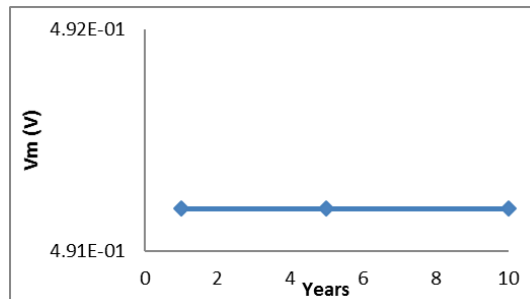


Figure 4. The relationship between switching speed and aging year

Another limiting factor in designing nano-scale circuits is the power dissipation. Hence, in this work, we include the analysis NBTI effect on power dissipation. As shown in Figure 5, the average power dissipation of the inverter is shown to be not affected by the NBTI as it is decreases as the year increases (Rossi et al., 2016). This is in agreement with (Wang & Zwolinski, 2008) where the delay that increase due to NBTI does not cause an increase in the power dissipation. The average power dissipation of 10 years of operation is lower than 1 year

of operation and at the same value during the 5 years of operation. It decreases by 4% from the start of operation until 10 years of operation. A capacitive coupling between input and output will trigger an injection of current into the supply, when the output briefly overshoots  $V_{DD}$  (Berkeley, 1999). As a result, it decreases exponentially inconsistent over 10 years and generate lesser power dissipation from zero year to 10 years of operation.

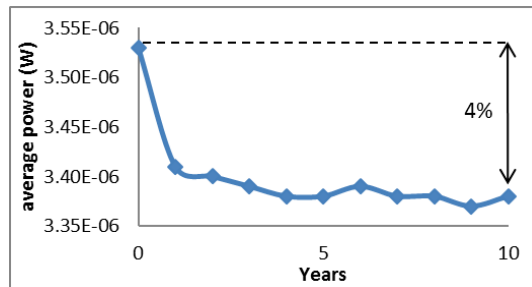


Figure 5. The relationship between average power and aging year

### Technology scaling

Scaling down technology node is a design technique that is used to improve the inverter performance. The technology nodes were varied from 16nm to 45nm and measured. Each PTM model uses different voltage supply such 0.7V, 0.8V, 0.9V, and 1.0V for 16nm, 22nm, 32nm and 45nm respectively. A comparison between models was done to study its effect on inverter performance.

As shown in Figure 6,  $\Delta V_{th}$  decreases as the technology nodes decreases. Over 10 years of operation, HP 16nm model produces the least  $\Delta V_{th}$  than other HP models.  $\Delta V_{th}$  of HP 16nm model are reduces up to 26.5%, 18.1% and 9.7% respectively from HP 45nm, HP 32nm and HP 22nm at 10 years of operation. Therefore, threshold voltage shift decreases as the technology models become smaller.

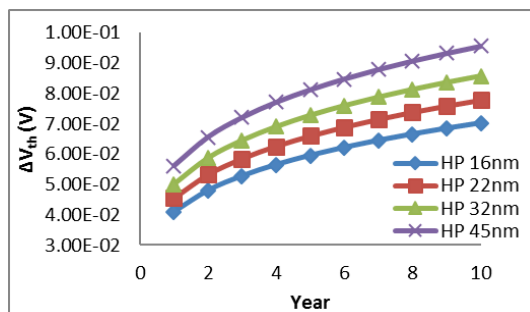


Figure 6. The relationship between threshold voltage shift and device lifetime for different technology scaling over 10 years

Figure 7 depicts the propagation delay trend for different technology nodes over device lifetime. The propagation delay increases as the technology node decreases. HP 45nm model shows the best propagation delay compared to other HP models. The propagation delay of HP 16nm model increases by 31.5%, 22% and 10% for HP 45nm, HP 32nm, and HP 22nm respectively. As the technology nodes become smaller, the nominal voltage supply,  $V_{DD}$  become smaller. Since the W/L ratio is constant, smaller  $V_{DD}$  is commonly used by designer to improve average power consumption as a trade-off to the propagation delay (Berkeley, 1999). Thus, the worst-case scenario for the propagation delay for the PTM model is HP 16nm model with the lowest voltage supply of 0.7V which evidence that the smaller technology will lead to poor reliability performance of CMOS inverter circuit.

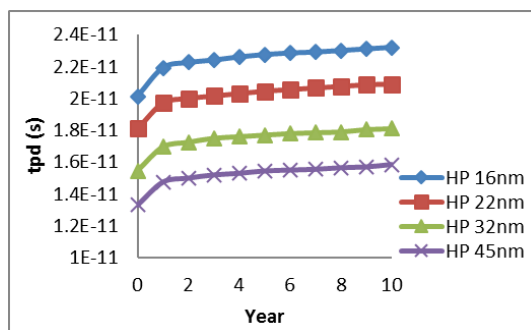


Figure 7. The relationship between propagation delay and device lifetime for different technology scaling over 10 years

Although switching speed and average power does not effected by NBTI, the inverter performance was evaluated. The switching speed ( $V_{sp}$ ) of the inverter decreases as the technology node decreases by referring to Figure 8. HP 16nm model show the lowest  $V_{sp}$  compared with other model.  $V_{sp}$  was reduced by 26.1% from HP 45nm model to HP 16nm model. Switching speed reduces as the nominal supply voltage decreases from the technology scaling. Reducing nominal supply voltage will results in lower oxide field,  $E_{ox}$  which was in agreement with (Chenouf, Djeddar, Benadelmoumene, Tahi, & Goudjil, 2015).

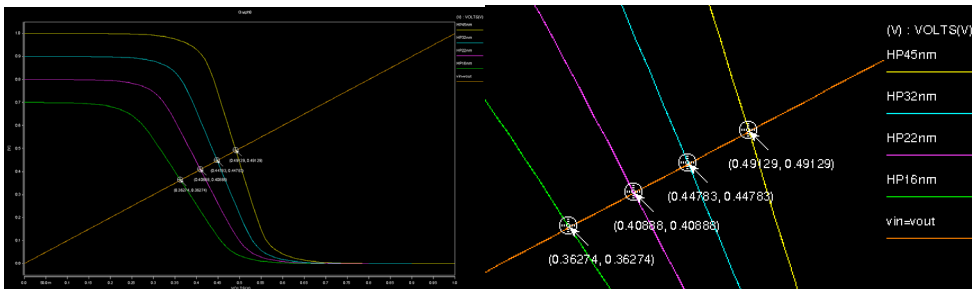


Figure 8. Switching speed and technology scaling

Based on the VTC graph above, noise margin for high logic level (NMH) and low logic level (NML) were obtained. Noise margins were evaluated to see how well the gate perform under noisy condition. Basically, an ideal noise margin is when  $NM_H = NM_L = V_{DD}/2$ . Table 1 shows the noise margins that were obtained from VTC graph. The noise margin decreases as the technology model becomes smaller. Smaller technology nodes results in decreasing of the threshold voltages. Decreasing the threshold voltage leads to reducing the threshold voltage shift. It was observed that noise margin decreases as the threshold voltage decreases in the previous study (Mukherjee, Mondal, & Reddy, 2010). Thus, it can be concluded that somehow threshold voltage has a relationship with noise margin.

Table 1  
Noise margin for different technology models

Technology Models	$V_{OH}$ (V)	$V_{IH}$ (V)	$N_{MH}$ (V)	$V_{OL}$ (V)	$V_{IL}$ (V)	$N_{ML}$ (V)
HP 16nm	0.7	0.475	0.225	0	0.25	0.25
HP 22nm	0.8	0.525	0.275	0	0.30	0.30
HP 32nm	0.9	0.55	0.35	0	0.35	0.35
HP 45nm	1.0	0.575	0.425	0	0.40	0.40

Average power consumption reduction is mainly because of using a low supply voltage. Figure 9 shows that HP 16nm model has lower average power consumption compared to other models. In HP 16nm models average power reduction is 59.4% than of HP 45nm models at 10 years of device lifetime. Since NBTI mainly focused on threshold voltage shift and not voltage supply. It can be concluded that NBTI effect does not influence the average power consumption compared with the NBTI aging effect (Rossi et al., 2016). Hence, average power consumption reduce as the supply voltage decreases due to technology and the device stress time increases.

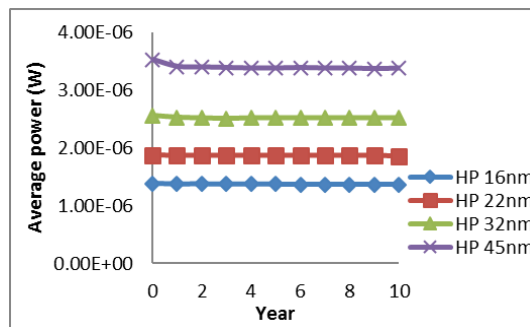


Figure 9. The relationship between average power and device lifetime for different technology scaling over 10 years

## CONCLUSION

In this paper, the study of inverter performance and reliability following increases voltage which leads to NBTI degradation was undertaken. Aging effect and technology scaling are the parameters used to study the NBTI effect on device performance and reliability. Results

threshold voltage shift increases as the stress time increases and the technology model increases. In addition, the propagation delay increases as the stress time increases and technology model decreases. Stress time gives no effect on the switching speed, but smaller technology model gives smaller switching speed. Noise shown to decrease as the technology model decrease. The average power consumption is not affected by NBTI which it is reduced as the stress time increases and the technology model becomes smaller.

## ACKNOWLEDGMENTS

The authors would like to thank Institute of Research Management and Innovation (IRMI) UiTM and Ministry of Higher Education for the financial supports. This research work is conducted at the Integrated Microelectronic Systems and Applications Research Group, Faculty of Electrical Engineering, Universiti Teknologi MARA (UiTM), Malaysia under the support of Fundamental Research Grant Scheme (FRGS: 600-RMI/FRGS 5/3 (31/2015)) and the Lestari Grant 600-RMI/DANA 5/3/LESTARI (2/2015).

## REFERENCES

- Berkeley. (1999). *The cmos inverter* (pp. 144–192). Retrieved from [http://bwrcs.eecs.berkeley.edu/Classes/icdesign/ee141\\_f01/Notes/chapter5.pdf](http://bwrcs.eecs.berkeley.edu/Classes/icdesign/ee141_f01/Notes/chapter5.pdf)
- Bild, D. R., Dick, R. P., & Bok, G. E. (2012). Static NBTI reduction using internal node control. *ACM Transactions on Design Automation of Electronic Systems (TODAES)*, 17(4), 45. <http://doi.org/10.1145/0000000.0000000>
- Chenouf, A., Djeddar, B., Benadelmoumene, A., Tahi, H., & Goudjil, M. (2015). Reliability analysis of CMOS inverter subjected to AC & DC NBTI stresses. In *Proceedings of 2014 9th International Design and Test Symposium, IDT 2014* (pp. 142–146). <http://doi.org/10.1109/IDT.2014.7038602>
- Chenouf, A., Djeddar, B., Benadelmoumene, A., Tahi, H., & Goudjil, M. (2015). Reliability analysis of CMOS inverter subjected to AC & DC NBTI stresses. In *Proceedings of 2014 9th International Design and Test Symposium, IDT 2014* (pp. 142–146). <http://doi.org/10.1109/IDT.2014.7038602>
- Deal, B. E., Sklar, M., Grove, A. S., & Snow, E. H. (1967). Characteristics of the Surface-State Charge (Q<sub>ss</sub>) of Thermally Oxidized Silicon. *Journal of The Electrochemical Society*, 114(d), 266. <http://doi.org/10.1149/1.2426565>
- Franco, J., Kaczer, B., & Groeseneken, G. (2014). Reliability of High Mobility SiGe Channel MOSFETs for Future CMOS Applications. *Springer Series in Advanced Microelectronics* (Vol. 47). <http://doi.org/10.1007/978-94-007-7663-0>
- Haggag, A., Anderson, G., Parihar, S., Burnett, D., Abeln, G., Higman, J., & Moosa, M. (2007). Understanding SRAM high-temperature-operating-life NBTI: Statistics and permanent vs recoverable damage. In *Annual Proceedings - Reliability Physics (Symposium)* (pp. 452–455). <http://doi.org/10.1109/RELPHY.2007.369932>
- Ho, C. H., Panagopoulos, G., & Roy, K. (2013). A self-consistent electrothermal model for analyzing NBTI effect in p-Type Poly-Si thin-film transistors. *IEEE Transactions on Electron Devices*, 60(1), 288–294. <http://doi.org/10.1109/TED.2012.2228657>

- Lee, M. C., Chen, Y. G., Huang, D. K., & Chang, S. C. (2011, January). NBTI-aware power gating design. In *16th Asia and South Pacific Design Automation Conference (ASP-DAC 2011)* (pp. 609-614). IEEE.
- Mahapatra, S., Goel, N., Desai, S., Gupta, S., Jose, B., Mukhopadhyay, S., ... Alam, M. A. (2013). A comparative study of different physics-based NBTI models. *IEEE Transactions on Electron Devices*, *60*(3), 901-916. <http://doi.org/10.1109/TED.2013.2238237>
- Mukherjee, D., Mondal, H. K., & Reddy, B. V. R. (2010). Static Noise Margin Analysis of SRAM Cell for High Speed Application. *IJCSI International Journal of Computer Science Issues*, *7*(5), 175-180.
- Nekovei, R. (2006). Design Hierarchy In HSPICE Use of Subcircuits , measurement , and Parameters.
- Parthasarathy, K., Eee, B. E., & Advisor, T. (2014). *Aging Analysis and Aging-Resistant Design for Low-Power Circuits*. (Doctoral dissertation). University of Cincinnati.
- Rossi, D., Tenentes, V., Yang, S., Khursheed, S., & Al-hashimi, B. M. (2016). Reliable Power Gating With NBTI Aging Benefits. *IEEE Transactions on Very Large Scale Integration (VLSI) Systems*, *24*(8), 1-10.
- Schroder, D. K. (2007). Negative bias temperature instability: What do we understand? *Microelectronics Reliability*, *47*(6), 841-852. <http://doi.org/10.1016/j.microrel.2006.10.006>
- Sridharan, A. (1988a). *HSPICE: 4. Transient Analysis*. Retrieved April 28, 2016, from [https://www.utdallas.edu/~akshay.sridharan/index\\_files/Page10411.htm](https://www.utdallas.edu/~akshay.sridharan/index_files/Page10411.htm).
- Sridharan, A. (1988b). *HSPICE: 5. DC Simulation*. Retrieved April 28, 2016, from [https://www.utdallas.edu/~akshay.sridharan/index\\_files/Page10690.htm](https://www.utdallas.edu/~akshay.sridharan/index_files/Page10690.htm).
- Synopsys. (2009). HSPICE ® User Guide : Simulation and Analysis, (September).
- Wang, Y., & Zwolinski, M. (2008). Impact of NBTI on the performance of 35nm CMOS digital circuits. In *International Conference on Solid-State and Integrated Circuits Technology Proceedings, ICSICT* (pp. 440-443). <http://doi.org/10.1109/ICSICT.2008.4734569>



## **Compound Learning Control for Formation Management of Multiple Autonomous Agents**

**Syafiq Fauzi Kamarulzaman<sup>1\*</sup> and Hayyan Al Sibai<sup>2</sup>**

*<sup>1</sup>Faculty of Computer System & Software Engineering, Universiti Malaysia Pahang, Lebuhraya Tun Razak 26300, Kuantan, Pahang Malaysia*

*<sup>2</sup>Faculty of Engineering Technology, Universiti Malaysia Pahang, Lebuhraya Tun Razak 26300, Kuantan, Pahang Malaysia*

---

### **ABSTRACT**

Having cooperation between multiple autonomous devices against one task is difficult due to each device having their own decision management based on self-deterministic protocol. Within the self-deterministic protocol, a formation management task should be considered along another task in order to provide cooperation and consideration between the operating autonomous devices. In this research, a compound learning control system for formation management of multiple control agents is proposed by managing coordination between multiple autonomous agents along with other tasks simultaneously in an operation. A series of simulation based on an autonomous robot was conducted to evaluate the effectiveness of learning through compound knowledge for providing consideration among achieving goals or coordination configuration against partner robot. The proposed system was able to provide consideration in coordination among operating partners in a task of achieving goal.

*Keywords:* Learning control, multi-agent, formation management, reinforcement learning, intelligent control

---

### **INTRODUCTION**

Manual control is when a human performs tasks such as monitoring the state of the

system, generating performance options, selecting the options in decision making and physical implementation on a device (Sutton et al., 1998). A device that is able to handle tasks done manually can be categorized as an autonomous device, capable of monitoring, deciding a control action and operating its own actuators for an assigned task. Having cooperation between multiple autonomous devices against one task is difficult due to each

---

#### **ARTICLE INFO**

*Article history:*

Received: 24 August 2016

Accepted: 02 December 2016

---

*E-mail addresses:*

syafiq29@ump.edu.my (Syafiq Fauzi Kamarulzaman),

mhdhayyan@gmail.com (Hayyan Al Sibai)

\*Corresponding Author

device having their own decision management based on self-deterministic protocol (Busoniu et al., 2008).

Various research has been conducted on formation management where the operation of multiple control agents is monitored by one intelligent system (Egerstedt et al., 2001) (Rui, 2010). A multi- agent control that is constrained by formation provides control of multiple devices that constrained the movement of the agents based on certain formation (Egerstedt et al, 2001). More application can be seen in (Rui, 2010) where multiple control agents in a form of unmanned aerial vehicle, UAV was operated according to formation assigned by an intelligent system. Within these research, each control agent was operated based on a primary decision that was provided by the main protocol. Thus, lack of the self-deterministic property of an autonomous device.

In this research, a compound learning control system for the management of multiple control agents is proposed for managing coordination between multiple autonomous agents. Earlier research was focused on multi-tasking by compound learning function for goal attainment as obstacle avoidance (Syafiq et al., 2013, 2014). From the previous research, it is understood that the compound learning function could consider multiple control knowledge (state-action rule) with each monitoring different state for producing the optimum action that can satisfy the rules within each control knowledge. Here, the research objective is for the compound learning function to consider a new task, which is the distance from operation partners, where the rules for partner's coordination has to be satisfied along with rules from other control knowledge concerning other tasks; In this case, a control knowledge for goal attainment. Therefore, the compound learning control system that is proposed in this research would consider goal attainment, and partner's coordination as dynamic constraints for having an effective autonomous control.

## METHOD & DESIGN

The tasks performed by the Compound Learning Control System is operated by Learning Agents. These Learning Agents provide information on the control knowledge for each task to a compound function, with which the collection of this information is analysed and rearranged into a compound state-action rule defined by Compound Knowledge. Construction of control knowledge through Reinforcement Learning applies Q-learning, where value function  $Q$  is developed through states  $S$  and actions  $A$  conditions. Actions are selected among the options through preference value stored in the value function  $Q(S, A)$  as  $q$  and later updated after a control attempt through rewards  $r$ . In this research, Learning Control is used to apply control action to the main controller during a control operation, where here, the control object is a two-wheeled differential robot. Therefore, control action  $A$  is in the form of target rotation angle  $\theta$  and target transition  $\Delta \mathbf{r}$ , where  $A = \{\theta, \Delta \mathbf{r}\}$ . Here, two learning control functions were applied on the control device where the control decision is unified by compound function. These two Learning Control functions require the functions to develop at almost similar phase by which



minimum and maximum preference value  $q$  in the value function  $Q(S, A)$  had to be constrained between 0 and 1. Therefore, the applied algorithm in the whole system is as,

$$Q(S, A) = (1 - \alpha)Q(S, A) + \alpha \left[ r + (1 - Q(S, A)) \max_A Q(S, A) \right]. \tag{1}$$

### Learning Agent for Goal Attainment

The Learning Agent for goal attainment updates its value function according to rewards  $r$ , obtained according to the distance between the control device and the goal location as shown in Figure 1. Rewards are determined by comparing the distance of the control device to the goal from its last position with the distance to the goal from its current position. Based on Q-learning, the value function of the Learning Agent is updated by the distance towards goal  $\Delta G$  according to the conducted action  $A_G$  that propels the control device closer to the goals, as

$$Q_1(\Delta G, A_G) = (1 - \alpha)Q_1(\Delta G, A_G) + \alpha \left[ r + (1 - Q_1(\Delta G, A_G)) \max_{A_G} Q_1(\Delta G, A_G) \right]. \tag{2}$$

### Learning Agent for Partner Consideration

The Learning Agent for partner consideration updates its value function according to rewards  $r$ , obtained according to the distance between the control device and the operation partner as shown in Figure 2. Rewards are determined by comparing the distance of the control device to partner from its last position with the distance to partner from its current position. Based on Q-learning, the value function of the Learning Agent is updated by the distance towards partner  $\Delta P$  according to the conducted action  $A_p$  that propels the control device to maintain the distant to the partner, as

$$Q_2(\Delta P, A_P) = (1 - \alpha)Q_2(\Delta P, A_P) + \alpha \left[ r + (1 - Q_2(\Delta P, A_P)) \max_{A_P} Q_2(\Delta P, A_P) \right]. \tag{3}$$

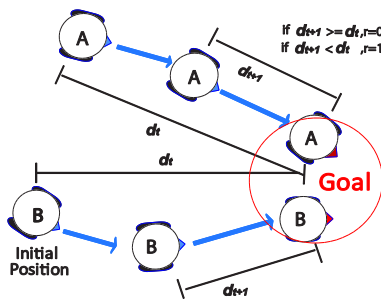


Figure 1. Rewarding in goal attainment function

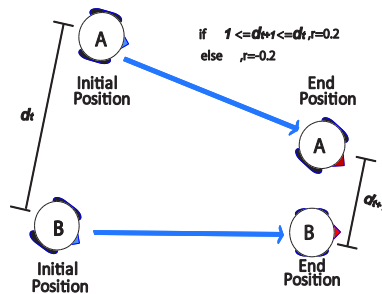


Figure 2. Rewarding in partner consideration function

### Compound Learning Control System with Formation Management

The proposed system utilizes a Compound Function in a Learning Control System. Learning agents for Goal Attainment  $Q_G$ , and Partner Consideration  $Q_P$  which are the control knowledge for specific tasks, contains value function that is converted into a new value function denoted as Compound Control Knowledge, **CQ**. The learning agents are converged and a new value functions, listing actions  $A$  according to the minimum preference value  $q$  when comparing the list of actions in those learning agents based on state  $S_t$ , creating the Compound Knowledge as,

$$Q_{All} = \min_{n=1,2} Q_n(S_t, A) \tag{4}$$

where the Learning Agent accountable for the list of actions is denoted as  $N$ ,

$$N_t(S_t, A) = n, \tag{5}$$

defining the Compound Control Knowledge **CQ** as,

$$f(x) = \sum_{i=0}^{N-1} \alpha_i y_i \exp(-\|x - x_i\|^2 / 2\sigma^2) + b \tag{6}$$

Therefore, the overall system of Compound Learning Control for Formation Management of multiple autonomous agents is designed as shown in Figure 3.

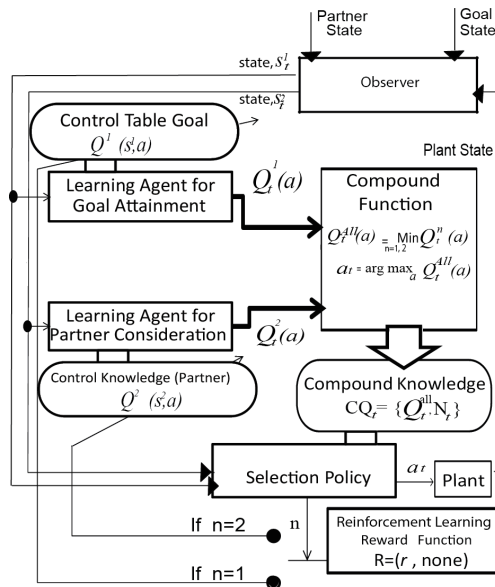


Figure 3. Diagram of Compound Function System for Partner Consideration

### SIMULATION SETTINGS

The Compound Learning Control System was applied in simulation of multiple two-wheeled differential robots. The properties of the robots are determined by the specification of the device in Figure 4 and Figure 5. Details of the device specification are described in Table 1. Both Learning Control functions applied in the Compound Learning Control System are based on the parameters given in Table 2. The controllers involved in managing the target transition and turning was created based on Proportional-Derivative (PD) controller. Intervals defined in Table 2 described that the states and targets were analysed in discrete form, where, for example, there are five options of turning angle and three options of transition.

Table 1  
*Robot Physical Specifications*

Parameter	Values
Weight	0.515 [kg]
Size	Diameter: 0.19 [m] Height: 0.85 [m]

Table 2  
*Robot Physical Specifications*

	Parameters	Range	Intervals
State, $\mathcal{S}$	$(Q_1)$ Goal	-	2
	Distance	10	
	$\Delta \mathbf{G}(x_i, y)$ [m]	$< \Delta \mathbf{G} < 10$	
	$(Q_2)$ Partner	1	0.5
	Distance	$< \Delta \mathbf{G} < 10$	
	$\Delta \mathbf{G}(x_i, y)$ [m]		
Action, $\mathcal{A}$	Target Angle, $\theta$ [rad]	$-1 < 0 < 1$	0.5
	Target Position	$0.1 < r < 0.5$	0.2
	Distance, $r$ [m]		
Discount Rate, $\gamma = 0.3$		Learning Rate. $\alpha = 0.5$	

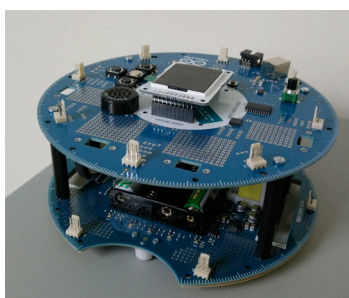


Figure 4. The robot which the simulation is based on (Arduino Mobile Robot Kit)

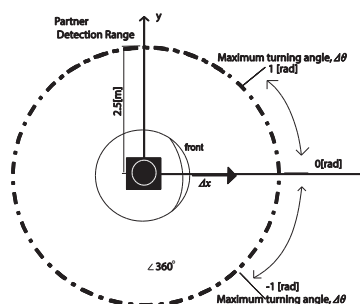


Figure 5. Specification of robot for simulation

The simulation was conducted in two phases; the first phase was the development phase, where value functions of both Learning Control Functions were developed through a series of basic simulation of goal training and partner coordination training. Two devices were simulated at once, where one of the devices is controlled through PD control entirely, and another one is embedded with the proposed system. Simulation concerning the development of both control function was conducted in 50 episodes for three assigned target without obstacles. However, during this phase, only the value functions for position control is updated during simulations with the goal, and only the value function for partner consideration is updated during the second simulation. The second phase was the operation phase, where value functions that have been developed in development phase were applied, united in the Compound Learning Control System, and was conducted in 50 episodes of iteration for two targets.

### SIMULATION RESULTS

The simulation provides results based on the movement of the simulated device after completing the assigned 50 episodes of operation iteration. Learning agent developed in the first phase is compared with the movement results in the second phase.

During the first phase of simulation, from the development of goal attainment control knowledge through learning control. The control operation successfully achieved the goals assigned as shown in the Figure 6. Through this result, the value function of the Learning Control function for goal attainment has been successfully developed towards creating an expert control knowledge for controlling the simulated device. Thus, shows that the Compound Learning Control System should be able to successfully operate goal attainment control in case of an absence of an operation partner. Figure 7 provides information on the control knowledge of goal attainment during simulation. The proposed system was required to reach all three targets consecutively after each 50 iterations. Win =1 describes success on reaching the goal, while win=0 describes failure in reaching the target. Total Value TA describes the improvement occurred in the control knowledge where rewards  $r$  increases the overall value of the goal attainment knowledge as iteration increases, which means, with more stable Total Value TA, more consistent control it will make to achieve the goal. Here, the crossing point

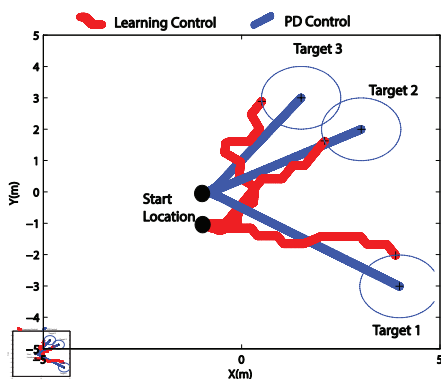


Figure 6. Control Result for target attainment

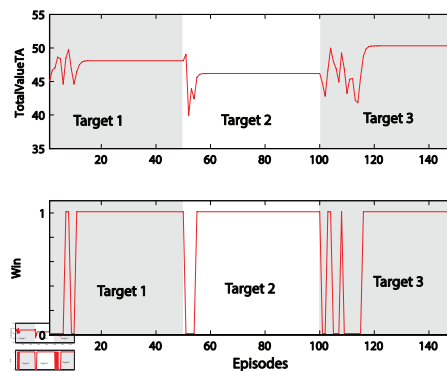


Figure 7. Improvement for Target Attainment Knowledge Learning

did not highlight the collision, since the time reach at that point is different according to each robot. The system was set to halt the robots, in the event of collision. .

During the first phase of the simulation, continues with the development of partner coordination control knowledge through learning control, the control operation successfully achieved the goals assigned as shown in the Figure 8. Through this result, the value function of the Learning Control function for partner coordination has been successfully developed towards creating an expert control knowledge for controlling the simulated device to follow the partner that was operated by PD control. Thus, shows that the Compound Learning Control System should be able to successfully operate partner coordination control in case of no goal information exists. The movement path is curved due to the requirement provided in the Learning Control where the control device has to maintain at least distance of 1[m] around the partner (save distance to avoid collision) to maintain the maximum reward, using path that helps avoid collisions, and gives movement room to the partner with PD control. Figure 9 provides understanding on how the control knowledge of partner coordination is developed during the simulation. The proposed system was required to reach all three targets consecutively after each 50 iterations of episodes. Total Value FM describes the improvement occurred in the control knowledge where rewards  $r$  increases the overall value of the partner coordination knowledge as iteration increases.

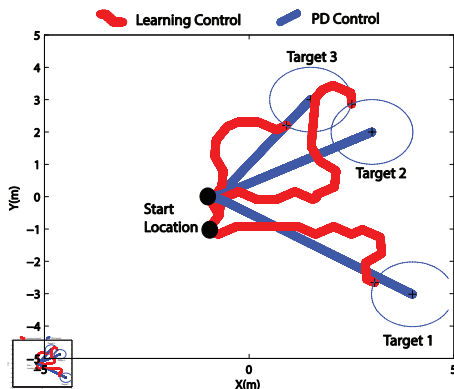


Figure 8. Improvement for Target Attainment Knowledge Learning

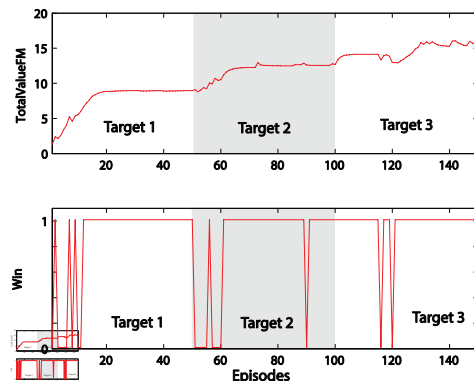


Figure 9. Control Knowledge Improvement for Partner Consideration Learning

During the second phase of the simulation, the control operation successfully achieved the goals assigned as shown in Figure 10. Through this result, the value function of the Learning Control function for partner coordination and goal attainment has been successfully applied and developed. towards creating priority for controlling the simulated device to coordinate with the partner that was operated by PD control while reaching the target area at an optimum movement. Thus, shows that the Compound Learning Control System were able to successfully operate partner coordination control along with goal attainment. The movement path is curved due to the requirement provided in the Learning Control where the control device has to maintain at least distance of 1[m] around the partner to maintain the maximum reward and conserve safety but still provide efforts to reach the target at the optimum movement.

Figure 11 shows how the control knowledge of partner coordination and goal attainment is developed during the second phase of simulation. The proposed system was required to reach all two targets consecutively for 50 iterations. Total Value TA and Total Value FM describes the improvement achieved in the control knowledge where rewards  $r$  increases the overall value of the partner coordination knowledge as iteration increases. Figure 12 provides understanding on how the control knowledge of partner coordination influence the goal attainment in the simulation. The movement path when applying compound function is slightly curved and delayed to preserve the distance between the robot partner but still completes the goal attainment task by optimum movement. Therefore, based on this figure, it is understood that the compound learning control method is applicable for formation management of multiple robots when completing a required task. Further study must include environmental constraints and also increase the number of partner robots in the operation.

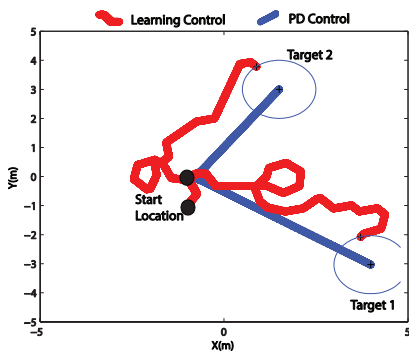


Figure 10. Result for Target Attainment and Partner Consideration using Compound Knowledge with partner using PD control)

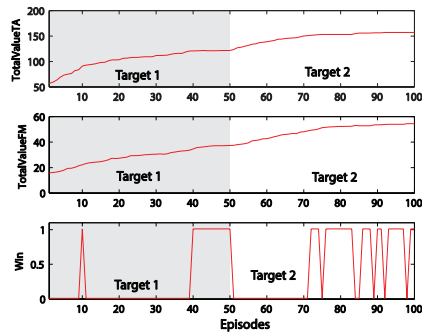


Figure 11. Control Knowledge Improvement using Compound Learning

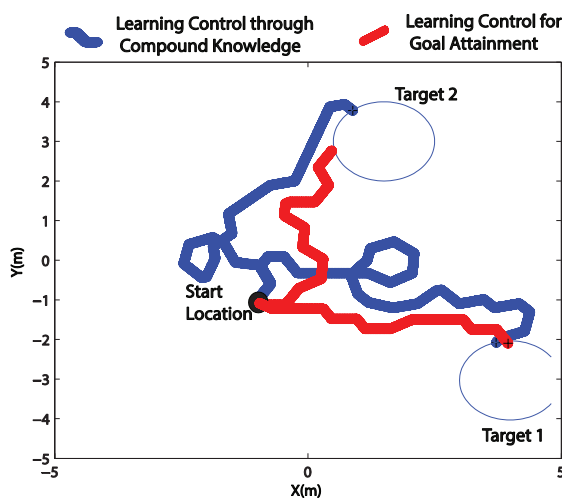


Figure 12. Comparing results using Compound Knowledge and normal Target Attainment Learning Control

## CONCLUSION

In this research, a compound learning control system for the management of multiple control agents by managing coordination between multiple autonomous agents along with other tasks simultaneously was proposed. The Compound Learning Control System makes use of multiple Learning Control functions to provide expert control knowledge of position transition and partner coordination for autonomous two-wheeled differential robots, united by compound function for selecting the best control target options for operating the device. Simulation based on an autonomous robot was conducted to evaluate the effectiveness of learning through compound knowledge for achieving goals or coordination configuration against partner robot. The results of applying compound knowledge was undertaken by analysing the differences in coordination among partner robots. Results show that the Compound Learning Control System was able to provide successful controls towards the goal position with consideration of operation partners location. Therefore, the Compound Learning Control System for position and formation control was achieved. Further study will be conducted in the future to evaluate the reliability in more than two devices within constrained environment.

## REFERENCES

- Busoniu, L., Babuska, R., & Schutter, B. D. (2008). A Comprehensive Survey of Multi-Agent Reinforcement Learning. *IEEE Transaction on Systems, Man, and Cybernetics*, 38(2), 156-172.
- Egerstedt, M., & Hu, X. (2001). Formation Constrained Multi-Agent Control. *IEEE Transactions on Robotics and Automation*, 17(6), 947-951.
- Endsley, M. R., & Kaber, D. B. (1999). Level of Automation Effects on Performance, Situation Awareness and Workload in Dynamic Control Task. *Ergonomics*, 42(3), 462-492.
- Rui, P. (2010). Multi-UAV Formation Manoeuvring Control Based on Q-Learning Fuzzy Controller. *Advanced Computer Control (ICACC)*, 4, 252- 257.
- Sutton, R. S., & Barto A. G. (1998). *Reinforcement Learning: An Introduction*. MIT Press.
- Syafiq, F. K., & Yasunobu, S. (2014). Cooperative Multi- Knowledge Learning Control System with Obstacle Consideration. In *Proceedings of IPMU International Conference* (pp. 505-515).
- Syafiq, F. K., & Yasunobu, S. (2015). Compound Learning Control for Autonomous Position and Obstacle Control of Aerial Hovering Vehicles. In *Proceedings of Asian Control Conference* (pp. 797-802).







## **Binary Classification using SVM for Sick and Healthy Chicken based on Chicken's Excrement Image**

**Nurhanna Abdul Aziz<sup>1</sup> and Mohd Fauzi Bin Othman<sup>1\*</sup>**

*<sup>1</sup>Malaysia-Japan International Institute of Technology, Universiti Teknologi Malaysia, Jln Sultan Yahya Petra, 54100 Kuala Lumpur, Malaysia*

### **ABSTRACT**

The purpose of this paper is to classify between healthy and sick chicken based on their dropping. Most chicken farm management system in Malaysia is highly dependent on human surveillance method. This method, however, does not focus on early disease detection hence, unable to and alert chicken farmers to take necessary action.. Therefore, the need to improve the biosecurity of chicken poultry production is essential to prevent infectious disease such as avian influenza. The classification of sick and healthy chicken based solely on chicken's excrement using the support vector machine is proposed. First, the texture is examined using grey-level co-occurrence matrix (GLCM) approach. A GLCM based texture feature set is derived and used as input for the SVM classifier. Comparison are made using more and then less extracted features, less extracted features and also applying Gabor filter to these features to see the effect it has on classification accuracy. Results show that having more features extracted using GLCM techniques allows for greater classification accuracy.

*Keywords:* Support vector machine, feature extraction, GLCM, Gabor filter

### **INTRODUCTION**

Poultry, especially chicken, is the primary source of protein in Malaysia. According to the recent USDA statistic chicken meat consumption in Malaysia is the highest in

the world. It has increased from 1.4 million metric tons in 2013 to 1.43 million metric tons in 2014. To meet this huge demand imports from China are needed. In order for Malaysia to become a trusted producer in the halal chicken meat industry, it should have a good poultry management system. The significant issues are diseases such as avian influenza. In this field, observation is highly consequential to discover diseases at an early stage because when the disease is in one of the last stages, the chicken is possibly not

#### **ARTICLE INFO**

*Article history:*

Received: 24 August 2016

Accepted: 02 December 2016

*E-mail addresses:*

nurhanna2@live.utm.my (Nurhanna Abdul Aziz),

mdfauzi@utm.my (Mohd Fauzi Bin Othman)

\*Corresponding Author

treatable anymore (den Boer, van den Hout, & Vervloed, 2014). Some of the signs are sudden diarrhoea, decreased egg production, sneezing, nasal discharge, coughing, gasping for air, lack of energy and appetite, swelling of tissues around the eyes and neck, purple discoloration of the wattles, combs and legs and depression, muscular tremors, drooping wings, twisting of head and neck, incoordination and complete paralysis. Chicken disease can also be recognized by its dropping's, colour and density. Early detection of disease and chicken health can facilitate the control of diseases through vector control of vaccination applications, disease-specific approach; and improved productivity. Previous work carried out by (Zhu, Peng, & Ji, 2009) mainly focused on detecting chicken that died. One way to improve the system is to examine chicken excrement images using Gabor- GLCM approach with SVM classification. This paper is divided into three sections. Section One discusses the importance of having early disease detection system in chicken poultry. Section Two emphasizes on the applied methodology, framework used and the experiment's result. We conclude our hypothesis and future work that need to be done in Section Three.

## METHODOLOGY

In the methodology section, this paper will describe briefly the designated framework, how the data is collected and pre-processed and also the feature extraction and the classifications methods.

### Framework

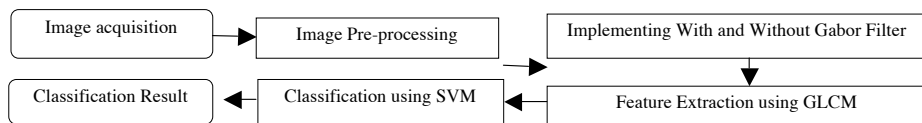


Figure 1. The chicken's disease detection framework

### Image Acquisition

Image acquisition of chicken's dropping was obtained by using a static digital camera. The distance of the camera has been set to be at least 90 degrees off the camera. All the photos were decoded in JPEG standard format in 4000x3000 pixels (dot). The manual identification of sick and normal chicken's excrement images was carried out based on their characteristic by an authorized veterinary. The data set contains 20 images of the same background. Figure 2 depicts some of the eight images that are classified as 'sick' or 'stressed' and Figure 3 is a sample of eight images classified as 'healthy' or 'normal'.



Figure 2. Sick chicken's excrement's images

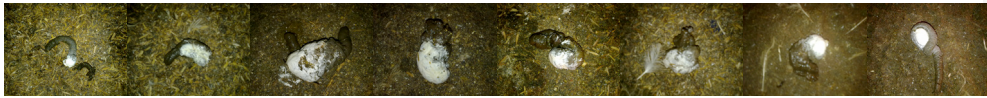


Figure 3. Healthy chicken's excrement's images

### Image Pre-processing

Image pre-processing is used to improve and enhance the quality of the images. Some of the images suffered from noise, blurry and low contrast of quality. Thus, the basic steps of image pre-processing were used and listed as follows:

1. Set the resolution of the images to 300x300 dpi.
2. Resize the image to 200x200 pixels
3. Convert the image from binary to the grayscale.

### Feature Extraction Using GLCM and Gabor Filter

One of the major tasks in image processing is feature extraction. It is believed that the nature of the surface can be characterized by the property of the texture (Hammouda & Jernigan, 2000). The texture itself contains much information about the structural arrangement and its relationship to its surrounding (Raju & Durai, 2013). Therefore, it is crucial to have feature extraction method so that the image can be easily classified. It is also a process that represents the raw image that can ease the decision-making process. As described by (Min et al, 2006), texture features are extracted by simulating the perceptual properties such as orientation, coarseness, fineness, and regularity. There are numerous ways to extract and classify the features, but this paper only focuses on Grey-level co-occurrence matrix (GLCM). GLCM is proven to be a very powerful tool for quantifying the intensity variation (Ahmed, Bayraktar, Bhunia, Hirleman, Robinson, & Rajwa, 2013). The use of the GLCM concept for texture can be seen in works done in (Siraj, Salahuddin, & Yusof, 2010; Arebey, Hannan, Begum, & Basri, 2012). As it is defined as the frequencies of grey-level values that occur in an image (thus some of the brief computation of texture feature extraction summarized (Level, Pramunendar, Supriyanto, Novianto, & Yuwono, 2013) is shown below.

$$entropy = - \sum_{i=0}^{N-1} p_{ij} \log p_{ij} \quad (1)$$

$$contrast = \sum_{i=0}^{N-1} n^2 \left\{ \sum_{i=0}^N \sum_{i,j=0}^N p_{ij} \right\}, |i - j| = n \quad (2)$$

$$\text{correlation} = - \sum_{i=0}^{N-1} \sum_{j=0}^{N-1} \frac{(i - \mu_x)(j - \mu_y)}{\sqrt{\sigma_x \sigma_y}} p_{ij} \quad (3)$$

$$\text{autocorr} = \sum_{i=0}^{N-1} \sum_{j=0}^{N-1} (ij) p_{ij} \quad (4)$$

$$\text{inertia} = \sum_{i=0}^{N-1} \sum_{j=0}^{N-1} (i - j)^2 p_{ij} \quad (5)$$

### Classification Using SVM

Support vector machine (SVM) is a novel type of learning machine, which is based on statistical learning theory (SLT). That is, an SVM is an approximate implementation of the method of structural risk minimization. SVM has shown to provide a better generalization performance than traditional techniques, including neural networks (Chih-Min et al, 2006). SVM demonstrates good classification performance in (Khedher, Ramírez, Górriz, Brahim, & Segovia, 2015; Dubey, 2014; Ahmed, Kang, Kang, Ko, Cho, Rhee, S. & Yu, 2015). SVM also has been applied in most of the fields such as face recognition, fingerprint, bioinformatics, and it has also been tested and applied to agriculture fields such as research works done by (Khedher et al., 2015; Sharaf-Eldeen, Moawad, El Bahnasy, & Khalifa, 2012). The basic idea of SVM is that it seeks to maximize the distance between two classes, and the distance between classes is traditionally defined by the closest points (Hammouda, K. & Jernigan, E., 2000). It is a very effective method for general purpose pattern recognition. (Chih-Min et al, 2006). SVM is popular for its capability in generalising in and predicting s with a good degree of accuracy. (Siraj et al., 2010). Optimal hyper- plane is derived in a high dimensional feature space that defines a maximum boundary margin between data samples in two classes which provides a better generalization property. With its latest extensions enabled the SVM to learn and classify multiple categories of data, overlapping classes and noisy data by the introduction of slack variables that enable the soft margin classifier (Elhariri et al, 2014). Basically, the SVM is modelled as in (Kazemian & Ahmed, 2015). This paper only classifies and compares sick and healthy chicken's excrement image only.

### Experiments and Classification Result

The experiments have been tested on a 4GB RAM, Intel Core i7 CPU 1.6 GHz using Matlab 2012b release. We had 20 samples of chicken's excrement images in which 20% of them is used as our test data, and the balance remains as our training data. GLCM statistical calculation is applied to extract the features which include autocorrelation, contrast, energy, entropy, homogeneity, cluster prominence, cluster shade, correlation, difference entropy, difference variance, dissimilarity, inverse difference moment, information measure of correlation 1, information measure of correlation 2, inverse difference, maximum probability, sum average, sum entropy, sum of squares and sum of variance. Thus, each image will have 19 features

subsequently. Based on these extracted features, we design four types of experiments. The first and second sets of experiment are to determine the accuracy rate of the classification by applying Gabor filters with five different orientations with only four features extracted out of 19. Experiments three and four focus on finding accuracy rate SVM classification without applying any Gabor filter with four extracted features and 19 extracted features consequently. Figures 5(a) and 5(b) show some samples of healthy and sick chicken dropping images that applied Gabor filter with different orientation approach while Figures 6(a) and 6(b) show some sample images with no Gabor filter applied.

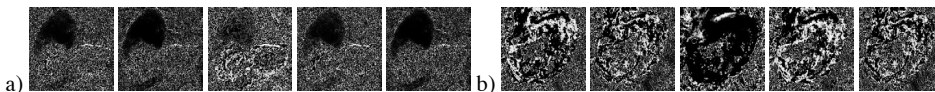


Figure 5. (a) A healthy chicken's excrement image with different orientations (0°, 45°, 90°, 135° and 180°) of Gabor filter; (b) Sick chicken's excrement image

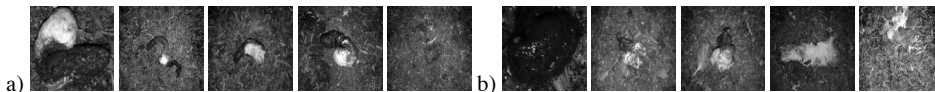


Figure 6. Sample of healthy chicken's excrement with no Gabor filter applied; (b) Sick chicken's excrement

Based on both Gabor and non-Gabor filter images, we applied the statistical calculation of GLCM to extract the features. Table 1 shows some of the GLCM calculation applied on both healthy and sick chicken's excrement images. The reason we choose autocorrelation, contrast, energy and entropy is based on the GLCM calculation in which the result outperform others features. Nevertheless, we still need to do the comparison with other 19 features to determine either this supporting features may affect the result of the classification or not.

Table 1  
GLCM statistical calculation applied on both sample healthy and sick images with 0° orientation of GABOR filter

Image#	Autocorrelation	Contrast	Energy	Entropy
Image Healthy 1	6.4733	9.9763	0.0723	3.0739
Image Healthy 2	6.8131	6.1299	0.0558	3.1496
Image Healthy 3	5.7578	4.7044	0.0682	2.952
Image Sick 4	4.9985	4.8265	0.0833	2.7861
Image Sick 5	11.194	53.899	0.0756	3.3975

After the GLCM implementation, all the dataset is scaled and normalised based on the minimum and maximum value of each row before running the classification method. Classification in SVM requires the dataset to be divided into two sets of data where one set of data is used

as a training set and another one as a test set. Each row of data contains its feature label. To implement the SVM approach, LibSVM 3.20 was used to fit this experiment purposes being a SVM library tool used widely in classifications (Zhang, 2014; Moraes, Valiati, Gavião, & Neto, 2013; Ahmed et al., 2012; Wang & Chung, 2013; Tang & Sazonov, 2014; Tong, et al., 2014). The toolbox was developed by Chang and Lin (2011) which solves the quadratic programming problem by using a sequential minimal optimization-type algorithm (Kang, S. et al, 2015). We used 80% of the total number of feature vectors as our training sample while the remaining 20% of a test sample. All the data must be converted into LibSVM format before classification can take place. We had labelled sick images equal to -1 and healthy images as one respectively. We used the radial basis kernel function as it is more significant to our case as compared to other kernel function as a polynomial and applied 10-cross validation in our dataset. We also set the parameter C equal to 1 for all the cases.

$$f(x) = \sum_{i=0}^{N-1} \alpha_i y_i \exp(- \| x - x_i \|^2 / 2\sigma^2) + b \tag{6}$$

Tables (2-3) compares the classification accuracy results between four extracted features (correlation, contrast, homogeneity, energy) and 19 extracted features (autocorrelation, contrast, energy, entropy, homogeneity, cluster prominence, cluster shade, correlation, difference entropy, difference variance, dissimilarity, inverse difference moment, information measure of correlation 1, information measure of correlation 2, inverse difference, maximum probability, sum average, sum entropy, sum of squares and sum of variance) by using GLCM techniques with Gabor filter applied. The value is set to be 3.05175 as it is the best value we had tested in our case.

Table 2  
Classification result- with GABOR and 4 extracted features within same dataset.  $O (= 3.05175)$

Kernel Type	Orientation	Classification Accuracy	#Iteration	#SV
Radial	0	81.25%	19	16
	45	81.25%	15	16
	90	75%	21	16
	135	68.75%	14	16
	180	81.25	13	16

Table 3  
SVM Classification result- with GABOR and 19 extracted features within the same dataset.  $O (= 3.05175)$

Kernel Type	Orientation	Classification Accuracy	#Iteration	#SV
Radial	0	81.25%	18	16
	45	81.25%	31	16
	90	81.25%	21	16
	135	75%	16	16
	180	81.25%	21	16

Both experiments use the same dataset for training and testing. It can be seen that by having more features extracted with Gabor filter applied to the images increase the accuracy rate compares with less feature extracted. Table (4-5) presents the accuracy rate for both four features and 19 features with 80% of the sample data is used for training and the remaining 20% for testing. Using the same training model, the accuracy rate for an image that has 19 extracted features yields much more than the image that only has four features extracted.

Table 4  
*SVM Classification result- with GABOR and 19 extracted features by using the test sample  $O = 3.05175$ ; # TEST SAMPLE=4; # TRAINING SAMPLE=16*

Kernel Type	Orientation	Classification Accuracy	Iteration	#SV
Radial	0	75%	18	16
	45	50%	31	16
	90	75%	21	16
	135	75%	16	16
	180	75%	21	16

Table 5  
*SVM Classification result- with GABOR and 4 extracted features by using the test sample  $O = 3.05175$ ; # TEST SAMPLE=4; # TRAINING SAMPLE=16*

Kernel Type	Orientation	Classification Accuracy	#Iteration	#SV
Radial	0	50%	19	16
	45	50%	15	16
	90	50%	21	16
	135	50%	14	16
	180	50%	13	16

Table (6-7) yields the accuracy rate comparison between fewer and more features but without any Gabor filter applied. It proves that even with no Gabor filter applied, the image which has 19 features extracted gives higher accuracy rate than four features extracted.

Table 6  
*SVM Classification result- with no GABOR and 4 extracted features ( $O = 3.05175$ )*

Kernel Type	Dataset	Accuracy Rate	#Iteration	#SV
Radial	Training	81.25%	13	13
	180	50%	13	16

Table 7  
*SVM Classification result- with no Gabor and 19 extracted features ( $O = 3.05175$ )*

Kernel Type	Dataset	Accuracy Rate	#Iteration	#SV
Radial	Training	93.75%	19	16



The performance measures are described regarding true and false positive and true and false negative.

- True Positive (TP): Sick chicken correctly identified as sick chicken.
- True Negative (TN): Healthy chicken correctly identified as healthy chicken.
- False Negative (FN): Sick chicken incorrectly identified as healthy chicken.
- False Positive (FP): Healthy chicken incorrectly identified as sick chicken.

As a conclusion, from Table (2- 7), it indicates that the accuracy rate improves if more features extracted as compared by extracting only four characteristics of the images with Gabor filter applied. It also shows that the implementation of Gabor filter bank does not give the major impact on the accuracy rate. The present finding support (Kazemian & Ahmed, 2015) research work which concluded that as the number of the dataset (in this case is the number of extracted features) increased, the accuracy also increases. Choosing the best optimum kernel for each of the cases also plays an important task in increasing the classification accuracy.

## CONCLUSION

This paper presents classification of texture images specifically of chicken's excrement using SVM classification approach and the GLCM method to extract the texture feature of images. It also applies the Gabor filter technique as part of feature extraction method. The paper draws a comparison between quantities of features that are extracted and conducted on g 20 sample images of chicken's dropping. We did four experimental studies. The first is between four features and 19 features by applying the Gabor filter. We found out that having more features extracted thru GLCM techniques yields results with better accuracy as compared with fewer features. The second study is between 4 features and 19 features but without Gabor filter applied which also proves that having more extracted features have more advantage than fewer features even though their result is much better than having Gabor filter applied on. Analysis of the results reveals that choosing the best optimization value for gamma in SVM modeler gives better accuracy. We also prove that having more features extraction for SVM classification give more accurate result specifically for chicken's excrement images in which there is a similarity in color between the features and background color. Our future work will be on texture feature extraction method as we believe that having a good extraction framework would provide better results. There is also the need to focus on identifying nearly sick chicken by analyzing the 'stressed' chicken images using the same framework with expansion on SVM algorithm.

## ACKNOWLEDGEMENT

Special thanks to Malaysia- Japan International Institute, Universiti Teknologi Malaysia and also Centre of Artificial Intelligence and Robotic (CAIRO) department.



## REFERENCES

- Ahmed, F., Al-Mamun, H. A., Bari, A. H., Hossain, E., & Kwan, P. (2012). Classification of crops and weeds from digital images: A support vector machine approach. *Crop Protection*, *40*, 98-104.
- Ahmed, W. M., Bayraktar, B., Bhunia, A. K., Hirtleman, E. D., Robinson, J. P., & Rajwa, B. (2013). Classification of bacterial contamination using image processing and distributed computing. *IEEE Journal of Biomedical and Health Informatics*, *17*(1), 232-239.
- Arebey, M., Hannan, M. A., Begum, R. A., & Basri, H. (2012). Solid waste bin level detection using gray level co-occurrence matrix feature extraction approach. *Journal of Environmental Management*, *104*, 9-18.
- Chen, C. M., Chen, C. C., & Chen, C. C. (2006, August). A Comparison of Texture Features Based on SVM and SOM. In *ICPR (2)* (pp. 630-633).
- den Boer, C. A., van den Hout, N., & Vervloed, L. (2014). Poultry farming
- Dubey, S. R., & Jalal, A. S. (2014). Adapted approach for fruit disease identification using images. arXiv preprint *arXiv:1405.4930*.
- Elhariri, E., El-Bendary, N., Fouad, M. M. M., Platoš, J., Hassanien, A. E., & Hussein, A. M. (2014). Multi-class SVM based classification approach for tomato ripeness. In *Innovations in Bio-inspired Computing and Applications* (pp. 175-186). Springer International Publishing.
- Hammouda, K., & Jernigan, E. (2000). *Texture segmentation using gabor filters*. Canada: Center for Intelligent Machines, McGill University.
- Kang, S., Kang, P., Ko, T., Cho, S., Rhee, S. J., & Yu, K. S. (2015). An efficient and effective ensemble of support vector machines for anti-diabetic drug failure prediction. *Expert Systems with Applications*, *42*(9), 4265-4273.
- Kazemian, H. B., & Ahmed, S. (2015). Comparisons of machine learning techniques for detecting malicious webpages. *Expert Systems with Applications*, *42*(3), 1166-1177.
- Khedher, L., Ramirez, J., Górriz, J. M., Brahim, A., Segovia, F., & Alzheimer's Disease Neuroimaging Initiative. (2015). Early diagnosis of Alzheimer's disease based on partial least squares, principal component analysis and support vector machine using segmented MRI images. *Neurocomputing*, *151*, 139-150.
- Moraes, R., Valiati, J. F., & Neto, W. P. G. (2013). Document-level sentiment classification: An empirical comparison between SVM and ANN. *Expert Systems with Applications*, *40*(2), 621-633.
- Pramunendar, R. A., Supriyanto, C., Novianto, D. H., Yuwono, I. N., Shidik, G. F., & Andono, P. N. (2013, November). A classification method of coconut wood quality based on Gray Level Co-occurrence matrices. In *Robotics, Biomimetics, and Intelligent Computational Systems (ROBIONETICS), 2013 IEEE International Conference on* (pp. 254-257). IEEE
- Raju, J., & Durai, C. A. D. (2013, February). A survey on texture classification techniques. In *Information Communication and Embedded Systems (ICICES), 2013 International Conference on* (pp. 180-184). IEEE.
- Sharaf-Eldeen, D. A., Moawad, I. F., El Bahnasy, K., & Khalifa, M. E. (2012, December). Learning and applying range adaptation rules in case-based reasoning systems. In *International Conference on Advanced Machine Learning Technologies and Applications* (pp. 487-495). Springer Berlin Heidelberg.

- Siraj, F., Salahuddin, M. A., & Yusof, S. A. M. (2010, September). Digital image classification for malaysian blooming flower. In *2010 Second International Conference on Computational Intelligence, Modelling and Simulation* (pp. 33-38). IEEE.
- Song, W., Xiong, B., Sun, Z., Mo, H., & Su, Q. (2010). Development and application of assistant system for diagnosing chicken diseases based on smart mobile phones. *Transactions of the Chinese Society of Agricultural Engineering*, *26*(4), 220-226.
- Tang, W., & Sazonov, E. S. (2014). Highly accurate recognition of human postures and activities through classification with rejection. *IEEE Journal of Biomedical and Health Informatics*, *18*(1), 309-315.
- Tong, T., Wolz, R., Gao, Q., Guerrero, R., Hajnal, J. V., Rueckert, D., & Alzheimer's Disease Neuroimaging Initiative. (2014). Multiple instance learning for classification of dementia in brain MRI. *Medical Image Analysis*, *18*(5), 808-818.
- Wang, S., Wang, J., & Chung, F. L. (2014). Kernel density estimation, kernel methods, and fast learning in large data sets. *IEEE Transactions on Cybernetics*, *44*(1), 1-20.
- Zhang, C. (2015). Applying data fusion techniques for benthic habitat mapping and monitoring in a coral reef ecosystem. *ISPRS Journal of Photogrammetry and Remote Sensing*, *104*, 213-223
- Zhu, W., Peng, Y., & Ji, B. (2009, December). An automatic dead chicken detection algorithm based on SVM in modern chicken farm. In *2009 Second International Symposium on Information Science and Engineering* (pp. 323-326). IEEE.



## A Single DC Source 41-level 115V, 400Hz Cascaded Multilevel Inverter

Ahmad, Syukri Mohamad<sup>1\*</sup> and Norman, Mariun<sup>2</sup>

<sup>1</sup>Department of Avionics, Malaysian Institute of Aviation Technology, Universiti Kuala Lumpur, Malaysia

<sup>2</sup>Center for Advance Power and Energy Research, Department of Electric and Electronic Engineering, Faculty of Engineering, Universiti Putra Malaysia, Malaysia

### ABSTRACT

Cascaded multilevel inverters are popular in fields such as oil and gas, power supply installations, and power quality devices. While there are many advantages of the cascaded multilevel inverter, its main disadvantage is the need for large numbers of multiple dc sources. In order to reduce total harmonics distortion (THD) of the output voltage waveform, the amount of output voltage level must be increased, hence the higher number of dc sources. This essentially complicated the inverter design, as most converter transform only one voltage source to another. In this paper a cascaded multilevel inverter topology with a single dc source is discussed. The topology is based on capacitors instead of cells as the multiple voltage sources. The cascaded multilevel inverter topology validity and functionality is verified by the Matlab Simulink simulation of a 100W and 1kW aircraft single phase 41-level inverter.

*Keywords:* Aircraft inverter, multilevel inverter, total harmonics distortion

### INTRODUCTION

Inverters as a power conversion device can be found in three main categories of application; power supply, motor drives and active filters (Tehrani et al., 2011). The multilevel inverter

is fast emerging as a popular choice of power inverter in many industries. Compared to two-level systems, multilevel inverter has a better power quality output and low total harmonics distortion (THD) thus providing better power efficiency (Al-Emadi et al., 2016).

Even though the cascaded multilevel inverter has many advantages, the need for multiple dc sources is its setback. In order to reduce the output THD level, the number of output levels need to be increased, and so too the number of dc sources. Apart from this the high number of power switches and related controlling devices makes this model

#### ARTICLE INFO

##### Article history:

Received: 24 August 2016

Accepted: 02 December 2016

##### E-mail addresses:

ahmadsyukri@unikl.edu.my (Ahmad, Syukri Mohamad),

norman@upk.edu.my (Norman, Mariun)

\*Corresponding Author

unattractive. As the number of output voltage levels are increased, the amount of switching devices are also increased greatly, making the inverter becoming more complex and expensive (Mailah et al, 2009). Although this issue is also important, this paper will only limit the scope of the discussion to only on the issue of multiple dc sources requirement.

## **AIRCRAFT INVERTER**

Onboard inverter became an important part of aircrafts when as aircraft systems became larger and more complex. This is because all these instruments use ac current while the main aircraft power supply at that time comes from 28V dc generator (Hayes & Ray, 1945).

As power electronics device availability increased static inverters became to be the preferred inverter choice for aircraft. The static inverter has no moving parts, the inverter is h more efficient and also smaller and lighter. The common technology is where a 400Hz oscillator is connected to the dc busbar and producing low voltage ac current. The low voltage output then stepped-up using a power transformer to the rated aircraft ac system voltage (Tooley & Wyatt, 2009).

The standard aircraft inverter input and output characteristics are as follows (EASA, 2003):

Input voltage:	28Vdc; tolerance + 2Vdc
Output voltage:	115V ac rms; tolerance +5%, -7%
Frequency:	400Hz; tolerance +1%
Output waveform:	sinusoidal
THD:	less than 7% under all load conditions

## **THE PROPOSED INVERTER**

The nature of a cascaded multilevel inverter operation is the dc sources are stacked on top of one another in series of successions. Care in switching time will create a stepped wave that is almost similar to a clean sinusoidal waveform. The stacked dc sources are connected in series, so the combined voltage output will be similar to a normal ac source.

At any time the inverter is operational dc sources are connected to the load or output terminals, while others may not be used. If the dc sources are replaced with capacitors, when they are not connected to the load, the capacitors can be charged in order to maintain the voltage level of the capacitors.

SDCS 41-level Cascaded Multilevel Inverter

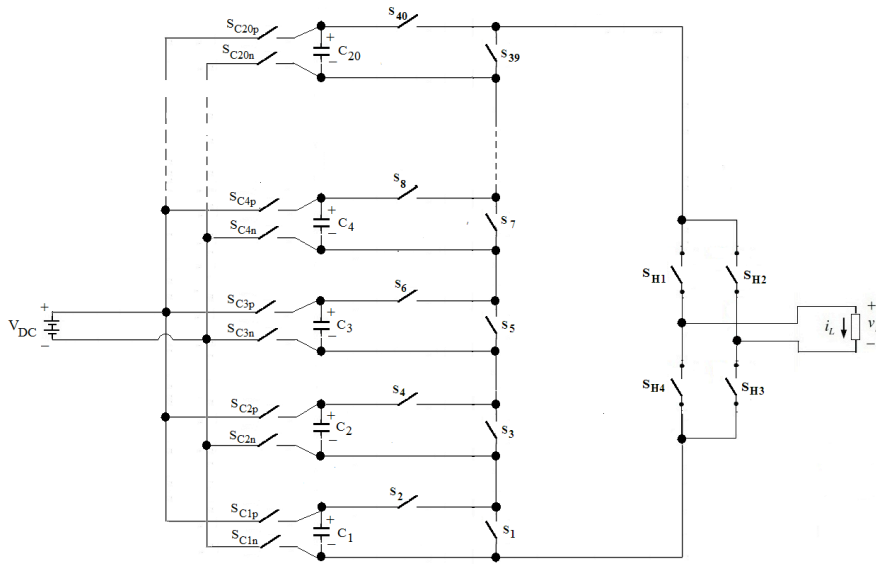


Figure 1. The proposed single dc source cascaded multilevel inverter topology

The proposed single dc source cascaded multilevel inverter topology is shown in Figure 1. The topology is based on the topology proposed by Babei and Hosseini (2009). This topology was chosen because it offers good switches reduction compared to the cascaded H-bridge topology. The topology is then modified by replacing the multiple dc sources with capacitors. The switches arrangement also modified to provide the means to charge the capacitors using a single dc source. The switching states of the switches is shown in Table 1.

Table 1  
The switching states of the switches and the resultant output voltage

Charged capacitors	Discharged capacitors	ON switches	OFF switches	Load voltage, VL
$C_1, C_2, \dots, C_{19}, C_{20}$	-	$S_{C1}, S_{C2}, \dots, S_{C19}, S_{C20}$ $S_1, S_3, \dots, S_{37}, S_{39}$ $S_{H1}, S_{H3}$	$S_2, S_4, \dots, S_{38}, S_{40}$ $S_{H2}, S_{H4}$	0V
$C_2, C_3, \dots, C_{19}, C_{20}$	$C_1$	$S_{C2}, S_{C3}, \dots, S_{C19}, S_{C20}$ $S_2, S_3, \dots, S_{37}, S_{39}$ $S_{H1}, S_{H3}$	$S_{C1}$ $S_1, S_4, \dots, S_{38}, S_{40}$ $S_{H2}, S_{H4}$	$V_{C1}$
$C_3, C_4, \dots, C_{19}, C_{20}$	$C_1, C_2$	$S_{C3}, S_{C4}, \dots, S_{C19}, S_{C20}$ $S_2, S_4, \dots, S_{37}, S_{39}$ $S_{H1}, S_{H3}$	$S_{C1}, S_{C2}$ $S_1, S_3, \dots, S_{38}, S_{40}$ $S_{H2}, S_{H4}$	$V_{C1} + V_{C2}$
•	•	•	•	•
•	•	•	•	•
•	•	•	•	•
•	•	•	•	•
•	•	•	•	•

Table 1  
The switching states of the switches and the resultant output voltage (continue)

Charged capacitors	Discharged capacitors	ON switches	OFF switches	Load voltage, VL
$C_{19}, C_{20}$	$C_1, C_2, \dots, C_{17}, C_{18}$	$S_{C19}, S_{C20}$ $S_2, S_4, \dots, S_{37}, S_{39}$ $S_{H1}, S_{H3}$	$S_{C1}, S_{C2}, \dots, S_{C17}, S_{C18}$ $S_1, S_3, \dots, S_{38}, S_{40}$ $S_{H2}, S_{H4}$	$V_{C1} + V_{C2} + \dots + V_{C17} + V_{C18}$
$C_{20}$	$C_1, C_2, \dots, C_{18}, C_{19}$	$S_{C20}$ $S_2, S_4, \dots, S_{38}, S_{39}$ $S_{H1}, S_{H3}$	$S_{C1}, S_{C2}, \dots, S_{C18}, S_{C19}$ $S_1, S_3, \dots, S_{37}, S_{40}$ $S_{H2}, S_{H4}$	$V_{C1} + V_{C2} + \dots + V_{C19}$
-	$C_1, C_2, \dots, C_{19}, C_{20}$	- $S_2, S_4, \dots, S_{38}, S_{40}$ $S_{H1}, S_{H3}$	$S_{C1}, S_{C2}, \dots, S_{C19}, S_{C20}$ $S_1, S_3, \dots, S_{37}, S_{39}$ $S_{H2}, S_{H4}$	$V_{C1} + V_{C2} + \dots + V_{C19} + V_{C20}$
$C_1, C_2, \dots, C_{19}, C_{20}$	-	$S_{C1}, S_{C2}, \dots, S_{C19}, S_{C20}$ $S_1, S_3, \dots, S_{37}, S_{39}$ $S_{H2}, S_{H4}$	- $S_2, S_4, \dots, S_{38}, S_{40}$ $S_{H1}, S_{H3}$	- 0V
$C_2, C_3, \dots, C_{19}, C_{20}$	$C_1$	$S_{C2}, S_{C3}, \dots, S_{C19}, S_{C20}$ $S_2, S_3, \dots, S_{37}, S_{39}$ $S_{H2}, S_{H4}$	$S_{C1}$ $S_1, S_4, \dots, S_{38}, S_{40}$ $S_{H1}, S_{H3}$	$-V_{C1}$
$C_3, C_4, \dots, C_{19}, C_{20}$	$C_1, C_2$	$S_{C3}, S_{C4}, \dots, S_{C19}, S_{C20}$ $S_2, S_4, \dots, S_{37}, S_{39}$ $S_{H2}, S_{H4}$	$S_{C1}, S_{C2}$ $S_1, S_3, \dots, S_{38}, S_{40}$ $S_{H1}, S_{H3}$	$-(V_{C1} + V_{C2})$
• • • • •	• • • • •	• • • • •	• • • • •	• • • • •
$C_{19}, C_{20}$	$C_1, C_2, \dots, C_{17}, C_{18}$	$S_{C19}, S_{C20}$ $S_2, S_4, \dots, S_{37}, S_{39}$ $S_{H2}, S_{H4}$	$S_{C1}, S_{C2}, \dots, S_{C17}, S_{C18}$ $S_1, S_3, \dots, S_{38}, S_{40}$ $S_{H1}, S_{H3}$	$-(V_{C1} + V_{C2} + \dots + V_{C17} + V_{C18})$
$C_{20}$	$C_1, C_2, \dots, C_{18}, C_{19}$	$S_{C20}$ $S_2, S_4, \dots, S_{38}, S_{39}$ $S_{H2}, S_{H4}$	$S_{C1}, S_{C2}, \dots, S_{C18}, S_{C19}$ $S_1, S_3, \dots, S_{37}, S_{40}$ $S_{H1}, S_{H3}$	$-(V_{C1} + V_{C2} + \dots + V_{C18} + V_{C19})$
-	$C_1, C_2, \dots, C_{19}, C_{20}$	$S_2, S_4, \dots, S_{38}, S_{40}$ $S_{H2}, S_{H4}$	$S_{C1}, S_{C2}, \dots, S_{C19}, S_{C20}$ $S_1, S_3, \dots, S_{37}, S_{39}$ $S_{H1}, S_{H3}$	$-(V_{C1} + V_{C2} + \dots + V_{C19} + V_{C20})$

**RESULTS AND DISCUSSION**

The performance of the inverter and the validity of the topology are tested using Matlab Simulink simulation. The switching timing are based on the algorithm discussed by Syukri Mohamad and Mariun (2012). Two load conditions are being tested – 100W and 1kW. This is because most of the large commercial aircrafts are equipped with a 1kW rated onboard inverter to provide the emergency power to the essential equipment in the event of emergency and normal power loss.

A 41-level inverter realization based on the proposed cascaded multilevel inverter topology is constructed based on the circuit shown in Figure 1 using Matlab Simulink modelling platform. The choice of power switches is Mosfet because as it has very fast switching time, simple gate circuit, virtually no gate current and negligible gate circuit loss (Rajashekara, 2002).

The inverter is supplied with a controlled single dc source, and the rated output voltage is 115Vrms, 400Hz. Peak voltage is about 163V. The measured parameters are shown in Figure 2 for 100W load condition and Figure 3 for 1kW load condition. Both loads are pure resistive loads.

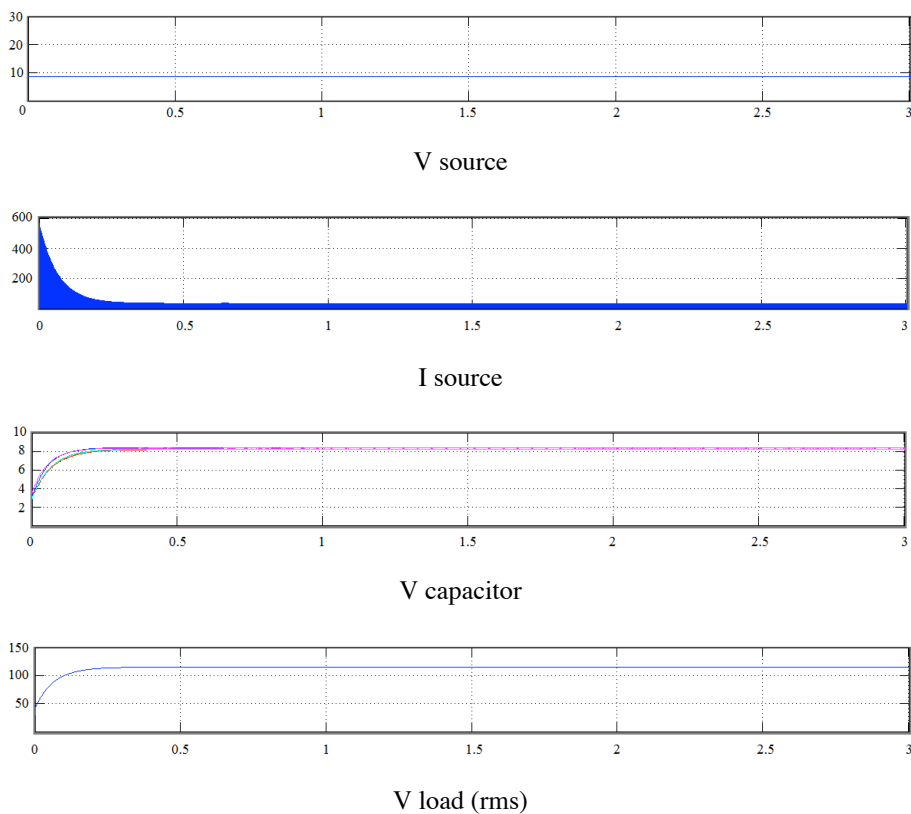


Figure 2. Measured parameters of the inverter when operating with 100W load

For the 100W load condition, the inverter input voltage is around 8.6V and the capacitors used are 12V, 0.12F capacitors. The initial current is very high, as can be expected of the charging process of the uncharged 20 capacitors.

As the capacitors built up the voltages, its current was also reduced to a constant level, with maximum value of 35A and rms value of 16.81A. The rms output voltage is 115V and the output voltage with the input current stabilizes after only about 0.3s.

The output power is measured at 99.95W while the input power is 144.566W, giving the efficiency of the inverter at 69.14%

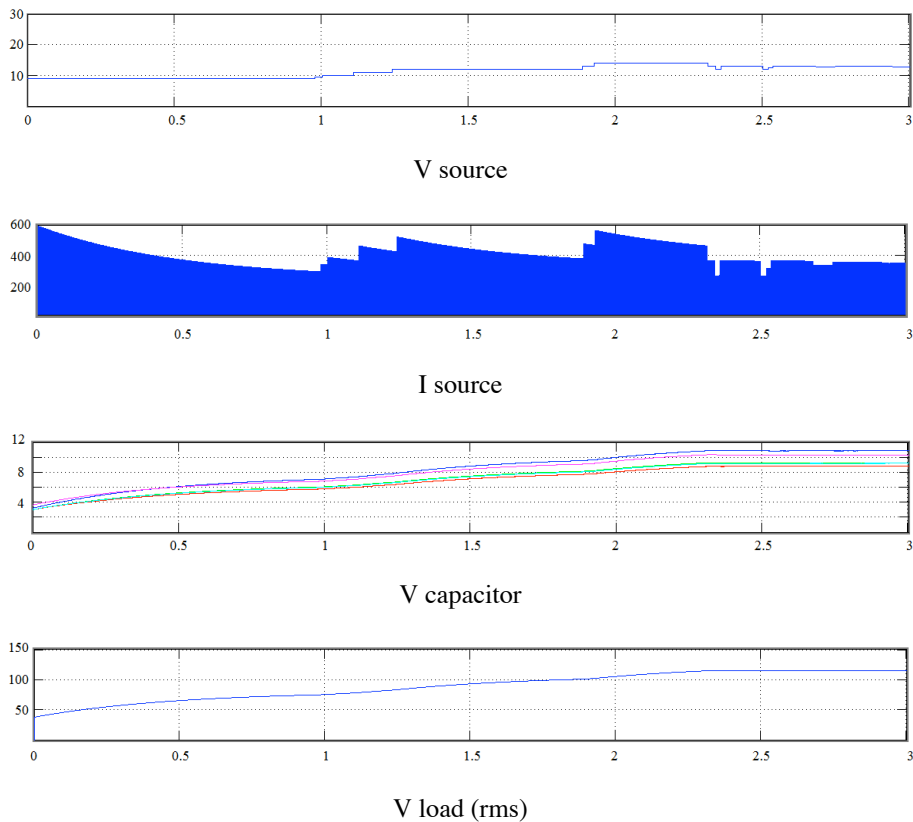


Figure 3. Measured parameters of the inverter when operating with 1kW load

For the 1kW load condition, the inverter input voltage changes around 9V to 14V during initial starting with the input voltage stabilized at 12.85V. The capacitors used are 16V, 1.2F capacitors. The source current fluctuates with the changing input voltage as the capacitors are very sensitive to any sudden voltage changes. The input current stabilizes at around 343A to 344A peak value, with the rms value settles at 165.5A.

As the capacitors built up the voltages, the capacitors voltage settles at a constant level, with values between 8.81V to 10.86V. The rms output voltage is 115V and the output voltage stabilizes after only about 2.3s. The output power is measured at 999.6W while the input power is 2126.675W, giving the efficiency of the inverter at 47.00%. The output waveform of the inverter is almost identical to a clean sinusoidal waveform (see Figure 4). The output THD reading at 100W load is 1.999% while at 1kW load is 3.307%.

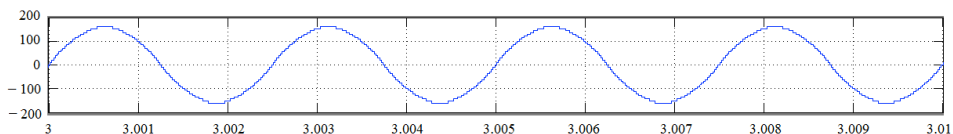


Figure 4. The inverter output voltage waveform



## CONCLUSION

A single dc source 41-level aircraft inverter has been successfully developed and constructed using Matlab Simulink modelling platform. The inverter is then simulated with the actual load rating, similar to the load condition of a large commercial aircraft inverter. The parameters are measured and compared to the standard set by aviation authority. The inverter output voltage is 115V rms, 400Hz, conforming with the conditions set out in the aviation standard. The output THD is also well below the 7% limit given in the standard. However, the efficiency of the inverter is relatively poor, with its high input current, which may be rectified using a dedicated current control method.

## REFERENCES

- Al-Emadi, N. A., Buccella, C., Cecati, C., & Khalid, H. A. (2016). A novel DSTATCOM with 5-level CHB architecture and selective harmonic mitigation algorithm. *Electric Power Systems Research*, 130, 251-258.
- Babaei, E., & Hosseini, S. H. (2009). New cascaded multilevel inverter topology with minimum number of switches. *Energy Conversion and Management*, 50(11), 2761-2767.
- Button, C. T. (1943). Aircraft Inverter Construction. *Transactions of the American Institute of Electrical Engineers*, 62(9), 598-602.
- European Aviation Safety Agency (2003). *European Technical Standard Order - Static Electrical Power Inverter*, ETSO-C73 pp. 4-5
- Franquelo, L. G., Rodriguez, J., Leon, J. I., Kouro, S., Portillo, R., & Prats, M. A. M. (2008). The age of multilevel converters arrives. *IEEE Industrial Electronics Magazine*, 2(2), 28-39.
- Hayes, C. P., & Ray, L. L. (1945). 400-Cycle Inverters for Military Aircraft. *Transactions of the American Institute of Electrical Engineers*, 64(5), 233-237.
- Mailah, N. F., Bashi, S. M., Aris, I., & Mariun, N. (2009). Neutral-point-clamped multilevel inverter using space vector modulation. *European Journal of Scientific Research*, 28(1), 82-91.
- Mohamad, A. S., & Mariun, N. (2012). Simulation of a 115V, 400Hz Aircraft Inverter Based on Cascaded Multilevel Inverter Topology. *Modelling and Simulations*, 5(1), 164-170.
- Rajashekara, K. (2002). Chapter 1 Power Electronics – Overview. *The Power Electronics Handbook, Industrial Electronics Series* (pp. 3-10). Florida, USA: CRC Press.
- Tehrani, K. A., Rasoanarivo, I., & Sargos, F. (2011). Power loss calculation in two different multilevel inverter models (2DM2). *Electric Power Systems Research*, 81(2), 297-307.
- Tooley, M. H., & Wyatt, D. (2009). *Aircraft electrical and electronic systems: principles, operation and maintenance* (pp. 131-132). Routledge.



## Dielectrophoresis and AC Electroosmosis Force on Fluid Motion in Microfluidic using Latex Particles

Nurul Amziah Md Yunus\*, Mohd Nazim Mohtar, Khaldon Mohammed Almadhagi and Izhal Abdul Halin

*Micro and Nano Electronic Systems Unit (MiNES), Department of Electrical and Electronic Engineering, Faculty of Engineering, Universiti Putra Malaysia, 43400 UPM, Serdang, Selangor, Malaysia*

### ABSTRACT

The use of electroosmotic is fast becoming a proven technique for manipulating particles in microfluidic systems. Several approaches were experimented to improve the force and thus the moving particles in the fluid. This paper will study the effect of microelectrode on the moving particles in latex using a particle image velocimetry and to test the velocity of particles movement at various frequencies from 10kHz to 500kHz. The result shows the behaviour of latex particles at different frequencies varying from low frequencies up to high frequencies under AC electrokinetic forces such as dielectrophoresis (DEP) and AC electroosmosis (ACEO).

*Keywords:* Electrical field, microfluidic, dielectrophoresis, electroosmotic flow, particle image velocimetry, charge density, Clausius-Mossotti factor

### INTRODUCTION

The considerable progress and development in the technology gave birth and growth to the miniaturisation, which is, integrated to all types of systems the thermal, chemical, and

electronic. This leads to a new field called MEMS (Micro-Electro-Mechanical Systems), which allows the fabrication of the systems. MEMS creates other applications and lead to other fields to improve and develop. One of the fields that had attracted attention was the fluid motion under the unexplored and unusual conditions which later known as the *Microfluidic* (Tabeling, 2005). Microfluidic is defined as the study of flows that are simple or complex, mono- or multiphase, which are circulating in synthetic microsystems, i.e. systems that are fabricated using new technologies (Tabeling, 2005; Pohl, 1978).

### ARTICLE INFO

#### *Article history:*

Received: 24 August 2016

Accepted: 02 December 2016

#### *E-mail addresses:*

amziah@upm.edu.my (Nurul Amziah Md Yunus),

nazim@upm.edu.my (Mohd Nazim Mohtar),

kma2013@gmail.com (Khaldon Mohammed Almadhagi),

izhal@upm.edu.my (Izhal Abdul Halin)

\*Corresponding Author

Generally, the electrical field causes the particles in the fluid to move depend on the voltage applied. A non-uniform electrical field induces a net force on a polarizable particle (Pohl, 1978). The field applied is either produced by direct current DC or alternative current AC. This will cause an electrokinetic phenomena. An AC electrokinetic phenomena uses electric fields to generate forces that act on fluids or suspended particles (Jones, 1995).

The dielectrophoretic (DEP) force is one of AC electrokinetic forces. It depends on the particle radius, complex permittivity and the Clausius-Mossotti factor (Jones, 1995; Tabeling, 2005; Cheri et al., 2014). The other main AC electrokinetic influence is the electroosmosis flow (EOF) under AC electroosmosis force (ACEO), which is the projecting mechanism for controlling fluid flow in micro and nano channels with embedded microelectrode in it that requiring surface charges. The surface charge on the microelectrode surface causes a diffuse layer of counter ions to form. When an electric field is induced, the outer layer of ions is attracted toward the oppositely charged electrode dragging with it the majority solution and making a net flow referred to as electroosmotic flow (EOF) (Feshbach, 1953). This mechanism of fluid motion causes a uniform velocity spreading across the microchannel, which is often advantageous. The electroosmotic velocity is

$$v_{eof} = \frac{\epsilon\zeta E}{4\pi\eta} \tag{1}$$

where  $\epsilon$  is the dielectric constant of the fluid,  $\eta$  is the fluid viscosity,  $E$  is the applied electric field strength, and  $\zeta$  is the zeta potential of the surface (A. Kitahara, 1984). The electroosmotic velocity is proportional to the applied electric field strength. The mobility ( $\mu_{eof}$ ) is the electroosmotic velocity normalised by the applied field:

$$(\mu_{eof}) = v_{eof} / E \tag{2}$$

Thus, altering the applied field, the properties of the solution, or altering the surface charge can affect  $v_{eof}$ .

In this study, latex beads will be tested and compared with different frequencies to check the characteristic of electroosmotic flow. Latex was chosen due to its density, which has slightly greater than water ( $1050 \text{ kg m}^{-3}$  compared to  $1000 \text{ kg.m}^{-3}$ ) (Arnold, 1987). Its dielectrophoretic properties, which show polarization of particles is dominated by the surface conductance (Baker, 1995; M.P. Hughes, 1999; N.G. Green, 1999). Dielectrophoresis and AC electroosmosis are the alternating fields, which used to manipulate particles. Dielectrophoresis arises via contact of the induced dipoles with non-uniform field. The output force is reliant on the gradient of the field squared  $\Delta E^2$  and the particle volume  $r^3$ , frequency and applied voltage (M.P. Hughes, 1999; Morgan, 2003). The dielectrophoresis force for spherical particle is written as

$$F_{DEP} = 2\pi\epsilon_m r^3 \text{Re}[f_{CM}(w)]\nabla E^2 \tag{3}$$

where  $r$  is the radius of the particle and  $\varepsilon_m$  is the dielectric constant in the medium,  $f_{CM}$  is the Clausius-Mossotti factor the effective polarizability of the particle.  $f_{CM}$  depends on the applied frequency  $\omega$ . The term  $Re[f_{CM}(\omega)]$  is bounded by -0.5 and 1. The sign of  $Re[f_{CM}(\omega)]$  depends on the applied frequency. Dielectrophoresis is a local effect and the DEP force decreases rapidly away from the electrode (Yunus, 2010). Another long-range electric force called electroosmosis is effective in manipulating biosamples (Pohl, 1978). As the particles moves under the influence of DEP, it can be assumed that the instantaneous velocity is proportional to the instantaneous DEP force so that for spherical particles such as latex

$$V_{DEP} = \frac{\pi a^3 \varepsilon_m Re[f_{CM}] \nabla |E|^2}{6\pi\eta a} \quad (4)$$

where  $V_{DEP}$  is dielectrophoretic velocity,  $a$  particle radius,  $f_{CM}$  Clausius-Mossotti factor,  $\varepsilon_m$  medium permittivity. It can be seen that for a spherical particle the dielectrophoretic mobility depends on the radius of the particle squared and the real part of the Clausius-Mossotti factor, together with the permittivity and viscosity of the fluid (Morgan, 2003).

In methodology section, shows the experimental setup, which includes the chemical solution, channels, and measurement of the velocity of the particles. In results and discussion, the particles velocity with the effect of different frequencies and at different distance are presented and compared. Finally, the important of the paper is concluded.

## METHODOLOGY

The paper presents a comprehensive study of electroosmotic properties of latex particles (test particle) as a function of fixed particle size, which is 2  $\mu\text{m}$  and Potassium Chloride, KCl electrolyte, with conductivity of 14.5  $\mu\text{S/m}$  acted as the medium (usually used in biology for normal cell respiration) and present viscosity (Pohl, 1978). The microfluidic chip was fabricated on glass substrate using direct-write electron beam lithography with Ti/Pt layer (10/200 nm thick) patterned and designed with a microchannel width of 500  $\mu\text{m}$  and 40  $\mu\text{m}$  height with array of interdigitated microelectrode of 20  $\mu\text{m}$  in width size and the gap between the electrodes is 20  $\mu\text{m}$ .

The electroosmotic flow (EOF) measured was based on placing the microchip under microscope with objective of 20x magnification until the particles are visible and easy to be captured. A series of video recording were accomplished under microscope and stored for later analysis as shown in Figure 1 below. Basically, the electrodes were supplied by an AC, 2Vpp power supply throughout the test, with varying the frequencies between 10kHz, 20kHz, 30kHz, 40kHz, 50kHz, 100kHz, 200kHz, 300kHz, 400kHz and 500kHz.

### *Particle Image Velocimetry Setup*

After acquiring the video, the video is analysed using MATLAB software, which converts the video into a series of images. This includes a series of image processing, region of interest (ROI), eliminate and mask the distortion and invert the background to smooth the image to maximize the result. After that, a moving window or interrogation area will be chosen to fit the particles size for the whole ROI. Furthermore, vector validation will take place whereby

it will select the most accumulated particles. Line graph will be drawn from the nearest point to electrode and to far point of the electrode, to study the velocity based on the movement of the particles (El-Gholabzouri, 2006). The velocity graph will be generated after calibrating the image to match the reality and this is done by selecting a reference point, which its length known prior to the study.

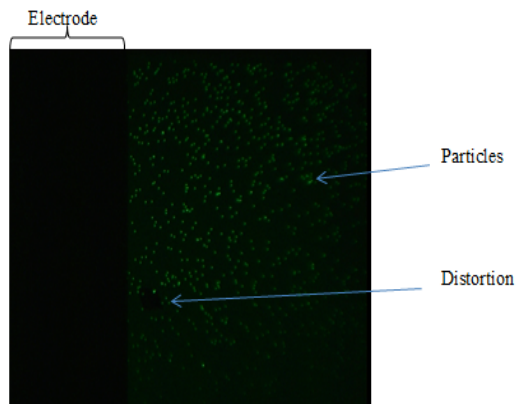


Figure 1. (a) Moving particles in KCl solution

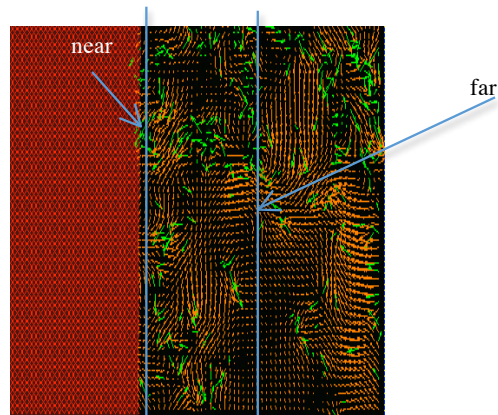


Figure 1. (b) Particles movement near mid and far from electrode

Figure 1a shows the basic layout of one frame. It was picked randomly from 350 frames. There are selected lines on Figure 1b to show the behaviour of particles near the electrode and far from the electrode. The movement (behaviour) of particles are represented by the arrows; as the bigger the arrow means the more electrical field its possessed and cause the particles to move further. The selected line near electrode was chosen to be  $5\ \mu\text{m}$  and the far selected line from electrode is chosen to be  $35\ \mu\text{m}$ . Identifying the line near and far from the electrode will provide consistency along the simulation. In the above experiment, the particles are the latex beads with all the same size of  $2\ \mu\text{m}$  in diameter. The electrode is located on the left hand side and the right hand side of the ROI. The particles are very active within electrode vicinity as compared to the particles in the middle region, which tend to approach zero. The middle region has less electrical field strength. Thus, the concentration of particles is observed lesser at the centre and increase when they get closer to the electrode as shown in Figure 2.

Figure 2 implies that, as the particles get closer to the electrode, they have been exposed to higher electrical field strength near the electrode hence obtain greater velocity. This behaviour is increasing in frequency as shown and discussed in the following section.

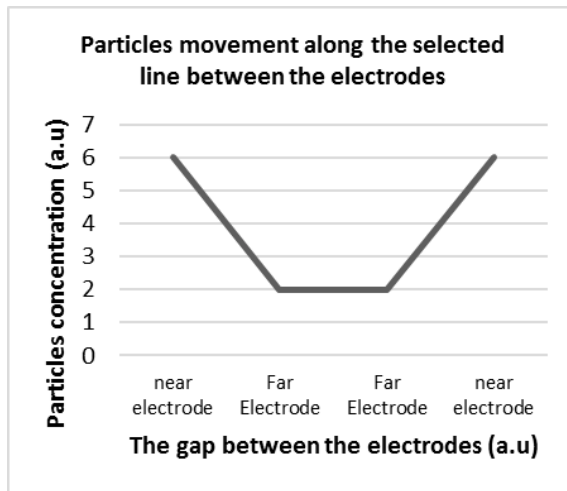


Figure 2. The behaviour of particles movement along the line

### RESULT AND DISCUSSION

The electric field strength generated by the parallel array of interdigitated microelectrodes produces sufficient dielectrophoretic forces to manipulate colloidal particles and macromolecules in microflows (Thielicke, 2014). As the electroosmotic velocity is proportional to the applied electric field strength and DEP force is proportional to the gradient in the electric field strength, it is instructive to look at the components of the electric field strength to gain a better intuition into the forces acting on target particles/species.

In this section, the observation was made on how the electroosmotic behaviour is reacting. It is based on different frequencies applied under voltage 2Vpp. Several results have been generated to serve the objective and this result was generated from the developed MATLAB

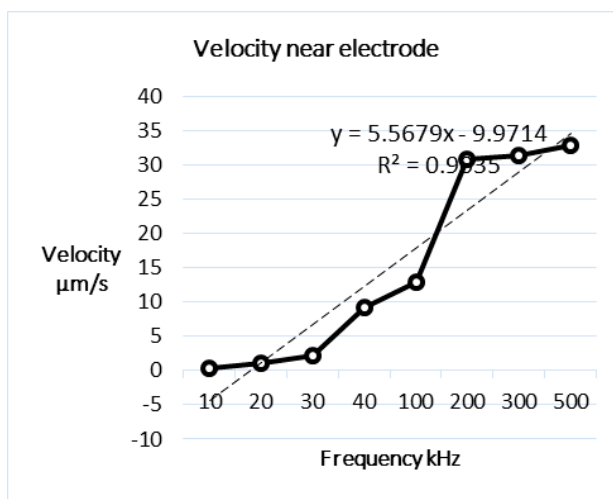


Figure 3. Velocity vs frequency near microelectrode

program. The data were collected for all videos with the same parameters as before. Figure 3 shows the velocity profile of particles taken vertically near the microelectrode. The dot lines represent the profile as the frequency increased.

Figure 3 shows that as the frequency increases, the velocity increases as well. The activity near the microelectrode is higher as compared with the one further away from the microelectrode. This is due to the fact that, as the particles are near the microelectrode, the electrical field is higher and the DEP force is present. It causes the particles move under certain velocity where ACEO is also present. Near the electrode, the velocity of particles increase and become hyper active as compared to the particles far away from the electrode as shown in Figure 4.

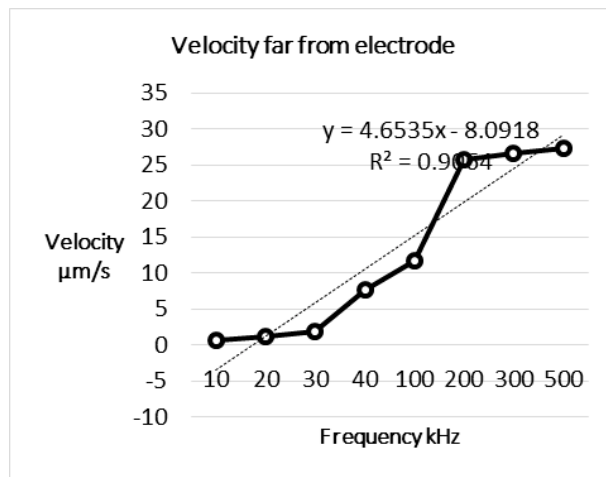


Figure 4. Velocity vs frequency far from microelectrode

Figure 4 shows the velocity of particles under the effect of DEP and ACEO far from microelectrode is lower as compared to their velocity shown in Figure 3. The result shows that as the DEP and ACEO present with the frequency increases, the particles will move under clear velocity. Whenever the particles travel away from the electrode, although the frequency is increased, the particles velocity will still decrease respectively due to weak DEP and ACEO further away from the electrode and this is proven by Clausius-Mossotti factor (Jones, 1995; Tabeling, 2005; Thomas B. J., 1995). Besides that, to further study the electroosmotic of latex particle, another analysis was carried out to fulfil the finding and the following graphs was generated. The graph in Figure 5a shows the velocity of latex particles at 40kHz. The velocity has been observed and measured along the selected line shown in Figure 5b.

Figure 5(a) indicates that the velocity of latex particles was high near the microelectrode and kept decreases until it reaches a very small value approximately 8 µm/s, where there is minimal electrical field presented. It starts to increase again up to 70 µm/s as it approaches the other microelectrode. The analysis was taken for frequencies varying from 10kHz up to 500kHz. It is noticed that, as the frequency is low, the particles behave unstably and in almost in circular motion e.g. moving forward and backward (oscillation) as the sufficient electrical field did not reach to start the electroosmotic of the latex particle.



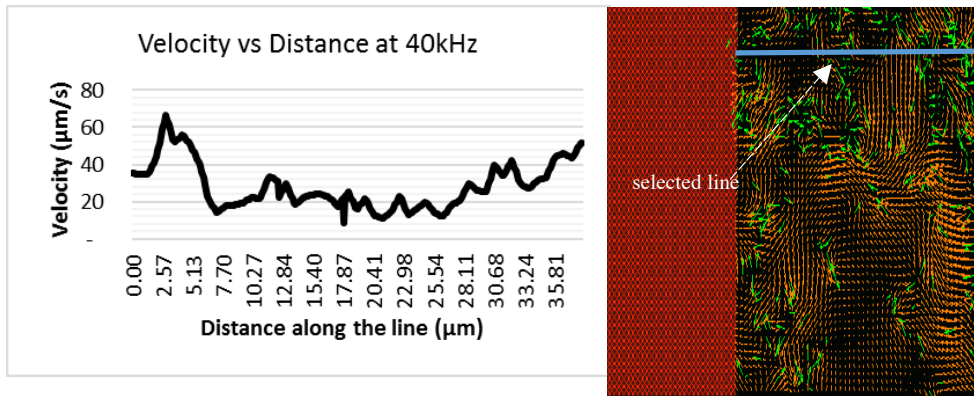


Figure 5. (a) Velocity vs distance at 40kHz

Figure 5. (b) Selected line used in Figure 5a & Figure 6

However, the starting frequency whereby the latex started to stop oscillating and generated proper velocity (of ACEO) was at 40kHz. The 40kHz was chosen after trying lower frequencies such as 10, 20, 30, and 40kHz. The 40kHz seems to give a better steady state and less circular motion and as the frequencies increased further the particles tend to respond better until it reach steady state movement. Once the steady motion is reached, the particles motion is observed at even higher frequency i.e. 500kHz. The graph on Figure 6 shows the electroosmotic flow velocity of latex particle at 500kHz.

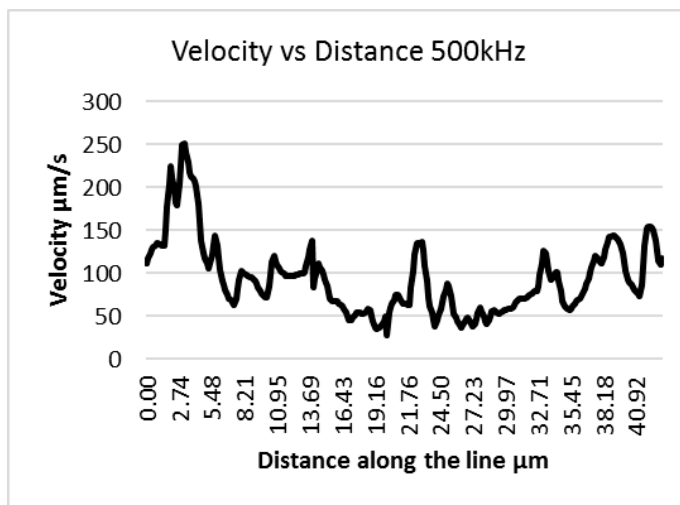


Figure 6. Velocity vs distance at 500kHz

The graph of Figure 6 shows the average particles electroosmotic velocity is increased up to 250 µm/s at 500kHz as compared to 70 µm/s at 40kHz. This is due to higher frequency and higher electrical field under DEP and ACEO effects (Chen et al., 2014; Feshbach, 1953). The comparison is made between Figure 5 and Figure 6. It is shown that, after increasing the

frequency, the particles tend to gain more velocity under the effect of DEP and ACEO. The parameters such as the latex particles size, electrolyte, PIV software environment, the location of the velocity measured are not changed at all processing frequencies.

## CONCLUSION

The study of AC electrokinetic forces, dielectrophoresis (DEP) and AC electroosmotic (ACEO), becoming the proven techniques for manipulating particles in microfluidic systems. The effect of electrical field on the moving particles of latex is studied using PIV, to test the velocity of particles movement at varying frequencies from 10k to 500kHz. The work has shown that, at lower frequency, latex particles are unstable and generating circular motion (oscillation). As the frequency increase, the particles start to stabilize and get higher velocity (higher electric field strength and force applied). This study could benefit the researchers for useful particles and fluid manipulation in term of particles behaviour at certain electrical properties environment. Further studies can be done by expanding the range of potential systems such as varying the voltage supplied and electric fields strength. Those parameters can be used to manipulate further the particle behaviour near and far from the microelectrodes in the microfluidic system. Besides that, by varying the electrolyte to Sodium hydroxide, NaOH (e.g. used for microfluidic mixer) and Potassium hydroxide, KOH (e.g. used for fungal cultures in microfluidic) (Persar, 2009; Saini, 2016) can also be promising study in the future.

## ACKNOWLEDGEMENT

This work was examined by researchers under research group, Micro and Nano Electronics System Engineering (MiNES) which, involved two laboratories, Advanced Material Synthesis and Fabrication Laboratory (AMSF) and Microelectronic and Nanoelectronic Laboratory (MNL), Department of Electrical and Electronic Engineering, UPM.

## REFERENCES

- Persat, A., Suss, M. E., & Santiago, J. G. (2009). Basic principles of electrolyte chemistry for microfluidic electrokinetics. Part II: Coupling between ion mobility, electrolysis, and acid–base equilibria. *Lab on a Chip*, 9(17), 2454-2469.
- Kitahara, A. W. (1984). *Electrical Phenomena at Interfaces*. New York: Marcel Dekker.
- Baker, D. R. (1995). *Capillary Electrophoresis*. New York: Wiley.
- Clague, D. S., & Wheeler, E. K. (2001). Dielectrophoretic manipulation of macromolecules: The electric field. *Physical Review E*, 64(2), 026605.
- El-Gholabzouri, O., Cabrerizo-Vilchez, M. Á., & Hidalgo-Álvarez, R. (2006). Zeta-potential of polystyrene latex determined using different electrokinetic techniques in binary liquid mixtures. *Colloids and Surfaces A: Physicochemical and Engineering Aspects*, 291(1), 30-37.
- Morse, P. M., & Feshbach, H. (1953). *Methods of theoretical physics* (Vol. 1, No. 2). New York: McGraw-Hill.
- Jones, T. B. (1995). *Electromechanics of Particles*. New York Cambridge University Press.

- M.P. Hughes, H. M., M.F. Flynn. (1999). *J. Colloid Interface Sci.*, 454–457
- Morgan, H., & Green, N. G. (2003). *AC Electrokinetics: Colloids and Nanoparticles: Research Studies Press.*
- N.G. Green, H. M. (1999). *J. Phys. Chem.*, 103.
- Pohl, H. A. (1978). *Dielectrophoresis*. Cambridge: Cambridge University Press.
- Ramos, A., Morgan, H., Green, N. G., & Castellanos, A. (1998). Ac electrokinetics: a review of forces in microelectrode structures. *Journal of Physics D: Applied Physics*, 31(18), 2338.
- Rouabah, H. A., Park, B. Y., Zaouk, R. B., Morgan, H., Madou, M. J., & Green, N. G. (2011). Design and fabrication of an ac-electro-osmosis micropump with 3D high-aspect-ratio electrodes using only SU-8. *Journal of Micromechanics and Microengineering*, 21(3), 035018.
- Saini, S., Bukosky, S. C., & Ristenpart, W. D. (2016). Influence of Electrolyte Concentration on the Aggregation of Colloidal Particles near Electrodes in Oscillatory Fields. *Langmuir*, 32(17), 4210-4216.
- Thielicke, W., & Stamhuis, E. (2014). PIVlab—towards user-friendly, affordable and accurate digital particle image velocimetry in MATLAB. *Journal of Open Research Software*, 2(1).
- Thomas, B, J. (1995). *Electromechanics of Particles*. New York: Cambridge University Press.
- Upadhyay, R. K., Soin, N., & Roy, S. S. (2014). Role of graphene/metal oxide composites as photocatalysts, adsorbents and disinfectants in water treatment: a review. *RSC Advances*, 4(8), 3823-3851. doi:10.1039/C3RA45013A
- W.M. Arnold, H. P. S., U. Zimmermann. (1987). *J. Phys. Chem.* (91), 509.
- Wang, H., Liu, Z., Kim, S., Koo, C., Cho, Y., Jang, D. Y., ... & Han, A. (2014). Microfluidic acoustophoretic force based low-concentration oil separation and detection from the environment. *Lab on a Chip*, 14(5), 947-956.
- Wang, X. B., Huang, Y., Burt, J. P., Markx, G. H., & Pethig, R. B. U. K. (1993). Selective dielectrophoretic confinement of bioparticles in potential energy wells. *Journal of Physics D: Applied Physics*, 26(8), 1278.
- Wang, X., Wang, X. B., Becker, F. F., & Gascoyne, P. R. (1996). A theoretical method of electrical field analysis for dielectrophoretic electrode arrays using Green's theorem. *Journal of Physics D: Applied Physics*, 29(6), 1649.
- Yunus, N. A. M., & Green, N. G. (2010). Fabrication of microfluidic device channel using a photopolymer for colloidal particle separation. *Microsystem Technologies*, 16(12), 2099-2107.
- Yunus, N. A. M., Jaafar, H., & Jasni, J. (2010). The Gradient of the Magnitude Electric Field Squared on Angled Microelectrode Array for Dielectrophoresis Applications. *Journal of the Japan Society of Applied Electromagnetics and Mechanics (JSAEM)*, 19.
- Yunus, N. A. M., Nili, H., & Green, N. G. (2013). Continuous separation of colloidal particles using dielectrophoresis. *Electrophoresis*, 34(7), 969-978



## Application of Sliding Mode Control with Extended High Gain Observer to Stabilize the Underactuated Quadrotor System

Elya M. N<sup>1\*</sup>, S. B. Mohd Noor<sup>1</sup>, Ribhan Zafira A. R.<sup>1</sup> and Syaril Azrad<sup>2</sup>

<sup>1</sup>Department of Electrical & Electronics Engineering, Universiti Putra Malaysia, 43400 UPM, Serdang, Selangor, Malaysia

<sup>2</sup>Department of Aerospace Engineering, Universiti Putra Malaysia

### ABSTRACT

This work proposes an output feedback controller for stabilization of the quadrotor underactuated system in the presence of time varying disturbances and model uncertainties. The proposed control is an improvement to the sliding mode control (SMC). An extended high-gain observer (EHGO) when combined with sliding mode control (SMC) able to give feasible performance beyond the performance of the standard sliding mode. It is able to bring the state trajectories of the closed-loop system close to the target system with a smaller ultimate bound of error and smaller control magnitude. The proposed method is illustrated by simulation.

*Keywords:* Extended high-gain observer, sliding mode control, underactuated system, output feedback control

### INTRODUCTION

The vertical take-off and landing (VTOL) vehicle such as quadrotor is perceived to have good potential in various applications such as monitoring, surveillance, and search

and rescue (SAR) mission. The quadrotor hovering capability makes it the best choice for near monitoring applications within confined areas. The quadrotor unmanned aerial vehicle (UAV) is in the group of underactuated system because of its four-input actuator that allows to control six degree of freedom outputs. It is classified as a second order nonholonomic, thus the controller design and stability analysis are complicated. The control problem of quadrotors has been confronted using several different approaches from leading research teams worldwide. Earlier works focuses on stabilization of the vehicle using linear approach (Bouabdallah

#### ARTICLE INFO

##### Article history:

Received: 24 August 2016

Accepted: 02 December 2016

##### E-mail addresses:

elyamnor@gmail.com (Elya M. N),

samsul@upm.edu.my (S. B. Mohd Noor),

ribhan@upm.edu.my (Ribhan Zafira A. R.),

syaril@upm.edu.my (Syaril Azrad)

\*Corresponding Author

et al., 2004) and nonlinear approach (Hoffmann et al., 2007; Bouabdallah & Siegwart, 2007; Benallegue et al., 2006). However, the stability is not guaranteed when the vehicle is flying in the presence of model uncertainties and external disturbances.

The controller design that includes uncertainties and disturbances and capable of disturbance rejection generally focuses on two direction, either adaptive method such as the work by Chen et al. (2014) or disturbance-observer (DOB) method. DOB has advantage as opposed to the adaptive technique in terms of flexibility and design simplicity (Dong et al., 2014). In DOB-based controller, the nominal model is retained while an observer is designed and added into the control to estimate and cancel the disturbance.

The study on robust control for trajectory tracking in real time is still new. A robust sliding-mode or high-gain observer can be used as the DOB-based controller to perform this mission. The use of sliding-mode observer had been reported by several authors (Benallegue et al., 2008; Besnard et al., 2012). However, the use of high-gain observer as DOB-based for robust trajectory control of a quadrotor is still lacking so far. According to (Freidovich & Khalil, 2008) the high-gain observer is simpler compared to the sliding-mode approach.

The backstepping technique combined with DOB for robust trajectory tracking of the quadrotor proposed by (Dong et al., 2014) is promising. However, the backstepping method is not suitable for a complex system because the controlling algorithm is based on a recursive method involving complex mathematics. In complex mission, the backstepping controller will involve heavy mathematical coding and computation which is time consuming and error prone during start up.

Sliding mode control is one of the well-known approaches for handling nonlinear systems that are under presence of uncertainties and external disturbances (Mokhtari & Cherki, 2015). The advantage of sliding mode control lies in its robustness and simplicity of implementation. However, the drawback of the sliding mode control is the chattering effect arising from high frequency switching. The chattering effect is usually solved by replacing the discontinuous switching to continuous switching. However, the drawback of using continuous switching is the error convergence of the states is uniformly ultimately bounded, instead of converging to zero in finite time.

A controller based on sliding mode control proposed by Xu and Özgüner (2008) for stabilizing a class of underactuated systems has an attractive sliding surface. The sliding surface presented is able to globally stabilize all degrees of freedom including those which are indirectly actuated through the nonlinear coupling. However, the ultimate bound of the steady state error it produces is large. In this paper, we propose an improvement to the controller proposed by (Xu & Özgüner, 2008). We use an extended high-gain observer (EHGO) as estimator to estimate the unknown states and the uncertainties and disturbances. The estimated states will be used in the controller and at the same time the estimated uncertainties and disturbances are continuously cancelled in the control. In simulation, we are able to show that our proposed method able to improve the performance of the standard sliding mode controller. The proposed control able to give smaller ultimate bound of error at a smaller magnitude of control signal.

This paper begins with a presentation of the dynamic model of the quadrotor vehicle and the transformation of the model to a cascade form for control design. This is followed with a presentation of proposed controller in a state feedback form. We assume that all states,

uncertainties and disturbances are known and available for the controller. An analysis between the proposed controller and standard SMC approach is undertaken and the proposed design of EHGO and output feedback control is presented. The efficiency of the proposed controller is illustrated through simulation using Matlab and Simulink.

## PRELIMINARIES

### Dynamic Model and Transformation

A simplified nominal model of a quadrotor UAV as shown in Figure 1 can be represented as follows. More detail of its configuration can be found in (Bouabdallah, 2007; Altug, Ostrowski, & Mahony, 2002)

$$\left. \begin{aligned} \begin{bmatrix} \ddot{x} \\ \ddot{y} \\ \ddot{z} \end{bmatrix} &= U_1 \begin{bmatrix} \cos\theta \sin\theta \cos\phi + \sin\theta \sin\phi \\ \sin\theta \sin\theta \cos\phi - \cos\theta \sin\phi \\ \cos\theta \cos\phi \end{bmatrix} - \begin{bmatrix} \frac{K_1 \dot{x}}{m} \\ \frac{K_2 \dot{y}}{m} \\ \frac{K_3 \dot{z}}{m} \end{bmatrix} - \begin{bmatrix} 0 \\ 0 \\ 1 \end{bmatrix} g \\ \begin{bmatrix} \ddot{\theta} \\ \ddot{\phi} \\ \ddot{\psi} \end{bmatrix} &= \begin{bmatrix} U_2 \\ U_3 \\ U_4 \end{bmatrix} - \begin{bmatrix} lK_4 \dot{\theta}/I_1 \\ lK_5 \dot{\phi}/I_2 \\ K_6 \dot{\psi}/I_3 \end{bmatrix} \end{aligned} \right\} \quad (1)$$

where  $[x, y, z]^T$  are the position in the  $x$ -axis,  $y$ -axis and  $z$ -axis ; and  $[\theta, \phi, \psi]^T$  are the pitch, roll and yaw, respectively;  $g$  is the acceleration of gravity,  $l$  is the half length of the helicopter,  $m$  is the total mass of the helicopter;  $I_i, K^i, U_i, (i = 1, 2, 3)$  are the moment of inertia with respect

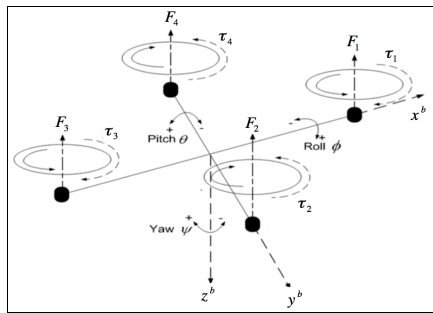


Figure 1. Quadrotor configuration

to the axes, the drag coefficients, and the control inputs, respectively.  $\psi$

The quadrotor system can be divided into two subsystems; a fully actuated and an underactuated. The quadrotor height ( $z$ ) and yaw motion are assumed to be fully actuated. Meanwhile, the positions in the longitudinal ( $x$ ) and lateral ( $y$ ) and the pitching and rolling angle are a multi-input multi-output (MIMO) underactuated subsystem represented as

$$\left. \begin{aligned} \begin{bmatrix} \ddot{x} \\ \ddot{y} \end{bmatrix} &= U_{1_1} \begin{bmatrix} \cos\theta & \sin\theta \\ \sin\theta & -\cos\theta \end{bmatrix} \begin{bmatrix} \sin\theta \cos\phi \\ \sin\phi \end{bmatrix} + \frac{1}{m} \begin{bmatrix} -K_1 \dot{x} \\ -K_2 \dot{y} \end{bmatrix} \\ \begin{bmatrix} \ddot{\theta} \\ \ddot{\phi} \end{bmatrix} &= \begin{bmatrix} U_2 \\ U_3 \end{bmatrix} + \begin{bmatrix} -lK_4 \dot{\theta}/I_1 \\ -lK_5 \dot{\phi}/I_2 \end{bmatrix} \end{aligned} \right\} \quad (2)$$

The controller design for the fully actuated subsystem is constructed using sliding mode and PID-based control following (Xu & Özgüner, 2008). In this paper, we will focus on the design of disturbance rejection mechanism to optimize the control performance for the underactuated subsystem Eq. (2) in the presence of time-varying disturbances and uncertainties. The control of underactuated system is important for stabilizing the vehicle in the longitudinal and lateral motion during trajectory.

We define new state variable as  $x_1 = \begin{bmatrix} x \\ y \end{bmatrix}$ ,  $x_2 = \begin{bmatrix} \dot{x} \\ \dot{y} \end{bmatrix}$ ,  $x_3 = \begin{bmatrix} \theta \\ \varphi \end{bmatrix}$ ,  $x_4 = \begin{bmatrix} \dot{\theta} \\ \dot{\varphi} \end{bmatrix}$  to obtain the transformation of system Eq. (2) into

$$\left. \begin{aligned} \dot{x}_1 &= x_2 + d_1 \\ \dot{x}_2 &= f_1(x_3) + d_2 \\ \dot{x}_3 &= x_4 \\ \dot{x}_4 &= U + d_3 \end{aligned} \right\} \tag{3}$$

where  $x_1$  and  $x_2$  are the position and angular position, respectively,  $x_2$  and  $x_4$  are the position and angular velocity, respectively,  $U \in R^2$ ,  $U = \begin{bmatrix} U_2 \\ U_3 \end{bmatrix}$ ,  $f_1 = \begin{bmatrix} \sin\theta\cos\varphi \\ \sin\varphi \end{bmatrix}$ ,  $d_1 \in R^2$ ,  $d_1 = \frac{\ddot{u}_1}{u_1} x_1$ ,

$d_2$  and  $d_3$  are a lumped of disturbances and uncertainties appearing in the translational link ( $x_1$  and  $x_2$ ) and rotational link ( $x_3$  and  $x_4$ ), respectively,  $d_2 = \begin{bmatrix} \frac{K_1 \ddot{x}}{m} + 0.03 \sin(0.5t) \\ \frac{K_2 \ddot{y}}{m} + 0.03 \sin(0.5t) \end{bmatrix}$ ,

$d_3 = \begin{bmatrix} \frac{IK_4 \ddot{\theta}}{I_1} + 0.003 \sin(0.5t) \\ \frac{IK_5 \ddot{\varphi}}{I_2} + 0.003 \sin(0.5t) \end{bmatrix}$ , and  $x_1$  and  $x_2$  are available for measurement. Assumptions are made as follows:

*Assumption 1:*  $d_1$ ,  $d_2$ , and  $d_3$  belongs to a compact set and are bounded.  $\ddot{d}_2$  and  $\ddot{d}_3$  are bounded.

*Assumption 2:*  $\frac{df_1}{dx_3}$  is invertible,  $\frac{df_1}{dx_3}$  and  $b(\bullet)$  are continuously differentiable with locally Lipschitz derivatives.

We define the error variable  $e_1 = x_1 - x_{1d}$ ,  $e_2 = x_2$ ,  $e_3 = f_1$ , and  $e_4 = \frac{df_1}{dx_3}$ , the switching surface

$$s = c_1 e_1 + c_2 e_2 + c_3 e_3 + e_4 \tag{4}$$

is defined. The dynamics of the switching surface

$$\dot{s} = f_k + f_d + gU \tag{5}$$

where  $f_k = c_1 x_2 + c_2 f_1 + c_3 \left[ \frac{df_1}{dx_3} \right] x_4 + \frac{d}{dt} \left[ \frac{df_1}{dx_3} \right] x_4$ ,  $f_d = c_1 d_1 + c_2 d_2 + d_3$  and  $g = \frac{df_1}{dx_3}$ . The control goal is to design the control  $U$  that is able to bring the sliding surface,  $s$  in Eq. (4) to zero in finite time under presence of  $d_2$  and  $d_3$ . This will result in improved performance of position trajectory specifically, smaller ultimate bound of position error,  $e_1$  with lesser magnitude of control signal.



## CONTROL DESIGN

### Standard Sliding Mode Control

We first present the standard sliding mode control algorithm for the underactuated system proposed by (Xu & Özgüner, 2008). The sliding mode control and the closed-loop control of the sliding surface are represented as Eqs. (6) and (7), respectively, as following.

$$U = g^{-1}(-f_k - M_1 \text{sat}\left(\frac{s}{\mu}\right) - \lambda s) \quad (6)$$

$$\dot{s} = -M_1 \text{sat}\left(\frac{s}{\mu}\right) - \lambda s + d \quad (7)$$

The closed-loop control of the sliding surface is obtained by combining Eq. (5) - (6).  $d$  represents the lumped of  $d_2$  and  $d_3$ , and  $M_1$  is the saturation level which is determined based on the upper bound of  $d$ .

### Proposed EHGO based Sliding Mode Control

We proposed an observer to estimate  $d_2$  and  $d_3$  and then continuously cancelling the estimated terms in the sliding mode control. The control algorithm of the proposed technique and the closed-loop control of the sliding surface are represented as in Eqs. (8) and (9), respectively.

$$U = g^{-1}(-f_k - f_{\hat{d}} - M_1 \text{sat}\left(\frac{s}{\mu}\right) - \lambda s) \quad (8)$$

$$\dot{s} = -M_1 \text{sat}\left(\frac{s}{\mu}\right) - \lambda s \quad (9)$$

where  $f_{\hat{d}}$  is the estimated disturbance which will be generated by the EHGO in the next subsection. In our proposed method,  $M_1$  can be any value smaller than the value chosen in standard SMC Eq. (6).  $M_1$  does not need to depend on the upper bound of the disturbance and uncertainties because it is cancelled in the control.

### Analysis of Ultimate Bound of $|s|$

The sliding surface trajectory of Eq. (4) is analysed. The performance of the sliding surface outside the boundary layer  $\{|s| \geq \mu\}$  is the same using the proposed method Eq. (8) and using the standard SMC Eq. (6). Both controllers are able to bring the sliding surface to the boundary layer in finite time.

However, inside the boundary layer  $\{|s| \leq \mu\}$ ,  $s\dot{s} \leq -\left(\frac{M_1}{\mu} + \lambda\right)s + s|a|$ ,  $a \gg |d|$ . In the standard SMC, the disturbance  $d$  is dominated. Therefore, the ultimate bound of  $|s|$  will be equal to  $\frac{\alpha}{\mu + \lambda}$ , where the bound will depend on the size of  $\alpha$ . In contrast, the proposed control Eq. (8) results in ultimate bound of  $|s|$  to be equal to  $\frac{M_1}{\mu + \lambda}$ , due to cancellation of the disturbance. Theoretically, the error bound of  $|s|$  is zero for proposed control.

*Design of EHGO and Output Feedback Control*

The EHGOs for the position and rotational dynamics are designed as two different observer (Khalil, 2014):

$$\left. \begin{aligned} \hat{\dot{x}}_1 &= \hat{x}_2 - \left(\frac{v_1}{u_1}\right) \hat{x}_1 + \frac{\alpha_{11}}{\varepsilon} (x_1 - \hat{x}_1) \\ \hat{\dot{x}}_2 &= f_1(x_3) - \left(\frac{v_1}{u_1}\right) \hat{x}_2 + \hat{d}_2 + \frac{\alpha_{12}}{\varepsilon^2} (x_1 - \hat{x}_1) \\ \hat{\dot{d}}_2 &= \frac{\alpha_{13}}{\varepsilon^3} (x_1 - \hat{x}_1) \end{aligned} \right\} \tag{10}$$

$$\left. \begin{aligned} \hat{\dot{x}}_3 &= \hat{x}_4 + \frac{\alpha_{21}}{\varepsilon} (x_3 - \hat{x}_3) \\ \hat{\dot{x}}_4 &= \hat{d}_3 + u + \frac{\alpha_{22}}{\varepsilon^2} (x_3 - \hat{x}_3) \\ \hat{\dot{d}}_3 &= \frac{\alpha_{23}}{\varepsilon^3} (x_3 - \hat{x}_3) \end{aligned} \right\} \tag{11}$$

Eq. (10) is the EHGO for position and Eq. (11) is the EHGO for rotational subsystem,  $\hat{d}_2$  and  $\hat{d}_3$  denote the estimate of disturbance and uncertainties in the translational and rotational link, respectively. The constants  $\alpha_{ji}$  for  $i = 1,2$  and  $j = 1,2,3$  are chosen such that the following polynomials  $s^3 + \alpha_{i1}s^2 + \alpha_{i2}s + \alpha_{i3}$ , for  $i = 1,2$  are Hurwitz and  $\varepsilon$  is a small positive number. Combining Eqs. (8), (10) -(11), the output feedback control is obtained as follows:

$$U = -g^{-1}\{-f_k - f_{\hat{d}} - M_1 sat\left(\frac{\hat{s}}{\mu}\right) - \lambda \hat{s}\} \tag{12}$$

Due to the high-gain term,  $\varepsilon$  in the EHGO, peaking will occur before the transient response. The smaller the  $\varepsilon$ , the higher the peaking (Khalil & Praly, 2014). The peaking destabilizes the control system. Therefore, to protect the system from peaking we saturate the control outside compact set of interest. The saturation function  $sat(\bullet)$  is used. Saturating the expression of  $U$  at  $\pm M_2$  using  $sat(\bullet)$  we arrived at the output feedback controller

$$U = M_2 sat\left(\frac{-g^{-1}\{-f_k - f_{\hat{d}} - M_1 sat\left(\frac{\hat{s}}{\mu}\right) - \lambda \hat{s}\}}{M_2}\right) \tag{13}$$

The saturation value  $M_2$  is determined such that the saturation functions will not be invoked under state feedback.

**Theorem 1:** Consider the closed-loop system formed of the plant Eq. (3), the observer Eqs. (10) -(11) and the controller Eq. (13). Suppose Assumptions 1-2 are satisfied. The initial states of the observer belong to a compact subset of  $R^{n+1}$ , and the initial states of the system belong to a compact set interior of  $\Omega_c$ . Then, there exists  $\bar{\varepsilon} > 0$  such that for  $\varepsilon \in (0, \bar{\varepsilon})$ :

- all trajectories are bounded;
- $\|x(t) - x^*(t)\| \rightarrow 0$  as  $\varepsilon \rightarrow 0$ , uniformly in  $t, t \geq 0$ ;
- $\|x(t)\|$  is uniformly ultimately bounded by  $\delta(\varepsilon)$ , where  $\delta(\varepsilon) \rightarrow 0$  as  $\varepsilon \rightarrow 0$

*Proof of Theorem 1*

A singular perturbation method is used to analyse the EHGO. First, the error between the actual states and estimated states are defined as follows

$$\eta_{1x} = \frac{x_1 - \hat{x}_1}{\varepsilon^2}, \quad \eta_{2x} = \frac{x_2 - \hat{x}_2}{\varepsilon}, \quad \eta_{3x} = d_2 - \hat{d}_2. \tag{14}$$

Differentiating  $\eta_{1x}$ ,  $\eta_{2x}$ ,  $\eta_{3x}$  in Eq. (14) and substituting into Eq. (3), the following matrix is obtained:

$$\varepsilon \dot{\eta}_{ix} = A\eta_{ix} + \varepsilon \Delta_1 \eta_{ix} + \Delta_2 \dot{d}_2, \quad i = 1, 2, 3 \tag{15}$$

where  $A = \begin{bmatrix} -\alpha_1 & 1 & 0 \\ -\alpha_2 & 0 & 1 \\ -\alpha_3 & 0 & 0 \end{bmatrix}$ ,  $\Delta_1 = \begin{bmatrix} -\left(\frac{\dot{u}_1}{u_1}\right) & 0 & 0 \\ 0 & -\left(\frac{\dot{u}_1}{u_1}\right) & 0 \\ 0 & 0 & 0 \end{bmatrix}$ ,  $\Delta_2 = \begin{bmatrix} 0 \\ 0 \\ 1 \end{bmatrix}$ . If  $\frac{\dot{u}_1}{u_1}$  and  $\dot{d}_2$  are bounded,

then after short period of time,  $\dot{\eta}_{ix} = 0(\varepsilon)$ , for  $i = 1, 2, 3$ .

**SIMULATION**

The simulation is done using Matlab SIMULINK. The quadrotor model parameters are:  $m = 2kg, l = 0.2m, g = 9.8m/s^2, I_1 = I_2 = 1.25Ns^2/rad, I_3 = 2.5Ns^2/rad, K_1 = K_2 = K_3 = 0.010Ns/m, K_4 = K_5 = K_6 = 0.012Ns/rad$ . The state feedback controller described by Eq. (6) was implemented using the following parameter values:  $c_1=20, c_2=22, c_3=8, M_1=6, \mu=0.1, \eta=0.1$ .

The proposed output feedback controller which is described by Eq. (13) was implemented using the same parameter values as the state feedback mentioned above. The saturation limits are chosen to be slightly greater than the maximum absolute values of the states, respectively, observed in state feedback control simulations. Meanwhile, the following parameter value were used for EHGO Eq. (10)-(11):  $\alpha_{11} = \alpha_{12} = \alpha_{21} = \alpha_{22} = 3$ , and  $\alpha_{13} = \alpha_{23} = 1$ . The initial states of state feedback and output feedback are  $x_1(0) = 2, x_2(0) = 0, x_3(0) = 0.5$ , and  $x_4(0) = 0$ . The initial conditions set for EHGO are  $\hat{x}_1(0) = 0.1, \hat{x}_2(0) = 0.1, \hat{x}_3(0) = 0, \hat{x}_4(0) = 0, \hat{d}_2(0) = 0$  and  $\hat{d}_3(0) = 0$ .

To investigate the performance of the proposed control with regard to the standard SMC, we simulate the closed-loop system using proposed control Eq.(13) at three cases : EHGO at  $\varepsilon = 0.01, \varepsilon = 0.002$  and  $\varepsilon = 0.001$ . The results are shown in Figure 2 and 3. Although the transient response trajectories as shown in Figures (2a)(2c) and Figures (3a)(3c) are showing large deviation in the overshoot and settling time as compared to the standard SMC, however as  $\varepsilon$  reduces, the overshoot and settling time improves slightly. It is expected that the proposed controller to produce slight deviation in the transient response from the standard SMC. This is because the proposed control is an output feedback form while it is compared to the standard SMC that is in a state feedback form. In the standard SMC Eq. (6), we assumed all states are known and available to be used in the control. However, this assumption is not valid in

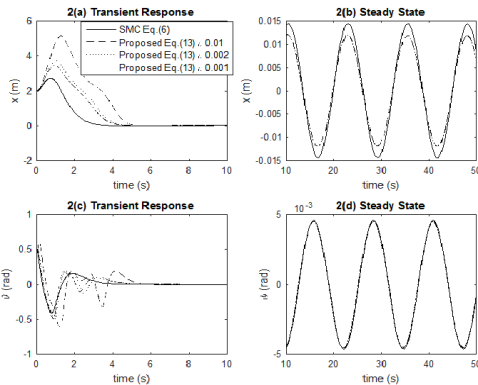


Figure 2. Trajectories of  $x$  and  $\theta$

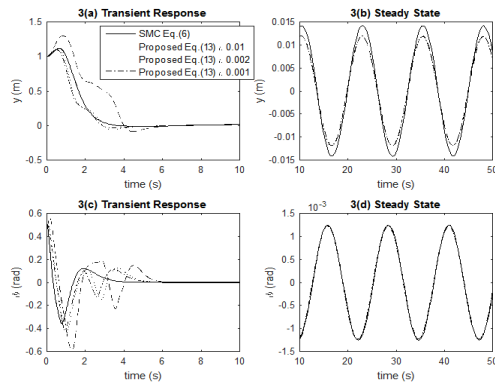


Figure 3. Trajectories of  $y$  and  $\psi$

practical settings due to limitation of sensors. Contrary to that, the proposed method is more practical because it assumes limited sensors are available and uses robust observer to estimate other unknown states.

The efficiency of our proposal is obvious at the steady state as shown in Figure 2(b) and 2(d) and Figure 3(b) and 3(d). The proposed technique and standard SMC able to bring the trajectory of  $x$  and  $y$  to converge to ultimate bound around zero. However, inside the boundary layer the proposed technique able to bring the trajectory to smaller ultimate bound which means closer to the desired position as shown in Figure 2(b) and Figure 3(b). The performance of the proposed method also depends on the gain  $\alpha_1, \alpha_2, \alpha_3$  from the EHGO. As the gains increases as shown in Figure 4, the overshoot and the settling time are getting smaller and the transient response is closely following the standard SMC. The proposed technique can be implemented at smaller control magnitude as presented in Figure 5. The result justifies t using disturbance estimator for the purpose of estimating the disturbance and then cancel it in the control gives smaller ultimate bound in the position trajectory with smaller control effort needed to produce that performance, as compared to dominating the disturbance.

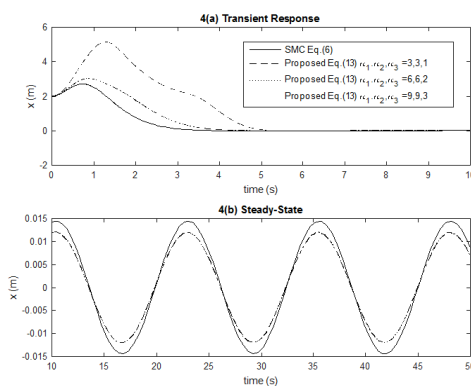


Figure 4.  $x$  trajectories at 0.001 and varying  $\alpha_1, \alpha_2, \alpha_3$

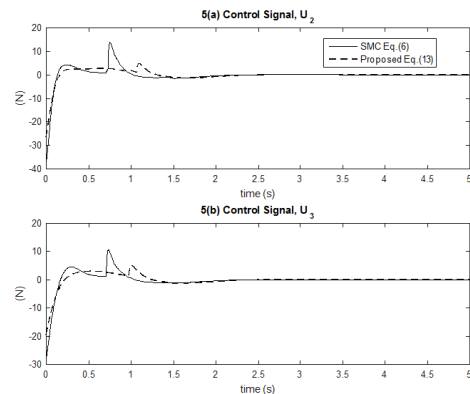


Figure 5. Control signal

## CONCLUSION

We presented a more robust output feedback controller for stabilization of the under-actuated part of the quadrotor system which is continuous and time-varying. An EHGO is used to estimate the unmeasured states and to compensate for the disturbances and uncertainties that appear in the positional and rotational link of the quadrotor. The efficiency of the proposed technique was compared over the standard sliding mode control. Numerical simulation carried out shows that the proposed output feedback control produces the same output response as the state feedback sliding mode control, with the exception of some short overshoot and higher settling time. However, the proposed output feedback is able to improve the steady state error utilizing smaller magnitude of control signal.

## ACKNOWLEDGMENT

The first author gratefully acknowledges Professor Dr. Hassan Khalil from Michigan State University for the learning attachment.

## REFERENCES

- Altug, E., Ostrowski, J. P., & Mahony, R. (2002). Control of a quadrotor helicopter using visual feedback. In *Proceedings of IEEE International Conference on Robotics and Automation*, 1(May) (pp. 72–77). doi:10.1109/ROBOT.2002.1013341
- Benallegue, A., Mokhtari, A., & Fridman, L. (2006). Feedback linearization and high order sliding mode observer for a quadrotor UAV. In *International Workshop on Variable Structure Systems, (VSS'06)* (pp. 365–372). doi:10.1109/VSS.2006.1644545
- Benallegue, A., Mokhtari, A., & L. Fridman. (2008). High-order sliding-mode observer for a quadrotor UAV. *International Journal of Robust and Nonlinear Control*, 18(May 2007), 557–569. doi:10.1002/mc
- Besnard, L., Shtessel, Y. B., & Landrum, B. (2012). Quadrotor vehicle control via sliding mode controller driven by sliding mode disturbance observer. *Journal of the Franklin Institute*, 349(2), 658–684. doi:10.1016/j.jfranklin.2011.06.031
- Bouabdallah, S. (2007). *Design and control of quadrotors with application to autonomous flying*. (Doctoral dissertation). Ecole Polytechnique Federale de Lausanne.
- Bouabdallah, S., & Siegwart, R. (2007). Full control of a quadrotor. *2007 IEEE/RSJ International Conference on Intelligent Robots and Systems, (I)*, 153–158. doi:10.1109/IROS.2007.4399042
- Bouabdallah, S., Noth, A., & Siegwart, R. (2004, September). PID vs LQ control techniques applied to an indoor micro quadrotor. In *Intelligent Robots and Systems, 2004.(IROS 2004)*. In *Proceedings 2004 IEEE/RSJ International Conference on* (Vol. 3, pp. 2451-2456). IEEE.
- Chen, F., Lu, F., Jiang, B., & Tao, G. (2014). Adaptive compensation control of the quadrotor helicopter using quantum information technology and disturbance observer. *Journal of the Franklin Institute*, 351(1), 442–455. doi:10.1016/j.jfranklin.2013.09.009

- Dong, W., Gu, G.-Y., Zhu, X., & Ding, H. (2014). High-performance trajectory tracking control of a quadrotor with disturbance observer. *Sensors and Actuators A: Physical*, *211*, 67–77. doi:10.1016/j.sna.2014.03.011
- Freidovich, L. B., & Khalil, H. K. (2008). Performance recovery of feedback-linearization-based designs. *IEEE Transactions on Automatic Control*, *53*, 2324–2334. doi:10.1109/TAC.2008.2006821
- Hoffmann, G. M., Huang, H., Waslander, S. L., & Tomlin, C. J. (2007). Quadrotor Helicopter Flight Dynamics and Control : Theory and Experiment. *American Institute of Aeronautics and Astronautics*, *4*(August), 1–20. doi:10.2514/6.2007-6461
- Khalil, H. K. (2014). *Nonlinear Control* (1 edition.). Pearson Higher Ed.
- Khalil, H. K., & Praly, L. (2014). High-gain observers in nonlinear feedback control. *International Journal of Robust and Nonlinear Control*, *24*, 991–992. doi:10.1002/rnc.3156
- Mokhtari, M. R., & Cherki, B. (2015). A new robust control for minirotorcraft unmanned aerial vehicles. *ISA Transactions*, *56*, 86–101. doi:10.1016/j.isatra.2014.12.003
- Xu, R., & Özgüner, Ü. (2008). Sliding mode control of a class of underactuated systems. *Automatica*, *44*(1), 233–241. doi:10.1016/j.automatica.2007.05.014

**REFEREES FOR THE PERTANIKA  
JOURNAL OF SCIENCE AND TECHNOLOGY**

**VOL. 25(S) JAN. 2017**  
*Special Edition*

**Contemporary Issues Towards Smart Sustainable Engineering Solution**

The Editorial Board of the Journal of Science and Technology wishes to thank the following:

Ahmad Farid Abidin  
*(UiTM, Malaysia)*

Aida Fazliana Abd Kadir  
*(UTEM, Malaysia)*

Anuar Mikdad Muad  
*(UKM, Malaysia)*

Ashrani Aizzuddin Abd Rahni  
*(UKM, Malaysia)*

Asrulnizam Abd Mana  
*(USM, Malaysia)*

Che Hang Seng  
*(UM, Malaysia)*

Chong Shin Horng  
*(UTEM, Malaysia)*

Chong Yu Zheng  
*(UTAR, Malaysia)*

Fairul Azhar Abdul Shukor  
*(UTEM, Malaysia)*

Gan Kok Beng  
*(UKM, Malaysia)*

Hafiz Rashidi Harun@ Ramli  
*(UPM, Malaysia)*

Hamza Rouabah  
*(Algeria, South Africa)*

Haslina Md Sarkan  
*(UTM, Malaysia)*

Hazlina Selamat  
*(UTM, Malaysia)*

Hiroaki Yamada  
*(Yamaguchi University, Japan)*

Ibrahim Ahmad  
*(UNITEN, Malaysia)*

Ibrahim Faye  
*(Universiti Teknologi Petronas, Malaysia)*

Intan Helina Hasan  
*(UPM, Malaysia)*

Jasronita Jasni  
*(UPM, Malaysia)*

M.M. Aliyu  
*(UKM, Malaysia)*

Mario Alberto Garcia Ramirez  
*(UANL, Mexico)*

Md Arafatur Rahman  
*(UMP, Malaysia)*

Miszaina Osman  
*(UNITEN, Malaysia)*

Mohamed Edardar  
*(Tripoli, Libya)*

Mohd Amrallah Mustafa  
*(UPM, Malaysia)*

Mohd Faisal Ibrahim  
*(UKM, Malaysia)*

Mohd Nabil  
*(UTM, Malaysia)*

Mohd Nizar Hamidon  
*(UPM, Malaysia)*

Mohd Razal Mohamad Sapiee  
*(UTEM, Malaysia)*

Mohd Tafir Mustaffa  
*(USM, Malaysia)*

N. Rugthaicharoencheep  
*(IEEE, Malaysia)*

Norhayati Soin  
*(UM, Malaysia)*

Norzanah Rosmin  
*(UTM, Malaysia)*

Raja Nor Firdaus Kashfi Raja Othman  
*(UTEM, Malaysia)*

Ramizi Mohamed  
*(UKM, Malaysia)*

Rosmina Jaafar  
*(UKM, Malaysia)*

Rosmiwati Mohd Mokhtar  
(USM, Malaysia)

Rozita Jailani  
(IEEE, Malaysia)

Ruhaida Abdul Rashid  
(UNIKL, Malaysia)

Sawal Hamid Md Ali  
(UKM, Malaysia)

Siti Fauziah Toha  
(IIUM, Malaysia)

Siti NoorJannah  
(IIUM, Malaysia)

Suresh Thanakodi  
(UPNM, Malaysia)

Suriati Paiman  
(UPM, Malaysia)

Suryanti Awang  
(UMP, Malaysia)

Taha Hussein Alaaldeen Rassem  
(UMP, Malaysia)

Tan Tong Boon  
(Universiti Teknologi Petronas, Malaysia)

Zuhaila Mat Yasin  
(UiTM, Malaysia)

Zulkifli Ibrahim  
(UTEM, Malaysia)

---

IEEE - Institute of Electrical and Electronics Engineers  
IIUM - International Islamic University Malaysia  
UANL - Autonomous University of Nueno Leon, Mexico  
UITM - Universiti Teknologi Mara  
UKM - Universiti Kebangsaan Malaysia  
UMP - Universiti Malaysia Pahang  
UPM - Universiti Putra Malaysia  
UNITEN - Universiti Tenaga Nasional  
UNIKL - Universiti Kuala Lumpur  
UPNM - Universiti Pertahanan Nasional Malaysia  
USIM - Universiti Sains Islam Malaysia  
UTAR - Universiti Tunku Abdul Rahman  
UTEM - Universiti Teknikal Malaysia

---

While every effort has been made to include a complete list of referees for the period stated above, however if any name(s) have been omitted unintentionally or spelt incorrectly, please notify the Chief Executive Editor, *Pertanika* Journals at [nayan@upm.my](mailto:nayan@upm.my).

Any inclusion or exclusion of name(s) on this page does not commit the *Pertanika* Editorial Office, nor the UPM Press or the University to provide any liability for whatsoever reason.



## *Pertanika Journals*

*Our goal is to bring high quality research to the widest possible audience*

### **INSTRUCTIONS TO AUTHORS** (Manuscript Preparation & Submission Guide)

Revised: June 2016

Please read the Pertanika guidelines and follow these instructions carefully. Manuscripts not adhering to the instructions will be returned for revision without review. The Chief Executive Editor reserves the right to return manuscripts that are not prepared in accordance with these guidelines.

## **MANUSCRIPT PREPARATION**

### **Manuscript Types**

*Pertanika* accepts submission of mainly **four** types of manuscripts for peer-review.

#### **1. REGULAR ARTICLE**

Regular articles are full-length original empirical investigations, consisting of introduction, materials and methods, results and discussion, conclusions. Original work must provide references and an explanation on research findings that contain new and significant findings.

*Size:* Generally, these are expected to be between 6 and 12 journal pages (excluding the abstract, references, tables and/or figures), a maximum of 80 references, and an abstract of 100–200 words.

#### **2. REVIEW ARTICLE**

These report critical evaluation of materials about current research that has already been published by organizing, integrating, and evaluating previously published materials. It summarizes the status of knowledge and outline future directions of research within the journal scope. Review articles should aim to provide systemic overviews, evaluations and interpretations of research in a given field. Re-analyses as meta-analysis and systemic reviews are encouraged. The manuscript title must start with "Review Article:".

*Size:* These articles do not have an expected page limit or maximum number of references, should include appropriate figures and/or tables, and an abstract of 100–200 words. Ideally, a review article should be of 7 to 8 printed pages.

#### **3. SHORT COMMUNICATIONS**

They are timely, peer-reviewed and brief. These are suitable for the publication of significant technical advances and may be used to:

- (a) report new developments, significant advances and novel aspects of experimental and theoretical methods and techniques which are relevant for scientific investigations within the journal scope;
- (b) report/discuss on significant matters of policy and perspective related to the science of the journal, including 'personal' commentary;
- (c) disseminate information and data on topical events of significant scientific and/or social interest within the scope of the journal.

The manuscript title must start with "*Brief Communication:*".

*Size:* These are usually between 2 and 4 journal pages and have a maximum of three figures and/or tables, from 8 to 20 references, and an abstract length not exceeding 100 words. Information must be in short but complete form and it is not intended to publish preliminary results or to be a reduced version of Regular or Rapid Papers.

#### 4. OTHERS

Brief reports, case studies, comments, concept papers, Letters to the Editor, and replies on previously published articles may be considered.

**PLEASE NOTE: NO EXCEPTIONS WILL BE MADE FOR PAGE LENGTH.**

#### Language Accuracy

Pertanika **emphasizes** on the linguistic accuracy of every manuscript published. Articles must be in **English** and they must be competently written and argued in clear and concise grammatical English. Contributors are strongly advised to have the manuscript checked by a colleague with ample experience in writing English manuscripts or a competent English language editor.

Author(s) **must provide a certificate** confirming that their manuscripts have been adequately edited. A proof from a recognised editing service should be submitted together with the cover letter at the time of submitting a manuscript to Pertanika. **All editing costs must be borne by the author(s)**. This step, taken by authors before submission, will greatly facilitate reviewing, and thus publication if the content is acceptable.

Linguistically hopeless manuscripts will be rejected straightaway (e.g., when the language is so poor that one cannot be sure of what the authors really mean). This process, taken by authors before submission, will greatly facilitate reviewing, and thus publication if the content is acceptable.

#### MANUSCRIPT FORMAT

The paper should be submitted in one column format with at least 4cm margins and 1.5 line spacing throughout. Authors are advised to use Times New Roman 12-point font and *MS Word* format.

##### 1. Manuscript Structure

Manuscripts in general should be organised in the following order:

##### Page 1: Running title

This page should **only** contain the running title of your paper. The running title is an abbreviated title used as the running head on every page of the manuscript. The running title should not exceed 60 characters, counting letters and spaces.

##### Page 2: Author(s) and Corresponding author information.

This page should contain the **full title** of your paper not exceeding 25 words, with name(s) of all the authors, institutions and corresponding author's name, institution and full address (Street address, telephone number (including extension), hand phone number, and e-mail address) for editorial correspondence. First and corresponding authors must be clearly indicated.

The names of the authors may be abbreviated following the international naming convention. e.g. Salleh, A.B.<sup>1</sup>, Tan, S.G<sup>2\*</sup>., and Sapuan, S.M<sup>3</sup>.

**Authors' addresses.** Multiple authors with different addresses must indicate their respective addresses separately by superscript numbers:

George Swan<sup>1</sup> and Nayan Kanwal<sup>2</sup>

<sup>1</sup>Department of Biology, Faculty of Science, Duke University, Durham, North Carolina, USA.,

<sup>2</sup>Office of the Deputy Vice Chancellor (R&I), Universiti Putra Malaysia, Serdang, Malaysia.

A **list** of number of **black and white / colour figures and tables** should also be indicated on this page. Figures submitted in color will be printed in colour. See "5. Figures & Photographs" for details.

##### Page 3: Abstract

This page should **repeat** the **full title** of your paper with only the **Abstract** (the abstract should be less than 250 words for a Regular Paper and up to 100 words for a Short Communication), and **Keywords**.

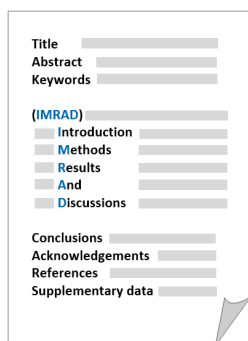
**Keywords:** Not more than eight keywords in alphabetical order must be provided to describe the contents of the manuscript.

#### Page 4: Introduction

This page should begin with the **Introduction** of your article and followed by the rest of your paper.

#### 2. Text

Regular Papers should be prepared with the headings *Introduction, Materials and Methods, Results and Discussion, Conclusions, Acknowledgements, References, and Supplementary data* (if available) in this order.



Title \_\_\_\_\_  
 Abstract \_\_\_\_\_  
 Keywords \_\_\_\_\_  
 (IMRAD)  
 Introduction \_\_\_\_\_  
 Methods \_\_\_\_\_  
 Results \_\_\_\_\_  
 And \_\_\_\_\_  
 Discussions \_\_\_\_\_  
 Conclusions \_\_\_\_\_  
 Acknowledgements \_\_\_\_\_  
 References \_\_\_\_\_  
 Supplementary data \_\_\_\_\_

#### MAKE YOUR ARTICLES AS CONCISE AS POSSIBLE

Most scientific papers are prepared according to a format called IMRAD. The term represents the first letters of the words Introduction, Materials and Methods, Results, And, Discussion. It indicates a pattern or format rather than a complete list of headings or components of research papers; the missing parts of a paper are: Title, Authors, Keywords, Abstract, Conclusions, and References. Additionally, some papers include Acknowledgments and Appendices.

The Introduction explains the scope and objective of the study in the light of current knowledge on the subject; the Materials and Methods describes how the study was conducted; the Results section reports what was found in the study; and the Discussion section explains meaning and significance of the results and provides suggestions for future directions of research. The manuscript must be prepared according to the Journal's instructions to authors.

#### 3. Equations and Formulae

These must be set up clearly and should be typed double spaced. Numbers identifying equations should be in square brackets and placed on the right margin of the text.

#### 4. Tables

All tables should be prepared in a form consistent with recent issues of Pertanika and should be numbered consecutively with Roman numerals. Explanatory material should be given in the table legends and footnotes. Each table should be prepared on a new page, embedded in the manuscript.

*When a manuscript is submitted for publication, tables must also be submitted separately as data - .doc, .rtf, Excel or PowerPoint files- because tables submitted as image data cannot be edited for publication and are usually in low-resolution.*

#### 5. Figures & Photographs

Submit an **original** figure or photograph. Line drawings must be clear, with high black and white contrast. Each figure or photograph should be prepared on a new page, embedded in the manuscript for reviewing to keep the file of the manuscript under 5 MB. These should be numbered consecutively with Roman numerals.

Figures or photographs must also be submitted separately as TIFF, JPEG, or Excel files- because figures or photographs submitted in low-resolution embedded in the manuscript cannot be accepted for publication. For electronic figures, create your figures using applications that are capable of preparing high resolution TIFF files. In general, we require **300 dpi** or higher resolution for **coloured and half-tone artwork**, and **1200 dpi or higher** for **line drawings** are required.

Failure to comply with these specifications will require new figures and delay in publication.

**NOTE:** Illustrations may be produced in colour at no extra cost at the discretion of the Publisher; the author could be charged Malaysian Ringgit 50 for each colour page.

#### 6. References

References begin on their own page and are listed in alphabetical order by the first author's last name. Only references cited within the text should be included. All references should be in 12-point font and double-spaced.

**NOTE:** When formatting your references, please follow the **APA reference style** (6th Edition). Ensure that the references are strictly in the journal's prescribed style, failing which your article will **not be accepted for peer-review**. You may refer to the *Publication Manual of the American Psychological Association* for further details (<http://www.apastyle.org/>).

## 7. General Guidelines

**Abbreviations:** Define alphabetically, other than abbreviations that can be used without definition. Words or phrases that are abbreviated in the introduction and following text should be written out in full the first time that they appear in the text, with each abbreviated form in parenthesis. Include the common name or scientific name, or both, of animal and plant materials.

**Acknowledgements:** Individuals and entities that have provided essential support such as research grants and fellowships and other sources of funding should be acknowledged. Contributions that do not involve researching (clerical assistance or personal acknowledgements) should **not** appear in acknowledgements.

**Authors' Affiliation:** The primary affiliation for each author should be the institution where the majority of their work was done. If an author has subsequently moved to another institution, the current address may also be stated in the footer.

**Co-Authors:** The commonly accepted guideline for authorship is that one must have substantially contributed to the development of the paper and share accountability for the results. Researchers should decide who will be an author and what order they will be listed depending upon their order of importance to the study. Other contributions should be cited in the manuscript's Acknowledgements.

**Copyright Permissions:** Authors should seek necessary permissions for quotations, artwork, boxes or tables taken from other publications or from other freely available sources on the Internet before submission to Pertanika. Acknowledgement must be given to the original source in the illustration legend, in a table footnote, or at the end of the quotation.

**Footnotes:** Current addresses of authors if different from heading may be inserted here.

**Page Numbering:** Every page of the manuscript, including the title page, references, tables, etc. should be numbered.

**Spelling:** The journal uses American or British spelling and authors may follow the latest edition of the Oxford Advanced Learner's Dictionary for British spellings.

## SUBMISSION OF MANUSCRIPTS

Owing to the volume of manuscripts we receive, we must insist that all submissions be made electronically using the **online submission system ScholarOne™**, a web-based portal by Thomson Reuters. For more information, go to our web page and [click "Online Submission"](#).

### Submission Checklist

1. **MANUSCRIPT:** Ensure your MS has followed the Pertanika style particularly the first four pages as explained earlier. The article should be written in a good academic style and provide an accurate and succinct description of the contents ensuring that grammar and spelling errors have been corrected before submission. It should also not exceed the suggested length.

**COVER LETTER:** All submissions must be accompanied by a cover letter detailing what you are submitting. Papers are accepted for publication in the journal on the understanding that the article is **original** and the content has **not been published** either **in English** or **any other language(s)** or **submitted for publication elsewhere**. The letter should also briefly describe the research you are reporting, why it is important, and why you think the readers of the journal would be interested in it. The cover letter must also contain an acknowledgement that all authors have contributed significantly, and that all authors have approved the paper for release and are in agreement with its content.

The cover letter of the paper should contain (i) the title; (ii) the full names of the authors; (iii) the addresses of the institutions at which the work was carried out together with (iv) the full postal and email address, plus telephone numbers and emails of all the authors. The current address of any author, if different from that where the work was carried out, should be supplied in a footnote.

The above must be stated in the cover letter. Submission of your manuscript will not be accepted until a cover letter has been received

2. **COPYRIGHT:** Authors publishing the Journal will be asked to sign a copyright form. In signing the form, it is assumed that authors have obtained permission to use any copyrighted or previously published material. All authors must read and agree to the conditions outlined in the form, and must sign the form or agree that the corresponding author can sign on their behalf. Articles cannot be published until a signed form (*original pen-to-paper signature*) has been received.

Please do **not** submit manuscripts to the editor-in-chief or to any other office directly. Any queries must be directed to the **Chief Executive Editor's** office via email to [nayan@upm.my](mailto:nayan@upm.my).

Visit our Journal's website for more details at <http://www.pertanika.upm.edu.my/home.php>.

### **HARDCOPIES OF THE JOURNALS AND OFF PRINTS**

Under the Journal's open access initiative, authors can choose to download free material (via PDF link) from any of the journal issues from Pertanika's website. Under "**Browse Journals**" you will see a link, "*Current Issues*" or "*Archives*". Here you will get access to all current and back-issues from 1978 onwards.

The **corresponding author** for all articles will receive one complimentary hardcopy of the journal in which his/her articles is published. In addition, 20 off prints of the full text of their article will also be provided. Additional copies of the journals may be purchased by writing to the Chief Executive Editor.



## Why should you publish in

# Pertanika?

### BENEFITS TO AUTHORS

**PROFILE:** Our journals are circulated in large numbers all over Malaysia, and beyond in Southeast Asia. Our circulation covers other overseas countries as well. We ensure that your work reaches the widest possible audience in print and online, through our wide publicity campaigns held frequently, and through our constantly developing electronic initiatives such as Web of Science Author Connect backed by Thomson Reuters.

**QUALITY:** Our journals' reputation for quality is unsurpassed ensuring that the originality, authority and accuracy of your work are fully recognised. Each manuscript submitted to Pertanika undergoes a rigid originality check. Our double-blind peer refereeing procedures are fair and open, and we aim to help authors develop and improve their scientific work. Pertanika is now over 38 years old; this accumulated knowledge has resulted in our journals being indexed in SCOPUS (Elsevier), Thomson (ISI) Web of Science™ Core Collection, Emerging Sources Citation Index (ESCI), Web of Knowledge [BIOSIS & CAB Abstracts], EBSCO, DOAJ, ERA, AGRICOLA, Google Scholar, ISC, TIB, Journal Guide, Citefactor, Cabell's Directories and MyCite.

**AUTHOR SERVICES:** We provide a rapid response service to all our authors, with dedicated support staff for each journal, and a point of contact throughout the refereeing and production processes. Our aim is to ensure that the production process is as smooth as possible, is borne out by the high number of authors who prefer to publish with us.

**CODE OF ETHICS:** Our Journal has adopted a Code of Ethics to ensure that its commitment to integrity is recognized and adhered to by contributors, editors and reviewers. It warns against plagiarism and self-plagiarism, and provides guidelines on authorship, copyright and submission, among others.

**PRESS RELEASES:** Landmark academic papers that are published in Pertanika journals are converted into press-releases as a unique strategy for increasing visibility of the journal as well as to make major findings accessible to non-specialist readers. These press releases are then featured in the university's UK and Australian based research portal, ResearchSEA, for the perusal of journalists all over the world.

**LAG TIME:** The elapsed time from submission to publication for the articles averages 3 to 4 months. A decision on acceptance of a manuscript is reached in 3 to 4 months (average 14 weeks).



Address your submissions to:  
The Chief Executive Editor  
Tel: +603 8947 1622  
[nayan@upm.my](mailto:nayan@upm.my)

Journal's Profile: [www.pertanika.upm.edu.my/](http://www.pertanika.upm.edu.my/)

## Call for Papers 2017-18

now accepting submissions...

*Pertanika* invites you to explore frontiers from all key areas of agriculture, science and technology to social sciences and humanities.

Original research and review articles are invited from scholars, scientists, professors, post-docs, and university students who are seeking publishing opportunities for their research papers through the Journal's three titles; JTAS, JST & JSSH. Preference is given to the work on leading and innovative research approaches.

*Pertanika* is a fast track peer-reviewed and open-access academic journal published by Universiti Putra Malaysia. To date, Pertanika Journals have been indexed by many important databases. Authors may contribute their scientific work by publishing in UPM's hallmark SCOPUS & ISI indexed journals.

Our journals are open access - international journals. Researchers worldwide will have full access to all the articles published online and be able to download them with zero subscription fee.

*Pertanika* uses online article submission, review and tracking system for quality and quick review processing backed by Thomson Reuter's ScholarOne™. Journals provide rapid publication of research articles through this system.

For details on the Guide to Online Submissions, please visit [http://www.pertanika.upm.edu.my/guide\\_online\\_submission.php](http://www.pertanika.upm.edu.my/guide_online_submission.php)

## About the Journal

*Pertanika* is an international multidisciplinary peer-reviewed leading journal in Malaysia which began publication in 1978. The journal publishes in three different areas — Journal of Tropical Agricultural Science (JTAS); Journal of Science and Technology (JST); and Journal of Social Sciences and Humanities (JSSH). All journals are published in English.

**JTAS** is devoted to the publication of original papers that serves as a forum for practical approaches to improving quality in issues pertaining to tropical agricultural research- or related fields of study. It is published four times a year in *February, May, August* and *November*.

**JST** caters for science and engineering research- or related fields of study. It is published twice a year in *January* and *July*.

**JSSH** deals in research or theories in social sciences and humanities research. It aims to develop as a flagship journal with a focus on emerging issues pertaining to the social and behavioural sciences as well as the humanities, particularly in the Asia Pacific region. It is published four times a year in *March, June, September* and *December*.



An Award-winning  
International-Malaysian Journal  
— CREAM AWARD, MoHE  
—Sept 2015





Evaluation of Inverter Reliability Performance Due to Negative Bias Temperature Instability (NBTI) Effects in Advance CMOS Technology Nodes <i>M. F. Zainudin, H. Hussin and A. K. Halim</i>	295
Compound Learning Control for Formation Management of Multiple Autonomous Agents <i>Syafiq Fauzi Kamarulzaman and Hayyan Al Sibai</i>	305
Binary Classification Using SVM for Sick and Healthy Chicken Based on Chicken's Excrement Image <i>Nurhanna Abdul Aziz and Mohd Fauzi Bin Othman</i>	315
A Single DC Source 41-level 115V, 400Hz Cascaded Multilevel Inverter <i>Ahmad, Syukri Mohamad and Norman, Mariun</i>	325
Dielectrophoresis and AC Electroosmosis Force on Fluid Motion in Microfluidic using Latex Particles <i>Nurul Amziah Md Yunus, Mohd Nazim Mohtar, Khaldon Mohammed Almadhagi and Izhal Abdul Halin</i>	333
Application of Sliding Mode Control with Extended High Gain Observer to Stabilize the Underactuated Quadrotor System <i>Elya M. N, S. B. Mohd Noor, Ribhan Zafira A. R. and Syaril Azrad</i>	343

Double Series Resonant DC-DC Converter with Uniform Voltage Stress on High Voltage Transformers <i>Nor Azura, Samsudin, Soib, Taib and Shahid, Iqbal</i>	187
PCA based Feature Extraction for Classification of Stator-Winding Faults in Induction Motors <i>Thanaporn Likitjarernkul, Kiattisak Sengchuai, Rakkrit Duangsoithong, Kusumal Chalermyanont and Anuwat Prasertsit</i>	197
Effect of Boron and Oxygen Doping to Graphene Band Structure <i>Siti Fazlina bt Fauzi and Syarifah Norfaezah bt Sabki</i>	205
Seasonal Variation of Transmission Line Outages in Peninsular Malaysia <i>I. Mohamed Rawi, M.Z.A. Ab-Kadir and M. Izadi</i>	213
FDTD Computational Simulation for SAR Observation towards Breast Hyperthermia Cancer Procedure <i>Kasumawati Lias and Norlida Buniyamin</i>	221
Application of Evolutionary Programming for the Placement of TCSC and UPFC for Minimisation of Transmission Losses and Improvement of Voltage Profile <i>Nur Ashida Salim, Nabila Ismail, Muhammad Murtadha Othman</i>	231
Method of Determining Load Priority using Fuzzy Logic for Adaptive Under Frequency Load Shedding Technique <i>A. I. M. Isa, H. Mohamad, K. Naidu, N. Y. Dahlan and I. Musirin</i>	239
Synchronous Reference Frame Fundamental Method in Shunt Active Power Filter for Mitigation of Current Harmonics <i>S. Musa and M. A. M. Radzi</i>	249
A Study of Negative Bias Temperature Instability (NBTI) in p-MOSFET Devices <i>H. Hussin and M. F. Zainudin</i>	257
Planar Sensors Array for Water Contaminants Detections <i>Aizat Azmi, Sallehuddin Ibrahim, Ahmad Amsyar Azman, and Mohd Amri Md Yunus</i>	267
Optimising PID Controller using Slope Variation Method for Positioning Radio Telescope <i>N. Mohamad Zaber, A. J. Ishak, A. Che Soh, M. K. Hasan and A. N. Ishak</i>	275
Enhanced Time of Use Electricity Pricing for Commercial Customers in Malaysia <i>Nur Azrina Mohd Azman, Md Pauzi Abdullah, Mohammad Yusri Hassan, Dalila Mat Said and Faridah Hussin</i>	285

Control of Wastewater Treatment by using the Integration MATLAB and LabVIEW <i>Ilanur Muhaini Mohd Noor and Muhamad Kamal M. A.</i>	77
LLC Resonant Converter with Series-Connected Primary Windings of Transformer for PEV Battery Charging <i>Shahid Iqbal, M. Imran Shahzad and Soib Taib</i>	85
Partial Measurement of Planar Surface Ion Balance Analysis <i>Sayan Plong-ngooluam, Nattha Jindapetch, Phairote Wounchoum and Duangporn Sompongse</i>	95
Reliably Optimal PMU Placement using Disparity Evolution-based Genetic Algorithm <i>Yoshiaki Matsukawa, Mohammad Lutfi Othman, Masayuki Watanabe and Yasunori Mitani</i>	103
Statistical Optimisation of Process Parameters on the Efficiency of N-TiO <sub>2</sub> Dye Sensitised Solar Cell Using Response Surface Methodology (RSM) <i>Buda Samaila, Suhaidi Shafie, Suraya Abdul Rashid, Haslina Jafaar and Ali Khalifa</i>	111
Classification of Aromatic Herbs using Artificial Intelligent Technique <i>A. Che Soh, U. K. Mohamad Yusof, N. F. M. Radzi, A. J. Ishak and M. K. Hassan</i>	119
A Corrective Action Scheme for Contingency Monitoring of Transmission Line Overloading <i>Mohammad Lutfi Othman, Mahmood Khalid Hadi and Noor Izzri Abdul Wahab</i>	129
Electrical Characteristics of Rubber Wood Ash Filled Natural Rubber at High Frequency <i>Salakjit Nilborworn, Krerkchai Thongnoo and Pornchai Phukpattaranont</i>	139
Unbalanced Self-Sensing Actuation Circuit Effects on Vibration Control in Piezoelectric Systems <i>Kiattisak Sengchuai, Boworn Panyavoravaj and Nattha Jindapetch</i>	149
Parametric Tracking Across Multiple Cameras <i>Patrick Sebastian, Yap Vooi Voon and Richard Comley</i>	159
Optimal Location and Size of Distributed Generation to Reduce Power Losses based on Differential Evolution Technique <i>Noor Izzri Abdul Wahab, Ahmed Sahib Hammadi and Mohammad Lutfi Othman</i>	169
Simulation of Interleaved Current Fed Full Bridge Converter for Fuel Cell Electrical Vehicle <i>Koay Boon Kit, Nasrudin Abd Rahim and Siti Rohani Sheikh Raihan</i>	179

**Contents**

**Contemporary Issues Towards Smart Sustainable Engineering Solution**

- Impact of Different Lifting Height and Load Mass on Muscle Performance using Periodogram 1  
*Shair, E. F., Ahmad, S. A., Abdullah, A. R., Marhaban, M. H. and Mohd Tamrin, S. B.*
- A single-stage LED driver with voltage doubler rectifier 9  
*Nurul Asikin, Zawawi, Shahid Iqbal and Mohamad Kamarol, Mohd Jamil*
- An Integrated System Wide Reactive Power Management Strategy for Transmission and Distribution System based on Techno Economic Analysis 19  
*Jun Huat Tang, Mau TengAu, Asnawi bin Mohd Busrah, Mohd Hafiz bin Mat Daud, Lau Chee Chong, Khairuddin bin Abdullah*
- Opportunity for Using WLAN with IEC 61850 and the Future of this Protocol 25  
*N. H. Ali, Borhanuddin. M. Ali, O. Basir, M. L. Othman, F. Hashim and E. Aker*
- Enhancement of DNA Microarray Images using Mathematical Morphological Image Processing 39  
*Asral Bahari Jambek, Khairul Anuar Mat Said and Nasri Sulaiman*
- Memory Polynomial with Binomial Reduction in Digital Pre-distortion for Wireless Communication Systems 49  
*Hong Ning Choo, Nurul Adilah Abdul Latiff, Pooria Varahram and Borhanuddin Mohd Ali*
- Performance Comparison of Image Normalisation Method for DNA Microarray Data 59  
*Omar Salem Baans, Asral Bahari Jambek, Uda Hashim and Nor Azah Yusof*
- Real-time Human Motion Analysis and Grasping Force using the OptiTrack System and Flexi-force Sensor 69  
*N. F. Elya Saidon, Chikamune Wada, Siti A. Ahmad, Ribhan Zafira Abdul Rahman, Kiyotaka Eguchi, Yoshiyuki Tomiyama and Farida Izni Abd Rahman*



**Pertanika Editorial Office, Journal Division**  
Office of the Deputy Vice Chancellor (R&I),  
1st Floor, IDEA Tower II,  
UPM-MTDC Technology Centre  
Universiti Putra Malaysia  
43400 UPM Serdang  
Selangor Darul Ehsan  
Malaysia

<http://www.pertanika.upm.edu.my/>  
E-mail: [executive\\_editor.pertanika@upm.my](mailto:executive_editor.pertanika@upm.my)  
Tel: +603 8947 1622

**PENERBIT**  
**UPM**  
UNIVERSITI PUTRA MALAYSIA  
**PRESS**

<http://penerbit.upm.edu.my>  
E-mail : [penerbit@putra.upm.edu.my](mailto:penerbit@putra.upm.edu.my)  
Tel : +603 8946 8855/8854  
Fax : +603 8941 6172

